NATIONAL TECHNICAL UNIVERSITY OF ATHENS

DOCTORAL THESIS

Manufacturing of Advanced Materials:

Simulation of High Precision Ring Rolling via Finite Element Analysis

---

Author:
Ioannis PRESSAS

Supervisor:
Dimitrios MANOLAKOS
Professor Emeritus

A thesis submitted in fulfillment of the requirements for the degree of:

Doctor of Philosophy

in the

School of Mechanical Engineering
Department of Manufacturing Technology

ΕΘΝΙΚΟ ΜΕΤΣΟΒΙΟ ΠΟΛΥΤΕΧΝΕΙΟ

ΔΙΔΑΚΤΟΡΙΚΗ ΔΙΑΤΡΙΒΗ

Διαμορφωσιμότητα Προηγμένων Υλικών:

Προσομοίωση Έλασης Δακτυλίων Υψηλής Ακρίβειας με Ανάλυση Πεπερασμένων Στοιχείων

Συγγραφέας:

Ιωάννης ΠΡΕΣΣΑΣ

Επιβλέπων:

Δημήτριος ΜΑΝΩΛΑΚΟΣ
Ομότιμος Καθηγητής

Μια διατριβή που υποβλήθηκε στα πλαίσια της εκπλήρωση των απαιτήσεων για την απονομή του τίτλου του:

Διδάκτορος Φιλοσοφίας

στον

Τομέα Τεχνολογίας των Κατεργασιών

της

Σχολής Μηχανολόγων Μηχανικών

NATIONAL TECHNICAL UNIVERSITY OF ATHENS
SCHOOL OF MECHANICAL ENGINEERING
DEPARTMENT OF MANUFACTURING TECHNOLOGY

Manufacturing of Advanced Materials:

Simulation of High Precision Ring Rolling via Finite Element Analysis

DOCTORAL THESIS

OF

IOANNIS PRESSAS

Advisory Committee:
Dimitrios E. MANOLAKOS, Professor Emeritus *(Supervisor)*
Georgios - Christoforos VOSNIAKOS, Professor
Aggelos P. MARKOPOULOS, Associate Professor

Approved by the seven-member examination committee at . . . / . . . / . . . .

(Signature)	(Signature)	(Signature)
. . . .	. . . .	. . . .
Dimitrios E. MANOLAKOS Professor Emeritus NTUA	Georgios - Christoforos VOSNIAKOS Professor NTUA	Aggelos P. MARKOPOULOS Associate Professor NTUA

(Signature)	(Signature)	(Signature)	(Signature)
. . . .	. . . .	. . . .	. . . .
Christoforos PROVATIDIS Professor NTUA	Panorios BENARDOS Associate Professor NTUA	Efstathios THEOTOKOGLOU Professor Emeritus NTUA	Spyridon PAPAEFTHYMIOU Professor NTUA

ΕΘΝΙΚΟ ΜΕΤΣΟΒΙΟ ΠΟΛΥΤΕΧΝΕΙΟ
ΣΧΟΛΗ ΜΗΧΑΝΟΛΟΓΩΝ ΜΗΧΑΝΙΚΩΝ
ΤΟΜΕΑΣ ΤΕΧΝΟΛΟΓΙΑΣ ΤΩΝ ΚΑΤΕΡΓΑΣΙΩΝ

Διαμορφωσιμότητα Προηγμένων Υλικών:

Προσομοίωση Έλασης Δακτυλίων Υψηλής Ακρίβειας με Ανάλυση Πεπερασμένων Στοιχείων

ΔΙΔΑΚΤΟΡΙΚΗ ΔΙΑΤΡΙΒΗ

ΤΟΥ

Ιωάννη ΠΡΕΣΣΑ

Συμβουλευτική Επιτροπή: Δημήτριος Ε. ΜΑΝΩΛΑΚΟΣ, Ομότιμος Καθηγητής *(Επιβλέπων)*
Γεώργιος - Χριστόφορος ΒΟΣΝΙΑΚΟΣ, Καθηγητής
Άγγελος Π. ΜΑΡΚΟΠΟΥΛΟΣ, Αναπληρωτής Καθηγητής

Εγκρίθηκε από την επταμελή εξεταστική επιτροπή στις . . . /. . . /. . . . . . .

(Υπογραφή)	(Υπογραφή)	(Υπογραφή)
. . . .	. . . .	. . . .
Δημήτριος Ε. ΜΑΝΩΛΑΚΟΣ Ομότιμος Καθηγητής Ε.Μ.Π.	Γεώργιος – Χριστόφορος ΒΟΣΝΙΑΚΟΣ Καθηγητής Ε.Μ.Π.	Άγγελος Π. ΜΑΡΚΟΠΟΥΛΟΣ Αναπληρωτής Καθηγητής Ε.Μ.Π.

(Υπογραφή)	(Υπογραφή)	(Υπογραφή)	(Υπογραφή)
. . . .	. . . .	. . . .	. . . .
Χριστόφορος ΠΡΟΒΑΤΙΔΗΣ Καθηγητής Ε.Μ.Π.	Πανώριος ΜΠΕΝΑΡΔΟΣ Αναπληρωτής Καθηγητής Ε.Μ.Π.	Ευστάθιος ΘΕΟΤΟΚΟΓΛΟΥ Ομότιμος Καθηγητής Ε.Μ.Π.	Σπυρίδων ΠΑΠΑΕΥΘΥΜΙΟΥ Καθηγητής Ε.Μ.Π.

Declaration of Authorship

I, Ioannis PRESSAS, declare that this thesis titled, “Manufacturing of Advanced Materials:, *Simulation of High Precision Ring Rolling via Finite Element Analysis*” (“*Διαμορφωσιμότητα προηγμένων υλικών*: *Προσομοίωση Έλασης Δακτυλίων Υψηλής Ακριβείας με Ανάλυση Πεπερασμένων Στοιχείων*”) and the work presented in it are my own. I confirm that:

- This work was done wholly or mainly while in candidature for a research degree at the National Technical University of Athens.
- Where any part of this thesis has previously been submitted for a degree or any other qualification at this University or any other institution, this has been clearly stated.
- Where I have consulted the published work of others, this is always clearly attributed.
- Where I have quoted from the work of others, the source is always given. With the exception of such quotations, this thesis is entirely my own work.
- I have acknowledged all main sources of help.
- Where the thesis is based on work done by myself jointly with others, I have made clear exactly what was done by others and what I have contributed myself.
- Three papers were published as a part of the current research, namely:
  - Gavalas, E., **I. S. Pressas**, and S. Papaefthymiou (July 2017). “Mesh Sensitivity analysis on implicit and explicit method for rolling simulation”. In: International Journal of Structural Integrity 9 (4), pp. 465–474.
  - **Pressas, I. S.**, S. Papaefthymiou, and D. E. Manolakos (2022). “Evaluation of the roll elastic deformation and thermal expansion effects on the dimensional precision of flat ring rolling products: A numerical investigation”. In: Simulation Modelling Practice and Theory 117, pp. 102499.
  - **Pressas, I. S.**, S. Papaefthymiou, and D. E. Manolakos (2024). "On the Fundamentals of Reverse Ring Rolling: A Numerical Proof of Concept". In: Materials 17 (9), pp. 2055.
- The LaTeX thesis template I used for my dissertation was openly available on the internet. It was created by Steve R. Gunn and modified into a template by Sunil Patel.

Overall this thesis contains a total of 110,026 words including appendices, bibliography, footnotes, tables and equations and has a total of 233 figures.

Signed: ....

Date: ....

"Γηράσκω δ' αεί πολλά διδασκόμενος."

Πλούταρχος, *Σόλων*, κεφ. 31

"I grow old ever learning many things."

Plutarch, *Solon*, ch. 31

NATIONAL TECHNICAL UNIVERSITY OF ATHENS

Abstract

School of Mechanical Engineering
Department of Manufacturing Technology

Doctor of Philosophy

Manufacturing of Advanced Materials:
Simulation of High Precision Ring Rolling via Finite Element Analysis

by Ioannis PRESSAS

Ring Rolling is widely considered as a near-net manufacturing process, due to the rough and the relatively imprecise final products. In most relevant industrial productions, a Ring Rolling cycle is followed by multiple, and sometimes extensive, machining cycles to achieve the required dimensional accuracy. Given that metallic ring products are widely used in some crucial applications, producing more dimensionally accurate products at less time through Ring Rolling can significantly increase the production quantities and reduce the production cost per piece.

In the current dissertation, multiple different precision increasing techniques and methods of a typical (flat), hot Ring Rolling process were thoroughly investigated. The proposed methodologies corresponded to several practices of a Ring Rolling manufacturing line and thus they covered all production stages – from billet to final product. Moreover, the time required for these additional corrective practices was significantly lower than running lengthy post-process machining cycle, since the former would be performed using the same Ring Rolling mill, without a need for re-positioning or intermediate storage of the workpiece.

The entire analysis of the current dissertation was performed numerically, since the necessary equipment for an experimental research was not available. The conducted numerical models were prepared using the commercial FEA software ANSYS/LS-DYNA, which offered the necessary tools and algorithms for these simulations. After a fully validated model was established, it was used as a basis for every subsequent analysis performed. In that way, the conducted simulations could act as a strong indicator towards the feasibility of the proposed methodologies and practices.

Initially in the *first chapter* of the current dissertation, a thorough literature review of the relevant experimental, analytical, and numerical research performed on Ring Rolling was conducted. Additionally, the principles of Ring Rolling and the necessary equipment required were presented. Finally, based on all of the above, the research questions that would drive the current dissertation were set.

In the *second chapter*, a step-by-step development of a typical, hot Ring Rolling simulation of an IN718 ring was performed. The developed numerical model was validated with corresponding experimental data found in literature. The choices that were made during the develop-ment of the aforementioned model were based on thorough literature and/or trial-and-error analyses, so that the physical phenomena that occur during the process would be properly simulated. In the end, the numerical model simulated the actual experiment very realistically, while several points of interest were detected and further analyzed.

In the *third chapter* of the current dissertation, three different process attributes taking place before or during Ring Rolling and that affect the dimensional accuracy of the process were investigated. These attributes were: (a) the precise volume estimation of the initial workpiece billet, (b) the effects of the thermo-elastic tool deformations, and (c) the effects of the support tool movement algorithm and its relationship to the material of the ring. For the precise billet volume estimation, a novel semi-analytical methodology was developed, which facilitates a combination of analytical equations and numerical models of every preceding process to Ring Rolling, in order to calculate the required billet volume for a final ring with specific dimensions. The proposed methodology was validated via a series of simulations, with the divergencies of the final product being far less than 1 %. In the case of the effects of the thermo-elastic tool deformations on the dimensional accuracy of Ring Rolling, three different numerical models were developed. In each model, the deformability of the tools varied (rigid, only elastic, coupled thermo-elastic) and the final results from the three models were compared to one another. From the aforementioned comparisons, it was clarified that even small deformations of the tools could lead to greater dimensional imprecisions on the product (especially in cases of high-precision products). Lastly for the analysis of the support roll movement algorithm, an AA5754 product Ring Rolling simulation was performed and compared to the IN718 simulation from the second chapter. The two simulations were then repeated, but with higher order polynomials describing the movement of support rolls. The final results revealed a dependence of the final ring dimensions from the material of the workpiece, while the higher order polynomials affected defect generation, as well as the growth rate of the ring.

In the *fourth chapter*, a newly proposed process for the "correction" of dimensional imprecisions right after a Ring Rolling process was introduced. This novel process was named "Reverse Ring Rolling". From its conceptualization, Reverse Ring Rolling involves a specific movement pattern of the tools, which leads to the reduction of the ring's diameters (both internal and external), and a subsequent increase in its height. The whole process could be distinguished into two separate steps: (a) one in which both diameters are reduced, and (b) a second in which only the external diameter is reduced. The feasibility of this process was validated via numerical modeling and the calculated results revealed a high-precision final product. Additionally, several important process parameters were futher analyzed, with the number of support rolls and the velocity of all tools proven to be the most affecting ones.

Finally in the *fifth chapter* of the dissertation, a novel approach for the production of metallic polygonal products using a typical Ring Rolling mill was introduced. This practice was presented mainly as a proof of concept, since a more in depth analysis would diverge significantly from the main scope of the current dissertation. However, since the core mechanics of this process are explained to some extent, any future research on the subject will not have to start from scratch. The basic idea of this approach lies with the simultaneous movement of support rolls in the same direction, which led to the formation of straight edges on the product. Through a carefully calculated sequence of tool movements and velocities, the manufacturing of a polygonal product was simulated as a proof of concept, while the most crucial attributes of the aforementioned process were briefly discussed. Overall, the proposed process was proven to be feasible, although further research should be conducted.

ΕΘΝΙΚΟ ΜΕΤΣΟΒΙΟ ΠΟΛΥΤΕΧΝΕΙΟ

ΠΕΡΙΛΗΨΗ

Σχολή Μηχανολόγων Μηχανικών
Τομέας Τεχνολογίας των Κατεργασιών

για τον τίτλο του Διδάκτορος Φιλοσοφίας

Διαμορφωσιμότητα Προηγμένων Υλικών:
Προσομοίωση Έλασης Δακτυλίων Υψηλής Ακρίβειας με Ανάλυση Πεπερασμένων Στοιχείων

από τον Ιωάννη ΠΡΕΣΣΑ

Η έλαση δακτυλίων θεωρείται ευρέως ως μία κατεργασία ημι-τελικών προϊόντων, εξαιτίας των τραχέων και σχετικά ανακριβών τελικών εργοτεμαχίων. Στις περισσότερες αντίστοιχες βιομηχανικές παραγωγές, ένας κύκλος της εν λόγω κατεργασίας ακολουθείται από πολλαπλούς, και συχνά εκτεταμένους, κύκλους αφαίρεσης υλικού ώστε να επιτευχθεί η απαραίτητη διαστασιολογική ακρίβεια. Δεδομένου ότι τα μεταλλικά δακτυλιοειδή προϊόντα χρησιμοποιούνται σε ορισμένες κρίσιμες εφαρμογές, η παραγωγή αυτών των προϊόντων με μεγαλύτερη διαστασιολογική ακρίβεια σε μικρότερο χρόνο μέσω της έλασης δακτυλίων μπορεί να αυξήσει σημαντικά τις παραγόμενες ποσότητες και να μειώσει το κόστος παραγωγής ανά τεμάχιο.

Στην παρούσα διατριβή, διερευνήθηκαν διεξοδικά πολλαπλές διαφορετικές τεχνικές και μέθοδοι που μπορούν να αυξήσουν την ακρίβεια μιας τυπικής (ορθογωνικής), εν θερμώ κατεργασίας έλασης δακτυλίων. Οι προτεινόμενες μεθοδολογίες αφορούν διαφορετικές πρακτικές σε μια παραγωγική γραμμή της κατεργασίας και έτσι καλύπτουν όλα τα διαφορετικά στάδια της εν λόγω παραγωγής – από την μπιγιέτα ως το τελικό προϊόν. Επιπλέον, ο απαιτούμενος χρόνος για τις προαναφερθείσες διορθωτικές ενέργειες ήταν σημαντικά μικρότερος σε σύγκριση με έναν πλήρη κύκλο φινιρίσματος, αφού οι ενέργειες αυτές μπορούν να πραγματοποιηθούν με τα ίδια εργαλεία, χωρίς να απαιτείται επανατοποθέτηση ή ενδιάμεση αποθήκευση του κατεργαζόμενου τεμαχίου.

Ολόκληρη η ανάλυση της παρούσας διατριβής πραγματοποιήθηκε αριθμητικά, λόγω έλλειψης του απαραίτητου εξοπλισμού για μια αντίστοιχη πειραματική διερεύνηση. Τα αριθμητικά μοντέλα αναπτύχθηκαν με το πρόγραμμα πεπερασμένων στοιχείων ANSYS/LS-DYNA, το οποίο περιλάμβανε τα απαραίτητα εργαλεία και τους κατάλληλους αλγορίθμους για τις αντίστοιχες προσομοιώσεις. Μετά από την ανάπτυξη ενός πλήρως πιστοποιημένου μοντέλου της κατεργασίας, αυτό χρησιμοποιήθηκε ως η βάση για όλες τις μετέπειτα αναλύσεις. Με τον τρόπο αυτό, οι προσομοιώσεις των μετέπειτα αναλύσεων μπορούν να θεωρηθούν ως μια ισχυρή ένδειξη για τη δυνατότητα πραγματοποίησης των προτεινόμενων μεθοδολογιών και πρακτικών, σε μια πραγματική εφαρμογή.

Αρχικά στο *πρώτο κεφάλαιο* της παρούσας διατριβής, πραγματοποιήθηκε μια ενδελεχής βιβλιογραφική ανασκόπηση των σχετικών πειραματικών, αναλυτικών, και αριθμητικών ερευνών που έχουν γίνει πάνω στην Έλαση Δακτυλίων. Επιπρόσθετα, παρουσιάστηκαν οι βασικές αρχές της εν λόγω κατεργασίας και ο απαραίτητος πειραματικός εξοπλισμός. Τέλος, βάσει όλων των παραπάνω, τέθηκαν τα ερευνητικά ερωτήματα που θα οδηγούσαν την παρούσα διατριβή.

Στο *δεύτερο κεφάλαιο*, παρουσιάστηκε βήμα-βήμα η ανάπτυξη της προσομοίωσης μιας τυπική, εν θερμώ Έλασης Δακτυλίων ενός δακτυλίου από IN718. Το αριθμητικό μοντέλο που αναπτύχθηκε, στη συνέχεια πιστοποιήθηκε με πειραματικά δεδομένα από τη βιβλιογραφία. Οι επιλογές που έγιναν για το εν λόγω μοντέλο, βασίστηκαν στα συμπεράσματα ενδελεχούς βιβλιογραφικής ανασκόπησης ή/και σε αναλύσεις δοκιμής-και-σφάλματος, ούτως ώστε τα φυσικά φαινόμενα που λαμβάνουν χώρα κατά την κατεργασία να προσομοιωθούν κατάλληλα. Στο τέλος, το αριθμητικό μοντέλο που αναπτύχθηκε μπορούσε να προσομοιώσει την πειραματική διεργασία πολύ ρεαλιστικά, ενώ πολλά σημεία ενδιαφέροντος μπόρεσαν να προσδιοριστούν και να αναλυθούν περαιτέρω.

Στο *τρίτο κεφάλαιο* της παρούσας διατριβής, διερευνήθηκαν τρία διαφορετικά στοιχεία της Έλασης Δακτυλίων, τα οποία λαμβάνουν χώρα πριν ή κατά τη διάρκεια της κατεργασίας και τα οποία επιδρούν στη διαστασιακή της ακρίβεια. Τα τρία αυτά στοιχεία ήταν: (α) ο υπολογισμός του ακριβούς όγκου της αρχικής μπιγέτας του εργοτεμαχίου, (β) η επίδραση των θερμο-ελαστικών παραμορφώσεων των εργαλείων, και (γ) η επίδραση του αλγορίθμου κίνησης των υποστηρικτικών ραούλων και η συσχέτισή του με το υλικό του δακτυλίου. Για τον υπολογισμό του ακριβούς όγκου της μπιγέτας αναπτύχθηκε μια νεωτεριστική, ημι-αναλυτική μεθοδολογία, η οποία χρησιμοποιεί έναν συνδυασμό αναλυτικών εξισώσεων και αριθμητικών μοντέλων κάθε προγενέστερης κατεργασίας της Έλασης Δακτυλίων, με σκοπό να υπολογιστεί ο ακριβής όγκος μπιγέτας για την κατεργασία ενός τελικού δακτυλίου με συγκεκριμένες διαστάσεις. Η προταθείσα μεθοδολογία πιστοποιήθηκε μέσα από μια σειρά προσομοιώσεων, με τις αποκλείσεις του τελικού προϊόντος να είναι πολύ μικρότερες από 1%. Για την περίπτωση της επίδρασης των θερμο-ελαστικών παραμορφώσεων των εργαλείων στη διαστασιακή ακρίβεια της Έλασης Δακτυλίων, αναπτύχθηκαν τρία διαφορετικά μοντέλα. Σε κάθε ένα από τα εν λόγω μοντέλα, η παραμορφωσιμότητα των εργαλείων ποίκιλε (άκαμπτα, ελαστικά παραμορφώσιμα μόνο, και συζευγμένα θερμο-ελαστικά παραμορφώσιμα) και τα τελικά αποτελέσματα από τα τρία μοντέλα συγκρίθηκαν μεταξύ τους. Από τις προαναφερθείσες συγκρίσεις προέκυψε ότι ακόμα και μικρές παραμορφώσεις των εργαλείων μπορούν να οδηγήσουν σε μεγαλύτερες διαστασιακές αποκλίσεις των προϊόν (ειδικά σε περιπτώσεις προϊόντων υψηλής ακρίβειας). Τέλος για την ανάλυση του αλγορίθμου κίνησης των υποστηρικτικών ραούλων, πραγματοποιήθηκε μια προσομοίωση Έλασης Δακτυλίου με τεμάχιο από AA5754, και στη συνέχεια συγκρίθηκε με την αντίστοιχη προσομοίωση του τεμαχίου από IN718 που αναπτύχθηκε στο δεύτερο κεφάλαιο. Οι δύο αυτές προσομοιώσεις επαναλήφθηκαν, στη συνέχεια, όμως με ένα πολυώνυμο υψηλής τάξης να περιγράφει την κίνηση των υποστηρικτικών ραούλων. Τα τελικά αποτελέσματα αποκάλυψαν μια εξάρτηση των διαστάσεων του τελικού δακτυλίου από το υλικό του εργοτεμαχίου, ενώ το υψηλής τάξης πολυώνυμο επηρέασε τη δημιουργία ελαττωμάτων, όπως επίσης και τον ρυθμό ανάπτυξης του δακτυλίου.

Στο *τέταρτο κεφάλαιο*, προτάθηκε μια νέα κατεργασία για τη “διόρθωση” διαστασιακών ανακριβειών, η οποία μπορεί να διεξαχθεί αμέσως μετά την Έλαση Δακτυλίων. Αυτή η νεωτεριστική κατεργασία ονομάστηκε “Αντίστροφη Έλαση Δακτυλίων”. Από τη σύλληψή της, η Αντίστροφη Έλαση Δακτυλίων περιλαμβάνει μια συγκεκριμένη κινηματική των εργαλείων, η οποία οδηγεί στη μείωση των διαμέτρων του δακτυλίου (και της εσωτερικής και της εξωτερικής), και σε μια επακόλουθη αύξηση του ύψους του. Η εν λόγω κατεργασία χωρίζεται σε δύο διακριτά βήματα: (α) ένα όπου και οι δύο διάμετροι μειώνονται, και (β) ένα δεύτερο όπου μόνο η εξωτερική διάμετρος μειώνεται. Η βιωσιμότητα αυτής της κατεργασίας πιστοποιήθηκε μέσω αριθμητικής μοντελοποίησης και τα υπολογισμένα αποτελέσματα κατέδειξαν υψηλή διαστασιολογική ακρίβεια. Επιπλέον, αναλύθηκαν περαιτέρω ορισμένες σημαντικές παράμετροι της κατεργασίας, με τον αριθμό των υποστηρικτικών ραούλων και την ταχύτητα των εργαλείων να είναι τα πιο επιδραστικά.

Τέλος στο *πέμπτο κεφάλαιο* της διατριβής, παρουσιάστηκε σύντομα μια νεωτεριστική προσέγγιση της χρήσης ενός τυπικού ελάστρου δακτυλίων για την παραγωγή πολυγωνικών μεταλλικών προϊόντων. Η εν λόγω πρακτική παρουσιάστηκε κυρίως ως μια απόδειξη της ιδέας, αφού μια εις βάθος ανάλυση θα απόκλινε σημαντικά από το κύριο θέμα της διατριβής. Παρόλα αυτά, αφού οι βασικές αρχές της έλασης πολυγωνικών δακτυλίων επεξηγούνται σε κάποιον βαθμό, οποιαδήποτε μελλοντική έρευνα στο θέμα δεν θα χρειαστεί να ξεκινήσει από το μηδέν. Η βασική ιδέα αυτής της προσέγγισης βασίζεται στη συγχρονισμένη, ομοδιευθυντική κίνηση των υποστηρικτικών ραούλων για τη δημιουργία ευθείων πλευρών στο προϊόν. Μέσα από μια καλά μελετημένη κίνηση των εργαλείων, η κατεργασία πολυγωνικών προϊόντων προσομοιώθηκε σαν απόδειξη της ιδέας, ενώ τα πιο κρίσιμα χαρακτηριστικά της μεθόδου συζητήθηκαν σε πρώτο επίπεδο. Συνολικά, η προταθείσα διεργασία αποδείχθηκε βιώσιμη, αν και περαιτέρω μελέτη θα πρέπει να διεξαχθεί.

Acknowledgements

Undertaking this PhD has been a dream of mine since the beginning of my academic years and it would not have been possible to do without the support and guidance of some very special people.

Initially, I would like to express my sincere gratitude to my supervisor Professor Emeritus Dr. Dimitrios Manolakos for his continuous support during my Ph.D study and all of the related research, as well as for his patience, motivation, and immense knowledge. This work would not be completed without his guidance and on-point observations. His proposition to turn this research in the finite element analysis route proved to be the right way to go, while it opened a lot more professional opportunities for me. I would like to thank him for encouraging my research and for allowing me to grow as a researcher.

Additionally, I would like to thank the rest of my thesis committee: Professor Dr. George - Christofer Vosniakos and Associate Professor Dr. Aggelos Markopoulos for their insightful comments and encouragement, but also for their hard questions which incented me to widen my research in various perspectives. I want to thank all of them for letting my defense be an enjoyable moment, as well as for their brilliant comments and suggestions.

Special thanks go to Professor Dr.-Ing. Spyros Papaefthymiou, for all his insiteful comments and assistance that helped me proceed my research. For all the time he spent on helping me further my investigation, as well as pinpointing its weaknesses and helping me improve, I will always be thankful to him.

Moreover, I would like to thank Dr. Evangelos Gavalas for our excellent collaboration and our insightful conversations that helped me take a look from a different perspective on certain parts of my research.

Furthermore, I would like to thank Dr.-Ing. Protesilaos Kostazos for helping me become accustomed to using LS - DYNA, a software package which was used to complete the greatest part of the current thesis. By introducing me to the world of finite elements analysis, Dr. Kostazos helped me find my personal calling in research.

Most importantly, I would like to express my deepest gratitude to my parents and my brother for their help and support. Their patience and encouragement all these years are the reason that this thesis became a reality.

Last but not least, I would like to express my love and gratitude to my wife Afrodite Savrida-Psarra for all her support and her continuous care. For she has been the best companion I could have asked for in my life and for always making me want to try even harder. This thesis is dedicated to her, our son and to my parents.

This research was financially supported by Special Account for Research Funding of N.T.U.A. (Ε.Λ.Κ.Ε. Ε.Μ.Π.), which provided a 2-year scholarship to the author of the current dissertation.

Table of Contents

Declaration of Authorship **xi**

Abstract **xv**

Abstract (Greek) **xvii**

Acknowledgements **xix**

1 Introduction **1**
1.1 Introduction . . . 1
1.1.1 Experimental Approaches of Ring Rolling . . . 2
1.1.2 Analytical Approaches of Ring Rolling . . . 12
1.1.3 Numerical Approaches of Ring Rolling . . . 19
1.2 Fundamentals of Ring Rolling Process . . . 45
1.3 Applications of Ring Rolling Products and Recent Trends . . . 48
1.4 Fundamentals of Finite Element Analysis (*Zienkiewicz, Taylor, and Zhu, 2013*) . 50
1.4.1 Finite Element Analysis of a Linear Structural System . . . 52
1.4.2 Finite Element Analysis of a Nonlinear Structural System (Hallquist, 2006) . . . 56
1.5 Scope of the Current Dissertation . . . 60

2 Numerical Modelling of the Ring Rolling Process **63**
2.1 Introduction . . . 63
2.2 Fitting Simulation Type – 2D or 3D . . . 64
2.3 Finite Element Method Formulation – Implicit vs. Explicit . . . 65
2.3.1 D'Alembert's Principle . . . 65
2.3.2 Implicit Formulation . . . 66
2.3.3 Explicit Formulation . . . 68
2.3.4 Optimum Formulation for Ring Rolling . . . 69
2.4 Geometries . . . 71
2.5 Optimum Mesh Density . . . 72
2.6 Material Properties . . . 76
2.7 Proper Finite Element Type (Hallquist, 2006) . . . 83
2.7.1 Solid Element Type . . . 85
2.7.2 SOLID_ELEMENT_1 Governing Equations . . . 86
2.7.3 SOLID_ELEMENT_2 Governing Equations . . . 86
2.8 Contact Definition . . . 89
2.8.1 Interfacial Penetration Reduction . . . 89
2.8.2 Interfacial Heat Transfer . . . 91
2.9 Tool Movement . . . 94
2.10 Boundary and Initial Conditions . . . 97
2.10.1 Initial Conditions . . . 97
2.10.2 Boundary Conditions . . . 98

2.11 Hourglass Control (Hallquist, 2006) 103
2.12 Optimum Mass Scaling 106
2.12.1 Conventional Mass Scaling (CMS) 107
2.12.2 Selective Mass Scaling (SMS) 108
2.12.3 Chosen Mass Scaling Method 109
2.13 Software Parameters 110
2.13.1 Control Parameters 110
2.13.2 Result Parameters 112
2.14 Solution 113
2.15 Validation of the Numerical Results 113
2.15.1 Deformational Results Validation 113
2.15.2 Load Results Validation 115
2.15.3 Thermal Results Validation 117
2.16 Numerical Model Results 118
2.16.1 Deformational Results 118
2.16.2 Stress and Strain Results 122
Equivalent Von Mises Stress Results 122
Effective Von Mises Strain Results 128
2.16.3 Load Results 133
2.16.4 Thermal Results 135
2.17 Discussion and Conclusions 139

3 Precision Increase of the Ring Rolling Process: Proof of Concepts 143
3.1 Introduction 143
3.2 Initial Billet Volume Precision 144
3.2.1 Billet Upsetting 144
Upsetting Parameter Evaluation via Finite Element Analysis 145
Initial Blank Volume Estimation Methodology 153
3.2.2 Upset Billet Piercing 155
3.2.3 Initial Billet Volume Calculation Methodology 157
3.2.4 Methodology Test Simulations 158
Initial Billet Volume Calculation 159
Billet Upsetting Test Model 161
Billet Central Forging Test Model 163
Billet Piercing Test Model 168
Pierced Billet Ring Rolling Test Model 179
Thermal shrinkage during cooling 182
3.2.5 Initial Billet Volume Precision Results Evaluation 184
3.3 Thermal Expansion and Elastic Deformation of the Tools 185
3.3.1 Numerical Model Setups 187
3.3.2 Numerical Model Results and Result Comparisons 191
Stress and Temperature Distributions on the Deformable Tools 191
R model - to - *NO_TE model* Results Comparison 195
NO_TE model - to - *TE model* Results Comparison 199
Combined Thermo-Elastic Tool Effects 203
3.3.3 Results and Result Comparisons Discussion 204
R model - to - *NO_TE model* Results Comparison Discussion 204
NO_TE model - to - *TE model* Results Comparison Discussion 206
Combined Thermo-Elastic Tool Effects Discussion 208
3.4 Support Rolls Movement Law and Ring Material Effects 209
3.4.1 Ring Rolling Simulation of an AA5754 Ring 210

Aluminum Ring Rolling Model Setup 210
Aluminum Ring Rolling Model Results 216
3.4.2 Higher Degree Ring Growth Algorithms 228
IN718 Ring Material Results 229
AA5754 Ring Material Results 233
3.4.3 Ring Material and Support Roll Movement Law Results and Discussion 235
3.5 Discussion and Conclusions 235

4 Reverse Ring Rolling Process **239**
4.1 Introduction 239
4.2 Characteristics of Reverse Ring Rolling Process 240
4.3 Reverse Ring Rolling Simulations 243
4.3.1 "Collaring" Model Setup 244
4.3.2 "Collaring" Model Results 246
Deformational Results ("Collaring" Model) 246
Stress and Strain Results ("Collaring" Model) 249
Load Results ("Collaring" Model) 254
Temperature Results ("Collaring" Model) 257
4.3.3 "Pulling" Model Setup 259
4.3.4 "Pulling" Model Results 261
Deformational Results ("Pulling" Model) 261
Stress and Strain Results ("Pulling" Model) 265
Load Results ("Pulling" Model) 268
Temperature Results ("Pulling" Model) 270
4.4 Crucial Reverse Ring Rolling Process Parameters 272
4.4.1 Tool Linear Velocity 273
Different Velocity Reverse Ring Rolling Models Setup 273
Different Linear Velocity "Collaring" Models Results 274
Different Linear Velocity "Pulling" Models Results 280
4.4.2 Number of Support Rolls 286
"Four-Point" Reverse Ring Rolling Models Setup 287
"Four-Point" Reverse Ring Rolling Models Results - Preliminary Runs 287
"Four-Point" Reverse Ring Rolling Models Results - Half Velocity Models 290
4.4.3 Initial Ring Temperature 297
Cold Reverse Ring Rolling Models Setup 297
Cold Reverse Ring Rolling Models Results Comparison 298
4.5 Discussion and Conclusions 308

5 Polygonal Ring Rolling Process **311**
5.1 Introduction 311
5.2 Mechanics of Polygonal Ring Rolling 312
5.3 Polygonal Ring Rolling Simulation 318
5.3.1 Polygonal Ring Rolling Model Setup 318
5.3.2 Polygonal Ring Rolling Model Results 321
Deformational Results 322
Stress and Strain Results 324
Load Results 326
Thermal Results 328
5.4 Discussion and Conclusions 329

6 General Conclusions and Future Research **331**
6.1 General Conclusions 331
6.2 Future Research 332

A LS-DYNA Example Keyword File **335**

B Python Scripts **343**
B.1 3D Surface Plot Script 343
B.2 Polynomial Function Calculation Script 344
B.3 Squared Polynomial Function Calculation Script 345
B.4 Squared Polynomial Function Integral Calculation Script 345

Bibliography **347**

CV **365**

Extended Review (Greek) **367**

List of Figures

1.1 Typical flat Ring Rolling setup . . . 46
1.2 Phases of a typical Ring Rolling process . . . 47
1.3 Most crucial methodologies leading to present-day *finite element method*. (**Zienkiewicz, Taylor, and Zhu, 2013**) . . . 51
1.4 *Standard discrete structural system* example with linear, elastic behavior (loosely based on a corresponding figure found in **Zienkiewicz, Taylor, and Zhu, 2013**) 52
1.5 Analysis of a deformable body, with simultaneous movement and deformation (figure taken from **Hallquist, 2006**) . . . 56

2.1 Recommended finite element formulation per application . . . 70
2.2 Rolling implicit vs. explicit analysis setup overview (figure taken from **Gavalas, Pressas, and Papaefthymiou, 2018**) . . . 71
2.3 Rolling implicit vs. explicit analysis solution time comparison per number of nodes in the numerical model (figure taken from **Gavalas, Pressas, and Papaefthymiou, 2018**) . . . 72
2.4 Geometric representation of Ring Rolling setup . . . 73
2.5 Mesh Independence Analysis - Experiment Setup . . . 74
2.6 Mesh Independence Analysis - Main Rolling Load Results . . . 75
2.7 Meshed bodies before simulation . . . 75
2.8 Stress - Strain - Temperature Surfaces for a Strain Rate Range of $\dot{\epsilon} = 0.01 - 10$ s^{-1} (IN718) . . . 78
2.9 Young's Modulus vs. Temperature (IN718) . . . 78
2.10 Poisson's Ratio vs. Temperature (IN718) . . . 79
2.11 Yield Strength vs. Temperature (IN718) . . . 79
2.12 Coefficient of Thermal Expansion vs. Temperature (IN718) . . . 80
2.13 Thermal Conductivity vs. Temperature (IN718) . . . 80
2.14 Specific Heat Capacity vs. Temperature (IN718) . . . 81
2.15 Emissivity vs. Temperature (IN718) . . . 81
2.16 Thermal Conductivity vs. Temperature (AISI H13) . . . 82
2.17 Specific Heat Capacity vs. Temperature (AISI H13) . . . 82
2.18 Eight node solid hexahedron element . . . 83
2.19 Bending mode for a fully integrated brick . . . 88
2.20 Contact Conductance Curves vs. Time . . . 94
2.21 Representation of changes during two time iterations of Ring Rolling . . . 97
2.22 Density of air versus Temperature (**Keenan, Chao, and Kaye, 1983**) . . . 100
2.23 Dynamic Viscosity of air versus Temperature (**Touloukian, Saxena, and Hestermans, 1975**) . . . 100
2.24 Specific Heat Capacity of air versus Temperature (**Keenan, Chao, and Kaye, 1983**) . . . 101
2.25 Thermal Conductivity of air versus Temperature (**Touloukian, Liley, and Saxena, 1970**) . . . 101

2.26 The hourglass modes of an eight-node element with one integration point are shown. A total of twelve modes exist . . . 104
2.27 Kinetic-to-internal energy ratio $\left(\frac{E_k}{E_{int}}\right)$ vs. Simulation Time . . . 109
2.28 Comparison between the experimental and numerical results of the outer and inner ring radii . . . 114
2.29 Comparison between the experimental and numerical results of the ring height 114
2.30 Comparison between the experimental and numerical results of the main rolling load . . . 115
2.31 Comparison between the experimental and numerical results of the axial rolling load . . . 116
2.32 Comparison between the experimental and numerical results of the ring's average temperature . . . 117
2.33 Workpiece deformation instances during Ring Rolling . . . 118
2.34 Common ring defects during Ring Rolling (t = 24 s): (a) Fishtail defect and (b) bulge defect . . . 119
2.35 Outer and inner radii results (experimental and numerical) . . . 120
2.36 Average ring height results (experimental and numerical) . . . 120
2.37 Outer and Inner diameter percentage ovality curves calculated during Ring Rolling . . . 122
2.38 Equivalent Von Mises stress distributions in multiple time instances during the simulation (Cross-section of the workpiece in the main rolling bite) . . . 123
2.39 Equivalent Von Mises stress distributions in multiple time instances during the simulation (Cross-section of the workpiece in the conical rolling bite) . . . 123
2.40 Equivalent Von Mises stress distributions in multiple time instances during the simulation (Cross-section of the workpiece in contact with support roll 1) 124
2.41 Equivalent Von Mises stress distributions in multiple time instances during the simulation (Cross-section of the workpiece in contact with support roll 2) 124
2.42 Equivalent Von Mises stress distributions along main rolling bite due to heat loss and during the first contact with the tools (at t = 4 s) . . . 128
2.43 Effective Von Mises strain distributions in multiple time instances during the simulation (Cross-section of the workpiece in the main rolling bite) . . . 129
2.44 Effective Von Mises strain distributions in multiple time instances during the simulation (Cross-section of the workpiece in the conical rolling bite) . . . 129
2.45 Effective Von Mises strain distributions in multiple time instances during the simulation (Cross-section of the workpiece in contact with support roll 1) . . 130
2.46 Effective Von Mises strain distributions in multiple time instances during the simulation (Cross-section of the workpiece in contact with support roll 2) . . 130
2.47 Effective strain distributions along main rolling bite due to heat loss and during the first contact with the tools (at t = 4 s) . . . 132
2.48 Main rolling load experimental and numerical result curves (full simulation duration) . . . 133
2.49 Axial rolling load experimental and numerical result curves (full simulation duration) . . . 134
2.50 Experimental and numerical average surface temperature result curves (full simulation duration) . . . 135
2.51 Temperature distributions in multiple time instances during the simulation (Cross-section of the workpiece in the main rolling bite) . . . 137
2.52 Temperature distributions in multiple time instances during the simulation (Cross-section of the workpiece in the conical rolling bite) . . . 138

3.1 Meshed nominal upsetting model . . . 147

3.2 Billet deformation at the final time instance of the nominal upsetting model . 147
3.3 Billet equivalent Von Mises stress distribution at the final time instance of the nominal upsetting model 148
3.4 Billet effective plastic strain distribution at the final time instance of the nominal upsetting model 148
3.5 Billet temperature distribution at the final time instance of the nominal upsetting model 148
3.6 Upsetting factor B deviation with the change in pressure plate velocity, $v_{tool,upsetting}$ 150
3.7 Upsetting factor B deviation with the change in friction coefficients, FS and FD 151
3.8 Upsetting factor B deviation with the change in initial billet diameter, d_0 . . . 151
3.9 Upsetting factor B deviation with the change in initial billet height, h_0 152
3.10 Edge profile functions and equivalent radius function 154
3.11 Stages of the billet at the end of each preparation process: (a) after billet upsetting, (b) after billet central forging and (c) after billet piercing 155
3.12 Billet upsetting test model setup - Initial time instance 162
3.13 Billet upsetting test model setup - Final time instance 162
3.14 Representative central forging tool geometry (presented upside down) 164
3.15 Initial states of the conducted billet central forging simulation steps 167
3.16 Final deformation of the billet at the end of the central forging process 167
3.17 Billet outer diameter evolution during the central forging process in correlation to the small tool diameter used in every step. Square marks represent the resulting correlation points, while the dotted line represents a fitted 3^{rd} degree polynomial 168
3.18 Piercing model meshed bodies at the initial time instance 169
3.19 Effective Plastic Failure Stain vs Stress Triaxiality vs Lode Parameter surface of IN718 171
3.20 Effective Plastic Failure Strain vs Stress Triaxiality vs Temperature surfaces for a Strain Rate Range of $\dot{\epsilon} = 0.001 - 10\ \mathrm{s}^{-1}$ 171
3.21 Effective Plastic Failure Strain Unitless Scale Factor vs Element Size 172
3.22 Billet's deformation during piercing process: (A) Initial state, (B) intermediate state (t = 5 s) and (C) final state 174
3.23 Zoomed image of the shear surface at the end of the piercing process 175
3.24 Typical zones created on a metal's shear surface during punching/blanking processes (figure taken from **Sahli et al., 2020**) 175
3.25 Equivalent Von Mises stress results at an intermediate state of the piercing model (t = 4.5 s) 176
3.26 Effective plastic strain results at an intermediate state of the piercing model (t = 4.5 s) 176
3.27 Effective plastic strain distribution around the cutoff edge of the billet at the end of the piercing process 177
3.28 Actual and equivalent billet volumes after piercing process 178
3.29 Final state of the Ring Rolling evaluation model of the billet volume calculation methodology 180
3.30 Billet volume calculation methodology and experimental outer radius result curves 180
3.31 Billet volume calculation methodology and experimental inner radius result curves 181
3.32 Billet volume calculation methodology and experimental average ring height result curves 181
3.33 Outer and inner radii shrinkage due to ring cooling 183
3.34 Average ring height shrinkage due to ring cooling 184

3.35 Anticipated roll deformations during Ring Rolling in each model 186
3.36 Modified numerical model setup for the tool elastic deformation and thermal expansion analysis 187
3.37 Density versus temperature (AISI H13 steel) 188
3.38 Young's Modulus versus temperature (AISI H13 steel) 189
3.39 Poisson's Ratio versus temperature (AISI H13 steel) 189
3.40 Yield Strength versus temperature (AISI H13 steel) 190
3.41 Coefficient of Thermal Expansion versus temperature (AISI H13 steel) 190
3.42 Calculated stress fields on process tools (t = 20.5 s): (a) main roll, (b) mandrel, (c) conical roll (top), (d) support roll 1 and (e) support roll 2 192
3.43 Calculated temperature fields on process tools (t = 20.5 s): (a) main roll, (b) mandrel, (c) conical roll (top), (d) support roll 1 and (e) support roll 2 194
3.44 Outer and inner ring diameters elastic differences 195
3.45 Average ring height elastic difference 196
3.46 Mandrel, main roll and conical rolls average elastic deformations 197
3.47 Support rolls average elastic deformations 197
3.48 NO_TE minus R average main and conical rolling force differences 198
3.49 Outer and inner ring diameters thermal differences 199
3.50 Average ring height thermal difference 200
3.51 Mandrel, main roll and conical rolls average thermal deformations 201
3.52 Support rolls average thermal deformations 202
3.53 TE minus NO_TE average main and conical rolling force differences 202
3.54 Outer and inner ring diameters thermo-elastic differences 203
3.55 Average ring height thermo-elastic difference 204
3.56 Allowances and tolerance charts for as-rolled carbon, alloy, and stainless steel seamless rings. Allowances are given in **boldface** type; tolerances are in regular type. Closed areas represent the maximum ring sizes for the corresponding allowances and tolerances (both given in μm) (**Bolin, 2005**) 209
3.57 Density vs. Temperature (AA5754) 211
3.58 Stress - Strain - Temperature Surfaces for a Strain Rate Range of $\dot{\epsilon}$ = 0.01 – 10 s^{-1} (AA5754). The edges of the input surfaces are presented zoomed in, on the upper right corner. 212
3.59 Young's Modulus vs. Temperature (AA5754) 212
3.60 Poisson's Ratio vs. Temperature (AA5754) 213
3.61 Yield Strength vs. Temperature (AA5754) 213
3.62 Coefficient of Thermal Expansion vs. Temperature (AA5754) 214
3.63 Thermal Conductivity vs. Temperature (AA5754) 214
3.64 Specific Heat Capacity vs. Temperature (AA5754) 215
3.65 Comparison between the IN718 and AA5754 numerical results of the ring's outer and inner radii 217
3.66 Comparison between the IN718 and AA5754 numerical results of the average ring's height 217
3.67 Comparison between the IN718 and AA5754 numerical results of the ring's thickness 218
3.68 Outer and Inner diameter percentage ovalities during Ring Rolling (AA5754 ring) 219
3.69 Deformation of AA5754 ring and support roll positions at specific time instance 220
3.70 Common defects formed during Ring Rolling at a time instance of t = 24 s (AA5754): (a) Fishtail defect and (b) bulge defect 220

3.71 Equivalent Von Mises stress distributions in multiple time instances during the simulation of the AA5754 Ring Rolling process (Cross-section of the workpiece in the main rolling bite) . . . 221
3.72 Equivalent Von Mises stress distributions in multiple time instances during the simulation of the AA5754 Ring Rolling process (Cross-section of the workpiece in the conical rolling bite) . . . 222
3.73 Effective strain distributions in multiple time instances during the simulation of the AA5754 Ring Rolling process (Cross-section of the workpiece in the main rolling bite) . . . 223
3.74 Effective strain distributions in multiple time instances during the simulation of the AA5754 Ring Rolling process (Cross-section of the workpiece in the conical rolling bite) . . . 224
3.75 Main and axial rolling loads result curves (AA5754) . . . 225
3.76 Temperature distributions in multiple time instances during the AA5754 Ring Rolling simulation (Cross-section of the workpiece in the main rolling bite) . 226
3.77 Temperature distributions in multiple time instances during the AA5754 Ring Rolling simulation (Cross-section of the workpiece in the conical rolling bite) 226
3.78 Average outer peripheral and upper ring surface temperature result curves (AA5754) . . . 227
3.79 Comparison between the outer and inner radii results from the 5^{th} degree ring growth polynomial and the reference models (IN718) . . . 229
3.80 Bulge defect comparison at a time instance of t = 45 s: (a) Reference IN718 model and (b) Polynomial ring growth algorithm model . . . 230
3.81 Comparison between the average ring height results from the 5^{th} degree ring growth polynomial and the reference models (IN718) . . . 231
3.82 Outer and inner diameter percentage ovality curves calculated during Ring Rolling (Reference and Polynomial Models - IN718) . . . 232
3.83 Comparison between the outer and inner radii results from the 5^{th} degree ring growth polynomial and the reference models (AA5754) . . . 233
3.84 Comparison between the average ring height results from the 5^{th} degree ring growth polynomial and the reference models (AA5754) . . . 234
3.85 Outer and inner diameter percentage ovality curves calculated during Ring Rolling (Reference and Polynomial Models - IN718) . . . 234

4.1 Outer and inner radii reduction in pottery (images taken from two time instances of a pottery related video on YouTube) . . . 239
4.2 Applicable pottery techniques to Reverse Ring Rolling: (a) Six-point "Collaring" (image taken from **Hardwicke and Lea, 2019)** and (b) "Pulling" (image taken from **Leach and Dehnert, 2013**) . . . 240
4.3 Applied movement on the rolls in each of the Reverse Ring Rolling process simulations: (a) "Collaring" model and (b) "Pulling" model . . . 242
4.4 Ring rolling setup used in the simulation of the "collaring" and "pulling" processes . . . 243
4.5 Cross-sections of the ring at the final time instance of the "collaring" model: (a) cross-section at the center of the main rolling bite and (b) cross-section in contact with a support roll . . . 246
4.6 "Collaring" model outer and inner radii results . . . 247
4.7 "Collaring" model average ring height results . . . 248
4.8 Outer and inner diameter ovality results ("Collaring" model) . . . 249
4.9 Ring thickness results ("Collaring" model) . . . 250

4.10 Signed Von Mises stress distributions at multiple time instances of the "collaring" Reverse Ring Rolling process simulation (Main Rolling Bite) 251
4.11 Signed Von Mises stress distributions at multiple time instances of the "collaring" Reverse Ring Rolling process simulation (cross-section in contact with Support Roll 3) 251
4.12 Signed equivalent Von Mises stress distributions at $t = 5$ s of the "collaring" Reverse Ring Rolling process simulation: (a) Top view and (b) cross-section at the middle of the ring's height. The black arrows indicate the radial compression from the rolls, the red curved double arrows indicate ring segments where tension is dominant, and the blue curve double arrows indicate ring segments where compression is dominant (along the inner peripheral surface). 253
4.13 Effective strain distributions at multiple time instances of the "collaring" Reverse Ring Rolling process simulation (Main Rolling Bite) 254
4.14 Load result curves from the "collaring" Reverse Ring Rolling process simulation (Main roll and mandrel) 255
4.15 Load result curves from the "collaring" Reverse Ring Rolling process simulation (Support rolls) 256
4.16 Temperature result curves from the "collaring" Reverse Ring Rolling process simulation 257
4.17 Temperature distributions at multiple time instances of the "collaring" Reverse Ring Rolling process simulation (Main Rolling Bite) 259
4.18 Global shape defects on the final product of a "pulling" process simulation, due to improper tool velocities 260
4.19 Cross-sections of the ring at different time instances of the "pulling" model: (a) initial time instance and (b) final time instance 261
4.20 "Pulling" model outer and inner radii results 262
4.21 "Pulling" model average ring height results 262
4.22 Outer and inner diameter ovality results ("Pulling" model) 264
4.23 Ring thickness results ("Pulling" model) 265
4.24 Signed Von Mises stress distributions at multiple time instances of the "pulling" Reverse Ring Rolling process simulation (Main Rolling Bite) 266
4.25 Signed Von Mises stress distributions at multiple time instances of the "pulling" Reverse Ring Rolling process simulation (cross-section in contact with Support Roll 3) 266
4.26 Effective strain distributions at multiple time instances of the "pulling" Reverse Ring Rolling process simulation (Main Rolling Bite) 268
4.27 Load result curves from the "pulling" Reverse Ring Rolling process simulation (Main roll and mandrel) 269
4.28 Load result curves from the "pulling" Reverse Ring Rolling process simulation (Support rolls) 269
4.29 Temperature result curves from the "pulling" Reverse Ring Rolling process simulation 271
4.30 Temperature distributions at multiple time instances of the "pulling" Reverse Ring Rolling process simulation (Main Rolling Bite) 272
4.31 Final time instance of the half velocity "collaring" model 274
4.32 Final time instance of the double velocity "collaring" model 275
4.33 Ring's cross-section at the final time instance of each model: (a) "Collaring" model, (b) Half velocity "collaring" model and (c) Double velocity "collaring" model. All cross-sections were taken from the main rolling bite, thus the outer peripheral surface is located on the right of each cross-section 275

4.34 "Collaring" model vs. half velocity "collaring" model vs. double velocity "collaring" model outer radii results comparison 276
4.35 "Collaring" model vs. half velocity "collaring" model vs. double velocity "collaring" model inner radii results comparison 276
4.36 "Collaring" model vs. half velocity "collaring" model vs. double velocity "collaring" model average ring height results comparison 278
4.37 "Collaring" model vs. half velocity "collaring" model vs. double velocity "collaring" model thickness results comparison 278
4.38 "Collaring" model vs. half velocity "collaring" model vs. double velocity "collaring" model outer and inner ovality results comparison 279
4.39 Final time instance of the half velocity "pulling" model 280
4.40 Final time instance of the double velocity "pulling" model 281
4.41 Ring deformation during multiple time instances during the double velocity "pulling" process simulation 281
4.42 Ring's cross-section at the final time instance of each model: (a) "Pulling" model, (b) Half velocity "pulling" model and (c) Double velocity "pulling" model. All cross-sections were taken from the main rolling bite, thus the outer peripheral surface is located on the right of each cross-section 282
4.43 "Pulling" model vs. half velocity "pulling" model vs. double velocity "pulling" model outer radii results comparison 283
4.44 "Pulling" model vs. half velocity "pulling" model vs. double velocity "pulling" model inner radii results comparison 283
4.45 "Pulling" model vs. half velocity "pulling" model vs. double velocity "pulling" model average ring height results comparison 284
4.46 "Pulling" model vs. half velocity "pulling" model vs. double velocity "pulling" model thickness results comparison 285
4.47 "Pulling" model vs. half velocity "pulling" model vs. double velocity "pulling" model outer and inner ovality results comparison 286
4.48 Initial Reverse Ring Rolling numerical model setup ("4P-collaring" model) . . 288
4.49 Final time instance of the "4P-collaring" model 288
4.50 Ring deformation during multiple time instances during the "4P-collaring" simulation 289
4.51 Final time instance of the "4P-pulling" model 289
4.52 Ring deformation during multiple time instances during the "4P-pulling" process simulation 290
4.53 Final time instance of the "4P-updated collaring" model 291
4.54 Ring's cross-section at the final time instance of each model: (a) Half velocity "collaring" model and (b) "4P-updated collaring" model. All cross-sections were taken from the main rolling bite, thus the outer peripheral surface is located on the right of each cross-section 292
4.55 Half velocity "collaring" model vs. "4P-updated collaring" model outer radii results comparison 292
4.56 Half velocity "collaring" model vs. "4P-updated collaring" model inner radii results comparison 293
4.57 Half velocity "collaring" model vs. "4P-updated collaring" model average ring height results comparison 293
4.58 Half velocity "collaring" model vs. "4P-updated collaring" model thickness results comparison 294
4.59 Half velocity "collaring" model vs. "4P-updated collaring" model outer and inner ovality results comparison 295
4.60 Final time instance of the "4P-updated pulling" model 296

4.61 Ring deformation during multiple time instances during the "4P-updated pulling" process simulation . . . 297
4.62 Final time instance of the cold "collaring" model . . . 299
4.63 Ring's cross-section at the final time instance of each model: (a) "Collaring" model and (b) Cold "collaring" model . . . 299
4.64 Cold "collaring" model vs. "collaring" model outer radii results comparison . 300
4.65 Cold "collaring" model vs. "collaring" model inner radii results comparison . 300
4.66 Cold "collaring" model vs. "collaring" model average ring height results comparison . . . 301
4.67 Cold "collaring" model vs. "collaring" model thickness results comparison . . 302
4.68 Cold "collaring" model vs. "collaring" model outer and inner ovality results comparison . . . 302
4.69 Ring deformation during multiple time instances during the cold "pulling" process simulation . . . 303
4.70 Ring's cross-section at t = 10 s from each model: (a) "Pulling" model and (b) Cold "pulling" model . . . 304
4.71 Cold "pulling" model vs. "pulling" model outer radii results comparison . . . 305
4.72 Cold "pulling" model vs. "pulling" model inner radii results comparison . . . 305
4.73 Cold "pulling" model vs. "pulling" model average ring height results comparison . . . 306
4.74 Cold "pulling" model vs. "pulling" model thickness results comparison 307
4.75 Cold "pulling" model vs. "pulling" model outer and inner ovality results comparison . . . 308

5.1 Basic hollow polygon dimensions (a pentagon is presented as a reference design) . . . 312
5.2 Main phases of a Polygonal Ring Rolling process: (a) Polygon side formation and (b) Workpiece rotation. In both instances, the green body represents the final state of the corresponding step and the hatched blue body represents its initial state, while the red and orange bodies are the mandrel and the main roll, respectively. . . . 315
5.3 Schematic explanation for the calculation of the workpiece's linear travel . . . 316
5.4 Basic rounded corner polygon dimensions (a pentagon is presented as a reference design) . . . 317
5.5 Linear displacement and rotational velocity applied on mandrel during Polygonal Ring Rolling simulation . . . 320
5.6 Linear displacement applied on both support rolls during Polygonal Ring Rolling simulation . . . 320
5.7 Polygonal Ring Rolling numerical model setup . . . 321
5.8 Deformation of the workpiece at multiple time instances of a Polygonal Ring Rolling process simulation (Top view) . . . 322
5.9 Example of fishtail defects formed around the top and bottom surfaces of the manufactured polygon's corners . . . 323
5.10 Signed equivalent Von Mises stress distributions during the side forming phase of a Polygonal Ring Rolling process simulation (Top view) . . . 324
5.11 Signed equivalent Von Mises stress distributions during the rotation phase of a Polygonal Ring Rolling process simulation (Top view) . . . 324
5.12 Effective strain distributions at the final times instance (t = 13.1 s) of a Polygonal Ring Rolling process simulation (Top view) . . . 326
5.13 Main roll and mandrel resultant reaction load curves . . . 327
5.14 Support rolls resultant reaction load curves . . . 327

5.15 Conical rolls resultant reaction load curves 328
5.16 Temperature distributions at the final times instance (t = 13.1 s) of a Polygonal Ring Rolling process simulation (Top view) 329

List of Tables

2.1 Tool dimensions 72
2.2 Mesh independence analysis parameters 73
2.3 Material properties (IN718) 77
2.4 Material properties (AISI H13) 77
2.5 Friction Coefficients 91
2.6 Heat transfer mechanisms in contacts 92
2.7 Definition of C and a constants (**Shapiro, 2012**) 102
2.8 Hourglass base vectors 103

3.1 Nominal upsetting model properties 146
3.2 Upsetting factor (*B*) affecting parameters tested 150
3.3 Material properties (IN718) - MAT_224 170
3.4 Material elastic thermo-plastic properties (AISI H13) 188
3.5 Material properties (AA5754) 211

5.1 Polygonal Ring Rolling initial ring and tool dimensions 318
5.2 Basic polygon dimensions and fundamental process parameters used in the Polygonal Ring Rolling simulation 319

List of Abbreviations

AA5754	**A**luminium **A**lloy 5754
ALE	**A**rbitrary **L**agrangian **E**ulerian *(Method)*
CAD	**C**omputer **A**ided **D**esign
FEA	**F**inite **E**lement **A**nalysis
FEM	**F**inite **E**lement **M**ethod
IN718	**IN**conel 718
MRB	**M**ain **R**olling **B**ite
CRB	**C**onical **R**olling **B**ite
UBET	**U**pper-**B**ound **E**lemental **T**echnique *(Method)*
UDF	**U**ser **D**efined **F**unction
2D/3D	**2D**imensional/**3D**imensional

My thesis is dedicated to my caring wife, my lovely son, my dear parents and to the memory of my late godfather . . .

Chapter 1

Introduction

1.1 Introduction

The manufacturing process of Ring Rolling has been utilized as a manufacturing process since the early 1840s **(Harbord and Hall, 1904)**. The process seems to have been born and spread widely, due to the rise of the steam locomotive. During that era, the worn locomotive wheels used to be substituted completely. However, when Ring Rolling become commonly used, outer steel tires were produced and shrunk into a cast wheel, when the previous tire got worn off **(Johnson and Needham, 1968a)**. This practice led to a significant reduction in the service cost of the locomotive wagons.

Since then, Ring Rolling has been utilized to manufacture a wide variety of different products. Some very common applications of the process, which have been mentioned in a large number of citations, involve:

- Bearing casings **(Egan, 1974; Salimi and Hawkyard, 1988; Yang, Kim, and Hawkyard, 1991; Shivpuri and Eruç, 1993; Milutinović et al., 2005; Hua, Deng, and Qian, 2015)**

- Rims and wheels **(Hutcheon and Hawkyard, 1984; Moussa and Hawkyard, 1986; Ong, 1990; Lee et al., 2014)**

- Locomotive tires **(Johnson and Needham, 1968a; Eruç and Shivpuri, 1992a; Szabo and Dittrich, 1996; Davey and Ward, 2000; Ceretti, Giardini, and Giorleo, 2010)**

- Automotive, naval and aerospace components **(Mamalis, Hawkyard, and Johnson, 1976; Hu et al., 1994; Lu et al., 2011; Giorleo, Giardini, and Ceretti, 2013; Zhu et al., 2016a)**

- Ring gear blanks **(Hawkyard, Appleton, and Johnson, 1973; Hawkyard, Navaratne, and Johnson, 1975; Onoda and Nakagawa, 1984; Omori et al., 1984; Guo and Yang, 2011b)**

- Power generation plants' components (e.g.nuclear reactor shells, wind generator turbine components etc) **(Parvizi, Abrinia, and Salimi, 2011; Parvizi, Abrinia, and Hamedi, 2012b; Giorleo, Ceretti, and Giardini, 2013; Yeom et al., 2014)**

- Pipeline applications and pressure vessel supporting rings **(Eruç and Shivpuri, 1992a; Joun, Chung, and Shivpuri, 1998;Wang et al., 2007; Moon, Lee, and Joun, 2008)**

- Valves and flanges **(Eruç and Shivpuri, 1992b; Szabo and Dittrich, 1996; Alfozan and Gunasekera, 2002; Luo et al., 2014)**

- Dies in food manufacturing setups **(Casotto et al., 2005; Bolin, 2005)**

The utilization of the process continued for almost a century until some initial scientific research was performed (e.g. **Weber, 1959**). Furthermore, the first research work on the finite element analysis of the Ring Rolling process was not published until the 1980s (e.g. **Yang and Kim, 1988**). Since then a wide variety of parameters of this process were investigated experimentally, analytically and numerically. A large part of the conducted research found during literature review, is discussed below.

1.1.1 Experimental Approaches of Ring Rolling

Ring rolling as a manufacturing process was first established around the early 1840s (**Harbord and Hall, 1904**), during the later years of the industrial revolution. During this period, the process was used mainly for producing locomotive wheels. This process continued to be of utmost importance due to the fact that the rings produced that way were seamless, thus had no inherent weaknesses, while it was more profitable than other commonly used processes for the same or similar products (**Johnson and Needham, 1968a**).

These first ring rolling setups went into constant transformations and modifications until their final forms, elements of which can be found in modern setups. The geometry of the produced rings of that era could not be very complex (mainly plain (rectangular) rings were produced, (**Johnson and Needham, 1968a**), however more complex setups led to the creation of more complex products (**Bolin 2005**).

Although the manufacturing process has been utilized since the early 1840s, the first analysis of the key factors and the mechanics of the process did not appear until the late 1950s.

More specifically, in 1959 Weber presented a number of different forging and ring rolling experiments, in order to determine the deformation of different segments of the workpieces during ring rolling (**Weber, 1959**). In his research, Weber observed that the percentage of roll indentation significantly affected which ring segments would deform, while he noticed that the segments near the mandrel were much more deformed than those near the main roll.

Later, Potter presented a new type of ring rolling setup, in which he attempted to determine the optimum position of the guide rolls and observed the deformed grains of the rings after various ring rolling experiments (**Potter, 1960**). In this work, Potter mentioned that the guide rolls could be positioned at a specific distance from the mandrel - main roll centerline axis, with the only affecting parameter for the value of the distance being the ring - shaped area of the workpiece. As for the grain deformation, it was proven that it followed the circumferential extension of the ring.

Some very interesting research works were published in 1968, from a pioneering research team on the subject from Cambridge University. Their works mainly involved various experiments performed at a purely experimental ring rolling mill, in order to investigate a number of different process parameters and their effects on the produced rings. The first research paper from this team was presented by Johnson and Needham and involved a sensitivity analysis of ring diameter strain and circumferential ring velocity and their effectiveness on roll load, torque and diameter strain in the ring rolling of lead - tellurium rings (**Johnson and Needham, 1968a**). Although this work tackled the subject both experimentally and analytically, several key aspects of the material were not accounted for, some simplifying assumptions were considered and a number of important process parameters were not in line with those of actual production. Moreover, by using an experimental ring rolling setup, the presented conclusions could be considered questionable in the case of productive Ring Rolling lines, where the production of much larger rings was the norm.

The next work from the same research team was presented also by Johnson and Needham. In this work, the hypothesis proposed by the authors' in their previous paper (**Johnson and Needham, 1968a**), involving the formation of a plastic hinge in the rings opposite to the roll grip, was investigated (**Johnson and Needham, 1968b**). The experiments were performed in a number of identical ring blanks which were annealed and etched in order for the deformation zones to become visible. The experiments verified the presence of a formed plastic hinge after the static indentation of the rolls, thus the authors mentioned that special care should be given in the cases where the initial indentation is relatively large.

Following their previous work, Johnson, MacLeod and Needham presented a new Ring Rolling setup where a number of Ring Rolling experiments of aluminum and steel rings was conducted (**Johnson, MacLeod, and Needham, 1968**). This work bore some very interesting results that connected the improperly applied force of the guide rolls to several s (e.g. polygon - shaped defects). Moreover, ring blank material, as well as the friction conditions between the blank and the rolls seemed to affect the creation of a *"flashover"* defect in the produced ring. Finally, the effects of lubrication in Ring Rolling were first tackled in this research, proving that the use of lubricants severely reduced both the amount of *"flashover"* and the required work. It is worth mentioning that this research involves the first mentioning for the effects of support rolls on the process.

In the same year Caddell, Needham and Johnson studied the effects induced on the ring material from the Ring Rolling process (**Caddell, Needham, and Johnson, 1968**). The authors in their work noticed that the strain hardening after the Ring Rolling process was not similar to that of a uniaxial compression for the same material and strain percentage, even though the ring was generally strain hardened (especially in cold working). What is more, the yield strength of the final product seemed to be mostly uniform in all direction, although significantly lower than what the same material in a uniaxial compression test and for the same effective strain would have. Finally, the results in this work showed that the final ring yield strength could be better predicted if the ring thickness reduction was considered instead of an effective compressive strain.

One year later, Beseler proposed several different setups for Ring Rolling mills (**Beseler, 1969**). With the proposed differences, the production of profile rings (as mentioned by **Barve, 2005**) and constant cross-section, non-circular products (as mentioned by **Allwood, Tekkaya, and Stanistreet, 2005b**) is possible.

In the same year, Hawkyard, Appleton, and Johnson performed various experiments, in order to test a new Ring Rolling setup in **Hawkyard, Appleton, and Johnson, 1973**. In their research, the authors proposed a new Ring Rolling mill with the same tools and mechanics that are still used today. The conducted experiments involved 6xxx series aluminum alloy blanks of various diameters and heights. The proposed setup performed well in the conducted experiments, with the dimensions of the produced rings being fairly accurate.

Soon after, Hawkyard, Navaratne, and Johnson performed experiments in order to create gears through a profile Ring Rolling process with a proper rotating die **(Hawkyard, Navaratne, and Johnson, 1975)**. The authors performed a series of experiments in steel as well as in softer ring materials. The entirety of the experiments was successful with no visible defects, thus proving the feasibility of gear production through the aforementioned process. The importance of lubrication was mentioned, as the gear teeth would be most likely damaged during extraction otherwise.

The same year, Mamalis, Hawkyard, and Johnson presented their work on the mechanism of cavity formations during profile Ring Rolling. In this work, lead-tellurium blanks were used and all of the experiments were performed on an experimental setup. The authors concluded that cavities initiated at a specific ring thickness-to-profile root thickness ratio, while the tool feed in correspondence to the overall thickness reduction should also be accounted for. This last fact was also presented via the slip line fields, although the overall slip line field analysis was omitted from the final paper.

The following year, the same team of authors further studied the flow mechanisms and the corresponding patterns of profile ring rolled blanks in their work **Mamalis, Hawkyard, and Johnson, 1976**. It this work, the authors scribed a specific mesh in the all sides of 6xxx series aluminum and tellurium-lead blanks and proceeded to Ring Roll them both in plain and profile rings. Moreover, metallic implants were used to track the deformation patterns in the inner segments of the rolled rings. Mamalis, Hawkyard, and Johnson concluded that the feed rate of the mandrel, the total ring thickness reduction and the geometric characteristic of the rolls (e.g. the roll radii ratio and the thickness-to-profile root thickness ratio) were the major factors that affected the magnitude and/or the form of the spread patterns, with a combination of bending and shearing stress being primarily exerted during the process.

Again in 1976, Mamalis, Johnson, and Hawkyard presented another work (**Mamalis, Johnson, and Hawkyard, 1976b**)on the distribution of stress between the rolls and the blank. The authors presented novel roll designs for both the main roll and the mandrel, that would allow for the measurement of the stress distribution on these tools via the *"pin load cell technique"*. Tellurium-lead blanks were rolled in the presented setup, both in plain (rectangular) Ring Rolling and in T-shape profile Ring Rolling. The experimental results showed that the stress distribution on the rolls presented its maximum value near the entry point of the blank in the bite and falling rapidly towards the exit point (making a characteristic *"knee"* formation on the diagram), a behavior that according to the authors is opposite from what was previously observed for the stress distribution results on the rolls of flat strip rolling. Furthermore, the stress distribution on the Ring Rolling process seemed to be heavily affected by the total thickness reduction of the blank and the magnitude of the linear feed of the mandrel, while the authors hinted that increased friction may also be the cause of some of the observed effects.

Following their previous paper, Mamalis, Johnson, and Hawkyard continued their work on the stress distribution on the rolls (**Mamalis, Johnson, and Hawkyard, 1976c**), by employing the previously presented in **Mamalis, Hawkyard, and Johnson, 1976** Ring Rolling setup and performing a number of experiments on 6xxx series aluminum alloy blanks, both as plain rings and as T-shaped profiled rings. The results in this analysis resembled those of the tellurium-lead rings, although their distribution, in this case, was much smoother across the ring-roll contact length. The majority of experimental conclusions of this study remain the same to those of **Mamalis, Hawkyard, and Johnson, 1976**, except for the plane strain fitting analysis performed in this case. The latter revealed that plane strain conditions were not applicable in the early stages of Ring Rolling, while the deviation grew even further as the process progressed.

The same authors reviewed their previous work in **Mamalis, Johnson, and Hawkyard,**

1976a and **Mamalis, Johnson, and Hawkyard, 1976e**, where more experimental graphs and photographs from the calculated deformations and the deformed blanks were presented. What is more, some roll force and torque analytical expressions previously presented in **Mamalis, Johnson, and Hawkyard, 1976c** were also briefly mentioned.

Another relative work to Ring Rolling was presented in 1984 by Hutcheon and Hawkyard in **Hutcheon and Hawkyard, 1984**. In this paper, the authors presented an alternative method of producing aluminum alloy bicycle wheel rims via profile Ring Rolling, contrary to the then common extrusion, rimming and welding production process. Moreover, several profile Ring Rolling process parameters and methods were reviewed from other works (e.g. the advantages of multi-stage rolling of the rims as presented in **Hawkyard and Ingham, 1979**), while a brief techno-economical analysis of the subject was also presented. It is worth noting that Hutcheon and Hawkyard in this work proposed a fully automated setup for the aforementioned wheel rim production, something that was rarely seen in previous similar works.

Another experimental work of 1984 was presented by Yang et al. in **Yang et al., 1984**. The scope of this work was the presentation of a new CNC Ring Rolling setup, fully automated via CAM. In the aforementioned setup, several tests were performed on steel blanks in high temperature (880 °C to 900 °C). The authors noticed the effects of the elevated temperature and strain rate on the effective stress exerted on the blanks, while the roll force and torque were also estimated.

Two years later, Moussa and Hawkyard presented an experimental study on the multi-stage process of producing aluminum bicycle wheel rims via consequent profile Ring Rolling procedures (**Moussa and Hawkyard, 1986**). The authors performed some preliminary tests on a process with three stages, but after the proper modifications, they concluded on a two-stage process. Furthermore, the most common problems faced during the aforementioned process (in all stages) were noted and the proper correcting measures for each problem were proposed.

Some years later, a new study was presented by Salimi and Hawkyard, in which a new experimental setup for producing rings with a V-shaped cross-section was introduced (**Salimi and Hawkyard, 1988**). After describing the geometric details of the rolls and their functionality in terms of the final ring geometry, some experimental tests were performed in the proposed setup. The received experimental roll force data were subsequently compared to the roll force predicted by an analytical approach also presented in the study, while the final ring product was examined in terms of its geometry. Additionally, some correcting measures that would eliminate common production defects of the introduced setup were also proposed. The authors noted a satisfactory agreement between the experimental and analytical results.

Another experimental work of 1988 was presented by Boucly, Oudin, and Ravalard in **Boucly, Oudin, and Ravalard, 1988**. In this work, the authors presented a new Ring Rolling setup along with three different wax-based materials, which could simulate the mechanical behavior of several steel and aluminum alloys in hot and warm forging processes. A combination of these three different materials could also be used (in the proper ratios), in order to simulate other metallic alloys. After some early tests and comparisons, the simulation materials' equations of state were approached and validated. However, as the authors mentioned, some extended preliminary experimental testing should be performed with the proposed materials, before estimating the exact process parameters of the actual production of metallic rings.

In 1992, Koppers presented an adaptive control system that could be utilized in existing Ring Rolling setups, in order to minimize the production costs (**Koppers, 1992**). The author proposed a complete schedule of the process that would help determine and track all the crucial parameters needed for the production of the desired ring. Additionally, a reverse simulation of the process was advised, in order to determine the dimensions of the preform for a given product result. Moreover, Koppers mentioned that a constant measurement of the process parameters and an estimation of the next rotation's parameters should be followed as a practice for the better control of Ring Rolling. Furthermore, some basic techniques for avoiding common shape defects in various plain (rectangular) and profiled rings were also presented. Finally, a fully automatic schedule, involving the adaptive controller was proposed by the author.

In the same year, Eruç and Shivpuri presented a two-part summary of various research works conducted around that period for the Ring Rolling process (**Eruç and Shivpuri, 1992a** and **Eruç and Shivpuri, 1992b**). In the first part of the summary, the authors presented various common and uncommon Ring Rolling setups and their respective final products. Additionally, they mentioned different variations of Ring Rolling, as well as the different stages of a typical Ring Rolling process. Moreover, Eruç and Shivpuri noted the effects that some key aspects bring in the process, and they concluded with the layouts of some characteristic process plants. The second part of the summary described some important factors and how they affected the flow of the metal during the manufacturing process. Furthermore, some major difficulties and some common defects were also mentioned. What is more, a typical process schedule and the key parameters that need to be monitored were noted, while the importance of simulating Ring Rolling within this procedure was highlighted. Finally, at the end of the summary, the Ring Rolling research subjects with the most interest of the time were mentioned.

The same authors published a new work the following year, regarding the utilization of a developed software that could assist in the Ring Rolling production lines (**Shivpuri and Eruç, 1993**). In their work, Shivpuri and Eruç presented the software *"ERCRNGROL"*, which provided the user with a techno-economic analysis of the process. The user could input the desired dimensions of the final ring, the bill of materials, the available equipment and the ring production lot and the software would estimate the least costly production schedule and the corresponding process parameters. Furthermore, several pieces of advice regarding preforming were provided by the authors in this study, based on prior experimental experience. Finally, the authors performed comparative research between the experimental results of a certain production line and the corresponding values their software estimated. Comparison between the two revealed that the production line could be further optimized using the estimated process parameter values, thus reducing its production cost.

Some years later, Szabo and Dittrich presented a study summarizing the aspects of a contemporary Ring Rolling setup (**Szabo and Dittrich, 1996**). The authors presented the basic mechanics of the Ring Rolling process, along with the flow of the blank material during deformation. What is more, several optimization tools and software packages used in Ring Rolling setups of the time to monitor and improve the whole process were noted by Szabo and Dittrich. Finally, the work is concluded with the presentation of a Ring Rolling setup layout, which involved the entirety of the optimization tools and software packages mentioned above.

The same year, Burge presented his master thesis on the validation of an already established numerical model of a profile Ring Rolling process (**Burge, 1996**). In his thesis, Burge performed several experiments that would check the validity of the developed model, while a number of different process parameters were tested as well. Comparison between the numerical and experimental results showed a good agreement in the estimated roll force and the percentage of the profile that was filled. Moreover, the experimental results revealed a connection between the thickness reduction rate (per pass) and roll force, while lubrication and initial blank thickness had no significant impact on the same parameter.

In 2004, Alexis and Satheesh presented a system for the optimization of hot Ring Rolling processes (**Alexis and Satheesh, 2004**). In their work, after presenting some roll force (radial and axial) estimation equations found in other works, the authors proposed a novel system that used the estimated values, along with the final dimensions of the ring, for the optimum control of the Ring Rolling setup. Alexis and Satheesh mentioned that the proposed system was validated by a leading aeronautical production company in India.

The following year, Milutinović et al. developed software that assisted in the production of bearing raceways (**Milutinović et al., 2005**). After demonstrating the fundamental geometric equations for the manufacturing of a raceway during all of the production steps, the authors presented a newly developed software that could assist in the optimal design of the process. The developed software used the final product geometry and available tools as input and produced a step-by-step production plan, some proposed process parameters, as well as the most suitable Ring Rolling setup for the desired bearing raceway.

The same year, Allwood, Tekkaya, and Stanistreet published a two-part review regarding Ring Rolling (**Allwood, Tekkaya, and Stanistreet, 2005a** and **Allwood, Tekkaya, and Stanistreet, 2005b**). In the first part of the review (**Allwood, Tekkaya, and Stanistreet, 2005a**), the authors presented a complete production schedule and various productive details of different Ring Rolling processes. Furthermore, some commonly faced defects in Ring Rolling were discussed. Finally, the first part concluded with the tools and setups required for each of the possible Ring Rolling products, as well as the evolution of various Ring Rolling setups over the years. In the second part of the review (**Allwood, Tekkaya, and Stanistreet, 2005b**), Allwood, Tekkaya, and Stanistreet briefly presented the experimental research methods that have been used for the evaluation of various mechanisms and the estimation of a variety of different Ring Rolling process parameters over time. Furthermore, several applications used for the process optimization and the improved tool control were also presented.

The following year, Stanistreet, Allwood, and Willoughby presented a more flexible Ring Rolling machine design (**Stanistreet, Allwood, and Willoughby, 2006**). Initially, the authors investigated several Ring Rolling machine designs capable of producing a wide range of ring products. Seeing that a single machine design would not be sufficient to produce several different ring geometries, Stanistreet, Allwood, and Willoughby opted for a modular Ring Rolling machine design, capable of adding or removing tools depending on the ring design produced each time. The authors tested their machine with a plasticine physical model ring, in order to verify the functionality of their Ring Rolling machine design and to identify potential critical points in it. The physical model results were in relatively good agreement to the target product dimensions.

In 2011, Zuo, Tan, and Li presented a novel ring rolling setup aimed at rolling thin-walled rings (**Zuo, Tan, and Li, 2011**). In this work, the authors presented their initial experimental attempt of a thin-walled ring rolling setup, which could both expand and shape a ring. The setup had twelve pairs of driven and idle rolls. Zuo, Tan, and Li performed ten different tests of creating a grooved twin-walled (0.3 mm) ring and identified several imperfections of the created setup and mentioned they would further investigate ways to correct them on a future research.

A novel approach for a combination of Ring Rolling and cross rolling processes was presented some years later in **Qian, Zhang, and Hua, 2013**. In this work, the authors proposed a different experimental Ring Rolling mill, which involved a moving main roll and three idle rolls with their positions fixed during the forming process. The whole process was divided into two separate steps: (a) a pure profile Ring Rolling step and (b) a cross rolling step up to the workpiece's final height. Additionally, Qian, Zhang, and Hua estimated the margin limits of several process parameters, in order to achieve stable and uniform manufacturing and then validated their proposed method both experimentally and numerically. From the conclusions of this work, the feasibility of the proposed manufacturing process was revealed, while the estimated value margins were shown to reassure the stable forming of the ring. It is worth mentioning that the proposed method was mainly aimed at the production of deep groove rings.

The next year, Arthington et al. presented a new method for measuring the evolution of ring inner and outer radii in **Arthington et al., 2014**. In this work, the authors developed a routine in MATLAB, which would analyze the image taken from a web camera and would estimate the boundaries of the produced ring. Although the conducted analysis was performed on a static image, the authors mentioned that future work would be concentrated in facilitating the proposed method in real-time, while the routine would be also modified to calculate more process values.

The following year, Hua, Deng, and Qian presented a work describing various methods of precision Ring Rolling (**Hua, Deng, and Qian, 2015**). In this work, the authors presented the most common methods utilized in the industry aimed at bearing raceway production of various sizes. Several pieces of information were involved in the aforementioned work, mainly regarding the process plan of both hot and cold, radial and radial-axial Ring Rolling processes, as well as various details and statistics of them. Additionally, Hua, Deng, and Qian proposed a new approach of casting the ring blank rather than preforming it, which would make the whole process faster and more economic from the reduction of material scrap.

The same year, Arthington et al. proposed a novel setup for the accurate measurement of the ring dimensions (**Arthington et al., 2015**). In this work, the authors used a previously developed optical method, in order to measure the dimensional changes, as well as some key process parameters in a typical radial-axial Ring Rolling setup. In order for the camera to be able to track the exact position and deformation of the blank, several radial lines were marked on the upper face of the product that the camera used for tracing. The changes in the ring's shape were stored in real-time on a computer, via a computer model with a single layer of elements in thickness. The proposed measurement method was verified experimentally, with very good accuracy.

The following year, Husmann and Kuhlenkötter investigated experimentally the main factors causing the ring climbing phenomenon, during a plain (rectangular) Ring Rolling process (**Husmann and Kuhlenkötter, 2016**). In their work, the authors chose four different experimental parameters mainly linked to ring climbing and designed a number of different experiments, in order to test their influence (separately and in pairs) on this phenomenon. From the experimental results, the most important of the tested factors for the aforementioned phenomenon were revealed. The authors further progressed their work in **Husmann and Kuhlenkötter, 2017**. In their second work, Husmann and Kuhlenkötter proposed an image analysis system that would monitor ring climbing and properly adjust tool positions and velocities. The proposed system was implemented in a plain (rectangular) Ring Rolling setup and several validation experiments were performed. From these experiments, the majority was considered to be successful by the authors, with ring climbing being heavily reduced. Husmann and Kuhlenkötter concluded that the proposed system, although being further progressed, could be used for research purposes.

Again in 2016, Cleaver et al. presented an investigation on the production of rings with varying thickness along their perimeter (**Cleaver et al., 2016**). In this work, the authors proposed a mandrel feed plan that could allow for the control of the ring's thickness, throughout the product's perimeter. Moreover, the importance of guide and axial rolls for the maintenance of the final product's circularity was also noted. A part of the same research team presented another experimental work relative to Ring Rolling in 2017 (**Cleaver and Allwood, 2017**). In this work, Cleaver and Allwood proposed the facilitation of an axially moving mandrel, which would allow the production of several different profiled ring through the same setup. In order to achieve this, a set of axial rolls and several guide-constraining rolls were also necessary, so as to ensure the stability of the aforementioned process. The authors performed several experiments in their proposed setup, in order to estimate the optimum schedule for each one. Overall, Cleaver and Allwood concluded that through further research, the presented method could become feasible in industrial applications.

The next year, Qian et al. presented their experimental study on the feasibility of warm Ring Rolling of bearing grade steel rings (**Qian et al., 2017**). In this work, the authors conducted two series of experiments on bearing grade steel samples: (a) a warm compressive test and (b) a warm plain (rectangular) Ring Rolling test. From the comparison between the experimental results of both processes, it was revealed that the warm Ring Rolling samples had a microstructure similar to that of post-annealed warm compression samples, thus proving the feasibility of the method with no further steps.

The same year, two different reviews regarding the up-to-date technology and the recent research trends of Ring Rolling were presented (**Hua and Deng, 2017** and **Qi and Li, 2017**). The review conducted by Hua and Deng involved the fundamentals, as well as the basic experimental setups required for radial, radial-axial and combined Ring Rolling processes, while their evolution throughout the recent years was briefly covered. The second review conducted by Qi and Li mentioned previous works regarding blank size, key process parameters and some common defects of profile Ring Rolling processes. What is more, the same authors also mentioned some finite element simulations of profile Ring Rolling processes found in the literature.

Another work presented in 2017, involved the use of logged process data online in order to avoid the creation of forming defects during Ring Rolling (**Husmann, Husmann, and Kuhlenkötter, 2017**). In this work, Husmann, Husmann, and Kuhlenkötter performed four Ring Rolling experiments, half with and half without ovality defects, and subsequently their process data were extracted and analyzed, in order to detect significant differences. From the analysis of the data, it was revealed that differences were present prior to the creation of significant ovalities, thus proper tool manipulation could help reduce these defects. At the end, the authors proposed a coupling of this methodology with machine learning and/or data mining techniques, in order to train an algorithm that could use the logged data in real time to reduce Ring Rolling forming defects.

The following year, Uchibori, Matsumoto, and Utsunomiya conducted experimental research, in order to investigate the peripheral velocity of the ring during a plain (rectangular) Ring Rolling process (**Uchibori, Matsumoto, and Utsunomiya, 2018**). In their work, the authors measured the peripheral velocity of the workpiece during a plain (rectangular) Ring Rolling process with the aid of a Full HD camera. The camera tracked the movement of a hole drilled in a specific section of the ring. Furthermore, the effect of mandrel feed on the peripheral velocity of the workpiece was also discussed. Based on the measured results, the evolution of the outer diameter of the ring was estimated. Additionally, a comparison between the rotational velocities of the ring and the main roll was conducted, while the feed-to-rotational velocity ratio's effects on the products ovality was also investigated.

In 2019, an experimental research was presented by Gontarz and Surdacki (**Gontarz and Surdacki, 2019**). In their work the authors performed a series of radial Ring Rolling processes in order to investigate the conditions of slip occurrence between the workpiece and the rolls. From their investigations, Gontarz and Surdacki were able to correlate slip occurrence with thickness reduction. This analysis was performed for every phase of the process, as well as with the limiting thickness reduction expression presented by Lin and Zhi (**Lin and Zhi, 1997**).

The same year, Zhang et al. presented a system that would measure and correct tool movement in real time during a ring rolling process (**Zhang et al., 2019**). In their work, the authors used an online laser detection system to measure the cross-section of a stationary ring. The measured data were de-noised by a Kalman time division multiplexed particle filter and the de-noised data were then used to structure a parameter cubic spline curve via the Hermite interpolation. The structured curve was used to calculate the position deviation and the dislocation of the ring's cross-section, thus allowing for a compensation of the tools' position. The results of the current research showed a good agreement between the fitted curve and the expected ring geometry.

Also in 2019, Wu et al. presented their work on the homogenization via thermal stress relief of the residual stresses induced on the ring during ring rolling (**Wu et al., 2019**). In their work, the authors rolled several rings, which they subsequently heated for different durations. They, also, conducted and presented the corresponding numerical models, created with SIMUFACT/DEFORM. The results from the two methods were compared and showed a very good agreement between one another. Wu et al. concluded that the thermal stress relief method had very good results in the homogenization of the residual stresses, while numerical simulations could function as a good alternative to corresponding experiments for this process.

The following year, Michl, Sydow, and Bambach performed Ring Rolling on wire arc additive manufacturing products (**Michl, Sydow, and Bambach, 2020**). The authors of this work manufactured six ring blanks via wire arc additive manufacturing and proceeded to manufacture them with Ring Rolling. Furthermore, half of the produced rings proceeded to be heat treated. Afterwards, various samples were extracted from the rolled rings on different directions, which were subsequently examined through tensile test and metallographic observations. The results from the tensile tests and the metallographic observations revealed the existence of defects and voids from the additive manufacturing process. Moreover, the non-heat treated samples had varying ultimate tensile strengths depending on the sample direction, while the heat treated samples had the same ultimate tensile strengths regardless of the sample direction.

The same year, Zhou, Wei, and Liu investigated the effects of hot Ring Rolling on the final metallurgy of a steel ring (**Zhou, Wei, and Liu, 2020**). In this work, the authors rolled several 100Cr6 steel rings to different percentages of thickness reductions. Afterwards, samples were received from each ring and their microstructure was analyzed via SEM and EBSD. Additionally, Zhou, Wei, and Liu performed finite element simulations of the same process to calculate the effective plastic strain of each ring from the process. Finally, the results from the two methods were compared and correlated to one another. From these comparisons it was found that there was an inversely proportional relationship between the grain size and the increase of plastic strain, as well as between the pearlite lamellar spacing and the increase of plastic strain.

A similar work was presented again in 2020, in which the evolution of Al_2Cu secondary phase particles in an Al2219 ring due to an improved Ring Rolling process plan, was investigated (**Mao et al., 2020**). In this work, Mao et al. performed two different experimental Ring Rolling process plans, a conventional and an improved, and then took samples from the two produced rings. The extracted samples were observed metallographically, and a correlation between the duration of certain process phases and the precipitation of specific Al2219 phases was made. Moreover, the effects of the evolved secondary phases on the mechanical properties of the material were calculated from empirical formulas. Moreover, two different Ring Rolling process plans were discussed in another published work of the same research group, again in 2020 (**Guo et al., 2020**). In this work too, Guo et al. performed three different Ring Rolling processes, (one conventional, one contrastive and one improved) in order to investigate the evolution of secondary Al_2Cu phases in Al2219 alloy rings. Afterwards, the authors took samples from the produced rings and examined them metallographically. The microstructural differences because of the different process plans were then evaluated, with the improved process results being superior to the other two. Finally, the mechanical properties of the manufactured ring material were calculated based on empirical formulas.

Again in 2020, Guenther, Schwich, and Hirt investigated the bond formed between the different layers of a two-steel alloy composite ring (**Guenther, Schwich, and Hirt, 2020**). In this work, the authors rolled several two-steel alloy composite rings, under different conditions, in order to identify those manufacturing parameters that would allow for the formation of the least interlayer oxidation and thus the strongest formed bond. After the Ring Rolling of the composite rings, samples were taken and were subsequently tested in terms of their tensile strength, as well as metallographically. In most cases, the two ring components were bonded to some extend along their height. Finally, the authors included a bond formation routine on an existing finite element model of the same process, in order to investigate further reasons during the process, which could lead to the debonding of the two components.

The possibility of pre-coating a ring blank prior to a ring rolling process were discussed in 2020 (**Kuhlenkötter et al., 2020**). In this work, Kuhlenkötter et al. spray-coated a steel ring and proceeded to roll it. Part of the coating surface were broken and fell during ring rolling, thus the whole process was reported as unsuccessful by the authors. However, the authors reported that spray-coating the ring prior to ring rolling may lead to a better mechanical behavior. Overall, Kuhlenkötter et al. concluded that further research on the simultaneous ring rolling and thermal spraying is required.

Another work presented in 2020, involved a novel hot ring rolling process of a composite blank (**Jiadong et al., 2020**). In this work, Jiadong et al. created a ring blank from two smaller ring components. The two ring components were assembled in one and were subsequently surface welded in an oxygen-free environment. The welded blank was then processed through hot ring rolling. After the completion of the ring rolling process, samples were extracted from the manufactured ring. The samples were mechanically tested and metallographically observed. No gaps were reported from the metallographic observations, which relates to an interfacial healing that occurred as a result of the hot ring rolling. Furthermore, a mechanical strength close to that of the pure metal was found from the mechanical tests of the composite rolled ring samples.

The following year, Cleaver, Lohmar, and Tamimi investigated the process parameters that could produce an L-shaped ring from an initially formed rectangular ring, but without a simultaneous growth in diameter (**Cleaver, Lohmar, and Tamimi, 2021**). In this work, the authors used a flexible ring rolling setup, in order to determine the process parameters that would allow for the aforementioned shaping of a rectangular ring. The ring's height, thickness and thickness reduction per pass were used as the free parameters for the problem. Using multiple free parameter combinations, Cleaver, Lohmar, and Tamimi performed corresponding experiments on Pb rings to determine an applicable operating window for each combination. The determined operation windows were then tested numerically on IN718 rings, in order to verify their transferability on more robust materials. The authors reported a relatively good agreement from the comparison between the two methods.

Another work presented in 2021, investigated the effects of ring rolling on the microstructure of a centrifuginally cast magnesium alloy ring (**Ma et al., 2021**). In this work, Ma et al. used centrifugal casting to manufacture magnesium alloy ring blanks, which were subsequently rolled with different percentages of thickness reduction. The mechanical properties of the rolled rings were estimated through mechanical tests, while their microstructures were also examined. The authors reported an increase in the mechanical strength of the rings proportional to the thickness reduction. Finally, an aging process was also applied to the ring with the highest thickness reduction. The aging process significantly increased the mechanical strength of the corresponding workpiece, while these results were correlated to the microstructure of the aged ring.

1.1.2 Analytical Approaches of Ring Rolling

The first attempt to qualify some of the core parameters of the experimental ring rolling process was found in technical manuals from the Ring Rolling equipment manufacturer Wagner & Company of Dortmund that presented some empirical laws predicting the roll force and torque. Being purely empirical, these laws involved a number of different parameters that needed further justification and/or validation (**Johnson and Needham, 1968a**).

The first purely scientific research involving an analytical approach of several fundamental values of Ring Rolling was presented in 1968 by Johnson and Needham in their work **Johnson and Needham, 1968a**. In this research, an initial attempt to calculate the ring diameter strain and circumferential ring velocity and their effectiveness on roll load, torque and diameter strain was made. Johnson and Needham presented several analytical methods for determining the aforementioned process parameters and compared the results from the two methods. The comparison revealed some deviation in the roll load results, thus proving that a complex compression and bending mechanism takes place near the roll grip. The analytical results were compared to corresponding experimental results presented in the same work, however, only lead-tellurium rings were considered in the study. It is worth noting that the roll force equation in this research was similar to that of the manufacturing process of forging, while an upper-bound analysis of the same value was also presented.

Later, Johnson, MacLeod, and Needham in their work **Johnson, MacLeod, and Needham, 1968** presented some quantitative results involving the rolling load and torque as a function of the main roll rotational velocity. The results from the empirical equations that were introduced for the calculation of the roll force had a satisfactory agreement with the results from similar formulas of flat rolling presented by Ford and Alexander in **Ford and Alexander, 1963–64**, for a similar roll radius. The analytical results were comparable to the experimental results, with the width percentage reduction being the major factor for a set Ring Rolling velocity and setup. However, the authors pointed out that the rolling force and torque may vary based on the material and the temperature of the ring, thus making the proposed equations not so accurate.

In 1973, Hawkyard, Appleton, and Johnson proposed an approach for the estimation of the rolling load in their work (**Hawkyard, Appleton, and Johnson, 1973**). The proposed expression was proved to be heavily depended on the strain rate of the process, with the predicted load values requiring a correcting factor depending on the experiment's strain rate.

In the same year Hawkyard et al. proposed some analytical equations for determining the roll force and torque during Ring Rolling, based on the slip-line theory (**Hawkyard et al., 1973**). The analytical results were then validated with previously conducted experiments in **Hawkyard, Appleton, and Johnson, 1973**. Comparison between the analytical and experimental results showed good agreement in the prediction of roll force for thin rings, while the analytical torque results had some deviation, possibly due to ring slip. Additionally, several other process parameters were addressed, thus different variations of the same equations were presented. However, Hawkyard et al. pointed out that the proposed analyses were not suited for hot Ring Rolling processes, due to a lack of necessary material data.

Later, Hawkyard, Navaratne, and Johnson presented a new method for gear production via profile Ring Rolling (**Hawkyard, Navaratne, and Johnson, 1975**). In their work, the authors proposed a formula for predicting the roll force of the process, which they would proceed to validate from their experimental results. The proposed formula was fairly accurate for a friction coefficient value of 0.1 to 0.15, while the corresponding roll force for the complete creation of the gear teeth was also determined. It is worth noting that the strain rate was not accounted for in this research.

The following year Mamalis, Hawkyard, and Johnson in their work **Mamalis, Hawkyard, and Johnson, 1976** presented a simple geometric equation, which predicted the average thickness of a ring during a T- shape profile Ring Rolling process. The presented equation takes into account the geometric characteristics of the blank and the profile rolls, although a radial Ring Rolling setup is only considered with no axial rolls involved.

Similar to their previous work, Mamalis, Johnson, and Hawkyard attempted to estimate the roll force and torque of cold Ring Rolling (**Mamalis, Johnson, and Hawkyard, 1976c**), based on the slip-line field method as it was presented by Hill in **Hill, 1950**. Apart from the aforementioned values, the authors also presented different expressions for predicting the contact length between the roll and the blank, the thickness reduction rate and the mean strain rate in Ring Rolling. Compared to the experimental results presented in the same work, the predicted roll force values had a maximum difference of 15%, while the predicted torque values were within a 15% margin for plain (rectangular) Ring Rolling and underestimated by approximately 20% for profile Ring Rolling.

An interesting analysis for the estimation of roll torque in L-shaped profile Ring Rolled blanks was presented in 1981 by Yang et al. in **Yang et al., 1981**. For this analysis, the authors established a novel expression for the roll torque resulting from the upper-bound solution of the total power required for the process (mentioned as upper-bound roll-torque). The analytical results were compared to similar experimental results performed for the needs of this work and were in relatively good agreement with one another. It is worth noting that in this work, an expression of the contact length between the roll and the ring was presented, which would be used by multiple other relevant works in the future.

Some years later, some of the same authors presented their work on the inclusion of rolling velocity for the Ring Rolling torque estimation (**Ryoo, Yang, and Johnson, 1984**). Ryoo, Yang, and Johnson presented different expressions for the velocities of the material due to the movement of the main roll and due to the pressure of the rolls in the bite. Subsequently, the two velocity fields were superposed and the total velocity field was used to estimate the strain rates. Additionally, by utilizing the upper-bound theorem on the overall roll power while considering the superposed velocity field, an updated form of the upper-bound torque was established. Comparison between the analytical and experimental results of **Yang et al., 1981** and the analytical results of this work showed that the consideration of a total velocity field led to a more accurate prediction of the roll torque.

Then, Ryoo, Yang, and Johnson performed a parametric analysis on several key characteristics of Ring Rolling and their effects on torque, roll force and power (**Ryoo, Yang, and Johnson, 1986**). The authors used the superposed upper-bound velocity field presented in **Ryoo, Yang, and Johnson, 1984** in order to establish the analytical expressions of the upper-bound torque, the power and the roll force and to define their dependence on some key geometric and dynamic process parameters, namely the feed velocity of the pressure roll, its diameter and the rotational velocity of the main roll.

The same year, Moussa and Hawkyard in their work **Moussa and Hawkyard, 1986** presented a supplementary analysis on the flange folding mechanism of the edge formations of the aluminum bicycle wheel rim premades. The presented approach involved the estimation of hinge formation in the cross-section of the rim via dynamic analysis. Moreover, the maximum radial stress on a simple radial element of the rim premade was also estimated.

The following year, Lugora and Bramley presented their work on the hoop spread mechanism of the ring during Ring Rolling (**Lugora and Bramley, 1987**). The authors utilized the analysis method presented by Hill in **Hill, 1963**, in order to determine the hoop deformation of the blank during its simultaneous thickness and height reduction. The calculated results from this analytical approach (calculated as a function of the imposed mandrel feed) were compared to the experimental results presented by Mamalis (**Mamalis, 1975**). Comparison between the two revealed that the proposed approach could be utilized for high feed rate values, but was lacking in lower feed values.

The same year, Yang and Ryoo published an analytical work, in which the rolling load and torque were correlated with one another (**Yang and Ryoo, 1987**). In this work, after presenting some fundamental geometric and dynamic equations of the process, the authors used the upper-bound torque theorem, in order to estimate the relationship between the roll force and torque. The aforementioned correlation of the two values was performed via the newly proposed *"equivalent friction coefficient"*, which was mainly affected by the feed and the initial blank dimensions. The analytical results were verified with similar experimental results.

In 1988, Salimi and Hawkyard presented an analytical study on the mechanics and dynamics of a V-shaped cross-sectioned ring production from the corresponding profile Ring Rolling process (**Salimi and Hawkyard, 1988**). The authors investigated the applied forces on a circumferential element of the ring, as well as the moment distribution that would develop on the same segment. Thus, an approximation of the final geometry and the parameters that affected this were determined. Moreover, the analytical results were compared to similar experiments, with the two being in a relatively good agreement given the assumed simplifications of the analytical model.

Some years later, Lin and Zhi presented an analytical work that estimated the supremum and infimum values of certain process parameters (**Lin and Zhi, 1997**). The authors proposed several equations that could be used to calculate the minimum and maximum acceptable values of thickness reduction rate, feed velocity, tool diameters (only minimum values) and blank height (only maximum value) for a given Ring Rolling setup. The proposed equations were established from a combination of simple geometrical functions and force equilibrium expressions. At the end of this study, Lin and Zhi mentioned that the analytical results of the aforementioned equations were validated with the experimental results presented in **Hawkyard et al., 1973** and the experimental values were well within the predicted value ranges.

Later in 2003, Puller presented a number of different analytical equations in his Ph.D. thesis (**Puller, 2003**). Initially, the author presented some simple geometrical relationships for the estimation of the contact length between the blank and each of the working rolls. Moreover, the velocity field functions of the flowing material were presented, which were subsequently used to determine the plastic strain rate and plastic work expressions. Finally, from the volume constancy principle, an equation for the axial deformation of the ring was presented. It is worth noting that results from the aforementioned axial deformation equation were compared with the corresponding results from the performed experiments, with which they were in good agreement.

Two years later, Yang, Guo, and Zhan proposed some analytical approaches for the estimation of the optimum friction coefficient (**Yang, Guo, and Zhan, 2005**). The authors in this work used the analysis presented in **Lin and Zhi, 1997** and further progressed the work of Lin and Zhi, in order to establish a time-dependent friction coefficient expression. This analytical expression was subsequently used to validate the proposed numerical routine, also presented in the same study.

The same year, Allwood, Tekkaya, and Stanistreet, in their two-part review on Ring Rolling, presented various analytical methods that were used for the estimation of some core process parameters of Ring Rolling (**Allwood, Tekkaya, and Stanistreet, 2005b**).

Two years later, Yan, Hua, and Wu proposed some analytical relationships for the estimation of a ring mean diameter growth and feed velocity (**Yan, Hua, and Wu, 2007**). In this work, the authors used the volume constancy principle on the ring segment located in the bite, in order to establish the mean diameter growth rate and linear feed expressions. Moreover, the connection between the two values was determined to be non-linear, with an increase in feed leading to a non-linear decrease in mean diameter growth rate and vice versa. Additionally, by combining the proposed equations with the work presented in **Lin and Zhi, 1997**, the extremum values of mean diameter growth rate were estimated. The presented expressions were validated in four different ring productions, for which the authors reported to have acceptable results.

Also in 2007, Tiedemann et al. investigated the creation of complex ring profiles through the vertical movement of a simple-profiled mandrel (**Tiedemann et al., 2007**). The authors in their current work presented a methodology to estimate the optimum profile strategy and material flow, given the desired ring profile geometry. Then, Tiedemann et al. conducted corresponding experiments with a wax-based material to validate their established methodology. A good agreement between the analytical and experimental results was reported.

The same year, Hua et al. presented a new approach to the guide roll movement (**Hua et al., 2007**). In this work, the authors considered a single guide roll setup, for which they estimated the center of rotation of the guide roll arm. By using simple geometric equations, Hua et al. estimated the initial and final positions of the guide roll's center. After these positions had been defined, the inner and outer radius evolution equations were determined and subsequently the velocity and acceleration functions were estimated from them.

Some years later, Zhao and Qian investigated the effects of grooves in groove-profiled Ring Rolling processes in their work **Zhao and Qian, 2010**. The authors, after estimating theoretically different classes of rolling ratio (the ratio between the groove depth and the ring thickness), they facilitated a finite element model (received from a previous work of theirs), in order to test their analytical approaches. The rolling ratio seemed to affect the final dimensions of the ring, as well as the roll force and torque required for the process. Furthermore, Zhao and Qian performed similar experiments and validated both the analytical and numerical approaches.

The following year, Parvizi, Abrinia, and Salimi facilitated the slab method in a plain (rectangular) Ring Rolling process (**Parvizi, Abrinia, and Salimi, 2011**). In their work, Parvizi, Abrinia, and Salimi used the slab method on the bite segment of a 2D plain (rectangular) Ring Rolling process, in order to determine the roll forces and torque applied on the workpiece during manufacturing. For the better approximation of the aforementioned stress fields, two distinct sections with different boundary conditions were considered. Moreover, the effects of varying friction coefficients, mandrel radius and feed values on the applied roll force and torque were also investigated.

In 2012, a research team from the University of Tehran presented a series of analytical works, regarding the facilitation of slab and upper-bound analysis methods in Ring Rolling. In **Parvizi, Abrinia, and Hamedi, 2012b**, the authors used the slab method analysis for the bite area of a plain (rectangular) Ring Rolling process, from which the roll force, roll pressure, torque and neutral point position were estimated. Furthermore, the effects of feed, rotational velocity and friction coefficient on the aforementioned parameters were also pointed out. It is worth noting that the analytical results from the slab method were validated with similar experiments, with the two being in relatively good agreement. In their second work (**Parvizi and Abrinia, 2012**), the author conducted an upper-bound analysis, in order to determine the velocity fields and strain rate functions governing that area. From these equations, Parvizi and Abrinia estimated parametrically the upper-bound power, with the neutral point position as the free parameter of the problem. The solution of the upper-bound power equation was performed numerically, as a straight solution was proven unsolvable. Furthermore, the upper-bound analysis results were validated with corresponding experimental data, with which they were considered to be close. Finally, in their third work (**Parvizi, Abrinia, and Hamedi, 2012a**) used again the upper-bound analysis method, but this time on a T-profile Ring Rolling process. As with the previous work, the velocity fields were estimated from the upper-bound analysis and were subsequently used to minimize the power of the manufacturing process. The analytical results involved the relationship of the rolling force with the ring diameter increase, while also taking into account the radial feed as a parameter. It is worth noting that this work too was verified through experiments, with the results from the two methods being relatively close. Finally, this research was further progressed by the same authors in **Parvizi and Abrinia, 2014** two years later. In this work, Parvizi and Abrinia considered the 2D velocity field proposed in **Ryoo, Yang, and Johnson, 1986** and **Yang and Ryoo, 1987** and estimated the forming load equation from the upper-bound theorem. The analytical results from this equation were validated both with a corresponding finite element model and an experiment, all three being in relatively good agreement with one another.

The same year, Xu et al. presented a novel mathematical approach for the estimation of ring diameter growth in a plain (rectangular) Ring Rolling process (**Xu et al., 2012**). In their work, the authors considered the full ring as an equivalent linear wedge element, through which the expansion rates of the dimensions were estimated. Moreover, both the initial and in-progress states of the ring were analyzed. The proposed method was facilitated in a 3D finite element model, which was validated with corresponding experiments. Comparison between the two processes revealed good predictability of the ring dimensions via the presented method and relatively poorer predictability of the velocity field in the bite region.

In 2013, Lee and Kim presented a newly proposed mathematical analysis, in order to determine the optimal manufacturing conditions (**Lee and Kim, 2013**). The authors used the volume constancy principle and a constant ring growth hypothesis, in order to estimate the limiting values for some important process parameters of Ring Rolling. The proposed values were then evaluated through corresponding experiments, as well as finite element models. Both validation means revealed that utilizing a value from the estimated margins, led to more smooth and uniform manufacturing of the workpiece.

Again in 2013, Wang and Hua presented an analytical approach to calculate the ring's growth during a vertical hot ring rolling process (**Wang and Hua, 2013**). The authors identified a linear relationship between the ring's outer diameter and the measuring roll's displacement and proceeded to fit the aforementioned relationship curve with corresponding experimental results. Then, Wang and Hua performed some verification experiments to prove the presented methodology, with a relatively good agreement between the two. It is worth noting that ring size error were taken into account and compensated for in the current work.

The following year, Xu et al. proposed some expressions that estimated the limiting values for plain (rectangular) ring blanks (**Xu et al., 2014**). In their work, the authors presented a series of extremum functions, which could be used to estimate the dimensions of a plain (rectangular) ring blank after the completion of the preforming procedure. The proposed functions were tested both experimentally and numerically, with the dimensional results from the two methods being fairly close.

The same year, Zamani proposed a novel method for estimating roll pressure and friction between the rolls and the ring blank (**Zamani, 2014**). The author of this work, divided the bite region blank segment to triangular elements, in order to determine the roll pressure and friction values affecting it. Moreover, the proposed expressions were used to determine the same values in the boundary regions (entry and exit points) of the bite. Finally, Zamani performed a sensitivity analysis of various process parameters, in order to investigate their effects on roll pressure, shearing stresses and equivalent friction coefficient.

The following year, Xu et al. proposed a novel quantitative approach on the process plan of plain (rectangular) Ring Rolling, which would ensure a stable ring manufacturing (**Xu et al., 2015**). In their work, the authors estimated the key process parameters of Ring Rolling, by considering the blank net as a continuous wedge. After estimating the allowable margins of the mandrel feed per outer diameter value that ensured stable and feasible manufacturing, the authors developed a finite element model in order to validate their quantitative approach. Comparison between the analytical and the numerical results revealed a relatively good agreement, while the forming of the ring in the simulation was proved to be fairly stable. Finally, both processes were verified with a corresponding experiment, from which similar conclusions derived.

Another mathematical approach for the tool motion prediction in plain (rectangular) Ring Rolling processes was presented the same year in **Berti, Guagliato, and Monti, 2015**. In this work, Berti, Guagliato, and Monti proposed a new mandrel velocity function, based on which all the ring geometry evolution equations were estimated. The proposed analytical model was tested through a series of finite element simulations, with the numerical results being relatively close to the corresponding experimental results received from literature. Quagliato and Berti presented another analytical work the next year, which involved the mathematical estimation of strain fields on the workpiece of a plain (rectangular) Ring Rolling process (**Quagliato and Berti, 2016**). In their later work, the authors considered a ring segment in a cylindrical coordinate axes system and introduced the equations that calculated each stain component in the system, as well as the equivalent strain equation. These equations were subsequently validated via numerical and experimental results found in the literature, with them being relatively close. Finally, the same research team presented another analytical work the following year (**Quagliato and Berti, 2017**). In this work, after presenting some basic geometric values of a plain (rectangular) Ring Rolling process, Quagliato and Berti proposed a semi-analytical method for calculating heat transfer from the workpiece to the tools and the environment, as well as an equivalent heat transfer coefficient expression. Additionally, the author facilitated the slip-line theorem, in order to introduce an equation that estimated the roll forces in the radial forming section of the process. Both of the introduced analytical approaches were subsequently implemented on Ring Rolling processes found in the literature, while their results were compared with the corresponding experimental and numerical ones from the aforementioned test cases. From the comparison between the different results, it was revealed that the estimated roll force and temperature values were in relatively good agreement with their corresponding experimental and numerical counterparts, thus verifying the importance of the introduced functions as prediction tools.

The possibility of producing ring segments and full rings with different curvatures was investigated by Cleaver and Allwood in **Cleaver and Allwood, 2019**. After thoroughly presenting the analytical formulas governing the creation of curvature during Ring Rolling found in literature, the authors proceeded to present a novel analytical approach based on force equilibrium. The results of the newly presented analytical model were compared to corresponding numerical models and lead experiments. From the aforementioned comparisons, it was concluded that the proposed model was fairly accurate in predicting the change in curvature of thin-walled rings, but not so accurate in the case of thick-walled rings. The tool size ratio and thickness reduction per revolution were found to be two of the most significant parameters that affect the developing curvature of the ring. Furthermore, Cleaver and Allwood proposed the use of their analytical formula to estimate the optimum mandrel size for a desired ring curvature. Finally, the authors mentioned that the positions and pathing of guide rolls were factors that could potentially affect the curvature of a ring and the overall stability of Ring Rolling, but were left to be studied in a future work.

In 2021, Li, Guo, and Wang proposed an instability criterion for ring rolling of ultra-wide rings, in four guide-roll ring rolling setups (**Li, Guo, and Wang, 2021**). In this work, the authors presented an analysis of the dynamics of a four guide-roll setup, mainly based on the positions of the guide rolls, and subsequently used this analysis to determine the minimum section bending moment on the ring. Based on the minimum section bending moments, the critical guide roll forces and the instability criterion were established. The proposed instability criterion was then tested numerically, using a ring rolling model of an ultra-wide aluminum alloy ring. From the numerical results, the authors reported a fairly good effectiveness of the proposed criterion, although the use of an adjustment coefficient was necessary.

1.1.3 Numerical Approaches of Ring Rolling

One of the earliest documented numerical approaches to a Ring Rolling model was performed by Yun and Cho, who presented their work on a novel approach for estimating the diameter of the produced ring (**Yun and Cho, 1985**). In their work, the authors developed a PID controller based on several dynamic equations. From the iterative solution of the system of equations, the optimal values of the weighting factors of the PID controller were determined. The optimization of weighting factors led to a final model that predicted fairly accurately the outer diameter, the outer diameter growth rate and the rolling force of a radial Ring Rolling process. What is more, the estimated results from the developed model were validated with the experimental results from a similar Ring Rolling process performed by the authors and differences between the proposed controller and P, PD and PI controllers were mentioned.

Another numerical approach to a proposed Ring Rolling model was presented by Lugora and Bramley in **Lugora and Bramley, 1987**. In this work, the authors concluded on an analytical expression for the estimation of the hoop widening of a ring during the simultaneous axial and radial deformation of the blank in Ring Rolling. Because of the complexity of the equation that was used to calculate the hoop widening (a fourth-order non-linear ordinary differential equation), a numerical solution using the same order Runge-Kutta method with Newtonian iterations was performed. The calculated curves were subsequently compared to the experimental results from **Mamalis, 1975**, with which they were in good agreement in certain test cases.

The first finite element approach to the manufacturing process of Ring Rolling was presented by Yang and Kim in 1988 (**Yang and Kim, 1988**). After presenting the system of non-linear differential equations, the authors established a 2D finite element model of the ring segment situated in the bite of a plain (rectangular) Ring Rolling process. From the established finite element model, the effectiveness of several friction coefficient values on the strain rate distribution, roll force and torque was investigated, with any changes in the friction conditions bringing little differences to the aforementioned parameters. Furthermore, the lack of friction between the rolls and the blank (frictionless conditions) was shown to significantly reduce the computational cost of the finite element model. Moreover, the roll force numerical results were compared to similar experimental results from **Yang et al., 1984** and the two appeared to be relatively close to one another.

The following year, Choi and Cho presented a new application of a real-time controller for Ring Rolling setups (**Choi and Cho, 1986**). This work was primarily based on the work presented in **Yun and Cho, 1985** and in **Choi and Cho, 1989**, thus it can be considered as an update of the controllers presented there. In this work, the main purpose of the facilitation of the real-time controller was to track several non-predictable parameters of the process, such as the roll pressure, and regulate the position of the mandrel accordingly. The efficiency of the presented adaptive controller was further validated with experimental results, with the comparison between the two revealing a very good agreement. This work was further progressed in **Choi, Cho, and Lee, 1990**, where the proposed adaptive controller was used to adjust the position of the guide rolls of the setup by monitoring their reaction forces.

Another finite element related work was published the same year by Kim, Machida, and Kobayashi in **Kim, Machida, and Kobayashi, 1990**. In their work, Kim, Machida, and Kobayashi, 1990 presented a three-dimensional rigid-plastic finite element program developed in order to simulate a Ring Rolling process. The program used a mixed mesh formulation, which involved a coarser mesh in the regions of the ring that did not deform in each time iteration and a finer mesh in the deforming region. In this way, the velocity and position of the ring could be calculated fairly accurately from the non-deforming region, while a more accurate spread of the ring was estimated in the deforming region. The authors used their newly developed program in order to study the ring spread in a plain (rectangular) and a T-shaped profile Ring Rolling processes. The simulation results were subsequently compared to the experimental results from **Mamalis, Hawkyard, and Johnson, 1976**, revealing a relatively accurate estimation of the ring spread in both the plain and the profile Ring Rolling simulations.

The same finite element program was used by Rachakonda et al., in order to design a Ring Rolling process schedule in **Rachakonda et al., 1991**. The authors created Ring Rolling models to simulate the whole process, both forward and backward. The backward simulation helped to better determine the dimensions of the blank that would be needed for a given final ring, while taking into account various defects appearing in an actual process. For the additional material needs, in order to make up for the process defects, the work of Koppers et al. (**Koppers et al., 1986**) was of utmost importance. The forward simulation was used to estimate the process parameters, which would produce the desired find product, such as the feed velocities of the mandrel. Although the authors acknowledged that the proposed schedule could be improved further, it could still function as guidelines for the user.

Another work that used the finite element method for the simulation of Ring Rolling was **Xu, Lian, and Hawkyard, 1991**. In this work, Xu, Lian, and Hawkyard simulated a segment of a blank, while it crossed the bite in a plain (rectangular) Ring Rolling process. The authors described the equations and the appropriate boundary conditions needed for the simulation, while the velocity fields of the blank and the rolls were considered as the variables that the model had to calculate iteratively. After the solution of the model, the roll force, torque, pressure distribution and defect formation results were received from the simulation and were subsequently compared to similar experimental results performed by the authors themselves, as well as from the experimental works presented in **Hayama, 1982** and **Polutin et al., 1972**. Comparison between the numerical and experimental results revealed that the proposed finite element model calculations were accurate, while the authors proposed that a multi-stage simulation would be their next goal. It is worth noting that due to the lack of the entirety of the blank and some of the tools in the proposed finite element model, some of the applied boundary conditions had to be over-constricting (e.g. zero normal velocities in the symmetry plane).

Again in 1991, Yang, Kim, and Hawkyard presented another relative study, which facilitated the finite element method to simulate the profile Ring Rolling process of T-shaped cross-section rings (**Yang, Kim, and Hawkyard, 1991**). In this work, the authors simulated a small segment of the blank, which passed through the bite of a simplified profile Ring Rolling setup that involved appropriate boundary conditions to simulate the actions of the main roll and the mandrel, while the effects from the axial conical rolls were omitted. Moreover, another set of boundary conditions was used to achieve axial symmetry in the process. The authors noted that a specific meshing technique had to be used in order to avoid stress concentration near the T-section, as well as to continuously monitor only the deformation zone around the bite. The final deformation of the numerical model was compared to the experimental cross-section deformation of a similar process presented in **Mamalis, Hawkyard, and Johnson, 1976**. Comparison between the two revealed that some discrepancies in the final geometry could be attributed to the relatively coarse mesh used in the numerical model. Furthermore, the effective strain and effective strain rate results showed an increased deformation near the entrance of the bite (especially around the main roll) and around the T-section root of the ring. Based on these results, the authors mentioned that a larger ring segment surpassing the entrance and exit point of the bite should be simulated in a future study.

In another work of 1991, Tszeng and Altan proposed a new approach for the finite element analysis of profile Ring Rolling, in order to simulate the flow of the material during the manufacturing process (**Tszeng and Altan, 1991**). The authors presented a 2D finite element model of the process with the appropriate boundary conditions and several simplifications to make up for the otherwise increased computational need. From the set boundary conditions, especially the zero velocity condition normal to the plane of ring radius growth is of increased importance in this study (mentioned as *"pseudo-plane-strain method* by the authors). The results of both a plain (rectangular) Ring Rolling and a T-shaped cross-section profile Ring-Rolling provided by the experimental work in **Mamalis, Hawkyard, and Johnson, 1976** and the analytical approach in **Yanagimoto and Kiuchi, 1989** were compared to the results of the presented analysis. Although the deformation results estimated by the proposed method were close to those of Yanagimoto and Kiuchi, they were divergent to the experimental results. Acknowledging this fact, Tszeng and Altan proposed the idea of a 3D model in future research.

The same year, Hahn and Yang presented a novel study in which they facilitated the Upper-Bound Elemental Technique (UBET) in two different profile Ring Rolling processes (**Hahn and Yang, 1991**), in order to estimate the required torque for each process, as well as some final geometry values (height of profile and mean diameter) of the profiled rings. For this analysis, the authors split a ring segment into simpler rectangular cross-section elements, while a suitable velocity field and some necessary simplifications were also considered. Comparison between the results from this analysis and similar experimental results revealed that the proposed analysis estimated the required torque relatively accurately. On the other hand, the geometrical results of the analysis had significant deviations from the corresponding experimental values, thus a more thorough investigation on this matter was proposed by the authors as future work.

The same research team presented another study based on the UBET method in 1994 (**Hahn and Yang, 1994**). In this work, Hahn and Yang introduced a new type of finite elements with uncommon geometry in each side, for which they developed the corresponding velocity field. The newly introduced element was used in order to estimate the torque and deformation values of two profile rings geometries: one including an internal semicircular path and another including an external formation with circular fillet sides. The simulation results were compared to similar experimental values, with the former agreeing in the same case to the latter (the torque results of the second geometry were almost identical to their experimental counterparts). The authors concluded that the proposed technique should be further optimized, although the presented results could be considered more accurate compared to other analytical techniques of the time.

The same year, Hu et al. presented one of the first 3D finite element models of Ring Rolling in **Hu et al., 1994**. In this research, the authors presented a simplified plain (rectangular) Ring Rolling setup with a newly proposed hybrid mesh technique for the ring, based on a modified Lagrangian finite element analysis method. The hybrid mesh involved the combination of a fine mesh in the deformation region and a coarser mesh in the rest of the ring, thus making the entire model much lighter during the solution. Although a coarser mesh was used to ensure the continuum of the ring, the deformation and load data occurring only on the finely meshed region were stored. The simulation results were compared to similar experiments performed by the authors and overall presented a similar behavior. Hu et al. concluded that the current analysis bore satisfactory results and the inclusion of the axial rolls, omitted in this study, would be the goal in their next relevant study.

Some years later, the same research team further progressed their previous work (presented in **Xu, Lian, and Hawkyard, 1991**) by developing a coupled thermo-mechanical model for the simulation of plain (rectangular) Ring Rolling in **Xu et al., 1997**. The inclusion of temperature as a parameter of the model was performed with the addition of a proper thermal matrix that involved the conduction, convection and radiation phenomena performed in the ring-tool and ring-environment interfaces. Additionally, the author chose to utilize an Euler mesh instead of a Lagrangian one in this work, thus some of the velocity equations had to be properly adjusted, while a new friction function for estimating the mandrel torque was also included. Similar to their previous work, Xu et al. in their work simulated only a small segment of the ring around the bite region. Finally, the authors concluded this study with a comparison of the roll force, torque and thickness spread results between this (temperature dependent) and their previous (non-temperature dependent) works and noted that the inclusion of ring temperature as a process parameter offered a more realistic approach.

The next year, Lim, Pillinger, and Hartley used a previously developed hybrid mesh method, in order to simulate titanium alloy plain (rectangular) and profile Ring Rolling processes in **Lim, Pillinger, and Hartley, 1998**. The facilitated meshing method in this study was the same as the one presented before in **Hu et al., 1994** by the same research team. Furthermore, a specialized support (guide) roll programming was developed in order to better control the expansion of the ring and to avoid common numerical defects, which are a result of the constantly rotating tools. The authors validated their model from the conducted plain Ring Rolling simulation (using experimental data from **Mamalis, Johnson, and Hawkyard, 1976b**) and then proceeded to simulate the V-shaped profile Ring Rolling process, in which the effectiveness of axial rolls was researched. Lim, Pillinger, and Hartley concluded that the facilitation of axial rolls significantly reduced the size of the *"fishtail"* defect, although it could not eliminate it.

The same year, Joun, Chung, and Shivpuri presented their approach on the finite element simulation of the profile Ring Rolling process for producing bearing raceways in **Joun, Chung, and Shivpuri, 1998**. In this work, a 2D axisymmetric model, similar to the process of forging, was proposed. The authors attempted to predict the flow of the material during Ring Rolling, while several forge factor values were tested. The simulation results were subsequently compared to similar experimental values. Comparison between the two revealed similar behavior for a forge factor value of $\epsilon = 0.01$, for which the mean final dimensions of the final ring were in relatively good agreement with those of the experiments.

Again in 1998, Dewasurendra presented her Ph.D. thesis on a numerical approach for the simulation of Ring Rolling processes (**Dewasurendra, 1998**). in her dissertation, Dewasurendra simulated plain (rectangular) and L-shaped profile Ring Rolling processes, using a hybrid mesh approach similar to the one seen in **Hu et al., 1994**. The basic principle of the hybrid mesh technique lied with two different meshes for the blank: (a) one finer in the bite region and coarser to the rest of the ring and, (b) one fine in the whole ring. During the simulation, mesh (a) was used to calculate the deformation occurring in the current iteration and the produced results would update mesh (b). At the end of the deformation step and after the results had updated mesh (b), mesh (a) would undergo a remeshing stage so that the new segment being in the bite region would be finely meshed now and the segment that had just exited the bite would be meshed more coarsely. Moreover, in order to make up for the movement difficulties due to the coarser mesh region, a smoothing equation would be used when estimating the velocity fields. The overall simulation process was described in detail and the numerical results were compared with experiment data from various past references (e.g. **Mamalis, Hawkyard, and Johnson, 1976**), with the two being in relatively good agreement. Dewasurendra concluded that the presented method could be considered fairly accurate, while its main advantage lied with the significant reduction of simulation time, when compared to other simulation methods of the time.

The following year, a master thesis was presented by Al-Mohaileb regarding the development of a model to simulate the heat transfer during profile Ring Rolling (**Al-Mohaileb, 2000**). After developing the corresponding mathematical equations, the author introduced them to a finite element model. Because not all the element had the same heat transfer response in each time iteration, five different types of element were proposed that covered all the heat transfer states during the process. After the thermal solution of the proposed model, the yield strength of each segment of the ring could be determined, thus a more accurate estimation of the ongoing deformation was possible.

The same year, a novel numerical approach of Ring Rolling was presented by Traoré, Montmitonnet, and Souchet in **Traoré, Montmitonnet, and Souchet, 2000**. In this work, the authors proposed an ALE methodology for the simulation of a plain (rectangular) Ring Rolling process, which was solved in two distinct step: (a) a Lagrangian formulation step for the estimation of velocities and temperature in each iteration and (b) a subsequent ALE formulation step for the estimation of deformation. The results from the second step would then be used to update the first step, and the method would be repeated from the beginning. Moreover, the mesh of the ring was split in various segments and each one was solved in a different processor. Traoré, Montmitonnet, and Souchet concluded that their approach was faster and adequately accurate compared to a finite element simulation of the same process, although several issues, such as the inclusion of strains and an automatic remeshing technique, would have to be resolved first.

Again in 2000, a new study about a novel dynamic approach to the simulation of Ring Rolling was presented in **Xie et al., 2000**.In their work, Xie et al. presented a newly developed 3D finite element program, which facilitated the explicit dynamics method in order to simulate a hot Ring Rolling process. The authors used a hybrid mesh for the ring in order to minimize the numerical effort, while special tool geometries and boundary conditions ensured the constant contact between the rolls and the workpiece, while they also helped to eradicate possible manufacturing defects. The aforementioned modeling method was used in two test cases: (a) a plain (rectangular) Ring Rolling process and (b) a L-shaped profile Ring Rolling process. The numerical results were compared to similar experiments performed by the authors and were in good agreement with one another.

Another study presented in 2000, involved an ALE analysis of the Ring Rolling simulation (**Davey and Ward, 2000**). In this work, Davey and Ward proposed the facilitation of the ALE formulation with a newly developed solver for the simulation of plain (rectangular) Ring Rolling processes. The ring in this study was meshed with the hybrid mesh method, similar to that used in previous works (e.g. **Hu et al., 1994**). The authors compared the numerical efficiency of their proposed solver to that of a Newton-Raphson solver and a Quasi-Newton solver, with the first being faster than both of them. Additionally, various pre-conditioners (user input artifacts that lead to a faster convergence of the numerical model) were tested, in order to detect the optimal for this procedure. All of the numerical models were constructed around and validated with the experimental work found in **Mamalis, Johnson, and Hawkyard, 1976d**. An update of this work was, also, presented by the same authors in 2002 (**Davey and Ward, 2002a**), in which the aforementioned simulation method with the same solver were used for the simulation of profile Ring Rolling processes, similar to those presented in **Mamalis, 1975** and **Salimi, 1988**. In this case too, the utilized method proved to be efficient with fairly accurate results, although several boundary conditions seemed to have a significant effect on the outcome of the corresponding model. The specifics for this profile Ring Rolling simulation process were presented in a supplementary work by the same authors (**Davey and Ward, 2002b**), where a more in depth analysis of the mesh update process and the utilized boundary conditions was made. Finally, the same modeling method was used by Davey and Ward again in **Davey and Ward, 2003**. After testing models with different friction conditions, in order to deduce if the zero friction condition was an acceptable simplification, the authors used their method on the Ring Rolling process of a wheel. For the wheel geometry, several modifications were required, as no mandrel could be included due to the lack of a central hole in the blank. The final results were proved to be acceptable in accuracy, should one take into account that the used simplifications brought some deviations to the calculated numerical results.

In 2001, Mori and Hiramatsu presented an alternative simulation method for profile Ring Rolling (**Mori and Hiramatsu, 2001**). The authors developed a 2D plane-strain model that was similar to the simulation of forging. Mori and Hiramatsu simulated two different profiled ring geometries with their proposed method, both of which were validated with the corresponding experiments. Overall, the proposed method showed good levels of accuracy in terms of the predicted ring dimensions.

The same year, Huez, Noyes, and Coupu presented a different finite element approach for a plain (rectangular) Ring Rolling process (**Huez, Noyes, and Coupu, 2001**). The authors proposed a mixed finite element approach, where two 3D models were used in the radial and axial deformation zones and two 2D models were used in the transitional zones from the radial to the axial deformation zones and vice versa. The simulation was performed in five steps: (a) a thermal estimation was performed, in order to estimate the temperature reduction during the transportation of the ring from the furnace to the setup, (b) a 3D thermo-mechanical calculation in the radial deformation zone was performed and the process parameters of the exit interface were estimated, (c) a thermal calculation on the 2D model, simulating the transition from the radial deformation zone to the axial deformation zone and estimating the temperature change during this state, was performed, (d) a 3D thermo-mechanical calculation in the axial deformation zone was performed, where the process parameters in the exit of this zone were estimated and (e) the temperature change during the transition of the axial to the radial deformation zone was estimated from a 2D thermal simulation. Then, steps (b) to (e) were repeated for a set number of ring rotations. The numerical results from the aforementioned model involved the strain and temperature distribution in the final ring. From them, the temperature results were validated from the microstructure of the metal in different states of the process, with which they were in good agreement. It is worth noting that this is one of the first studies that involved the Ring Rolling of IN718 rings.

Another IN718 Ring Rolling process was simulated by Song et al. in 2002 (**Song et al., 2002**). The authors of this work, developed a 2D simplified, coupled thermo-mechanical model of the whole ring, in order to simulate the hot radial Ring Rolling process of an IN718 blank. The presented model did not include the guide rolls, thus the whole simulation required less computational effort. However, several shape and centering defects could be also attributed to the lack of guide rolls. The numerical results were compared with experimental data from similar tests. Overall, the temperature, plastic strain and load results around the bite region were fairly close to their corresponding experimental values.

The same year, Utsunomiya et al. studied the basic characteristics of plain (rectangular) cold Ring Rolling processes (**Utsunomiya et al., 2002**). The main scope of this study was to research the initial stages of a Ring Rolling, where the process is not characterized as steady-state due to the occurring transitional phenomena (e.g. ring acceleration). In their work, Utsunomiya et al. proposed a 2D implicit finite element model, in order to simulate the early stages of a bearing raceway manufacturing. After the solution of the model, the stress and deformation results of specific elements located in the four sides of the initial blank were estimated and the authors gave some possible explanations for the observed results, compared to the relative position of these elements and the thickness reduction of the bite in each iteration.

Alfozan and Gunasekera presented another work in 2002, regarding the utilization of the UBET method for the simulation of profile Ring Rolling processes (**Alfozan and Gunasekera, 2002**). In this work, the authors used a pseudo 3D UBET analysis (a 2D analysis with a constant normal velocity for all elements) of the already formed ring and backwards calculated the deformation and forming energy rates of the process. For the estimation of the minimum forming energy rate consumption, various sets of different boundary conditions were considered, for two separate ring cross-section profiles. From these two profiles, one was validated with similar experiments, with which there was a relatively good agreement. Overall, Alfozan and Gunasekera concluded that their method produced acceptable results in a much quicker calculation than other methods (including experiments), although further optimization could be still performed.

The following year, Forouzan et al. presented a new method for substituting guide rolls in a Ring Rolling simulation (**Forouzan et al., 2003**). The mechanism of this method lied in the creation of a central node that was allowed to move only along the mandrel-main roll centerline axis. Subsequently, line elements connecting the central node to the nodes of the outer circle of the ring were created. As the process progressed, the movement of the central node corresponded to the displacement of the ring's center, while a proper thermal load in the line elements led to their thermal expansion, which was equal to the outer diameter increase of the ring. The authors introduced this so-called *"thermal spokes method"*, in order not to use guide rolls in their simulation, thus significantly reducing the computational effort and eliminating the need for position determination of these rolls. Moreover, with this method the centering and imbalance problems caused by the lack of guide rolls were also negated. The aforementioned method was tested in a 2D plain (rectangular) Ring Rolling simulation and the numerical results were compared to similar results from experiments. From the comparison between simulation and experiments, it was concluded that the roll force, torque and equivalent guide roll reaction force results were fairly accurate with one another, while a stiffening of the linear expansion coefficient was proved rather damaging than benefitting, as the result values tended to deviate as the stiffness of the line elements increased. The same research team further continued their study on this method in **Forouzan, Salimi, and Gadala, 2003**. In this work, Forouzan, Salimi, and Gadala performed a comparative study between a 3D finite element model including the proposed *"thermal spokes method"* and a similar 3D model excluding the method (with no guide rolls involvement). The results from both models were also compared with similar experimental results. After, the completion of the simulations, the authors concluded that the proposed method had similar results to those brought by the inclusion of guide rolls, while the torque, roll force and relative guide roll reaction force results were relatively close to the corresponding experimental values.

The same year, Yea et al. presented the numerical results of a commercial computational software, dedicated to simulating Ring Rolling processes through hybrid meshed finite element models (**Yea et al., 2003**). The authors compared the commercial software SHAPE-RR results in four different test cases of plain (rectangular) and T-shaped cross-section profile Ring Rolling, with their corresponding experimental counterparts. From this comparison, it was made clear that the aforementioned software produced fairly accurate results for the estimation of the final dimensions, while the pressure distribution and the roll force results had some acceptable deviations, in all of the simulated test cases.

Again in 2003, the same commercial software was used by Koo et al., in order to conduct a thermo-mechanical analysis (**Koo et al., 2003**). The authors of this study performed a 3D simulation of three separate plain (rectangular) aluminum Ring Rolling processes. Through their simulations, Koo et al. determined the effects that initial blank thickness and temperature had in the heat transfer and final dimensions of the rolled rings. What is more, the efficiency of axial rolls in eliminating *"fishtail"* defects was also researched. It is worth noting that in this work, only conduction and convection heat transfer mechanisms were considered.

Another relative work presented in 2003 was the Ph.D. thesis of Puller (**Puller, 2003**). In this study, the author developed a pseudo 3D model, in order to estimate the velocity field of the ring cross-section located in the bite. This process was performed both for a plain (rectangular) and a profiled ring, while the defect formation mechanisms (e.g. *"fishtail"* defect) were especially analyzed. The simulation results were compared to similar experimental values, and the final dimensions of both were in very good agreement.

The following year, Guo et al. presented a 3D finite element model of a plain (rectangular) Ring Rolling process, in order to determine a displacement rule for guide rolls (**Guo et al., 2004**). The authors, after mentioning some necessary simplifying conditions, proposed some expressions for the estimation of ring's thickness and radial increase velocity per second, as well as the total manufacturing time. Based on these expressions, the guide roll displacement rule was established and tested in a number of finite element models with varying mesh densities. What is more, the effectiveness of guide roll inclusion was presented through a series of finite element models. More specifically, two different types of defects (*"squaring"* and *"tilting"*), resulting from the lack of guide rolls, were depicted. Guo et al. noted that the actual defect that would prevail, when no guide rolls are included, was determined by the overall thickness reduction during the process.

Another work presented in 2004, involved the utilization of a new 3D approach of the UBET method (**Ranatunga et al., 2004**). The authors of this work utilized the UBET method on a 3D segment of a blank in a profile Ring Rolling process, in order to determine the final dimensions of the ring and the roll force required for the process. For this simulation, the segment located in the bite was considered, as the rest of the ring was thought to be unaffected. The initial segment was divided in triangular and rectangular elements, for which the linear velocity fields and the in-between interactions were determined. The estimated results from the proposed method were compared with those of similar experiments, with which they were considered to be close (within a 10% margin).

Again in 2004, Matsui, Takizawa, and Kikuchi presented a newly developed finite element method of Ring Rolling processes was presented (**Matsui, Takizawa, and Kikuchi, 2004**). The authors simulated a segment of the blank and performed a thermal and a mechanical analysis on it. The blank segment was modeled with an Eulerian mesh and the necessary velocity boundary conditions on the end surfaces, while an additional (mentioned as *"dummy model"* by the authors) ring segment was used for the thermal analysis. Additionally, another two models were proposed for the estimation of static grain growth and recrystallization of the material during the manufacturing process. For these models, a Lagrangian mesh was used on the whole ring. After the proper coupling of the aforementioned models, Matsui, Takizawa, and Kikuchi tested the developed simulation method in several multi-pass compression tests, as well as in an actual casing product. Comparison between the numerical and experimental results revealed a good agreement in the prediction of final ring geometry and material microstructure.

The same year, Moon et al. performed a finite element analysis for the prediction of certain defects in Ring Rolling processes (**Moon et al., 2004**). The authors created two hybrid mesh finite element models, in order to research the formation mechanisms of *"central cavity"* and *"polygonal shape"* defects, respectively. After the completion of simulations, Moon et al. concluded on the most common roots for the aforementioned defects and proposed some process parameter sets that could help minimize them. The same subject was further researched in 2008, by some of the same authors (**Moon, Lee, and Joun, 2008**). In this work, Moon, Lee, and Joun developed a 3D hybrid mesh finite element model, which simulated a plain (rectangular) hot Ring Rolling process with no guide rolls included. The main scope of this study was to determine the process parameters that could lead to the creation of a *"polygonal shape"* defect. After the numerical solution of the models was completed, the authors reviewed the results and observed that the core mechanism for this defect was the instability of the blank in the bite, caused mainly due to an exceeding feed-to-rotational velocity value, combined with poor support for the guide rolls. The numerical final ring geometry was also compared with a corresponding experimental product, both of which were fairly similar.

A very interesting study presented in 2004 by Pauskar, Sawamiphakdi, and Jin involved the comparative research between implicit and explicit formulations for the simulation of Ring Rolling processes (**Pauskar, Sawamiphakdi, and Jin, 2004**). After a brief presentation of each numerical method, the authors proceeded to simulate various cases of cold Ring Rolling with both of them. The final results revealed that both methods could be used for the simulation of cold Ring Rolling, given that the proper boundary conditions are considered. Furthermore, comparison between the two methods with one another revealed that the explicit method produced more accurate results (given the limitations of both methods and the computational capabilities of the time), thus it was suggested over the implicit method for this manufacturing process.

The next year, Yang, Guo, and Zhan researched the effects of friction in Ring Rolling, via finite element models (**Yang, Guo, and Zhan, 2005**). In their work, the authors used an already developed plain (rectangular) Ring Rolling model (created via the commercial FEM software ABAQUS), which was validated in a previous work of theirs. After presenting some analytical expressions for the friction coefficient in each time iteration, Yang, Guo, and Zhan proposed a friction coefficient estimation numerical routine, which was subsequently tested in two different simulation tests. From the numerical results, a good agreement was revealed between the proposed method and the analytical approaches. Furthermore, a sensitivity analysis of the friction coefficient on various process values was performed. The sensitivity analysis indicated that an increase in the friction coefficient, brought a decrease in both the axial and the radial spread of the blank, while the roll force and torque required for the process were roughly unaffected. It is worth noting that this analysis corresponded to all of the friction coefficients between the rolls and the blank.

Again in 2005, Casotto et al. presented a numerical model that would estimate deformations occurring during cooling of rolled rings (**Casotto et al., 2005**). The authors developed a 2D thermo-mechanical finite element model of a pain (rectangular) Ring Rolling process, while some UDFs that would estimate the effects from the phase transformation taking place during the cooling process were also included. The developed model was validated in a variety of test cases, where the numerical deformation results were in relatively good agreement with the corresponding experimental product dimensions.

Another study presented in 2005 was a two-part review on the various aspects of Ring Rolling processes (**Allwood, Tekkaya, and Stanistreet, 2005a** and **Allwood, Tekkaya, and Stanistreet, 2005b**). In the second part of this review, Allwood, Tekkaya, and Stanistreet discussed the various numerical methods that were used to simulate Ring Rolling processes, up to that time. It is worth noting that the majority of these numerical methods involved several variations of finite element modeling.

The same research team along with some more researchers presented another work the same year (**Allwood et al., 2005**). In their work Allwood et al. proposed a novel ring rolling setup, which could be used to create a variety of different profiled rings. The proposed setup was tested experimentally both large scale and in a scaled model. Furthermore, FE models of four of the tested case studies were simulated, which were then validated with the experimental results. Subsequently, a simplified model was created in order to test several tool movement paths, as well as the constraints of the FE models. From the whole analysis, some initial conclusions regarding some important process parameters of the proposed setup and the effects of different tools on the final products were reported.

The next year, Wang et al. presented a 3D thermo-mechanical finite element model of a plain (rectangular) Ring Rolling process (**Wang et al., 2006**). The presented finite element model was solved with an explicit formulation, while mass scaling was also included so as to reduce the solution time. The authors used their model to simulate two different Ring Rolling processes, which were subsequently validated with the experimental results found in past studies from other researchers (**Mamalis, Hawkyard, and Johnson, 1976** and **Song et al., 2002**). Comparison between the numerical and the corresponding experimental results revealed a relative good agreement in temperature and ring dimension values.

Again in 2006, Yang et al. conducted a numerical analysis of a cold ring rolling process, in order to estimate the effects of different material properties on certain process parameters (**Yang et al., 2006**). More specifically, the authors tested different values of Young's Modulus, yield strength, hardening coefficient, feed rate and rotational velocity in five different series of simulations. In each of the aforementioned simulation series, only one specific property or process parameter was variable, while the rest of the properties and parameters had constant values. Afterward, the effects from these variables on the ring's deformation, fishtail defect development, rolling load and rolling moment are calculated.

One year later, Wang et al. used the commercial FEM software LS-DYNA, in order to simulate profile Ring Rolling processes (**Wang et al., 2007**). After presenting some displacement approaches for the guide and axial rolls, the authors created three different models, which involved the Ring Rolling of a gear blank, a casing blank and a conical reactor shell. The final geometries of the rolled parts were subsequently compared with the expected final geometries, with which there was a fairly good agreement.

In 2008, Li et al. presented another method for the control of guide rolls in FEM simulations of Ring Rolling (**Li et al., 2008**). In this work, the authors developed an assisting numerical method, which included a system of line elements attached both to the axis of rotation of the guide rolls and to a hydraulic pressure piston. As the ring grew, pressure would start to build up on one end of the hydraulic piston (delivered through the line element system) and when a critical value was surpassed, the piston would draw back, thus allowing the displacement of the guide rolls. The numerical results were compared to similar results from a previous work (**Guo et al., 2004**, thus proving that the currently proposed method produced more accurate results. Furthermore, a numerical model of the experiment presented in **Mamalis, Hawkyard, and Johnson, 1976** was used to validate the method. Comparison between the experimental and numerical results revealed good agreement in the final dimensions of the produced profiled ring of the model.

The following year, Wang et al. facilitated FEM to simulate the plain (rectangular) Ring Rolling process of large diameter titanium alloy rings (**Wang et al., 2009**). After estimating the limiting values for the process parameters of feed and rotational velocity, the authors developed a 3D thermo-mechanical finite element model of a plain (rectangular) radial Ring Rolling process of Ti-6Al-4V rings. The numerical model was validated with similar experiments, with which there was a relatively good agreement. Additionally, the effects of various parameters (e.g. roll diameter, rotational velocity, blank initial dimensions etc.) on the thermo-mechanical behavior of the manufacturing process were tested with the developed model.

The same year, Hua, Qian, and Pan developed a FEM model of the Ring Rolling process of a L-shaped profiled ring, in order to study the plastic deformation mechanism (**Hua, Qian, and Pan, 2009**). The authors presented a simplified 3D finite element model of an L-shaped profile Ring Rolling process, which was subsequently validated with similar experimental procedures. A step-by-step study of the numerical model results revealed that the plastic deformation during the Ring Rolling process began from the outer surfaces of the blank and progressively extended towards the mean radius of the ring. Afterward, variations of the developed model were used, in order to evaluate the effects of feed and initial blank dimensions on the plastic deformation occurring during the process. Furthermore, a distinct movement analysis (solitary rotation, solitary feed and combined rotation and feed) was conducted for the same reason. All of the aforementioned analyses were also validated with similar experiments. The same researchers presented another Ring Rolling related FEM work in 2011 (**Zhou, Hua, and Qian, 2011**). In this work, the authors developed and subsequently verified (experimentally and analytically) a finite element model of a plain (rectangular) Ring Rolling process, which was then used to investigate the effects that differences on the rolls' radii and angles brought to the manufacturing process. After the solution of the FEM model, the aforementioned effects on plastic strain distribution, roll force, torque and ring temperature were presented and discussed.

Again in 2009, Ramaprasad published his M.Sc. thesis regarding the finite element simulation of plain (rectangular) Ring Rolling (**Ramaprasad, 2009**). In this work, Ramaprasad created a 2D simplified Ring Rolling model, in order to clarify the plastic deformation mechanism and evaluate the effects of several parameters on the process. From the numerical results of various test cases, the author observed that feed was the main factor that defined the plastic deformation mechanism in the bite. Also, the effects of an increasing feed seemed to be further amplified with a simultaneous decrease of the rotational velocity. Moreover, the substitution of the initial aluminum alloy to a softer aluminum alloy seemed to have negligible effects on the deformation mechanism. Finally, the required roll force and power increased with the feed increase, thus resulting in a more costly Ring Rolling process.

The next year, Schafstall and Barth presented a new numerical approach for Ring Rolling, as well as other forming processes (**Schafstall and Barth, 2010**). The authors developed a 3D thermo-mechanical finite element model, in order to simulate a profile Ring Rolling process. Schafstall and Barth paid special attention to the facilitation of an automatic control routine, that would adjust the position of the tools. The calculated results from the FEM model were compared with similar experiments, where the tool position paths and final ring dimensions were very close to one another. The presented method was also used for the simulation of a cogging process, although the presented results for this method were limited.

Another relative work of 2010 was presented by Ceretti, Giardini, and Giorleo and involved the 3D simulation of a plain (rectangular) Ring Rolling process (**Ceretti, Giardini, and Giorleo, 2010**). The authors of this work developed a 3D finite element model, meshed with a finer mesh around the deforming segments, while several simplifications were considered in order to reduce some of the computational effort. Additionally, Ceretti, Giardini, and Giorleo estimated the movement patterns of the tools from an actual experimental procedure and input this data in the numerical model. After the finite element model was solved, the calculated results were compared with the results from the aforementioned experiments, with which a good agreement in the dimensional values was met.

Again in 2010, Vimalnathan and Mears presented a finite element model of a plain (rectangular) Ring Rolling process, developed with the commercial FEA software ABAQUS (**Vimalnathan and Mears, 2010**). The authors developed a 2D Ring Rolling simulation with a fairly fine mesh and then proceeded to simulate a plane-strain 3D analysis of the same process, initially. As Vimalnathan and Mears mentioned, the transition from the 2D to the 3D analysis was very complex, as a lot of different factors could drastically change the stability of the 3D simulation, something not faced in the 2D analysis.

The same year, Wang et al. developed a finite element model and an optimization routine in order to introduce the virtual manufacturing of a plain (rectangular) Ring Rolling process (**Wang et al., 2010**). Through a series of geometric relationships, the authors estimated the limiting value expressions of the tool velocities of the process. These expressions were then implemented in a finite element model created via the commercial FEA software ANSYS/LS-DYNA. The numerical results were compared to similar experimental results, with which there was fairly good agreement. What is more, the authors, based on the presented optimization routine, proposed an alternative version for the production of the same ring, which involved a different initial blank geometry and which would reduce the overall manufacturing time.

Another finite element related work was presented in 2010 by Anjami and Basti, which facilitated the finite element method in order to study the effects of rolls' size in Ring Rolling (**Anjami and Basti, 2010**).In this work, Anjami and Basti developed a 3D coupled thermo-mechanical finite element model, which was subsequently validated with similar experiments. After estimating analytically the limiting values of feed, roll radii and contact lengths, the authors performed several numerical tests and studied the effects of rolls' diameter, feed and ring thickness on plastic strain, contact length and temperature distribution during Ring Rolling. Moreover, the overall ring growth and *"fishtail"* defect differences, during the deviation of the aforementioned parameters, were also investigated. Finally, graphs showing the rolls' radii effects on roll force and torque were presented as well.

The following year, Lu et al. used a plain (rectangular) Ring Rolling finite element model, in order to verify a proposed deformation curve for the process (**Lu et al., 2011**). After establishing the velocity expressions for the tools, the authors proposed a three-phase deformation of the blank during the process, which was later validated with a similar finite element model. Although the results from the two methods were not very close, Lu et al. mentioned that an optimum deformation curve could be estimated from the combination of the numerical and the proposed curves.

Again in 2011, Guo and Yang published a book chapter on the finite element modeling of radial-axial Ring Rolling processes, mainly aimed at aerospace applications (**Guo and Yang, 2011a**). After noting the requirements of the aerospace industry and how they could affect relative Ring Rolling products, the authors presented some of the most important parameters of a Ring Rolling simulation. The presented method was validated with similar experiments, with their results considered to be close. Additionally, a test case was simulated with the proposed method and the calculated numerical results were presented in this work. The same authors further the aforementioned work in **Guo and Yang, 2011a**. In this work, the authors developed a full 3D coupled thermo-mechanical model of the process, using the aforementioned finite element methodology. Furthermore, a steady growth rate was proposed, while the limiting values for several process parameters were estimated. The developed model was subsequently validated with corresponding experiments, while a relatively close agreement between the two was achieved. Afterward, the presented FEM model was used in multiple tests cases with varying mandrel and conical roll feed values, in order to determine the range of parameters that ensured a steady ring forming. It is worth mentioning that both studies were conducted with the commercial FEA software ABAQUS/Explicit.

The same year, Gheisari, Forouzan, and Maracy developed a coupled thermo-mechanical finite element model of a profile Ring Rolling process, to research the effects of varying feed and rotational velocity values on it (**Gheisari, Forouzan, and Maracy, 2011**). The authors simulated a simplified version of an experimental Ring Rolling setup (with the guide rolls lacking) and validated their model with the experimental results of **Mamalis, Hawkyard, and Johnson, 1976**. Afterward, the same modeling technique was used to research the effects of increased feed and rotational velocity values on the resulting ovality of a plain (rectangular) ring.

In order to investigate the difference between a pure mechanical (with no temperature differentiation) and a coupled thermo-mechanical finite element approach, Anjami and Basti conducted a relative comparative research study in 2011 (**Anjami and Basti, 2011**). In this work, an ALE approach of a plain (rectangular) Ring Rolling was developed, which was then validated with similar experimental results found in the literature. Then, the authors used the validated model and investigated the difference that temperature dependence brought to the manufacturing process. Comparison between the two models revealed that the temperature differentiation of the coupled thermo-mechanical model caused an increase in the yield strength of the material, thus increased roll forces and reduced ring spread were observed.

Again in 2011, Wang and Hua further progressed the work presented in **Hua et al., 2007**, by analyzing the guide roll variations of vertical Ring Rolling setups via FEM (**Wang and Hua, 2011**). After a brief description of the different guide roll setups and their corresponding mechanics for vertical Ring Rolling mills, the authors presented a 3D coupled thermo-mechanical plain (rectangular) Ring Rolling FEM model, in order to investigate the different effects of each of the presented guide roll setups on the manufacturing process. More specifically, the effects on the ring ovality (here mentioned as *"roundness error"*), eccentricity, as well as the final ring dimensions were researched. From the aforementioned study, an optimum guide roll setup was proposed. Additionally, the Wang and Hua compared the numerical results of two specific guide roll setup with similar experimental results, the two of which could be considered to be relatively close.

Another finite element related work was presented by Zhou et al. in 2011, regarding the utilization of the FEM method for the simulation of large aluminum Ring Rolling processes (**Zhou et al., 2011a**). In their work, the author developed a finite element model of a plain (rectangular) Ring Rolling process, which they proceeded to validate with corresponding experimental data. After the numerical model was solved, various equivalent plastic strain zones were observed on cross-section of the deformed blank, some of which could possibly lead to the creation of defects. Thus, a new Ring Rolling plan was proposed, which could lead to a more uniform deformation across the ring's cross-section. Moreover, the effects of different process parameters were also discussed.

The simulation of the manufacturing of large rings was also discussed in **Wang, 2011**. In this work, Wang simulated the hot plain (rectangular) Ring Rolling process of a large titanium alloy ring. From the numerical results, the stress and strain distribution fields per time increment around the bite were examined, thus the dependence of these fields with mandrel feed and initial blank dimensions was discussed. What is more, the most potent crack initiation points, based on the developed stress fields, were also mentioned.

Another work regarding the simulation of large ring manufacturing was presented by Zhou et al. the following year (**Zhou et al., 2012**). In this work, the authors utilized the FEM method to simulate the plain (rectangular) Ring Rolling of large steel rings. After the solution of the model was completed, the temperature and dimensions results of the simulation were compared with corresponding experimental results. Moreover, the effects of axial roll feed on plastic strain, temperature, axial and radial roll forces and axial and radial torque values were also investigated.

The same year, Zhu et al. researched the effects of total deformation and blank temperature on the final microstructure of titanium (Ti-6Al-2Zr-1Mo-1V) alloy rings, via finite element modeling (**Zhu et al., 2012**). After mentioning the constitutive equation and grain growth laws for the used titanium alloy, the author proceeded to evaluate the effects from the number of Ring Rolling passes and forming temperature on the resulting ring microstructure via two separate finite element models. The first model involved a compression simulation of a curved specimen, which was also validated with similar experimental results. The second model involved the simulation of multiple passes of a disk Ring Rolling process, from which the developed material grains were predicted as a function of the blank temperature and the total number of passes. The numerical results from both simulations were evaluated, while the differences between them and the corresponding experimental results were considered negligible.

The same research group presented another numerical work in 2012, regarding the effects of tool movement in Ring Rolling (**Wang, Yang, and Guo, 2012**). In this work, Wang, Yang, and Guo developed a plain (rectangular) Ring Rolling model of a titanium (Ti-6Al-4V) alloy ring, which was used to investigate the effects of varying feed and rotational velocities on radial roll force, plastic strain, deformation and temperature change of the manufactured workpiece. The authors concluded that a relatively high feed value would produce the best manufacturing results, but simultaneously an increase of roll force would also be expected.

Again in 2012, Kim, Kim, and Jin used FEM method to propose a Ring Rolling schedule that would minimize the roll force requirements (**Kim, Kim, and Jin, 2012**). The authors developed a hybrid mesh plain (rectangular) Ring Rolling model, which was then validated with similar experiments. The aforementioned model was subsequently used to estimate an optimum feed plan for both the mandrel and the axial rolls. The proposed mandrel and axial roll feed plan were shown to minimize the radial and axial roll force requirements, respectively.

The effects of mandrel feed and rotational velocity on a conical Ring Rolling process were discussed in **Xiaotao and Fan, 2012**. In this work, Xiaotao and Fan developed a 3D finite element model of a conical Ring Rolling process with external formations (commonly used as a turbojet component), which was used to research the effects of different feed and rotational velocity values on the applied plastic strain. Based on the numerical results, the authors concluded that a combination of a relatively high feed and a low rotational velocity produced the most uniform deformation of the ring.

Another numerical work presented in 2012, involved the development and numerical testing of a novel controller for Ring Rolling setups (**Jenkouk et al., 2012**). The authors, developed and validated (through conducted experiments) an ALE finite element model, which was used to test the newly proposed closed-loop controller. In order to achieve optimum control, the estimated plan was adapted appropriately to each manufacturing process, with some process parameters being considered beforehand, while others being controlled in real time. The simulation results revealed the feasibility of adopting the proposed control system in an industrial setup, although not all process parameters could be successfully estimated (either from the finite element model or the experimental tests).

The next year, Qian and Pan published a novel work on the combined simulation of a steel blank preparation and its subsequent Ring Rolling (**Qian and Pan, 2013**). After presenting the equations governing the macro and micro-scaled behavior of the material, the authors proceeded to estimate the ranges of various process parameters for both the preforming and Ring Rolling procedures. Afterward, Qian and Pan developed five implicit finite element models, which were solved serially. The final dimensions and the temperature distribution calculated from the simulations were verified through similar experiments, with which they were in good agreement. Furthermore, the resulting plastic strain and temperature distributions were also used, in order to estimate the average material grain size developed during the manufacturing processes. From the evaluation of the aforementioned numerical results, it was revealed that the processes proceeding Ring Rolling may bring some inherent defects, resulting from the non-uniform state of the initial workpiece.

Again in 2013, Giorleo, Giardini, and Ceretti presented a plain (rectangular) Ring Rolling simulation performed via a newly proposed computational method (**Giorleo, Giardini, and Ceretti, 2013**). The authors developed an ALE hybrid mesh model via the commercial software DEFORM-3D. The numerical results were validated with experimental data received from a corresponding industrial process. Overall, the presented simulation was considered fairly accurate, although Giorleo, Giardini, and Ceretti mentioned that further research was underway. The same numerical method was used by the authors again in **Giorleo, Ceretti, and Giardini, 2013**. In this work, Giorleo, Ceretti, and Giardini performed a number of simulations, in order to determine the final dimensions of the blank before Ring Rolling. Subsequently, the effects from the initial blank height on Ring Rolling, in terms of roll force and power, as well as defect formation, were examined through via a conducted sensitivity analysis.

The effects from preforming the blank were also examined by Wang, Geijselaers, and Boogaard in **Wang, Geijselaers, and Boogaard, 2013**. In this work, the authors used a combination of 2D and 3D finite element models, in order to investigate the residual stresses on the blank from the preforming processes. Afterward, the simulation of the Ring Rolling process of the pre-stresses blank was performed and the final stress results were evaluated. Moreover, two different preforming processes were tested with their results compared with one another and with an ideally preformed (rectangular) blank. This work was further progressed in **Wang et al., 2014a**, where the authors investigated the effects of feed, on the evolution of defects during Ring Rolling using the same finite element modeling method. The conclusions of both these works were presented in detail in the Ph.D. dissertation of one of the authors two years later (**Wang, 2016**).

Another numerical work of 2013 was presented by Feng and Champliaud, which involved the coupled thermo-mechanical simulation of a plain (rectangular) Ring Rolling process (**Feng and Champliaud, 2013**). In their work, the author simulated the vertical, single guide-roll Ring Rolling of a steel ring. The workpiece was simulated with 10-node tetrahedral elements, which led to the minimization of *"fishtail"* defect. Moreover, the stress-strain results showed a greater stress concentration around the inner radius of the forming ring. The presented numerical method was also extended in profile Ring Rolling processes by the same authors in **Feng and Champliaud, 2014**. In their second work, Feng and Champliaud attempted to simulate the manufacturing of a T-section profile ring, using the previously presented numerical models. The final results were considered acceptable from the authors, although the optimization of the presented model was proposed.

Again in 2013, Kim et al. proposed a simpler version of the dual-mesh numerical approach of Ring Rolling (**Kim et al., 2013**). In this work, the authors simulated a vertical radial-axial profile Ring Rolling process, using three different remeshing techniques. Although the first of the three remeshing techniques was the same as the one met in past works (e. g. **Hu et al., 1994**), the other two newly proposed methods were connected to the active deformation of the remeshed finite elements, thus further reducing the overall simulation time.

The same year, Li, Feng, and Yang proposed a novel material model for cold Ring Rolling simulations (**Li, Feng, and Yang, 2013**). In their research, the authors proposed a polycrystalic plastic material model based on Taylor theory, which was implemented in an explicit finite element Ring Rolling model. With the newly proposed material, the calculated stress field from the simulation would be updated in two steps, thus taking into account the effects from the polycrystalic structure, while the evolved workpiece texture after the completion of manufacturing could also be estimated. Comparison between the numerical and similar experimental results revealed a close agreement between the two, while the strain percentage of the different ring sections was also derived from the evolved texture. Furthermore, the effects of the material texture before Ring Rolling were also investigated.

The possibility of using FEA as an assisting tool for the designing process in Ring Rolling productions was investigated in **Jenkouk, Hirt, and Seitz, 2013**. In this work, Jenkouk, Hirt, and Seitz proposed the implementation of finite element models as a design tool, through which the user can inspect the final manufacturing product with a high degree of accuracy. Furthermore, because of the difficulty of predetermining the exact motion of the tools, the authors proposed the utilization of an industrial control system, which would automatically update the tool positions through a close-loop routine. The proposed numerical system was facilitated in an axial profile Ring Rolling simulation that was also validated with corresponding experiments.

The same year, two novel numerical works were presented by a research team from RWTH Aachen University. In the first work (**Kebriaei, Frischkorn, and Reese, 2013**), the authors developed a finite element model, in order to simulate the powder coating of plain (rectangular) rings in a Ring Rolling process. After introducing the appropriate material and tool motion equations for the model, Kebriaei, Frischkorn, and Reese used the proposed model in order to simulate both the coated and the uncoated plain (rectangular) rings manufacturing. The numerical models were also validated with corresponding experimental results, with which there were in good agreement. Moreover, special attention was given to a newly proposed method for an optimum coat density control of the produced rings that was achieved through the precise angular position of the guide rolls. In the second work presented by the same research team (**Kebriaei et al., 2013**), the authors used the same numerical model, in order to test the effectiveness of several parameters on the final results. More specifically, Kebriaei et al. conducted both 2D and 3D simulations of powder-coated Ring Rolling processes, with varying values for mesh density, different types of mesh (uniform and hybrid), as well as different guide roll angles. The calculated numerical results were subsequently validated with similar experiments, again with good agreement between one another. It is worth noting that the second work is one of the few numerical research that included a mesh independence analysis, even if it was only performed in the 2D models.

Another innovative work presented in 2013 discussed the manufacturing of dish shaped rings on conventional radial-axial Ring Rolling setup (**Seitz, Jenkouk, and Hirt, 2013**). In their work Seitz, Jenkouk, and Hirtinvestigated the mechanisms around ring dishing and ring climbing, previously considered as manufacturing forming errors, in order to facilitate them and create dish shaped seamless rings of specific geometries. The authors used both experiments and finite element modeling in order to validate their investigations. Finally, Seitz, Jenkouk, and Hirt concluded that although facilitating ring dishing and ring climbing to create dish shaped rings is plausible, a great amount of control and stabilization of the process is required and thus additional tools and methods are required and should be developed first.

The same year, Wang et al. numerically calculated the microstructure evolution of a Ti-alloy ring during ring rolling (**Wang et al., 2013**). In their work, Wang et al. used the VUMAT routine of ABAQUS/Explicit to simulate the evolution of β phase grain size and volume fraction in the Ti-alloy of the ring during its manufacturing. Moreover, the effectiveness of main roll's rotational velocity and the feed of the mandrel on the alloy's microstructure evolution were also investigated. Although the authors do not validate the calculated results, they mention that their work could provide the theoretical basis for other similar works.

The following year, Wang et al. used finite element modeling, in order to simulate profile Ring Rolling in a vertical Ring Rolling setup (**Wang et al., 2014b**). In this work, the authors developed a numerical model that would simulate a bearing raceway manufacturing in a single guide roll, vertical Ring Rolling setup. Additionally, a newly proposed manufacturing plan was also tested through this model. The novelty of the aforementioned model lied with the inclusion of a measuring roll, which could be used to control the forming simulation iteratively, while also several dimensional characteristics of the product could be monitored accurately. The numerical results were validated through similar experiments, with which the authors mentioned that there was a fairly good agreement.

Again in 2014, two works involving the simulation of conical Ring Rolling processes were presented by the same research team. In their first work (**Meng and Zhao, 2014**), the authors presented the details of developing a numerical model for simulating conical Ring Rolling processes. What is more, the effects of ring diameter evolution and tool dimensions on the plastic strain and temperature distribution on the ring during the manufacturing process were discussed. In their second work (**Meng and Zhao, 2014**), Meng and Zhao used their previously presented finite element model, in order to investigate the effects of mass scaling, time scaling and remeshing repeats on the volumetric strain rate and overall solution time. The same research team further investigated conical Ring Rolling with another two works the same year. In **Meng, Zhao, and Guan, 2014b**, the effects from the tool dimensions on the temperature and strain distribution on the conical ring are investigated, while in **Meng, Zhao, and Guan, 2014a** the effects of the mandrel's feed on the final conical ring are researched.

The same year, a research team from the Wuhan University of Technology presented four works on a novel process for producing cylinders via Ring Rolling. In their first work (**Han**

et al., 2014b), Han et al. proposed a new method for producing cylindrical products by using a hollow roll around the blank, in a vertical Ring Rolling setup. A finite element model of the proposed process preceded the experimental validation, in order to estimate the values of various process parameters. After the completion of both the numerical and the experimental processes, their corresponding dimensional results were compared, with a relatively good agreement between them. Moreover, several simulations were performed, to investigate the effects of various process parameters on the final product and the applied roll forces. In their second work (**Han and Hua, 2014**), the authors gave special attention to the effects of varying friction coefficient values on the same process, regarding the final geometry of the product, as well as the applied forces and torque. This analysis was performed purely via the previously developed finite element model. In their third work, Han et al. numerically studied the effects of the blank's initial dimensions on the manufactured cylinder (**Han et al., 2014c**). In this research, the authors investigated the effects of changing the blank's height, outer diameter and thickness in a combined radial - axial cylinder ring rolling process to achieve the optimum result in terms of homogeneity and surface quality. Although simplistic, the results presented in **Han et al., 2014c** can be used to perform a design of experiment for the aforementioned process. Finally, in their final work (**Han et al., 2014a**), Han et al. introduced a follow-up radial-axial Ring Rolling stage after the previously presented process, in order to produce cylindrical rings with low thickness and without the axial defects introduced in the cylindrical Ring Rolling. The developed numerical model of the multi-stage cylindrical Ring Rolling was validated with similar experiments and was then used to investigate the effects of the intermediate (between the two stages) blank geometry on the final cylinder dimensions and the applied forces and torque.

A numerical model was also developed by Luo et al., in order to investigate the effects of varying rotational velocities in a Ring Rolling process of magnesium alloy blanks (**Luo et al., 2014**). In their work, the authors developed a finite element model of a plain (rectangular) Ring Rolling process, which was subsequently used to simulate the same process with different rotational velocity values. The numerical results from the models were then evaluated and the effects of rotational velocity on the strain and temperature distribution, roll forces and torque, as well as the *"fishtail"* defect evolution were revealed.

Another work presented in 2014, involved the facilitation of mapping the deformation of the ring's cross-sections, in order to estimate the formability of the ring during Ring Rolling (**Kil, Lee, and Moon, 2014**). In their work, Kil, Lee, and Moon developed a finite element model of several plain (rectangular) Ring Rolling processes, to map the deformation vs. temperature distributions for different initial blanks. From the numerical results, the authors estimated the efficiency of power distribution along various cross-sections of the blanks during forming, while they also proposed the *"Formability index"* that could combine ring mass and current deformation to provide a process uniformity index. This work was presented again, in more detail, in **Kil, Lee, and Moon, 2015**.

Again in 2014, Schwich et al. developed a finite element model that could estimate the developed microstructure of the ring during Ring Rolling (**Schwich et al., 2014**). In this work, the authors presented a coupled thermo-mechanical numerical model of a plain (rectangular) Ring Rolling process, while the appropriate material equations estimating grain growth and dynamic recrystallization were also considered. After validating the developed finite element model, the effects of several thermal and mechanical properties on the material grain evolution were evaluated.

The same year, Kang conducted a numerical analysis to investigate the filling ratio of profile Ring Rolling processes (**Kang, 2014**). In his work, the author developed a finite element model that was used to investigate the filling ratio in some specific profile Ring Rolling productions. After the completion of the simulations, Kang used the numerical results to verify the reliability and limitations of certain proposed indexes that could estimate the filling of the produced ring profiles.

The behavior of Inconel 718 blanks during Ring Rolling processes was researched numerically by Alkorta et al. in **Alkorta et al., 2014**. The authors in this work developed a coupled thermo-mechanical finite element model of an IN718 plain (rectangular) Ring Rolling, in order to calculate the strain and temperature distributions during the process. After simulating several test cases, the authors concluded that the current model was sensitive to the strain path followed during the process, thus proving that non-monotonous material properties should be considered for the blank, as they could result in a rather different deformation behavior.

A newly developed finite element model with an automatically updated movement of the tools was also proposed by Zhu et al. in 2014 (**Zhu et al., 2014**). In this work, after defining the mandrel and axial rolls' feed functions, the authors developed a routine that would read and adapt the position of the tools in every iteration of the finite element analysis. The proposed routine was facilitated in a finite element model, which was previously validated with experimental results, in order to ensure a greater degree of control and a more uniform ring deformation. Zhu et al., also conducted a series of simulations, in order to investigate the effects of different radial-to-axial feed rates on the process. From these simulations, the final geometrical results, as well as the strain and temperature distributions during Ring Rolling, were evaluated.

The same year, Lee et al. presented a finite element analysis for the simulation of excavator idler rim production (**Lee et al., 2014**). In order to simulate the profile Ring Rolling process of the aforementioned excavator component, the authors proposed a three stage finite element analysis, which combined with the proper process parameters would produce the desired product accurately. Furthermore, the strain distribution fields on the ring were also evaluated. The proposed numerical analysis was validated from similar experiments, while a comparison between the final rim dimensions from the two processes revealed a fairly good agreement.

The following year, Kim and Kim developed a numerical method for the simulation of profile Ring Rolling of rings with multiple layers (**Kim and Kim, 2015**). In their work, the authors presented two separate finite element models: (a) a 2D model used to estimate the blank geometry after preforming and (b) a 3D hybrid mesh model used to simulate the profile Ring Rolling process. The numerical models were validated with similar experiments, and the comparison between the two showed a relatively good agreement. It is worth noting that the hybrid mesh modeling technique was verified with a corresponding fine mesh model, prior to using this technique on the multiple-layered ring.

In 2016, Zhu et al. presented another numerical analysis on the simulation of conical Ring Rolling (**Zhu et al., 2016a**). In this work, the authors proposed a new method of calculating the volume of the conical ring in each iteration and verified their method via a previously developed finite element model. Moreover, the effects from different initial blank dimensions on the conical ring evolution, as well as the strain and temperature distributions, were investigated. From the numerical results of the different simulations that were conducted, the optimal initial blank dimensions were identified. The same research team presented another numerical analysis the same year (**Zhu et al., 2016b**). In their second work, Zhu et al. developed a coupled thermo-mechanical finite element plain (rectangular) Ring Rolling model, which was validated with corresponding experiments. Subsequently, a design of experiment was performed in order to estimate the optimal feed power law, which would ensure a smooth and uniform ring manufacturing. The estimated feed function was, then, facilitated in the presented finite element model. The results from this final model were compared to those of the initial numerical and experimental approaches and verified the feed function validity, in terms of optimal manufacturing conditions and less tool wear.

The same year, Hua et al. facilitated a stiffness law in the numerical model of a plain (rectangular) Ring Rolling process (**Hua et al., 2016**). After presenting the proposed parametric stiffness law, which estimated the bending moment of a section of the produced ring with the relative angle of the guide rolls as the free parameter, the authors proceeded to validate their analytical approach via a 2D finite element model. Additionally, several similar analytical approaches were compared to the presented one, with the latter being the most accurate. Based on the proposed analytical model, Hua et al. developed a 3D radial-axial finite element model of the large diameter plain (rectangular) Ring Rolling process, which was used to establish a relationship between the relative pressure of the guide rolls and the size of the ring. The aforementioned 3D finite element model was also validated through similar experiments that verified the analytical and numerical conclusions of this work.

Another numerical analysis presented in 2016 involved the development of a numerical model, in order to validate an introduced analytical work (**Quagliato and Berti, 2016**). In their study, the authors introduced a novel set of equations used to calculate the different strain components, as well as the equivalent strain in a ring segment. In order to further verify their analytical results, Quagliato and Berti also developed a finite element model with tracing particles, through which the effects from the initial blank geometry on the estimated strain fields were evaluated. From the comparison between the analytical and numerical results, a fairly close agreement between the two was revealed.

Again in 2016, Li et al. used finite element modeling, in order to test a proposed feed planning algorithm (**Li et al., 2016**). In this work, after presenting their proposed real-time feed predicting algorithm, the authors developed a 3D finite element model of a profile Ring Rolling process, in which the aforementioned plan was implemented. From the comparison between the different results, a good agreement between the predicted outer diameter evolution in both the numerical and analytical models was revealed.

The possibility of reducing profile Ring Rolling passes by using a pre-formed blank was discussed the same year by Park et al. in **Park et al., 2016**. The authors of this work developed a numerical model to simulate the profile Ring Rolling process of several (different) pre-formed blanks, in order to manufacture a complex cross-section ring used to manufacture heavy-machinery bearings and gears, in a single-pass. The numerical model results were compared to those of pre-existing experiments in terms of dimensional accuracy and forming defects, in order to identify the optimum combination of blank geometry and rolling path. Although no set of blank geometry and rolling path produced the precise final geometry, a specific set of the aforementioned parameters was identified that led to a final product with a relatively dimensional small error.

In order to simulate damage evolution during ring rolling, Wang et al. presented a numerical model with a proper material routine the same year (**Wang et al., 2016**). In this work, the

authors created a model in LS-DYNA with a user-defined material routine, which can simulate the creation of porosity during ring rolling. The simulation results were compared to corresponding ultrasonic experiments and metallographic investigations. Overall, a good agreement between the numerical and experimental/metallographic results was reported by the authors.
The same year, Seitz et al. developed a finite element model, in order to simulate the Ring Rolling process of a composite ring (**Seitz et al., 2016**). In their work, the authors investigated numerically different forming scenarios of a plain (rectangular) Ring Rolling process of a ring blank composed of two separate materials. The developed finite element model was validated with similar experimental processes, with which a good agreement was achieved. The validated numerical model was subsequently used to investigate the influence of material thickness in the blank, as well as the influence of material properties and tool dimensions. Moreover, different experimental setups were also tested via FEM. This work was further progressed by the same researchers in **Guenther et al., 2017**. In their second work, Guenther et al. studied the bonding condition of a composite blank during Ring Rolling. Via their validated finite element model, the authors were able to pinpoint the process parameters that could lead to a fully bonded product or a final ring that was easy to debond or not bond at all. In order to simulate these conditions, Guenther et al. introduced a proper numerical subroutine in their finite element model. Moreover, members of the same research team published another work in 2016, regarding the use of conical modules on the support rolls of a traditional Ring Rolling mill, in order to achieve better and more consistent results when producing dish-shaped rings (**Seitz, Kordtomeikel, and Hirt, 2016**). In this work, Seitz, Kordtomeikel, and Hirt simulated the dishing Ring Rolling process of a steel ring, with the simultaneous ring axis shifting and use of conical modules on the support rolls. The simulation results were compared to corresponding experiments, with a relatively good agreement reported between the two. It is worth noting that Seitz, Kordtomeikel, and Hirt in **Seitz, Kordtomeikel, and Hirt, 2016** paid special attention in presenting the parameters for an optimum simulation of the discussed process. Finally, in ESAFORM 2016 conference, Schwich, Jenkouk, and Hirt presented an additional work discussing the kinematics of Ring Rolling tools (**Schwich, Jenkouk, and Hirt, 2016**). In this work, the authors presented some simple kinematic laws for all of the tools of a traditional Ring Rolling mill and proceeded to test the accuracy of these laws with finite element models. The conducted finite element analysis involved the Ring Rolling simulations of steel rings. The simulation results were compared to those of corresponding experiments, with a relatively good agreement reported between the two in terms of dimensional accuracy, load and torque.

Finally, another numerical work presented in 2016, involved the simulation of polygonal shaped ring production via Ring Rolling (**Arthington et al., 2016**). In this work, the authors developed an optimum mandrel feed plan that allowed the creation of a polygon-shaped product. The proposed plan was implemented in a finite element model, where different forming scenarios were tested. The developed finite element model was also validated experimentally, through a clay Ring Rolling process. The geometrical results from both the experimental and the numerical processes were in fairly good agreement with one another.

The following year, Franchi et al. developed a finite element model, in order to predict the microstructure evolution during a Ring Rolling process (**Franchi et al., 2017**). In this work, the authors simulated a plain (rectangular) Ring Rolling process via finite element modeling, which was subsequently used to test the effects of tool velocities on the ring microstructure. The microstructure evolution was estimated by the Avrami equations, while the proper equation parameters for the used material were found in the literature. From their numerical model, Franchi et al. estimated an optimum set of velocities, which led to a minimization of grain size. It is worth noting that no analytical approach or experimental validation of the model was conducted in this work.

Another numerical work presented in 2017 was conducted by Han et al. and involved a novel approach of producing eccentric rings (**Han et al., 2017**). In this work, the authors proposed the production of eccentric rings by enclosing the blank in a casing with an eccentric inner gap. As the combined body of blank-casing rotated around a fixed rotation axis dictated by the guide rolls, the workpiece ended up covering the voids of the casing's eccentricity, thus producing a counter-eccentric (compared to the casing) final product. The whole process shared the same manufacturing principles with cylindrical Ring Rolling, as the same setups were used. In order to test their approach, the authors developed a finite element model, which helped investigate the deformational behavior of the workpiece, as well as the roll forces. Furthermore, some major defects of the process were revealed. Based on the numerical results, Han et al. proposed an optimum blank geometry, which would counter the aforementioned defects. For this workpiece, an experimental process was also conducted, which produced good results overall.

During the 7th annual congress of WGP held in October of 2017, Krämer et al. presented their work, where they proposed a coupling between a finite element simulation of a ring rolling process and a simultaneous microstructure prediction (**Krämer et al., 2017**). In their work, Krämer et al. successfully coupled Simufact.forming (finite element simulation tool) and StrucSim (microstructure evolution tool) software programs while simulating the consecutive stages of an IN718 turbine disk manufacturing. The whole process was performed two times: one where the simulation and microstructure solutions were coupled and another where they were not. The results from both processes were compared to a set of experimental results, in order to be validated. The comparison between those results revealed an underestimation of the ring rolling load in the numerical models, which the authors attributed to differences in the process parameters and the material properties used in simulation. Thus, this work can be better considered as a proof of concept for the coupling of the finite element simulation and the numerical microstructure prediction for the manufacturing process of ring rolling.

The same year, Peng et al. developed the numerical models of a plain (rectangular) and a profile Ring Rolling, in order to investigate the effects of the conical and axial rolls' movement on each process (**Peng et al., 2017**). After presenting the equations estimating some crucial process parameters and the basic mechanics of the process, the authors developed two separate coupled thermo-mechanical finite element models: (a) a plain (rectangular) Ring Rolling model and (b) a profile Ring Rolling model. In both of them, a sensitivity analysis regarding the guide and axial rolls' movement was conducted. Additionally, an adaptive guide and axial roll controller was also developed and tested on the finite element models. After the simulation bore acceptable results, the now refined controller was implemented in an experimental setup. A comparison between the experimental and numerical results revealed a good agreement between the two.

Another work presented in 2017 by Tang et al. involved the use of a unified ISV material model to predict the microstructure evolution during ring rolling of an IN718 ring (**Tang et al., 2017**). The authors, after a brief explanation of the material model, presented the results of a multistep radial-axial ring rolling process. The microstructure evolution results predicted by the model were then compared to the metallographic observations of corresponding experiments, with a relatively good agreement between the two. Furthermore, the effects of mandrel and main roll diameters, initial blank temperature and rolling ratio on the microstructure evolution were investigated.

The next year, Hua et al. presented a numerical work on the microstructure evolution of the workpiece during hot Ring Rolling (**Hua et al., 2018**). In this work, after presenting the recrystallization laws for the used material, the authors developed a coupled thermo-mechanical finite element model of a hot plain (rectangular) Ring Rolling process, in which the aforementioned laws were implemented. The developed numerical model was validated with similar experiments, with their results being relatively close. Moreover, Hua et al. investigated the effects of the mandrel's feed pattern on the microstructure evolution via their numerical model and the optimum feed rate for achieving a relatively uniform microstructure was mentioned.

Again in 2018, Oh et al. studied the manufacturing defects of an L-shaped profile ring (**Oh et al., 2018**). The author in this work developed a finite element model of a specific industrial production of a L-shaped ring. Through step-by-step monitoring of the simulation, the roots of cause for the forming defects were noted and the deformation mechanisms were clarified. The developed model was validated for a number of tests with similar experiments, with the defect positions and sizes being close in both cases. Finally, the authors estimated via the finite element model the optimized initial blank and mandrel geometries, which would help reduce the observed manufacturing defects. The proposed geometries were subsequently tested experimentally, with the produced rings being significantly improved in terms of manufacturing defects.

The same year, Li et al. presented two numerical works, in which the same finite element model was used (**Li et al., 2018** and **Liang et al., 2018**). In the former work, after proposing the guide roll movement analytical model, Li et al. developed a coupled thermo-mechanical finite element model of a profile Ring Rolling process, in which the aforementioned guide roll control method was implemented. The numerical results revealed that the process was rather stable, with the ring oscillation and ovality errors being relatively small. In their later work, Liang et al. used the same finite element model, in which a real-time force adaptive controller was implemented. The developed controller would measure the radial force value in each time increment and, based on a pre-determined target radial force-mandrel feed curve, it would appropriately adapt the response of the tools. The simulation results revealed a relatively good fitting between the control and the achieved force curves, while the deformation of the workpiece was fairly uniform throughout the process.

Also in 2018, Sun, Xu, and Xing investigated the effects of mandrel feed on the forming quality of cold-rolled rings, both numerically and experimentally (**Sun, Xu, and Xing, 2018**). In this work, the authors created a numerical model to investigate the effects of mandrel feeding velocity and number of feed curve steps on the geometric and force results of a cold-rolled steel ring. The numerical results were compared to corresponding metallographic observations and the optimum mandrel feed conditions were determined.

The effects of rotational velocity of the main roll on the final geometry of the ring were discussed by Allegri, Giorleo, and Ceretti in 2018 (**Allegri, Giorleo, and Ceretti, 2018**). In this work, the authors simulated the Ring Rolling process of a steel ring with three different rotational velocity patterns (one increasing, one constant and one decreasing). The geometric results from the three simulations were compared to one another. From this comparison, the increasing rotational velocity pattern was deemed superior to the other two. The same authors continued this work the following year (**Allegri, Giorleo, and Ceretti, 2019**). In their second work, Allegri, Giorleo, and Ceretti investigated the optimum roll gap per rotation through three different simulations, with respect to the ring thickness per ring height ratio. Afterward, the geometric results from these simulations were compared to one another and the optimum roll gap per rotation was found. Finally, the optimum roll gap per rotation was tested with three different rotational velocities. From the comparison between these final simulations, it was proved that the lowest rotational velocity produced the most geometrically accurate ring, with the least fishtail defects.

Another work of 2018 was presented in the 9^{th} International Symposium on Superalloy by Büscher and Witulski (**Büscher and Witulski, 2018**). In this research, the authors created a 3D ring rolling model, while the appropriate equations for the prediction of recrystallization and grain growth were also considered in the simulation. The constants for these equations were defined from experimental data. Moreover, a process monitoring procedure was also utilized, using envelope curves for various process parameters to increase the uniformity of the final products. The numerical model was used to predict the microstructure and some important mechanical properties (e.g. its ultimate tensile strength) of two separate products, a flat and a profiled ring. The final numerical results were in good agreement with their corresponding experimental results.

The following year, Teja et al. presented an implicit Ring Rolling simulation (**Teja et al., 2019**). The authors created a 3D cold Ring Rolling model using ANSYS Mechanical Enterprise 14.5 in a static structural analysis. Aluminum 6061 was chosen as the material for the workpiece, while structural steel was chosen for the rolls. After the simulation, various results including the deformation fringes and the maximum equivalent Von Mises stress values were presented. However, the presented results were very low compared to the expected values from the forming of Al6061, something that the authors failed to mention at all. Also, the choice of simulating Ring Rolling via a static structural analysis can also be characterized as inappropriate.

Again in 2019, Brosius, Tulke, and Guilleaume tested a novel thermo-mechanical Ring Rolling process through finite element analysis (**Brosius, Tulke, and Guilleaume, 2019**). In this work, the authors tested the simultaneous controlled cooling of the ring during Ring Rolling, in order to introduce an in-process quenching of the workpiece. In order to validate the proposed process methodology, the authors created a 2D numerical model, while also performing the corresponding experiments. The microhardness results from the experimentally manufactured rings were compared to the plastic strain results of the numerical model, where a correlation between the two was proven.

Another work presented in 2019, involved the design of rolling paths (movement of tools in ring rolling) through the measurement of ring temperature (**Li et al., 2019**). In this work, Li et al. used a ring temperature-driven, tool motion subroutine to design the optimum tool paths during the simulation of a Ring Rolling process. Based on this methodology, Li et al. proceeded to investigate the effects that initial ring temperature and initial mandrel feed velocity had on the designed rolling paths. Although this seems to be a very interesting methodology, no experimental results that would validate the aforementioned procedure are presented by the authors.

The following year, Han, Hua, and Yang presented a new approach on the polygonal ring rolling process (**Han, Hua, and Yang, 2020**). In this work, the authors simulated an alternative process of creating polygonal rings, where a ring blank is placed inside a polygonal, immovable matrix. Afterward, a freely moving mandrel presses the blank against the matrix's inner walls, giving it the desired polygonal shape. Han, Hua, and Yang tested four different tool paths, in order to identify the optimum in terms of workpiece dimensional accuracy and lowest forming defects. Moreover, corresponding experiments of a soft clay workpiece were also conducted, in order to provide the necessary validation for the proposed process. It is worth noting that the current methodology, although called ring rolling, is more similar to a close-die forging process in terms of tool mechanics.

Again in 2020, Arthington, Havinga, and Duncan presented a methodology of manufacturing rings with variable thickness and/or curvature throughout their perimeter (**Arthington, Havinga, and Duncan, 2020**). In this work, the authors attempted to control the tools of a ring rolling setup, in order to manipulate the overall shape of the manufactured ring. In order to achieve a good dimensional accuracy, a combination of image analysis and active tool control was used. Afterward, Arthington, Havinga, and Duncan performed the numerical simulations on two target ring shapes (a D-shaped one and a square one), while they also performed the corresponding experimental validation using soft clay. The comparison between the results from the two methods revealed a relatively good accuracy of the proposed methodology.

The same year, Lisiecki et al. simulated the whole process cycle for the production of large rings, with special emphasis on the discontinuities of the material (**Lisiecki et al., 2020**). In this work, the authors used finite element analysis to simulate the upsetting, punching, piercing and ring rolling process steps of a large-sized ring manufacturing. From the analysis of the numerical results, special attention was paid to the relative density of the resulting ring, as well as to the movement of specific pre-determined points in the blank (representing material discontinuities) and their final position after the completion of ring rolling. The results from the overall analysis can be described as more qualitative than quantitative, as no validation of the finite element analysis was presented, while the scope of the current paper was rather vague.

Another work presented in 2020, involved the use of additional guide rolls, in order to control the temperature distribution of the manufactured ring (**Lohmar, Cleaver, and Allwood, 2020**). In this work, Lohmar, Cleaver, and Allwood simulated the radial ring rolling process of an IN718 with additional guide rolls, to investigate their effects on the temperature distribution and evolution of the ring during the process. After three different scenarios were simulated (with two, four and six guide rolls respectively), the authors concluded that the guide rolls play a major role on the temperature evolution of the ring, via the conducted heat through their bodies. Moreover, the simulations were performed for both thick and thin rings, to correlate the results to the thickness of the workpiece. Finally, Lohmar, Cleaver, and Allwood discussed the effects that different temperature evolution rates can bring to the microstructure of the manufactured ring.

In 2021, Lv et al. simulated the manufacturing of a complex cross-section steel rim through Ring Rolling (**Lv et al., 2021**). In this work, the authors used finite element analysis to simulate the radial-axial Ring Rolling process of a steel rim. Moreover, the effects of friction, feed and rotational velocity on the process were investigated. The simulation results were compared to corresponding experimental results, with a relatively good agreement between the two reported.

The same year, Lafarge et al. created a digital twin of an existing ring rolling setup to determine the optimum control strategy to achieve a desired ring microstructure (**Lafarge et**

al., 2021). In this work, the authors used an LS-DYNA model coupled with a deep neural network deformation model and a differential evolution algorithm for the estimation of the ring's temperature, in order to create a controller that could determine the control strategy that would produce a preset ring hardness. More specifically, the presented controller had the present and past deformation, temperature and microstructure data as inputs, in order to predict the process parameters that would achieve the target hardness in the ring. Lafarge et al. tested their digital twin model in two different cases with relatively good results. However, a facilitation of the predicted strategy on an experimental setup was not involved in this analysis.

The following year, Pressas, Papaefthymiou, and Manolakos simulated the elastic and thermal effects of a rectangular Ring Rolling process on the rolls (**Pressas, Papaefthymiou, and Manolakos, 2022**). In this work, the authors created a thermo-mechanical model of a rectangular Ring Rolling process, based on the experimental data presented in **Zhu et al., 2016b**. Three different sets of rolls were simulated: one completely rigid, a second with only elastic properties but no thermal expansion, and a third with the thermo-mechanical properties of the rolls considered. After validating the models, the results from the three simulations were compared with one another. From the comparison between these results, it was proven that the thermo-elastic deformations of the rolls were significant in terms of the final products dimensional accuracy, and thus they should always be compensated for.

Finally, the same group of authors presented another work two years later **Pressas, Papaefthymiou, and Manolakos, 2024**. In their most recent work, Pressas, Papaefthymiou, and Manolakos discussed the fundamentals of a novel, follow-up process to Ring Rolling, which they referred to as Reverse Ring Rolling. During this process, all tools move towards the center of the workpiece, thus shrinking the outer diameter of the product, to the expense of an increase in its height. Pressas, Papaefthymiou, and Manolakos proved numerically the feasibility of the aforementioned process, while the presented results led to a fairly dimensionally precise final product.

1.2 Fundamentals of Ring Rolling Process

Ring Rolling is mainly facilitated in order to produce seamless circular products of varying cross-sections. Based on the geometry of the product, the production setups may vary a lot in terms of tool geometry and number, although the same mechanics take place in every Ring Rolling process. Furthermore, the process parameters are heavily dependent on the material and the complexity of the final product. A typical flat Ring Rolling setup is presented in Fig.1.1:

During Ring Rolling, the workpiece is constantly rotated by the main roll while the workpiece's thickness is constantly reduced through the mandrel - main roll gap reduction. Because of the circular interfaces of the tools and the workpiece, as well as their rotating motion throughout the process, Ring Rolling can be characterized as a highly unstable process. Thus, the use of support rolls for stabilizing the side oscillation of the workpiece during the process is considered mandatory. Based on the number and position of the support rolls, different setups can be considered with slight variations on the mechanics of the process. Finally, in order to reduce and control the height of the final product, a pair of axial conical rolls is also facilitated that is used to control the height of the final product.

The aforementioned mechanics of a common Ring Rolling process show clear signs of a

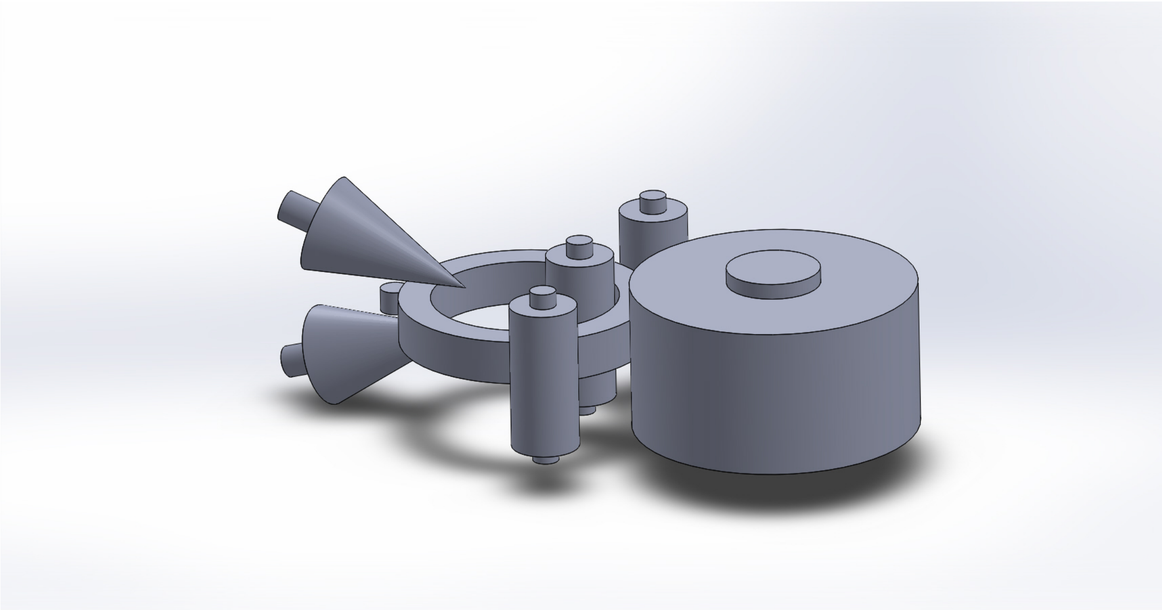

FIG. 1.1: Typical flat Ring Rolling setup

nonlinear process. A nonlinear structural process can involve the following factors responsible for the nonlinear behavior of the system (**Silveira, Pereira, and Gonalves, 2008**):

- *Geometry*: Shape-related effects on the stiffness of the system (e.g. non-constant shapes throughout the volume, drastic geometric changes during a process, etc.)
- *Material*: Stiffness changes due to the differentiations caused by the behavior of a material under stress (e.g. elastoplasticity, creep, etc.)
- *Kinematics*: Alterations in stiffness due to non-constant boundary conditions and contacts (e.g. on again - off again contacts, sudden object releases during a process, etc.)
- *Applied loads*: The application of time-dependent (non-constant) loads (e.g. vibrations, detonations, etc.)

Ring Rolling as a manufacturing process can be performed either cold or hot. Usually, a combination of both a hot and a cold stage of the process is practiced, in order to come close to the required dimensional accuracy of the final products. More specifically, the majority of thickness reduction in the blank is performed as a hot process, which allows for reduced main roll and conical roll loads and thus less energy requirements and tool wear. Once this part has been completed, the final few ring thickness millimeters are then reduced during a cold ring rolling process. This practice helps to reduce the fishtail and bulging defects, while an increased dimensional accuracy and a better surface quality can be achieved. However, in most industrial productions an exact dimensional accuracy is rarely or never achieved, as the rough processes of blank upsetting and protrusion, which always precede a ring rolling process, add a margin of uncertainty regarding the exact volume of the blank. With the blank's volume being impossible to be accurately estimated beforehand, the final dimensions of the final ring product tend to vary from the planned dimensions. Thus, several cycles of grinding and finishing processes usually follow a ring rolling process, in order to achieve the target dimensions of the ring (**Wu et al., 2019**). It is worth noting that warm plain (rectangular) Ring Rolling was also discussed in **Han et al., 2017** as a practice, however there are no known industrial applications of warm Ring Rolling.

The phases of a typical Ring Rolling process (**Yun and Cho, 1985**) are presented in Fig.1.2:

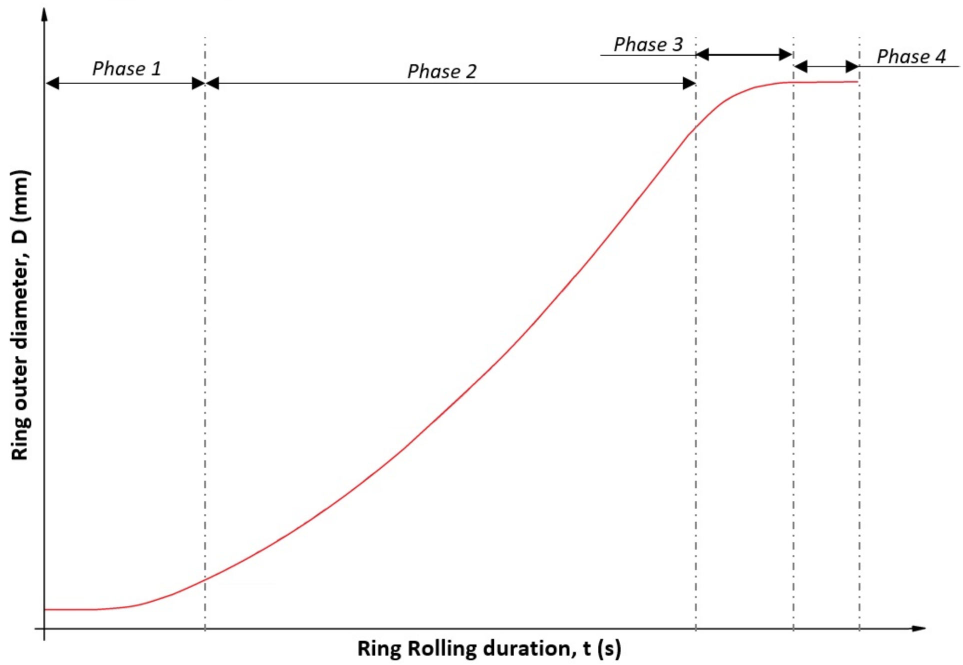

FIG. 1.2: Phases of a typical Ring Rolling process

In Fig.1.2 four different phases of the process can be distinguished. In each phase, different movement pattern are in effect for each tool, with their results being observed on the produced ring (**Meng, Zhao, and Guan, 2014a**):

1. In *Phase 1 (biting-in stage)*, the mandrel begins to move towards the main roll with a constant velocity, while the main roll begins to rotate with a constant acceleration until it reached its final rotational velocity. Because the feed of the mandrel is very low, the increase of the ring's outer diameter is usually very small (compared to the outer diameter of the final product). Additionally, the conical rolls begin the axial reduction of the blank during this phase. The duration of *Phase 1* depends on the properties of the setup and the initial ring blank, as the mass of the tools and the distance that the mandrel has to cover in order to have a constant and steady bite of the blank, are variable.

2. In *Phase 2 (steady forming stage)*, all tools have reached their final velocities and the thickness and height reduction of the blank proceed almost steadily. During this phase, the majority of the blank's forming is performed, and *Phase 2* concludes when the mandrel and the conical rolls stop their linear movements.

3. In *Phase 3 (final rolling stage)*, both the mandrel and the conical rolls have seized to move linearly, and the ring continues to rotate. During its rotation, the ring's variable thickness segments pass through the bite and a ring with a constant thickness occurs.

4. In *Phase 4 (roundness correction stage)* several more rotations of the ring are performed, in order to correct the ovality of the final product by equalizing the final thickness throughout the ring's perimeter, while also some large scale defects of the ring (e.g. ring bending) can often be corrected. Because no further thickness or height decrease occurs on the ring, the increase on the ring's outer diameter is very limited. Moreover,

it is very common during this phase, for a rapid cooling of the ring and an increase of the rotational velocity of the main roll to be simultaneously conducted, in order for the last rotations of the ring to be performed as a cold rapid process. Because of this, any forming defect on the ring (e.g. bulging, fishtailing, etc.) can be eradicated (via high strain rate, severe plastic deformation), while an increased surface hardness on the product can be achieved.

It is worth noting that additional heating cycles can interrupt the phase diagram presented in Fig.1.2, if the workpiece's temperature falls below annealing temperature or if the forming load is too great for the ring rolling setup capacity. However, a certain duration of Phase 4 can be performed in cold, to achieve higher dimensional accuracy and better surface quality.

Ring Rolling can be used to process a wide range of materials. Most commonly, either steel rings and nickel-based superalloy rings are manufactured, as these material families cover the largest amount of potential applications (e.g. bearings and other common engineering components, jet engine casing, etc.). However, materials such as aluminum, titanium and copper alloys have also been reported to be used in Ring Rolling (e.g. **Lee et al., 2017**, **Kim et al., 2007**, **Teja et al., 2019**, **Koo et al., 2003**), to produce various components varying from structural parts (e.g. aluminum bicycle wheels, titanium reinforcement rings, etc.) to more precise seamless ring components (e.g. copper motor short circuit rings, aluminum gears, etc.).

1.3 Applications of Ring Rolling Products and Recent Trends

As seen in section §1.1 the process underwent a number of changes, which resulted in the production of variable of ring products. These include plain (rectangular cross-section) rings (e.g. **Zhu et al., 2016a**) profiled and complex cross-section rings (e.g. **Barve, 2005** and **Lv et al., 2021**), cylinders (e.g. **Han et al., 2014a**) and even polygon-shaped products (e.g. **Arthington et al., 2016**).In the current section, these alternative forms of Ring Rolling are presented.

This large variability of the process allows for the manufacturing of seamless ring components aimed at many different aplications. Some major industries using seamless ring components are the following (**Group, n.d.(a), Ferralloy, n.d.**):

- *Aerospace industry*: Seamless ring components are used from simple aviation and space components (e.g. bearings, valves, etc.) to more vital components (e.g. jet-engine casings, helicopter gearboxes, space vehicle wheels, etc.). More exotic seamless ring components can be manufactured especially for space applications (e.g. precise, large diameter propulsion engine casings).
- *Automotive industry*: Multiple automotive part involve seamless ring components (e.g. bearings, axle drive wheels, brake disks, etc.).
- *Railway industry*: Traditionally, railway wheel rims are manufactured through Ring Rolling. Other applications involve bearing, hydraulic clutch components, spring rings, etc.
- *Electric power generation industry*: Regardless of the type of electric power generation plant, seamless ring components can be found in multiple parts of such plants (e.g. valves, flanges, etc.). In this case, too, more exotic components are also made through Ring Rolling, such as shell segments of pressure vessels.

- *Oil & Gas industry*: Seamless ring components can be found in parts and machinery used in both the extraction and manufacturing stages, in oil & gas industries (e.g. pipe fittings, valves, manway and vessel rings, shell of glass-lined reactors, etc.).
- *Marine and Shipbuilding industry*: Seamless ring components are used in ships (e.g. propeller shaft sleeves, bearings, etc.), submarines (e.g. manway rings, reinforcement rings, etc.), as well as other marine applications (e.g.submarine pipe fittings, valves, etc.).
- *Wind turbine manufacturing*: Some of the most important wind turbine parts involve seamless ring components (e.g. mast flanges, gearboxes, etc.).
- *Manufacturing industry*: As with much industrial machinery, manufacturing process setups involve multiple parts made with seamless ring components (e.g. deflector rolls, bearings, gearboxes, etc.).
- *Heavy-duty machinery*: Likewise to automotive industry, seamless ring components can be found in the vehicle parts of heavy-duty machinery (e.g. bearings, wheels, wtc.), while other ring components are used in their work-performing parts (e.g. bevel and swivel gears, swing bearings, pullies, etc.).
- *Robotics*: Several of the parts used in robotics applications involve seamless ring components (e.g. bearings, synchronizer rings, sliding coupling sleeves, etc.).

Over the last few years, several of the aforementioned applications have known increased interest. These mainly involve the automotive industry, where a turn to electric vehicles demanded for a decrease in component weight and wind turbine manufacturing, as green energy applications are gaining increasingly more space in the energy market every year. This fact has led researchers to find ways that could further improve the Ring Rolling process. Some of the most recent trends that are being researched at the moment are the following:

- *Flexible Ring Rolling setups* – Researchers from Cambridge University have published several works of a novel Ring Rolling setup with several independently-controlled support rolls, which can produced variable thickness and differently shaped ring components (**Group, n.d.(b)**).
- *Ring Rolling setups coupled with induction heating* – SMS Group has recently presented a novel Ring Rolling setup coupled with an induction heating system, which can accelerate the whole process by eliminating the intermittent reheating times (**Gellhaus and Langejürgen, n.d.**).
- *Ring Rolling setups including real-time ring manipulation systems* – SMS Group has filed for a patent of a Ring Rolling setup including a real-time robotic ring manipulation systems, which allows both for a faster loading and unloading of the manufactured items and for a more localized manufacturing of the workpiece (**Michl, Neumann, and Brenner, n.d.**).
- *Larger Ring Rolling setups* – The Chinese company Wuxi Paike New Materials Technology Co. placed an order on 2020 for a large-scale rolling mill capable of manufacturing jet engine rings with a height of up to 1500 mm and a diameter of up to 10 m (**Magazine, n.d.**).
- *Ring Rolling of additive manufacturing products* – The coupling of additive manufacturing and Ring Rolling has been discussed in many research publications (e.g. **Michl, Sydow, and Bambach, 2020**), with the majority of them discussing the successful

Ring Rolling of printed ring blanks. Should the coupling of these processes finally produces acceptable results, the time of Ring Rolling post-processes is expected to be significantly reduced, even eliminated completely.

Although Ring Rolling is a rather common manufacturing process, because of the need for seamless ring components in industry, in Greece there are no such industries. This can be attributed to the lack of major industries in the country that would function as the end-recipient of the aforementioned ring components. Thus, the few industries that require ring components, end up buying them from international markets. The only similar products produced in Greece are the small-scale copper and copper-alloy disks used for coins (e.g. from Epirus Metalworks, part of the Viohalco Group), however these are commonly manufactured through blanking and/or punching processes, and not Ring Rolling.

1.4 Fundamentals of Finite Element Analysis (*Zienkiewicz, Taylor, and Zhu, 2013*)

In most engineering applications, a system can be analyzed through a finite number of well-defined components. These systems are often call *discrete*. On the other hand, in cases where the behavior of a system can be described by an "infinite" amount of "infinitesimally" small components, such systems are referred to as *continuous*. Given the finite porous of a computational system, the analysis of a *continuous* system would seem impossible. However, it is possible to solve *continuous* system problems through mathematical manipulation. More specifically, if a system is discretized with a number of variables above a certain limit, then the behavior of a *continuous* system can be approximated. Mathematicians and engineers have approached these discretization techniques differently throughout the history, with the concept of *finite element method* being born eventually in 1960 (**Clough, 1960**). Since then, this method has evolved even more through the work of many researchers, as well as from the evolution of computational systems. Nowadays, finite element method is utilized widely in science and industry, with an emphasis on following purely mathematical and "direct analogy" approaches of existing problems. In general, the finite element method is regarded as *a general discretization procedure of continuum mechanics problems posed by mathematically defined statements*.

Over the years, a standard methodology has been developed to analyze *discrete* systems. In structural analyses, force-displacement relationships for each component of the assembly are calculated and then local equilibrium at each "node" or connecting point of the structure is established. The resulting equations can be solved for the definition of the unknown displacements. Similarly, in electrical and hydraulic analyses, a relationship between currents (fluxes) and potentials for individual elements is established, and then the system is assembled by ensuring continuity of said flows.

These analyses follow a standard pattern, which is common to *discrete* systems. It is thus possible to define a *standard discrete problem* with processes universally applicable, regardless of the field of science governing the analyzed system. Through the analysis of a *standard discrete problem*, an initial definition of the finite element method can be established. Thus, a *finite element method* is one that can be used to approximate continuum problems via the following steps:

- The continuum is divided into a finite number of parts (elements), the behavior of which is specified by a finite number of parameters.

- The solution of the complete system as an assembly of its elements follows precisely the same rules as those applicable to *standard discrete problems*.

Many individual mathematical and direct approximation procedures led to the development of present *finite element* methodology. A brief historical hierarchy of the most crucial of these procedures in the creation of the present-day *finite element method* is presented in Fig.1.3:

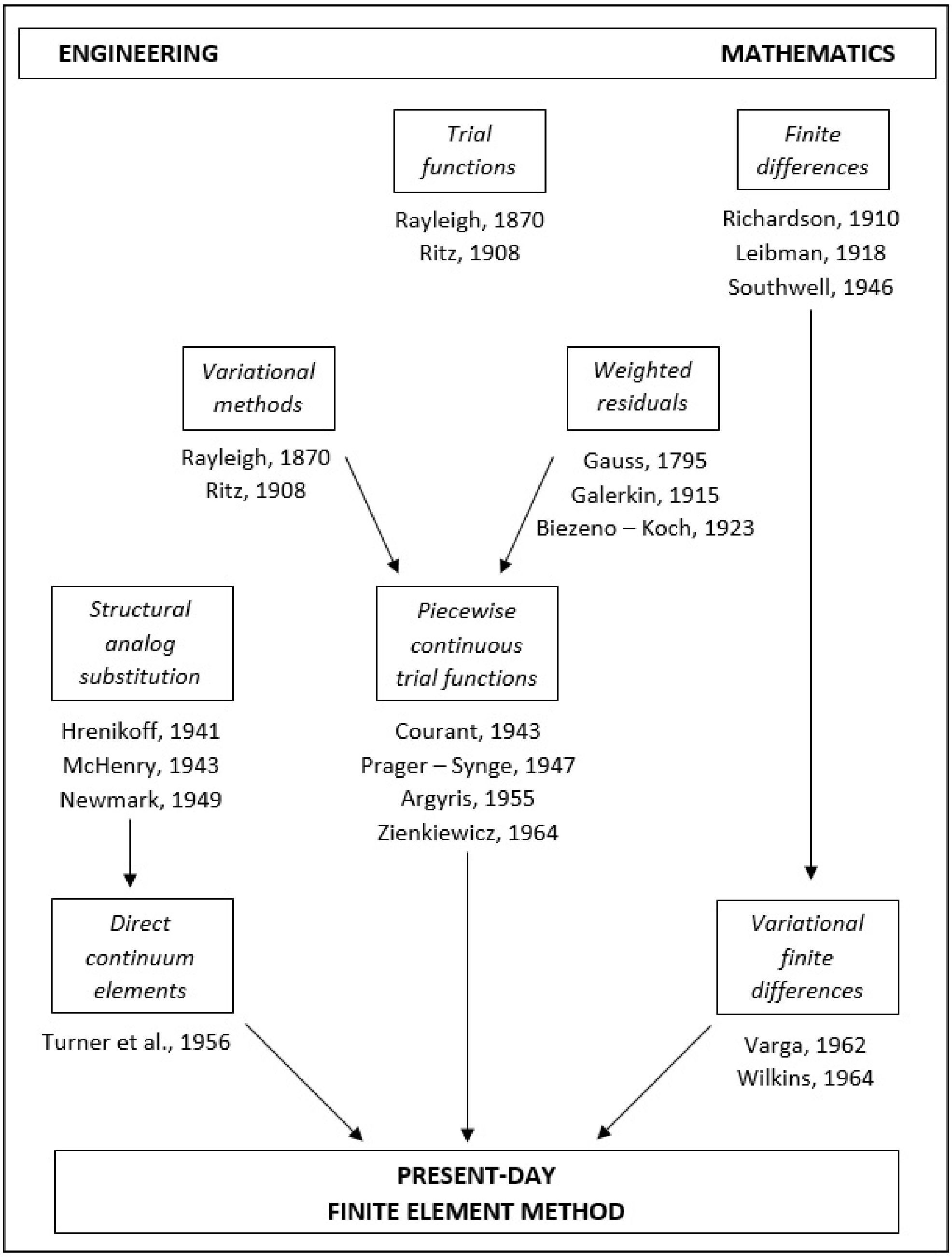

FIG. 1.3: Most crucial methodologies leading to present-day *finite element method*. (**Zienkiewicz, Taylor, and Zhu, 2013**)

It is worth noting that in Fig.1.3, the names of the methodologies that led to the development of present-day *finite element method* are framed, while their respective references are mentioned below each frame. Also, please note that the aforementioned references are not included in the Bibliography of the current dissertation and the reader should look for their precise titles and journals in **Zienkiewicz, Taylor, and Zhu, 2013**.

1.4.1 Finite Element Analysis of a Linear Structural System

Although similar, the analyses of different physical systems with the *finite element method* require different differential equation systems, in order to approach the governing physical laws of each system. Given that the scope of the current Ph.D. dissertation is the analysis of a manufacturing process, the methodology behind simulating structural systems will be analyzed in the current subsection.

Initially, the reader should be introduced to the analysis of a *standard discrete structural system* with linear, elastic behavior. An example of such a system is presented in Fig.1.4:

In Fig.1.4, an assembly comprised of four different components or elements (labeled in

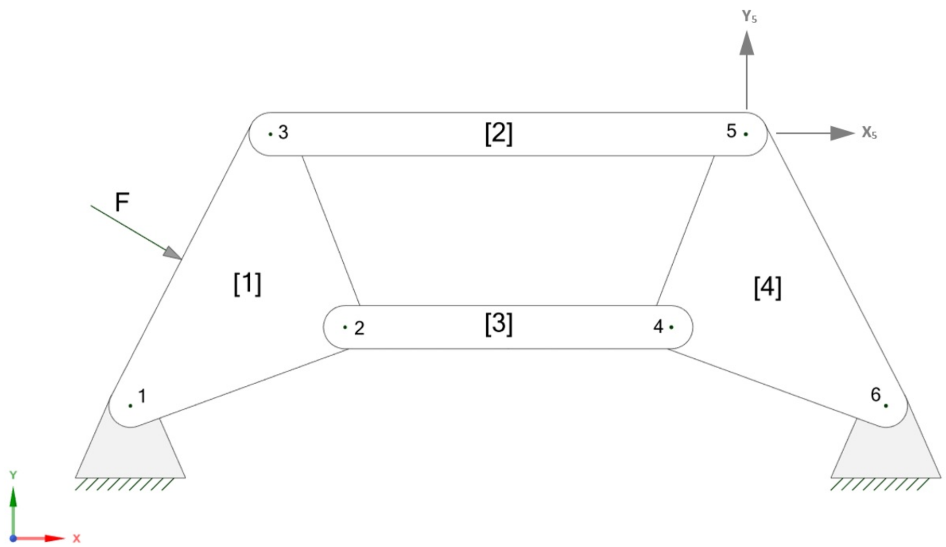

FIG. 1.4: *Standard discrete structural system* example with linear, elastic behavior (loosely based on a corresponding figure found in **Zienkiewicz, Taylor, and Zhu, 2013**)

bracketed numbers) and connected through the nodes 1–6, is presented. In order to simplify the problem, it is assumed that no moments can be transmitted through the nodes. Because of the load F, a rotation and a deformation of element [1] can be assumed, which can in turn be translated to a unique set of loads and displacements (*(U, V)*, respectively) on each individual node of element [1]. Apart from the external loads (e.g. load F in this example), any displacement of the nodes as a result of the actions of their neighboring elements, as well as any initial strain of the elements (e.g. thermal strains, preloading of the elements, etc.) are also considered in *(U, V)*. Thus for element [1], the corresponding matrix including the loads and velocities of all of its nodes will be:

$$\mathbf{r}^1 = \left\{ \begin{array}{c} \mathbf{r}_1^1 \\ \mathbf{r}_2^1 \\ \mathbf{r}_3^1 \end{array} \right\} \qquad \text{where,} \qquad \mathbf{r}_1^1 = \left\{ \begin{array}{c} U_1 \\ V_1 \end{array} \right\}, \text{etc.} \tag{1.1}$$

while the corresponding nodal displacements will be:

$$\mathbf{u}^1 = \left\{ \begin{array}{c} \mathbf{u}_1^1 \\ \mathbf{u}_2^1 \\ \mathbf{u}_3^1 \end{array} \right\} \qquad \text{where,} \qquad \mathbf{u}_1^1 = \left\{ \begin{array}{c} u_1 \\ v_1 \end{array} \right\}, \text{etc.} \tag{1.2}$$

It should be noted that in Eqs.1.1 and 1.2, the load and displacement vectors defined in the global coordinate system are mentioned in uppercase letters, while the corresponding vectors defined in their respective nodal (local) coordinate systems are given in lowercase letters. An example of a nodal coordinate system is presented in Fig.1.4 for node No. 5.

As the behavior of each element is considered to be linear and elastic, the characteristic relationship will have the form:

$$\mathbf{r}^1 = \mathbf{K}^1\mathbf{u}^1 - \mathbf{f}^1 \tag{1.3}$$

where:

- $\mathbf{r}^1$, is the vector of the forces induced by the displacement of the nodes
- $\mathbf{f}^1$, is the vector of the nodal forces required to maintain equilibrium on each element
- $\mathbf{K}^e$, is the *stiffness matrix* of the element e

Thus, in their generalized form for an element with n nodes, Eqs.1.1 and 1.2 will have the following form:

$$\mathbf{r}^e = \left\{ \begin{array}{c} \mathbf{r}_1^e \\ \mathbf{r}_2^e \\ \vdots \\ \mathbf{r}_n^e \end{array} \right\} \qquad \text{and} \qquad \mathbf{u}^e = \left\{ \begin{array}{c} \mathbf{u}_1^e \\ \mathbf{u}_2^e \\ \vdots \\ \mathbf{u}_n^e \end{array} \right\} \tag{1.4}$$

with each of the $\mathbf{r}_n^e$ and $\mathbf{u}_n^e$ having the same number of components or *degrees of freedom*. On the other hand, the *stiffness matrix* of the element will always be square and will have the following form:

$$\mathbf{K}^e = \begin{bmatrix} \mathbf{K}_{11}^e & \mathbf{K}_{12}^e & \dots & \mathbf{K}_{1n}^e \\ \mathbf{K}_{21}^e & \ddots & & \vdots \\ \vdots & \vdots & & \vdots \\ \mathbf{K}_{n1}^e & \dots & \dots & \mathbf{K}_{nn}^e \end{bmatrix} \tag{1.5}$$

where:

- $\mathbf{K}^e_{11}$, $\mathbf{K}^e_{12}$, etc. being submatrices which are again square and of size $l \times l$
- l is the number of force and displacement components to be considered at each node,

It is worth noting that for this approach the elements are considered undeformable. In such cases, the *stiffness matrices* are symmetrical, thus the following equation is in effect:

$$\mathbf{K}^e = (\mathbf{K}^e)^T \tag{1.6}$$

where:

- $(\cdot)^T$, denotes the transpose of a matrix

After the analysis of each individual element and the calculation of their corresponding load and displacement vectors, the interactions between the different elements in the assembly are analyzed. In any assembly, two basic conditions should be satisfied:

1. Displacement compatibility
2. Force and moment equilibrium

From these two conditions, the first one is satisfied with the consideration of all individual element displacement vectors, $\mathbf{u}^e_n$ in a single system:

$$\mathbf{u} = \left\{ \begin{array}{c} \mathbf{u}^1 \\ \mathbf{u}^2 \\ \vdots \\ \mathbf{u}^n \end{array} \right\} \tag{1.7}$$

For the second condition and given that equilibrium has already been satisfied within each individual element, all that is necessary is to establish equilibrium at the interactions points between the different elements of the assembly. On each of the interaction points or nodes, the resulting load vectors can be determined using Eq.1.3, with the nodal displacements being the unknown factors. The internal forces in each element are considered known, from the analysis of each element. Thus, for a typical node, a the equilibrium of all forces by the elements of the assembly are given by the following equation:

$$\sum_{e=(1)}^{n_e} \mathbf{r}^e_a = \mathbf{r}^{(1)}_a + \mathbf{r}^{(2)}_a + \cdots = \mathbf{0} \tag{1.8}$$

where:

- $\mathbf{r}^{(1)}_a$, is the loads affecting node a by element (1), $\mathbf{r}^{(2)}_a$ by element (2), etc.

Obviously, all elements not including node a contribute zero loads, even if they are included in the summation. Substitution of Eq.1.3 into Eq.1.8 and considering that the nodal displacements, $\mathbf{u}_a$ are common (thus omitting the superscript e), the following expression of Eq.1.8 is in effect:

$$\left(\sum_{e=(1)}^{n_e} \mathbf{K}^e_{a1} \right) \mathbf{u}_1 + \left(\sum_{e=(1)}^{n_e} \mathbf{K}^e_{a2} \right) \mathbf{u}_2 + \cdots - \sum_{e=(1)}^{n_e} \mathbf{f}^e_i = \mathbf{0} \tag{1.9}$$

If Eq.1.9 is applied on all nodes of the assembly and summed, a simplified form of the equilibrium equation is the following:

$$\mathbf{K}\mathbf{u} - \mathbf{f} = \mathbf{0} \tag{1.10}$$

where the corresponding submatrices can be calculated using the following summations:

$$\mathbf{K}_{ab} = \sum_{e=(1)}^{n_e} \mathbf{K}^e_{ab} \qquad and \qquad \mathbf{f}_a = \sum_{e=(1)}^{n_e} \mathbf{f}^e_a \tag{1.11}$$

where Eqs.1.11 including all elements of the assembly. *This general assembly process is a common and fundamental feature of all finite element calculations*. It is worth noting that if different types of structural elements are used, and they have to be coupled, the rules of matrix summation can be applied at each node only if the respective matrices are of identical size. In other words, all individual submatrices can be summed, only if they are being built up by the same number of individual components of force and displacement.

In order to solve the system of equations resulting from Eq.1.10, it is necessary to have some properly defined boundary conditions in the problem. For example, in Fig.1.4 the corresponding boundary conditions in effect are defined in nodes 1 and 6, as per the following considerations:

$$\mathbf{u}_1 = \mathbf{u}_6 = \begin{Bmatrix} 0 \\ 0 \end{Bmatrix} \tag{1.12}$$

Because of the form of Eq.1.12, the total system of equations (in this example 12 in total) is reduce by two, thus the total number of unknown displacements is also reduced to eight. In a steady-state problem without substitution of a minimum number of prescribed displacements to prevent rigid body movements of the components, it is impossible to solve this problem analytically (no unique force-to-displacement system exists). This fact leads to a mathematically singular *stiffness matrix* **K**, which cannot be inverted. However, the prescription of appropriate displacements after the assembly, will permit a unique solution to be obtained by reducing the appropriate rows and columns of the corresponding matrices.

Considering the entire system of equations of the assembly in the following form:

$$\begin{gathered} \mathbf{K}_{11}\mathbf{u}_1 + \mathbf{K}_{12}\mathbf{u}_2 + \mathbf{K}_{13}\mathbf{u}_3 + \cdots - \mathbf{f}_1 = \mathbf{0} \\ \mathbf{K}_{21}\mathbf{u}_1 + \mathbf{K}_{22}\mathbf{u}_2 + \mathbf{K}_{23}\mathbf{u}_3 + \cdots - \mathbf{f}_2 = \mathbf{0} \\ \mathbf{K}_{31}\mathbf{u}_1 + \mathbf{K}_{32}\mathbf{u}_2 + \mathbf{K}_{33}\mathbf{u}_3 + \cdots - \mathbf{f}_3 = \mathbf{0} \\ \text{etc.} \end{gathered} \tag{1.13}$$

and then substituting known displacements (e.g. $\mathbf{u}_1 = \bar{\mathbf{u}}_1$) in Eqs.1.13, while simultaneously eliminating the corresponding forces (e.g. $\mathbf{f}_1$ in this case), as it cannot be determined unless the rest of the displacements, $\mathbf{u}_i$ are determined, the system of equations that finally needs to be solved is the following:

$$\begin{gathered} \mathbf{K}_{22}\mathbf{u}_2 + \mathbf{K}_{23}\mathbf{u}_3 + \cdots + +(\mathbf{K}_{21}\bar{\mathbf{u}}_1 - \mathbf{f}_2) = \mathbf{0} \\ \mathbf{K}_{32}\mathbf{u}_2 + \mathbf{K}_{33}\mathbf{u}_3 + \cdots + +(\mathbf{K}_{31}\bar{\mathbf{u}}_1 - \mathbf{f}_3) = \mathbf{0} \\ \text{etc.} \end{gathered} \tag{1.14}$$

which has fewer equations than Eqs.1.13. Overall, after the substitution of all the known parameters from their corresponding boundary conditions, the number of equations and unknowns should always be the same.

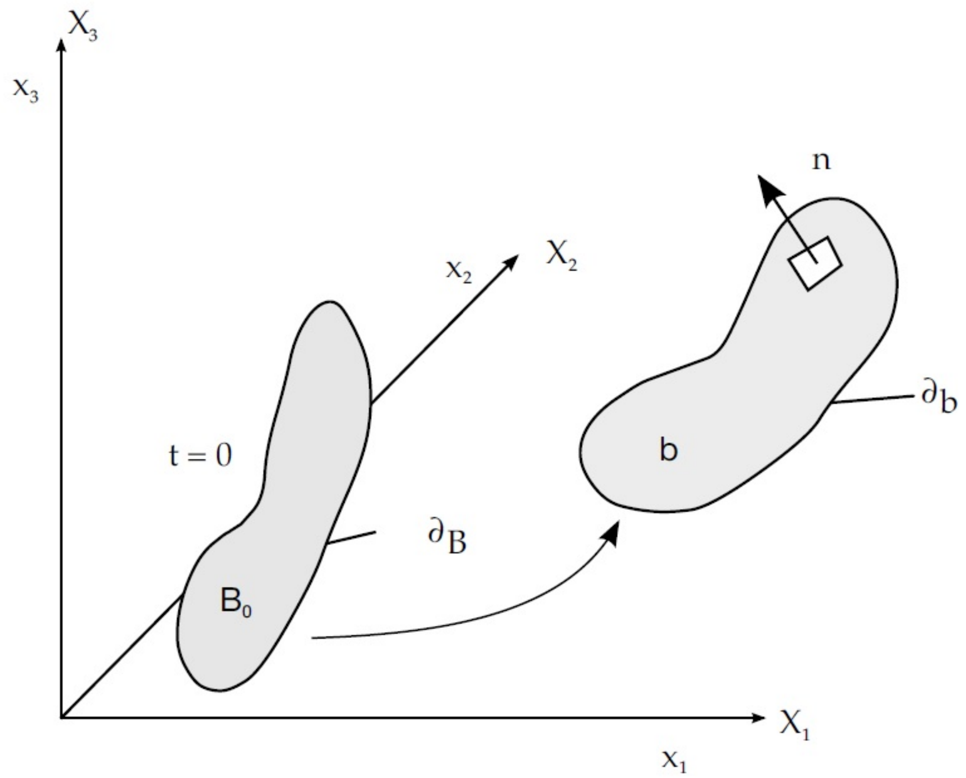

FIG. 1.5: Analysis of a deformable body, with simultaneous movement and deformation (figure taken from **Hallquist, 2006**)

1.4.2 Finite Element Analysis of a Nonlinear Structural System (Hallquist, 2006)

Although the methodology described in §1.4.1 corresponds to simple mechanical problems, in practice most engineering applications possess a higher degree of complexity. For the analysis of manufacturing processes in particular, the aspects of time-dependent phenomena (e.g. body accelerations, material strain-rate phenomena, etc.) and body deformations have to be considered in the system of equations that are solved. For this reason, a methodology for analyzing non-linear, time-dependent structural systems has to established.

In order to better describe the methodology of the analysis of a nonlinear structural system, the deformable body presented in Fig.1.5 is considered:

In Fig.1.5, a point a in the deformable body b at a t=0, moves to a new point, as body b moves and deforms. Both the initial, $\mathbf{X}_a$ and the final coordinates, $\mathbf{x}_i$ of point a are defined at the same coordinate system. Considering the vector of the initial coordinates as follows:

$$\mathbf{X}_a = \left\{ \begin{array}{c} X_1 \\ X_2 \\ X_3 \end{array} \right\} \tag{1.15}$$

and considering a Lagrangian formulation, the final coordinates will be a function of the initial coordinates $\mathbf{X}_a$ and time t, as follows:

$$\mathbf{x}_i = \mathbf{x}_i(\mathbf{X}, t) \tag{1.16}$$

where:

- i = 1, 2, 3, depending on the corresponding direction in the coordinate system

At a time t=0, the initial conditions of point a will be:

$$\begin{aligned} \mathbf{x}_i(\mathbf{X}, 0) &= \mathbf{X}_a \\ \dot{\mathbf{x}}_i(\mathbf{X}, 0) &= v_i(\mathbf{X}) \end{aligned} \tag{1.17}$$

where:

- v_i, is the vector of the initial velocities

In order to calculate the deformation of body b resulting from the applied forces, a series of equations has to be solved. Initially, the momentum conservation equation has to be solved. This is given in the following form:

$$\sigma_{ij,j} + \rho f_i = \rho \ddot{x}_i \tag{1.18}$$

In order for Eq.1.18 to have a unique solution, several boundary conditions have to be satisfied, namely when x_i^+=x_i^-:

- $\sigma_{ij} n_j = t_i(t)$, the traction boundary conditions, on boundary ϑb_1
- $x_i(X, 0) = D_i(t)$, the displacement boundary conditions, on boundary ϑb_2
- $\sigma_{ij}^+ - \sigma_{ij}^-) n_i = 0$, the contact discontinuity condition, along an interior boundary ϑb_3

where:

- σ, is the Cauchy stress vector
- ρ, is the current density
- $\mathbf{f}$, is the body force density
- $\ddot{x}$, is the acceleration vector

It is worth noting that the comma on $\sigma_{ij,j}$ denotes covariant differentiation, while n_j is a unit outward normal to a boundary element on ϑb.

Regarding the mass conservation, this is ensured by the following equation:

$$\rho V = \rho_0 \tag{1.19}$$

where:

- ρ_0, is the reference density
- V, is the relative volume, i.e., the determinant of the deformation gradient matrix F_{ij}
- F_{ij}=$\frac{\vartheta x_i}{\vartheta X_j}$

On the other hand, the energy conservation equation is integrated in time, and it is used for evaluation equations of state, as well as to track the global energy balance. The energy conservation equation is considered in the following form:

$$\dot{E} = V s_{ij} \dot{\epsilon}_{ij} - (p + q) \dot{V} \tag{1.20}$$

where:

- $s_{ij}=\sigma_{ij}+(p+q)\delta_{ij}$, is the deviatoric stress
- p=$-\frac{1}{3}\sigma_{ij}\delta_{ij}-q=-\frac{1}{3}\sigma_{kk}-q$, is the hydrostatic pressure
- q, is the bulk viscosity
- δ_{ij}, is the Kronecker delta ($\delta_{ij}=1$ if i=j; otherwise $\delta_{ij}=0$)
- $\dot{\epsilon}_{ij}$, is the strain rate tensor

If the principle of virtual work is applied on the system depicted in Fig.1.5, the following equation is received:

$$\int_v(\rho\ddot{x}_i-\sigma_{ij,j}-\rho f)\delta x_i dv+\int_{\vartheta b_1}(\sigma_{ij}n_j-t_i)\delta x_i ds+\int_{\vartheta b_3}(\sigma_{ij}^{+}-\sigma_{ij}^{-})n_j\delta x_i ds=0 \tag{1.21}$$

where δx_i satisfies all boundary conditions on ϑb_2, and the integrations are over the current geometry. Applications of the divergence theorem gives the following:

$$\int_v(\sigma_{ij}\delta x_i)_{,j}dv=\int_{\vartheta b_1}\sigma_{ij}n_j\delta x_i ds+\int_{\vartheta b_3}(\sigma_{ij}^{+}-\sigma_{ij}^{-})n_j\delta x_i ds \tag{1.22}$$

and noting that:

$$(\sigma_{ij}\delta x_i)_{,j}-\sigma_{ij,j}\delta x_i=\sigma_{ij}\delta x_{i,j} \tag{1.23}$$

leads to the weak form of the equilibrium equation:

$$\delta\pi=\int_v\rho\ddot{x}_i\delta x_i\delta v+\int_v\sigma_{ij}\delta x_{i,j}dv-\int_v\rho f_i\delta x_i dv-\int_{\vartheta b_1}t_i\delta x_i ds=0 \tag{1.24}$$

By superimposing a mesh of finite elements interconnected at nodal points on the reference configuraiton and the track particles through time, for example:

$$x_i(X_a,t)=x_i(X_a(\xi,\eta,\zeta),t)=\sum_{j=1}^{k}N_j(\xi,\eta,\zeta)x_i^j(t) \tag{1.25}$$

where:

- N_j, are shape (interpolation) functions in the parametric coordinates (ξ,η,ζ)
- k, is the number of nodal points defining the element
- x_i^j, is the nodal coordinate of the j^{th} node in the i^{th} direction

Each shape function has a finite support that is limited to the elements for which its associated node is a member (hence the name *finite* element method). Consequently, within each element the interpolation only depends on the nodal values for the nodes in *that* element, and hence expressions like Eq.1.25 are meaningful.

The condition $\delta\pi=0$ holds for all variations, δx_i and in particular it holds for variations along the shape functions. In each of the three Cartesian directions upon setting the variation to one of the shape functions, the weak form reduces to a necessary (but not sufficient) condition that must be satisfied by any solution so that:

$$\text{Number of eqautions} = 3\times\text{Number of nodes}$$

At this stage it is useful to introduce a vector space having dimension $\mathbb{R}^{(\text{number of nodes})}$ with a corresponding Cartesian basis, $\{\mathbf{e'}_i\}_{i=1}^{\text{number of nodes}}$. Since the body is discretized into n

disjoint elements, the integral in Eq.1.24 may be separated using the spatial additively of integration into n terms, where for each element becomes:

$$\delta\pi = \sum_{m=1}^{n} \delta\pi_m = 0 \tag{1.26}$$

The contribution from each element can be summed up from the following equation:

$$\delta\pi_m = \int_{v_m} \rho \ddot{x}_i \delta x_i dv + \int_{v_m} \sigma_{ij} \delta x_{i,j} dv - \int_{v_m} \rho f_i \delta x_i dv - \int_{\vartheta b_1 \cap \vartheta v_m} t_i \delta x_i ds \tag{1.27}$$

Assembling the element contributions back into a system of equations leads to the following:

$$\sum_{m=1}^{n} \left\{ \int_{v_m} \rho \ddot{x}_i (\mathbf{e}_i \otimes \boldsymbol{v}^m) dv + \int_{v_m} \sigma_{ij}^m (\mathbf{e}_i \otimes \boldsymbol{v}_{,j}^m) dv - \int_{v_m} \rho f_i (\mathbf{e}_i \otimes \boldsymbol{v}^m) dv - \int_{\vartheta b_1 \cap \vartheta v_m} t_i (\mathbf{e}_i \otimes \boldsymbol{v}^m) ds \right\} = 0 \tag{1.28}$$

In which:

$$v^m = \sum_{i=1}^{k} N_i \mathbf{e}'_{n_m(i)} \tag{1.29}$$

where:

- $\mathrm{n}_m(i)$, is the global node number

Applying the approximation scheme of Eq.1.25 to the dependent variables and substituting into Eq.1.28 yield the following:

$$\sum_{m=1}^{n} \left\{ \int_{v_m} \rho \mathbf{N}_m^T \mathbf{N}_m \mathbf{a} dv + \int_{v_m} \mathbf{B}_m^T \sigma dv - \int_{v_m} \rho \mathbf{N}_m^T \mathbf{b} dv - \int_{\vartheta b_1} \mathbf{N}_m^T \mathbf{t} ds \right\} = 0 \tag{1.30}$$

where:

- **N**, is an interpolation matrix
- σ^T=(σ_{xx}, σ_{yy}, σ_{zz}, σ_{xy}, σ_{yz}, σ_{zx}), is the stress vector
- **B**, is the strain-displacement matrix
- **a**, is the nodal acceleration vector
- **b**, is the body force load vector
- **t**, is the applied traction load

with:

$$\begin{bmatrix} \ddot{x}_1 \\ \ddot{x}_2 \\ \ddot{x}_3 \end{bmatrix} = \mathbf{N} \begin{bmatrix} a_x^1 \\ a_x^2 \\ \vdots \\ a_y^k \\ a_z^k \end{bmatrix} = \mathbf{Na}$$

$$\mathbf{b} = \begin{bmatrix} f_x \\ f_y \\ f_z \end{bmatrix}$$

$$\mathbf{t} = \begin{bmatrix} t_x \\ t_y \\ t_z \end{bmatrix}$$

It is worth noting that in order to calculate the derivatives of displacements in any coordinate system, the chain rule has to be used:

$$\frac{\vartheta N_a}{\vartheta \xi^i} = \frac{\vartheta N_a}{\vartheta x_j}\frac{\vartheta x_j}{\vartheta \xi^i} \tag{1.31}$$

or in matrix form:

$$\frac{\vartheta N_a}{\vartheta \boldsymbol{\xi}} = \mathbf{J}\frac{\vartheta N_a}{\vartheta \mathbf{x}} \tag{1.32}$$

which can be analyzed as:

$$\frac{\vartheta N_a}{\vartheta \boldsymbol{\xi}} = \begin{Bmatrix} \frac{\vartheta N_a}{\vartheta \xi} \\ \frac{\vartheta N_a}{\vartheta \eta} \\ \frac{\vartheta N_a}{\vartheta \zeta} \end{Bmatrix}, \frac{\vartheta N_a}{\vartheta \boldsymbol{x}} = \begin{Bmatrix} \frac{\vartheta N_a}{\vartheta x} \\ \frac{\vartheta N_a}{\vartheta y} \\ \frac{\vartheta N_a}{\vartheta z} \end{Bmatrix}, \text{and } \boldsymbol{J} = \begin{bmatrix} \frac{\vartheta x}{\vartheta \xi} & \frac{\vartheta y}{\vartheta \xi} & \frac{\vartheta z}{\vartheta \xi} \\ \frac{\vartheta x}{\vartheta \eta} & \frac{\vartheta y}{\vartheta \eta} & \frac{\vartheta z}{\vartheta \eta} \\ \frac{\vartheta x}{\vartheta \zeta} & \frac{\vartheta y}{\vartheta \zeta} & \frac{\vartheta z}{\vartheta \zeta} \end{bmatrix}$$

with **J** being the Jacobian transformation matrix between x_i and ξ_i. Using Eq.1.32, the shape function derivatives are given by the following equation:

$$\frac{\vartheta N_a}{\vartheta \boldsymbol{x}} = \boldsymbol{J}^{-1}\frac{\vartheta N_a}{\vartheta \boldsymbol{\xi}} \tag{1.33}$$

Overall, the equations presented in the current section (§1.4) are the fundamental equilibrium equations performed by every FEA code. From then on, each commercial software can perform different operations on an *element* level. A more detailed presentation on the *element* level operations, as these are performed by LS-DYNA, will be performed on the corresponding section (§2.7) and for the specific element types used for the current analyses.

1.5 Scope of the Current Dissertation

The manufacturing process of ring rolling has been researched extensively over the past 70 years, and various aspects of the process mechanics have been thoroughly investigated. Several works of research involving the effectiveness of Ring Rolling setup tools (e.g. **Hawkyard, Appleton, and Johnson, 1973**, **Stanistreet, Allwood, and Willoughby, 2006**), the evolution of the manufactured workpieces (e.g. **Szabo and Dittrich, 1996**, **Uchibori, Matsumoto, and Utsunomiya, 2018**) and various critical limits of the process (e.g. **Zhao and Qian, 2010**, **Xu et al., 2015**) have been presented and analyzed. Moreover, from the early 1990s various finite element models have been presented in a plethora of scientific papers, usually in addition to other experimental data (e.g. **Xu, Lian, and Hawkyard, 1991**, **Wang et al., 2009**) or as a means to validate various analytical or experimental methodologies (e.g. **Parvizi and Abrinia, 2014**, **Li, Guo, and Wang, 2021**).

However, the evolution of the various finite element analysis software programs that exist today, give the user many different tools to work with during the simulation of a manufacturing process, some of which can dramatically change the calculated results. Furthermore, although other Ph.D. dissertations (e.g. **Wang, 2016**) have been conducted on the simulation of the manufacturing process of Ring Rolling, only specific simulation methods are usually presented, many of which can be considered dated based on the capabilities of modern algorithms and software packages. Moreover, very little research has been conducted on the numerical aspects that allow for the proper simulation of the current manufacturing process, thus reproduction of reliable results that are free from the inherent numerical defects (e.g. result dependency on mesh quality, numerical artifacts on stress concentration points, etc.) is often impossible.

Additionally, as seen from the aforementioned literature review, Ring Rolling is a rather crude process, with dimensional inaccuracies being frequent on the final product. This results in extensive post-processing required at the end of each manufacturing cycle, in order to achieve the (usually) very strict dimensional demands expected of Ring Rolling products. Two major factors that lead to the aforementioned dimensional inaccuracies are the poor control of the tools and the roughly determined volume of the initial blank.

In the current Ph.D. dissertation, some key aspects and methodologies, which can potentially increase the dimensional accuracy of a flat Ring Rolling process were investigated through validated, coupled thermo-mechanical simulations. More specifically, the current dissertation has the following structure:

- In the *second chapter*, the simulation setup of the coupled thermo-mechanical Ring Rolling model is presented. The most suitable simulation parameters, along with an explanation of their suitability for the final model, are discussed. Finally, the results from the conducted simulation are compared to the corresponding experimental results of **Zhu et al., 2016b**, in order for the produced numerical model to be considered as fully validated.

- In the *third chapter*, three crucial parameters for increasing the dimensional accuracy of Ring Rolling products are investigated. Initially, the calculation methodology for the determination of a more precise initial blank volume are researched. Then, the effects of tool thermal and elastic deformation on the dimensions of the final ring product are evaluated. Finally, the effects of the movement pattern of the support rolls, based on the final growth rate of the ring, as well as the differences brought by different ring materials are shown.

- In the *fourth chapter*, a novel approach for *"correcting"* dimensional inaccuracies on the final ring products is presented. Apart from the core mechanics of this new process, some crucial parameters that affect the outcome of this approach are also investigated.

- Finally, in the *fifth chapter*, a novel approach for the manufacturing of polygonal products using a typical Ring Rolling mill is briefly introduced. This analysis was not conducted in depth, since it deviated from the main scope of the current dissertation. Instead, it is presented to the reader as a proof of concept.

For all of the conducted simulations, the commercial FEA software LS-DYNA™is used, with the preparation of each model being made with the LS-Pre-Post™4.10 pre-processor. LS-Pre-Post™4.10 offers a wide variety of tools and mathematical approaches that presented solutions for the problems faced on the current dissertation.

To the best of the author's knowledge, the presented analyses have not been presented elsewhere, while it is the author's intention that the readers will find the current thesis useful for their scientific work.

Chapter 2

Numerical Modelling of the Ring Rolling Process

2.1 Introduction

As seen in the previous section, several attempts have been performed in the past in order to simulate the manufacturing process of Ring Rolling. From the literature review many difficulties of the process derived, and several solutions were proposed. In all relative research items, however, rarely or never the authors provide all the aspects of a complete Ring Rolling simulation. Additionally, it is very common that several assumptions are made, in order to bypass some of the process problems that appear but are not connected with the goals of the corresponding research (e.g. considering an isothermal process (**Yang et al., 2006**) or simulating Ring Rolling as a 2D process (**Huez, Noyes, and Coupu, 2001**), often without mentioning the possible effects these assumptions have in the final results. The combination of the lack of necessary information and the consideration of several assumptions make the simulation of Ring Rolling a very challenging task.

In the current section of the dissertation, a step-by-step presentation of the simulation of Ring Rolling is presented. Due to the lack of experimental data in order to validate the presented model, the overall setup and the experimental data from **Zhu et al., 2016b** were used as a starting point. Apart from the necessary experimental data required for the successful validation of the numerical model, Zhu et al. also contained in their work most of the process parameters required to reproduce the model, while some of them could be concluded from the provided figures. Regarding the material properties of the model, some of them were taken directly from the work of Zhu et al. and the rest were found in literature. For the rest of the process parameters, a thorough analysis of the physical phenomena taking place in the process was performed, in order to end up with all the necessary information for the simulation.

In order to re-create successfully a manufacturing process via finite element analysis, it must be performed in specific and precise steps. More specifically, a complete simulation should involve the following steps:

1. Estimation of the most fitting simulation type – 2D or 3D
2. Definition of the appropriate finite element formulation
3. Precise re-creation of the manufacturing process's geometry
4. Estimation of the optimum mesh
5. Definition of the appropriate material properties

6. Estimation of the proper finite element type
7. Definition of contacts between the different bodies
8. Definition of the tools' movement
9. Estimation of the problem's constants and initial conditions
10. Definition of the software parameters
11. Estimation of the optimum mass scaling
12. Solution of the numerical model
13. Validation of the results

For the simulation of Ring Rolling performed in the current dissertation, the aforementioned simulation steps are presented in detail in the following sections of the current chapter.

2.2 Fitting Simulation Type – 2D or 3D

In the past, both 2D (e.g **Kim and Kim, 2015; Hua et al., 2016**) and 3D models (e.g. **Seitz et al., 2016; Peng et al., 2017**) of Ring Rolling have been presented in literature. Given the complicated combination of movements and the possible instabilities that result from them in a 3D setup of a Ring Rolling process, a 2D model is surely easier to be set. Furthermore, the reduced order of differential equations that need to be solved in the case of surface elements, combined with the reduced number of nodes that are affected, allow for a much greater number of finite elements to be used for a given solution duration of the model. On the other hand, the inability to involve the axial reduction of the ring leads to a false deformation mechanism and thus false final dimensional predictions than in an actual Ring Rolling. Under specific circumstances(e.g. no axial reduction and negligible forming defects assumptions), however, a 2D model may predict the final dimensions of the ring product within acceptable margins of error. As seen in literature, 2D models were mostly common in the past, when the capabilities of PCs were significantly reduced, thus a full 3D model was too expensive a solution.

In most Ring Rolling simulations nowadays, a full 3D setup is presented. This allows for a more realistic representation of the actual phenomena that take place in the process, which may involve important aspects of industrial productions, such possible defects from improperly chosen process parameters and limiting production parameter values. In this case, however, both the duration and the computational cost are fairly large. This often leads many researchers either to reduce the mesh density of the workpiece or to consider assumptions that will help with the convergence of the numerical algorithms (e.g. axial movement restriction on the ring). A proper setup of the Ring Rolling finite element model can help bypass most numerical issues, while a good prediction of the final properties of the ring will be achieved.

For the current dissertation and for the chosen experimental data, a 3D numerical model of the Ring Rolling process was the only option. Although challenging, the author of the current research analyzed to the best of his knowledge both the numerical and the physical aspects of the problem, in order for a thorough and robust Ring Rolling finite element model to be created.

2.3 Finite Element Method Formulation – Implicit vs. Explicit

Regarding the proper finite element method formulation, Ring Rolling simulations using both an explicit (e.g. **Guo and Yang, 2011a**) and an implicit method (e.g. **Teja et al., 2019**) have been presented in literature. Comparative researches between the two formulation methods, regarding the most suitable in simulating dynamic processes, are fairly old and numerous (e.g. **Lindgren and Edberg, 1990; Sun, Lee, and Lee, 2000; Harewood and McHugh, 2007**). Their results tend to differentiate according to the application each time, however explicit formulation seems to be preferable in the most manufacturing process simulations. For example, Gavalas, Pressas, and Papaefthymiou (**Gavalas, Pressas, and Papaefthymiou, 2018**) investigated the differences between implicit and explicit formulations in an aluminum rolling simulation, regarding the proper mesh density for the simulation of this process. Rolling is very similar to Ring Rolling in terms of tools mechanics and thus overall kinetics, thus the results presented by Gavalas, Pressas, and Papaefthymiou can be also considered to be applicable to the current research (the results from this researched are presented in more detail below). Furthermore, Pauskar, Sawamiphakdi, and Jin (**Pauskar, Sawamiphakdi, and Jin, 2004**) performed a similar investigation in a flat Ring Rolling simulation, which was unfortunately very limited from the significantly lower capabilities of computers at the time. Nevertheless, both of these investigations shifted towards explicit formulation as it has increased precision and less computational cost.

The most important difference between the two formulations lies with the segmentation of time (**Butcher, 2003**). More specifically, in an implicit analysis, an equation is solved numerically with information from both the current and later states of the analyzed system (*Backward Eulerian Method*). This fact creates the need for a globally converged solution in each and every time state of the model before proceeding to more localized analyses (e.g. in each finite element), which can be time-consuming. However, because all states have to reach equilibrium, the time increments can be rather long. On the other hand, in an explicit analysis, system equations are calculated for states at different times from the current one (*Eulerian Method*). Because of this, the global equilibrium in every state is taken as granted and only the localized analyses are performed. Thus, for this method to work, time increments have to be very short (in the order of μs or less), so that a stable solution may be achieved. For the aforementioned reasons, the chosen formulation for the simulation of a non-linear dynamic process can lead to great differences in the way that the differential equations will be solved.

2.3.1 D'Alembert's Principle

In every nonlinear simulation (including those of manufacturing processes), D' Alembert's principle should always be satisfied (**Hallquist, 2006**):

$$f_I + f_D + f_{int} = p(t) \tag{2.1}$$

where:

- $f_I = m\ddot{u}$, are the inertia forces
- $f_D = c\dot{u}$, are the damping forces
- f_{int}, are the internal forces
- $p(t)$, are the external forces

and:

- m, is the mass indicator
- c, is the damping indicator
- $\ddot{u} = \frac{d^2u}{dt^2}$, is the acceleration
- $\dot{u} = \frac{du}{dt}$, is the velocity
- u, is the displacement

Thus, Eq.2.1 becomes:

$$m\ddot{u} + c\dot{u} + f_{int}(u) = p(t) \tag{2.2}$$

or considering the corresponding linear form of Eq.2.2:

$$[M]\{\ddot{u}\} + [C]\{\dot{u}\} + \{F_{int}\} = \{F_{ext}\} \tag{2.3}$$

2.3.2 Implicit Formulation

In a nonlinear implicit analysis, initially the global matrix of equations should be in equilibrium, thus:

$$\{R\} = [M]\{\ddot{u}\} + [D]\{\dot{u}\} + \{F_{int}\} - \{F_{ext}\} = \{0\} \tag{2.4}$$

From Eq.2.4 an applied loads vector $\{F^a\}$ can be determined. Then, the global stiffness equation can be estimated (**Kohnke, 2009**):

$$[K(u)]\{u\} = \{F^a\} \tag{2.5}$$

where:

- $\left[\mathrm{K(u)}\right]$, is the nonlinear stiffness coefficient matrix

From Eq.2.5 a prediction of the global displacements can be estimated. Solving for {u}, Eq.2.5 gives:

$$\{u\} = [K(u)]^{-1}\{F^a\} \tag{2.6}$$

With the global displacement prediction estimated, the same process is repeated iteratively for each element of the model. For this, a slightly different expression of Eq.2.5 is used:

$$[Ki^T]\{\Delta u_i\} = \{F_i^{na}\} - \{F_i^{nr}\} \tag{2.7}$$

where:

- $\left[\mathrm{Ki}^T\right]$, is the Jacobian stiffness coefficient matrix (tangent matrix) at the current time iteration
- $\{\mathrm{F}_i^{na}\}$, is the vector of applied loads on the elements at the current time increment
- $\{\mathrm{F}_i^{nr}\}$, is the vector of restoring loads (element internal loads) at the current time increment

Thus, the displacement of the following iteration, i+1 can be approximated based on the calculated vector, $\{\Delta u_i\}$ and the initial displacement vector of the current iteration, $\{u_i\}$ as:

$$\{u_{i+1}\} = \{\Delta u\} + \{u_i\} \tag{2.8}$$

If the difference between the global displacement prediction, {u} and the displacement vector of the current iteration, $\{u_{i+1}\}$ is significant, the displacement vector for all elements is repeated until the two values converge. When a converged displacement solution is reached, the strain vector for each element at the next time iteration can be determined:

$$\{\epsilon_{i+1}\} = [B]\{u_{i+1}\} \tag{2.9}$$

where:

- $\{\epsilon_{i+1}\}$, is the strain vector for the next time iteration
- $\big[$B$\big]$, is the strain-displacement matrix, based on the element shape functions

Subsequently, the stress vector for each element is determined:

$$\{\sigma_{i+1}\} = [D]\{\epsilon_{i+1}\} \tag{2.10}$$

where:

- $\{\sigma_{i+1}\}$, is the stress vector for the next time iteration
- $\big[$D$\big]$, is the stress-strain matrix

Additionally, the Jacobian stiffness coefficient matrix, $\{K^T_{i+1}\}$ and the applied loads on the elements, $\{F^{na}_i\}$ at the next time iteration can also be determined:

$$\{K^T_{i+1}\} = \int_{\delta V} [B]^T[D][B]dV \tag{2.11}$$

where:

- δV, is the volumetric difference between the current time iteration and the next

and:

$$\{F^{na}_i\} = \{\delta u\}^{-T}\delta W \tag{2.12}$$

where:

- $\{\delta$u$\}$, is the displacement difference between the current time iteration and the next
- δW, is the external work difference between the current time iteration and the next

When the vectors from Eqs.2.8-2.12 have been determined for all elements, the whole process moves to the next time iteration as an initial point and the cycle begins anew. When the calculations for the final time increment are completed, the process terminates.

From all of the above, the implicit formulation is a time-consuming and quite expensive process. Some of the presented matrices and vectors, such as the $[K(u)]^{-1}$ matrix in Eq.2.6, can be very difficult to estimated, especially for large systems with numerous finite elements. In these cases, usually a large computational cost is required, while advanced iterative solvers are a necessity. If, however, the displacement vector $\{u\}$ is calculated, the rest of the vectors and matrices are easily calculated. Also, because a global equilibrium has been reached a priori, the whole process is unconditionally stable, thus the time iterations can be quite large. Generally, implicit formulation is usually avoided in the case of non-linear, dynamic simulations due to its computational complexity and increased cost.

2.3.3 Explicit Formulation

In the case of an explicit formulation analysis, it is assumed that all forces at a time t should be equal to mass × acceleration, or:

$$[M]\{\ddot{u}_t\} = \{F_t^{ext}\} - \{F_t^{int}\} \tag{2.13}$$

where:

- $\{F_t^{ext}\}$, is the applied force and body force vector
- $\{F_t^{int}\} = \sum \left(\int_V [B]^T \sigma_n dV + \{F^{hg}\} \right) + \{F^{contact}\}$, is the internal force vector
- $\left[B\right]$, is the strain-displacement matrix defined from an interpolation assumption in elements
- σ_n, is the stress induced on each element
- V, is the volume of each element
- $\{F^{hg}\}$, is the hourglass resistance force vector, which forbid the excess deformation of an element, thus working as a stiffness indicator for them
- $\{F^{contact}\}$, are the forces applied from the contact of the bodies

From the inversion of the diagonal mass matrix [M], the acceleration vector at time t can be estimated:

$$\{\ddot{u}_t\} = [M]^{-1}(\{F_t^{ext}\} - \{F_t^{int}\}) \tag{2.14}$$

Then, the velocity $\{\dot{u}\}$ and displacement $\{u\}$ vectors at time t+Δt can be estimated via central difference time integration:

$$\{\dot{u}_{t+\frac{\Delta t}{2}}\} = \{\dot{u}_{t-\frac{\Delta t}{2}}\} + \{\ddot{u}_t\}\Delta t_t \tag{2.15}$$

$$\{u_{t+\Delta t}\} = \{u_t\} + \{\dot{u}_{t+\frac{\Delta t}{2}}\}\Delta t_{t+\frac{\Delta t}{2}} \tag{2.16}$$

while the corresponding time iterations are:

$$\Delta t_{t+\frac{\Delta t}{2}} = \frac{1}{2}(\Delta t_t + \Delta t_{t+\Delta t}) \tag{2.17}$$

$$\Delta t_{t-\frac{\Delta t}{2}} = \frac{1}{2}(\Delta t_t - \Delta t_{t+\Delta t}) \tag{2.18}$$

After the calculation of the displacement vector $\{u\}$, the effects on the geometries in the finite element model can be estimated by adding the displacement increments to the initial (for the current state) geometry $\{x_0\}$, as follows:

$$\{X_{t+\Delta t}\} = \{X_0\} + \{u_{t+\Delta t}\} \tag{2.19}$$

When the geometric differences at the following time increment have been determined, the strain and stress vectors can be defined, as these were described by Eq.2.9 and Eq.2.10, respectively. Furthermore, the element forces can also be estimated from Eq.2.12. Once all vectors and matrices have been determined for the next time iteration, this iteration becomes the current and the process repeats. Once the calculations for all time iterations have been completed, the process terminates.

Explicit formulation is much more direct compared to implicit. Each equation is uncoupled from the others, and they can be solved directly, without the need for time-consuming repeats until a solution converges. Additionally, no matrix inversions are required, thus further reducing the computational cost. However, because the majority of the nonlinearities are taken into account in the internal loads vector, its estimation is quite expensive relative to the rest of the vectors.

The greatest drawback of this formulation is that in order for the whole process to be stable, each time iteration has to be very small. The size of time iterations has to satisfy Courant-Friedrichs-Levy criterion (**Courant, Friedrichs, and Levy, 1967**):

$$\Delta t \leq \Delta t^{critical} = \frac{2}{\omega_{max}} \tag{2.20}$$

where:

- ω_{max}=2 $\frac{c}{l}$, is the largest natural circular frequency
- c=$\sqrt{\frac{k}{m}}$, is the wave propagation velocity
- l, is the characteristic length of the smallest element
- k, is the stiffness of the elastic material
- m, is the mass of the elastic material

Thus, Eq.2.20 can be expressed as:

$$\Delta t \leq \Delta t^{critical} = \frac{l}{c} \tag{2.21}$$

From Eq.2.21, it is implied that the time increment in an explicit analysis should always be less than the time required for a mechanical wave to move through an elastic means of length l. The characteristic length l in the case of hexahedral solid element should not be mistaken for the least element edge, as it is commonly chosen as the least fraction of an element's volume by its corresponding maximum surface among all the elements in a model. This indicates that both element size and element quality affect the maximum time iteration in an explicit analysis.

Overall, the explicit formulation can be faster and more precise in large and complicated 3D finite element models, as no expensive and time-consuming numerical iterations as required. Even if, the significantly lower time increments may act as a false indicator of an increased overall duration for an explicit analysis, in cases of numerous elements per model and with many million more time iterations, the total time can and is usually in favor of the explicit analysis.

2.3.4 Optimum Formulation for Ring Rolling

As presented in the previous subsections, the two formulations have significant differences in the solution of a structural problem. Moreover, the complexity, duration and size of the said problem can establish a certain method as more suitable than the other. As a general rule-of-thumb showing which method is recommended in terms of the corresponding phenomenon's duration, a representative figure is presented below (Fig.2.1):

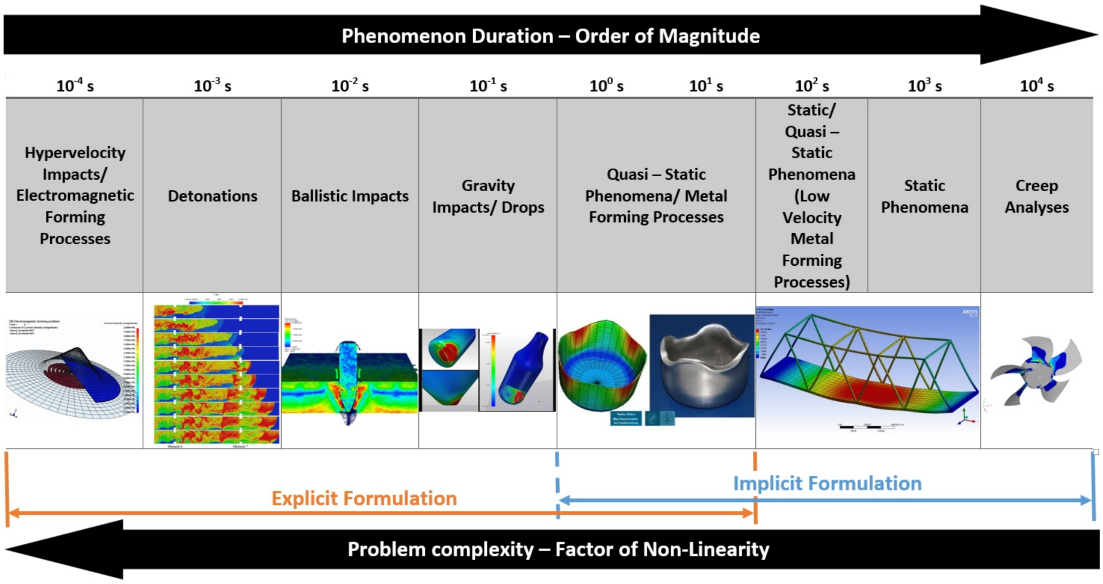

FIG. 2.1: Recommended finite element formulation per application

Observation over Fig.2.1 reveal that based on the common deformation rates of most conventional forming processes (usually around 10^{-1} – 10^{2} s), either formulation method can be used for their simulation.

Since, both formulations could be used based on the deformation rates of the analyzed problem (strain rate approximately 10^{-1} – 10^{0} s^{-1}, total duration approximately 40 s) a more thorough investigation had to be performed. As mentioned above, the author of the current dissertation and his colleagues investigated the recommended formulation of a typical aluminum rolling process (**Gavalas, Pressas, and Papaefthymiou, 2018**). Rolling as a manufacturing process has many similarities in its fundamental mechanism to that of Ring Rolling. More specifically, in both processes the material's deformation is conducted by rotating tools, while the material inside the rolling bite is squeezed through it. Ring Rolling has an additional level of complexity in that there is another rolling bite from the conical rolls, while the workpiece can be easily destabilized if any of the tools is not in its proper position. However, the similarities between the two processes in terms of their respective deformation mechanisms and tool kinetics make the results of **Gavalas, Pressas, and Papaefthymiou, 2018** (at the very least) applicable to the current analysis.

In their work, Gavalas, Pressas, and Papaefthymiou simulated one quarter of an actual aluminum rolling setup through multiple numerical models, with the number of elements changing between the different runs. For the implicit analyses, the author used the commercial FEA software ANSYS Mechanical, while for the explicit analyses they used LS-DYNA. In the aforementioned models, both the tools and the sheet were modeled as deformable bodies, thus the complexity of the simulation was significantly increased. In total, four different mesh densities were tested with the implicit formulation and another four with the explicit formulation. An overview of the simulated setup is presented in Fig.2.2 (**Gavalas, Pressas, and Papaefthymiou, 2018**):

After the solution of the models, a comparison between the required solution time and the number of elements (defined by the total node number in the model) was made. The resulting comparative diagram is presented in Fig.2.3:

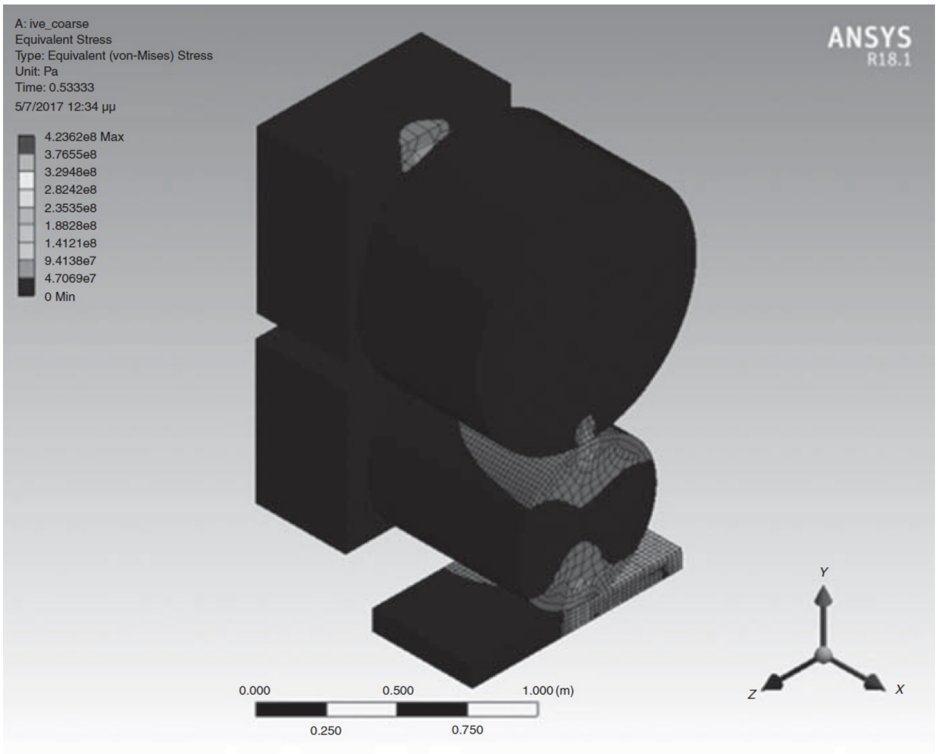

FIG. 2.2: Rolling implicit vs. explicit analysis setup overview (figure taken from **Gavalas, Pressas, and Papaefthymiou, 2018**)

Observations over Fig.2.3 reveal that in cases of rolling models with a relatively small number of nodes (approximately 10,000 nodes), the total solution time required begins to deviate from one another, with implicit formulation requiring significantly more simulation time than explicit. Based on these results and given that a fairly dense mesh will be used in order to precisely calculate the various aspects of Ring Rolling (also see §2.5), it was decided that **an explicit formulation** is the recommended formulation, and it would be used in the current research.

It is worth noting that in their work Gavalas, Pressas, and Papaefthymiou presented further analyses from the comparison of the two formulations (i.e. comparison of the calculated main rolling load, effects of friction coefficient on the total solution time, etc.). However, the rest of the presented results are mainly viable for simulations of rolling processes and thus beyond the scope of the current dissertation.

2.4 Geometries

The proper initial geometries are one of the most important aspects for an accurate simulation. In the reference work of Zhu et al., the geometries of tools are not provided. However, a 3D CAD drawing of the whole setup is presented in this work. Thus, based on the initial blank dimensions, which are provided in the reference, and the 3D CAD of the setup, a fairly precise approximation of the tools' dimensions was possible. The aforementioned approximated tool dimensions are summarized in Table 2.1:

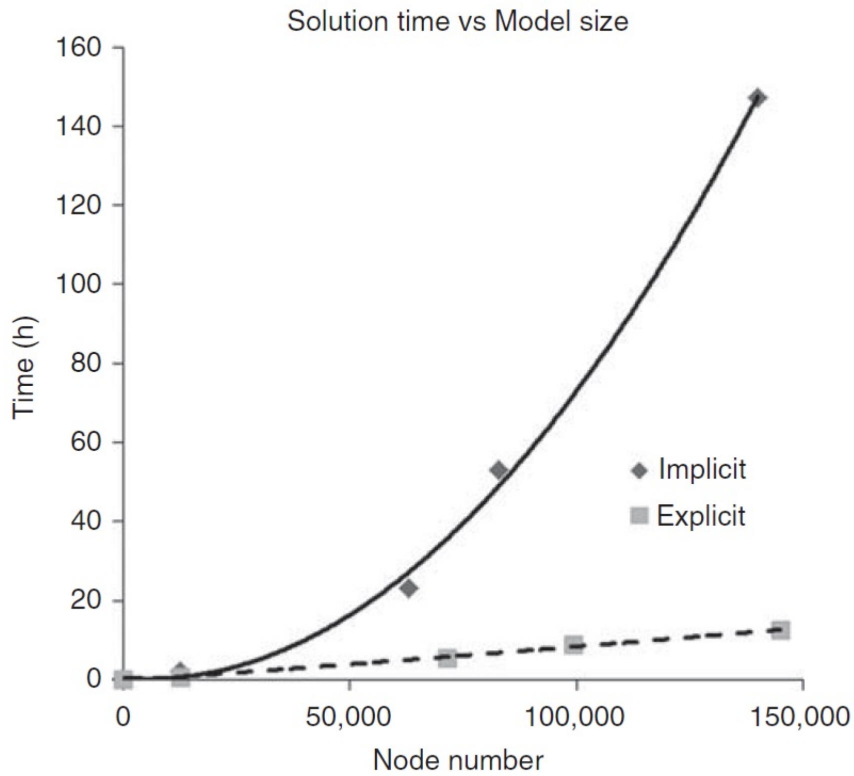

FIG. 2.3: Rolling implicit vs. explicit analysis solution time comparison per number of nodes in the numerical model (figure taken from **Gavalas, Pressas, and Papaefthymiou, 2018**)

TABLE 2.1: Tool dimensions

Tool	Diameter (mm)	Height (mm)	Semi-conical angle (°)
Main roll	780	250	–
Mandrel	190	250	–
Support rolls	110	250	–
Conical rolls	450	730	18°

With the tool dimensions estimated, the geometries of all bodies were input into LS-DYNA. The geometric bodies prior to meshing are presented in Fig.2.4:

It is worth noting that not the entire conical rolls' length was used for the corresponding geometric bodies, as it would not be used in the simulation, thus less finite elements would be required.

2.5 Optimum Mesh Density

Meshing the geometric bodies is an essential part of performing a simulation. Although a mesh of any quality can produce numerical results, the numerical results are susceptible to numerical errors. In general, the coarser the mesh on a body is, the greater the value of the numerical error. This is mainly because the numerical approximation performed during a iteration cycle are heavily affected by the average element length. If the average element length is too large, the margin of error between the approximated and the real values grows

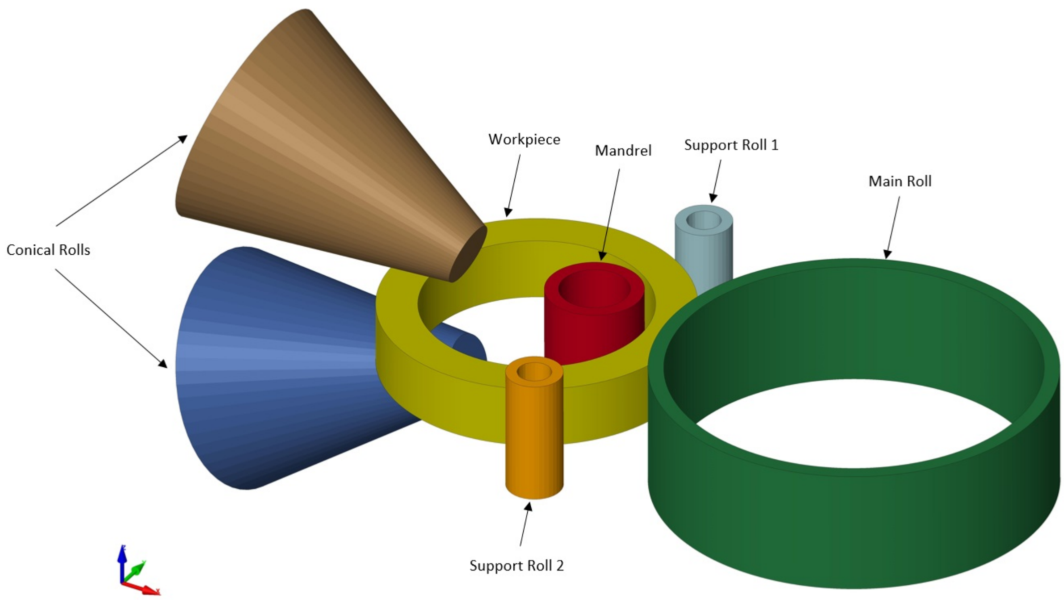

FIG. 2.4: Geometric representation of Ring Rolling setup

TABLE 2.2: Mesh independence analysis parameters

No of experiment	Average element length (mm)	Solution time (h)
1	12	52.9
2	6	235.7*
3	4	356.8
4	3	394.8

*Simulation was not completed for this case, thus the overall solution time was extrapolated from the end of the existing data to the predefined end time of the process.

larger. However, below a certain average element length, this margin of error becomes so little that the numerical model produces the same numerical results every time it repeats. Such numerical models are known as *"mesh independent"*.

For the model of Ring Rolling in the current thesis, a *"mesh independence"* experiment was designed. An early Ring Rolling model was repeated a number of times, until the numerical results had negligible differences between them. In each repeat, the mesh density of the ring blank was altered, with the average element length being reduced from one simulation to the next. The mesh of the tools was kept the same, as an early test with two different tool mesh densities showed no difference between their numerical results, mainly due to their rigid behavior. However, the mesh used for the tools in the final model was still comparable to that of the ring, so as not to have numerical errors building up in heat transfer calculations. It is worth noting that, the main rolling load was chosen as the reference point for the mesh independence analysis.

The parameters of the *"mesh independence"* analysis are summarized in Table 2.2, while an overview of the ring blanks' mesh are presented in Fig.2.5. It is worth noting that the solution time of Experiment 2 had to be approximated for the entirety of the model's duration, as the solution was not completed for this model.

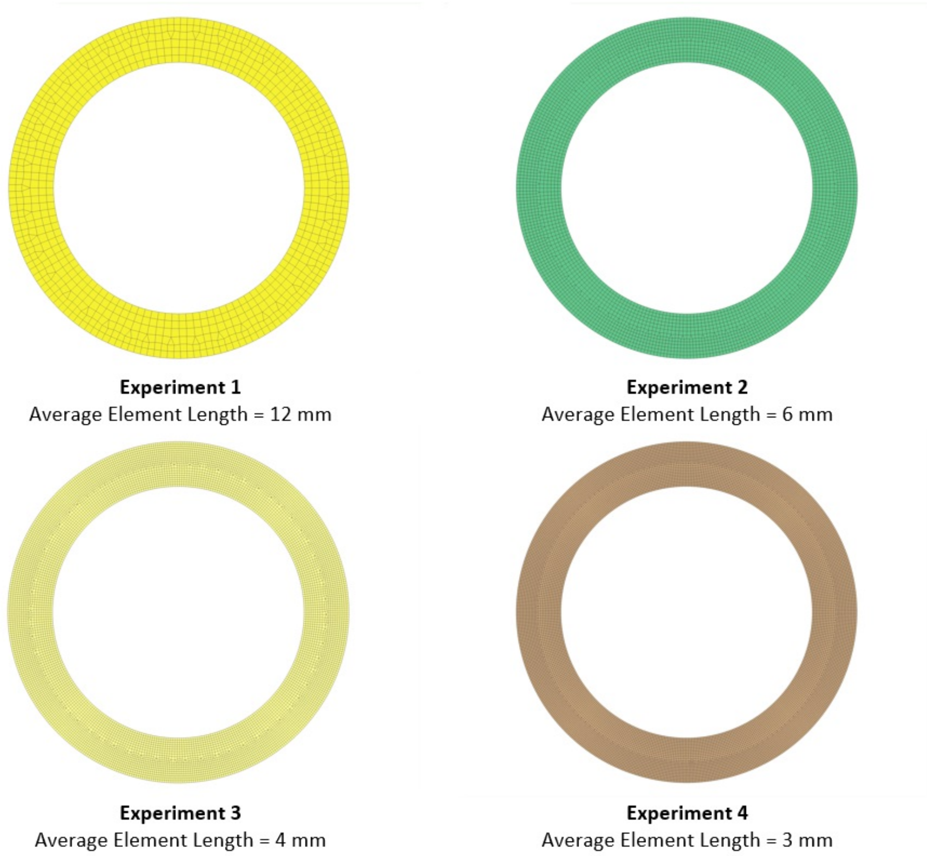

FIG. 2.5: Mesh Independence Analysis - Experiment Setup

After the numerical models for the mesh independence analysis were solved, the main rolling load results of each model were collected and compared to one another. The comparison between the main rolling load results are presented in Fig.2.6. It is worth noting that (as mentioned in Table2.2)the simulation of Experiment 2 was not completed, however the insufficiency of this specific mesh can be verified from the results received up to the interruption point.

From the comparison in Fig.2.6, it is clearly shown that the main rolling load results tend to converge in the case of experiments 3 and 4. Thus, a blank with **an average element length of 4 mm and below** should provide mesh independent numerical results. For this average element length, approximately 225,000 deformable elements are required for the simulation. From the corresponding results for rolling presented in Fig.2.3 and considering a similar implicit vs. explicit comparison for Ring Rolling, it is clear that for this number of elements, explicit formulation is the optimum choice.

It should be noted that the results deviations observed on the final segment of experiment 4 (Fig.2.6)are a result of a faulty movement of the support rolls, and thus they should not be taken into account.

The meshed bodies used in the Ring Rolling simulation are presented in Fig.2.7:

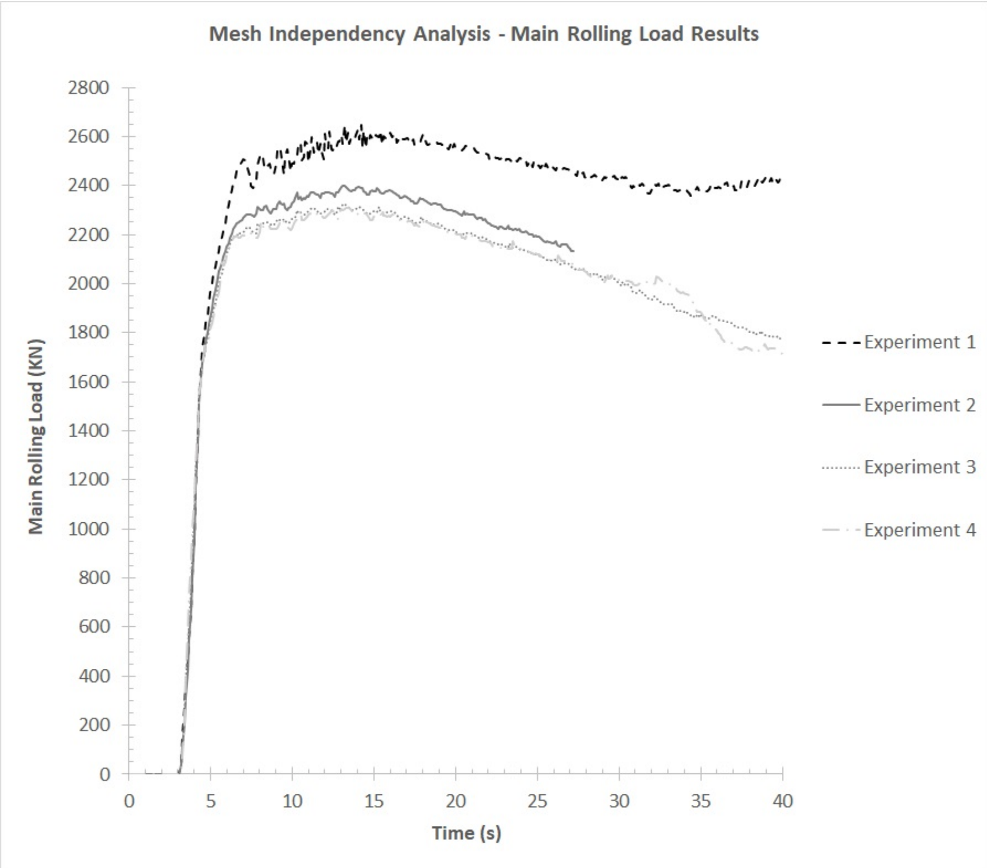

FIG. 2.6: Mesh Independence Analysis - Main Rolling Load Results

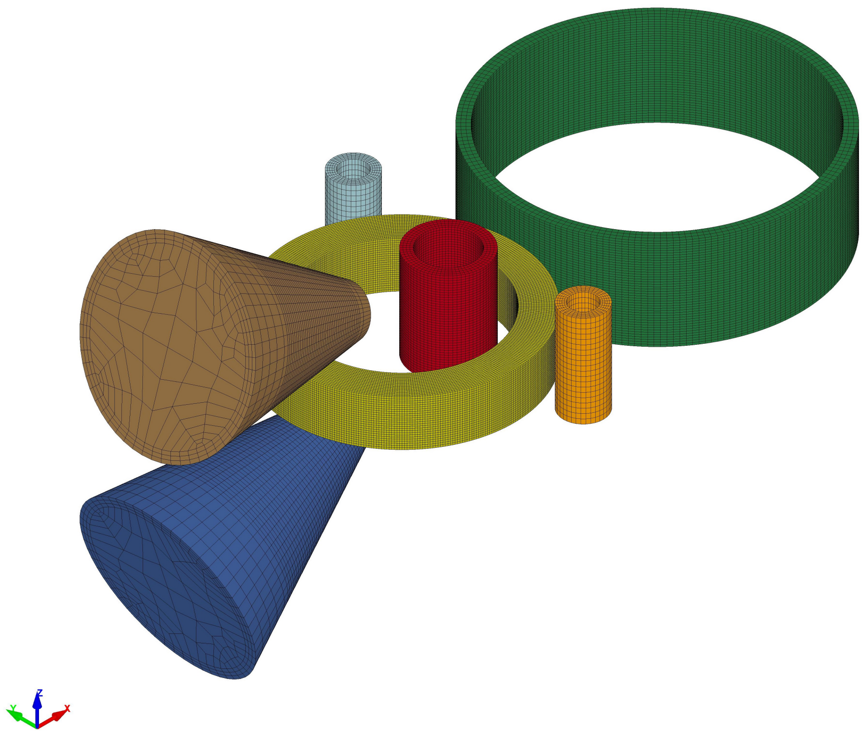

FIG. 2.7: Meshed bodies before simulation

2.6 Material Properties

A great part of a simulation's success lies with the proper definition of the mechanical properties of the blank and the tools. LS-DYNA offers a large library of material models that can be used to properly simulate the behavior of a vast list of materials. Based on the reference work used in the current dissertation, the ring's material is an **Inconel 718 alloy (IN718)**, while a tool steel (5CrNiMo) was used for the tools. Because of the lack of information for the aforementioned steel alloy, a very similar **hot work tool steel alloy (AISI H13)** was finally chosen and used in the current analysis.

As mentioned above, LS-DYNA provides a wide library of mathematical material models. After some preliminary tests, the most appropriate material model for the simulation of the workpiece ended up being MAT_106-ELASTIC_VISCOPLASTIC_THERMAL. In MAT_106,the user can directly input the stress-strain curves of the material. Moreover, if the stress-strain curves are correlated to their respective strain rate values (via DEFINE_TABLE), a temperature and strain rate dependent behavior of the material can also be simulated (via DEFINE_TABLE_3D). More specifically, the stress - strain curves have to be correlated to their respective strain rate values with the DEFINE_TABLE tool for each temperature point, and then the created stress-strain-strain rate surfaces have to be used as inputs in the DEFINE_TABLE_3D tool to correlate the aforementioned surfaces to their respective temperature values. Other necessary material properties that need to be defined are density, d, a curve correlating Young's Modulus, E with temperature, a curve correlating Poisson's ratio, v with temperature, yield strength, σ_Y with temperature and finally thermal expansion coefficient, α with temperature. Additionally and in order to simulate a body's thermal behavior, T10-THERMAL_ISOTROPIC_TD_LC material model was chosen. In this thermal material model, two curves correlating the the body's specific heat capacity, C with temperature and the body's thermal conductivity, K with temperature need to be input. Furthermore, the emissivity, ϵ of IN718 was estimated (**Greene, Finfrock, and Irvine, 1999**), as the thermal behavior of workpiece needs to be thoroughly characterized.

For the simulation of the tools, a different material model was chosen. As with most finite element simulations of manufacturing processes, the tools are usually simulated as perfectly rigid (undeformable) objects. For this reason, the mechanical behavior of tools was simulated with MAT_20-RIGID material model. In MAT_20, only some basic properties are required, namely density, d, Young's Modulus, E and Poisson's ratio, v, while some movement constrains for the bodies can also be input. The movement constrains can, however, be neglected, should other boundary conditions be defined. Seeing that no deformation occurs on the materials, the aforementioned mechanical properties are only required for the calculation of mass matrix and the estimation of the maximum iteration step from Courant-Friedrichs-Levy criterion. For the simulation of the thermal behavior of the tools, again T10-THERMAL_ISOTROPIC_TD_LC material model was used.

Regarding the values of the material properties input in the software for the analysis, they are summarized in Tables 2.3–2.4 and in Figs. 2.8–2.17:

TABLE 2.3: Material properties (IN718)

Property	Value or Curve	Reference
	IN718	
Density, d (kg m^{-3})	8240	*Zhu et al., 2016b*
Stress - Strain - Temperature surfaces for a Strain Rate Range of $\dot{\epsilon}$ = 0.01 – 10 s^{-1}	Fig.2.8	*Chaudhury and Zhao, 1992, Thomas et al., 2006, Iturbe et al., 2017, Jarugula et al., 2020*
Young's Modulus, E (GPa)	Fig.2.9	*Iturbe et al., 2017*
Poisson's Ratio, v	Fig.2.10	*Special_Metals_Corp., 2020*
Yield Strength for a Strain Rate Range of $\dot{\epsilon}$ = 0.01 – 10 s^{-1}, σ_Y (MPa)	Fig.2.11	*Chaudhury and Zhao, 1992, Thomas et al., 2006, Iturbe et al., 2017, Jarugula et al., 2020*
Coef. of Th. Expansion, α $\left(\cdot(10^{-6}) \text{ K}^{-1}\right)$	Fig.2.12	*Deshpande et al., 2011*
Thermal Conductivity, K (W m^{-1} K^{-1})	Fig.2.13	*Deshpande et al., 2011*
Specific Heat Capacity, C (J kg^{-1} K^{-1})	Fig.2.14	*Deshpande et al., 2011*

TABLE 2.4: Material properties (AISI H13)

Property	Value or Curve	Reference
	AISI H13	
Density, d (kg m^{-3})	7671	*Oh and Ki, 2019*
Young's Modulus, E (GPa)	190.6	*Tolcha and Lemu, 2019*
Poisson's Ratio, v	0.374	*Tolcha and Lemu, 2019*
Thermal Conductivity, K (W m^{-1} K^{-1})	Fig.2.16	*Tolcha and Lemu, 2019*
Specific Heat Capacity, C (J kg^{-1} K^{-1})	Fig.2.17	*Oh and Ki, 2019*

The material property values presented in Table 2.4 correspond to a temperature of 573.15K, which is the temperature of the tools at the beginning of the simulation.

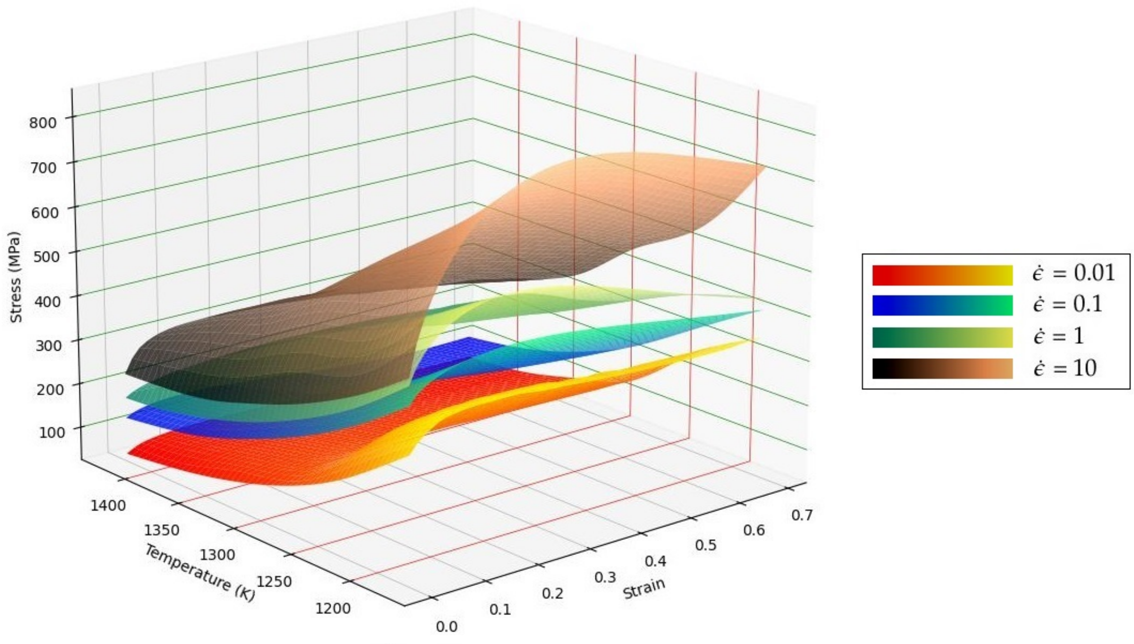

FIG. 2.8: Stress - Strain - Temperature Surfaces for a Strain Rate Range of $\dot{\epsilon} = 0.01 - 10\ \mathrm{s}^{-1}$ (IN718)

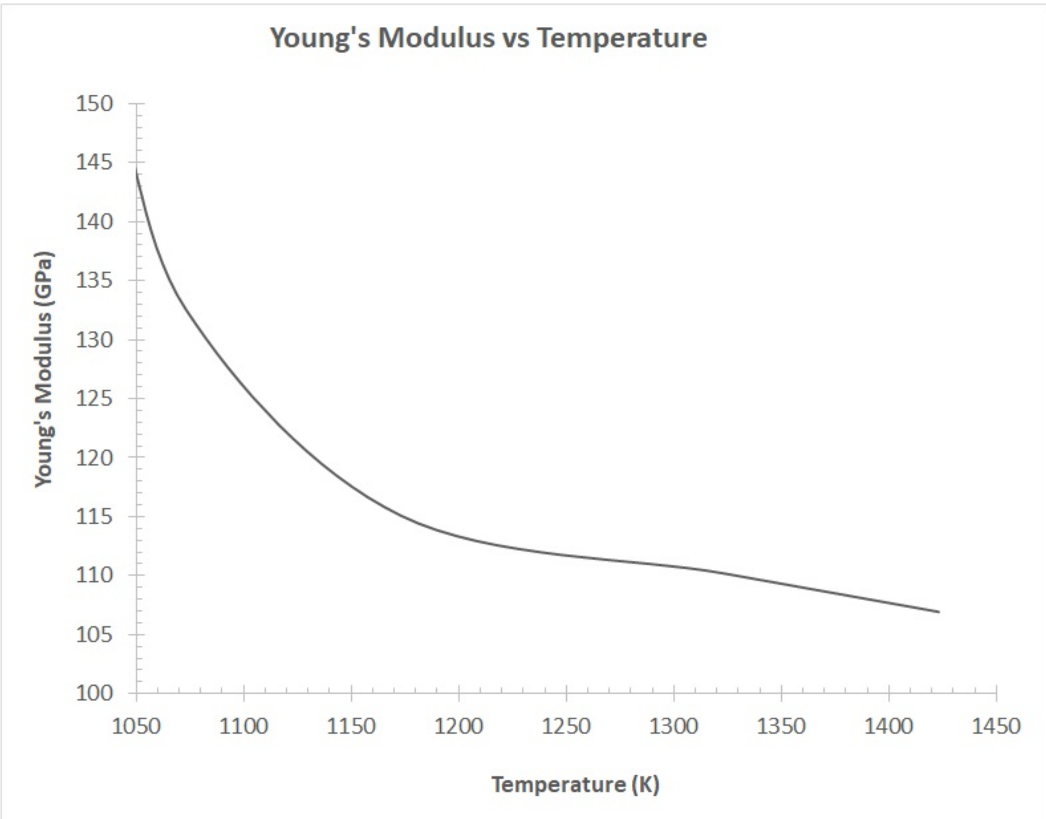

FIG. 2.9: Young's Modulus vs. Temperature (IN718)

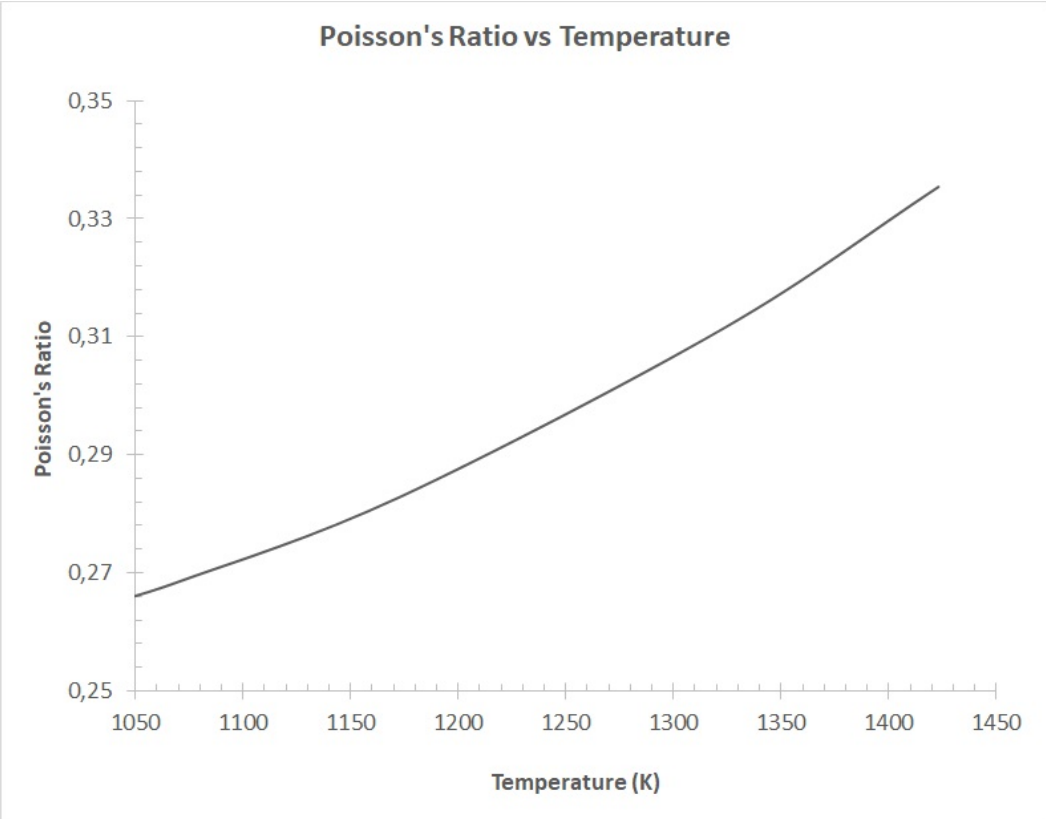

FIG. 2.10: Poisson's Ratio vs. Temperature (IN718)

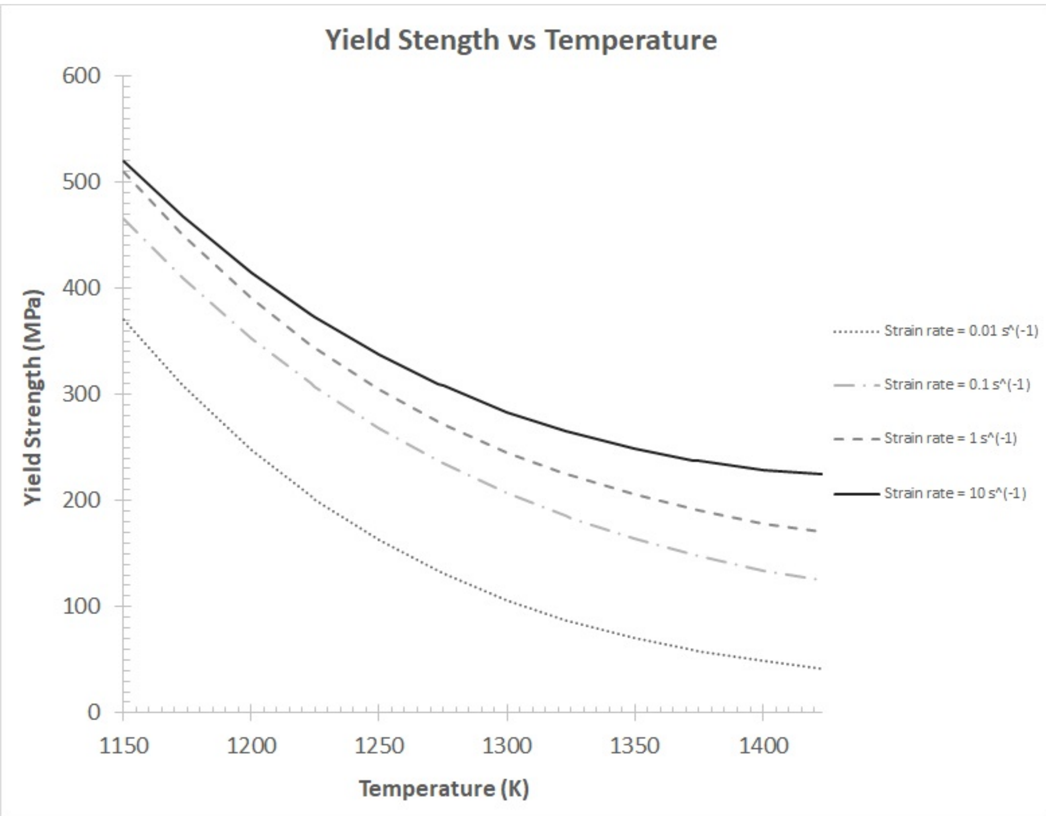

FIG. 2.11: Yield Strength vs. Temperature (IN718)

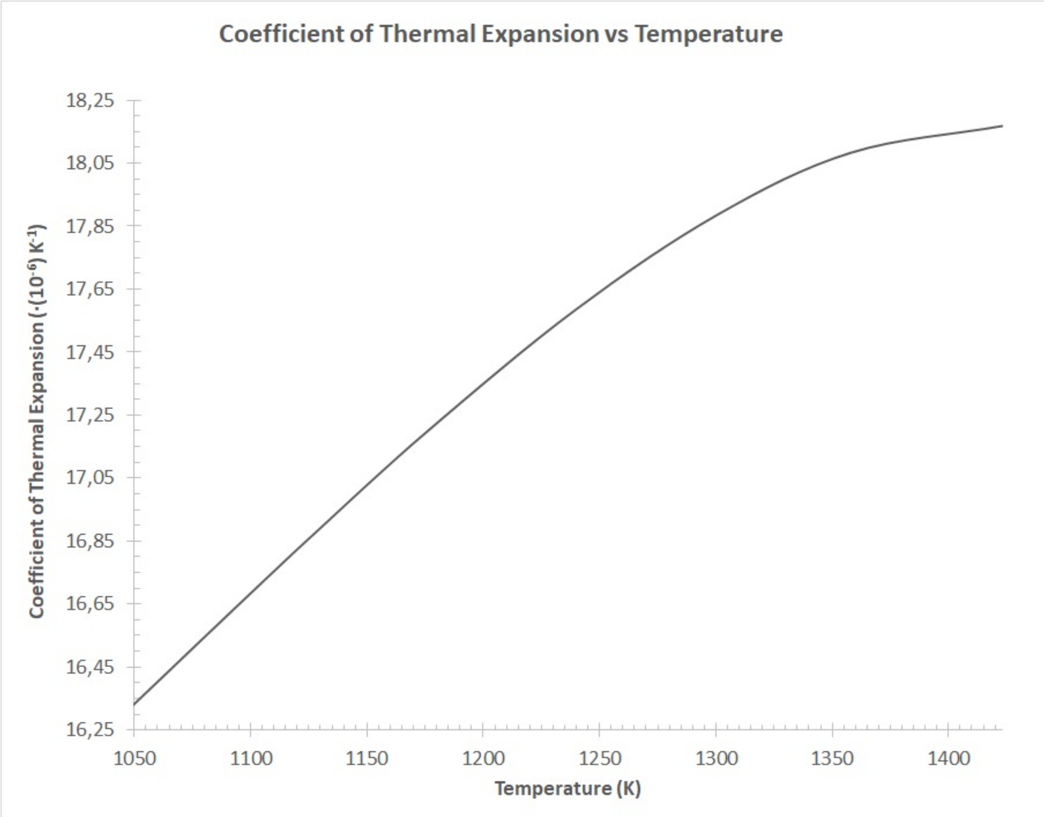

FIG. 2.12: Coefficient of Thermal Expansion vs. Temperature (IN718)

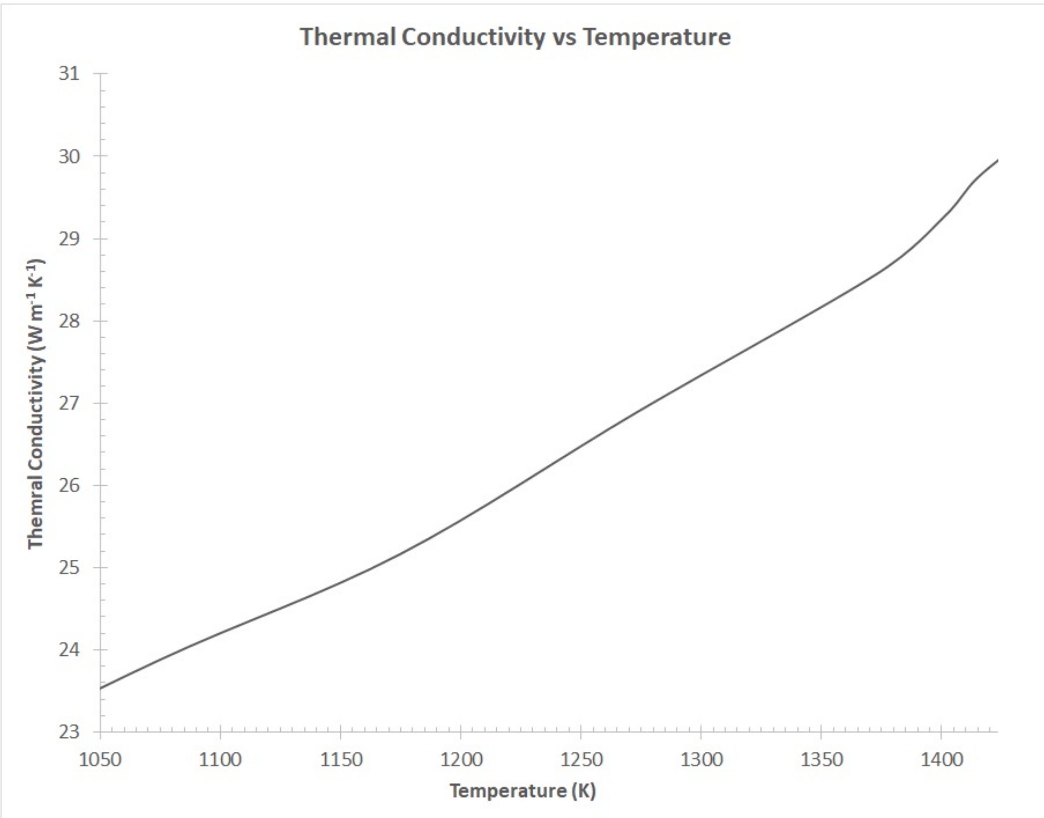

FIG. 2.13: Thermal Conductivity vs. Temperature (IN718)

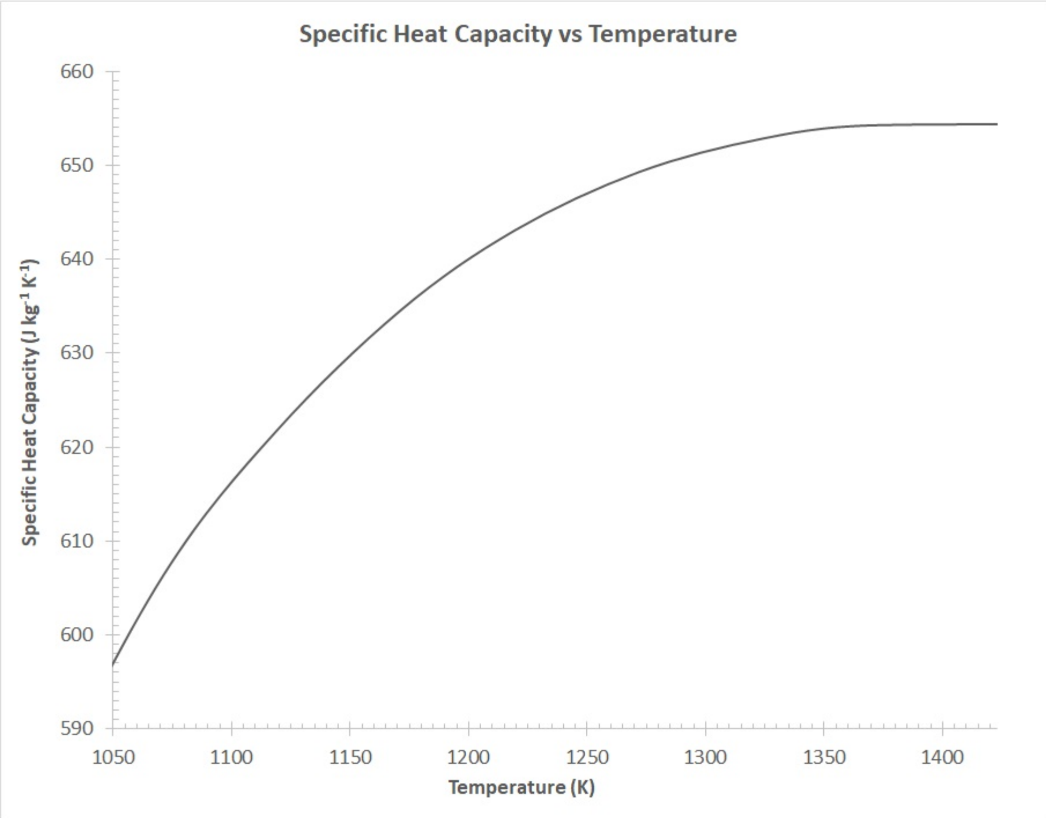

FIG. 2.14: Specific Heat Capacity vs. Temperature (IN718)

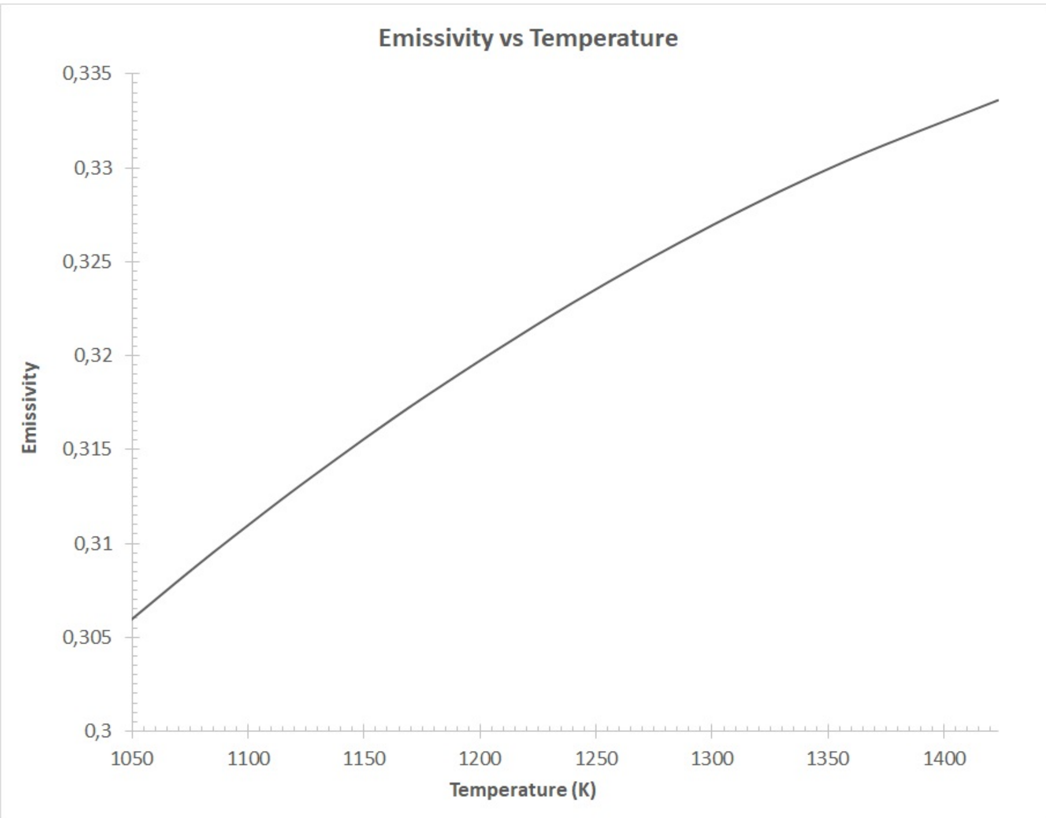

FIG. 2.15: Emissivity vs. Temperature (IN718)

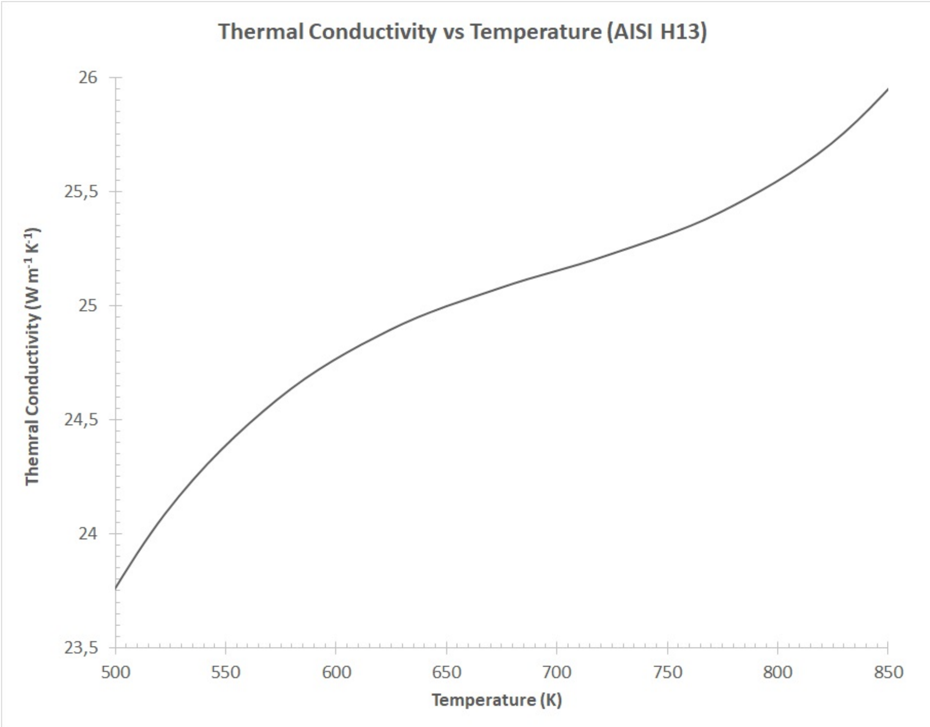

FIG. 2.16: Thermal Conductivity vs. Temperature (AISI H13)

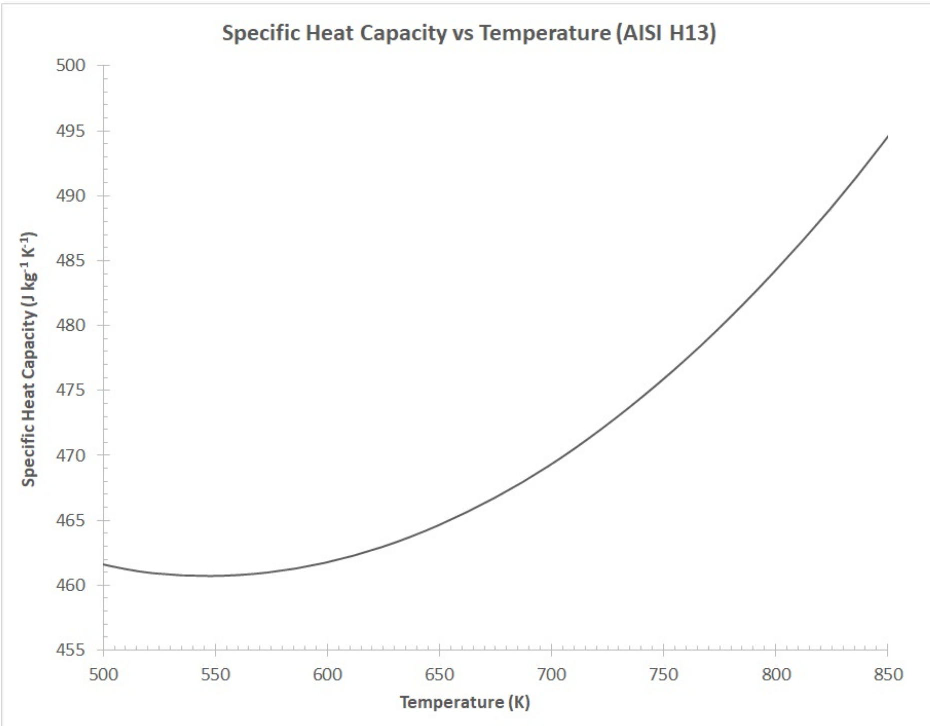

FIG. 2.17: Specific Heat Capacity vs. Temperature (AISI H13)

It is worth noting that, the properties presented in Figs.2.8–2.17 correspond to a slightly wider temperature range than the one that the corresponding bodies will go through during the simulation. Also, for the creation of Fig.2.8, a python script presented in Appendix B.1 was written and used.

2.7 Proper Finite Element Type (Hallquist, 2006)

The choice of the proper finite element type is fundamental for the accurate simulation of the manufacturing process. In general, in a mesh of 8-node hexahedron solid elements, Eq.1.25 becomes:

$$x_i(X_a,t) = x_i(X_a(\xi,\eta,\zeta),t) = \sum_{j=1}^{8} \phi_j(\xi,\eta,\zeta) x_i^j(t) \tag{2.22}$$

The shape function ϕ_j is defined for the 8-node hexahedron as:

$$\phi_j = \frac{1}{8}(1+\xi\xi_j)(1+\eta\eta_j)(1+\zeta\zeta_j) \tag{2.23}$$

where ξ_j, η_j, ζ_j take on their nodal values of (±1, ±1, ±1) and x_i^j is the nodal coordinate of the j$^t h$ node in the i$^t h$ direction (also see Fig.2.18):

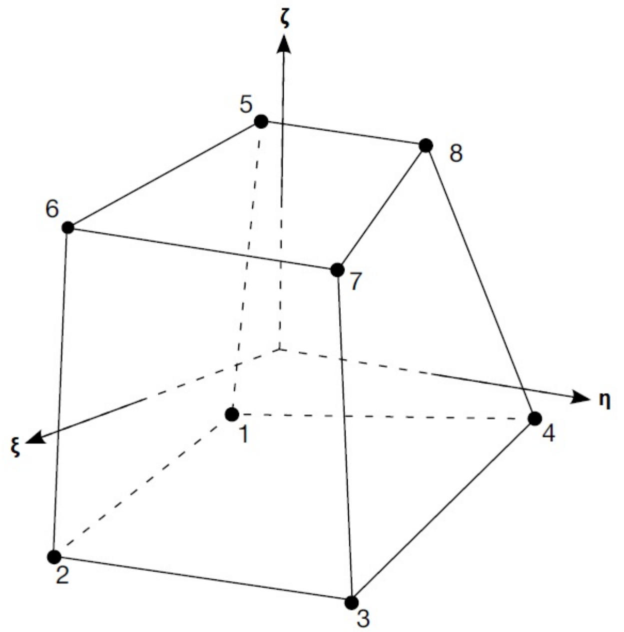

Node	ξ	η	ζ
1	-1	-1	-1
2	1	-1	-1
3	1	1	-1
4	-1	1	-1
5	-1	-1	1
6	1	-1	1
7	1	1	1
8	-1	1	1

FIG. 2.18: Eight node solid hexahedron element

For a solid element, N is the 3×24 rectangular interpolation matrix given by the following equation:

$$N(\xi,\eta,\zeta) = \begin{bmatrix} \phi_1 & 0 & 0 & \phi_2 & 0 & \dots & 0 & 0 \\ 0 & \phi_1 & 0 & 0 & \phi_2 & \dots & \phi_8 & 0 \\ 0 & 0 & \phi_1 & 0 & 0 & \dots & 0 & \phi_8 \end{bmatrix} \tag{2.24}$$

σ is the stress vector noted as:

$$\sigma = (\sigma_{xx}, \sigma_{yy}, \sigma_{zz}, \sigma_{xy}, \sigma_{yz}, \sigma_{zx}) \tag{2.25}$$

B is the 6×24 strain-displacement matrix:

$$\boldsymbol{B} = \begin{bmatrix} \frac{\vartheta}{\vartheta x} & 0 & 0 \\ 0 & \frac{\vartheta}{\vartheta y} & 0 \\ 0 & 0 & \frac{\vartheta}{\vartheta z} \\ \frac{\vartheta}{\vartheta y} & \frac{\vartheta}{\vartheta x} & 0 \\ 0 & \frac{\vartheta}{\vartheta z} & \frac{\vartheta}{\vartheta y} \\ \frac{\vartheta}{\vartheta z} & 0 & \frac{\vartheta}{\vartheta x} \end{bmatrix} \boldsymbol{N} \tag{2.26}$$

In order to achieve a diagonal mass matrix, the rows are summed, giving the kth diagonal term as per the following equation:

$$m_{kk} = \int_v \rho \phi_k \sum_{i=1}^{8} \phi_k dv = \int_v \rho \phi_k dv \tag{2.27}$$

since the basis functions sum to unity.

Terms in the strain-displacement matrix are readily calculated. Note that the shape function partial derivatives can be expressed as follows:

$$\begin{aligned} \frac{\vartheta \phi_i}{\vartheta \xi} &= \frac{\vartheta \phi_i}{\vartheta x}\frac{\vartheta x}{\vartheta \xi} + \frac{\vartheta \phi_i}{\vartheta y}\frac{\vartheta y}{\vartheta \xi} + \frac{\vartheta \phi_i}{\vartheta z}\frac{\vartheta z}{\vartheta \xi} \\ \frac{\vartheta \phi_i}{\vartheta \eta} &= \frac{\vartheta \phi_i}{\vartheta x}\frac{\vartheta x}{\vartheta \eta} + \frac{\vartheta \phi_i}{\vartheta y}\frac{\vartheta y}{\vartheta \eta} + \frac{\vartheta \phi_i}{\vartheta z}\frac{\vartheta z}{\vartheta \eta} \\ \frac{\vartheta \phi_i}{\vartheta \zeta} &= \frac{\vartheta \phi_i}{\vartheta x}\frac{\vartheta x}{\vartheta \zeta} + \frac{\vartheta \phi_i}{\vartheta y}\frac{\vartheta y}{\vartheta \zeta} + \frac{\vartheta \phi_i}{\vartheta z}\frac{\vartheta z}{\vartheta \zeta} \end{aligned} \tag{2.28}$$

which can be rewritten as:

$$\begin{bmatrix} \frac{\vartheta \phi_i}{\vartheta \xi} \\ \frac{\vartheta \phi_i}{\vartheta \eta} \\ \frac{\vartheta \phi_i}{\vartheta \zeta} \end{bmatrix} = \begin{bmatrix} \frac{\vartheta x}{\vartheta \xi} & \frac{\vartheta y}{\vartheta \xi} & \frac{\vartheta z}{\vartheta \xi} \\ \frac{\vartheta x}{\vartheta \eta} & \frac{\vartheta y}{\vartheta \eta} & \frac{\vartheta z}{\vartheta \eta} \\ \frac{\vartheta x}{\vartheta \zeta} & \frac{\vartheta y}{\vartheta \zeta} & \frac{\vartheta z}{\vartheta \zeta} \end{bmatrix} \begin{bmatrix} \frac{\vartheta \phi_i}{\vartheta x} \\ \frac{\vartheta \phi_i}{\vartheta y} \\ \frac{\vartheta \phi_i}{\vartheta z} \end{bmatrix} = \boldsymbol{J} \begin{bmatrix} \frac{\vartheta \phi_i}{\vartheta x} \\ \frac{\vartheta \phi_i}{\vartheta y} \\ \frac{\vartheta \phi_i}{\vartheta z} \end{bmatrix} \tag{2.29}$$

Thus, the desired terms can be calculated by inverting the Jacobian matrix **J** and solving the following:

$$\begin{bmatrix} \frac{\vartheta \phi_i}{\vartheta x} \\ \frac{\vartheta \phi_i}{\vartheta y} \\ \frac{\vartheta \phi_i}{\vartheta z} \end{bmatrix} = \boldsymbol{J}^{-1} \begin{bmatrix} \frac{\vartheta \phi_i}{\vartheta \xi} \\ \frac{\vartheta \phi_i}{\vartheta \eta} \\ \frac{\vartheta \phi_i}{\vartheta \zeta} \end{bmatrix} \tag{2.30}$$

Regarding the volume integration in solid elements, this is carried out with Gaussian quadrature. If g is some function defined over the volume and n is the number of integration points, then the following equation applies:

$$\int_v g dv = \int_{-1}^{1}\int_{-1}^{1}\int_{-1}^{1} g|\boldsymbol{J}|d\xi d\eta d\zeta \tag{2.31}$$

which can be approximated by:

$$\sum_{j=1}^{n}\sum_{k=1}^{n}\sum_{l=1}^{n} g_{jkl}|J_{jkl}|w_j w_k w_l \tag{2.32}$$

where:

w_j, w_k, w_l, are the weighting factors,

$g_{jkl} = g(\xi_j, \eta_k, \zeta_l)$

and J, is the determinant of the Jacobian matrix.

For a one-point quadrature the following are in effect:

$$n = 1$$
$$w_i = w_j = w_k = 2$$
$$\xi_1 = \eta_1 = \zeta_1 = 0$$

and Eq.2.31 can be written as:

$$\int g dv = 8g(0,0,0)|\boldsymbol{J}(0,0,0)| \tag{2.33}$$

Note that $8|J(0,0,0)|$ approximates the element volume.

Perhaps the biggest advantage to one-point integration is a substantial savings in computational time. An anti-symmetry property of the strain matrix at $\xi = \eta = \zeta = 0$ reduces the amount of effort required to compute the aforementioned matrix by more than 25 times over an 8-point integration. This cost savings extend to strain and element nodal force calculations, where the number of multiplications is reduces by a factor of 16. Because only one constitutive evaluation is needed, the time spent determining stresses is reduced by a factor of 8. It is worth noting that the anti-symmetry in the strain matrix is expressed as:

$$\begin{aligned} \frac{\vartheta\phi_1}{\vartheta x_i} &= -\frac{\vartheta\phi_7}{\vartheta x_i}, & \frac{\vartheta\phi_3}{\vartheta x_i} &= -\frac{\vartheta\phi_5}{\vartheta x_i}, \\ \frac{\vartheta\phi_2}{\vartheta x_i} &= -\frac{\vartheta\phi_8}{\vartheta x_i}, & \frac{\vartheta\phi_4}{\vartheta x_i} &= -\frac{\vartheta\phi_6}{\vartheta x_i} \end{aligned} \tag{2.34}$$

Other than the increased cost, another disadvantage of the 8-point or fully integrated element used in the solution of plasticity problems and problems where Poisson's ratio approaches 0.5 is that they tend to lock up in constant volume bending modes. In order to preclude locking, an average pressure must be used over the elements, thus consequently, the zero energy modes are resisted by the deviatoric stresses. If the deviatoric stresses are insignificant relative to the pressure or if the material failure causes loss of this stress state component, hourglassing will occur with no means of resisting it. However, both the increased cost and the additional effort to counter element locking may sometimes be justified by their increased reliability and if used sparingly they may actually increase the overall speed of the simulation.

The aforementioned methodology may be expanded to all solid element types, regardless of the problem simulated, given that the proper modifications on the corresponding Jacobian matrix and shape functions of each element type are taken into consideration.

2.7.1 Solid Element Type

For the needs of the analyses of the current dissertation and after searching through the relative literature (**Hallquist, 2006, *LS-DYNA Keyword Use's Manual – Volume 1* 2020, Schmied and Erhart, 2018**), two different element types were elected as the most compatible in terms of deformational behavior and total computational time, namely *SOLID_ELEMENT _1: Constant Stress Solid Element* and *SOLID_ ELEMENT_2: 8-Node Hexahedron*. A brief explanation of the governing system of equations is presented in the following subchapters, for both of the elected element types.

The reason for the choice of the aforementioned element types lies with the mechanics of the analyzed manufacturing process. More specifically, during Ring Rolling the elements are expected to progressively lose their initially cubic shape, thus favor poorer aspect ratios in them. This is mainly due to the fact that the elements elongate circumferentially and compress axially and radially. However, the aspect ratio on the final model transitioned from approximately 1:1 to an 1:2 ratio, which is not considered large enough to induce shear locking on the elements. Furthermore, only slight bending of the elements is expected, as the contacts with the tools are continuous with large contact surfaces. Thus, SOLID_ELEMENT_2 is considered as a good choice for the workpiece in order to eliminate any potential numerical instabilities, while SOLID_ELEMENT_1 with the proper HOURGLASS_CONTROL is considered for the tools in order to maintain the total computational cost as low as possible. It is worth noting that SOLID_ELEMENT_1 was maintained for the tools, even in the analyses where these deformed (elastically and/or thermally), as the aforementioned tool deformations were relatively small to cause any numerically instabilities.

It is worth noting that LS-DYNA includes two more recent, fully integrated solid element types (ELFORM = -1 and -2), which use a modified Jacobian matrix to reduce the spurious stiffness without affecting the true physical behavior of the finite elements, they add a considerable amount of computational cost to the overall process, thus rendering them as not so efficient. The same applies to other higher order element types (e.g. 20, 40 or 64-noded cubic elements), which increase the computational cost by adding more calculation points in their respective shape functions.

2.7.2 SOLID_ELEMENT_1 Governing Equations

SOLID_ELEMENT_1 is a constant stress solid 8-node element, with a single integration point. The constant stress is underintegrated on the elements, thus rank-deficient stiffness matrices are produced from this process. As a result, numerical instabilities can occur (**Jacquotte, 1985**). In order to overcome these instabilities, LS-DYNA requires hourglass stabilization when this element type is used. LS-DYNA offers many different hourglass formulations that create artificial stiffness of viscosity matrices, which stabilize their respective matrices during the numerical integration (for more information, please refer to §2.11). Seeing that SOLID_ELEMENT_1 has a single integration point, the governing equations presented above (namely, Eqs.2.22-2.34) apply to the current element type, as they are (no modifications are required for the shape function and Jacobian matrix). Overall, this solid element type is the default option for 3D solid simulations in LS-DYNA, as it is considered accurate and efficient even in simulations with severe deformations.

2.7.3 SOLID_ELEMENT_2 Governing Equations

SOLID_ELEMENT_2 is an 8-node fully, selective reduced integrated solid element, which generally regarded as too stiff, especially when the elements exhibit poor aspect ratio, i.e., when one element dimension is significantly smaller than the others. This occurs for instance when modelling thin walled structures, and the time for solving the problem prevents using a sufficient number of elements for maintaining close to cubic elements throughout the structure. The reason for the locking phenomenon is that the element is not able to represent pure bending modes without introducing transverse shear strains, and this may be bad enough to lock the element to a great extent. Overall, SOLID_ELEMENT_2 is regarded as a good choice in simulations where numerical instabilities may occur (no

HOURGLASS_CONTROL is required for this element type), even if it is slightly slower than SOLID_ELEMENT_1.

Regarding the governing system of equations of SOLID_ELEMENT_2, consider an 8-noded solid hexahedron element (Fig.2.18). Let x_{Ii} represent the nodal coordinate of dimension i and node I, and likewise v_{Ii} its velocity. Also, denote that the rectangular interpolation matrix becomes:

$$N_I(\xi_1,\xi_2,\xi_3) = \frac{1}{8}(1+\xi_1^I\xi_1+\xi_2^I\xi_2+\xi_3^I\xi_3+\xi_{12}^I\xi_1\xi_2+\xi_{13}^I\xi_1\xi_3+\xi_{23}^I\xi_2\xi_3+\xi_{123}^I\xi_1\xi_2\xi_3) \quad (2.35)$$

The shape function for the standard isoparametric domain is:

$$\begin{aligned}
\xi_1^* &= [-1 \quad 1 \quad 1 \quad -1 \quad -1 \quad 1 \quad 1 \quad -1] \\
\xi_2^* &= [-1 \quad -1 \quad 1 \quad 1 \quad -1 \quad -1 \quad 1 \quad 1] \\
\xi_3^* &= [-1 \quad -1 \quad -1 \quad -1 \quad 1 \quad 1 \quad 1 \quad 1] \\
\xi_{12}^* &= [\ 1 \quad -1 \quad 1 \quad -1 \quad 1 \quad -1 \quad 1 \quad -1] \\
\xi_{13}^* &= [\ 1 \quad -1 \quad -1 \quad 1 \quad 1 \quad -1 \quad 1 \quad -1] \\
\xi_{23}^* &= [\ 1 \quad 1 \quad -1 \quad -1 \quad -1 \quad -1 \quad 1 \quad 1] \\
\xi_{123}^* &= [-1 \quad 1 \quad -1 \quad 1 \quad 1 \quad -1 \quad 1 \quad 1]
\end{aligned} \quad (2.36)$$

Furthermore, assume the following conditions are true:

$$\begin{aligned}
\xi_{21}^I &= \xi_{12}^I \\
\xi_{32}^I &= \xi_{23}^I \\
\xi_{31}^I &= \xi_{13}^I
\end{aligned} \quad (2.37)$$

The isoparametric representation of the coordinates of a material point in the element is then given as follows (where the dependence on ξ_1,ξ_2,ξ_3 is suppressed for brevity):

$$x_i = x_{Ii}N_I \quad (2.38)$$

and its associated Jacobian matrix is:

$$J_{ij} = \frac{\vartheta x_i}{\vartheta \xi_j} = x_{Ii}\frac{1}{8}(\xi_j^I + \xi_{jk}^I\xi_k + \xi_{jl}^I\xi_l + \xi_{123}^I\xi_k\xi_l) \quad (2.39)$$

where:

- k=1+mod(j,3)
- l=1+mod(j+1,3)

For future reference, let the following be the Jacobian, evaluated in the element center and in the beginning of the simulation (i.e, at time zero):

$$J_{ij}^0 = x_{Ii}(0)\frac{1}{8}\xi_j^I \quad (2.40)$$

The velocity gradient computed directly from the shape functions and velocity components is:

$$L_{ij} = \frac{\vartheta v_i}{\vartheta x_j} = \dot{J}_{ik}J_{kj}^{-1} = B_{ijIk}v_{Ik} \quad (2.41)$$

where the gradient-displacement matrix, B_{ijIk} is given by:

$$B_{ijIk} = \frac{\vartheta N_I}{\vartheta \xi_l} J_{lj}^{-1} \delta_{ik} \tag{2.42}$$

It is worth noting that B_{ijIk} represents the element except for the alleviation of volumetric locking. The alleviation of the volumetric locking is further discussed below. Thus, the initial state of the element B^0_{ijIk} can be defined by the following expression:

$$\dot{\acute{J}}_{ik} \acute{J}_{kj}^{-1} = B^0_{ijIk} v_{Ik} \tag{2.43}$$

with $\acute{J}_{ij}$ being the element averaged Jacobian matrix and construct the gradient-displacement matrix used for the element as follows:

$$\acute{B}_{ijIk} = B_{ijIk} + \frac{1}{3}(B^0_{llIk} - B_{llIk})\delta_{ij} \tag{2.44}$$

This formulation is often called the B-bar method.

In order to alleviate transverse shear locking, certain modifications on the Jacobian matrix and the velocity gradient have to be done. Initially, a parallelepiped of dimensions $l_1 \times l_2 \times l_3$ is considered (solid-lined hexahedron in Fig.2.19):

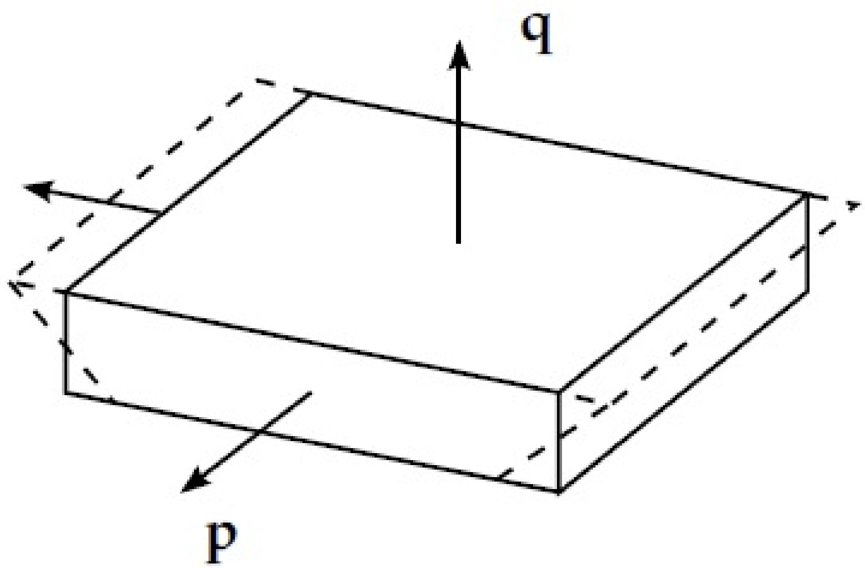

FIG. 2.19: Bending mode for a fully integrated brick

For this simple geometry the Jacobian matrix is diagonal, while the velocity gradient is expressed as follows:

$$L_{ij} = \frac{2}{l_j} \dot{J}_{ij} = \frac{1}{4l_j} v_{Ii}(\xi^I_j + \xi^I_{jk}\xi_k + \xi^I_{jl}\xi_l + \xi^I_{123}\xi_k\xi_l) \tag{2.45}$$

Let $i \neq p \neq q \neq i$, then a pure bending mode in the plane with normal in direction q and about axis p is represented by the following set of equations:

$$\begin{aligned} v_{Ii} &= \xi^I_{iq} \\ v_{Ip} &= 0 \\ v_{Iq} &= 0 \end{aligned} \tag{2.46}$$

and thus the velocity gradient is given as:

$$\begin{aligned} L_{ij} &= \tfrac{1}{4l_j}(\xi^I_{iq}\xi^I_{jk}\xi_k + \xi^I_{iq}\xi^I_{jl}\xi_l) \\ L_{pj} &= 0 \\ L_{qj} &= 0 \end{aligned} \tag{2.47}$$

for j=1,2,3. The nonzero expression above amounts to the following:

$$\begin{aligned} L_{ii} &= \tfrac{1}{4l_i}\xi_q \\ L_{ip} &= 0 \\ L_{iq} &= \tfrac{1}{4l_q}\xi_i \end{aligned} \tag{2.48}$$

Notably, from the set of Eqs.2.48, the last expression represents a pure bending mode that leads to a transverse shear strain. Assuming that l_q is small compared to l_i, this more often than not locks the element, preventing it from further displacement. It is worth noting that the term element locking refers to a phenomenon where under certain circumstances displacements that are orders of magnitude smaller than they should be, are calculated by the finite element method. The two most common types of locking are shear and pressure locking. Shear locking occurs when elements are subjected to bending, and pressure locking occurs when the material is incompressible. Locking commonly occurs in lower order elements because an element's kinematics aren't rich enough to represent the correct solution. Most of the research on reducing locking is devoted to elements with linear shape functions, with the remainder devoted to quadratic elements.

2.8 Contact Definition

In order to guarantee a proper interaction between the different bodies, contacts have to be well-adjusted. In LS-DYNA, apart from the setup of interactions between different bodies, there are various options that ensure different aspects in a numerical contact. From these, perhaps the most important ones have to do with avoiding interfacial penetrations in each contact pair and (in the case of thermo-mechanical simulations) ensuring the proper heat transfer between the bodies. These two major aspects are analyzed separately in the following subsections.

2.8.1 Interfacial Penetration Reduction

Interfacial penetrations are always a matter of concern in multi-body simulations. In most simulations, penetrations of nodes in the contacting body's surface is inevitable, thus measures of minimizing this phenomenon are usually taken. The most common and effective way in through the manipulation of pinball radius.

Pinball radius manipulation is a technique commonly used in finite element analyses. A pinball radius is a spherical numerical volume (with a radius equal to the pre-set pinball radius) created around nodes (usually) of a contacting body towards the target body. Should a node's spherical volume pass come in contact or pass through a target body's surface segment, the software can perform different actions (as per the definition of the user) to ensure a contacting behavior. Usually, a pinball radius acts as a trigger for contact recognition, with the target body starting to apply forces on the contacting node, when its spherical volume comes in contact with the target's surface segment. However, other options are also possible, for example applying damping effects or recognizing a full-contact of a percentage of pinball radius. Nevertheless, the appropriate choice of the pinball radius is of utmost importance, as a small pinball radii risks for penetrations of the surface segments of different bodies, while large pinball radii allow for pseudo-contacts, thus creating false effects.

In the case of Ring Rolling, the appropriate tool for controlling pinball radius was utilized (*OPTIONAL CARD A: Offset options* on the chosen CONTACT types). Initially, however, a proper contact type had to be chosen. Seeing that both the ring and the bodies had a circular circumference, AUTOMATIC_SURFACE_TO_SURFACE_SMOOTH contact type was chosen. This particular contact type has three different components, as shown by its name:

- The AUTOMATIC type contacts have null beams to the exterior edges of segments so that edge-to-edge treatment of the parts is applied. Also, when the AUTOMATIC option is used, the orientations of segment normals are automatic. Thus, after penetrating segments are found, an automatic judgment is made as to which is the master segment, and penalty forces are applied normal to that segment.
- In SURFACE_TO_SURFACE contacts, the contact algorithm checks for segments vs. segment penetration rather than node vs. segment. This is performed via mid surface vectors created automatically for each of the contacting segments.
- SMOOTH option considers a smooth curve-fitted surface, so that it can provide a more accurate representation of the actual surface for both the slave and master sides. This results in reducing the contact noise, and producing smoother results with coarser meshes.

For the chosen contact type, the rest of the options from *OPTIONAL CARD A: Offset options* had to be properly input:

- The soft constraint *SOFT=2* that was selected, is a segment based contact with the properties described above to work in here.
- *SOFSCL*, is the scale factor for constraint forces of soft constraint option. The default value of 0.10 was chosen in the current analysis.
- *MAXPAR*, is the maximum parametric coordinate in segment search. This parameter allows for a percentage of the average element length to be used for the searching of contacts. In this case, a value of 1.20 was used.
- *SBOPT*, is the contact options for *SOFT=2*. In the current analysis, *SBOPT=2* was chosen, which assumes planer segments in the contacts (it is the default option).
- Finally, *DEPTH* normally defines the search depth in automatic contacts or checks for nodal penetration through the closest contact segments. In the case of *SOFT=2*, however, this option has different functions. In the current analysis, a *DEPTH=5* was chosen, where both surface penetrations and edge-to-edge penetrations are checked.

Finally, for the estimation of both the static, *FS* and dynamic, *FD* friction coefficients, the corresponding options on *CARD 1* of each of the set contacts were used. LS-DYNA uses Eq.2.49 to estimate the friction coefficient each time:

$$\mu_C = FD + (FS - FD) \cdot e^{-DC \cdot |v_{rel}|} \tag{2.49}$$

where:

- *DC*, is the exponential decay coefficient currently set as zero (default value)
- v_{rel}, is the relative velocity between the two contacting surfaces

In order to reassure that no sliding occurs between the tools and the workpiece (sticking contact conditions), something that is widely accepted in well-set Ring Rolling processes (**Gontarz and Surdacki, 2019**), some fairly large friction coefficients were chosen. The chosen friction coefficients are presented in Table 2.5:

TABLE 2.5: Friction Coefficients

Contacting bodies	**FS**	**FD**	μ_C
Ring - Main Roll	0.6	0.5	0.6
Ring - Mandrel	0.5	0.4	0.5
Ring - Support Rolls	0.3	0.2	0.3
Ring - Axial Rolls	0.3	0.2	0.3

2.8.2 Interfacial Heat Transfer

Another crucial functionality of contacts is the definition of interfacial heat transfer properties. This function is activated from checking *OPTIONAL CARD: Thermal*. From the activation of *OPTIONAL CARD: Thermal*, it is possible to determine the thermal conductivity of a fluid between two surfaces (e.g. coolant), the radiated heat transfer and the conductance heat transfer, while the gap values can also be defined. More specifically, the following options are available:

- *K*, allow for the definition of thermal conductivity of a fluid between the contact surfaces. Considering a gap l_{gap} between the two surfaces, the conductivity coefficient is given by Eq.2.50:

$$h_{cond} = \frac{K}{l_{gap}} \tag{2.50}$$

  where l_{gap} is calculated automatically during the solution, given the deformation of the contacting surfaces each time.

- *FRAD*, is the radiation factor between the contact surfaces. It is given by Eq.2.51:

$$f_{rad} = \frac{\sigma}{\frac{1}{\epsilon_1} + \frac{1}{\epsilon_2} - 1} \tag{2.51}$$

  where:

  - σ, is the Stefan-Boltzmann constant
  - ϵ_1, is the emissivity of the master surface
  - ϵ_2, is the emissivity of the slave surface

LS-DYNA then estimates the radiant heat transfer coefficient between the two surfaces from Eq.2.52:

$$h_{rad} = f_{rad} \cdot (T_m + T_s) \cdot (T_m^2 + T_s^2) \tag{2.52}$$

where:

- T_m, is the temperature of the master surface
- T_s, is the temperature of the slave surface

- H_0 *or HTC*, is the heat transfer conductance for closed gaps.
- *LMIN*, is the minimum gap.
- *LMAX*, is the maximum gap.
- *BC_FLAG*, is a special flag type (ON-OFF) function, which allows or prohibits the rest of the thermal boundary conditions (e.g. radiation to the environment) to be active on particular segments, when they are in contact. More specifically, if one particular set of contacting segments (with $l_{gap} \leq LMAX$) is discovered at a specific time iteration during the solution, the rest of the thermal functions towards the environment will not be activated for as long as these segments are in contact. For the current analysis, a *BC_FLAG=1* was chosen (prohibit thermal boundary conditions for contacting segments).

In order for the software to identify which of the heat transfer mechanisms are is action in each time iteration, the definition of *LMIN* and *LMAX* must be present. In general, in case l_{gap} is less than *LMIN*, heat transfer via conductance is in action, whereas when l_{gap} is between *LMIN* and *LMAX*, heat transfer via conductivity (with the aid of a liquid) is active. Heat transfer via radiation is always active, supposing that the view factor between the two surfaces be non-zero. In the current analysis the values for *LMIN* and *LMAX* are 0.5 mm and 1 mm, respectively, thus, the heat transfer mechanisms present between two contacting bodies are as presented in Table 2.6:

TABLE 2.6: Heat transfer mechanisms in contacts

Condition of contacting surfaces	**Active mechanisms**
$0 \leq l_{gap} \leq 0.5$ mm	Conductance
0.5 mm $\leq l_{gap} \leq 1$ mm	Conductivity via liquid (and Radiation if applied and view factor non-zero)
1 mm $\leq l_{gap}$	No contact heat transfer

Regarding the definition of *K* and H_0, a deep and detailed analysis was required. The accurate representation of the thermal contact behavior is very important for the precise estimation of the mechanical properties, as these were presented in Figs.2.8-2.17. However, this was proven rather demanding, and numerous simulations were required for the trial – and – error analysis to estimate the different heat transfer coefficients of the problem. During this analysis, an initial analytical estimation of the heat transfer coefficients was performed via the corresponding equations (Eqs.2.53-2.54), as these are given in **Shapiro, 2012**:

$$K = h_{cond} \cdot l_{gap} \tag{2.53}$$

$$H_0 = h_{contact} = \frac{k\pi}{4\lambda}\left[1 + 85\left(\frac{P}{\sigma_r}\right)^{0.8}\right] \tag{2.54}$$

where:

- $h_{contact}$, is the contact conductance
- k, is the thermal conductivity of air
- λ, is the surface roughness
- P, is the interfacial pressure
- σ_r, is the stress rupture

As a rule of thumb it is commonly assumed that $h_{cond} = 600\frac{W}{m^2K}$, thus from Eq.2.53 and for an average gap length of $l_{gap} = 0.75mm$, the conductance coefficient is equal to $K = 0.45\frac{W}{mK}$. Furthermore, for the definition of contact conductivity (known as Shvets' formula (**Shvets and Dyban, 1964**)) in Eq.2.54, for an average surface roughness of approximately $\lambda = 60\mu m$, an average stress rupture of $\sigma_r = 350MPa$ (**Lu et al., 2014**) and contact pressures ranging from $P = 250 - 400MPa$ (estimated from preliminary runs of the model) a range of contact conductivity coefficients ranging from $H_0 = 8631.61 - 100094\frac{W}{m^2K}$ was calculated. It is worth noting that the air thermal conductivity k for the aforementioned calculations was estimated during the thermal boundary conditions calculations and will be presented in section 2.10.

After the preliminary runs with the analytically estimated heat transfer coefficients were concluded, a cycle of corrective trial – and – error runs was conducted. During this cycle of runs, it was decided that the simplistic approach presented in Eq.2.54 was inadequate, in order to reproduce the temperature results presented in **Zhu et al., 2016b**. Alternatively, a manually estimated *h(t)* curve had to be input in the program. For this reason, the CARD *T_Friction* was activated in all the defined contacts. From the available options under the *T_Friction* CARD, *LCH* was used:

- *LCH*, defines a load curve ID for h. If a positive value is provided, LS-DYNA correlates a curve with the same ID as the value given, as a heat transfer coefficient as a function of time. The aforementioned curve consists of *(t, h(t))* data pairs.

As mentioned above, the *h(t)* curves had to be estimated through a number of trial – and – error runs, since it was the only property that was not defined by Zhu et al. More specifically, two different *h(t)* curves had to be estimated: (a) one for the inner and outer peripheral surfaces of the ring and (b) one for the upper and lower end surfaces of the ring. Initially, both curves were estimated based on the results of Eq.2.54. Then, specific points of the *h(t)* curves were adjusted between runs, so that the average temperature results from the simulation were fitted to the experimental results presented in **Zhu et al., 2016b**. After the completion of the trial – and – error runs, the *h(t)* curves were estimated and are presented in Fig.2.20:

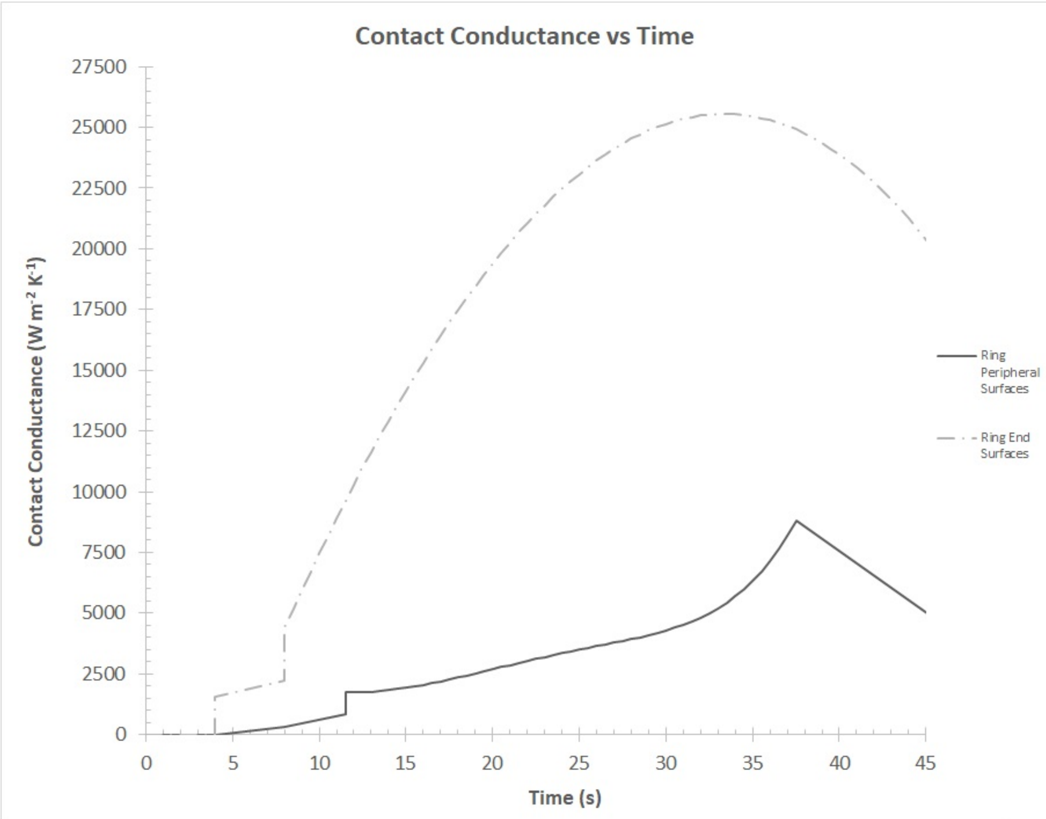

FIG. 2.20: Contact Conductance Curves vs. Time

Observations over the curves in Fig.2.20 reveal that both conductance curves have two regions: (a) a low initial region and (b) a higher final region. The initial region in both curves is composed of steps, as in the actual experiment a passivation film is created and subsequently broken during the first seconds of the process. Because of the different thermal properties of the aforementioned passivation film and their abrupt removal (scaling) from the workpiece, such sudden changes in contact conductance, H_0, are expected. On the other hand, the second region of each curve follows a smoother path up to the point when the corresponding contacting tools cease their movement. From that point on, the conductance values begin to decrease in both curves. This behavior can be explained from Eq.2.54, as the interfacial pressure, P, between the tools and the ring would begin decreasing rapidly, after the former have reached their final position.

2.9 Tool Movement

In the case of tool movement of the rolls, most of the velocities were already provided in the literature reference. These contain the following tool velocities:

- $v_{mandrel} = 0.89\ \frac{mm}{s}$, is the linear feed of mandrel
- $\omega_{MR} = 2.09\ \frac{rad}{s}$, is the rotational velocity of main roll
- $v_{CR} = 0.35\ \frac{mm}{s}$, is the linear feed of the top conical roll
- $\omega_{CR} = 7.71\ \frac{rad}{s}$, is the rotational velocity of the conical rolls (average)

Regarding the movement of support rolls, there were two different approaches that could be followed. In the first approach, a spring beam element was added on the opposite side (regarding the position of the ring) of each support roll, with a critical yielding spring load, F_{cr} described by Eq.2.55 (**Li et al., 2008**):

$$F_{cr} = \frac{W_z k_{safety} \sigma_Y}{r_m \sin\phi} \tag{2.55}$$

where:

- $W_z = \frac{h_0(R-r)^2}{6}$, is the section modulus for bending resistance
- k_{safety}, is a safety factor with $0 \leq k_{safety} \leq 1$
- σ_Y, is the yield strength of the ring's material
- $r_m = \frac{R+r}{2}$, is the mean radius of the ring
- ϕ, is the support roll angle relative to the ring center-main roll center axis
- h_0, is the initial height of the blank
- R, is the outer radius of the ring (in each time iteration
- r, is the inner radius of the ring (in each time iteration)

Although this approach was easy to implement on LS-DYNA, it was finally dismissed as numerous preliminary simulations were required in order to precisely define the value of k_{safety} per time, as from the aforementioned preliminary runs it was proven that k_{safety} was time-dependent due to its dynamic nature. Thus, a second approach was implemented for the movement of support rolls. In this second approach, the exact position of support rolls in each time iteration was directly input in LS-DYNA. For this reason, a ring growth algorithm had to be estimated. Although several researches have tackled this subject in the past (i.e. **Anjami and Basti, 2010**), their approaches did not have the expected results when tested in LS-DYNA. Thus, a new approach was estimated.

As with most other ring growth algorithm approaches, the volume constancy law (**Schuler, 1998**) was used initially. According to this approach, the ring growth algorithm given by Eq.2.56 was estimated:

$$R_{i+1} = \frac{1}{2}\left[\frac{1}{\Delta f}(R_i^2 - r_i^2)\frac{h_i}{h_{i+1}} + R_i - r_i - v\Delta t\right] \tag{2.56}$$

where:

- $\Delta f = R_{i+1} - r_{i+1}$, is the thickness of the ring in the following time iteration
- R_i, is the outer radius of the ring in the current time iteration
- r_i, is the inner radius of the ring in the current time iteration
- h_i, is the height of the ring in the current time iteration
- h_{i+1}, is the height of the ring in the following time iteration
- v, is the linear velocity of mandrel
- $\Delta t = t_{i+1} - t_i$, is the iteration timestep

The algorithm given by Eq.2.56 was tested in the developed model and was proven to produce inaccurate results. More specifically, an algorithm developed via the volume constancy law implies that any geometric deformation occurring in the blank (any part of it), changes the entire volume of the blank at the same time (e.g. a height reduction by the conical rolls, reduces evenly the ring's height as if it was compressed by a much larger set of compressive plates). However, this is not representing of the localized deformations occurring during Ring Rolling, as specific parts of the blank are deformed in each time iteration and thus a different ring growth algorithm is in action. Also, the formation of certain defects, namely bulging from the conical rolls and fishtailing from the bite (main roll - mandrel action on the ring), which are hard to be properly accounted for and cannot be eliminated during Ring Rolling, cause instabilities on the ideal shapes considered by the volume constancy law.

Thus, a power law approach on the ring growth algorithm was tested. This approach was resulted after observations on the Phase diagram of a typical Ring Rolling process (Fig.1.2), where an initial slow increase of the outer diameter of the ring (Phase one) is succeeded by a much higher increase rate, until the end of the second Phase. At this point, a different power law is active for the entirety of Phase three. Finally, at Phase four a linear increase (with an almost zero angle) is active. So, the ring growth algorithms for Phases one and two (a single algorithm was estimated for both these Phases) had the general equation form presented in Eq.2.57, while a different algorithm was estimated for Phase three, which is presented in Eq.2.58:

$$R_i = a \cdot t^c + b \tag{2.57}$$

$$R_i = a \cdot t^2 + b \cdot t + c \tag{2.58}$$

where:

- a and b, are constant parameters of the power law
- c, is the exponent of the power law

For the estimation of constants a, b and c, the proposed algorithm was fitted to the experimental data found in the reference and the final ring growth algorithms are presented in Eq.2.59 (Phases one and two) and Eq.2.60 (phase three):

$$R_i = 3.1003 \cdot 10^{-1} \cdot t^{1.7} + 301.7273 \tag{2.59}$$

$$R_i = -2.5097 \cdot 10^{-1} \cdot t^2 + 22.6085 \cdot t - 45.5521 \tag{2.60}$$

Regarding the aforementioned power laws, some preliminary trials proved that the a, b and c constants (for given initial and final ring dimensions) depended on the material properties of the ring and the tools, the linear velocities of the tools and the duration of the process. Some of these aspects are presented in more detail in Chapter 3.

Finally, based on the estimated ring growth algorithms, the displacement coordinates of each support roll was given by Eqs.2.61 and 2.62:

$$X_{SR} = R_i \cdot \cos\phi - \Delta c \tag{2.61}$$

$$Y_{SR} = \pm R_i \cdot \sin\phi \tag{2.62}$$

where:

- X_{SR}, is the X displacement (parallel to the mandrel center - main roll center axis) of support rolls
- Y_{SR}, is the Y displacement (perpendicular to the mandrel center - main roll center axis) of support rolls (positive for Support Roll 1, negative for Support Roll 2 (Fig.2.4))
- Δc, is the movement of the ring's center during Ring Rolling, relative to the constant position of main roll (also see Fig.2.21 that follows)

It is worth noting that a proper phase difference has to be considered for each support roll, as the same cross-section of the ring will meet each support roll at a different time. More specifically, for the specified angle ϕ and the clockwise rotation of the ring in the simulation, a phase difference of $\pi/3$ was used for support roll 2, while a phase difference of $5\pi/3$ was used for support roll 1.

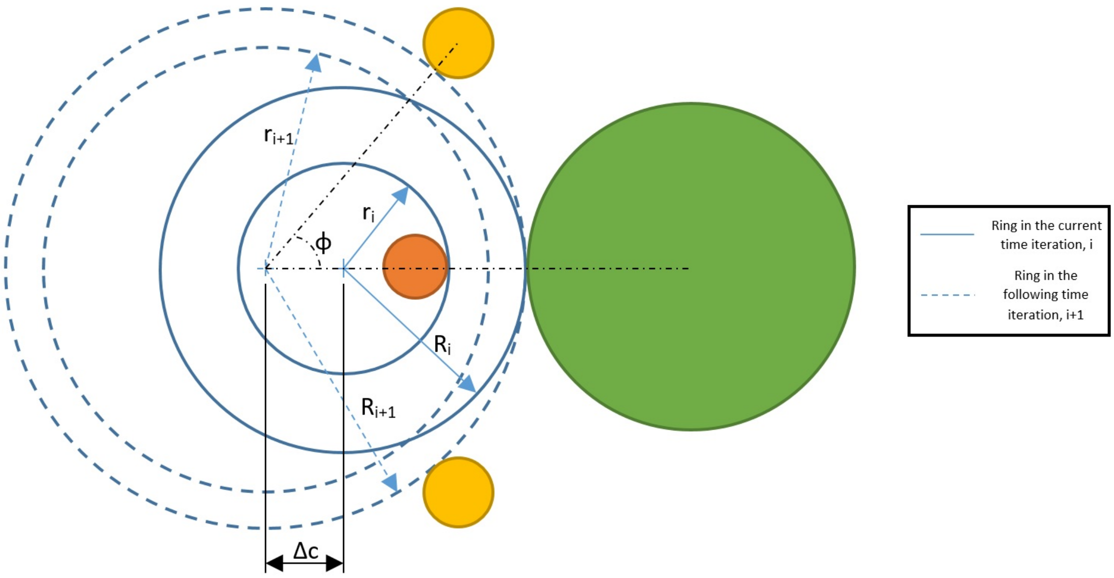

FIG. 2.21: Representation of changes during two time iterations of Ring Rolling

2.10 Boundary and Initial Conditions

Boundary and initial conditions are a key parameter in every simulation. A faulty set of either boundary or initial conditions will significantly affect the final results of a numerical model, or can make the problem unsolvable. In the numerical models that were developed for the current research, the boundary and the initial conditions had to do either with thermal conditions or with tool movement.

2.10.1 Initial Conditions

In LS-DYNA, initial conditions are parameters that are active only at the very first time iteration. A wide variety of load, geometric, movement and thermal parameters can be set as initial conditions.

In the model of the current research, the only initial conditions that had to be set were the initial temperatures of the ring and the tools. More specifically, the initial temperature of the ring was set as $T_{ring,periphery}$ = 1290.1 K on the peripheral surfaces and $T_{ring,ends}$ = 1291.1 K on the end surfaces (based on the experimental results presented in **Zhu et al., 2016b**), while the initial temperature of the tools was set as T_{tools} = 573.15 K.

In order for the initial temperatures to be input in LS-DYNA, initially, the nodes with the same initial temperature have to be grouped. For this, the SET DATA_SET_NODE option from the Create Entity menu was used. Three separate node sets were created:

- One set containing all the ring's nodes, except from the nodes of the ring's end surfaces.
- A second set containing only the nodes of the end surfaces.
- A third set containing the nodes of the tools.

Then, the initial temperature from each of the created node sets can be defined with the INITIAL_TEMPERATURE_SET menu. With this menu, an initial temperature value is applied to each node set via the TEMP option. The defined initial temperatures will be active at the beginning of the simulation (T_0), and will be used for the initial calculations of the thermal analysis.

2.10.2 Boundary Conditions

Regarding the boundary conditions, LS-DYNA offers a wide variety of selections in this case too. These may involve movement, thermal and restrictive (in terms of displacement and load) conditions, while some boundary conditions allow for the repetition of certain segments of the model (e.g. CYCLIC) or for the change of the element method during the model's solution (e.g. ELEMENT_METHOD_CONTROL). In the current analysis, two types of boundary conditions were considered.

The first type involved the correlation of the movement laws to the corresponding bodies. For the movement laws, the reader is advised to read the corresponding section of the current dissertation (Section 2.9).

The second type of boundary conditions involved the thermal behavior of each body to the environment, namely their thermal convective and radiative behavior of the bodies to the environment.

For the convective behavior of the bodies, menu BOUNDARY_CONVECTION_SET was used. In this function, the surface segments of the ring and the tools were grouped and set, in order to define the thermal surfaces in each body. Subsequently, the convective coefficient, h_{conv} of each body to the environment and the temperature of the environment, $T_{\infty} - 293.15$ were input. Based on these data, a set of dimensionless numbers, namely Nusselt, *Nu*, Prandtl, *Pr*, Reynolds, *Re* and Grashof, *Gr* had to be estimated via their definition, as these are given in Eqs.2.63:

$$\begin{aligned} Nu &= \frac{h_{conv} \cdot L}{k} \\ Pr &= \frac{C_P \cdot \mu}{k} \\ Re &= \frac{v \cdot L \cdot \rho}{\mu} \\ Gr &= \frac{\rho^2 \cdot g \cdot \beta \cdot (T_{surf} - T_\infty) \cdot L^3}{\mu^2} \end{aligned} \tag{2.63}$$

where:

- L, is the equivalent height of the body*
- k, is the thermal conductivity of air at a temperature of T_{film}
- C_P, is the specific heat capacity of air at a temperature of T_{film}
- μ, is the dynamic viscosity of air at a temperature of T_{film}
- v, is the air velocity in the case of forced convection
- ρ, is the air's density at a temperature of T_{film}
- g, is the acceleration of gravity
- β, is the coefficient of thermal expansion (equal to approximately $1/\mathrm{T}$, for ideal gases)
- T_{surf}, is the surface temperature of the body

* In the case of the equivalent height of a body, a different approach is taken in the case of cylindrical and planar bodies, where:

- L = height of the cylinder (for cylindrical bodies)
- L = $\frac{2 \cdot Area}{Semi-perimeter}$ (for planar bodies)

For the estimation of the air properties, these have to be estimated at a film temperature, T_{film}, which is given by Eq.2.64:

$$T_{film} = \frac{T_{surf} - T_\infty}{2} \tag{2.64}$$

The film temperature is estimated by LS-DYNA in each time iteration, and then the corresponding properties for air at the calculated film temperature are used. The aforementioned thermal properties of air are presented in Figs.2.22-2.25 that follow:

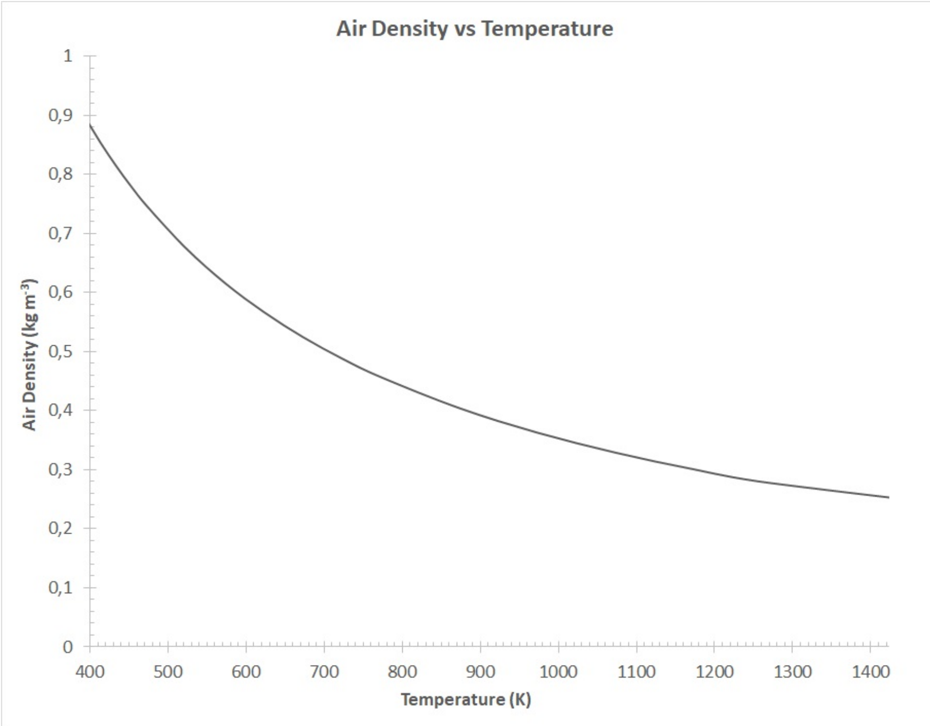

FIG. 2.22: Density of air versus Temperature (**Keenan, Chao, and Kaye, 1983**)

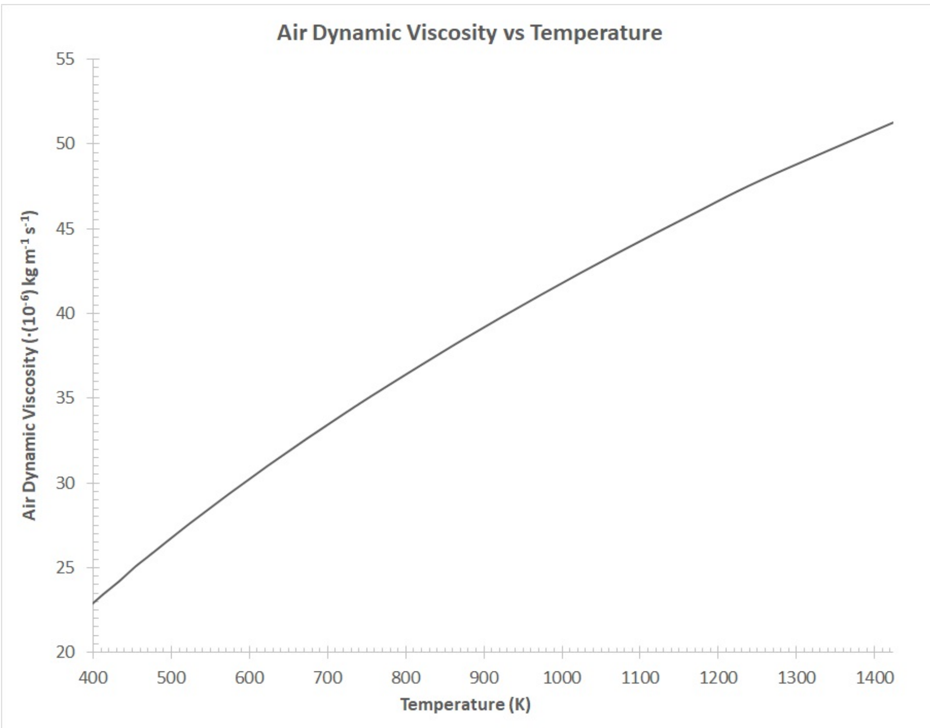

FIG. 2.23: Dynamic Viscosity of air versus Temperature (**Touloukian, Saxena, and Hestermans, 1975**)

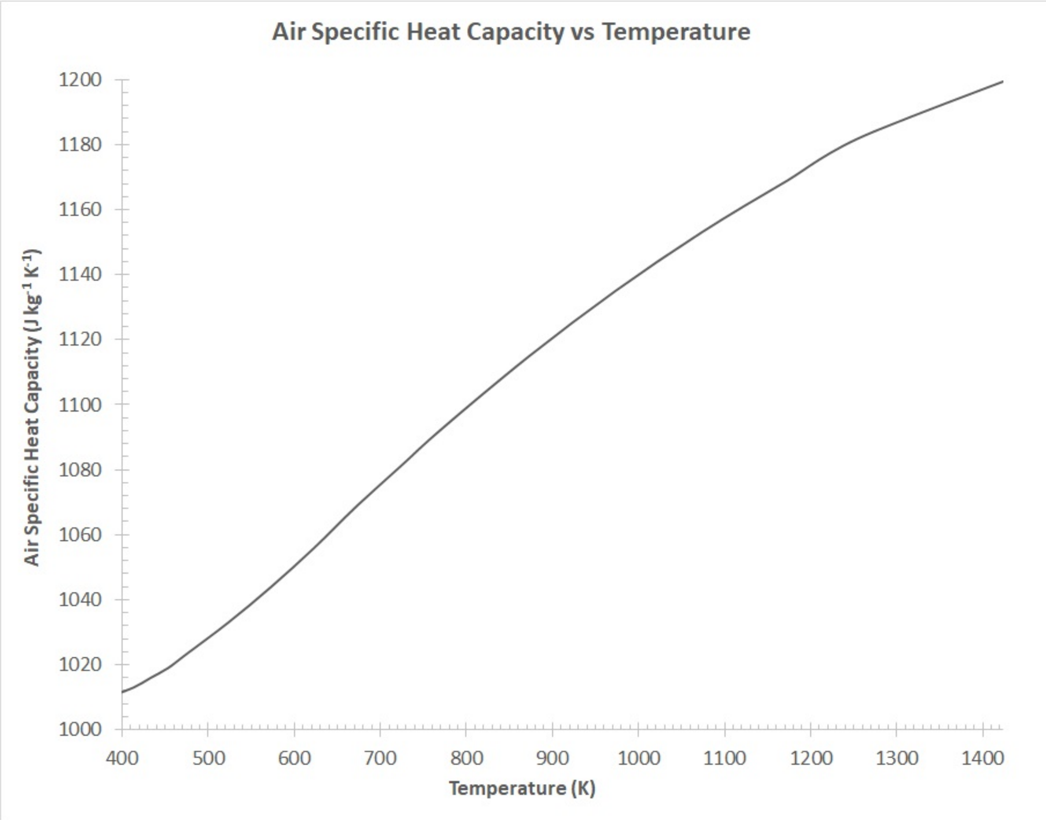

FIG. 2.24: Specific Heat Capacity of air versus Temperature (**Keenan, Chao, and Kaye, 1983**)

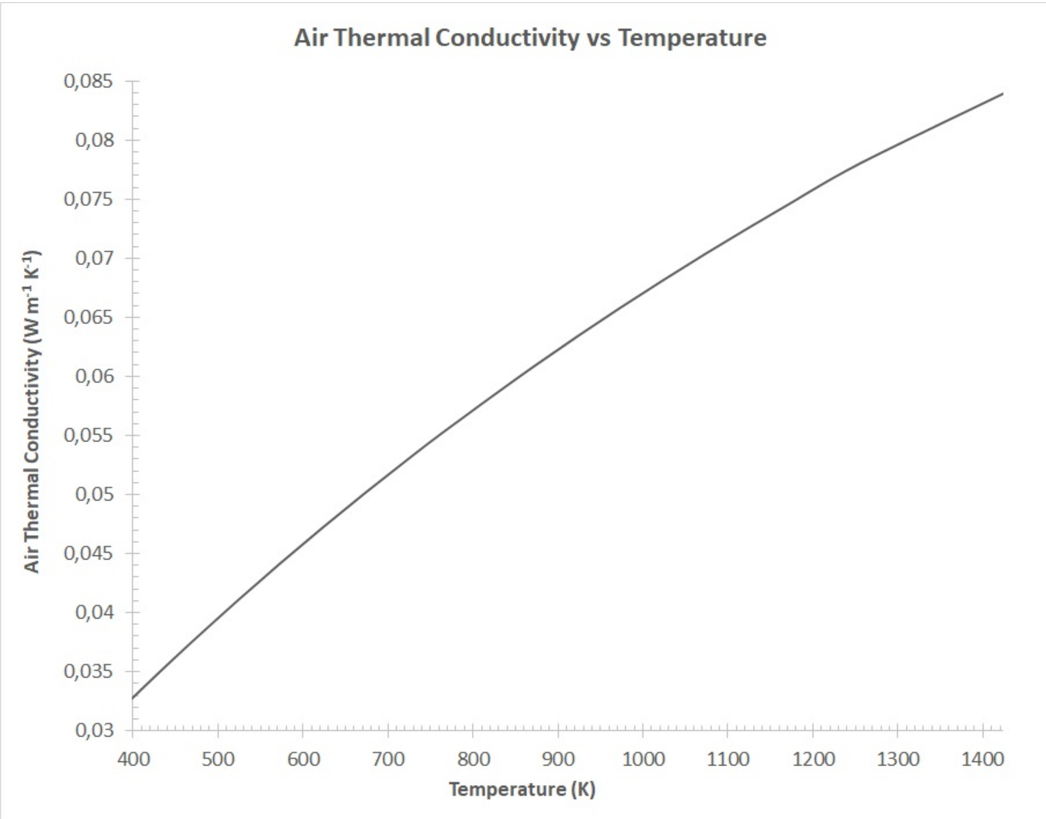

FIG. 2.25: Thermal Conductivity of air versus Temperature (**Touloukian, Liley, and Saxena, 1970**)

With the dimensionless numbers defined, the convective behavior of the bodies in the model is defined by different equations, in the cases of either free (Eq.2.65) or forced convection (Eq.2.66) **Shapiro, 2012**:

$$Nu = C \cdot (Gr \cdot Pr)^a \tag{2.65}$$

$$Nu = C \cdot (Re \cdot Pr)^a \tag{2.66}$$

where the constants C and a can be defined according to Table 2.7:

TABLE 2.7: Definition of C and a constants (**Shapiro, 2012**)

Geometry	Laminar	Turbulent	Equivalent L
Vertical plate or cylinder	GP $\leq 10^9$, C=0.59, a=$\frac{1}{4}$	GP>10^9, C=0.13, a=$\frac{1}{3}$	Cylinder height
Upper horizontal plate	GP $\leq 10^7$, C=0.54, a=$\frac{1}{4}$	GP>10^7, C=0.14, a=$\frac{1}{3}$	$\frac{2 \cdot Area}{Semi-perimeter}$
Lower horizontal plate	GP $\leq 10^{10}$, C=0.27, a=$\frac{1}{4}$		$\frac{2 \cdot Area}{Semi-perimeter}$

Thus, based on the definition of Nusselt's number presented in Eq.2.63, the convective coefficient can be input as an equation in LS-DYNA (Eqs.2.67):

$$\begin{aligned} h_{conv} &= \frac{k}{L} \cdot C \cdot (Gr \cdot Pr)^a, \text{ free convection} \\ h_{conv} &= \frac{k}{L} \cdot C \cdot (Re \cdot Pr)^a, \text{ forced convection} \end{aligned} \tag{2.67}$$

It is worth noting that both the free and the forced convection equations were used in the conducted simulations, as because of the relative velocity between the ring and the air, a forced convective behavior can be considered during the ring's rotation.

Finally, for the radiative boundary conditions, the function BOUNDARY_RADIATION_SET was used. Similarly to the convective boundary conditions, both the surface segments of the bodies and the environmental temperature, $T_\infty = 293.15K$ were input. However, in this case the radiation coefficient, h_{rad} is different and follows Eq.2.68:

$$h_{rad} = \sigma \cdot \epsilon \cdot F \tag{2.68}$$

where:

- σ, the Stefan-Boltzmann constant
- ϵ, the emissivity of body (presented in Fig.2.15)
- F, the view factor (equal to 1, for heat radiation towards the environment)

Note that in order to simulate heat radiation towards the environment, BOUNDARY_ RADIATION_SET menu's TYPE option must be set to TYPE=1.

2.11 Hourglass Control (Hallquist, 2006)

The term hourglass mode refers to a nonphysical, zero-energy mode of deformation that produces zero strain and no stress. It usually occurs only in under-integrated (with a single integration point) finite elements. Undesirable hourglass modes tend to have periods that are typically much shorter than the periods of the structural response, and they are often observed to be oscillatory. However, hourglass modes with periods that are comparable to the structural response periods may be a stable kinematic component of the global deformation modes and must be admissible.

In order to comprehend the formation mechanism of hourglass modes, the strain rate calculation equation for an height-node solid element should be examined:

$$\dot{\epsilon}_{ij} = \frac{1}{2} \cdot \left(\sum_{k=1}^{8} \frac{\vartheta \phi_k}{\vartheta x_i} \cdot \dot{x}_j^k + \frac{\vartheta \phi_k}{\vartheta x_j} \cdot \dot{x}_i^k \right) \tag{2.69}$$

Whenever diagonally opposite nodes have identical velocities, i.e.,

$$\dot{x}_i^1 = \dot{x}_i^7, \quad \dot{x}_i^2 = \dot{x}_i^8, \quad \dot{x}_i^3 = \dot{x}_i^5, \quad \dot{x}_i^4 = \dot{x}_i^6$$

the strain rates are identically zero:

$$\dot{\epsilon}_{ij} = 0,$$

due to the asymmetries in Eq.2.34. It is easy to prove the orthogonality of the hourglass shape vectors, which are listed in Table 2.8 and shown in Fig.2.26 with the derivatives of the shape functions:

$$\sum_{k=1}^{8} \frac{\vartheta \phi_k}{\vartheta x_i} \cdot \Gamma_{\alpha k} = 0, \quad i = 1, 2, 3, \quad \alpha = 1, 2, 3, 4.$$

TABLE 2.8: Hourglass base vectors

	$\alpha = 1$	$\alpha = 2$	$\alpha = 3$	$\alpha = 4$
Γ_{j1}	1	1	1	1
Γ_{j2}	1	-1	-1	-1
Γ_{j3}	-1	-1	1	1
Γ_{j4}	-1	1	-1	-1
Γ_{j5}	-1	-1	1	-1
Γ_{j6}	-1	1	-1	1
Γ_{j7}	1	1	1	-1
Γ_{j8}	1	-1	-1	1

The product of the base vectors with the nodal velocities is zero when the element velocity field has no hourglass component,

$$h_{i\alpha} = \sum_{k=1}^{8} \dot{x}_i^k \cdot \Gamma_{\alpha k} = 0 \tag{2.70}$$

while they are nonzero if hourglass modes are present. The twelve hourglass-resisting force vectors, $f_{i\alpha}^k$, are given by the following equation:

$$f_{i\alpha}^k = \alpha_h \cdot h_{ia} \cdot \Gamma_{\alpha k} \tag{2.71}$$

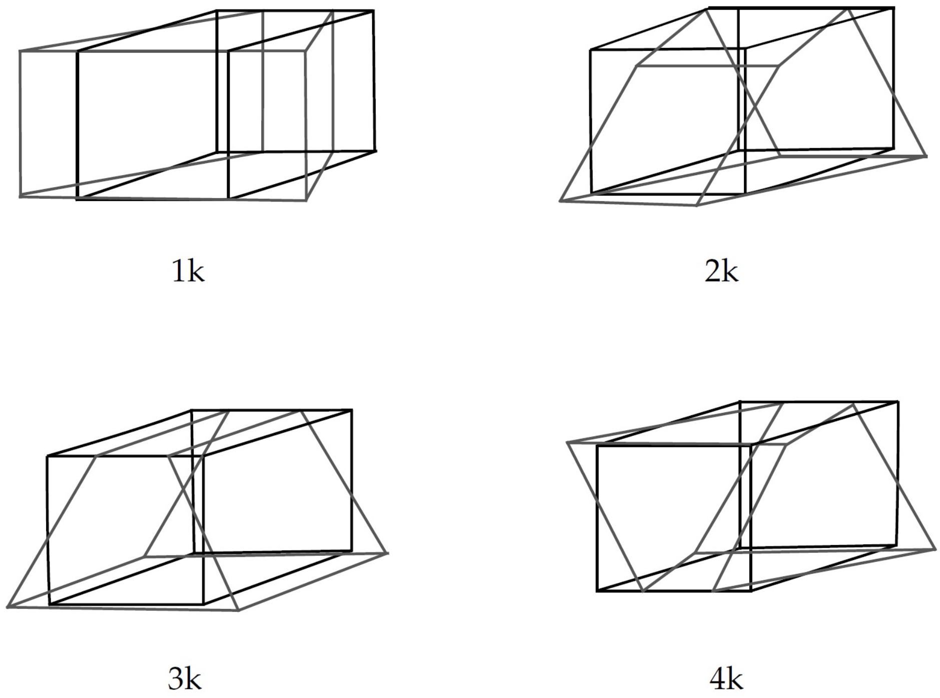

FIG. 2.26: The hourglass modes of an eight-node element with one integration point are shown. A total of twelve modes exist

in which,

$$\alpha_h = Q_{HG} \cdot \rho \cdot v_e^{2/3} \cdot \frac{c}{4} \tag{2.72}$$

where:

- v_e, is the element volume
- c, is the speed of sound in the analyzed material
- Q_{HG}, is a user-defined constant, usually set to a value between 0.05 and 0.15

It is worth noting that Eq.2.71 is the basic hourglass control equation of hourglass control algorithm type 1.

Hourglassing is a rather common occurrence during preliminary analyses, thus various methods have be found to tackle this phenomenon:

- Refine the mesh – A rather effective way to eliminate hourglassing, which is usually performed in parallel with the mesh independence analysis.
- Review the method of loading – Pressure loading is preferred over single-point loading, as the latter is likely to excite hourglassing modes.
- Facilitate triangular shell and tetrahedral solid elements – these elements do not have hourglassing modes, but they usually have an overly stiff behavior.
- Switch to fully-integrated or selectively reduced (S/R) integration elements – A more expensive element type and with a tendency to "shear-lock" in cases with poor shape ratio in the elements.

- Apply viscous damping or small elastic stiffness – This is performed via dedicated hourglass control algorithms in LS-DYNA.

In case single-point integration elements are used, the most common way to avoid the hourglassing modes is by applying an hourglass control algorithm. As mentioned above, this is possible via the homonym CONTROL_HOURGLASS menu. The viscous damping and/or small elastic stiffness in the simulation applied through these algorithms offer a way of resisting undesirable hourglassing by stopping the formation of anomalous modes, while having negligible effects on the stable global modes.

Identifying whether the effects of hourglass control can be considered negligible or not, can be a debatable issue. The most common way of evaluating the effects of hourglass control is via the hourglass energy dissipation. Since, the hourglass deformation modes are orthogonal to the strain calculations, work done by the hourglass resistance is neglected in the overall energy calculation. This leads to a slight energy loss. The energy dissipated by the hourglass forces reacting against the formation of the hourglass modes is tracked and reported in the output files *MATSUM* and *GLSTAT* (also see §2.13.2). If the dissipated energy is small relative to the peak internal energy for the part on which the hourglass control has been applied to, then the effects from hourglass control can be considered negligible. As a general rule-of-thumb, the ratio of the hourglass energy over the internal energy for the same part should be <10%.

In the current analysis, an hourglass control algorithm had to be used in the case of SOLID_ELEMENT_1. This specific element type was used for the elastic segment of the tools in section §3.3. After some preliminary simulations, hourglass control algorithm types 4 and 5 were elected as the most appropriate. The aforementioned hourglass control types are based on a slightly different form of Eq.2.71, which is:

$$f_{i\alpha}^{k} = \alpha_h \cdot g_{ia} \cdot \gamma_{\alpha k} \tag{2.73}$$

in which, $\gamma_{\alpha k}$ is an equation that defines the hourglass shape vectors in terms of the base vectors:

$$\gamma_{\alpha k} = \Gamma_{\alpha k} - \phi_{k,i} \cdot \sum_{n=1}^{8} x_i^n \cdot \Gamma_{\alpha n} \tag{2.74}$$

and $g_{i\alpha}$ is the analogue for Eq.2.70:

$$g_{ia} = \sum_{k=1}^{8} \dot{x}_i^k \cdot \gamma_{\alpha k} = 0 \tag{2.75}$$

Hourglass control types 4 and 5 evaluate hourglass stiffness, contrary to Eq.2.73 that evaluates hourglass viscosity. This is performed by multiplying hourglass rates of Eq.2.73 by the solution time step to produce increments of hourglass deformation. The hourglass stiffness is scaled by the element's maximum frequency so that stability is maintained, as long as the hourglass scale factor, α_h, is sufficiently small. The choice of focusing more in evaluating the stiffness of the elements was obvious, given that the corresponding hourglass control would be applied to improve the deformational behavior of the tools, thus a stiffer response would be closer to the actual process.

Finally, between hourglass control types 4 and 5, type 5 was selected as the most appropriate for the current analysis. The main difference between these aforementioned hourglass control types lies with the evaluation of the respective shape function derivatives. More specifically, in type 4 control the shape function derivatives are evaluated at the origin of the referential coordinate system, while in type 5 control they are evaluated at the centroid of each element. Thus, in type 5 control an exact element volume is produced (as this is given by Eq.2.33), although an increased number of computations is required, as the anti-symmetry property of Eq.2.34 is not true in this case. Seeing that the elastic deformations of the tools can be in an order of magnitude of microns to tens of microns, an exact volume calculation is essential, in order to perform calculations with increased accuracy (also see §3.3).

It is worth noting that regarding the user-defined constant, Q_{HG}, various values were tested during the preliminary runs. After the conclusion of the preliminary trials, a value of Q_{HG} = 0.04 was chosen. This Q_{HG} value was low enough so that any nonphysical stiffening of the model's mechanical response would be minimized, while at the same time it was high enough to effectively counter the inhibiting hourglass modes.

2.12 Optimum Mass Scaling

Mass scaling refers to a technique where non-physical mass is added to a structure in order to achieve a larger explicit time step and reduce total simulation time (**LS-DYNA_Support, 2019**). Anytime nonphysical mass is added to increase the time step in a dynamic analysis, the results may be affected similarly to Newton's second law $F = m \cdot a$. Sometimes the effects from the added mass are insignificant, and in those cases adding non-physical mass can be justified and permitted. This mainly involves cases where small and noncritical elements are affected and/or in simulations where velocity is low, and the kinetic energy is relatively smaller compared to the internal energy (such as in quasi-static simulations).

The addition of non-physical mass in an LS-DYNA model can be performed in one of two ways (**Olovssin, Simonsson, and Unosson, 2005**):

- *Conventional Mass Scaling (CMS)*: The mass of small or stiff elements is increased to prevent a very small timestep. Thus, artificial inertia forces are added, which can influence all eigenfrequencies. This includes rigid body modes. Thus, this additional mass must be used very carefully so that the resulting non-physical inertia effects do not dominate the global solution.

- *Selective Mass Scaling (SMS)*: Using selective mass scaling, only the high frequencies are affected, whereas the low frequencies (rigid body modes) are not influenced. Thereby, a lot of artificial mass can be added to the system without adulterate the global solution. This method is very effective, if it is applied to limited regions with very small critical timesteps.

In both methods, the diagonal (lumped) mass matrix is updated. In order to better understand that, one should first comprehend the way timestep is defined in an explicit finite element analysis. As mentioned before, the geometry in an explicit analysis is update from one iteration to the next through the system of equations 2.76:

$$\begin{aligned} \mathbf{a}_n &= \mathbf{M}^{-1}(\mathbf{f}_n^e - \mathbf{f}_n^i) \\ \mathbf{v}_{n+1/2} &= \mathbf{v}_{n-1/2} + \mathbf{a}_n \Delta t \\ \mathbf{u}_{n+1} &= \mathbf{u}_n + \mathbf{v}_{n+1/2} \Delta t \end{aligned} \tag{2.76}$$

The general form of the diagonal mass matrix is given by the following equation (Eq.2.77):

$$\mathbf{M} = \sum_e \mathbf{m}_e, \text{ with } \mathbf{m}_e = \frac{m_e}{n}\mathbf{I} \tag{2.77}$$

Thus, the original form of the critical timestep is given by Eq.2.78:

$$\Delta t \approx \frac{2}{\omega_{max}} \approx \sqrt{\frac{\rho}{E}} \cdot l_{e,min} = \sqrt{\frac{M_e}{E \cdot l_{e,min}}} \tag{2.78}$$

where:

- $\boldsymbol{a}_n$, is the acceleration vector
- $\boldsymbol{M}$, is the global mass matrix
- $\boldsymbol{f}_n^e$, is the external load vector
- $\boldsymbol{f}_n^i$, is the internal load vector
- $\boldsymbol{v}_n$, is the velocity vector
- $\boldsymbol{u}_n$, is the displacement vector
- Δt, is the critical timestep
- $\boldsymbol{m}$, is the element diagonal mass matrix
- ω_{max}, is the maximum eigenfrequency
- ρ, is the material density E, is the Young's Modulus
- $l_{e,min}$, is the minimum element length of the smallest element

2.12.1 Conventional Mass Scaling (CMS)

Based on the chosen mass scaling method, an updated mass matrix will be used for the calculation of the new critical timestep. In the case of Conventional Mass Scaling (CMS) method, the respective equations will be the following:

$$\mathbf{M} = \sum_e (\mathbf{m}_e + \Delta\mathbf{m}_e), \text{ with } \Delta\mathbf{m}_e = \frac{\Delta m_e}{n}\mathbf{I} \tag{2.79}$$

$$\Delta t_{new} \approx \sqrt{\frac{m_e + \Delta m_e}{E \cdot l_{e,min}}} \Rightarrow \frac{\Delta t_{new}}{\Delta t} = \sqrt{1 + \frac{\Delta m_e}{m_e}} \tag{2.80}$$

Thus, the total calculation time is calculated from the following equation:

$$t_{CPU} \sim N \cdot (t_{CMS} + t_{other}) \cdot \frac{\Delta t}{\Delta t_{new}} \tag{2.81}$$

The additional diagonal mass Δm_e considered in Eq.2.79 can be performed simply by altering the density of specific materials or by considering a positive value in DT2MS option in CONTROL_TIMESTEP. Although this method can be sufficient for lowering the critical timestep, the addition of diagonal mass affects all eigenmodes equally. This can be rather problematic in the case of rigid bodies and structures with low frequency modes, which tend to deform in low frequency modes. In other word, using CMS to equally add diagonal mass causes inertia effects to significantly increase, thus putting a practical limit to the allowable critical timestep used.

2.12.2 Selective Mass Scaling (SMS)

In the case of Selective Mass Scaling (SMS), the respective system of equations will be the following:

$$\mathbf{M} = \sum_e (\mathbf{m}_e + \Delta\mathbf{m}_e), \text{ with } \Delta\mathbf{m}_e = \frac{\Delta m_e}{n}\left(\mathbf{I} - \sum_i \mathbf{e}_i\mathbf{e}_i^T\right) \tag{2.82}$$

while Eqs.2.80 is the same in this case, too. The total calculation time is estimated from the following equation:

$$t_{CPU} \sim N \cdot (t_{SMS} + t_{other} \cdot \frac{\Delta t}{\Delta t_{new}}) \tag{2.83}$$

Regarding the rigid body modes, $\mathbf{e}_i$, no inertia is added as the following applies:

$$\mathbf{e}_i^T\mathbf{e}_j = \delta_{ij} \Rightarrow \Delta\mathbf{m}_e\mathbf{e}_i = \mathbf{0} \tag{2.84}$$

Thus, projecting out translational rigid body modes only, allows for the estimation of the added mass matrix as follows:

$$\mathbf{e}_1 = (\mathbf{1} \quad \mathbf{0} \quad \mathbf{0})^T \quad \mathbf{e}_2 = (\mathbf{0} \quad \mathbf{1} \quad \mathbf{0})^T \quad \mathbf{e}_3 = (\mathbf{0} \quad \mathbf{0} \quad \mathbf{1})^T \tag{2.85}$$

$$\Delta\mathbf{m}_e = \frac{\Delta m_e}{4}\begin{pmatrix} \mathbf{m}_4 & & \\ & \mathbf{m}_4 & \\ & & \mathbf{m}_4 \end{pmatrix}, \quad \text{with} \quad \mathbf{m}_4 = \frac{1}{4}\begin{pmatrix} 3 & -1 & -1 & -1 \\ -1 & 3 & -1 & -1 \\ -1 & -1 & 3 & -1 \\ -1 & -1 & -1 & 3 \end{pmatrix} \tag{2.86}$$

The added diagonal mass presented in Eq.2.86 can be generalized to other elements, with no further alterations. In general, SMS does not simply add mass in the manner of CMS. It is designed to provide a more physical dynamic solution compared to CMS, as it adds mass only to elements whose timestep would be less than the one chosen for the SMS and which would not affect the critical frequency modes of the model. Thus, only high frequency modes are affected in the model, while the low frequency modes are left unaffected.

On the other hand, SMS requires additional memory and CPU. That is because with SMS, the solution of a sparse system of linear equations is performed in every time step. As a result of this process, the mass matrix can no longer be diagonal. Storing the non-diagonal matrix in every time step requires additional memory, while the explicit solution takes additional CPU time. The aforementioned system of linear equations is solved iteratively using a Preconditioned Conjugate Gradient solver with a Jacobi preconditioner. In order to achieve linear convergence, the number of iterations should approximate the condition number of the system matrix $\mathbf{M}$, as per Eq.2.87:

$$\left.\begin{array}{r} n_{iter} \sim \sqrt{\kappa(\mathbf{M})} \sim \frac{\Delta t_{new}}{\Delta t} \\ t_{iter} \sim N \end{array}\right\} \quad t_{CPU} \sim N \cdot \left(t_{SMS} + t_{other} \cdot \frac{\Delta t}{\Delta t_{new}}\right) \tag{2.87}$$

Regarding the critical timestep increase of the SMS, its calculation follows the same pattern to that of CMS (supposing the same mesh for the system), however an updated added mass matrix is considered in every timestep. It is worth noting however that in large problems, a saturation in CPU time can be manifested.

Similarly to CMS, enabling SMS in LS-DYNA is performed via the DT2MS option in CONTROL_TIMESTEP. The main difference to the CMS is that a negative value should be input in DT2MS, with ∣DT2MS∣ being the desirable timestep value.

2.12.3 Chosen Mass Scaling Method

From the two aforementioned methods, SMS was finally chosen because of its several advantages over CMS. However, choosing the proper mass scaling method is not a straightforward issue. The desirable timestep set in DT2MS has to be verified through a preliminary trial – and – error analysis. The main reason is that the optimum timestep is case dependent, while a poor choice of timestep can heavily affect the simulation results and overall model response. Too small of a timestep will add no benefits to the model. Too large of a timestep will only add inertia to the model with no added benefits, but rather affect the calculated kinetic energy because of the aforementioned added inertia.

During the preliminary analysis to estimate the optimum timestep, two different factors evaluated as reference points:

- The fraction $\frac{E_k}{E_{int}}$ (E_k is the kinetic energy of the models and E_{int} is the internal energy of the model) had to be less than 10% (**Patil, Baratzadeh, and Lankarani, 2017**)
- No extreme deformations should occur in any body of the model

After the completion of the preliminary runs, a timestep value of DT2MS=4 μs was finally chosen, as this was the maximum value that satisfied both evaluation factors. With this DT2MS value, no extreme deformations were observed in the model, while the corresponding E_k and E_{int} diagrams vs solution time are presented in Fig.2.27:

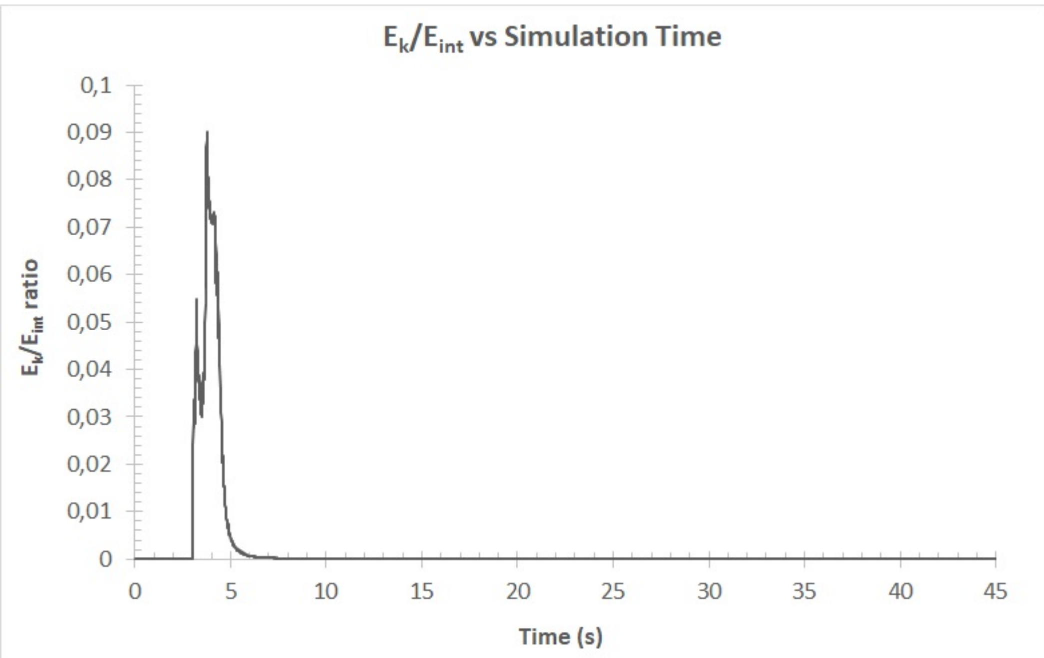

FIG. 2.27: Kinetic-to-internal energy ratio $\left(\frac{E_k}{E_{int}}\right)$ vs. Simulation Time

Observations over Fig.2.27 reveal that for the majority of the simulation's duration, the kinetic-to-internal energy ratio was close to zero, where a value less than 10% was expected.

This fact verifies the choice of the timestep value, to not have affected the results of the simulation. The only instances where the aforementioned energy ratio increased was around the time when the tools came in contact with the workpiece. However, in no time instance was the energy ratio equal to or greater than 10%, thus the chosen timestep value is considered appropriate for the current analysis. It is worth mentioning that the kinetic-to-internal energy ratio was checked for every simulation performed and the 10% threshold was not surpassed in any of them.

2.13 Software Parameters

With the parameters presented so far, the majority of the model has been set up. However, there are some important parameters that need to defined, in order to conduct a simulation. These parameters can be split in two categories:

- Control parameters, which act as rules for the algorithm of LS-DYNA to function properly
- Result parameters, which define the outputs of the simulation after its solution

These two categories are presented separately in the following subsections.

2.13.1 Control Parameters

Control parameters in LS-DYNA are defined through the CONTROL option. As mentioned above, these parameters involve the necessary rules by which the solver will perform the solution. More specifically, from the entirety of the potential options available in LS-DYNA, CONTROL parameters function as flags enabling specific of these options. These may involve both essential parameters for the model to be completed (e.g. model termination time) or special functions aimed at specific simulations (e.g. special mass scaling function for rotating bodies).

From the entirety of the available CONTROL parameters, the following were used for the simulations of the current analysis:

- *ACCURACY*, includes control parameters that improve the accuracy of the calculations. From the available parameters the following were activated:
  - *OSU*, is a global flag for second order objective stress updates (set to *OSU* = 1)
  - *INN*, sets invariant node numbering for solid elements (set to *INN* = 3)
- *CONTACT*, alters the default parameters for computations with contact surfaces. The following parameter was set:
  - *ISLCHK*, is a flag for checking initial penetrations in contact surfaces (set to *ISLCHK* = 2)
- *HOURGLASS*, redefines the default values of hourglass control type and coefficient. The following parameters were set/activated:
  - *IHG*, is the flag for the default hourglass control type (set to *IHQ* = 5)
  - *QH*, is the flag for the default hourglass coefficient (set to *QH* = 0.1)
- *SOLUTION*, is used to specify the solution procedure if combined thermo-mechanical analysis is performed. The following parameter was set:

  - *SOLN*, is the flag for the active solver of the analysis (set to *SOLN* = 2, for a combined thermo-mechanical solver)

- *TERMINATION*, is used to define the total simulation time. The following parameter was set:
  - *ENDTIM*, sets the total simulation time and its mandatory for any LS-DYNA model (set to *ENDTIM* = 45.0)

- *THERMAL_NONLINEAR*, sets certain parameters for a nonlinear thermal analysis or a combined thermo-mechanical analysis. In this option, the default parameters were maintained.

- *THERMAL_SOLVER*, sets certain parameters for the thermal part of the combined thermo-mechanical solver. The following parameters were set/activated:
  - *ATYPE*, sets the analysis type (set to *ATYPE* = 1, for a transient analysis)
  - *PTYPE*, defines the type of the thermal problem (set to *PTYPE* = 2, for a nonlinear problem with material properties evaluated at element average temperature)
  - *FWORK* = 0.8, defines the Taylor-Quinney coefficient or the ratio of plastic work turned to heat during the process, which has been proven to depend on the loading mode (**Rittel, Zhang, and Osovski, 2017**) and on strain rate effects (Ż**aba et al., 2021**). The value of *FWORK* = 0.8 was reported for IN718 by Dolci et al. (**Dolci et al., 2016**)
  - *SBC*, defines the Stefan-Boltzmann constant (defined as *SBC* = 5.67e-11, based on the system of units used in the current analysis)

- *THERMAL_TIMESTEP*, is used to define the thermal timestep controls for the thermal part of the combined thermo-mechancal analysis. The following parameters were set:
  - *TS*, defines the timestep control (set to *TS* = 1, for a variable timestep)
  - *DTEMP*, defines the maximum temperature change in each timestep, above which the thermal timestep will decrease (set to *DTEMP* = 20.0)

- *TIMESTEP*, is used to define the timestep controls for the structural part of the combined thermo-mechancal analysis. The following parameters were set:
  - *DT2MS*, is the timestep size for mass scaled solutions (set to *DT2MS* = -4.0e-6, to trigger selective mass scaling)
  - *ERODE*, is a flag permitting the deletion of elements causing the decrease of timestep below the value of *DT2MS* (set to *ERODE* = 0, to deny the deletion of elements)
  - *IMSCL*, is a flag for defining which bodies will undergo selective mass scaling (set to *IMSCL* = 1, so that all parts will undergo selective mass scaling)
  - *RMSCL*, is a flag for including the rotational option in selective mass scaling (set to *RMSCL* = 1.0, to include the rotational option)
  - *IHDO*, changes the method for calculating timestep for solid elements (set to *IHDO* = 1, to improve timestep continuity through a modified calculation method)

It is worth noting that for every CONTROL option included in the analysis, the default values were considered for the rest of their individual parameters that were not altered.

2.13.2 Result Parameters

With the definition of the aforementioned options and parameters, the model can be simulated and concluded successfully. However, no results would be recorded for a post-simulation evaluation. In order for the results to be recorded in LS-DYNA, certain parameters must be defined through the DATABASE option. These parameters act as flags indicating the chosen result values that will be exported after each timestep. It is a very important step, as in case some results are not set to be recorded during solution, the whole solution has to be repeated with the respective flag activated this time.

From all the available result parameters provided by LS-DYNA, the following were chosen and activated.

- *ASCII_options*, are different result values that LS-DYNA records as numeric values per timestep. Depending on the individual option, these can refer to result values on nodes, elements or entire parts. The following ASCII_options were activated in the current analysis:
  - *BNDOUT*, records the forces and energies on the boundary conditions
  - *DEFGEO*, records the deformed geometry of the bodies in the analysis
  - *GLSTAT*, records the global statistics and energies of the entire analysis
  - *MATSUM*, records the energy results on each part individually
  - *RBDOUT*, records the motion of rigid bodies in their respective coordinate system
  - *RCFORC*, records the resultant contact interaction forces
  - *TPRINT*, records the thermal outputs from a coupled thermo-mechanical analysis
- *BINARY_D3PLOT*, is an option that records the stress, deformation and energy database for the entire model. Enabling this option is the only way to receive animated results after a simulation.
- *EXTEND_BINARY*, enables the extension of the recorded content of *D3PLOT*. From the available parameters, the following were activated:
  - *THERM*, allows the output of thermal results to *D3PLOT* (set to *THERM* = 2)
  - *INTOUT*, allows the output of stress/strain results at all integration points (set to *INTOUT* = ALL)
  - *NODOUT*, allows the output of stress/strain results at connectivity nodes (set to *NODOUT* = ALL)
  - *DTDT*, allows the recording of transient thermal results to *D3PLOT* (set to *DTDT* = 1)
  - *RESPLT*, allows the recording of translational and rotational residual forces to *D3PLOT* (set to *RESPLT* = 1)

It is worth noting that for all the ASCII options a recording timestep of 0.01 s was applied, while for D3PLOT a recording timestep of 0.5 s was applied.

Finally, although it is not an actual result file, the option of *INTERFACE_SPRINGBACK_LSDYNA* was also activated for the models of the current analysis. The main purpose of this option is to record the stresses and effective plastic strains at the final state of the model. Additionally, several thermal results can be included in the output file, when a specific flag is activated. From all the available parameters of *INTERFACE_SPRINGBACK_LSDYNA*, the following were considered:

- *PSID*, denotes the set of parts, whose results will be included in the output file (set to the number of part set including the workpiece and the deformable segment of the tools)
- *NHSV*, defines the number of history variables to be included in the output file (set to *NHSV* = 100, in order to include all possible results)
- *FTYPE*, defines the type of output file (set to *FTYPE* = 2, for ASCII and binary file format)
- *NTHHSV*, defines the number of thermal history variables to be included in the output file (set to *NTHHSV* = 100, in order to include all possible thermal results)
- *FSPLIT*, is a flag that enables the division of the output file to one including only geometric results and another including the stress and strain results (set to *FSPLIT* = 1, to enable division of the output file)

2.14 Solution

After all parameters of the model have been set, a keyword file (.k file) was created. This file contains all the parameters of the numerical model in a specific format. A sample of a .k file created for one of the models of the current dissertation is presented in Appendix A.

The solution of each Ring Rolling model lasted approximately 300–320 h, on an Intel Core i7-4790, 32 GB RAM computer with an SSD disk for greater read/ write speeds. For the solution, six parallel logical processors were used, in order to accelerate the whole process based on the available resources.

After the simulation was solved, the results were inspected for errors and were compared with the reference experimental results to be validated. The aforementioned validation between the numerical and experimental results will be presented in section §2.15.

2.15 Validation of the Numerical Results

In order to validate the performed simulations, the numerical results had to be compared with their corresponding results from **Zhu et al., 2016b**. In the current analysis, deformational (outer radius, inner radius and ring height), load (main and axial rolling loads) and ring temperature results were validated.

2.15.1 Deformational Results Validation

Regarding the calculated deformations, comparisons for the outer and inner radii of the ring, as well as the ring height results were performed. For the measurement of the ring diameters (both inner and outer) and height, twelve result sets were exported and the respective average results were subsequently calculated. For each result set, appropriate node couples were used (e.g. diametrically opposite nodes for the outer diameter, etc.), which were uniformly situated across the periphery of the ring. The comparisons of deformational results from the two methods are presented in Figs.2.28-2.29:

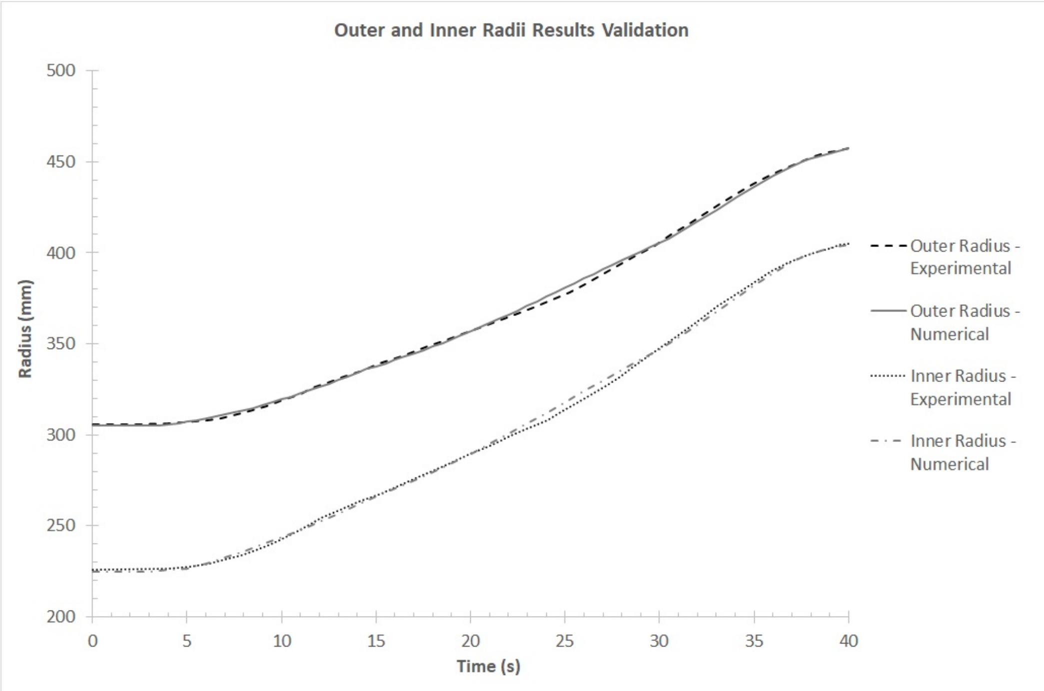

FIG. 2.28: Comparison between the experimental and numerical results of the outer and inner ring radii

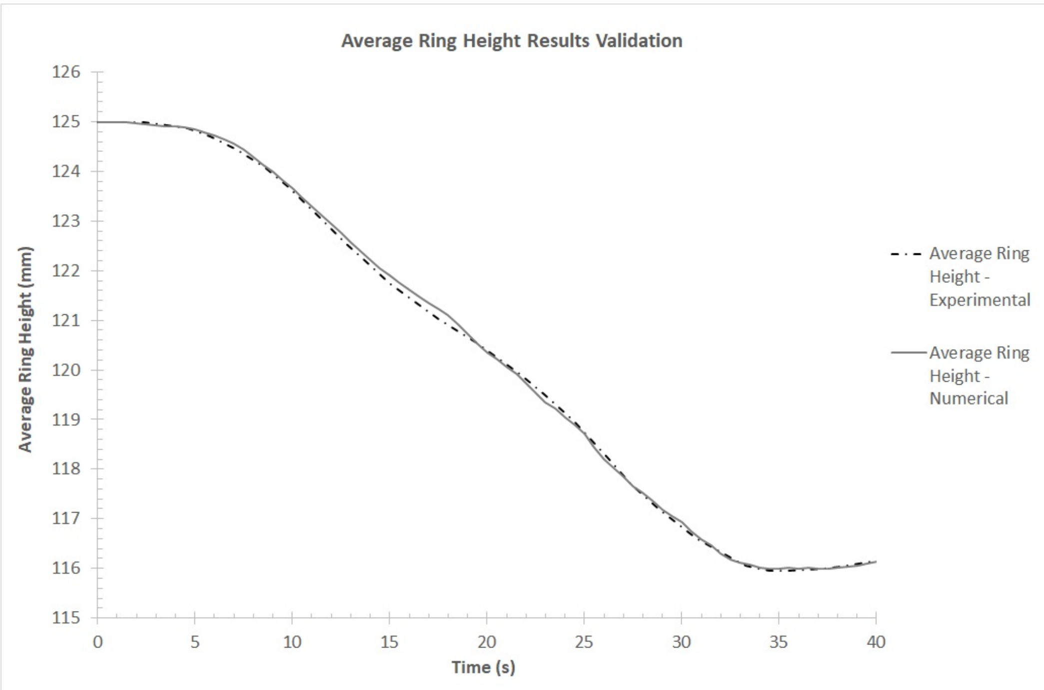

FIG. 2.29: Comparison between the experimental and numerical results of the ring height

Observations over Figs.2.28-2.29 reveal close deformational behaviors in the two methods. The recorded results from the numerical model followed a steady state deformation rates, with little to no deviations. This is slightly different for the experimental results, where a change in the deformation rate was observed at approximately t = 25 s in both figures.

However, the final deformation results from both methods were almost identical, thus rendering the numerical model validated in terms of the calculated ring deformation.

A closer inspection over the experimental results of both the inner and outer ring radius deformations reveals that the corresponding curves did not progress linearly through Phase 2 of the process (also see §1.2), as it would be expected. This indicates a non-linearity in the process, which could be the result of various factors (e.g. change in mandrel velocity, "ring climbing" manifestation, etc.). Although no such phenomenon was reported by Zhu et al., a change of the linear velocity of the mandrel could be further investigated as the most possible cause. If the mandrel's velocity was changed, the ring growth algorithm would be different from the one described by Eq.2.59, and instead it should be approached by a higher order polynomial (the effects of higher order polynomials describing mandrel linear feed are investigated in section 3.4).

In the case of the ring's height and contrary to the outer and inner diameters, a slight decrease in the corresponding deformation rate was observed between t = 17 s and t = 25 s, approximately (Fig.2.29). Although this behavior can be attributed to a non-constant axial velocity of the conical roll, similarly to before, the simultaneous existence of deformation rate changes in both ring diameters and ring height, around the same time instances render the manifestation of a ring imbalance as the most possible cause for these changes.

2.15.2 Load Results Validation

Regarding the load results' comparisons, these are presented in Figs.2.30-2.31:

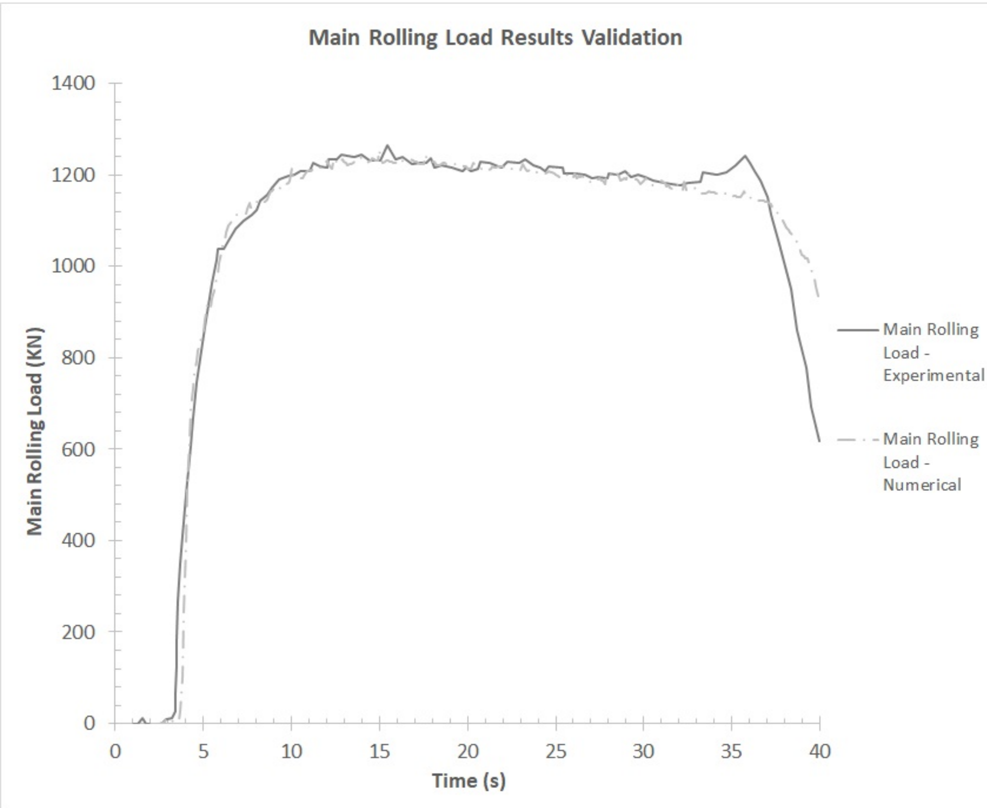

FIG. 2.30: Comparison between the experimental and numerical results of the main rolling load

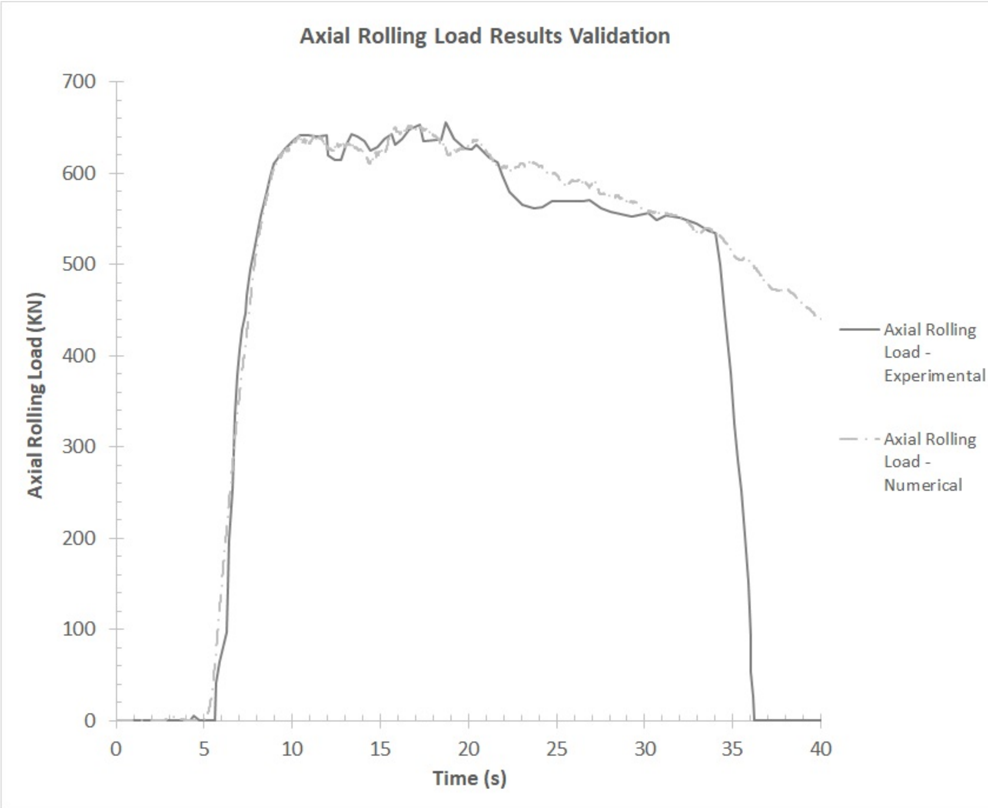

FIG. 2.31: Comparison between the experimental and numerical results of the axial rolling load

Observations over Figs.2.30-2.31 reveal a fairly close comparison between the results from the two meth-ods, but with some points of interest.

In the case of the main rolling load (Fig.2.30), the curves from the two methods were almost identical for most of the process's duration, with only the very final segment of the experimental curve differentiating. More specifically, a peak was observed on that segment, which was probably a result of a sudden (and thus dynamic) change in the movement of the mandrel. More specifically, the sudden increase of the experimental curve indicates that the mandrel moved at an accelerated rate towards the ring (similar to an impact), thus causing additional thinning than what was expected. Supposing that the mandrel had a predetermined final position and that it returned to it after its sudden forward movement, the subsequent, fast main rolling load decrease could also be explained, as the size of the bite would be slightly larger than the ring's thickness. On the other hand, such a phenomenon was not considered in the numerical model, thus the corresponding load curve had a much steadier behavior, with no unexpected peaks.

Regarding the axial rolling load (Fig.2.31), the two curves followed an almost identical path, until an unexpected drop of the experimental curve was manifested at t = 25 s, approximately. From then on the two curves were slightly different from one another until approximately t = 32 s, when the two curves resumed their identical path again, until t = 36 s approximately. The aforementioned unexpected load drop at approximately t = 25 s can be correlated to the corresponding observations made previously for the deformational results, further indicating an unexpected phenomenon (most probably an imbalance in the workpiece). After t = 36 s, approximately, the experimental curve dropped suddenly to zero, which indicates a contact loss between the conical rolls and the ring. This practice is not common in a typical Ring Rolling process, as the conical rolls should remain at their final axial positions, in order to eliminate the formation of fishtail defects during the final stages of the process. Such a removal of the conical rolls was not included in the simulation, thus a reaction load remained until the end of the process in the numerical result curve, as a result of the continuous flattening of small fishtail defects on the ring.

2.15.3 Thermal Results Validation

Finally, for the validation of model's thermal behavior, a comparison of the ring's temperatures was performed. For this comparison, the ring's temperatures had to be measured in its outer peripheral and upper surfaces, similarly to the respective measurements found in the literature reference (**Zhu et al., 2016b**). Seeing that no information regarding the temperature measurements in the experiment was provided by Zhu et al., the average temperature from every node in the corresponding surfaces was calculated in each timestep. The resultant time - temperature curves were then compared to the respective curves from **Zhu et al., 2016b** and they are presented in Fig.2.32:

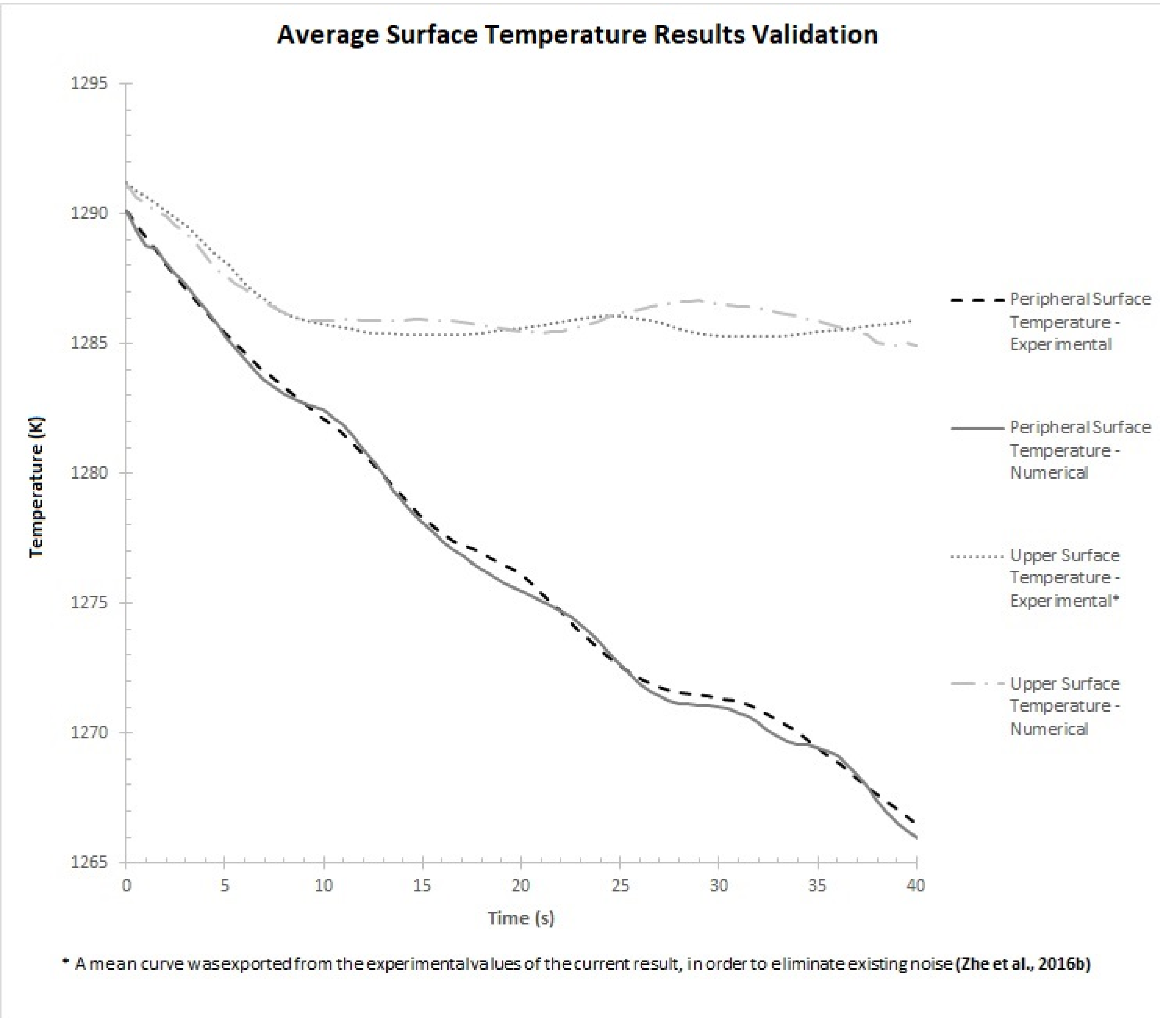

FIG. 2.32: Comparison between the experimental and numerical results of the ring's average temperature

Observations over Fig.2.32 reveal a fairly close relationship between the ring temperatures from the two methods, during the whole process. In the case of the outer peripheral surface temperatures, the numerical curve was almost identical to the corresponding experimental curve, with the greatest difference between the two being less than a degree (at approximately t = 18 s and t = 33 s). Similarly, the upper surface temperature curves from the two methods were very close, as well. The maximum temperature differences in this case were observed at approximately t = 30 s and at the end of the process, with their respective temperature differences being approximately ΔT_{30s} = 1.3 K and ΔT_{40s} = 1 K. It is worth noting that for the comparison in Fig.2.32, a mean of the experimental upper surface temperature curve was used, as the corresponding results were presented with an amount of noise in **Zhu et al., 2016b**.

Overall, the temperature results of the numerical model were almost the same to those of the actual process, thus the thermal behavior of the model can be considered validated.

2.16 Numerical Model Results

After successfully validating the numerical model, the rest of the results could be evaluated. In the current section, different results from the numerical model are presented in four separate subsections, namely deformational results (§2.16.1), stress and strain results (§2.16.2), load results (§2.16.3) and thermal results (§2.16.4).

2.16.1 Deformational Results

Initially, the deformation of the ring throughout the process was evaluated. Although the outer and inner radii of the ring were validated to those of the experiment, a visualization of the ring's deformation in multiple timesteps during the simulation can provide additional information regarding localized forming on the workpiece. The aforementioned deformation instances are presented in Fig.2.33:

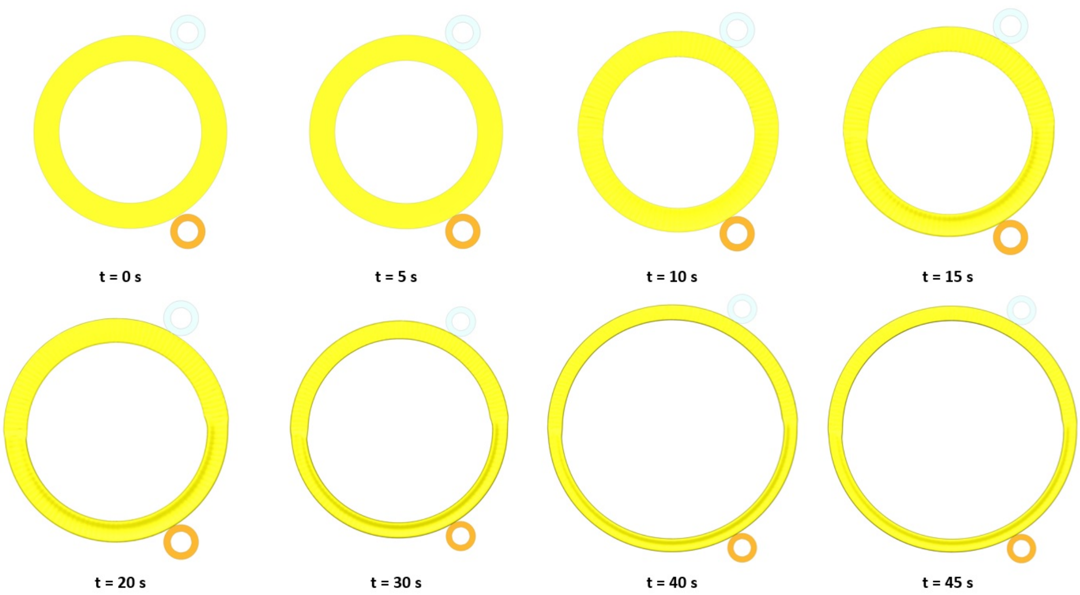

FIG. 2.33: Workpiece deformation instances during Ring Rolling

Observations over Fig.2.33 reveal the different individual deformations occurring simultaneously on the workpiece on each time instance. The two main deformation mechanisms were the workpiece's thickness reduction (observed at the rightmost segment of each instance) and the workpiece's height reduction (observed at the leftmost segment of each instance). A closer inspection of the deformation instances also reveals the two common defects that occur during Ring Rolling, namely fishtail defects on the lower half of the workpiece and bulges on the upper half. In the case of fishtail defects, their forming was rather asymmetric. More specifically, fishtail segments formed in the inner diameter side of the ring are larger in height than the corresponding segments in the outer diameter side. Both defects are presented in more detail through a cross-section of the ring, at a time instance of t = 24 s (Fig.2.34):

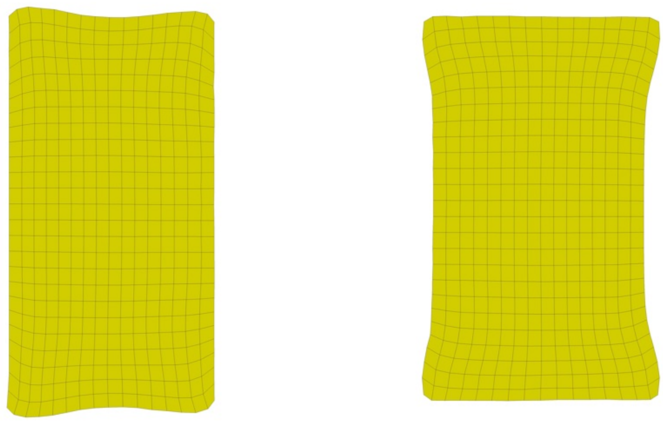

FIG. 2.34: Common ring defects during Ring Rolling (t = 24 s): (a) Fishtail defect and (b) bulge defect

Observations over Fig.2.34 further confirm the asymmetrical forming of fishtail defects, with their inner diameter segments (left side of Fig.2.34(a)) being slightly larger than their outer diameter segments (right side of Fig.2.34(a)). On the other hand, bulge defects (Fig.2.34 (b)) were rather symmetrical, with their segments on both diameters of the ring being almost equally sized.

Finally, the outer and inner radii results, as well as the average ring height results are presented for the entirety of the process's duration in Figs.2.35 and 2.36, respectively:

In the case of the outer and inner radii (Fig.2.35), both dimensions increased slightly after the end of the corresponding experimental curves (t = 40–45 s), which is expected to occur during Phase 4 of a typical Ring Rolling process (also see §1.2). More specifically, an additional increase of approximately ΔR = 4 mm was observed for the outer ring radius, while an additional increase of approximately Δr = 3 mm was observed for the inner ring radius, leading to a final outer radius of R_f = 461.03 mm and a final inner radius of r_f = 408.16 mm, approximately. The choice to omit Phase 4 from the experimental results was rather peculiar. During Phase 4, the ring attains its final circularity and height, as a result of the final thickness that is applied throughout the ring's perimeter. Furthermore, any fishtail and bulge defects are eliminated during Phase 4. Thus, the inner and outer radii are slightly increased from the combination of these actions, leading to slightly increased final dimensions. Compared to the experimental outer and inner radii results, as well as the

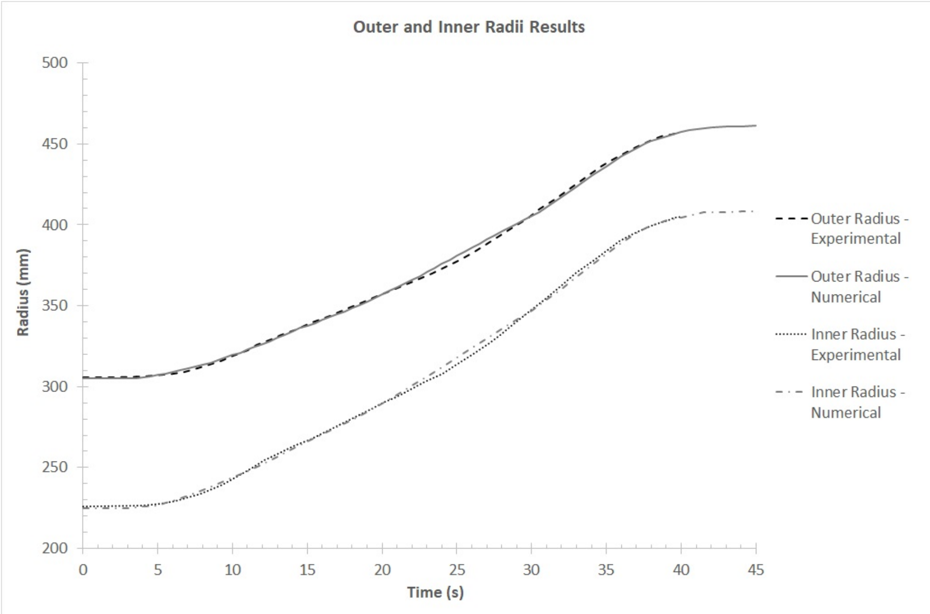

FIG. 2.35: Outer and inner radii results (experimental and numerical)

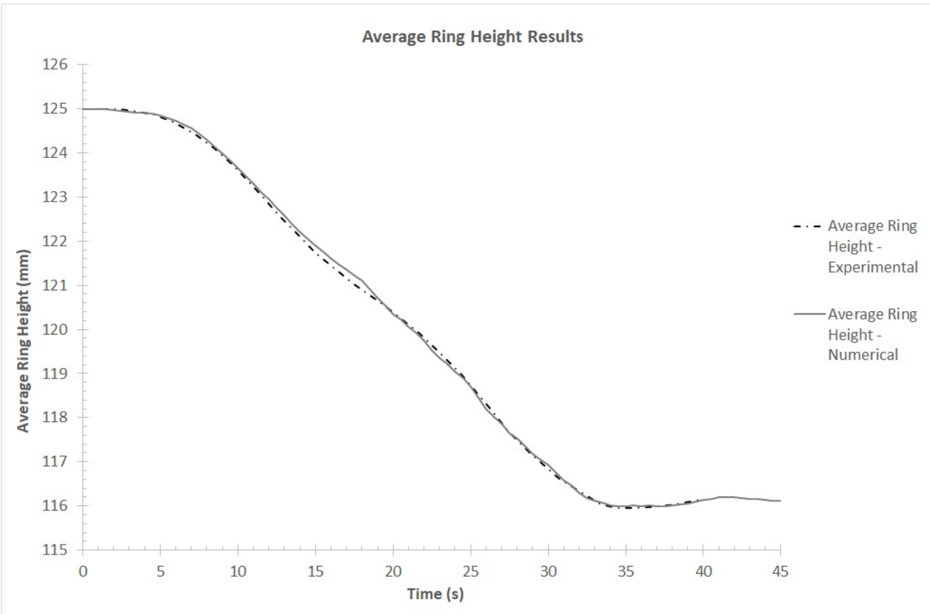

FIG. 2.36: Average ring height results (experimental and numerical)

target ring dimensions presented in **Zhu et al., 2016b** ($R_{f,target}$ = 450 mm and $r_{f,target}$ = 400 mm), the aforementioned radii differences from the inclusion of Phase 4 in the analysis led to an outer radius percentage overshoot of 2.4% and an inner radius percentage overshoot of just over 2%, approximately. Such dimensional differences are usually considered inappropriate, as for most simple engineering applications or near-net products a threshold of 2% in dimensional divergence is set as a common hard limit, while in more critical application the acceptable dimensional divergences may range from some microns to a few tens of microns. It is worth mentioning that any divergence from the target radii values is usually irreversible, especially in the case of the inner radius.

Observations over Fig.2.36 reveal a different behavior in the case of the average ring height.

In this case, after the end of the experimental results (t = 40–45 s) the average ring height in the simulation slightly increased until approximately t = 42 s. From that point and until the end of the simulation, the average ring height decreased again and stabilized at its final height of H_f = 116.1 mm, at the final instances of the simulation (t = 44–45 s). Compared to the final experimental value of $H_{f,experimental}$ = 116.2 mm, the difference was approximately ΔH = 0.1 mm or 0.09%, which can be considered negligible. Moreover, compared to the target final average ring height of $H_{f,target}$ = 115 mm, both the experimental and numerical results had an overshoot of approximately 1%, which can be considered acceptable in common engineering applications and near-net products, especially since further post-processes can be performed to achieve the target ring height (commonly several post-process grinding cycles). In the case of the numerical results, the aforementioned height difference (compared to $H_{f,target}$) can be attributed to the existence of slight fishtail defects in the final workpiece, which were included in the calculation of the average ring height.

It is worth noting that during Phase 4, a significant rotational velocity increase and a rapid cooling are applied and thus common process defects, such as fishtails and bulges, are eradicated via high strain rate, severe plastic deformation of the ring. This process was not simulated in the current analysis, as the necessary process parameters were unknown. In case this information was available, the final ring height would be relatively constant throughout the workpiece and close to the target ring height, while the final ring radii would be slightly larger.

Finally, the ovality of the inner and outer diameters of the produced ring were evaluated. For the calculation of the ring's ovality, Eq.2.88 was used (**Uchibori, Matsumoto, and Utsunomiya, 2018**):

$$C = \frac{\sqrt{\frac{1}{n_d}\sum_{i=1}^{n_d}(D_i(t) - \overline{D}(t))^2}}{\frac{1}{n_d}\sum_{i=1}^{n_d} D_i(t)} \tag{2.88}$$

where:

- C, is the calculated ovality
- n_d, is the number of diameter inputs used for the calculation
- $D_i(t)$, are the individual diameter inputs at each time instance used for the calculation
- $\overline{D}(t)$, is the average diameter value at each time instance

Regarding the inputs used in Eq.2.88, twelve outer diameter and twelve inner diameter growth curves, equally distanced around the perimeter of the ring during the entire process, were used. The resulting outer and inner diameter ovality curves (presented here in percentage form) are presented in Fig.2.37:

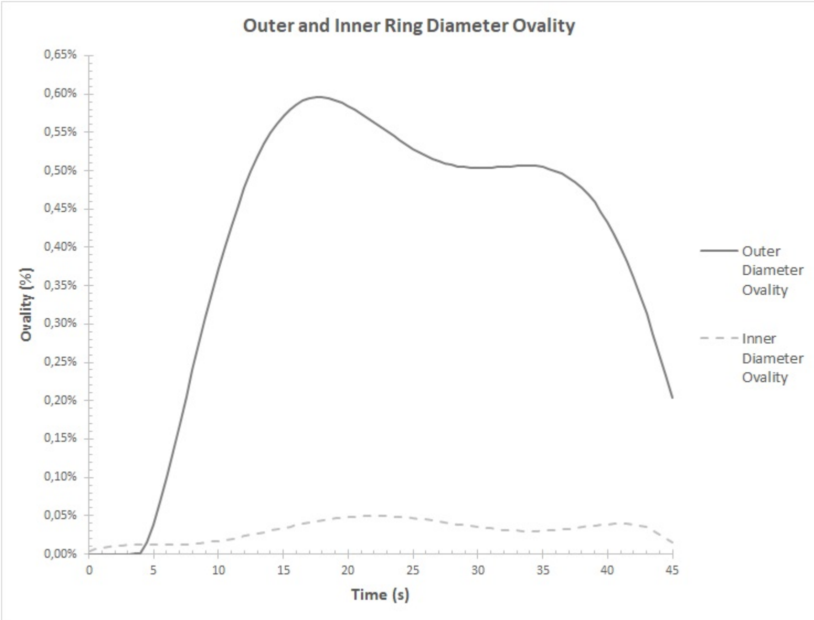

FIG. 2.37: Outer and Inner diameter percentage ovality curves calculated during Ring Rolling

Observations over Fig.2.37 reveal very small percentage ovalities in both diameters of the produced ring. More specifically, in the case of the outer diameter's ovality, a rapid increase of the value was observed at the early stages of the process, until the maximum ovality of approximately 0.59% was reached at t = 18 s. From that point onwards, ovality began reducing and an ovality value of 0.20% approximately was finally observed at the end of the process. On the other hand, the inner diameter ovality had significantly lower values throughout the process. In this case too, an early ovality increase was observed until it reached its maximum value of 0.05% at t = 22 s, followed by a subsequent ovality reduction until the end of the process. The inner ovality value at the end of the process was 0.01%, approximately. Interestingly, the most rapid ovality reduction rates, for both the inner and outer diameter, were observed after t = 40 s (Phase 4 of Ring Rolling), thus further verifying that diameter normalization occurred at the final stages of the process. Overall, both of the calculated ovalities maintained at low enough values that the ring can be considered as perfectly round. These low ovality values can be directly correlated to the proper support of the ring, and thus the precise movement laws applied on both support rolls. It should be noted that an ovality of zero indicates a perfectly round workpiece.

2.16.2 Stress and Strain Results

In the case of stress and strain results, multiple cross-sections of the ring during the process's duration were extracted from the model and evaluated. For a better presentation of the current section, each of the stress and strain results will be discussed separately in different subsections.

Equivalent Von Mises Stress Results

In the case of the stress results, the equivalent Von Mises stress distributions of multiple cross-sections along the ring's perimeter were extracted. The cross-sections that were chosen for the analysis were those being in contact with the tools during the process, namely: (a) between the mandrel and the main roll (main rolling bite), (b) between the two conical rolls (conical rolling bite) and (c) those being in contact with each of the support rolls.

The equivalent Von Mises stress distribution in multiple time instances during the process for these cross-sections are presented in Figs.2.38-2.41. It is worth noting that the limits of the color scale used in Figs.2.38-2.41 correspond to the maximum and minimum equivalent Von Mises stress values recorded during the entirety of the simulation.

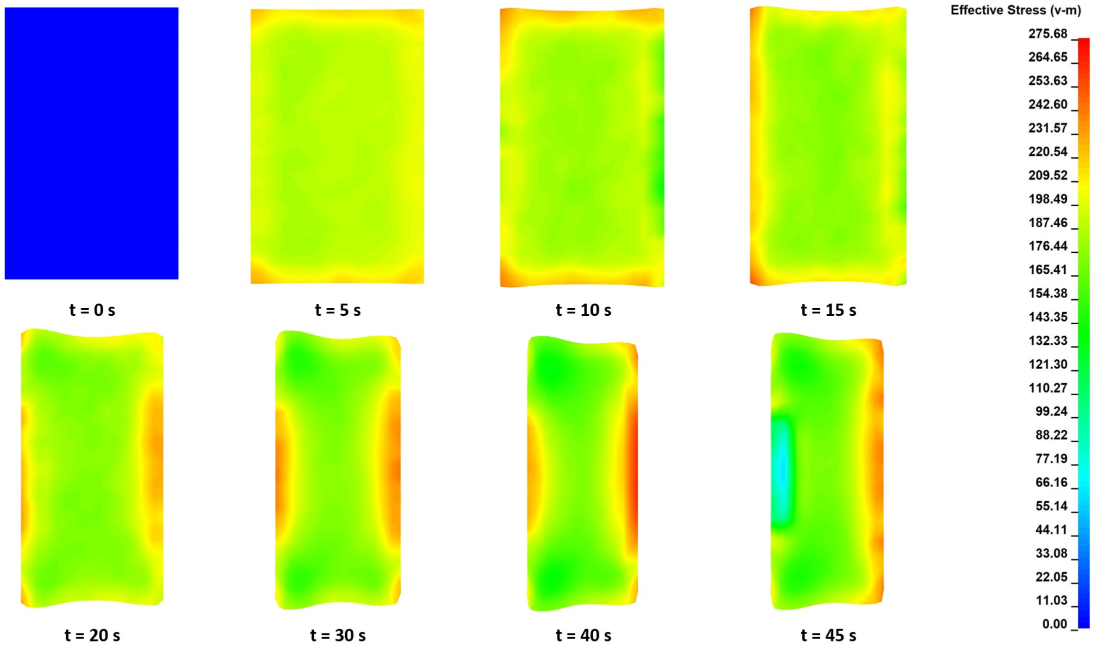

FIG. 2.38: Equivalent Von Mises stress distributions in multiple time instances during the simulation (Cross-section of the workpiece in the main rolling bite)

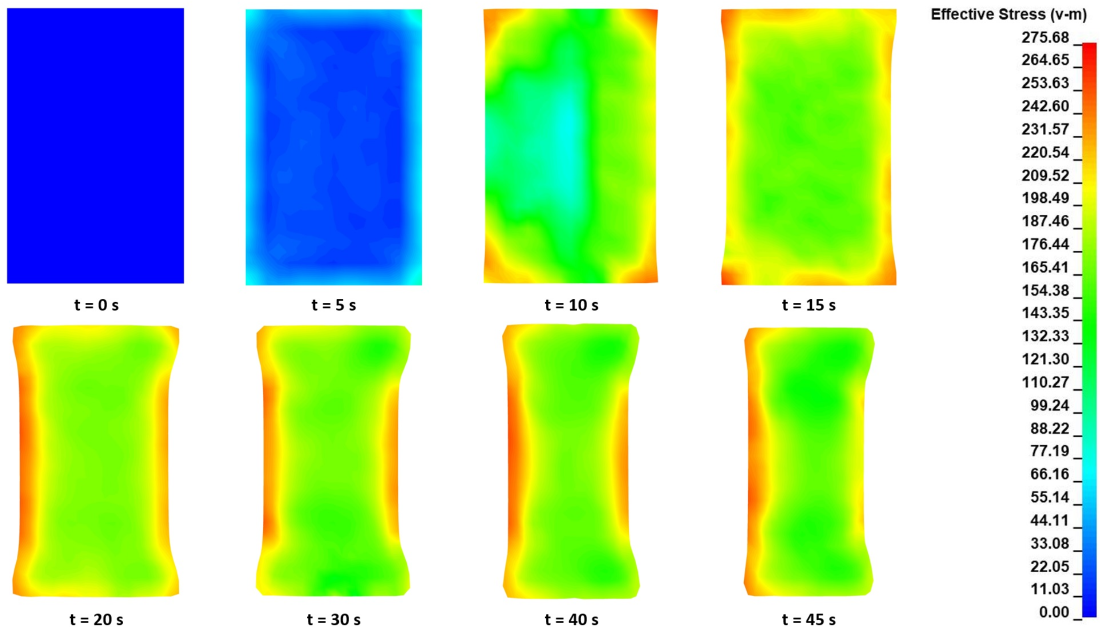

FIG. 2.39: Equivalent Von Mises stress distributions in multiple time instances during the simulation (Cross-section of the workpiece in the conical rolling bite)

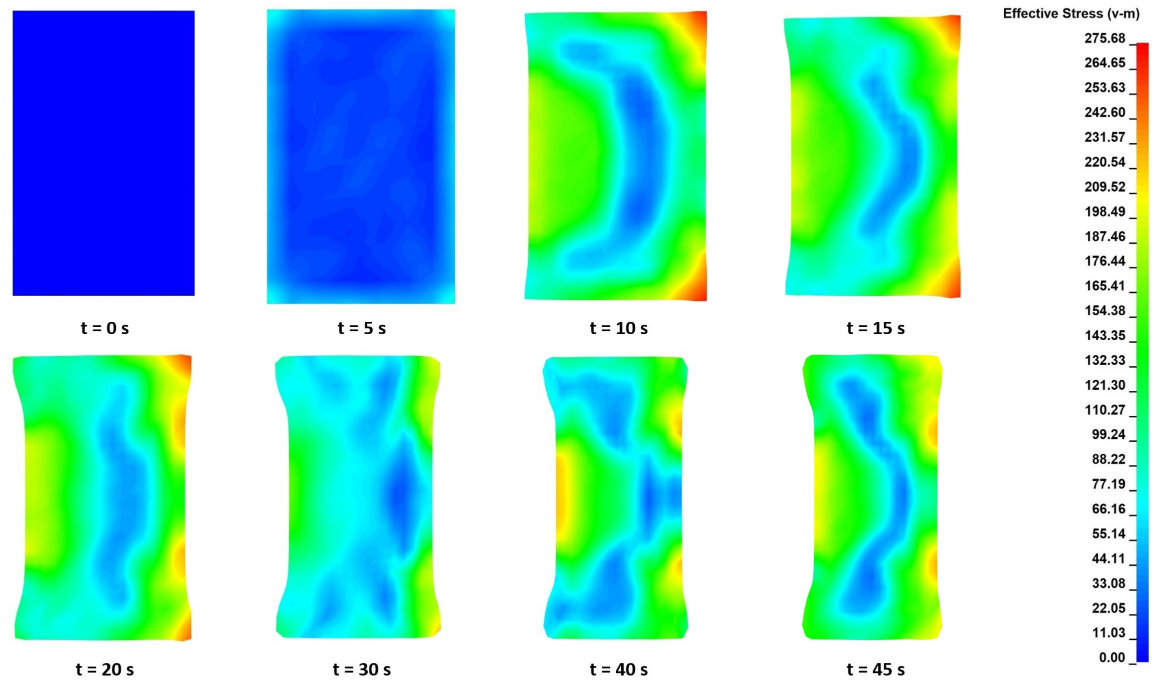

FIG. 2.40: Equivalent Von Mises stress distributions in multiple time instances during the simulation (Cross-section of the workpiece in contact with support roll 1)

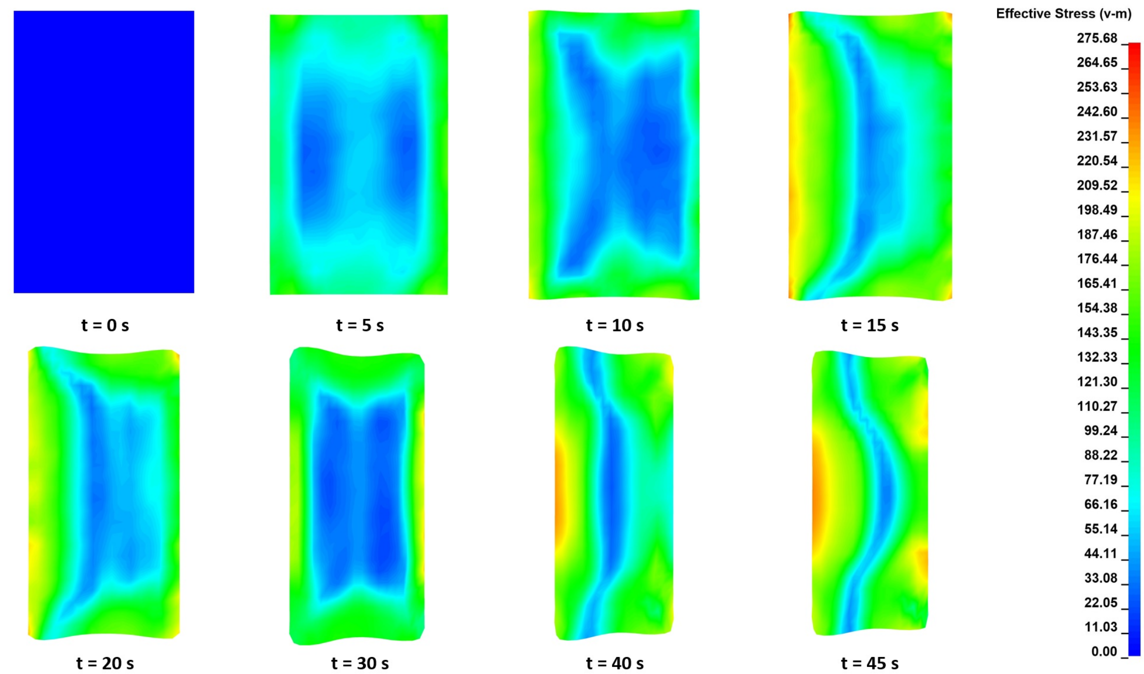

FIG. 2.41: Equivalent Von Mises stress distributions in multiple time instances during the simulation (Cross-section of the workpiece in contact with support roll 2)

In the case of Fig.2.38, the eq. Von Mises stress distributions around the main rolling bite area are presented. In the instances of Fig.2.38, the inner diameter of the ring was on the left side of each cross-section, while the outer diameter was on the right side. During the early forming stages of the process t = 5–10 s approximately), the highest stress values appeared on the bottom and top surfaces of the workpiece, and especially on the four corners of the corresponding cross-sections. These high stress values were approximately 230–250 MPa, and they can be attributed to a combination of residual stresses from the action of the conical rolling bite and the ironing of the bulge defects from the main rolling bite. Stresses caused by the main rolling bite during the same time were lower at approximately 195–210 MPa. From that point and until the end of the main rolling bite action (t = 15–40 s approximately), the stresses on the top and bottom surfaces seemed to relax significantly, while the stresses caused by the main rolling bite prevailed. The maximum recorded stress values during this time were approximately 240–275 MPa. Interestingly, after t = 20 s the highest stress values from the two main rolls seemed to concentrate around the middle of the ring's height, thus indicating an ironing of a barrel-like shape formed previously in the conical rolling bite. Additionally, the increased stress values at the four corners of the cross-sections remained, as bulge defects were ironed. Finally, during the final stages of the simulation (t = 45 s), the highest stress values were those around the contact with the main roll at approximately 220–240 MPa, as the main roll continues to rotate the ring for the entirety of the simulation's duration. These stresses were almost equally distributed throughout the height of the ring, thus indicating that no further barreling was caused by the conical rolls. On the other hand, the stresses previously seen around the contact with the mandrel were almost completely relaxed (50–70 MPa, approximately), as the thickness of the ring was constant throughout its perimeter during that time. The sequential decrease of the mandrel side stresses can be observed in the last three cross-section instances of Fig.2.38 (t = 30–45 s), as a result of the mandrel stopping its movement and thus ceasing any further radial forming. Moreover, the corner stresses on the mandrel side also reduced, as the bulges formed during this time were small in size. It is worth mentioning that for the majority of instances in Fig.2.38, the fishtail defects created on the mandrel side were larger than those on the main roll side, as mentioned previously in chapter §2.16.1.

On the side of the conical rolling bite (Fig.2.39), the stress distributions observed on the workpiece presented some slight differences. Initially, it should be mentioned that in Fig.2.39, the inner diameter of the ring was on the right side of each instance, while the outer diameter was on the left side. On the very early stage of the process (t = 0–5 s) only low stress values were observed, as the movement of the conical rolls had just initiated. The maximum recorded stress values during this time were observed around the four corners of the cross-section, calculated at approximately 65–85 MPa. Other than that, almost equal stresses in size and value appear in the four edges of the cross-section. Afterward and during the initial forming stages (t = 10–15 s), greater stresses appeared on the corners and the four sides of the corresponding cross-sections in a fairly symmetrical pattern, and with values of approximately 200–240 MPa. The maximum stress values during this time remained at the corners. During the later stages of the process (t = 20–40 s), a similar stress distribution to that observed in Fig.2.38 was seen here too. More specifically, the stresses on the top and bottom ring surfaces relaxed, and greater stresses were observed around the inner and outer diameter surfaces of the ring. The highest recorded stress values were mainly concentrated around the outer diameter surface at approximately 240–275 MPa, with the distribution around the inner diameter surface following at slightly lower values (200–240 MPa). The great stresses observed at this time were a combination of residual stresses from the main rolling bite and compressive stresses from the ironing of the fishtail defects. Finally, during the final stages of the simulation (t = 45 s), all stresses gradually dropped to lower values, although the overall distribution remained the same. The highest recorded values during this time were approximately 230–250 MPa, again concentrated around the outer diameter surface.

Regarding the stress distributions on the cross-sections being in contact with the two support rolls, these had significant differences compared to the corresponding distributions of the main and conical rolling bites, but also to one another. Initially, in the case of the cross-section in contact with support roll 1 (ring-to-support roll contact on the right side of each cross-section), the corresponding stress distributions are presented in Fig.2.40. During the very early stage of the process (t = 0–5 s), the stress distributions were almost identical to those observed in Fig.2.39, thus the same conclusions can be drawn. Later and during the initial forming stages (t = 10–20 s), a unique stress distribution was manifested. More specifically, the greater stresses concentrated around the edges of these cross-sections, leaving a crescent-like distribution of low stresses in the middle. The highest stress values during this time were observed at the corners on the side of the support roll at approximately 250–275 MPa, followed by residual stresses on the inner diameter of the ring (at approximately 175–195 MPa) and some localized stresses on the ring-support roll interface. The latter gradually increased (from 85 MPa to 225 MPa, approximately) during this, as a result of the outwards bending of the bulge defects, which caused a localized stretching of the material. From these observations, it can be concluded that support roll 1, apart from stabilizing the ring also partially formed it, through a mixed mechanism of ironing the bulge defects and bending them outwards. Should support roll 1 only stabilize the ring, the low stresses observed in the middle of the cross-section would have more of an X-like distribution. During later forming stages of the process (t = 30–40 s), the stresses in the interface with support roll 1 relaxed significantly at first (t = 30 s), indicating that support roll 1 simply stabilized the ring at that time, and later (t = 40 s) the outwards bending of the bulges manifested again. The highest recorded stress values were again at the corners being in contact with support roll 1 and at the inner diameter of the ring, at approximately 175–205 MPa (t = 30 s) and 205-225 MPa (t = 40 s), respectively. Interestingly, the stresses around the middle of the ring's height in its interface with support roll 1 were fairly low, as support roll 1 was mainly in contact with the bulge defects during that time. Finally, during the last stage of the process (t = 45 s), stress distribution was similar to that observed previous at t = 40 s, although stress levels around the inner and outer diameter surfaces of the ring were slightly higher and more uniformly distributed. On the outer diameter surface, the localized stresses resulting from the combined ironing and bending of the bulges were present, at approximately 200–225 MPa, while the stresses around the middle of the ring's height on the same surface were slightly higher than before (90–110 MPa approximately). On the inner diameter surface, stresses around the middle of the ring's height were slightly lower than before (180–200 MPa approximately), while the corner stresses were slightly higher (130–150 MPa approximately). Thus, it can be concluded that during the final stage of the process the ironing of the fishtail defects (by the conical rolls) and the bulges (by support roll 1) continued, even if their size was not so great. What is more, the uniformity of the distribution indicates a stabilization of the whole process.

For the stress distribution on the ring-support roll 2 interface, these are presented in Fig.2.41. In Fig.2.41, the contact with support roll 2 is on the right side of each cross-section. During the very early stages of the process (t = 0–10 s), some relatively high stresses appeared on the surfaces previously formed by the main rolling bite. Additionally, another two relatively high stress protrusions were observed in the top and bottom surfaces of the ring, which seemed to persist throughout the duration of the process. These protrusions were a result of the ring's thickness reduction and the fishtail defect formation, which caused the ring's material to flow outwards around the corners. This mechanism, combined with a slight barreling caused by the main rolling bite, led to the creation of an X-like low stress field in the middle of the analyzed cross-sections (mainly at t = 10 s). The highest recorded stress values during this time were approximately 200–210 MPa, observed at the two corners on the inner diameter surface of the ring (t = 10 s), while the majority of the aforementioned relatively high stress fields were approximately 140–160 MPa. Later and during the early forming stages of the process (t = 15–20 s), the pressure from support roll 2 increased initially (t = 15 s) and gradually decreased later (t = 20 s), as the previously manifested X-like low stress field changed to a more crescent-like shape at first and then began changing to an X-like shape again. The existence of a crescent-like stress field was a result of the increased stresses in the outer diameter surface around the corners of the cross-section during that time, caused by the ironing of bulge defects. Moreover, the stress fields on the inner diameter surface of the ring were increased, resulting from the mandrel's movement towards the ring. The highest recorded stress values during this time were approximately 200–220 MPa, mainly located around the inner diameter surface of the ring and at the corners of the outer diameter ring surface. Afterward and during later forming stages of the process (t = 30 s), a rather symmetrical stress field was observed with an X-like, low stress field at the center of the cross-section and the highest stress fields along the inner and outer diameter surfaces of the ring. The highest recorded stress values during this time were approximately 200–240 MPa, mainly along the contact with support roll 2. Finally and during the final stages of the process (t = 40–45 s), a rather constant stress distribution was observed with relatively high stress fields on the inner diameter surface of the ring at approximately 230-250 MPa. Furthermore, relatively high stress fields (approximately 200–220 MPa) could be seen around the corners on the outer diameter surface side, which moved towards the center of the ring's height at the end (t = 45 s). Also, a crescent-like, low stress field was observed in the middle of the ring's thickness, running from the top to the bottom ring surface. The aforementioned stress fields during these last stages of the process indicate strong residual stress fields caused by the mandrel and the ironing of bulge defects from the main roll, which persisted beyond the main rolling bite. What is more, at time t = 40 s a simple stabilization of the ring by support roll 2 was implied by their relaxed stress field, which however gradually increased towards the end of the simulation (t = 45 s), thus with the normalization of the ring's thickness and the subsequent diameter expansion, the latter was pressed more towards support roll 2.

Apart from the equivalent stresses from the interaction of the ring with tools, LS-DYNA can also fringe plot the equivalent Von Mises stress fields due to the loss of heat to the environment. A presentation of the equivalent Von Mises stresses solely due to heat loss are presented in Fig.2.42:

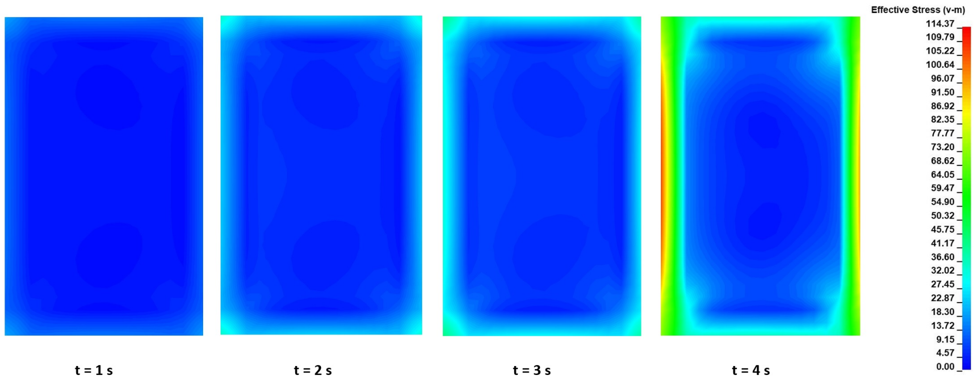

FIG. 2.42: Equivalent Von Mises stress distributions along main rolling bite due to heat loss and during the first contact with the tools (at t = 4 s)

In Fig.2.42, the equivalent Von Mises stress distributions on the ring due to heat loss to the environment are presented. Also, the equivalent stress distribution during the first contact with the tools of the main rolling bite is depicted on the same figure. It should be noted here, that since the heat exchange with the environment is constant throughout the ring during the first few seconds of the simulation, cross-sections of the ring around the main rolling bite were chosen as an example.

Observations over the first three seconds of the simulation in Fig.2.42 reveal a gradual increase in the thermal stresses in all four surfaces of the ring. Since thermal stress values and temperature change are governed by an inversely proportional relationship, the highest recorded thermal stresses were in the four corners of the corresponding cross-sections, with their maximum values being approximately 35–45 MPa at t = 3 s. However, from the comparison of the stress distributions between t = 3 s and t = 4 s, when the ring comes in contact with the tools (no forming had occurred yet) and thus heat conductance through the bodies of the mandrel and main roll and coolant conductivity were introduced, a major stress increase was recorded resulting from a great (although localized) temperature drop. More specifically, the highest recorded stress values at t = 4 s were approximately 95–115 MPa, observed along the inner and outer diameter surfaces. These stress values are large enough that in elevated temperatures and for low strain rates, they could cause localized plastic deformations on the workpiece (also see Fig.2.11). However, such phenomena were not observed in the current simulation, as the actual manufacturing process began immediately after the ring's contact with the tools, thus significantly higher stress field were introduced into the workpiece. It is worth reminding that during the first three seconds of the simulation only radiation and heat conductivity mechanisms contributed towards cooling the workpiece, while after t = 4 s heat conductance and coolant conductivity were added to the heat transfer mechanisms.

Effective Von Mises Strain Results

Similarly to the equivalent stress, for the analysis of the effective strain distributions, these were plotted on multiple different cross-sections of the ring for the duration of the simulations. Once again, the cross-sections in contact with the tools were mainly observed. The effective Von Mises strain distributions for the aforementioned cross-sections are presented in Figs.2.43-2.46. It is worth noting that in this case, the limits of the color scale in Figs.2.43-2.46 were manually selected, to avoid shadowing the strain distributions by using the extremum values recorded during the simulation. However, the maximum recorded values on each time instance and for each cross-section will be mentioned in the corresponding analysis of each figure.

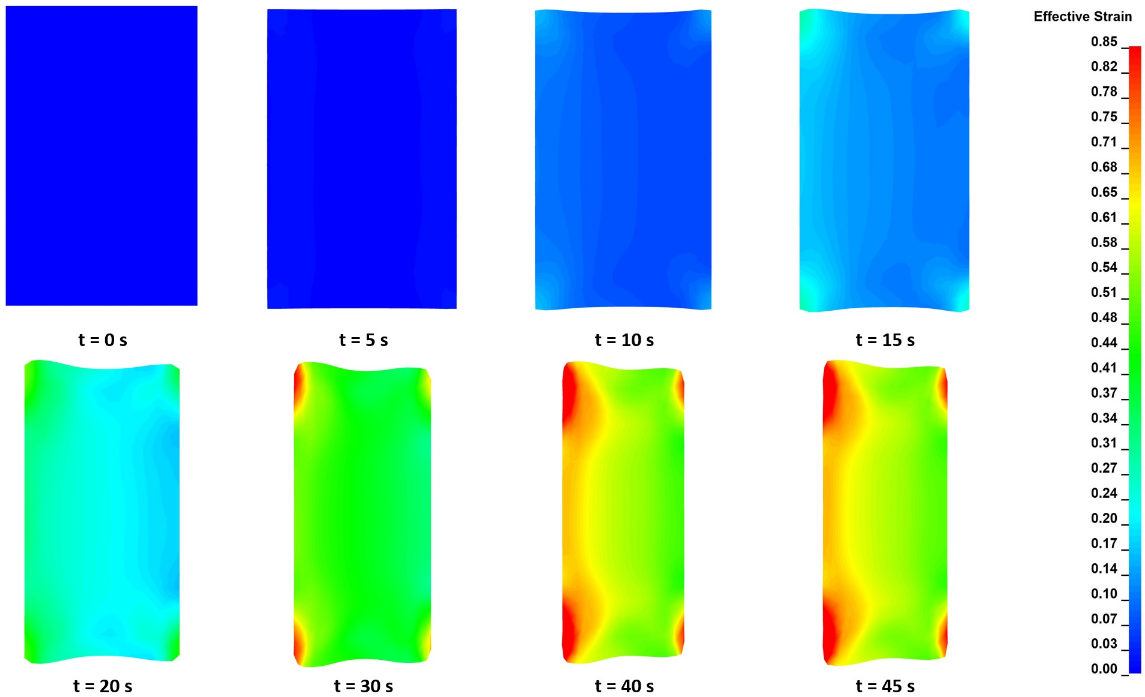

FIG. 2.43: Effective Von Mises strain distributions in multiple time instances during the simulation (Cross-section of the workpiece in the main rolling bite)

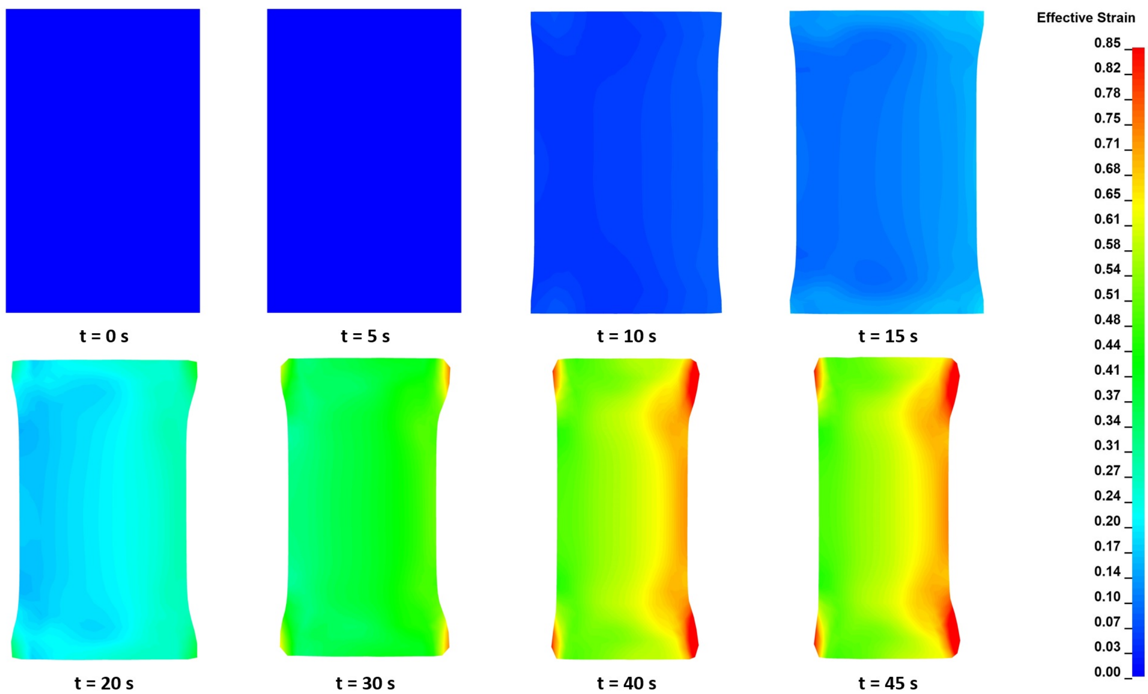

FIG. 2.44: Effective Von Mises strain distributions in multiple time instances during the simulation (Cross-section of the workpiece in the conical rolling bite)

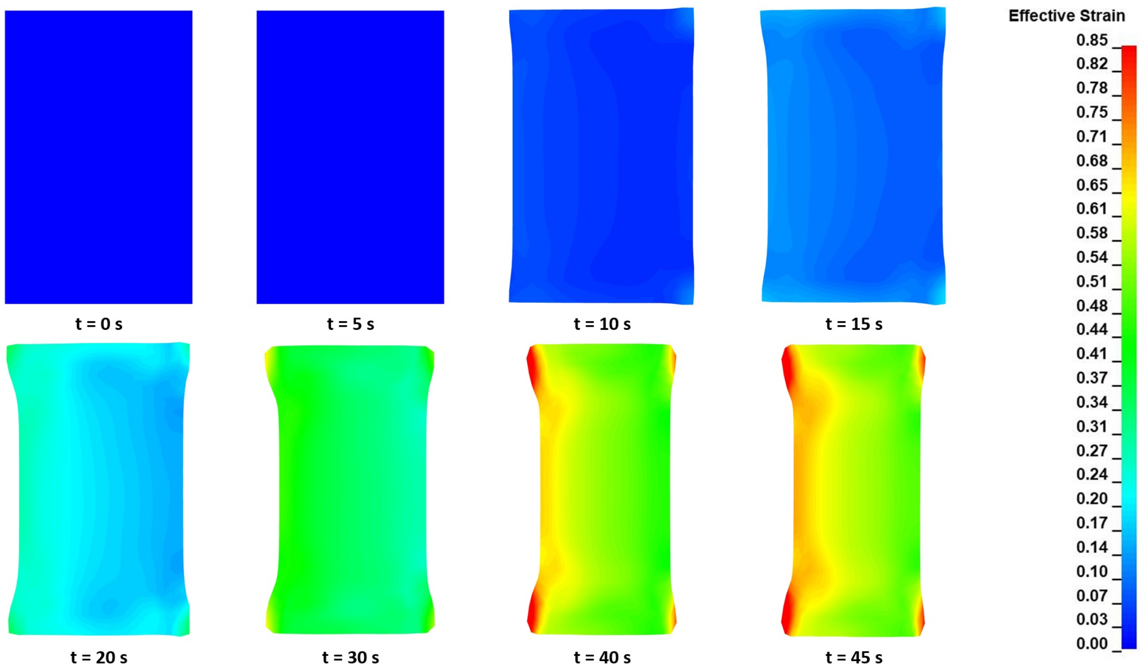

FIG. 2.45: Effective Von Mises strain distributions in multiple time instances during the simulation (Cross-section of the workpiece in contact with support roll 1)

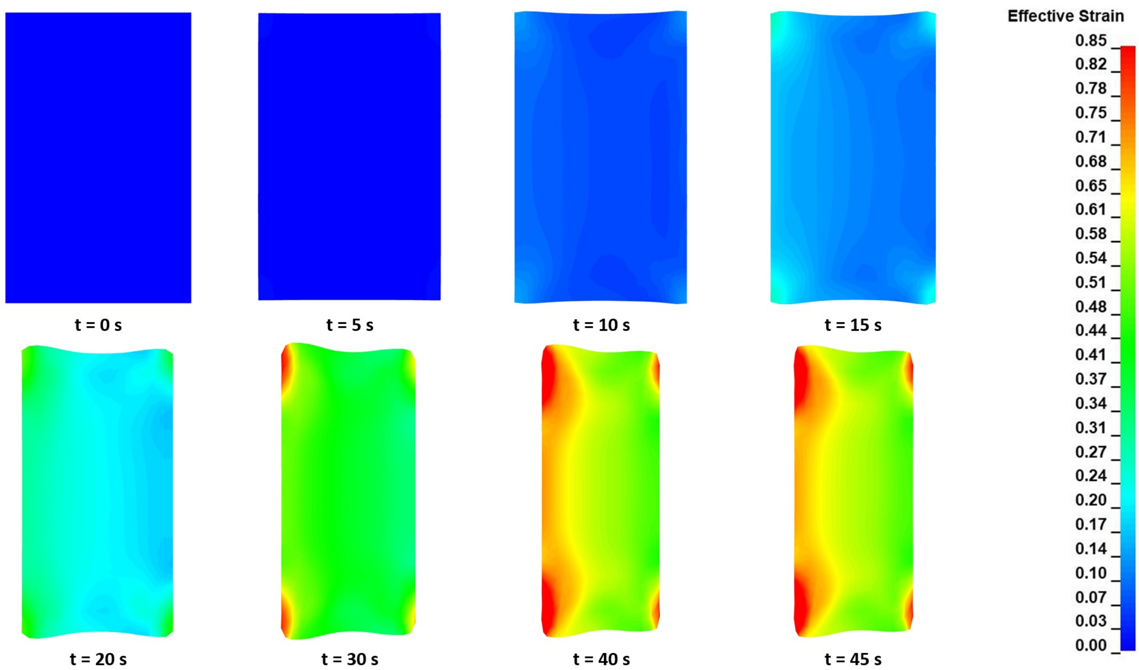

FIG. 2.46: Effective Von Mises strain distributions in multiple time instances during the simulation (Cross-section of the workpiece in contact with support roll 2)

Observations over Fig.2.43 reveal a rather expected strain distribution throughout the simulation process. Initially, it should be noted that in Fig.2.43 the contact with the mandrel is on the left side of each cross-section, while the contact with the main roll is on their right side. During the first few time instances of the simulation (t = 0–5 s) the majority of strain are almost zero, with the highest of them being distributed along the inner and outer diameter surface (contact areas with the mandrel and the main roll, respectively) at approximately 0.01–0.02. During the early forming stages of the process (t = 10–15 s), some measurable strains were observed, mainly on the interface with the mandrel and around the four corner. The aforementioned effective strain fields were a result of the mandrel indentation on the workpiece and the ironing of the bulge defects in the main rolling bite. The maximum recorded strain values during this time were approximately 0.27–0.30, located on the two corners on the inner diameter surface side. Next and during later forming stages of the process (t = 20–40 s), the aforementioned strain distribution gradually increased with no distinctive change in its pattern. The maximum recorded values at the end of the forming process were again at the two corners of the inner diameter surface size at approximately 1.00–1.10, followed by the strain values at the opposite corners of the surface and the indentation of the mandrel, both at approximately 0.75–0.85. Finally and during the last instances of the simulation (t = 45 s), the same strain pattern persisted, slightly increased at the same areas. The highest recorded strain values at the end of the process were observed again at the inner diameter side corners, at approximately 1.00–1.14.

In the case of Fig.2.44 similar strain distributions to those of the main rolling bite (Fig.2.43) were observed. In Fig.2.44 the inner diameter surface in on the right side of each cross-section, while the outer diameter surface is on their right side. During the very first time instances (t = 0–5 s), no strain fields were observed on the cross-section, as the conical roll just came in contact with the workpiece, and the pair of conical rolls have yet to start deforming it. Next and during the early forming stages (t = 10–15 s), some slight strain fields appeared, mainly on the four corners of the cross-section and on the inner diameter surface. These strain fields are a combination of the ironing of fishtail defects by the conical rolling bite and of residual strain fields from the main rolling bite. The maximum strain values during this time were located along the inner diameter surface at approximately 0.09–0.11. Afterward and during later forming stages of the process (t = 20–40 s), the residual strain fields from the main rolling bite prevailed, while they gradually intensified until the end of the forming process. The maximum strain values recorded at this time were approximately 0.90–1.00 again at the inner diameter side corners. Lastly, during the final time instances of the process (t = 45 s), the same strain fields remained, again slightly intensified. The maximum effective strain values at the end of the simulation were the inner diameter side corner strain at approximately 0.95 -1.05. It is worth noting that from a general overview in all the time instances of Fig.2.44, the effective strain fields caused by the ironing of fishtail defects seized to be relevant after t = 20 s approximately, when the much more severe residual strain fields from the main rolling bite prevailed.

Regarding the contact with support roll 1, the corresponding effective strain distributions are presented in Fig.2.45. In Fig.2.45, contact with support roll 1 is made on the right side of each cross-section (outer diameter ring surface). During the very first instances of the process (t = 0–5 s), no strain fields were observed on the workpiece as contact with support roll 1 was just made (no deformed cross-sections have yet reached support roll 1) at the end of this time. Then and during the early forming stages of the process (t = 10–20 s), the higher effective strain fields appeared on the four corners of the corresponding cross-sections, followed by increased strain fields on the inner diameter side and on the top and bottom surfaces. The maximum recorded strain values during this time were approximately 0.30–0.35

at the corners of the cross-section at t = 20 s. The aforementioned strain fields were a result of residual strains from the mandrel and the conical rolling bite. Later and during later forming stages of the process (t = 30–40 s), the top and bottom surface strain fields attenuated, while the corner and inner diameter surface strain fields prevailed. The maximum recorded strain values during this time were observed at the inner diameter side corners at approximately 0.90–1.00. Finally, during the final time instances of the process (t = 45 s), the aforementioned strain fields observed during the last forming stages of the process remained and were slightly intensified. The maximum recorded effective strain values at the end of the process were approximately 0.95–1.05, once again located at the inner diameter side corners of the cross-section. It is worth mentioning that from a closer inspection of the effective strain fields in Figs.2.45 and 2.44, the presented strain distributions were almost identical to one another, with the corresponding strain values in Fig.2.45 being slightly decreased

Regarding the effective strain fields from the contact of the workpiece with support roll 2, these are presented in Fig.2.46. Comparing the effective strain fields in Figs.2.46 and 2.43 revealed that they are almost identical both in pattern of distribution and in values. Thus, the same conclusion drawn previously for the results of Fig.2.43, also stand true for the effective strain results in Fig.2.46.

Finally, the effective strains caused by heat loss during the first few time instances of the simulation were analyzed. The corresponding effective strain distributions during these first time instances are presented in Fig.2.47. Similarly to the thermal stresses analyzed before in Fig.2.42, cross-sections in the main rolling bite were chosen as representative for the whole ring, in this case too.

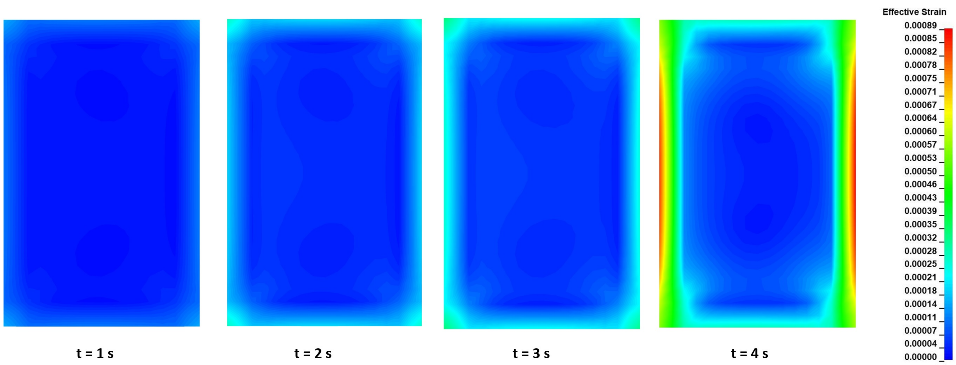

FIG. 2.47: Effective strain distributions along main rolling bite due to heat loss and during the first contact with the tools (at t = 4 s)

Observations over Fig.2.47 reveal that during all the presented time instances, the recorded effective strains were far below the proportional limit of the material. More specifically, during the initial three time instances, a symmetrical strain distribution was observed with gradually increasing intensity. The highest strains were distributed along the four edges of the cross-section, while the maximum recorded values were recorded at its four corners at approximately 0.0002–0.0003. At t = 4 s, when the tools first came in contact with the workpiece (no forming had yet occurred), the strain distributions along the contact faces intensified with the maximum recorded values at approximately 0.00065–0.0009. Similarly to the thermal stress analysis, the intensification of strains when the tools came in contact with the workpiece can be attributed to the inclusion of additional mechanisms (conductance and coolant convection) to heat transfer. However, the absolute effective strain values were low enough that they could be neglected.

2.16.3 Load Results

Although a comparison between the experimental and numerical load results was performed previously in §2.15.2, in the current section the analysis of the full length curve was performed. Special attention was paid to the segment of the numerical load curve after the completion of the corresponding experimental results.

Regarding the main rolling load, the corresponding numerical result curve is presented in Fig.2.48. Although the following analysis mainly corresponds to the numerical load results, in Fig.2.48 the corresponding experimental load curve was also included for comparative reasons.

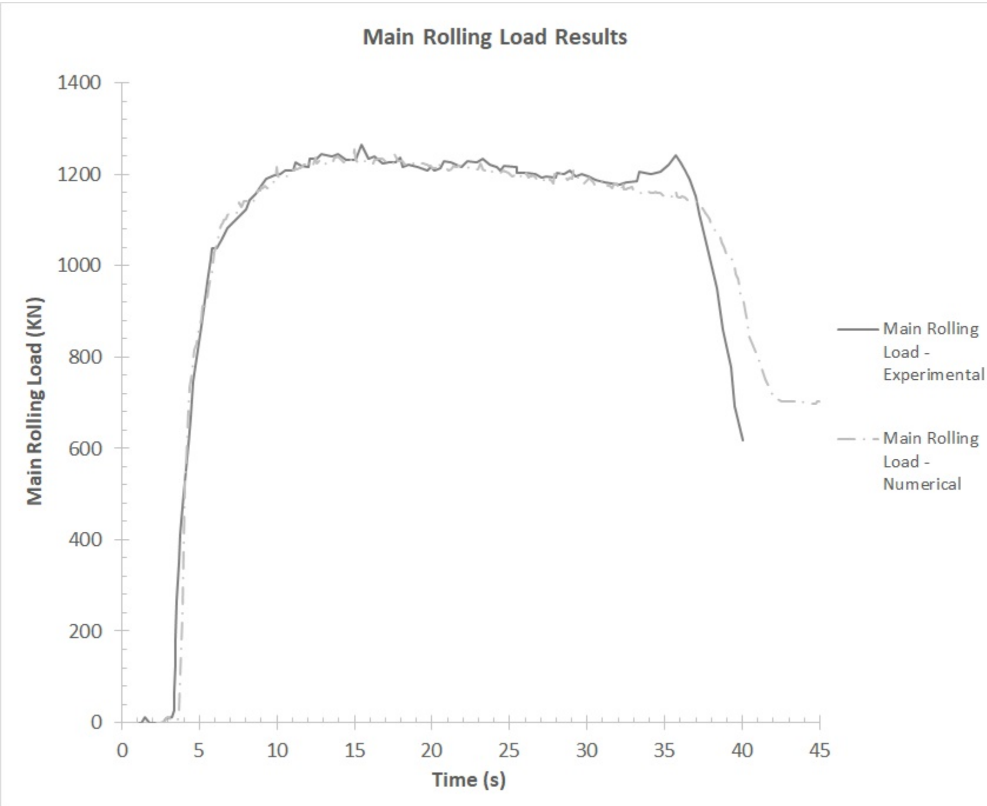

FIG. 2.48: Main rolling load experimental and numerical result curves (full simulation duration)

Observations over Fig.2.48 revealed a rather expected load curve form. The main rolling load began increasing after $t = 4$ s, when the mandrel first came in contact with the ring and the main rolling bite closed. Then, a rapid increase of the load was observed until $t = 5$ s approximately, at which point the aforementioned load increase rate was reduced. However, the main rolling load continued to increase until approximately $t = 14$ s, when the maximum recorded value of $F_{max,MRL} = 1240$ KN was reached. This main rolling load increase between $t = 5$–14 s, can be correlated to the formation of the first bulge defects during the same time (also see Fig.2.44), which led to additional material (in each cross-section) passing through the main rolling bite. From that point onward, the main rolling load began reducing at an almost constant rate, until t = 37.5 s approximately when the mandrel reached its final position. This behavior was rather expected, as the ring's thickness was progressively reducing during that time and thus less forming load was gradually required. Then from t = 37.5 s until t = 42.5 s, the main rolling load decreased rapidly, as during that time the ring's thickness was equalized throughout the entirety of its perimeter and much less forming load was required for this process. Finally, from t = 42.5 s and until the end of the simulation, the main rolling load maintained an almost constant value of approximately 700 KN, which can be analyzed as a combination of load required for the ironing of bulge defects, as well as load required for the movement of the ring. This specific load curve segment was absent from the corresponding experimental results, as the experiment's duration was not extended beyond t = 40 s (Phase 3 of Ring Rolling). As a result, whether this behavior was manifested later or not, cannot be verified. However, the final segment of the numerical load curve could be considered as a possible outcome of Ring Rolling Phase 4.

Regarding the analysis of the axial rolling load results, the corresponding experimental and numerical curves are presented in Fig.2.49:

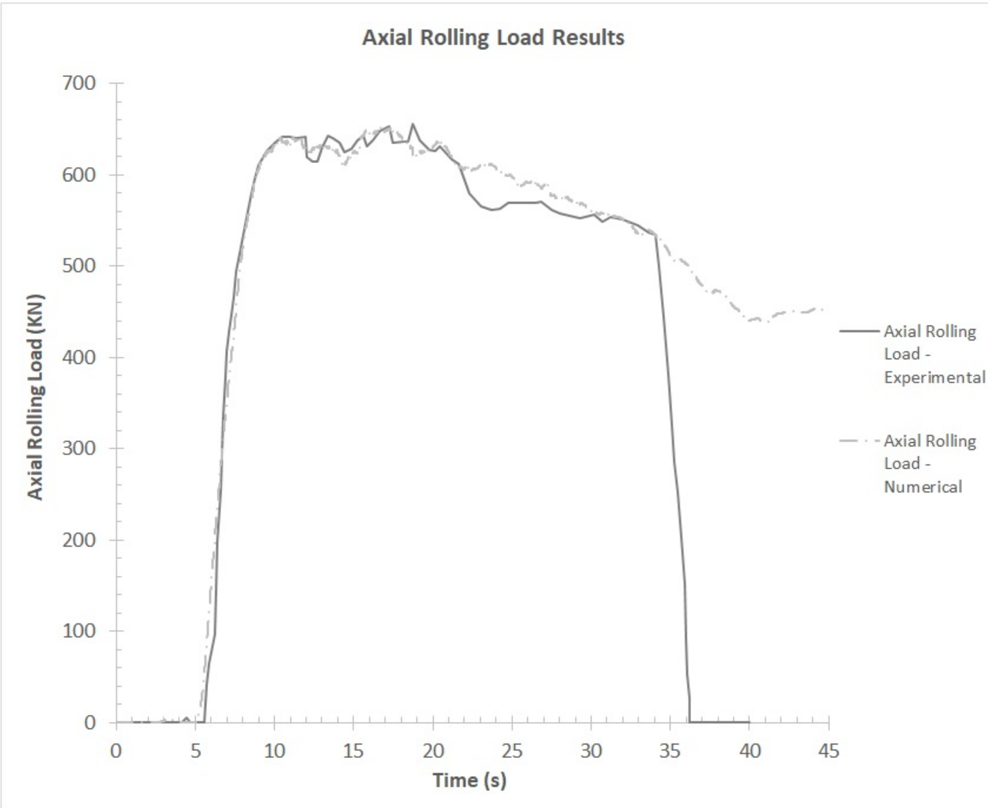

FIG. 2.49: Axial rolling load experimental and numerical result curves (full simulation duration)

Observations over Fig.2.49 revealed a similar curve form to that of main rolling load, although some differences between the two were presented. In this case, the first contact of the top conical roll with the ring was made at t = 5.5 s approximately, at which point the axial rolling load began increasing at an accelerated rate. Likewise, main rolling load, this rapidly increasing load rate was reduced after t = 9 s, and a more gradual load increase was observed until t = 17 s. At that point, the maximum recorded axial load was reached, at a value of $F_{max,ARL}$ = 647 KN approximately. The aforementioned axial load increase between t = 9–17 s can be correlated to the fishtail defect formation, which became significant during the same time and thus increased the cross-sectional material being processes by the conical rolling bite. From that point onward, the axial load began decreasing at a relatively low rate, until approximately t = 40 s. Similarly to the decrease of the main rolling load, this behavior can be attributed to the progressive height reduction of the ring, which led to the respective reduction in axial load requirements. Finally, between t = 40–42 s a slight increase of the axial load was observed, which was then stabilized between t = 42–45 s at a value of approximately 450 KN. This behavior follows the corresponding increase and stabilization of the ring's height previously observed in Fig.2.36, thus a correlation between the two can be made.

2.16.4 Thermal Results

Regarding the thermal results from the entire process, a comparison of the experimental average surface temperature curves to the corresponding numerical results was performed previously in §2.15.3. For this comparison, the numerical results only up to the end of the corresponding experimental curves were used. The numerical average surface temperature curves for the full duration of the simulation are presented in Fig.2.50, in which the corresponding experimental curves were also included for comparative reasons.

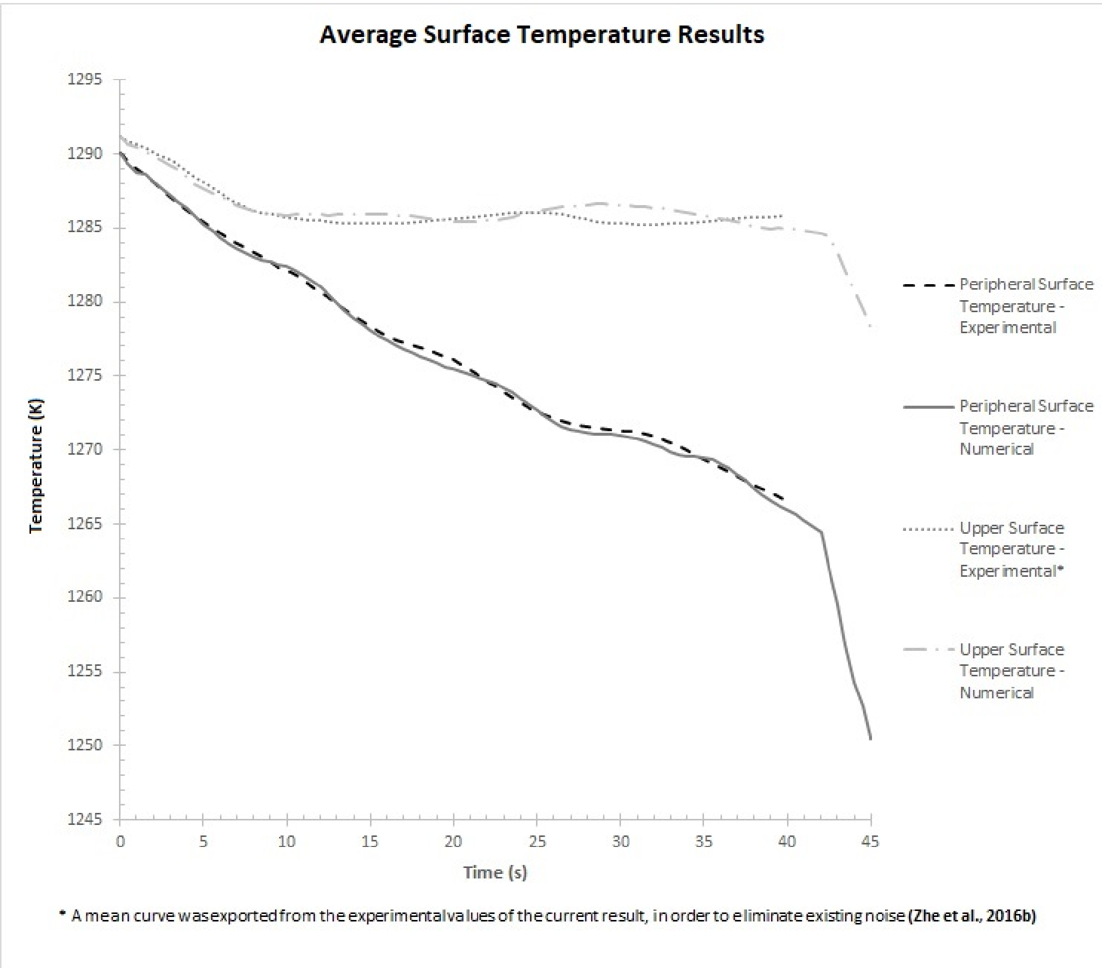

FIG. 2.50: Experimental and numerical average surface temperature result curves (full simulation duration)

In the case of the average outer peripheral surface temperature curve (Fig.2.50), an almost steady decrease rate was observed for the majority of the process's duration (t = 0–42.5 s). Then during the last few seconds of the simulation (t = 42.5–45 s), a sudden drop of approximately $\Delta T_{peripheral,42.5-45s}$ = 12 K was observed. This sudden temperature drop can be attributed to a combination of the constant movement (and thus cooling) of the ring, mainly through conductance with the tools and convection with the coolant, and the completion of all localized forming processes, leaving only the slight bulge and fishtail defect ironing to be conducted after t = 42.5 s. From all of the above, it can be concluded that plastic work from forming was the main source of reheating the ring during the process, seeing that the lack of it (t = 42.5–45 s) led to a severe and rapid temperature decrease. Overall, a gradual temperature drop of approximately $\Delta T_{peripheral,0-42.5s}$ = 28 K was observed throughout the duration of the ring's forming (up to t = 42.5 s, when the ring's thickness was equalized throughout its perimeter) and an additional rapid temperature drop of approximately $\Delta T_{peripheral,42.5-45s}$ = 12 K was observed for the remaining duration of the simulation.

Regarding the average upper surface temperature results presented in Fig.2.50, three distinct segments were observed in the corresponding curves. In the first segment (t = 0–9 s, approximately), a temperature decrease of $\Delta T_{upper,0-9s}$ = 5 K was observed. During that time, defects were almost non-existent in the workpiece, thus only the plastic work from the main forming actions were contributing to the reheating of the workpiece. In the second segment (t = 9–42.5 s) of the curve, an almost constant average upper surface temperature was observed, with the maximum temperature deviation being approximately $\Delta T_{upper,9-42.5s}$ = 1.3 K. Finally in the last segment of the curve (t = 42.5–45 s), a sudden temperature drop was observed in this case, too. This temperature decrease was approximately $\Delta T_{upper,42.5-45s}$ = 7 K, and it can be correlated to a combination of the completion of any severe forming process, whilst all heat transfer mechanisms were still in effect.

Although the aforementioned average surface temperature results provided some insight on the thermal state of the ring, little to no information was given about the temperature distribution inside the volume of the workpiece. Seeing that the forming behavior of the ring is heavily affected by the temperature of the entire cross-section at each time instance, this aspect was further investigated. More specifically, the temperature distributions of the cross-sections in the main and conical rolling bites were extracted at various time instances during the manufacturing process, and they are presented in Figs.2.51 and 2.52, respectively. It is worth noting that the temperature distributions in Figs.2.51 and 2.52 were presented with a different color scale in each time instance, as using a universal scale for the entirety of the process's duration led to severe shadowing effects of the presented results (the majority of the cross-sections would be entirely red). The limits of each color scale were the minimum and maximum temperature values at the current time instance. Moreover, it should be noted that the inner and outer diameter surfaces in Figs.2.51 and 2.52 are the same as their respective figures presented in previous chapters (e.g. Figs.2.38 and 2.39 in §2.16.2).

Observations over Fig.2.51 reveal that for most of the process's duration, the inner segments of the cross-section in the main rolling bite were hotter than the surfaces. More specifically, during the very first seconds of the process the entirety of the cross-section had the same temperature (T_{0s} = 1290.1 K), except from the top and bottom surfaces, which were slightly hotter ($T_{upper,0s}$ = 1291.17 K). It should be mentioned that the initial temperature were based on the corresponding experimental curves (Fig.2.50). Then at t = 5 s, when the mandrel and main roll had just come in contact with the workpiece, a rapid cooling of the inner and outer diameter surfaces was observed. The temperature of these surfaces was approximately

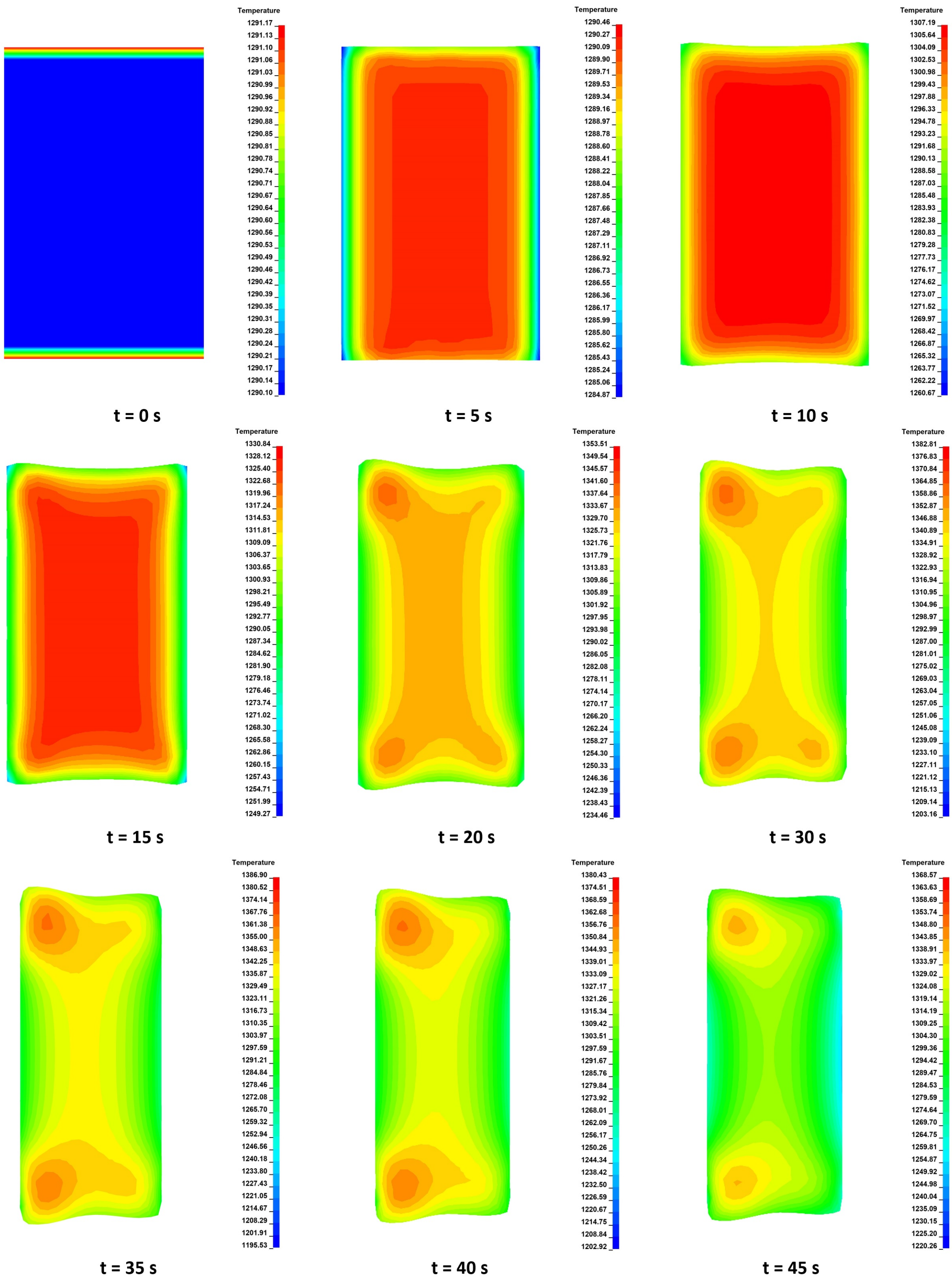

FIG. 2.51: Temperature distributions in multiple time instances during the simulation (Cross-section of the workpiece in the main rolling bite)

$T_{peripheral,5s}$ = 1285 K, while the maximum recorded temperature value was approximately $T_{max,5s}$ = 1290.5 K at the center of the cross-section. Similar temperature distributions were observed for all the early forming stages of the process, with the corresponding maximum

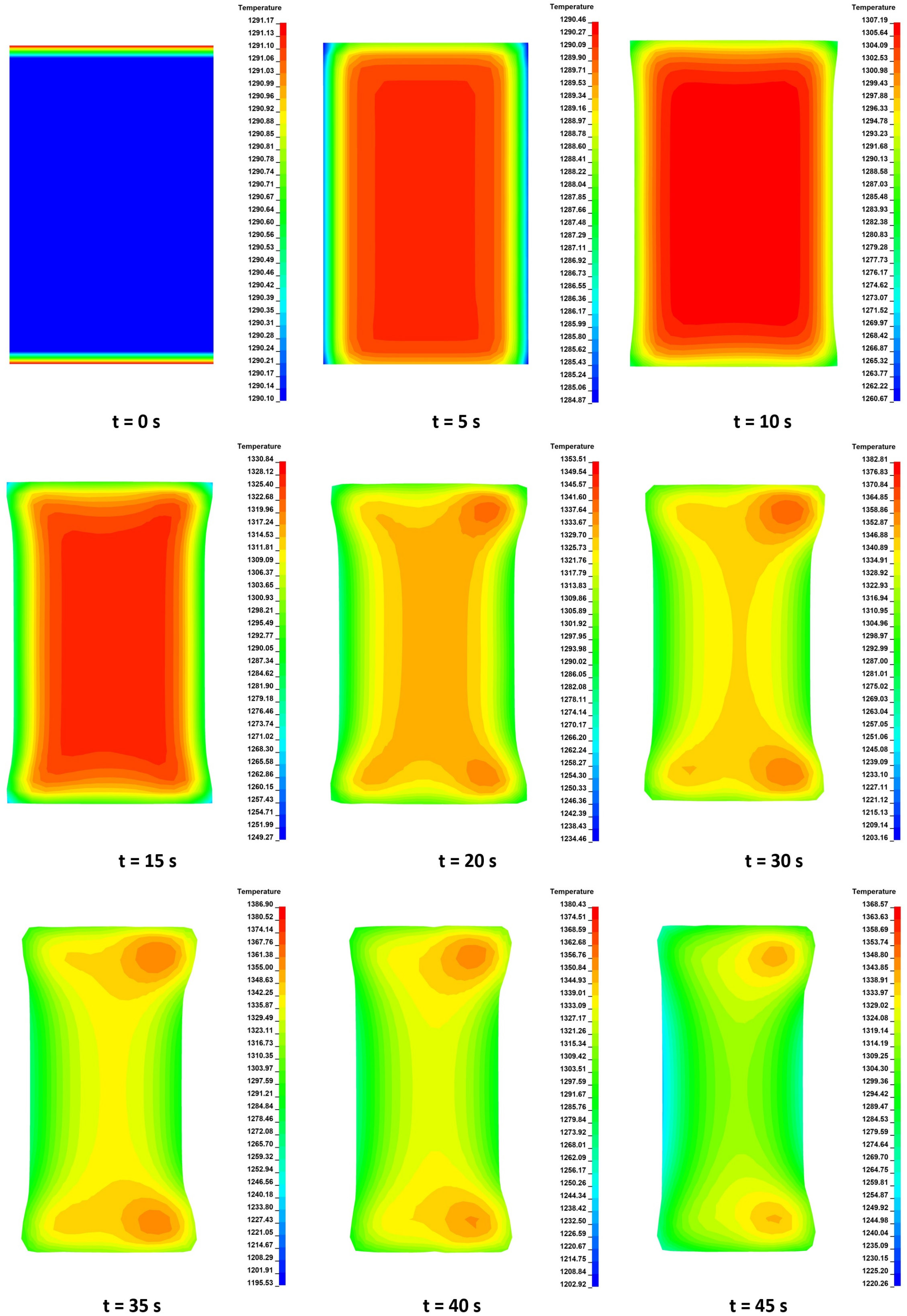

FIG. 2.52: Temperature distributions in multiple time instances during the simulation (Cross-section of the workpiece in the conical rolling bite)

temperature value being approximately $T_{max,15s}$ = 1331 K, again at the center of the cross-section. Since all tools were in contact with the workpiece at that time, all of its surfaces were comparably cooler. Interestingly, at t = 15 s, a noticeable deviation in the temperature distribution was observed, as the areas around the ironed bulges remained slightly hotter than the middle of their neighboring edges. This tendency became more obvious during later forming stages of the process (t = 20–40 s), when the center of the corresponding cross-sections remained at a temperature of approximately T_{center} = 1330–1335 K, while the areas around the ironed bulge defects (especially around the inner diameter surface) continued heating up. The all-time maximum recorded temperature was observed at t = 36 s around the ironed bulge defects area from the inner diameter surface, and had a value of $T_{max,MRB}$ = 1389 K approximately. Finally, at the final seconds of the simulation (t = 45 s), an overall temperature decrease in the entire cross-section was observed, but without deviations in the distribution compared to previous time instances. The maximum recorded temperature at the end of the simulation was observed again around the inner diameter surface ironed bulge defects, at $T_{max,45s}$ = 1345 K, approximately.

In the case of the temperature distributions in the conical rolling bite, similar conclusions can be drawn. The observed temperature distributions in Fig.2.52 were almost identical to those previously observed in the main rolling bite, while the recorded values were hardly the same or slightly lower (ΔT = 9 K, at most) than the corresponding values in Fig.2.51. The all-time maximum temperature value was again recorded at t = 36 s around the inner diameter surface defects and at approximately $T_{max,CRB}$ = 1380 K.

Finally, from the comparison between the temperature distributions in the two bites, it can be concluded that the highest temperatures resulted from the reheating of the workpiece, mainly due to the ironing of bulge defects in the main rolling bite. These increased temperatures did not have sufficient time to dissipate completely when the same cross-section reached the conical rolling bite, thus those heated areas were still present. Other than that, the temperature distributions in both bites followed the same pattern throughout the process, with the inner volume of the workpiece being anywhere from 6 K (early time instances) to 60 K (later forming stages) hotter than its surfaces.

2.17 Discussion and Conclusions

From the analysis that preceded, it was made clear that simulating hot Ring Rolling is a fairly complex process. Several advanced simulation techniques had to be used to describe the various deformation mechanisms taking place, as well as the proper movement of the workpiece. Furthermore, some critical information had to be thoroughly investigated and/or precisely defined, in order to achieve validity of the simulation results. Although LS-DYNA includes a plethora of tools capable of simulating the aforementioned manufacturing process, some specific capabilities of the software had to be researched in depth to determine the proper way of setting them up.

If a classification of the most important simulation techniques and/or LS-DYNA tools had to be made for the simulation of hot Ring Rolling, this would be summed up to the following:

- *Mesh independence analysis*: It is considered a fundamental step for any finite element simulation.

- *Temperature and strain rate dependent material model*: It was one of the most significant aspects in the current analysis, as it heavily affected the calculated results. In LS-DYNA, only MAT_106 material model could combine temperature and strain rate dependency phenomena.
- *Interfacial heat transfer (Conductance)*: The proper definition of heat conductance curves was the most affecting parameter for the temperature calculation during the process. From the rest of heat transfer mechanisms, heat radiation and coolant convection followed, although with much less impact on the calculated thermal results.
- *Support roll movement*: The definition of a proper movement pattern for the support rolls was one of the most important parameters for the proper deformation of the workpiece during the process. Apart from the simulation, proper and unobstructed movement of support rolls is one of the rudimentary aspects of Ring Rolling as a manufacturing process.
- *Mass scaling*: Determination of the maximum allowable selective mass scaling factor allowed for a significant reduction in simulation time, which would otherwise be prohibitive.

For most of the aforementioned parameters a thorough research for corresponding input data was required, most notably in the case of the temperature and strain rate dependent material properties, which required an in depth investigation in literature. On the other hand, other of these parameters were determined after numerous trial – and – error runs, with the most characteristic examples being mesh density and conductance coefficient curves. Regarding the rest of the simulation parameters and although several of them (not including the aforementioned) could affect the quality of the calculated results (e.g. element type, contact definition, etc.), in most cases they could be adjusted via multiple alternative ways, thus it was easier for them to be set up in the final model. It is worth reminding that the work of **Zhu et al., 2016b** was one of the few (if not the only) viable references for simulating, as from the necessary parameters only the conductance curves were not included as input data, and thus they could be approximated though trial – and – error. The rest of the simulation parameters were either provided (e.g. tool velocities, heat transfer coefficients, initial conditions, etc.) or could be found in literature (e.g. material properties).

Regarding the validity of the calculated results, the conducted numerical model can be considered as an accurate alternative to the reference Ring Rolling process, based on the comparisons of the results from the two methods. The observed deviations in the deformational and thermal results were negligible, apart from some unpredictable points in the movement of the tools (not mentioned in the reference). Overall, the close agreement between the compared results allowed for the conducted numerical modeling to be considered as validated.

Finally, an overview of the calculated numerical results revealed several key aspects of the process and helped to further clarify some inconsistencies:

- From the deformational results, the evolution of the main ring dimensions over the course of the process was observed. Both the ring diameters and the average ring height were in good agreement to the corresponding experimental results, although in both methods the final ring dimensions were larger than those initially prescribed. More specifically, the final outer ring radius was approximately R_f = 461 mm, the final inner ring radius approximately r_f = 408 mm and the final average ring height approximately H_f = 116 mm, whereas their respective target values were $R_{f,target}$ =

450 mm, $r_{f,target}$ = 400 mm and $H_{f,target}$ = 115 mm. Furthermore, the calculated ovality curves proved that the ring maintained an almost perfectly round shape throughout the manufacturing process, both in its inner and its outer periphery. Finally, a general overview of the two major defects was made, although the actual evolution of these defects was better presented in the following stress and strain results.

- From the equivalent stress results, the corresponding stress distribution fields of the ring cross-sections being in contact with the tools were highlighted. The observed stress distributions had significant differences between one another and with a lot of variance throughout the process's duration, however their results could be justified. The highest recorded stress values were observed around the contacts with the mandrel and the main roll, with an all-time maximum value of σ_{max} = 276 MPa recorded during the process. Lastly, some minor thermal stress distributions manifested over the first few seconds of the process were briefly discussed.

- Similarly to the equivalent stress distributions, the effective strain fields in the cross-sections being in contact with the tools and throughout the process's duration were also observed. The greatest effective strains were manifested around the defect ironing areas, while an all-time maximum strain value of approximately ϵ_{max} = 1.14 was recorded. Additionally, the purely elastic thermal strains over the initial seconds of the simulation were briefly discussed.

- Regarding the calculated load results, the full extent of the resultant main and axial load curves was analyzed. From the comparison between the calculated main and axial load curves and their corresponding experimental results, it was made clear that some inconsistencies observed in the experimental curves should not be present during a regular Ring Rolling process. Moreover, a rapid removal of the tools after t = 40 s was implied from the aforementioned comparisons, thus Phase 4 was skipped during the experiment. The maximum recorded load values were observed relatively early during the process (at t = 14 s for the main rolling load and at t = 17 s for the axial rolling load), with their corresponding values being $F_{max,MRL}$ = 1240 KN and $F_{max,ARL}$ = 647 KN. Overall, the review of the calculated load results revealed several interesting facts about the experimental recordings and thus the details and the sequence of events in the conducted experiment.

- Lastly, regarding the calculated thermal results, both the average surface temperatures and the temperature distributions inside the volume of the workpiece were discussed. The average surface temperature results were in close agreement between the two methods, while the extended thermal behavior of the workpiece (including Phase 4) was observed in the case of the numerical model. Furthermore, the temperature distributions observed in the main and conical rolling bite cross-sections of the workpiece revealed that the highest temperatures manifested inside the volume of the workpiece, as a result of the plastic work turning into heat. The maximum recorded temperature value was approximately T_{max} = 1389 K, located in the main rolling bite cross-section and around the inner diameter corners. It is worth noting that these results would require a very elaborate experimental setup in order to be recorded (if at all possible).

Chapter 3

Precision Increase of the Ring Rolling Process: Proof of Concepts

3.1 Introduction

In the previous chapter, the necessary steps to conduct a validated numerical simulation of a Ring Rolling process were presented. During the simulation, certain points showing noncompliance between the experimental and numerical results became apparent. The aforementioned noncompliance mainly lied with the dimensional differences between the simulated and the experimentally produced rings, especially given that Ring Rolling Phase 4 was completely omitted from the experimental results. Apart from that, another major issue that derived from the conducted analysis of Chapter §2 was the divergence between the target dimensions of the final product and the actual final ring dimensions. This divergence could be largely attributed to the inexact volumes between the initial blank and the target workpiece, which would inadvertently lead to different ring dimensions even considering some volume loss due to scaling of other manufacturing defects.

From these observations, the issues of a high precision Ring Rolling process and how to achieve it, arisen. More often than not, in actual Ring Rolling processes the differences between the target and the produced ring dimensions can be considerable, thus further post-processes, such as grinding and finishing, are necessary to achieve dimensional accuracy (e.g. **Rachakonda et al., 1991, Wu et al., 2019**, etc.). This fact can be even more imperative and time-consuming for ring products aimed at critical applications, such as high grade bearings and aerospace components, where the tolerance limits are usually very strict.

Based on all of the above, in the following sections, an attempt to further analyze some precision affecting parameters of Ring Rolling is made. After each of these parameters is investigated, their importance on the quality of the final product will be discussed and ways of manipulating their effects towards a high precision ring will be proposed. It is worth noting that the analyses presented in the current Chapter will be mainly focused on factors affecting the dimensional precision of the final product before and during Ring Rolling.

Some of the most crucial parameters that heavily affect the precision of the produced rings, and thus will be the main focus in the current Chapter, are the following:

- The volume precision of the initial blank
- The thermal expansion and elastic deformation of the tools
- The polynomial law applied for the movement of support rolls, combined with the ring's material

Any precision increase resulting from the analysis of these parameters can bring significant advantages in a Ring Rolling production, both in terms of cost and duration. More specifically, an increased dimensional accuracy can lead to the minimization of post-processes required and/or their durations, as well as to a better product quality (both dimensional and surface). Additionally, reducing or discarding any additional post-process can lead to a reduction in the complexity of the production line, and thus to its better overall control, with lower production times and costs.

Given that actual experimental setups and ring production lines were not available for the conducted simulations, the analyses in the current Chapter will be performed solely via finite element modeling. For each of the investigated parameters, multiple numerical models will be created and the key parameters that mostly affect the precision of the final product will be estimated from these simulations.

3.2 Initial Billet Volume Precision

One of the most important factors that heavily affects the final dimensions of a Ring Rolling product is the precise estimation of the initial blank volume. Considering that in any forming process, including Ring Rolling, the volume constancy law applies (**Schuler, 1998**), an inaccurate initial volume of the blank will inevitably lead to inaccurate final product dimensions, no matter how precise the actual process is.

In Ring Rolling, apart from the initial dimensions of the blank, the volume that will proceed to be manufactured is also defined by the two processes that precede it, namely the billet upsetting and piercing. Both of these processes are performed hot, however their actual mechanisms are vastly different. Because of their differences, in the current section, each of these processes will be analyzed separately.

3.2.1 Billet Upsetting

In an upsetting process, the initially cylindrical billet is compressed to a lower, more manageable height. The final height after upsetting is equal to the initial workpiece height for the Ring Rolling process. Because of the compression, the upset billet has a barrel-like shape at the end of this process. This specific shape makes the prediction of the initial billet volume challenging, even more so because the actual shape of barreling can be affected by multiple parameters of the process.

In order to measure the change of the billet dimensions caused by the upsetting process, Roebuck et al. (**Roebuck et al., 2002**) proposed the use of the upsetting factor, B as this is defined in Eq.3.1:

$$B = \frac{h_f \cdot d_f^2}{h_0 \cdot d_0^2} \tag{3.1}$$

where:

- h_f, the height of the blank after upsetting
- d_f, the maximum diameter of the blank after upsetting
- h_0, the height of the billet before upsetting
- d_0, the diameter of the billet before upsetting

It is worth noting that the billets being upset before Ring Rolling are a result of extrusion, thus the initial billet diameter can be considered constant throughout its height.

Upsetting Parameter Evaluation via Finite Element Analysis

In order to investigate the parameters that affect the upsetting factor B, and due to the lack of an experimental setup to perform the necessary trials, a series of simulations was decided to be conducted. In these simulations, specific parameters such as friction coefficient between tool and billet, tool velocity and initial billet dimensions were investigated and their effects on B factor were evaluated. More specifically, the parameters that were investigated in the conducted trials were the following:

- Tool-to-billet friction coefficient
- Initial billet dimensions
- Tool velocity

It is worth noting that although other parameters (e.g. billet initial temperature, billet material, etc.) may affect the final billet dimensions and thus upsetting factor B, their definition and/or knowledge can vary significantly. As a result, further researching such parameters is considered to be beyond the scopes of the current dissertation, as upsetting process is not the main point of focus.

For the upsetting numerical models, a simple axisymmetric approach was chosen. Only three bodies were including in the current simulation, namely the billet, and the top and bottom pressure plates. From the two pressure plates, the bottom was immobilized throughout the process, while the top pressure plate moved towards the billet at a constant velocity. Both pressure plates had a radius of r_{plates} = 470 mm. In order to enable the axisymmetric analysis, half of the billet's and tools' cross-sections were simulated, with their central axis used as the axis of symmetry for these bodies. In LS-DYNA, setting an axisymmetric model is possible only when the axis of symmetry is aligned with the global Y-axis of the model. Other than that, the solver will conduct the aforementioned analysis only if *ELFORM = 14* or *15* is chosen in *SECTION_SHELL (_THERMAL)*, in which case the created shell elements are treated as axisymmetric solid elements by the software.

Most of the model parameters were exactly the same as the Ring Rolling model presented in Chapter §2. Most notably, material model MAT_106 and thermal material model MAT_T10 with the properties of Table 2.3, heat transfer mechanism with the coefficients presented in sections 2.8 and 2.10, hourglass control settings as presented in section 2.11, initial conditions and movement conditions as in section 2.10 (although with different initial temperature and velocity values) and software parameters as in section 2.13 were defined with the same exact keyword.

Other than that, some keywords had to be defined differently than the previously conducted models, mainly in order to accommodate for the 2D axisymmetric analysis. Initially, and as mentioned above, element definition was one of the model parameters that had to be setup via the *SECTION_SHELL_THERMAL* keyword. The most crucial parameters in *SECTION_SHELL_THERMAL* and a short description of them are presented below:

- *ELFORM = 15*, defines volume-weighted axisymmetric solid elements
- *NIP = 4*, considers 4 integration points for each axisymmetric solid element

- *SETYP = 1*, defines a Lagrangian 2D solid element type
- *T1 – T4 = 1.0*, defines a shell thickness of 1.0 mm at each of the elements corner nodes

Additionally, the contacts between the billet and the two pressure plates were defined via the keyword *CONTACT_2D_AUTOMATIC_SINGLE_SURFACE_THERMAL*, although the parameters defined in this keyword were the same as those presented in section 2.8. Special attention was paid to the friction coefficients *FS* and *FD*, which were investigated as parameters affecting upsetting factor, *B*. Finally, an additional keyword for exporting the final stress results had to be considered. This was performed via *INTERFACE_SPRINGBACK* keyword, which created a .dynain file containing all the residual stress results from the final time instance of the model. The .dynain file could be then imported to a subsequent analysis, in order to include the stress state of the workpiece at the end of the previous process.

Before conducting the evaluation of the aforementioned parameters on the upsetting factor, *B*, a nominal upsetting model had to be solved, to act as a reference. The initial and the most crucial parameters of the nominal upsetting model are presented in Table 3.1:

TABLE 3.1: Nominal upsetting model properties

Property	Value or Reference
Billet Material Properties	Table 2.3
Tool Material Properties	Table 2.4
Initial billet diameter, d_0 (mm)	533.4
Initial billet height, h_0 (mm)	150
Initial billet temperature, T_0 (K)	1173.15
Tool diameter, d_{tools} (mm)	305.7
Initial tool temperature, T_0 (K)	573.15
Tool velocity, v_{tool} (mm/s)	0.1667
Friction coefficients (Static/Dynamic), *FS/FD*	0.5/0.4
Total simulation time, t_{total} (s)	151.2

It is worth noting that the simulation termination time for the nominal model was estimated in such a way that the final height of the upset billet would be approximately $h_{f,upsetting}$ = 125 mm, which was the initial workpiece height of the Ring Rolling process.

For the nominal upsetting model, the corresponding bodies were meshed with approximately 1300 deformable shell elements for the billet and approximately 230 rigid shell elements for the tools. The mesh of the billet was non-uniform, so as to have a more refined mesh around the edges of the billet, where the greatest deformations were expected. In Fig.3.1, the meshed nominal upsetting model prior to its solution is presented:

After the solution of the nominal upsetting model, some results were extracted and reviewed. Initially, the final dimensions of the upset billet were measured. Since it was predefined, the final height of the upset billet was measured at the end of the simulation, and

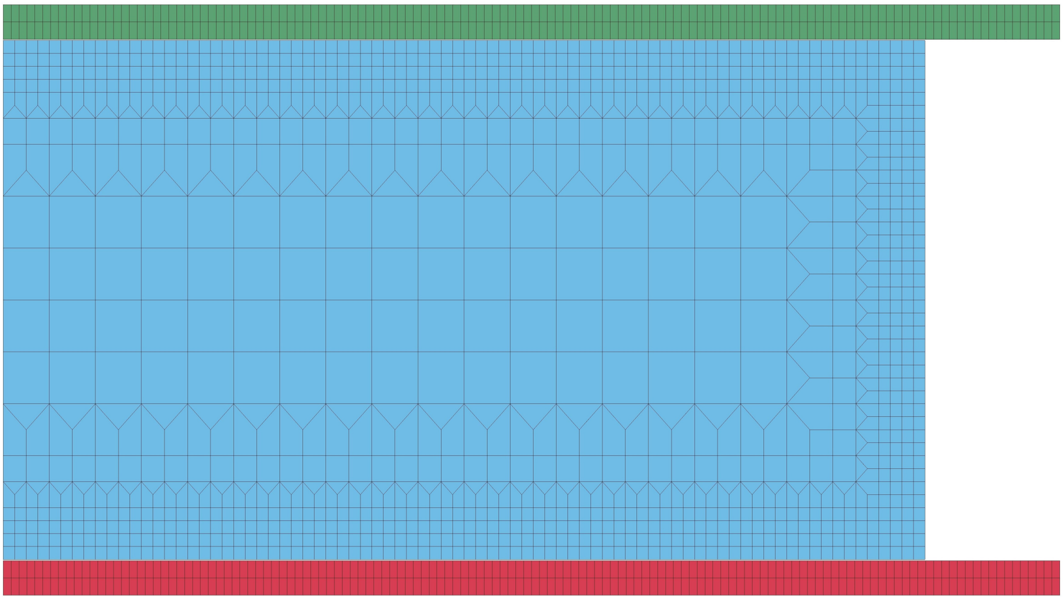

FIG. 3.1: Meshed nominal upsetting model

it was equal to $h_{f,upsetting}$ = 125.15 mm. In the case of the final diameter of the billet, the maximum measured diameter value (accounting for the barreling of the workpiece) was equal to $d_{f,upsetting}$ = 587.4 mm, approximately. The deformation of the billet at the final time instance of the nominal upsetting model is presented in Fig.3.2:

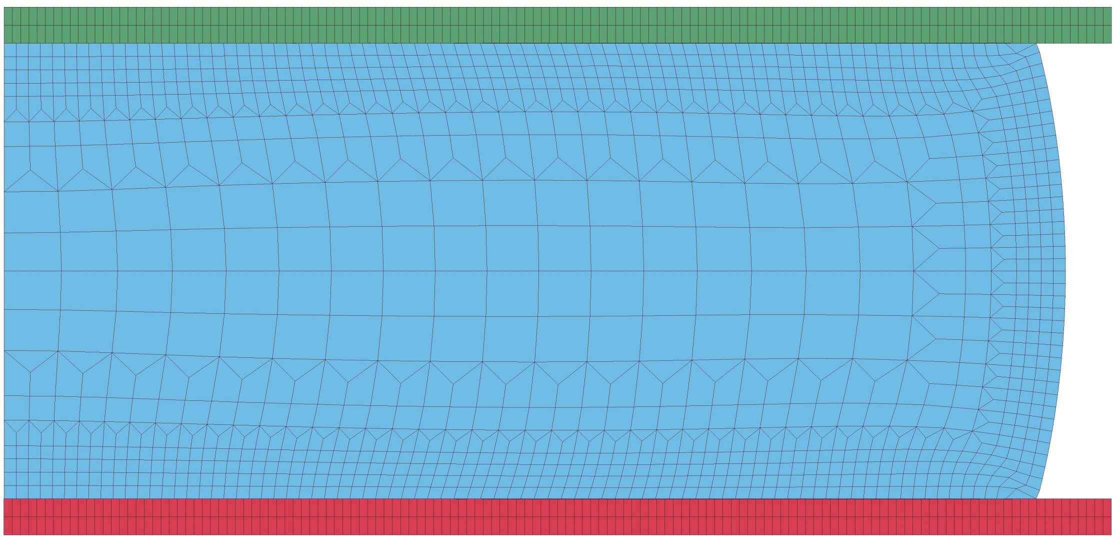

FIG. 3.2: Billet deformation at the final time instance of the nominal upsetting model

Afterward, a brief review of the equivalent Von Mises stress, effective plastic strain and temperature distribution fields at the end of the upsetting process was performed. The aforementioned fields review is not considered necessary for the estimation of upsetting factor, B, however it was performed for the sake of completeness. The corresponding distribution fields (as mentioned above) are presented in Figs.3.3-3.5, respectively:

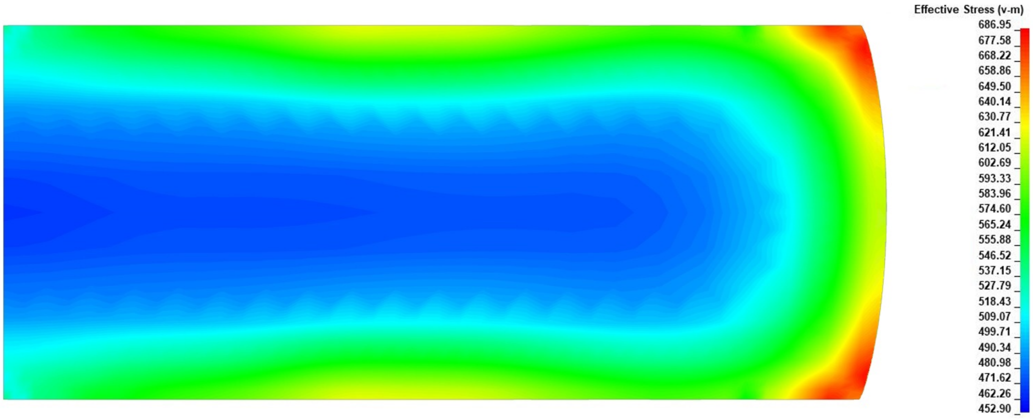

FIG. 3.3: Billet equivalent Von Mises stress distribution at the final time instance of the nominal upsetting model

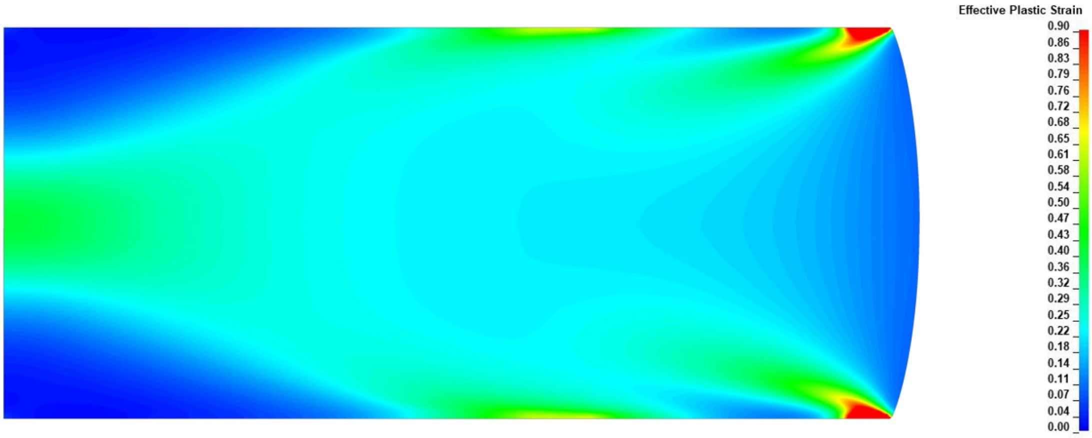

FIG. 3.4: Billet effective plastic strain distribution at the final time instance of the nominal upsetting model

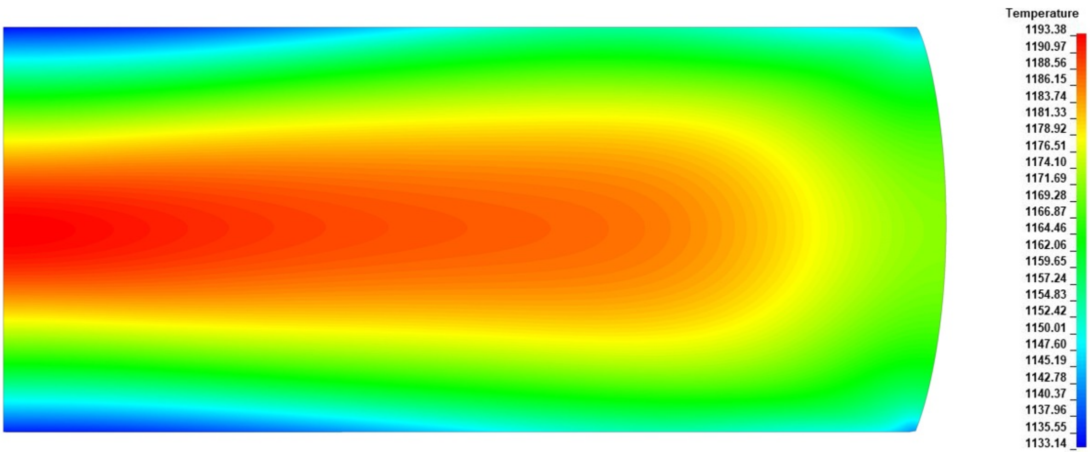

FIG. 3.5: Billet temperature distribution at the final time instance of the nominal upsetting model

Observations over Figs.3.3-3.5 reveal rather expected distributions from an upsetting process.

The stress distribution in Fig.3.3 revealed a high stress concentration around the surfaces of the upset billet, with the stress values increasing towards the periphery of the billet. The maximum stress values were approximately 690 MPa, located at the corner edges of the billet. On the other hand, the minimum stress values were observed around the center of the billet and around its axis of symmetry, where the corresponding elements were suspended to the least deformation, with the corresponding stress values being approximately 450 MPa.

In the case of the plastic strain distribution in Fig.3.4, significant plastic strains were observed on the upper and lower surfaces of the upset billet and around the corner edges, as a result of the maximum deformations of these areas. The maximum recorded plastic strain value was approximately 0.90, located at the aforementioned areas. Regarding the minimum strain values, these were observed along the symmetry axis and around the contacts with the pressure plates. Interestingly, an X-like formation of relatively increased strains was observed extending from the corner edges towards the center of the billet. This specific strain distribution is typical in open-die billet forging processes such as upsetting (e.g. **Buckingham et al., 2016**), and can be attributed to the increased shear stresses present at the corresponding areas.

Finally in the case of the temperature distribution in the upset billet (Fig.3.5), a rather typical temperature field was observed. The greatest temperatures could be seen around the center of the billet, where the least amount of heat could be transferred outwards. Moreover, the plastic work turned to heat, led to an increase of temperature in that area at approximately $T_{upsetting,max}$ = 1190 K, which is beyond the initial temperature of the billet at the beginning of the process (T_0 = 1173.15, Table 3.1). The temperature of the billet reduced gradually towards the surfaces of the billet, with the lowest values recorded around the center of the contacts with the pressure plates, at approximately $T_{upsetting,min}$ = 1130 K.

After the review of the nominal upsetting model, it was concluded that all results were as expected and without any notable errors, thus it could be considered validated. Based on the aforementioned results and Eq.3.1, the upsetting factor, B, for the nominal model was calculated to be $B_{nominal} = \frac{125.15 \cdot 586.3^2}{150 \cdot 533.4^2} = 1.012$.

In order to investigate the aforementioned factors that affect the upsetting factor, B, the nominal model was used as the base for the following simulations. More specifically, various values for the friction coefficients, the initial billet radius, the initial billet height and the tool velocity were used with the nominal model, although only a single parameter was altered at each subsequent simulation. A summary of the investigated process parameters and their corresponding tested values are presented in Table 3.2:

TABLE 3.2: Upsetting factor (B) affecting parameters tested

Tested parameter	Value
Tool velocity, $v_{tool,upsetting}$ (mm/s^3)	0.16667 (nominal), 0.33334, 0.83335, 1.6667
Friction coefficients, *FS/FD*	0.0/0.0, 0.2/0.15, 0.3/0.2, 0.5/0.4 (nominal), 0.6/0.5, 1.0/1.0
Initial billet diameter, d_0 (mm)	300, 400, 533.4 (nominal), 600
Initial billet height, h_0 (mm)	135, 150 (nominal), 180

After the solution of the twelve models (excluding the nominal model which was already solved), the final deformational results from each model were reviewed. Based on these results, the corresponding upsetting factor, B could be calculated for each of the conducted simulations.The corresponding curves with the calculated upsetting factors, B from these models, are presented in Figs.3.6–3.9:

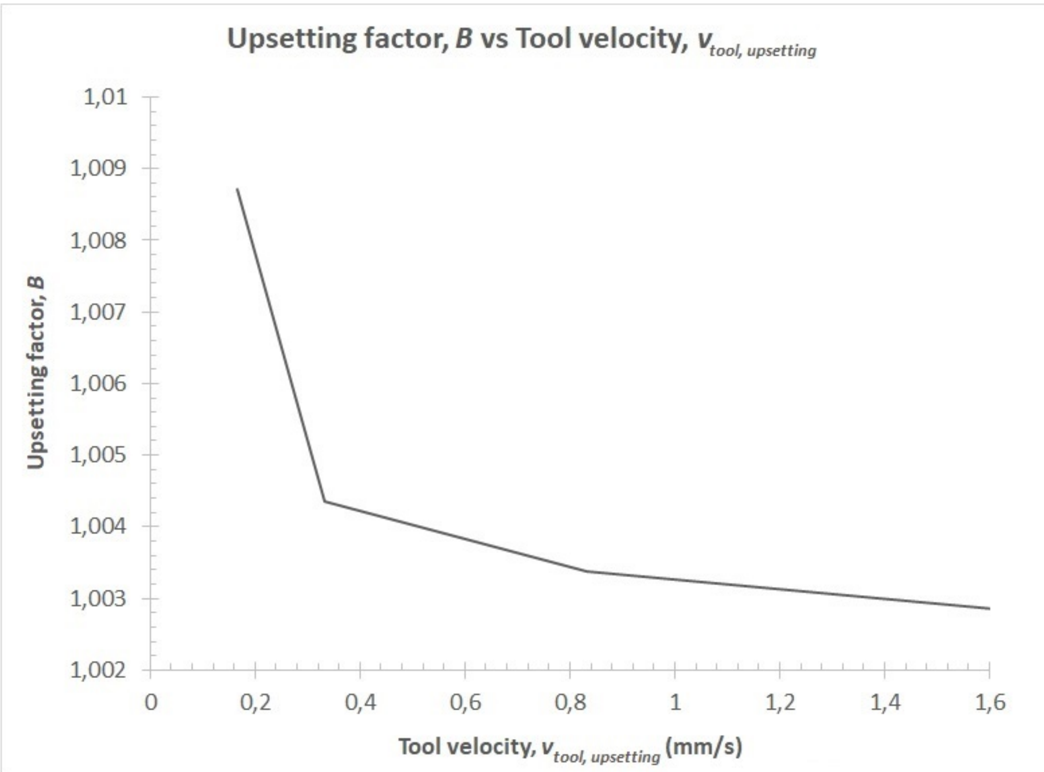

FIG. 3.6: Upsetting factor B deviation with the change in pressure plate velocity, $v_{tool,upsetting}$

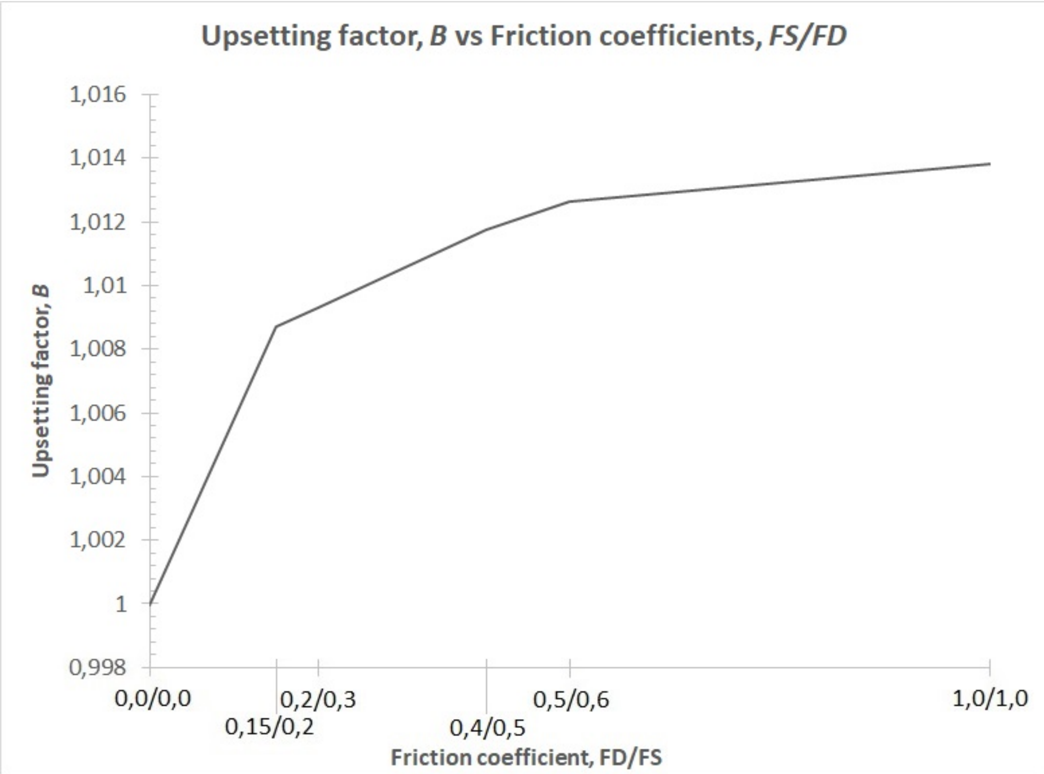

FIG. 3.7: Upsetting factor B deviation with the change in friction coefficients, FS and FD

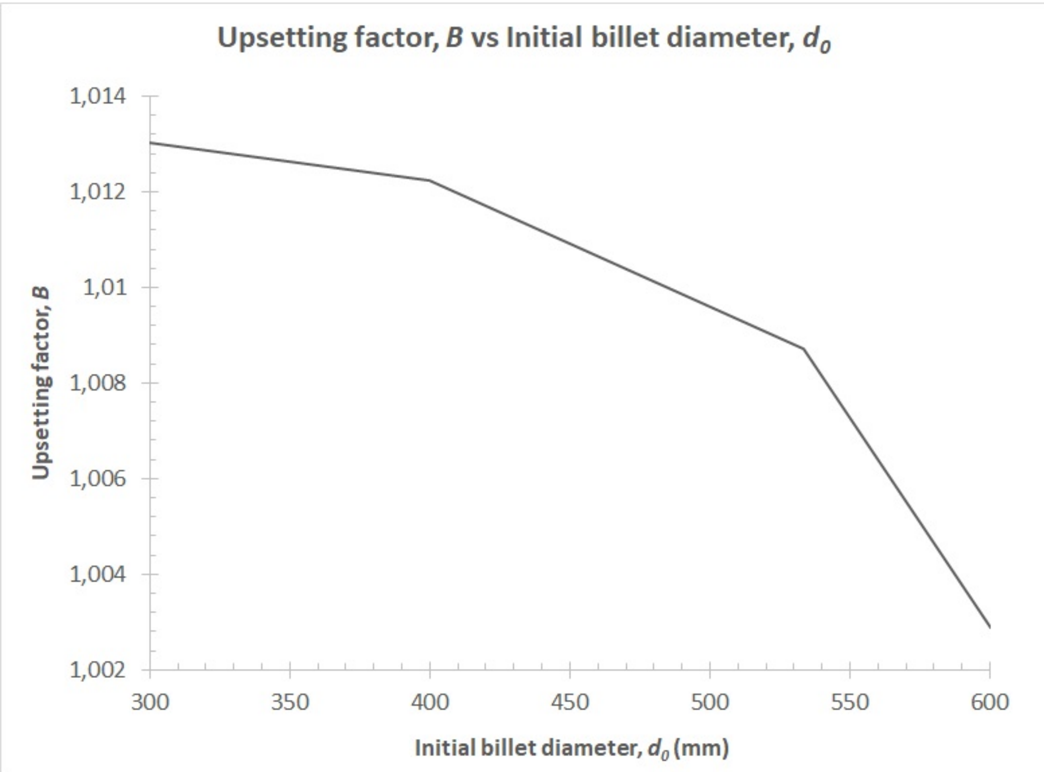

FIG. 3.8: Upsetting factor B deviation with the change in initial billet diameter, d_0

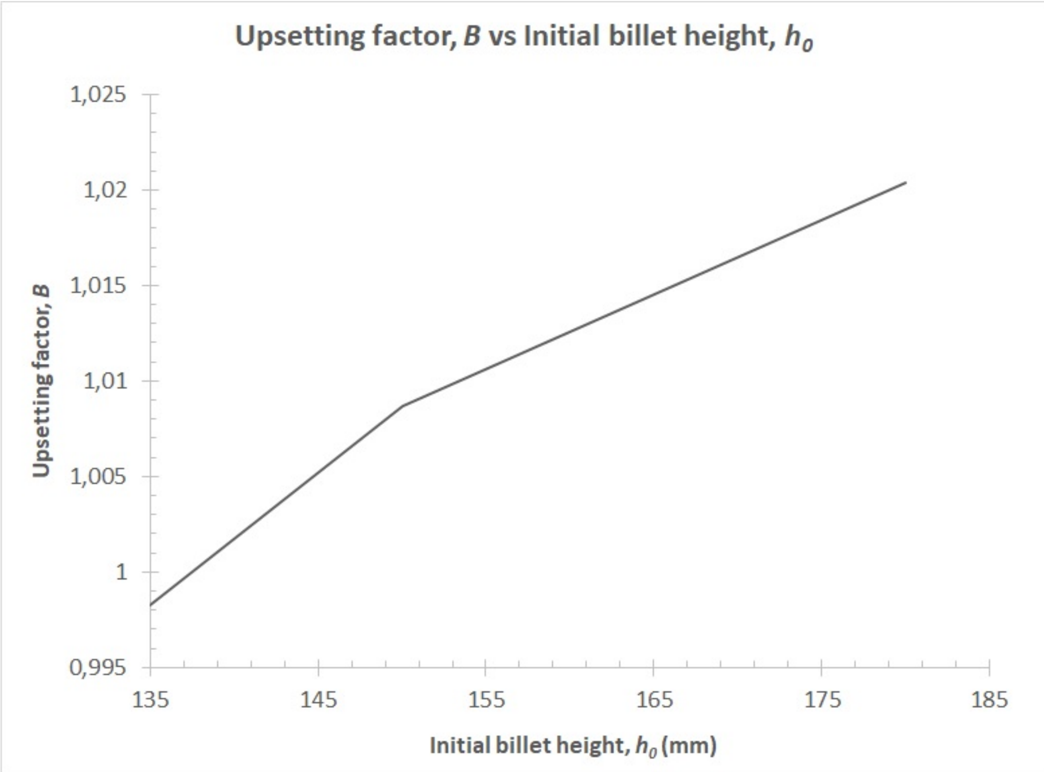

FIG. 3.9: Upsetting factor B deviation with the change in initial billet height, h_0

Observations over Figs.3.6–3.9 reveal correlations between all four of the investigated parameters and the upsetting factor, B. Since each parameter was investigated separately from the rest, the presented results in Figs.3.6–3.9.

Regarding the correlation of the upsetting factor, B with the pressure plate velocity, the two parameters seem to have an inversely proportional relationship based on the results presented in Fig.3.6. More specifically, lower pressure plate velocity values led to an increase of the calculated final diameter of the billet and thus an increase of factor B. However, the relative difference of factor B, over the entire range of tool velocities that were tested, was marginally small (from 1.009 to 1.003, approximately), proving that tool velocity is not one of the most affecting parameters.

In the case of friction coefficients, FS and FD, the presented results in Fig.3.7 reveal a proportional relationship between them and the upsetting factor, B. The difference of factor B over the entire range of friction coefficients tested varied from 1 to 1.014, which can be considered relatively large compared to the rest of the parameter evaluations of the current analysis. It is worth noting that for the evaluation of the current parameter, the entire range of possible friction coefficients was investigated, as in LS-DYNA a friction coefficient of 0.0 indicates a frictionless contact, while a coefficient of 1.0 causes the contacting elements to stick to one another.

Finally, the relationship between the initial billet dimensions and the upsetting factor, B, was presented in Figs.3.8 and 3.9. In the case of the initial billet diameter and its effects on factor B, d_0, an inversely proportional relationship was observed from Fig.3.8. A difference of approximately 0.01 (from 1.013 to 1.003) was recorded for factor B, which, similarly to friction coefficients, can be considered as relatively large. On the other hand, a proportional relationship was observed between the initial billet thickness, h_0 and the upsetting factor, B, as it was presented in Fig.3.9. More specifically, a factor B difference of approximately 0.022 (from 0.998 to 1.020 approximately) was observed across the entire initial height margin tested. This was the highest recorded difference recorded in the current analysis and over a relatively small range of initial heights, thus rendering this parameter as the most affecting for the upsetting factor, B. It is worth noting that in most upsetting applications, a billet's initial diameter and initial height are usually interdependent, as a specific initial volume, defined by both these dimensions, is required.

Overall, the following conclusions were drawn from the research of the most affecting upsetting factor parameter:

- Increasing the tool velocity led to a decrease of the upsetting factor, B, although the differences were negligible.
- Increasing the friction coefficients led to an increase of the upsetting factor, B.
- Increasing the initial billet diameter led to a decrease of the upsetting factor, B.
- Increasing the initial billet height led to an increase of the upsetting factor, B.
- Based on the presented results, initial billet height seems to be the most affecting upsetting parameter, while tool velocity seems to be the least affecting parameter.

After the completion of the aforementioned analysis and based on the conducted simulations, the parameters of the nominal upsetting model seemed to be fairly realistic, thus the upsetting factor, $B = 1.012$ calculated from this model was used for the following steps of the current methodology.

Initial Blank Volume Estimation Methodology

Based on the aforementioned results and in order to estimate the optimum initial billet dimensions, a new property of the equivalent radius, r_{eq} had to be established. The equivalent radius, r_{eq} can be defined as the radius of a perfect cylinder that has the same volume as the upset blank. In order to calculate r_{eq}, the function of the blank's outlining edge, *f(y)* should be estimated initially. This is usually a higher order (e.g. a 4^{th} order or greater) polynomial estimated from the vertical positions of the aforementioned outlining edge's points, hereafter mentioned as y_i. Furthermore, an additional line connecting the lowermost to the uppermost points of the outlining edge, hereafter mentioned as *g(y)*, should also be estimated. With *f(y)* and *g(y)* known, the upset billet's total volume, V_1 can be calculated through Washer's Method (**Anton, 1984**), as per Eq.3.2:

$$V_1 = \int_{y_l}^{y_u} \pi \cdot \left[\left[f(y) \right]^2 - \left[g(y) \right]^2 \right] \mathrm{d}y \tag{3.2}$$

where:

- y_l, the vertical position of the lowermost point of the edge profile
- y_u, the vertical position of the uppermost point of the edge profile

Finally, a vertical line that creates a profile with *g(y)* and a revolute volume of V_2 should be established. This line is located at a radial distance of r_{eq} from the axis of rotation, or in functional form:

$$x = r_{eq} \tag{3.3}$$

Thus, a second revolute volume between Eq.3.3 and *g(y)* can be calculated, as per Eq.3.4:

$$V_2 = \int_{y_l}^{y_u} \pi \cdot \left[r_{eq}^2 - [g(y)]^2 \right] \mathrm{d}y \tag{3.4}$$

The aforementioned functions and volumes are presented in Fig.3.10:

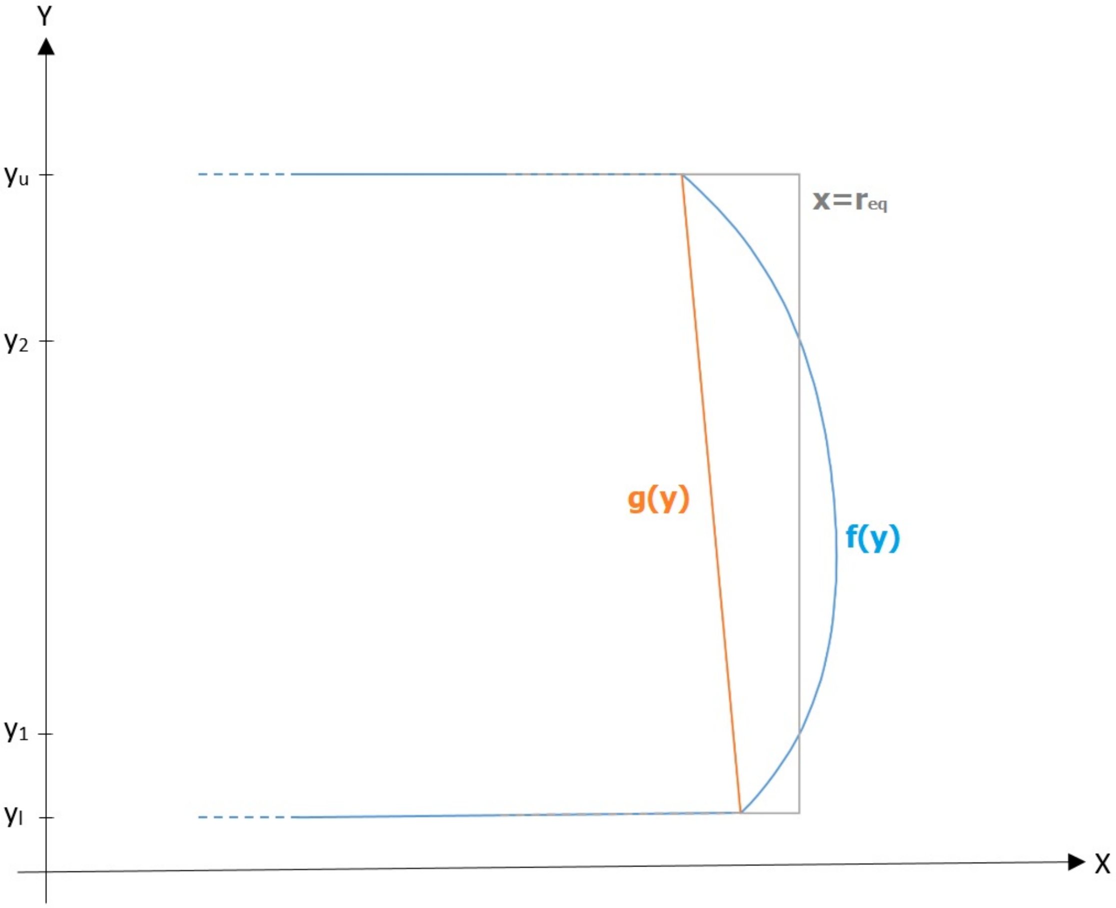

FIG. 3.10: Edge profile functions and equivalent radius function

Observations over Fig.3.10 reveal that *f(y)* and Eq.3.3 share common points, let their vertical positions be y_1 and y_2 respectively, which should satisfy the equation:

$$f(y) = r_{eq} \tag{3.5}$$

Thus and in order to calculate the equivalent radius, r_{eq}, an equation between volumes V_1 (Eq.3.2) and V_2 (Eq.3.4) should be satisfied, as per Eq.3.6:

$$\begin{gathered} V_1 = V_2 \Leftrightarrow \\ \Leftrightarrow \int_{y_l}^{y_u} \pi \cdot \left[[f(y)]^2 - [g(y)]^2 \right] \mathrm{d}y = \int_{y_l}^{y_u} \pi \cdot \left[r_{eq}^2 - [g(y)]^2 \right] \mathrm{d}y \Leftrightarrow \\ \Leftrightarrow r_{eq} = \sqrt{\frac{1}{y_u - y_l} \cdot \int_{y_l}^{y_u} [f(y)]^2 dy} \end{gathered} \tag{3.6}$$

The definition of r_{eq} allows for the estimation of an ideal cylinder instead of a barrel-shaped blank with the same volume, thus a more accurate prediction of the final volume of the ring is possible. Furthermore, the estimated cylinder can also be used in the following analysis, namely billet piercing, where a subsequent barreling of the upset billet is expected. It is worth noting that since the billet surface profile is given as an ordinate dependent function, a variable change to transform it into an abscissa dependent function should be performed, in order to solve Eq.3.6.

3.2.2 Upset Billet Piercing

After the volume and equivalent radius of the ideal cylinder has been estimated after the upsetting process, the billet piercing process can be performed. Billet piercing can be divided in two separate sub-processes:

1. An initial billet center forging (also called as piercing), which deforms a central portion of the workpiece, in order to reduce the volume that will be removed during the upcoming piercing process, up to an adequately thin disk ($\frac{1}{4} \cdot \mathrm{h}_f \leq \mathrm{h}_{disk} \leq \frac{1}{3} \cdot \mathrm{h}_f$). The aforementioned central forging is usually performed from both ends of the billet, while this process can also be performed in multiple steps, in case the initial billet volume and material require to do so.

2. The thin disk of the blank is pierced (in a process also known as shear piercing), thus a portion of the initial billet volume is removed. The pierced billet is then proceeded for Ring Rolling.

The three stages of the billet, after the end of each of the aforementioned preparation processes, are presented in Fig.3.11:

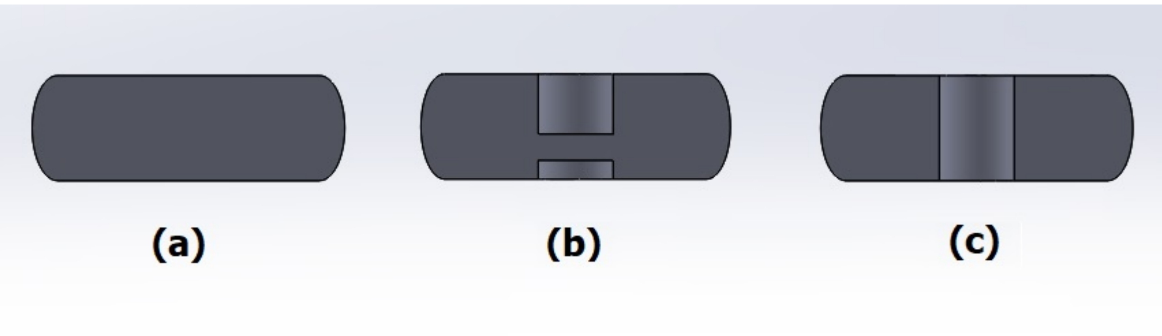

FIG. 3.11: Stages of the billet at the end of each preparation process: (a) after billet upsetting, (b) after billet central forging and (c) after billet piercing

In order for the central forging and piercing processes to be stable and without defects, Xu et al. established certain constraint conditions that have to be satisfied (**Xu et al., 2014**), as per the relationships presented in Eqs.3.7 :

$$\begin{gathered}\gamma \leq 1 \\ \frac{1}{5} \leq m \leq \frac{1}{3} \\ \frac{2}{3} \leq v \leq \frac{3}{4}\end{gathered} \tag{3.7}$$

where:

- $\gamma = \frac{h_f}{d_f}$, blank's height to diameter ratio
- $m = \frac{d}{d_f}$, tool's diameter to blank's diameter ratio
- $v = \frac{h}{h_f}$, tool's penetration depth to blank's height ratio

and:

- d, the tool's diameter
- h, the total penetration depth of the tool into the billet
- d_f, is the diameter of the upset billet
- h_f, is the height of the upset billet

During the initial stages of the billet central forging, a cylindrical tool with an outer diameter of d is used to compress the middle segment of the upset billet. Let the total penetration depth be h. As the tool moves into the upset billet, the material is forced to move radially, as the height of the blank is kept constant by a restrictive plate. Since the overall volume of the billet is maintained during this process, the outer radius of the workpiece at the end of central forging, r' further increases compared to the end of the upsetting process. Due to the friction between the billet and the restriction plates, as well as the asymmetrical penetration (greater from the top of the billet), the result of central forging is expected to be a non-uniform barrel-shaped final body. However, since the methodology of an equal volume cylinder greatly simplifies the necessary calculations, r', in this case too, is the equivalent radius of such an idealized cylinder (at least regarding the outer radius of the billet). From all of the above, a simple calculation of r' at the end of central forging can be performed through Eq.3.8:

$$r' = \sqrt{r_{eq}^2 + \frac{d^2}{4} \cdot v} \tag{3.8}$$

It is worth noting that in cases of very large billets and/or robust materials, the central forging process can be performed progressively in multiple steps. In such cases, multiple tools with progressively increasing diameters are used. Should central forging be performed in multiple steps, only the diameter and penetration depth of the final step are required in Eq.3.8. Moreover, the tool's penetration in the aforementioned analysis is considered perfect (an ideal $\frac{\pi d^2}{4} \cdot h$ hole is left after the forging), thus no defects caused by the tool's penetration that would cause a slight, additional increase in r' were considered. Finally, it is fairly common that penetration tools have a slight conicity, to help with their extrusion from the billet. Should such tools be used, their effects on the pierced billet's geometry can be taken into account, through a correction in the second factor of Eq.3.8. More specifically, considering a single or two different truncated conical tools penetrating the workpiece (one from each side of the upset billet), Eq.3.8 would be transformed either to Eq.3.9 or to Eq.3.10, respectively:

$$r' = \sqrt{r_{eq}^2 + \frac{1}{3} \cdot v \cdot (r_t^2 + r_t \cdot R_t + R_t^2)} \tag{3.9}$$

$$r' = \sqrt{r_{eq}^2 + \frac{1}{3 \cdot h_f} \cdot \left[h_t \cdot (r_t^2 + r_t \cdot R_t + R_t^2) + h_b \cdot (r_b^2 + r_b \cdot R_b + R_b^2)\right]} \tag{3.10}$$

where:

- r_t, the small radius of the top penetrating truncated conical tool

- R_t, the large radius of the top penetrating truncated conical tool
- h_t, the penetration depth of the top penetrating truncated conical tool
- r_b, the small radius of the bottom penetrating truncated conical tool
- R_b, the large radius of the bottom penetrating truncated conical tool
- h_b, the penetration depth of the bottom penetrating truncated conical tool

It should be mentioned that the estimation of r' from Eqs.3.8–3.10 is based on the hypothesis that the height of the workpiece before and after the central forging and piercing processes will remain the same. In case this is not the case, a billet with greater initial height should be forwarded to central forging and piercing, to compensate for potential height deviations. Furthermore, different heights should be considered in Eqs.3.8–3.10. To the author's best knowledge, this phenomenon is not clarified in literature. However, further analysis of the subject at hand is beyond the scopes of the current dissertation.

One very important aspect of the central forging process is that the penetration tool must follow the empirical equations proposed by Xu et al. (Eqs.3.7). Should the required initial hole be larger than Eqs.3.7 allow, or (as mentioned above) the combination of a large billet and/or robust material suggest otherwise, central forging should be performed in multiple steps. Although no dedicated work (to the best of the author's knowledge) has been presented so far regarding the workpiece preparation of Ring Rolling, multi-stage central forging processes have been analyzed in literature (e.g. **Paetzold et al., 2018**). The constraints of Eqs.3.7 can thus be used as a rough indicator for the number of piercing steps required for the completion of the process up to the predetermined size. Alternatively, machining or drilling processes may follow some initial smaller forging of the billet. It is worth noting that, due to the lack of relevant information, in 3.2.2 a single-step central forging process was considered.

With the completion of the central forging and the piercing processes, a new billet volume, V_{ring} has occurred. Supposing that the aforementioned thin disk, which was removed from at the center of the billet, had a volume equal to V_{disk}, the billet's volume before and after piercing are connected by Eq.3.11:

$$\begin{aligned} V_{billet} &= V_{ring} + V_{disk} \Leftrightarrow \\ \Leftrightarrow V_{billet} &= \pi \cdot h_f \cdot \left(r'^2 - \frac{d^2}{4} \cdot v \right) \end{aligned} \tag{3.11}$$

3.2.3 Initial Billet Volume Calculation Methodology

By following the aforementioned calculations in reverse, the initial volume for the blank can be estimated. More specifically, the following steps may be followed:

1. From the dimensions of the final ring product, calculate the total volume of the required material.
2. Given the total ring volume, and the dimensions of the Ring Rolling setup, two out of three from the initial ring dimensions must be chosen. These involve the outer initial radius of the ring R_0, the inner initial radius of the ring r_0 and the initial height of the ring H_0. The third dimension is considered a free dimension, and it is calculated through volume constancy.

3. Supposing a constant diameter throughout the workpiece's height, r' is set as the outer radius (r′ = R_0), d is set as the inner diameter (d = 2 · r_0) and h_f is set as the height of the workpiece (h_f = H_0) before Ring Rolling.

4. Use r' to calculate the limits of the equivalent radius of the upset billet, r_{eq} (Eqs.3.8 - 3.10), based on the limiting values of the constraint condition for v (see Eqs.3.7).

5. With h_f either chosen or calculated, choose the value of forging tool penetration depth, h, while verifying that the constraint condition for v (Eqs.3.7) is satisfied. This particular step can be further improved with experience, since the optimum penetration depth, h, will eventually be estimated accurately after a few production cycles.

6. With r', h_f, d and h (and thus v) estimated, the initial volume of the billet V_{billet} can be calculated from Eq.3.11. Subsequently, the equivalent radius of the upset billet, r_{eq} can be estimated using V_{billet} ($V_{billet} = \pi \cdot r_{eq}^2 \cdot h_f$). The estimated r_{eq} should be within the limits previously estimated in step 4.

7. Check the rest of constraint conditions of Eqs.3.7 and in case any of the factors are not satisfied, proceed to proper actions. More often than not, the diameter ratio factor, m, will be out of bounds, thus multiple central forging steps or a combination of central forging and machining should be considered.

8. Based on supplier capabilities and the dimensions of the upsetting setup, estimate the initial billet dimensions h_0 and d_0 (one must be known or chosen and the other calculated through Eq.3.1 – upsetting factor B must have been previously estimated).

The aforementioned methodology was subsequently tested numerically, through a series of models. In the following subsection, simulations that were conducted to test the billet volume estimation methodology will be presented.

3.2.4 Methodology Test Simulations

In order to verify the preceding process methodology presented in the current section of the dissertation, several numerical models had to be created and solved.

Initially, an example that would be tested had to be decided. Given the work performed for the simulation of the Ring Rolling process in the previous chapter (Chapter §2), the example chosen involved the correct prediction of the initial billet required for the creation of the target ring presented by Zhu et al. (**Zhu et al., 2016b**). In this reference, a ring of 900 × 800 × 115 (D_f × d_f × H_f) was the target at the end of the conducted Ring Rolling process. For such a ring, a pierced billet volume of approximately 15,354,534.1 mm^3 was required. However, the process began with a pierced billet of 610 × 450 × 125, resulting to a total volume of 16,650,441.1 mm^3. Based on the measurements of the final ring from the experimental process (914 × 810 × 116.2), the corresponding final volume of the ring was approximately 16,363,138.6, which is very close to the initial billet volume. It is worth noting that the slight difference between the two volumes of the experimental process can be attributed to a combination of lost material due to scaling and small defects in the final product, which were not taken into account during the final product measurements.

Seeing that such a difference can lead to relatively significant dimensional overshoots (at least in terms of high dimensional accuracy products), a numerical repeat of the entire process was conducted, while elaborating the proposed billet volume calculation methodology (see section 3.2.3). More specifically, the target of this exercise is to manufacture a ring with the target dimensions mentioned in **Zhu et al., 2016b** ($D_f \times d_f \times H_f$ = 900 × 800 × 115). However, instead of the initial pierced billet considered in the experimental process, a more precise (in terms of volume) billet will be estimated and used in a subsequent Ring Rolling simulation.

Initial Billet Volume Calculation

Before proceeding to the test simulations, the initial volume and the corresponding dimensions of the billet before the upsetting process had to be calculated, using the methodology presented in subsection §3.2.3. For a better comprehension, the following calculations were conducted in the same step-by-step way that the corresponding methodology was presented above:

1. Final ring volume, V_{ring} calculation:

$$V_{ring} = \pi \cdot (R_f^2 - r_f^2) \cdot H_f \Leftrightarrow$$

$$\Leftrightarrow V_{ring} = \pi \cdot (450^2 - 400^2) \cdot 115 \Leftrightarrow$$

$$\Leftrightarrow V_{ring} = 15,354,534.1 \ mm^3$$

2. Pierced workpiece initial dimensions, R_0, r_0, H_0 estimation:

Chosen dimensions: r_0 *= 225 mm and* H_0 *= 125 mm*

$$V_{ring} = \pi \cdot (R_0^2 - r_0^2) \cdot H_0 \Leftrightarrow$$

$$\Leftrightarrow R_0 = \sqrt{\frac{V_{ring}}{\pi \cdot H_0} + r_0^2} \Leftrightarrow$$

$$\Leftrightarrow R_0 = 299.54 \ mm$$

3. Link initial Ring Rolling workpiece dimensions to the corresponding of the final piercing process product:

$$r' = R_0 = 299.54 \ mm$$

$$d = 2 \cdot r_0 = 450 \ mm$$

$$h_f = H_0 = 125 \ mm$$

4. Calculation of the upsetting billet's equivalent radius limits, $r_{eq,lower}$, $r_{eq,upper}$:

$$r' = \sqrt{r_e q^2 + \frac{d^2}{4} \cdot v} \Leftrightarrow$$

$$\Leftrightarrow r_{eq} = \sqrt{r'^2 - \frac{d^2}{4} \cdot v} \Leftrightarrow$$

$$\Leftrightarrow r_{eq,lower} = \sqrt{299.54^2 - \frac{450^2}{4} \cdot \frac{3}{4}} \text{ and } r_{eq,upper} = \sqrt{299.54^2 - \frac{450^2}{4} \cdot \frac{2}{3}} \Leftrightarrow$$

$$\Leftrightarrow r_{eq,lower} = 277.50 \ mm \text{ and } r_{eq,upper} = 236.59 \ mm$$

5. Central forging tool penetration depth, h estimation:

Chosen constraint condition: $v = 0.72\ \left(\frac{2}{3} \leq m \leq \frac{3}{4}\right)$

$$v = \frac{h}{h_f} \Leftrightarrow$$

$$\Leftrightarrow h = v \cdot h_f \Leftrightarrow$$

$$\Leftrightarrow h = 90\ mm$$

6. Initial billet volume, V_{billet} and equivalent radius, r_{eq} calculations:

   Calculation of the initial billet volume, V_{billet}*:*

$$V_{billet} = \pi \cdot h_f \cdot \left(r'^2 - \frac{d^2}{4} \cdot v\right) \Leftrightarrow$$

$$\Leftrightarrow V_{billet} = \pi \cdot 125 \cdot \left(299.54^2 - \frac{450^2}{4} \cdot 0.72\right) \Leftrightarrow$$

$$\Leftrightarrow V_{billet} = 20,921,043.6\ mm^3$$

   Calculation of the equivalent radius, r_{eq}*:*

$$V_{billet} = \pi \cdot r_{eq}^2 \cdot h_f \Leftrightarrow$$

$$\Leftrightarrow r_{eq} = \sqrt{\frac{V_{billet}}{\pi \cdot h_f}} \Leftrightarrow$$

$$\Leftrightarrow r_{eq} = \sqrt{\frac{20,921,043.6}{\pi \cdot 125}} \Leftrightarrow$$

$$\Leftrightarrow r_{eq} = 230.81\ \mathrm{mm}$$

7. Verification of the rest of the constraint conditions, γ *and* m:

$$\gamma = \frac{h_f}{d_f} = \frac{h_f}{s \cdot r_{eq}} = \frac{125}{461.63} = 0.27 \leq 1\ (\gamma \leq 1, \text{thus satisfied})$$

$$m = \frac{d}{d_f} = \frac{450}{461.63} = 0.97 \geq 0.33\ \left(\frac{1}{5} \leq m \leq \frac{1}{3}, \text{thus not satisfied}\right)$$

   Since the second constraint condition is not satisfied, the central forging cannot occur in a single step. Thus, it is chosen that the corresponding process will be performed in multiple steps. Since it more common for large billets, a single conical tool penetration will be simulated, with a cone semi-angle of θ = 20° (constant in all tools) and the following tool diameters considered:

   - *Step 1*: $d_{t,1}$ = 44.26 mm/ $D_{t,1}$ = 111.80 mm
   - *Step 2*: $d_{t,2}$ = 111.80 mm/ $D_{t,2}$ = 179.34 mm
   - *Step 3*: $d_{t,3}$ = 179.34 mm/ $D_{t,3}$ = 246.87 mm
   - *Step 4*: $d_{t,4}$ = 246.87 mm/ $D_{t,4}$ = 314.41 mm
   - *Step 5*: $d_{t,5}$ = 314.41 mm/ $D_{t,5}$ = 381.95 mm

- *Step 6*: $d_{t,6}$ = 424.38 mm/ $D_{t,6}$ = 491.92 mm

*The number of steps was determined after a number of preliminary runs. As it is common in most punching blanking/punching processes, the diameter of the tool can create several deformation defects on the punched workpiece, with some common defects being the inner diameter bulges and the dishing of the workpiece (**Wang et al., 2016, El-Wakil, 2019**). In order to reduce or avoid the formation of these defects, the central forging and subsequent piercing of the billet had to be performed in multiple steps with small tool diameter increase between consecutive steps. Additionally, the use of two tools in the subsequent piercing process is expected to significantly reduce the creation of burrs and further dishing of the billet, similarly to a fine blanking process (**El-Wakil, 2019**). It is worth noting that the same penetration depth h = 90 mm will be maintained for all steps.*

8. Calculation of the initial billet dimensions, h_0, d_0:

   Chosen dimension: h_0 *= 150 mm*

   Upsetting factor value: B = 1.012

$$B = \frac{h_f \cdot d_f^2}{h_0 \cdot d_0^2} \Leftrightarrow$$
$$\Leftrightarrow d_0 = \sqrt{\frac{h_f \cdot d_f^2}{h_0 \cdot B}} \Leftrightarrow$$
$$\Leftrightarrow d_0 = \sqrt{\frac{125 \cdot 461.63^2}{150 \cdot 1.012}} \Leftrightarrow$$
$$\Leftrightarrow d_0 = 418.90mm$$

The proposed methodology needed to be verified. For this reason, a numerical model for each process step was created and solved. Some more information for each of the conducted simulations, as well as their respective results, are presented in the following sections.

Billet Upsetting Test Model

Initially, a numerical model simulating the upsetting process was created. For this model, the same setup as that presented in section § 3.2.1 was used. The only difference in this model was the initial diameter of the billet, d_0, which was d_0 = 418.90 mm. The 2D axisymmetric upsetting test model before and after its solution is presented in Figs.3.12 and 3.13, respectively:

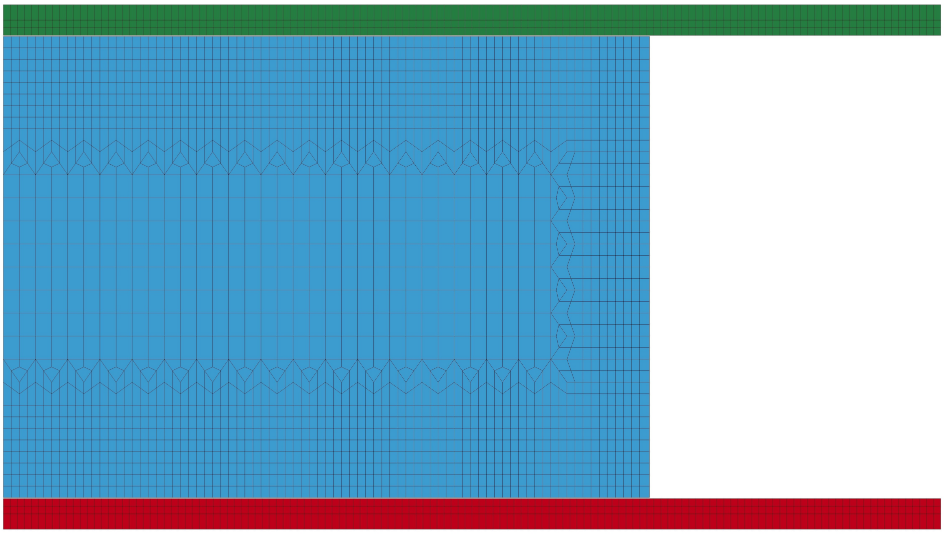

FIG. 3.12: Billet upsetting test model setup - Initial time instance

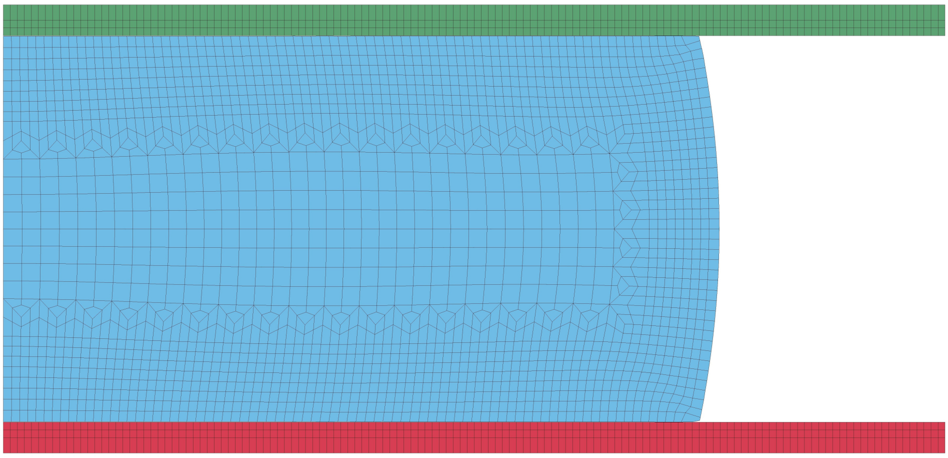

FIG. 3.13: Billet upsetting test model setup - Final time instance

After the model was solved, its results were inspected for errors and then evaluated. Since a validation of the aforementioned methodology was the main scope of the current simulation, the coordinates of the nodes located at the peripheral edge of the 2D model were exported. The coordinates of the peripheral nodes were subsequently used to fit a polynomial function that could be used for the precise estimation of the equivalent radius, r_{eq}, as described by Eq.3.6.

For the better and automated fitting of the aforementioned polynomial function, a script estimating it was written in Python. This script is presented in Appendix B.2. From the Python script in Appendix B.2, multiple polynomial functions of different degrees were examined, to determine the minimum polynomial degree that would have the best regression to the model's peripheral node coordinates. A coefficient of determination, $R^2 = 0.999$ was chosen as a minimum requirement for the polynomial (also calculated by the written script).

Substitution of the nodal coordinates in the Python script resulted in a 6^{th} degree polynomial as the infimum fitted function. The aforementioned polynomial is expressed by Eq.3.12:

$$\begin{aligned} f(y) = -4.3225 \cdot 10^{-11} \cdot y^6 + 1.9136 \cdot 10^{-8} \cdot y^5 - 3.4161 \cdot 10^{-6} \cdot y^4 + 3.1326 \cdot 10^{-4} \cdot y^3 \\ -1.7690 \cdot 10^{-2} \cdot y^2 + 7.1103 \cdot 10^{-1} \cdot y + 216.0036 \end{aligned} \tag{3.12}$$

Regarding the high degree of the fitted polynomial, several lower and higher order polynomials could be used just as well. In this case, the higher degree polynomials (of 6^{th} degree or greater) were proven to systematically produce accurate results, regardless of the mesh density used in the corresponding model. However, if the complexity of the 6^{th} degree polynomial is high, a lower degree polynomial could also be applied but with a relatively fine mesh or with an adaptive mesh.

The calculated polynomial (Eq.3.12) had to be raised to the power of 2 and integrated, in order to be substituted in Eq.3.6. For this reason, a second Python script was written for the power raise of the polynomial (Appendix B.3), while a third Python script estimating the indefinite integral of the squared polynomial was used for the final calculations (Appendix B.4). The resulting polynomial was finally substituted in Eq.3.6, after the corresponding integral limits have been considered (Eq.3.6 requires a definite integral). After the necessary calculations were performed, the equivalent radius of the upset billet test model was equal to r_{eq} = 228.64 mm.

From the comparison of the equivalent radius from the test model to that estimated in section 3.2.4 ($r_{eq,methodology}$ = 230.81 mm), a percentage difference of approximately Δr_{eq} = 0.94% was estimated, which can be considered as acceptable given the slight uncertainty inserted by the numerical modeling method. Furthermore, the numerical value was within the r_{eq} limits that were calculated in step 4 ($r_{eq,lower}$ = 227.50 mm, $r_{eq,upper}$ = 236.59 mm). Potential factors that would have led to the aforementioned small r_{eq} deviation are the need for a slightly finer mesh or a small accumulation of numerical error. However, and as mentioned above, this difference is negligible.

Since the produced error in the equivalent radius, r_{eq} calculated by the numerical model was not significant, this value was used as the initial state of the subsequent central forging model.

Billet Central Forging Test Model

With the conclusion of the billet upsetting simulation, the following two manufacturing processes, namely central forging and piercing of the billet, needed to be simulated. Since the central forging process by itself had to be performed in multiple steps (as per the results of Section §3.2.4), a sequential model had to be created. More specifically, each central forging step was simulated in a separate numerical model, with the results (mainly the final billet deformation) of each step was used as the initial state of the next. After the completion of the last central forging step, the final billet geometry was input as the initial state of the piercing process numerical model.

During the central forging model, the simulation of a truncated conical tool creating a central hole in the middle of the billet and then expanding it with each subsequent forging cycle was conducted. The dimensions of the truncated conical tools were those mentioned in section §3.2.4, while a slightly greater height of h = 92.78 mm was set as the height of the truncated cone. The reason for this slight deviation in the height of the tool was to compensate for the slight change in the equivalent radius of the upset billet. More specifically, based on the equivalent radius calculated from the numerical model (r_{eq} = 228.64 mm), a slightly different upset billet volume occurred. Thus and in order not to deviate from the previously estimated pierced billet volume, the volume of the removed material, V_{disk}, needed to be corrected. After performing the necessary calculations using Eqs.3.8 and 3.11, a constraint condition v = 0.74 was calculated, which subsequently led to a forging tool penetration depth of h = 92.78 mm. Seeing that the maximum penetration depth should be equal to the height of the conical tool, the aforementioned value for h was used as the height of the cone. Other than that, an upsetting plate was also embedded on the upper part of the aforementioned tools. The main role of this upsetting plate was to iron out any bulges formed around the edge of the central hole during the process. The aforementioned upsetting plate should come in contact with the entire upper surface of the billet at the exact time when the maximum penetration depth is achieved. In the conducted simulations, the embedded upsetting plate had a radius of r_{plate} = 350 mm in all the forging tools. A presentation of one of the forging tools modeled for the central forging model is presented in Fig.3.14. It should be mentioned that the forging tool in Fig.3.14 is presented upside down, while the most important dimensions are also noted.

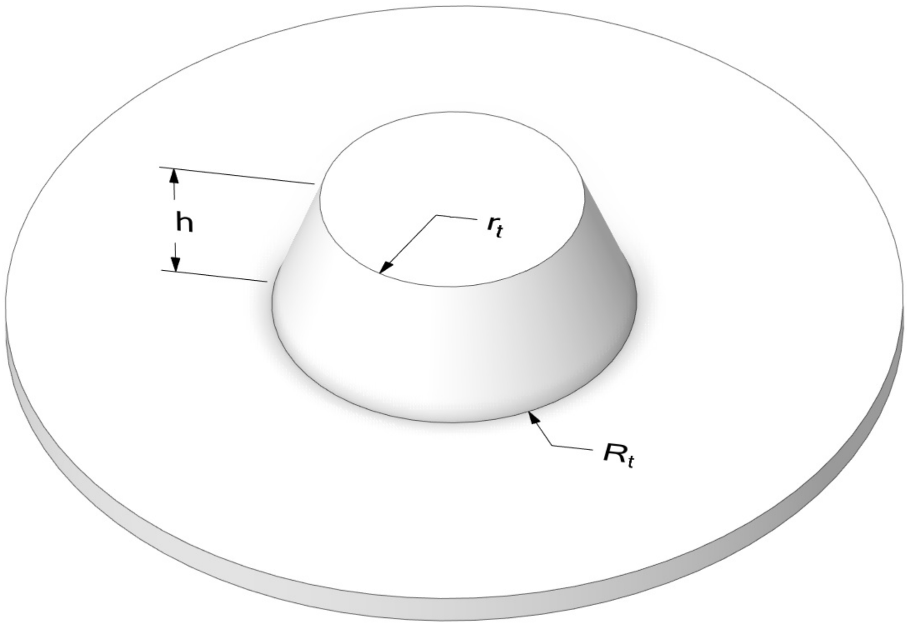

FIG. 3.14: Representative central forging tool geometry (presented upside down)

As mentioned above, for the initial billet geometry of the first central forging step the equivalent radius estimated from the previous billet upsetting model was used (r_{eq} = 228.64 mm), in order to include any additive error in the current models (thus calculating the worst case scenario). On the other hand, the height of the upset billet prior to central forging was equal to the final height of the upsetting process, h_f = 125 mm. On this point, it should be repeated that in the current analysis, no height deviation was simulated for the billet. This was made possible with the application of a very small velocity on the forging tools ($v_{forging}$ = 0.2 mm/s), which made the process quasi-static and allowed for a localized deformation of the billet mainly around the penetration of the tool. The author acknowledges that such small velocities are uncommon in actual forging processes, however delving deeper into the forging process was beyond the scopes of the current dissertation. It should be mentioned that the total travel of each tool into the forged billet was equal to the tools' height of h = 92.78 mm.

Lastly, the lower plate from the billet upsetting test model was included in this model, too. Similarly to the upsetting test model, the lower plate provided the necessary reaction forces, so that central forging could be simulated. The radius of the lower plate, in this case too, was r_{plates} = 470 mm. The lower plate remained immobilized during all central forging process cycles.

Because of the very small forging velocity, an average simulation time of $t_{f,forging}$ = 463.9 s was required for the tools to reach the maximum penetration depth. Reviewing the recommended formulation map presented in Fig.2.1, such slow phenomena are better simulated using implicit analysis, and thus this was the formulation chosen for these corresponding models. By default, all numerical models in LS-DYNA are solved using explicit formulation. However, the chosen formulation can be switches to implicit, if the proper option from *CONTROL_IMPLICIT* menu are activated. In the current analysis, the following *CONTROL_IMPLICIT* menus were facilitated:

- *CONTROL_IMPLICIT_GENERAL*, which is the necessary menu to activate the implicit analysis and define the core parameters. From the available options, *IMFLAG* = 1 was chosen to activate a fully implicit analysis, while *DT0* = 0.01 defined an initial implicit time iteration step of 0.01 s.
- *CONTROL_IMPLICIT_SOLVER*, which defines the type of implicit solver that will be used in the analysis. From the available options, *LSOLVR* = 6 was chosen for the current analysis, thus defining a direct, sparse, double precision solver to be used in the current analysis.
- *CONTROL_IMPLICIT_FORMING*, which provides specific routines for assisting with the solution convergence in forming problems. From the available options, *IOPTION* = 2 defined a binder closing and/or flanging problem (closer to the forging problem simulated), while *NSMIN* = 150 and *NSMAX* = 150000 defined the minimum and maximum number of implicit steps, respectively.
- *CONTROL_IMPLICIT_SOLUTION*, in which the type of solution (linear or non-linear) is defined. In this menu, the default options were left unchanged for the current analysis.
- *CONTROL_IMPICIT_DYNAMICS*, allowed for the compensation of potential dynamic loads occurring during the process. In this menu, the default options were left unchanged for the current analysis.

Apart from the implicit related options, some additional options had to be enabled for the current analysis. These involved the following:

- The *CONTACT_2D_AUTOMATIC_SINGLE_SURFACE_THERMAL* menu should be turned on for the recognition of the self-contacting segments of the billet. From the available options of this menu, *INIT* = 1 should be included, in order to compensate for the compression of the workpiece and reduce numerical defects, while option *ISTIFF* = 2 would allow for a better scaling of the calculated stiffness of each element.

- A minor offset between the contacting surfaces should be considered through the *SLDSO* options in all the included *CONTACT* menus, so that potential penetrations of the tools in the workpiece would be reduced. Typical offset values could be approximately *SLDSO* = 0.05–0.15.
- The inclusion of an adaptive mesh is crucial for the successful simulation of forging processes. In LS-DYNA, adaptive mesh can be turned on through a combination of *CONTROL_ADAPSTEP* and *CONTROL_ADAPTIVE* menus, while option *ADPOPT* = 2 should be considered for the formed body through the *PART_PART* menu. In *CONTROL_ADAPSTEP* menu, the default values were proved adequate for the central forging simulations. On the other hand, in *CONTROL_ADAPTIVE* menu the following options should be considered:
  - *ADPFREQ* = 0.5 dictates the time between two consecutive remeshings.
  - *ADPTOL* = 1.0 sets the average element size of the adaptive mesh (in the case of *ADTYP* = 8).
  - *ADTYP* = 8 defines the type of remeshing rules that will be followed in the analysis. Options -8 and 8 are the only valid options for an axisymmetric 2D solid analysis.
  - *ADPASS* = 1 dictates a single pass adaptivity per time iteration.
  - *LADPCL* = 1 allows for element fusion to be included.
  - *NCFREQ* = 1 defines the element fusion will occur after every remeshing step.
  - *ADPCTL* = 1.0 defines the element thickness threshold below which element fusion will occur.

Since the model presented in section §3.2.1 was used as the basis for the central forging test model, the rest of the included menus and options in LS-DYNA remained the same to that model.

The initial states of the six billet central forging steps are presented in Fig.3.15. In the states presented in Fig.3.15, the red body is the billet, the blue body is the forging tool and the green body is the bottom plate.

Observations over the initial states presented in Fig.3.15 reveal several interesting points. Initially, the shape of the consecutively expanding central gap followed the shape of the corresponding forming tool with good agreement. Only in the cases of Steps 4 and 5 (results of the forging processes performed during Steps 3 and 4, respectively), some minor deviations from the outline of the tool could be seen at the bottom corner of the forged gaps, which were a result of the billet's material wrapping onto itself during the process. Other than that, the combination of the low forging velocity and the embedded upsetting plate on the tool resulted in no significant changes in the billet's height after each central forging step. Because of this, any deformation that occurred as a result of the tool penetration, resulted only in a billet radius expansion. Finally, the remaining material below the formed gap had the same height in all the presented states, as a result of the same tool penetration travel and the constant billet height.

After the conclusion of the final central forging step (Step 6), the final geometry of the billet before proceeding to the piercing process was evaluated. This final deformation state is presented in Fig.3.16:

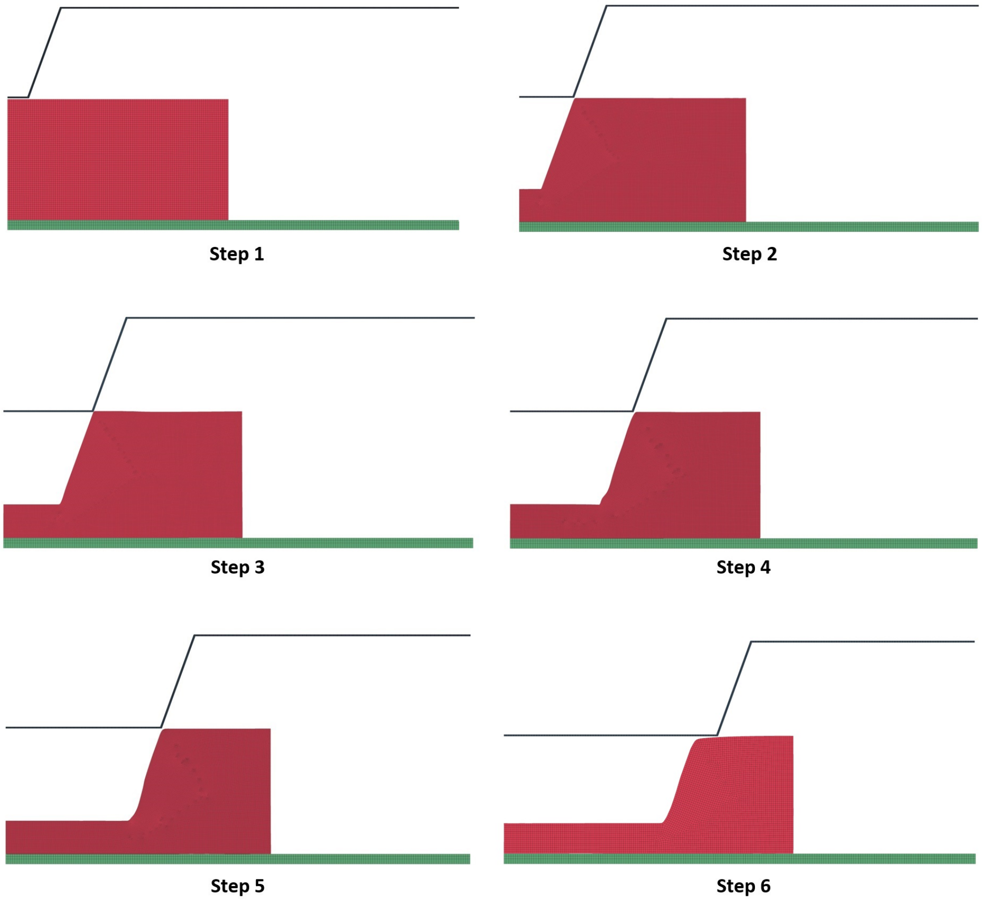

FIG. 3.15: Initial states of the conducted billet central forging simulation steps

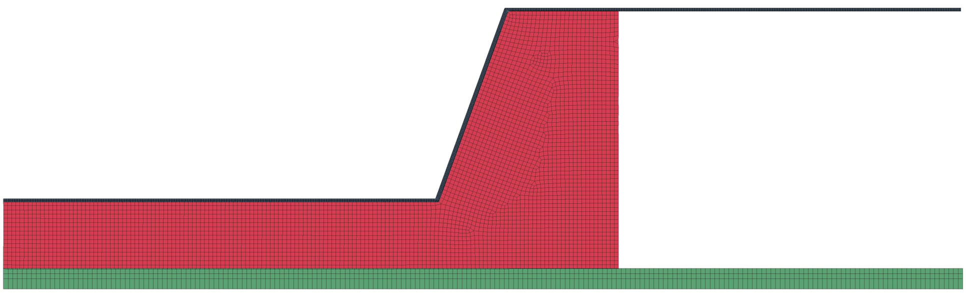

FIG. 3.16: Final deformation of the billet at the end of the central forging process

The final state of the central forging simulation (final time instance of Step 6) reveal a rather expected billet deformation. More specifically, the formed gap at the center of the billet followed almost perfectly the outline of the final forging tool, except from a minor difference in the radius of the top edge of the gap. Moreover, the outer radius of the billet was almost constant throughout its height. The average final outer radius at the end of the central forging process was equal to $r' = 299.79$ mm. Comparing this value to the corresponding value estimated with the proposed methodology in section §3.2.4 ($r'_{methodology} = 299.54$ mm) reveal a difference of approximately 0.08%, which can be considered negligible. Since the difference in the outer radius between the methodology and the corresponding central forging model was so close, the proposed methodology can be considered valid in this case, too.

Finally, the evolution of the outer billet radius during the consecutive central forging steps was further investigated. For this reason, the outer billet radius, r', at the end of each forging step was correlated to the corresponding small diameter of the forging tool, d_t. The resulting points were then compared in a figure and a polynomial was subsequently fitted to them. The corresponding figure with the resulting points (square marks) and the fitted polynomial (dotted line) is presented in Fig.3.17:

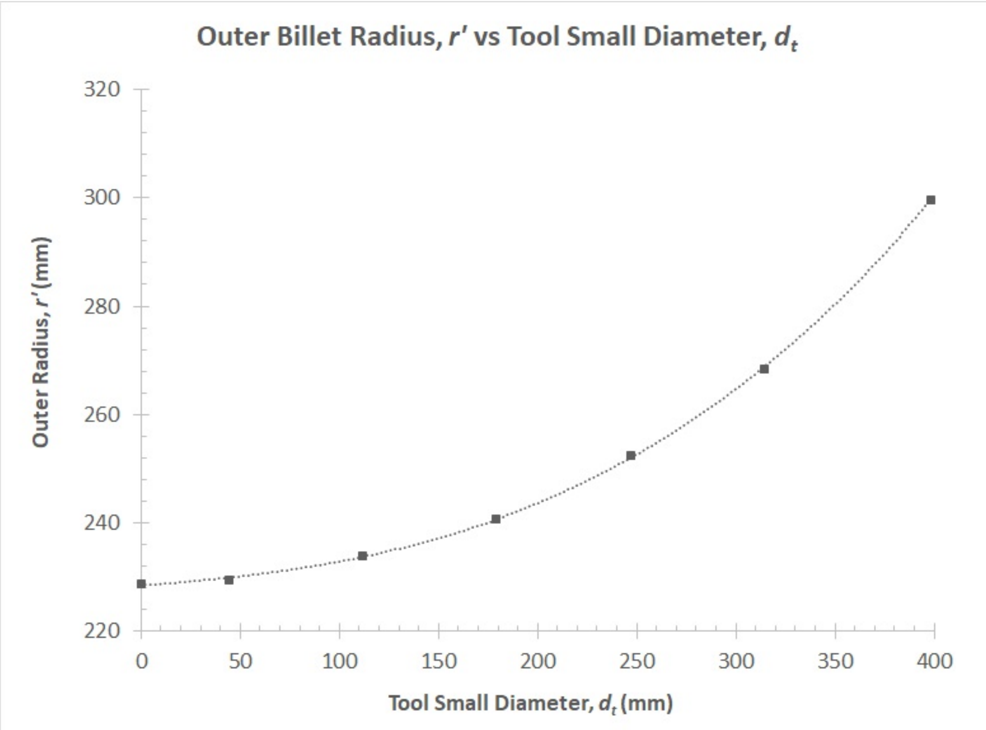

FIG. 3.17: Billet outer diameter evolution during the central forging process in correlation to the small tool diameter used in every step. Square marks represent the resulting correlation points, while the dotted line represents a fitted 3^{rd} degree polynomial

Observations over Fig.3.17 reveal a non-linear evolution of the outer billet diameter during the central forging process. More specifically, during the initial forging steps, the billet's radial expansion was limited to a few millimeters (less than 10 mm after forging step 2). After the second forging step, however, a significant increase in the outer radius's growth rate was observed. Finally, the polynomial that was fitted to the resulting correlation points satisfied Eq.3.13:

$$r' = -6.804 \cdot 10^{-7} \cdot d_t^3 + 1.1131 \cdot 10^{-4} \cdot d_t^2 - 2.6336 \cdot 10^{-3} \cdot d_t + 228.4292 \tag{3.13}$$

It is worth noting that the coefficient of determination of Eq.3.13 was equal to $R^2 = 0.9999$.

Billet Piercing Test Model

After step 6 of the central forging simulation was completed, the final deformation of the billet was extracted and subsequently used to create the piercing process model. In this model, the central disk segment of the billet would be removed. The remaining billet material would be measured and the equivalent inner and outer radii would be calculated using a properly modified Eq.3.9 and Eq.3.6, respectively.

In the case of the billet geometry, a small modification had to be done. Since an adaptive mesh is vital for this type of simulations, even more so with relatively small element length, remeshing the entire workpiece with such a fine mesh would lead to a huge number of finite elements and a corresponding increase in solution time. Thus and in order to limit mesh adaptive refinement only around the shear region, the mass of the billet was spit around that area. More specifically, specific billet elements from its initial mesh were set as a second, independent part in the model, which was allowed to remesh adaptively. In order to maintain the continuity of the workpiece's material, the proper contact conditions between the two parts had to be applied. The applied contact conditions are further discussed below.

Apart from the billet, a pair of piercing tools and a pair of pressure plates were also included in the numerical model. The pair of piercing tools had a cylindrical shape, while the pressure plates were simulated as hollow disks. The outer diameter of each piercing tool was equal to the small diameter of the forging tool used in step 6, namely $d_{t,6}$ = 424.38 mm, while the inner and outer diameters of each pressure plates were equal to $d_{i,plate}$ = 424.48 mm and $d_{o,plate}$ = 724.64 mm, respectively. From the aforementioned tool dimensions, a tolerance of 0.05 mm can be identified. This specific value is within the allowable tolerance values mentioned in literature (**Swift and Booker, 2013**). Furthermore, an edge radius was considered in the case of the piercing tool equal to 0.1 mm. Tool edge radius is mentioned as a very significant parameter in literature (e.g. **Bohdal et al., 2022**), which can heavily affect the shear surface of the pierced workpiece. The chosen edge radius of 0.1 mm can be considered as a relatively small value, thus indicating a brand-new tool or one with little wear.

The meshed bodies at the initial time instance of the piercing model are presented in Fig.3.18:

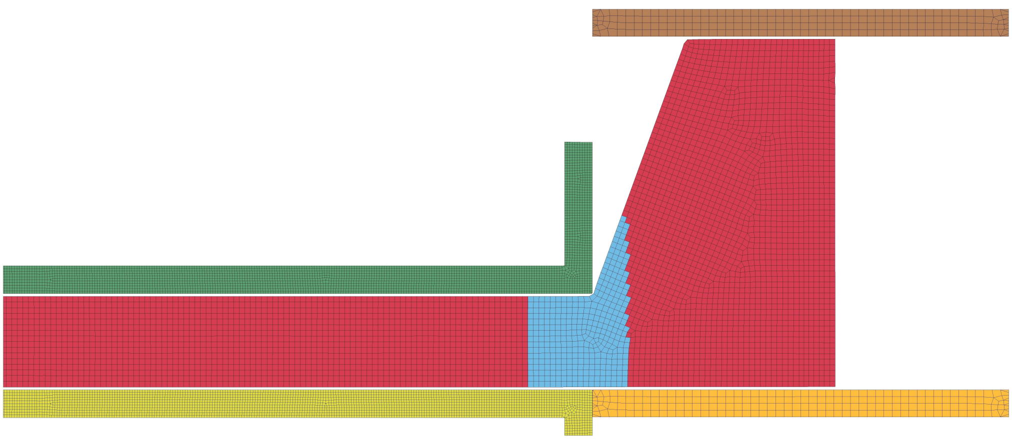

FIG. 3.18: Piercing model meshed bodies at the initial time instance

Regarding the movement of the tools, a constant downwards velocity of $v_{piercing}$ = 5 mm/s was applied in both of the piercing tools. This specific tool velocity was found in literature (**Komori et al., 2022**) for a punching process of steel samples. Since no experimental data of a relevant process were available, the aforementioned tool velocity value was adopted.

One of the most crucial parameters for the piercing simulation is the proper consideration of material failure for IN718. For this reason, a different material model was considered for the billet in the current simulation. More specifically, *MAT_224-TABULATED_JOHNSON_COOK* material model was used. *MAT_224* is a more generalized form of Johnson-Cook material model, in which the material's behavior is correlated to temperature and strain rate phenomena. Additionally, material failure is also considered, through triaxiality and lode parameter curves/surfaces. In the case of IN718, the required material properties for *MAT_224* were found in literature. More specifically, the material property inputs used in the current model, their respective references and the corresponding figures are summed up in Table 3.3 and presented individually in Figs.3.19–3.21:

TABLE 3.3: Material properties (IN718) - MAT_224

Property	**Value or Curve**	**Reference**
	IN718	
Density, *d* (kg m^{-3})	8240	*Zhu et al., 2016b*
Stress - Strain - Temperature surfaces for a Strain Rate Range of $\dot{\epsilon}$ = 0.01 – 10 s^{-1}	Fig.2.8	*Chaudhury and Zhao, 1992, Thomas et al., 2006, Iturbe et al., 2017, Jarugula et al., 2020*
Young's Modulus, *E* (GPa)	Fig.2.9	*Iturbe et al., 2017*
Poisson's Ratio, v	0.282	*Special_Metals_Corp., 2020*
Specific Heat Capacity, *C* (J kg^{-1} K^{-1})	637	*Deshpande et al., 2011*
Effective Plastic Failure Strain - Triaxiality - Lode Parameter Surface	Fig.3.19	*Dolci, 2021*
Effective Plastic Failure Strain - Temperature Triaxiality Surfaces for a Strain Rate Range of $\dot{\epsilon}$ = 0.001 – 10 s^{-1}	Fig.3.20	*Rodríguez-Millán et al., 2021*
Effective Plastic Failure Strain (Scale Factor) - Element Size	Fig.3.21	*Dolci, 2021*

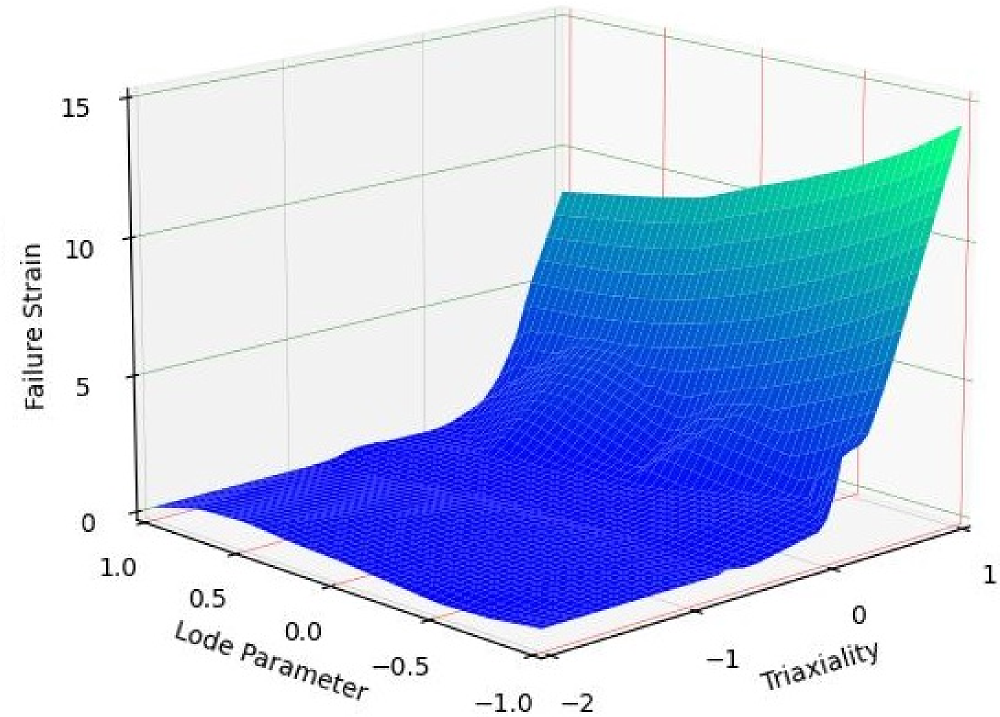

FIG. 3.19: Effective Plastic Failure Stain vs Stress Triaxiality vs Lode Parameter surface of IN718

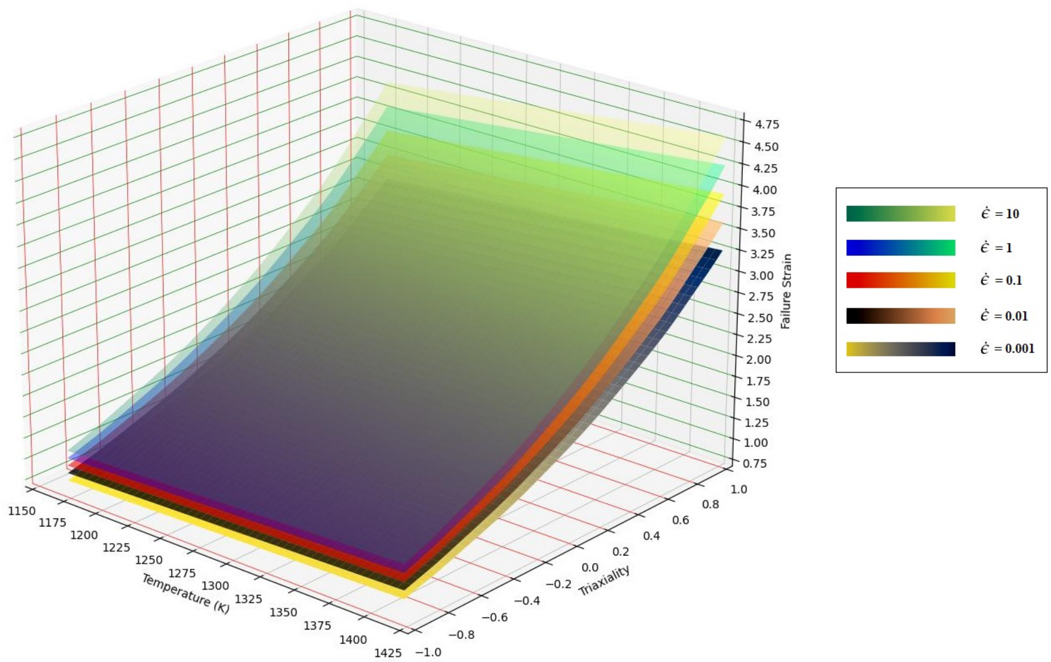

FIG. 3.20: Effective Plastic Failure Strain vs Stress Triaxiality vs Temperature surfaces for a Strain Rate Range of $\dot{\epsilon} = 0.001 - 10\ \mathrm{s}^{-1}$

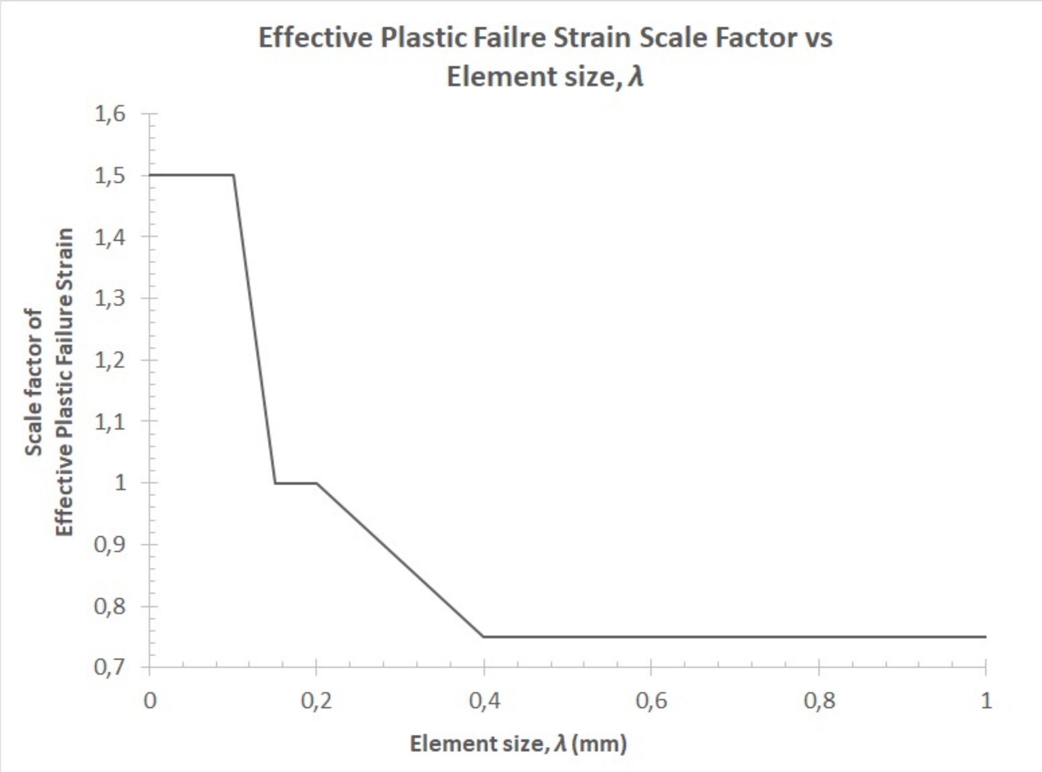

FIG. 3.21: Effective Plastic Failure Strain Unitless Scale Factor vs Element Size

The material properties presented in Table 3.3 were subsequently input in *MAT_224*. The corresponding options of this material model that were activated, and their respective values were the following:

- *R0*, which defines the density of the material. The corresponding value of Table 3.3 was input in this option.
- *E*, which defines the material's Young's Modulus. For this property, the Young's Modulus - Temperature curve presented in Fig.2.9 was input via *DEFINE_CURVE* menu and then was applied on the aforementioned option of *MAT_224*.
- *PR*, which defines the material's Poisson ratio. A value of *PR* = 0.282 was applied, which is the Poisson's ratio for the initial temperature of T = 1173.15 K (as per Fig.2.10).
- *CP*, which defines the material's specific heat capacity. A value of *CP* = 637 J kg^{-1} K^{-1} was applied, which is the specific heat capacity for the initial temperature of T = 1173.15 K (as per Fig.2.14).
- *TR*, which defines the room temperature in the analysis. A value of *TR* = 293.15 K was applied.
- *BETA*, which defines the fraction of plastic work converted into heat. A value of *BETA* = 0.8 was applied (also see §2.13).
- *LCK1*, which defines the true stress - true plastic strain curves for multiple strain rates. For this option, the corresponding curves were taken from Fig.2.8 and input via a combination of *DEFINE_CURVE* and *DEFINE_TABLE* menus.

- *LCKT*, which defines the true stress - true plastic strain curves for multiple temperatures. For this option, the corresponding curves were taken from Fig.2.8 and input via a combination of *DEFINE_CURVE* and *DEFINE_TABLE* menus.
- *LCF*, which defines the effective plastic failure strain-triaxiality curves for multiple lode parameter values. For this option, the corresponding curves were taken from Fig.3.19 and input via a combination of *DEFINE_CURVE* and *DEFINE_TABLE* menus.
- *LCG*, which defines the effective plastic failure strain - strain rate curves. For this option, the corresponding curves were taken from Fig.3.20 and input via a combination of *DEFINE_CURVE* and *DEFINE_TABLE* menus. It is worth noting that since *LCF* was input as a nominal curve, the effective plastic failure strain in *LCG* had to be converted into a corresponding scale factor, with the failure strain value of $\dot{\epsilon} = 1\ \mathrm{s}^{-1}$ being the nominal value.
- *LCH*, which defines the effective plastic failure strain - temperature curves. For this option, the corresponding curves were taken from Fig.3.20 and input via a combination of *DEFINE_CURVE* and *DEFINE_TABLE* menus. It is worth noting that since *LCF* was input as a nominal curve, the effective plastic failure strain in *LCH* had to be converted into a corresponding scale factor, with the failure strain value of $T = 1173.15$ K being the nominal value.
- *LCI*, which defines the unitless effective plastic failure strain scale factor - (average) element size curve. For this option, the corresponding curve from Fig.3.21 was input via *DEFINE_CURVE* menu and subsequently applied on *LCI*.

Regarding the rest of the numerical model's options and inputs, these were mostly the same as those of the central forging simulations. The menus and options that were activated uniquely for the piercing model involve those presented below. It is worth noting that similarly to the central forging models, the piercing model was also solved using implicit formulation.

- From the *PART* menu, the option *ADAPTIVE_FAILURE* was enabled for the shear zone of the billet, in order to allow for the separation and remeshing of the initial mesh during piercing. A threshold of $T = 1.0$ was selected as the minimum element thickness before remeshing.
- From the *CONTROL_ADAPTIVE* menu, the option *ADPTOL* = 0.3 was activated only for the shear zone part of the billet (blue segment in Fig.3.18).
- An additional contact was activated between the shear zone of the billet and the rest of the workpiece, via *CONTACT_2D_AUTOMATIC_TIED_THERMAL*. From this menu, activating option *TIEDGAP* = -10.0 was crucial, since it ensured the contact between the two billet pieces regardless of the level of adaptive remeshing that occurred in the shear zone. The rest of the options in this contact were the same as those of the central forging models.
- A total simulation time of *ENDTIM* = 9.0 was required to complete this simulation (activated in *CONTROL_TERMINATION* menu).

After the piercing simulation setup was completed, the model was solved and its results were evaluated. Initially, the billet's deformation results were extracted. The deformation of the billet in three time instances during the piercing process are presented in Figs.3.22, while the zoomed image of the shear zone at the end of the process is presented in Fig.3.23:

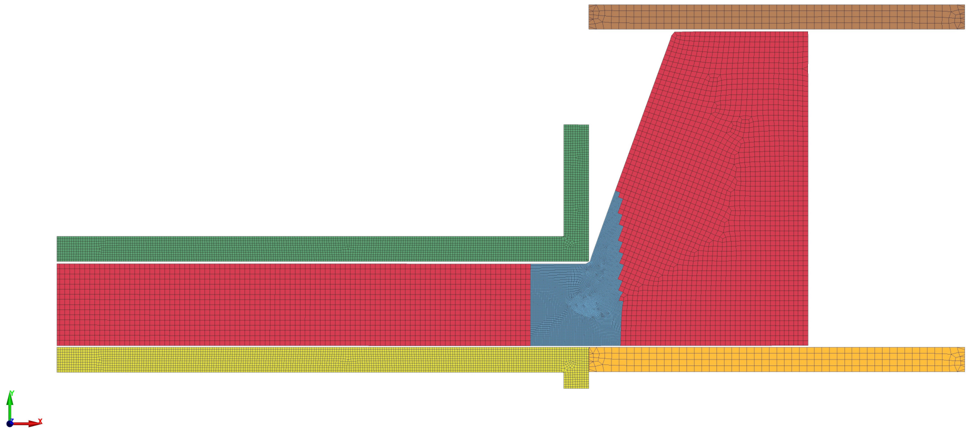

(A)

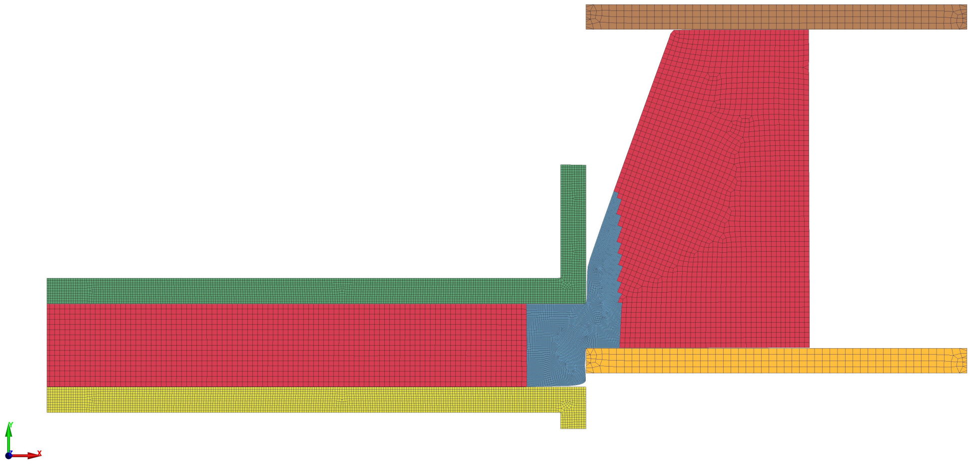

(B)

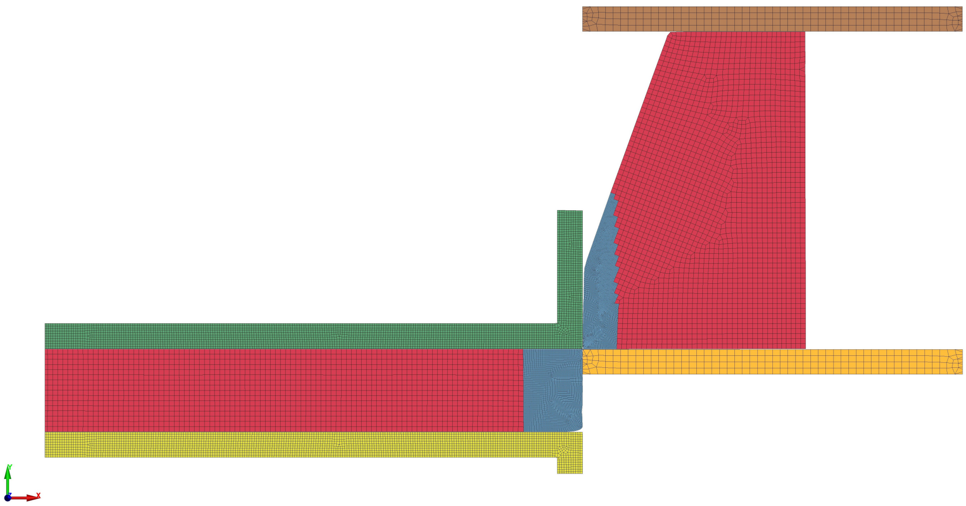

(C)

FIG. 3.22: Billet's deformation during piercing process: (A) Initial state, (B) intermediate state (t = 5 s) and (C) final state

Observations over Figs.3.22 and 3.23 reveal a rather expected shearing behavior of the material. The use of a piercing tool pair (punch and counter-punch) combined with the small

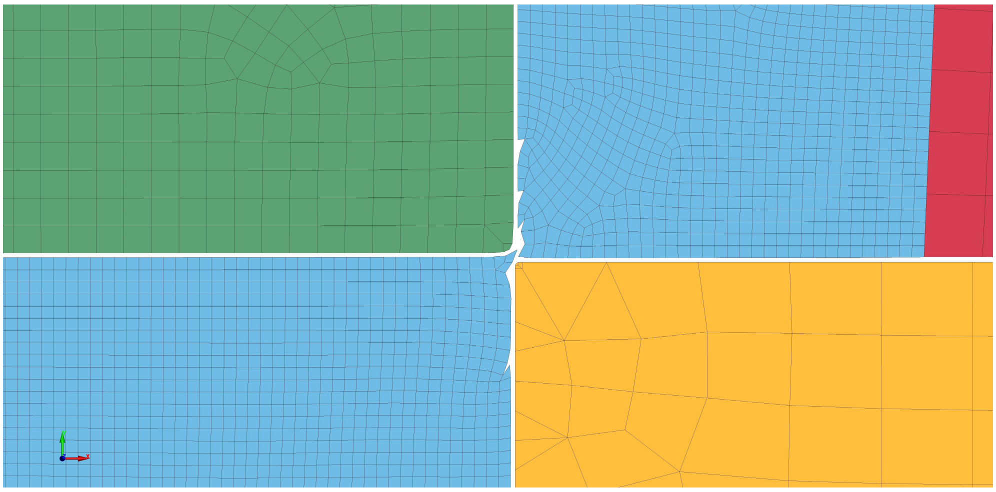

FIG. 3.23: Zoomed image of the shear surface at the end of the piercing process

clearance between the tools and the pressure plates allowed for a clean shear surface, with little to no defects manifesting. This fact became apparent from the lack of burrs at the bottom surface of the pierced billet (Fig.3.23). Moreover, the adaptive remeshing of the shear zone allowed for a more precise calculation of the inner surface's final geometry, while the expected fracture surface zones (Fig.3.24) described in literature (**Sahli et al., 2020**) were also observed. More specifically, in Fig.3.23 both the shear zone and the fracture zone were clearly distinguishable. Finally, the mesh adaptivity was made apparent from the comparison between the three instances in Fig.3.22, in which a constantly adjusting mesh was shown. Overall, the deformation results from the piercing model had the anticipated behavior, with the central disk removed and no further geometrical changes on the remaining workpiece.

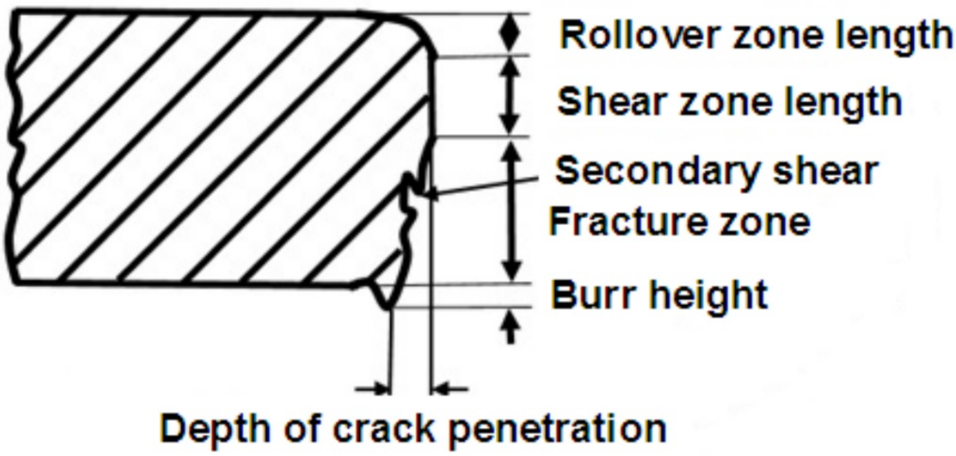

FIG. 3.24: Typical zones created on a metal's shear surface during punching/blanking processes (figure taken from **Sahli et al., 2020**)

Apart from the deformational results, the equivalent Von Mises stress and the effective plastic strain results during an intermediate time iteration of the process were evaluated. The aforementioned results are presented in Figs.3.25 and 3.26, respectively. It is worth noting that since no corresponding experimental data were available for the creation of the current simulation, the stress and plastic strain results are presented only for the sake of completeness.

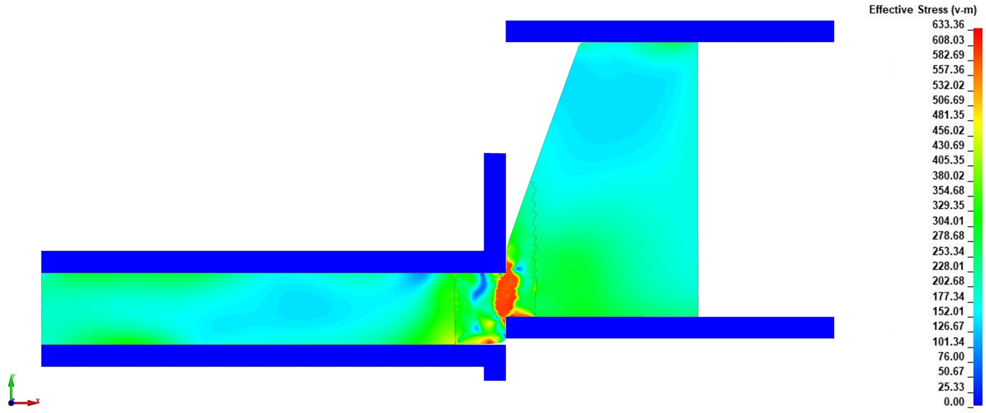

FIG. 3.25: Equivalent Von Mises stress results at an intermediate state of the piercing model (t = 4.5 s)

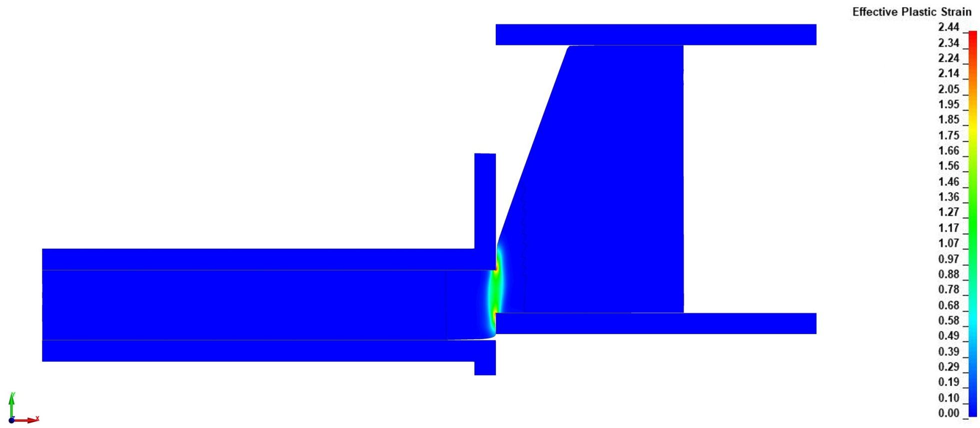

FIG. 3.26: Effective plastic strain results at an intermediate state of the piercing model (t = 4.5 s)

Observations over Fig.3.25 reveal a typical stress distribution of a punching process. More specifically, the greatest stress values seem to connect the two shear fronts around the edges of the top piercing tool and the bottom pressure plate. The stress path connecting the two shear fronts indicates a proper tool clearance, based on similar cases described in literature (**Sahli et al., 2021**). Other than that, relatively increased stress fields could also be observed around the top outer corner of the remaining billet material, which indicates a tendency of the material to bend (similar to a dishing defect mechanism). This phenomenon was, however, averted by the top pressure plate, which restricted any further movement of the billet.

Likewise, the effective plastic strain distribution was that expected during a metal punching process. The increased strain distribution field is situated along the path connecting the two shear fronts. The maximum recorded plastic strains were located around the shear fronts, which were in fact maintained after the end of the piercing process around the points formed in the fracture zone (see Fig.3.27).

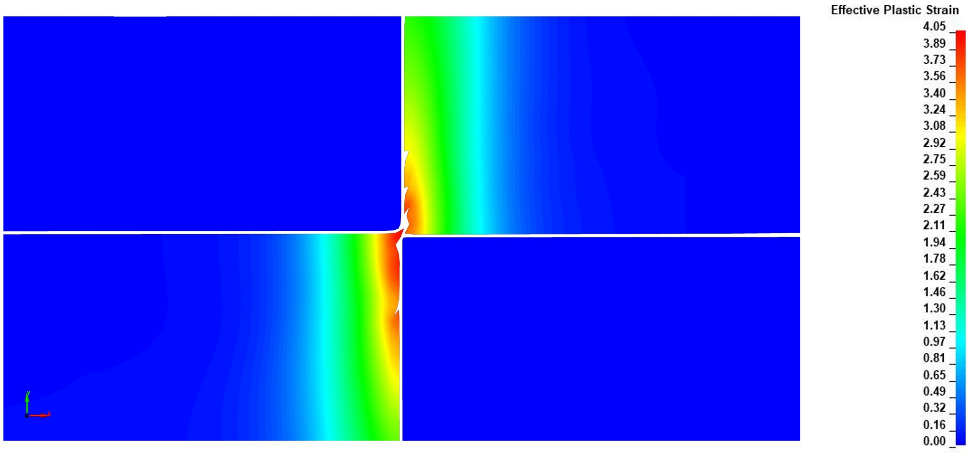

FIG. 3.27: Effective plastic strain distribution around the cutoff edge of the billet at the end of the piercing process

Finally, the equivalent inner and outer billet radii needed to be measured and then compared to the corresponding values, as these were estimated from the presented methodology in section §3.2.4. More specifically, from the final time instance of the piercing model, the nodal coordinates of the inner and outer billet surfaces were initially extracted. In the case of the outer billet surface nodes, their coordinates were input in the corresponding python scripts presented in Appendices B.2–B.4 and the script outputs were used in Eq.3.6. On the other hand, and regarding the inner billet surface nodes, these were separated into two different groups: (a) the cylindrical segment nodes and (b) the conical segment nodes. Beginning with the cylindrical segment nodes, the same procedure as that of the outer billet surface nodes was followed. The resulting equivalent cylindrical radius was substituted along with the maximum and minimum conical radii in a properly modified form of Eq.3.9, with r_0 considered equal to r_t.

Using the outer billet surface nodes in the python script presented in Appendix B.2 produced the 6^{th} order polynomial presented in Eq.3.14:

$$\begin{aligned} f_{outer}(y) = &-8.015 \cdot 10^{-12} \cdot y^6 + 3.1818 \cdot 10^{-9} \cdot y^5 - 5.0813 \cdot 10^{-7} \cdot y^4 \\ &+4.1858 \cdot 10^{-5} \cdot y^3 - 1.8609 \cdot 10^{-3} \cdot y^2 + 3.8007 \cdot 10^{-2} \cdot y + 300.08 \end{aligned} \tag{3.14}$$

Substituting the polynomial of Eq.3.14 in Eq.3.6 and performing the rest of the calculations finally resulted in an equivalent outer billet radius of r' = 300.18 mm.

Regarding the inner billet surface, performing the same calculations for the cylindrical segment resulted in a 7^{th} order polynomial presented in Eq.3.15:

$$\begin{aligned} f_{inner,cyl}(y) = &-1.7206 \cdot 10^{-9} \cdot y^7 + 2.6786 \cdot 10^{-7} \cdot y^6 - 1.6756 \cdot 10^{-5} \cdot y^5 \\ &+5.4143 \cdot 10^{-4} \cdot y^4 - 9.698 \cdot 10^{-3} \cdot y^3 + 9.6478 \cdot 10^{-2} \cdot y^2 - 4.9526 \cdot 10^{-1} \cdot y + 213.454 \end{aligned} \tag{3.15}$$

Using Eq.3.6 and performing the calculations with Eq.3.15 resulted in an equivalent cylindrical segment radius of $r_{eq,cyl}$ = 212.59 mm. Finally, the equivalent inner billet surface equivalent radius was calculated from a modified form of Eq.3.9. The aforementioned modification had to do with the consideration of a small square ring volume being equal to a small segment of the actual billet after the piercing process, which consisted of a hollow cylinder and a wedge-sectioned ring. The cross-sections of the aforementioned volumes are schematically presented together with the rest of the billet's volume in Fig.3.28. In

Fig.3.28, the equivalent small square ring volume is presented in blue, the small segment to be equalized is presented in green and the remaining of the billet's volume is presented in red. Additionally, the most characteristic radii are also noted in this figure.

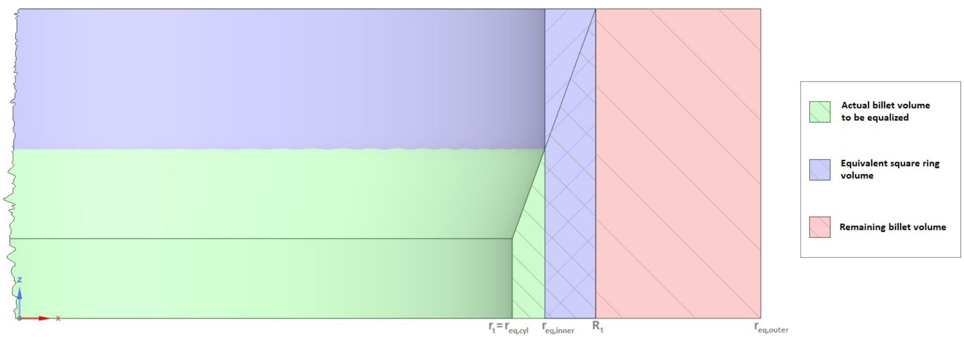

FIG. 3.28: Actual and equivalent billet volumes after piercing process

The modified equation that was used to calculate the equivalent inner billet surface radius is presented in Eq.3.16:

$$
\begin{gathered}
V_{actual} = V_{equivalent} \Leftrightarrow \\
\Leftrightarrow \pi \cdot (R_t^2 - r_{eq,inner}^2) \cdot h_f = \pi \cdot (R_t^2 - r_t^2) \cdot (h_f - h) + \pi \cdot \left[R_t^2 - \frac{1}{3} \cdot h \cdot (r_t^2 + r_t \cdot R_t + R_t^2) \right] \Leftrightarrow \\
\Leftrightarrow r_{eq,inner} = \sqrt{\frac{(3 - 2 \cdot v) \cdot r_t^2 + v \cdot r_t \cdot R_t + v \cdot R_t^2}{3}}
\end{gathered}
\tag{3.16}
$$

Thus, after substituting r_t (= $r_{eq,cyl}$), R_t and v into Eq.3.16 and performing the calculations, an equivalent inner billet surface radius of r_0 = 225.38 mm.

Finally, the resulting equivalent radii values from the simulation were compared to those calculated by the methodology presented in section 3.2.3. Initially, comparing the inner equivalent radius r_0 from the piercing model (r_0 = 225.38 mm) to the corresponding value resulting from the presented methodology ($r_{0,methodology}$ = *225 mm*), a percentage difference of approximately 0.17% could be calculated between the two values. Similarly, comparing the corresponding outer radii values from the model (r' = 300.18 mm) and the methodology ($r'_{methodology}$ = 299.54 mm), a percentage difference of 0.21% could be calculated. Both of these differences are small enough to be considered negligible, thus further validating the proposed methodology.

It is worth noting that from the comparison of r' at the end of the piercing simulation (r' = 300.18 mm) to the corresponding value at the end of the central forging simulation (r' = 299.79 mm), a small difference was observed between the two values. This indicates that during a piercing process, the billet is partially deformed as well. Given the amount of conducted billet deformation can be affected by the process parameters (mainly the piercing velocity), some additional, unpredicted material removal can occur. In such a case, some correction should be applied to the proposed methodology.

Pierced Billet Ring Rolling Test Model

After the conclusion of the piercing process test model, the newly estimated billet geometry was proceeded to a Ring Rolling model. For this simulation, the same model setup presented in detail in Chapter §2 was used, with the main difference being the initial geometry of the workpiece. As a result of the different workpiece geometry, some slight adjustments should also be made to the movement of the support rolls and the total simulation time of the model. The rest of the model parameters were the same as those presented in Chapter §2.

In the case of the initial workpiece geometry, a square ring with the following initial dimensions was considered:

- $H_0 = h_f$ = 125 mm
- r_0 = 225.38 mm
- $R_0 = r'$ = 300.18 mm

Similarly to the previous simulations, the decision to use the slightly different dimensions from the billet piercing model was so that the worst case scenario would be simulated, and thus the maximum divergence would occur at the end of the Ring Rolling simulation.

Regarding the total solution time of the simulation and given that the same constant mandrel feed velocity of $v_{mandrel}$ = 0.89 mm/s was used in the current model, solution time had to be reduced to approximately t = 27.87 s. In that way, the thickness of the ring would be reduced from t_0 = 74.8 mm to its final value of t_f = 50 mm, as this can be estimated from the target dimensions of the ring ($D_f \times d_f \times H_f$ = 900 × 800 × 115). The total process time was then increased by approximately 10 s, in order to achieve thickness normalization during phase 4 of the Ring Rolling process, as well as to close any initial gap before the beginning of the process. Finally, the total simulation time was set as *ENDTIM* = 37.87 s in the *CONTROL_TERMINATION* menu.

Finally, the movement of support rolls had to be properly adjusted. In order to determine the power law that governed the movement of support rolls (also see section §2.9), a number of trial runs were performed. After the trial – and – error procedure was completed, the ring growth algorithm, which the movement of support rolls was based on (Eqs.2.61 and 2.62) was that presented in Eqs.3.17 (for Ring Rolling Phases 1 and 2) and 3.18 (for Ring Rolling Phase 3):

$$R_i = 3.6974 \cdot 10^{-1} \cdot t^{1.7} + 295.607 \tag{3.17}$$

$$R_i = -4.8294 \cdot 10^{-1} \cdot t^2 + 36.8365 \cdot t - 252.331 \tag{3.18}$$

Afterward, the simulation was solved, and its results were subsequently evaluated. The state of the model at the end of the process is presented in Fig.3.29.

From the result of the Ring Rolling methodology evaluation model, the final dimensions were mainly focused on. Likewise, Chapter §2, the average curves of the outer and inner radii, as well as the average height of ring results were evaluated. The aforementioned results were also compared to the corresponding experimental results from **Zhu et al., 2016b**, in order to evaluate both the overall evolution of each dimension and the final values estimated from each method. The outer and inner radii comparisons and the average ring height comparison are presented in Fig.3.30, 3.31 and 3.32, respectively:

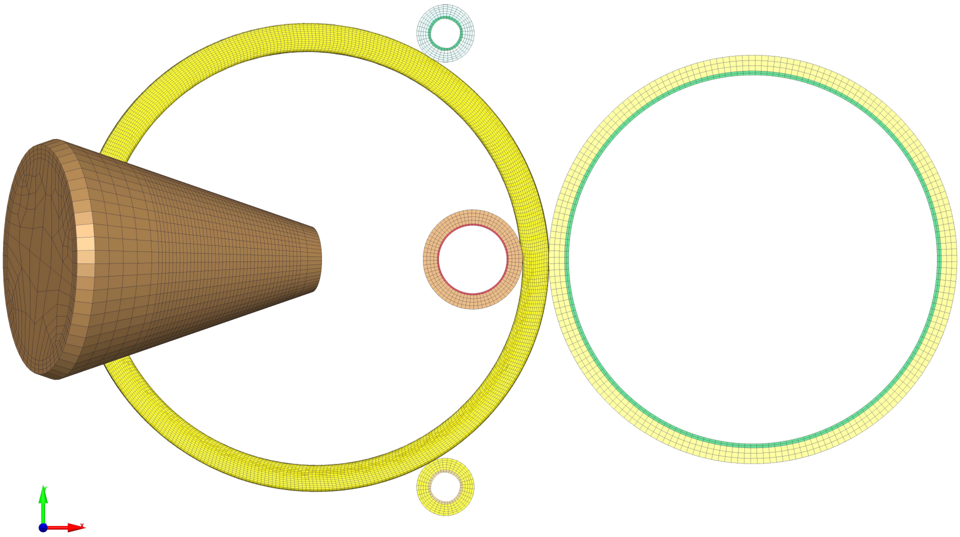

FIG. 3.29: Final state of the Ring Rolling evaluation model of the billet volume calculation methodology

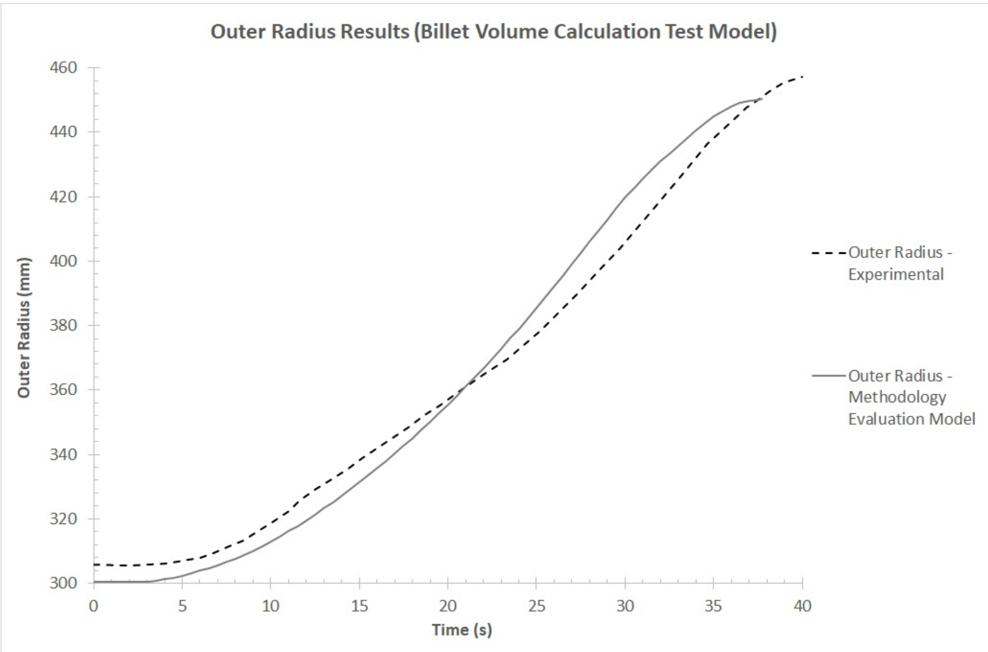

FIG. 3.30: Billet volume calculation methodology and experimental outer radius result curves

Observations over Fig.3.30 revealed differences between the two methods, as was expected. More specifically, and apart from the different terminations of the two curves, which were expected given the different initial dimensions, a slightly different growth rate was observed. In the case of the experimental curve, a more sudden radius evolution could be seen during the early stages of the process, which was reduced during the middle part of the process and was subsequently increased again after t = 25 s, approximately. On the other hand, the outer ring radius from the Ring Rolling model increased steadily during most of the process's duration, with no significant changes in its growth rate. Regarding the final outer radius values from the two methods, an outer radius of R_f = 450.23 mm was

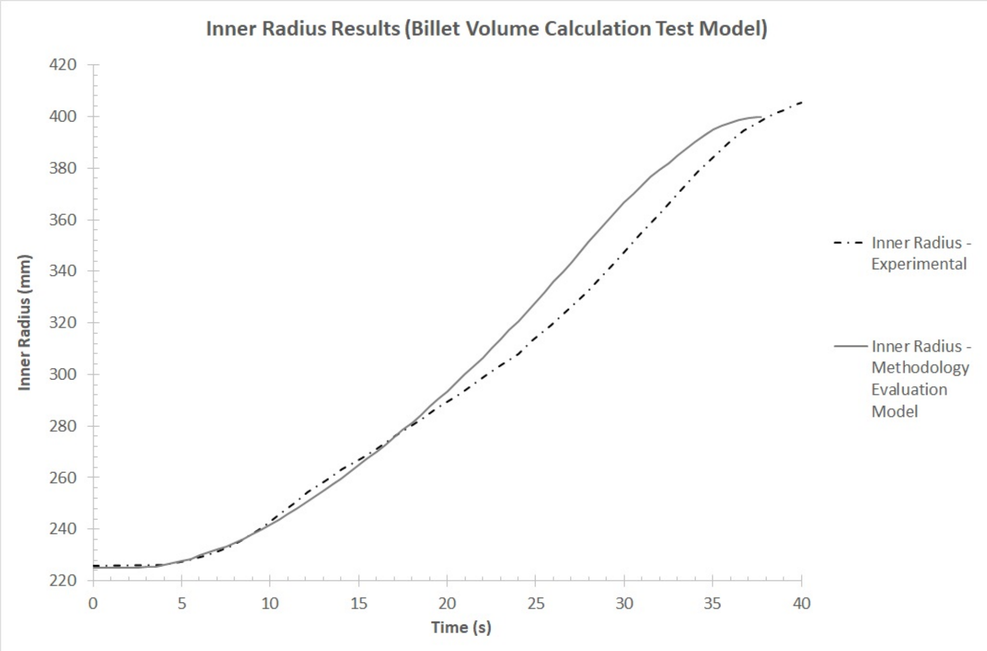

FIG. 3.31: Billet volume calculation methodology and experimental inner radius result curves

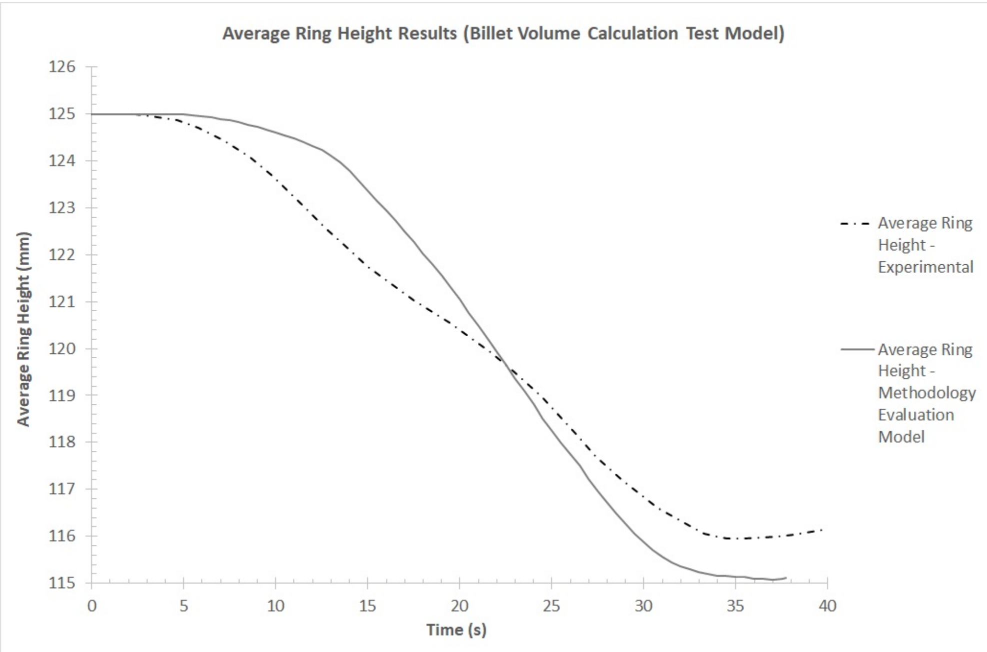

FIG. 3.32: Billet volume calculation methodology and experimental average ring height result curves

recorded at the end of the numerical model, while the corresponding value was approximately $R_{f,experimental}$ = 457.35 mm at the end of the experiment. From the comparisons of these values to the target outer ring radius mentioned by, Zhu et al. ($R_{f,target}$ = 450 mm) it can be concluded that the proposed methodology produced a very close result, which overshoot the target value only by 0.05%. On the contrary, the corresponding percentage difference of the experiment value was approximately 1.63%, which, although close enough, should require additional manufacturing to reach the target outer radius.

In the case of Fig.3.31, similar conclusions to those of the outer ring radius could be drawn. Initially, the same differences in the inner radius growth rates were observed between the two method. What is more, the final inner radii values from the two methods were r_f = 399.72 mm and $r_{f,experimental}$ = 405.18 mm, respectively. Compared to the target inner radius value of $r_{f,target}$ = 400 mm, percentage differences of 0.07% to the numerical model and 1.3% to the experimental process were observed. Similarly to the conclusions drawn for the outer ring radius, both of these percentage differences were relatively small, however the overshoot of the experimental inner radius beyond the target value may be considered unacceptable for some product applications.

Finally, in the case of the average height results (Fig.3.32), a similar behavior to that of the other two dimensions was observed. The height reduction rate during the experiment was not constant throughout the process's duration, while the average height reduction rate during the simulation was mostly constant. The final average ring height values from the experimental and the numerical results were approximately $H_{f,experimental}$ = 116.2 mm and H_f = 115.1 mm, respectively. Comparing these values to the target average ring height of $H_{f,target}$ = 115 mm led to percentage differences of 1.04% and 0.09%, respectively. In practice, both of these percentage differences are small enough that they can be considered negligible.

Overall, the final results of the Ring Rolling model proved that the proposed methodology led to a product with high dimensional accuracy, compared to the requirements that were initially considered.

Thermal shrinkage during cooling

The main goal of the current analysis was to achieve a dimensional precision of the final workpiece, based on the results provided by Zhu et al. However, in **Zhu et al., 2016b** the author describe their process up to the end of hot Ring Rolling. In an actual Ring Rolling process, the ring may continue to rotate with a constant or increased rotational velocity and with additional cooling after the final thickness has been normalized throughout the ring's perimeter. In order to evaluate the amount of dimensional shrinkage during the cooling of the workpiece, a separate numerical model was prepared and solved.

In this simulation, the final model setup of the methodology evaluation analysis was used. The final geometry of the ring and all tools in their final positions were input in the model and a simple rotation of the ring was applied. The rotational velocity was equal to that presented in Chapter §2, due to the lack of corresponding experimental data. Furthermore, the majority of model parameters and options were maintained. The only differences were the initial temperature of the workpiece and the tools, as well as a slight movement of the support rolls, so that they could follow the shrinkage of the workpiece. More specifically, the initial temperature of the ring was equal to $T_{i,shrink,ring}$ = 1250.5 K, while the initial temperature of all tools was considered equal to $T_{i,shrink,tools}$ = 298.15 K. It should be noted that the tool temperature remained constant throughout the current simulation, in order to achieve a ring temperature decrease to room temperature. In an actual Ring Rolling process, this can be achieved with excessive outer cooling of the tools combined with inner tool cooling. Once again, the initial temperatures were input in the model using the *TEMP* option of the INITIAL_TEMPERATURE_SET menu. Regarding the movement of the support rolls, it was based on the ring shrinkage algorithm that was determined after a few trial models. The aforementioned ring shrinkage law is given in Eq.3.19:

$$R_{shrink} = -3.3146 \cdot 10^{-3} \cdot t + 450.23 \tag{3.19}$$

Likewise previous Ring Rolling simulations the movement coordinated of the support rolls were then calculated by substituting Eq.3.19 in Eqs.2.61 and 2.62.

The total simulation time was approximately t_{shrink} = 2098 s. The author of the current dissertation recognizes that such process times are not realistic in practice, and that it would be significantly reduced with additional cooling. However, since the thermal behavior of the workpiece can be affected by multiple physical parameters and in multiple alternative ways, maintaining the same cooling in the model was finally chosen for simplicity. It is worth saying that the total solution time was reduced by enabling a non-linear, thermal solution for the model (*SOLN* = 1 option in CONTROL_SOLUTION menu) and by imposing a greater thermal timestep (*ITS* = 1.0 option in CONTROL_THERMAL_TIMESTEP menu).

After the model was solved, its results were inspected for errors. In order to evaluate the dimensional divergence due to thermal shrinkage, the outer and inner radii, as well as the average ring height versus temperature curves were extracted, and they are presented in Figs.3.33–3.34:

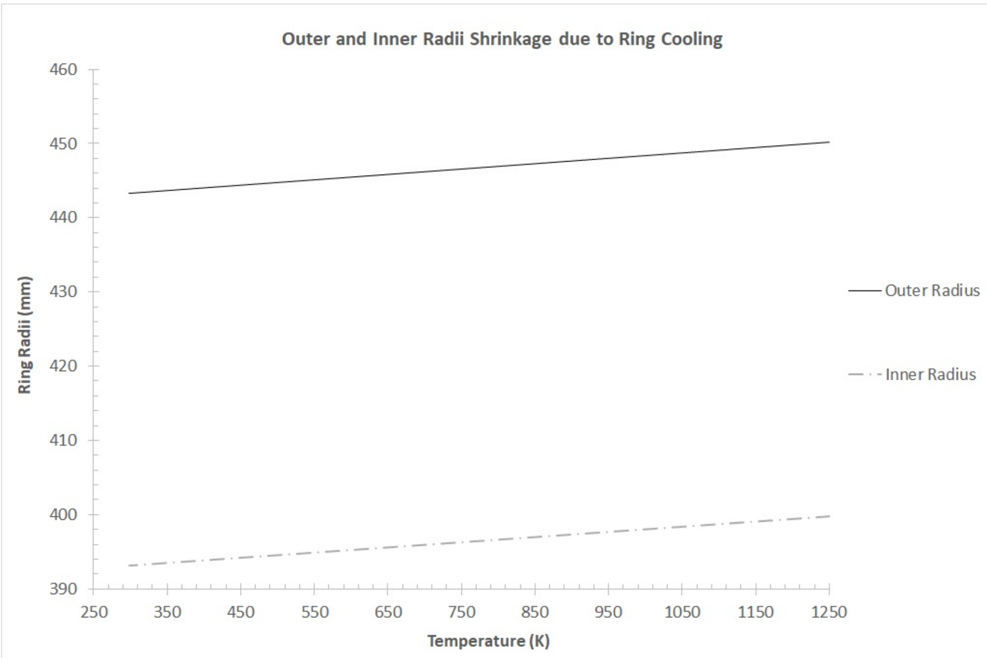

FIG. 3.33: Outer and inner radii shrinkage due to ring cooling

Observations over Figs.3.33 and 3.34 reveal an expected behavior. In the case of the outer and inner ring radii (Fig.3.33), both dimensions were reducing with the temperature reduction, with an almost linear rate (although different between one another). The maximum outer radius shrinkage at room temperature (T_{room} = 298.15 K) was approximately ΔR_{shrink} = 6.95 mm, while the corresponding shrinkage for the inner radii was approximately Δr_{shrink} = 6.59 mm. On the other hand, and regarding the average ring height shrinkage, an almost linear reduction was observed in this case, too, with the maximum height shrinkage at room temperature being approximately ΔH_{shrink} = 4.31 mm. The combination of these individual shrinkages add up to a volumetric shrinkage of approximately 4.06% at room temperature.

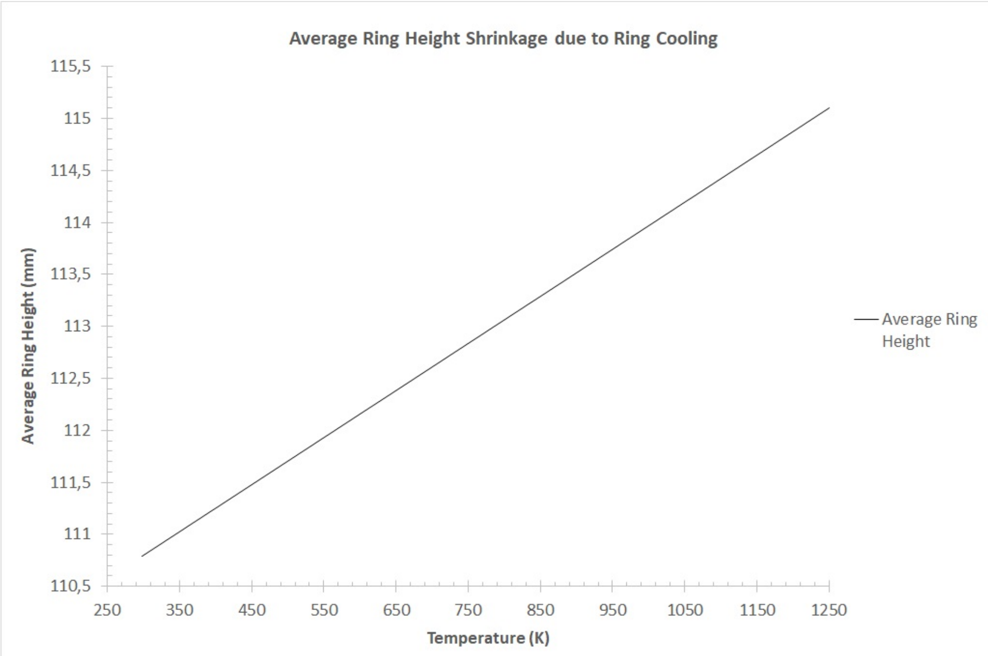

FIG. 3.34: Average ring height shrinkage due to ring cooling

Similar volumetric percentage shrinkage values have been reported in literature (**Kumar and Jebaraj, 2021**), in the case of IN718 samples.

Such dimensional differences are relatively large, and they should be taken into account when designing a Ring Rolling process production and calculating the initial volume of the workpiece. More specifically, this can be introduced as an overestimation of the initial billet volume, close or equal to the resulting percentage volumetric shrinkage.

3.2.5 Initial Billet Volume Precision Results Evaluation

The methodology presented in the current section of the dissertation was proposed as a helping tool for a better initial billet volume calculation. In that way, the dimensions of the final product would be much closer to those requested, and thus less corrective post-processing would be required after Ring Rolling. Additionally, since common ring productions are a result of serial production lines and given that there are three different manufacturing processes that take place before Ring Rolling, any dimensional error occurring during an early process would be passed to the next steps of the production chain. This point should be taken under consideration, as small dimensions divergences during an early step of the production may lead to larger forming defects in subsequent processes.

From the conducted analysis, the proposed methodology seemed to be validated with a good level of agreement between the predicted workpiece dimensions and the results of the corresponding numerical models. Moreover, the most important factors for each of these processes were identified and can be summed up as follows:

- In the case of the billet upsetting process, a good estimation of the upsetting factor B is considered essential. From the conducted analysis, pre – upsetting billet height and tool – to – billet friction coefficients seemed to be the most affecting parameters for B.
- Regarding the central forging process, the number of forging steps, as well as tool velocity had the greatest influence on the final billet geometry. Especially in the case

of tool velocity, in case a small enough value cannot be applied, performing the same process as closed – die forging should be considered, in order to reduce potential forming defects (e.g. dishing).

- In billet piercing and similarly to the central forging process, tool velocity was the most affecting factor. In case tool velocity is very high, a combined mechanism of forming and piercing takes place, thus any attempt of predicting the final volume of the pierced workpiece will be very difficult. Additionally, the use of a counter – punch is heavily advised, in order to further reduce potential forming defects and to achieve better billet quality (e.g. no burr formation).
- Finally, during the Ring Rolling process and as it was previously mentioned in Chapter §2, tool movement seems to be one of the most crucial parameters. A faulty movement of the Ring Rolling tools may lead to severe forming defects that more often than not cannot be reversed in any way.
- It is important to remember that a volumetric overestimation of the billet should be performed, in order to compensate for the shrinkage of the produced workpiece due to its cooling to room temperature.

Overall, the close results between the volume calculations and the numerical models were an important step towards producing more dimensionally precise ring products. Although the dimensions of the final product in the conducted test were almost identical to those initially set as target, the author of the current dissertation would recommend towards a slight initial volume increase. The main reason for this correction would be to compensate for some material losses that may occur (e.g. due to scaling or imprecise piercing), as well as minor volume inconsistencies innate to the numerical modeling process (especially if this tool is facilitated as a part of the production). The amount of this volume increase should be decided based on the importance of the product's dimensional precision, as well as the capability and cost of further post-processing the products.

3.3 Thermal Expansion and Elastic Deformation of the Tools

Apart from the preceding processes that affect the dimensional accuracy of the final ring product, various parameters of Ring Rolling can cause deviations in the quality of the ring. Examples of such parameters are the elastic deformation of tools and their thermal expansion during Ring Rolling. These parameters have not been investigated in Ring Rolling thoroughly, while in most simulations of the process, tools are considered perfectly rigid. Thus, in the current section, a numerical investigation regarding the effects of elastic deformation and thermal expansion of tools is conducted.

For this investigation, three distinct numerical models had to be simulated:

1. One with undeformable tools
2. Another where tools can deform but the thermal expansion of the rolls was omitted
3. The last one where the tool can deform, and their thermal expansion was considered

In that way, the effects from the deformation and displacement of the rolls can be separated from the deformation caused by their thermal expansion. Numerical modeling is the only possible method that can be used to perform the aforementioned investigation, as the isolation of the thermal expansion of rolls is impossible in an experimental approach.

The presented investigation consists of two separate parts. In the first part, a comparison between a FE model with elastic tools but without considering their thermal expansion (mentioned hereafter as *NO_TE model*) and another with perfectly undeformable tools (mentioned hereafter as *R model*) is performed to evaluate the effects of tool elastic deformation in the process. In the second part, a comparison between the *NO_TE model* and another with the thermal expansion considered (mentioned hereafter as *TE model*), is conducted to evaluate the effects of tool thermal expansion in the process. The anticipated roll deformations during Ring Rolling for each model are quite different from one another and are roughly (and in an exaggerated degree) presented in Fig.3.35:

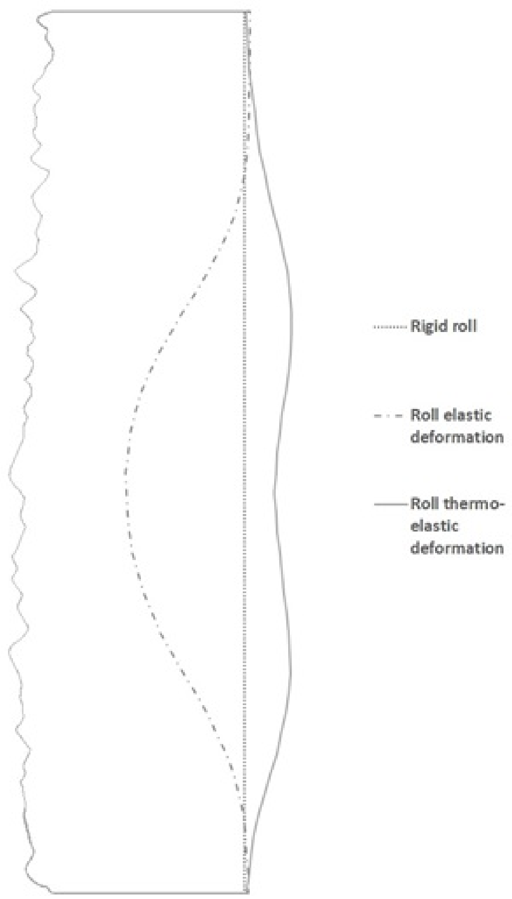

FIG. 3.35: Anticipated roll deformations during Ring Rolling in each model

In Fig.3.35, the anticipated elastic roll deformations in this process are a result of the Hertz type of contact between the tool and the ring. The addition of thermal expansion on the tools lead the same Hertz type contacts to become more localized, with the total roll deformation in this case to vary, depending on the roll – ring material combination. In the current analysis and seeing that the anticipated deformation profiles were not constant throughout the height of the rolls, the average radii for the roll in both the elastic and thermo-elastic models were considered.

It is worth noting that the current subsection was also published as a scientific article (**Pressas, Papaefthymiou, and Manolakos, 2022**).

3.3.1 Numerical Model Setups

Regarding the conducted simulations, the one presented in Chapter §2 was used as the *R model*. For the other two models and in order to make up for the different properties of the tools required in the current analysis, most roll were simulated as two-layered bodies. The inner layer of these rolls were perfectly rigid, but smaller in dimensions from those given in Table 2.1. Thus, the tool velocities could be properly set, without variation due to the tools' deformation. On the other hand, the outer layer of the rolls reached up to the outer dimensions mentioned in Table 2.1, with their corresponding mechanical properties being carefully selected to properly represent each model. The only exceptions were the conical rolls, which were considered as deformable, and a rigid "motor" body was added on each of their corresponding large diameter ends. In order to separate the non-thermal expansion from the thermal expansion models, an elastoplastic material numerical routine with zero thermal expansion coefficients was selected for *NO_TE model* (MAT_106-ELASTIC_VISCOPLASTIC_THERMAL) and the same elastoplastic routine but with the appropriate thermal expansion coefficients was selected for *TE model*. The initial geometries of the ring and rolls are presented in Fig.3.36:

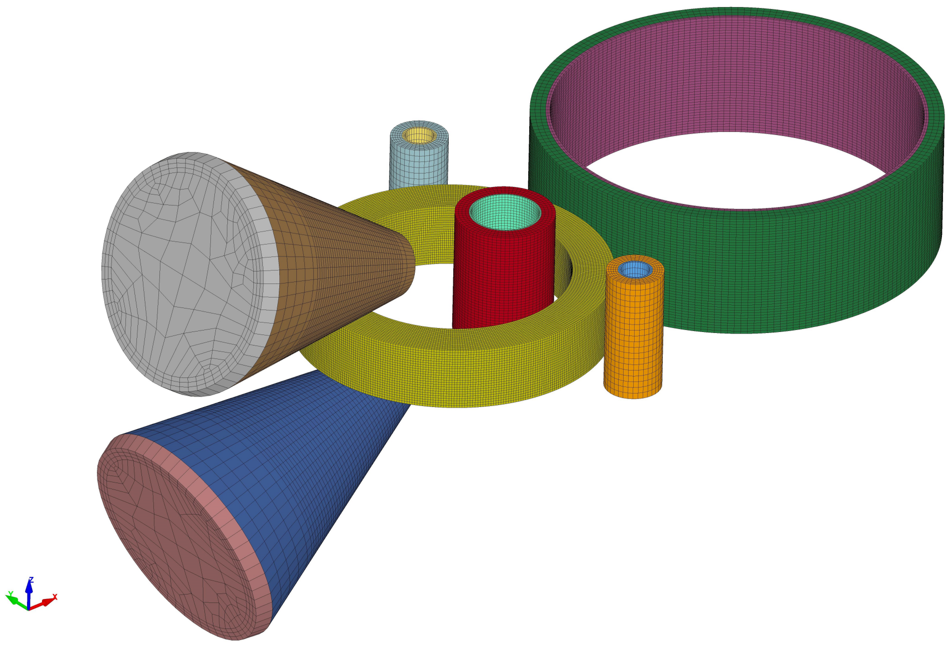

FIG. 3.36: Modified numerical model setup for the tool elastic deformation and thermal expansion analysis

Regarding the material properties of the tools, the material properties presented in Table 2.4 were used in the case of rigid bodies, while the corresponding properties for the deformable rolls had to be estimated. The mechanical properties used for the deformable tools in the current analysis are presented in Table 3.4 and in Figs.3.37-3.41, while the thermal properties previously presented in Figs. 2.16 and 2.17 from Chapter §2 were used for every tool in the analysis:

TABLE 3.4: Material elastic thermo-plastic properties (AISI H13)

Property	Value or Curve	Reference
AISI H13		
Density, d (kg m^{-3})	Fig.3.37	*Oh and Ki, 2019*
Young's Modulus, E (GPa)	Fig.3.38	*Tolcha and Lemu, 2019*
Poisson's Ratio, v^*	Fig.3.39	*Tolcha and Lemu, 2019*
Yield Strength, σ_Y (MPa)	Fig.3.40	*Uddeholm, 2020*
Coef. of Th. Expansion, α $\left(\cdot(10^{-6})\ \mathrm{K}^{-1}\right)$	Fig.3.41	*Tolcha and Lemu, 2019*
Thermal Conductivity, K (W m^{-1} K^{-1})	Fig.2.16	*Tolcha and Lemu, 2019*
Specific Heat Capacity, C (J kg^{-1} K^{-1})	Fig.2.17	*Oh and Ki, 2019*

*For the estimation of Poisson's ratio vs temperature for AISI H13, the equation $v = \frac{E}{(2 \cdot G)-1}$ (**Frost and Ashby, 1982**) was used, based on the Shear Modulus, G and Young's Modulus, E data received from **Tolcha and Lemu, 2019**.

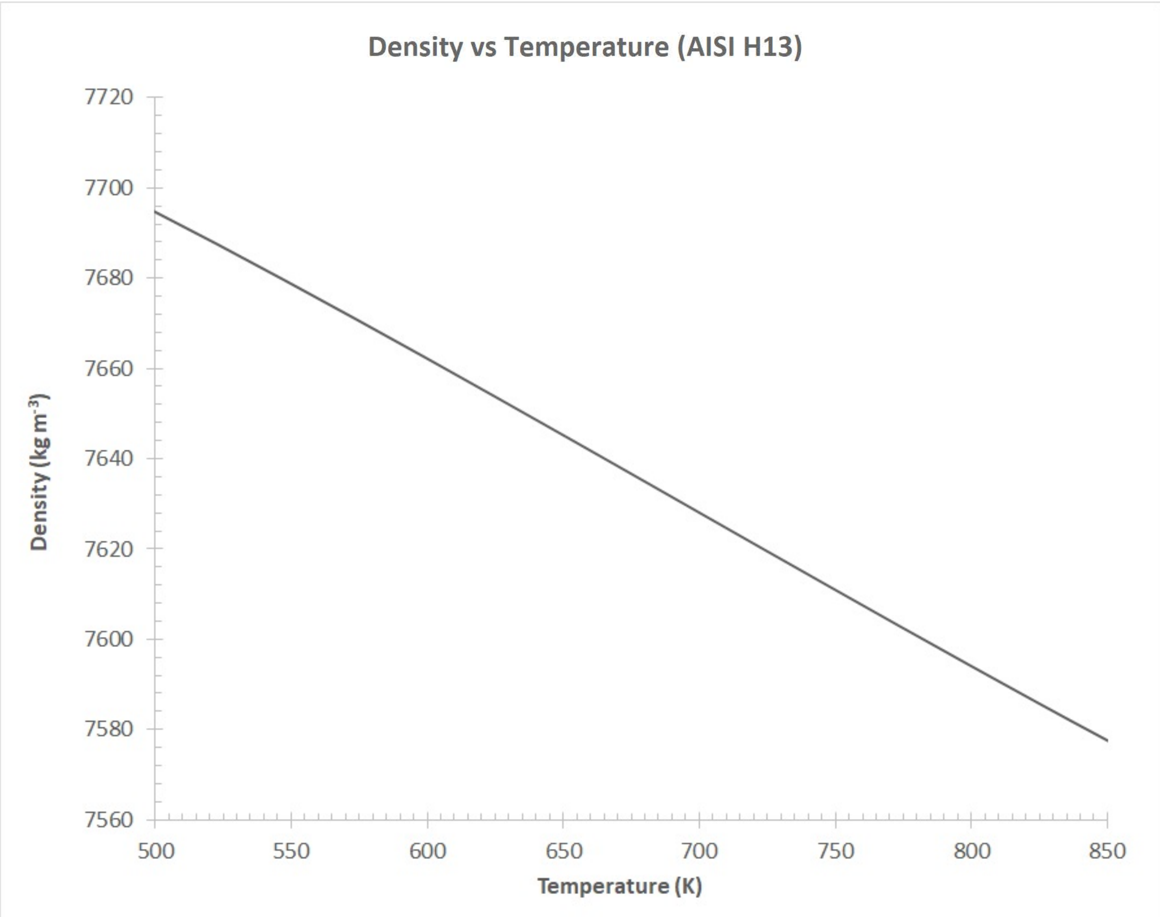

FIG. 3.37: Density versus temperature (AISI H13 steel)

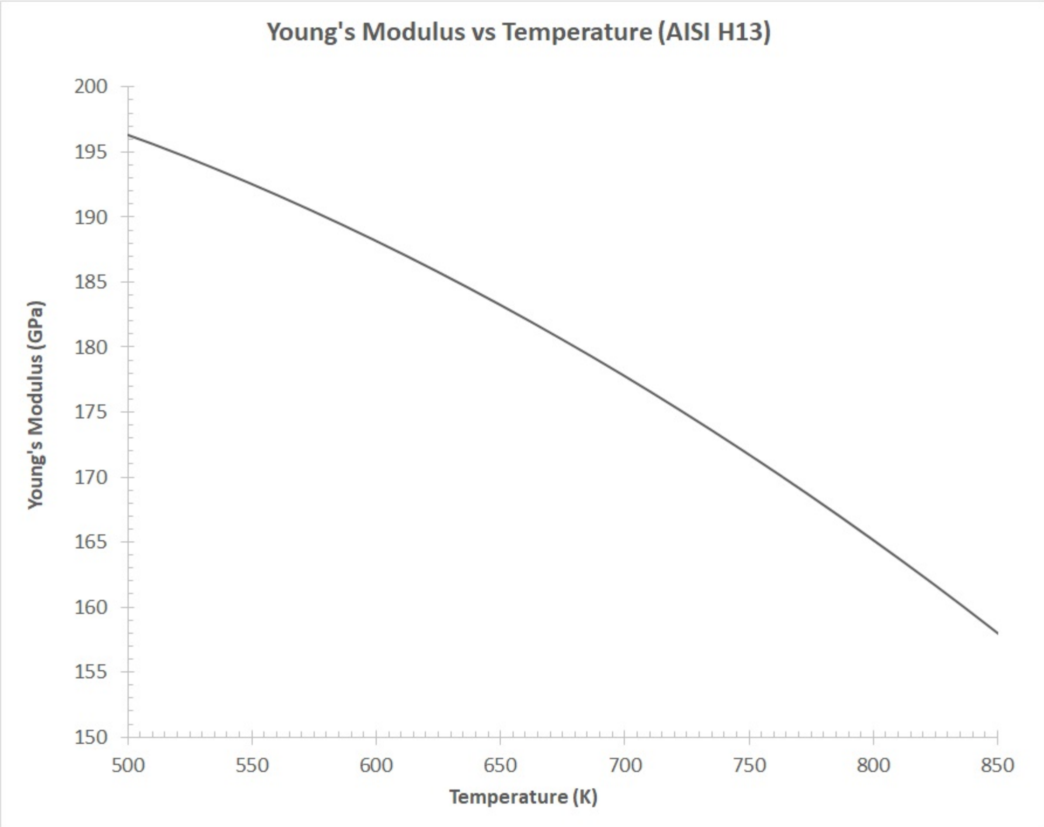

FIG. 3.38: Young's Modulus versus temperature (AISI H13 steel)

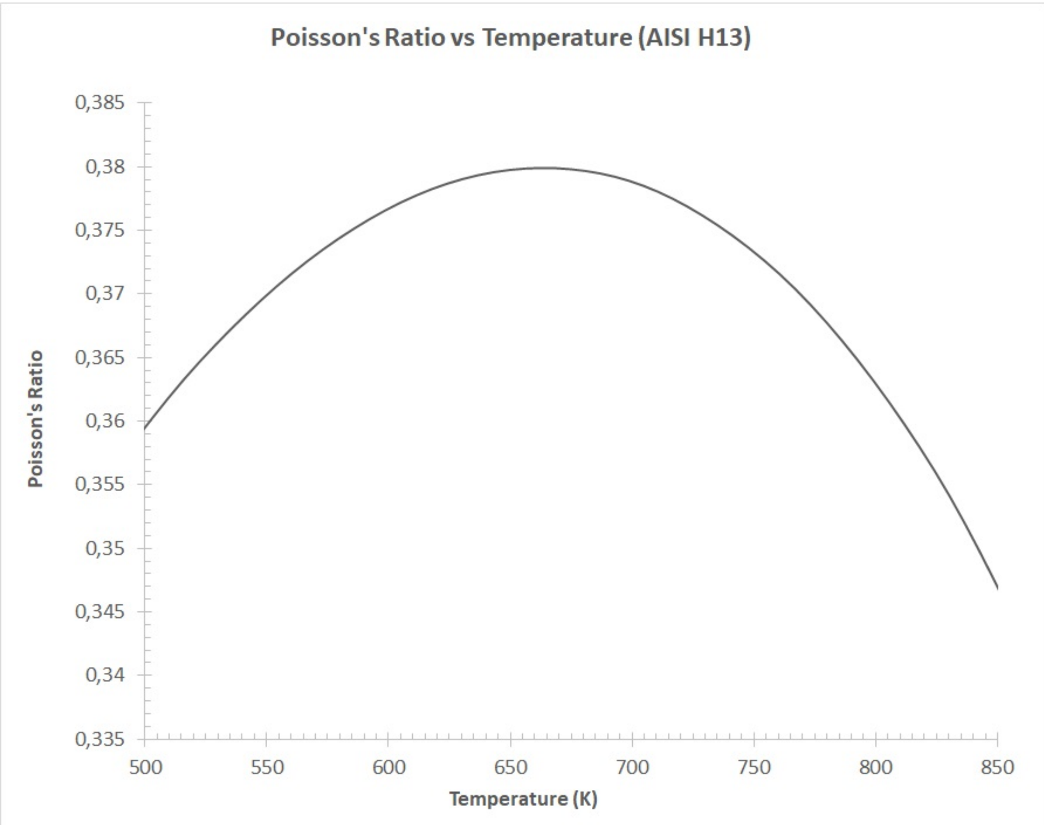

FIG. 3.39: Poisson's Ratio versus temperature (AISI H13 steel)

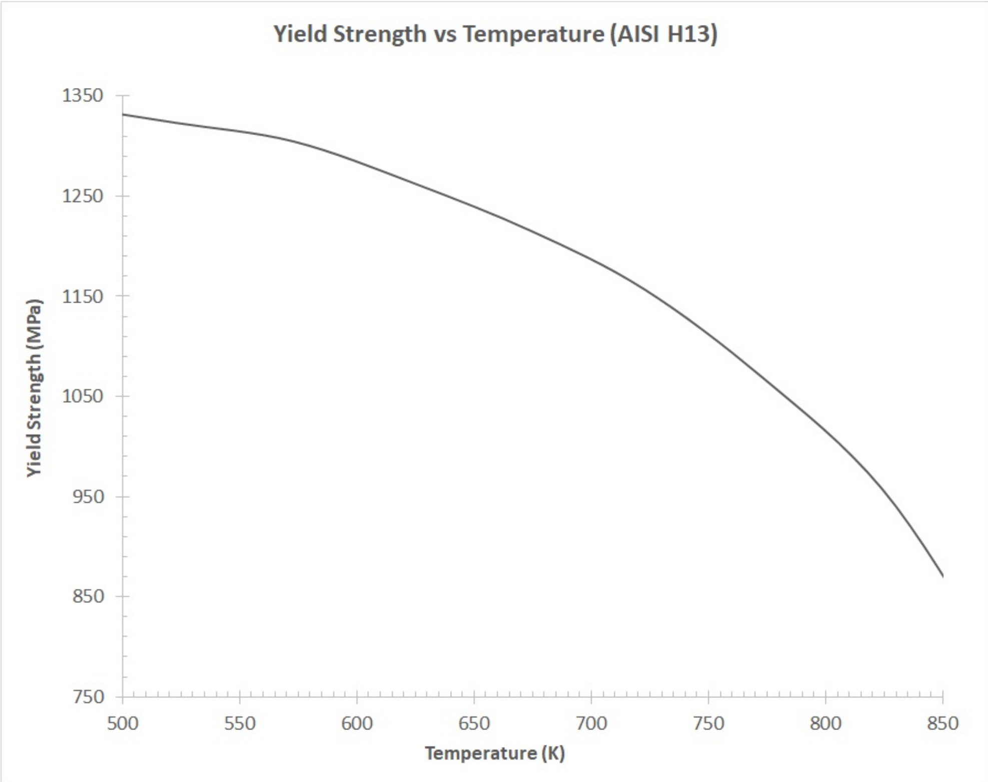

FIG. 3.40: Yield Strength versus temperature (AISI H13 steel)

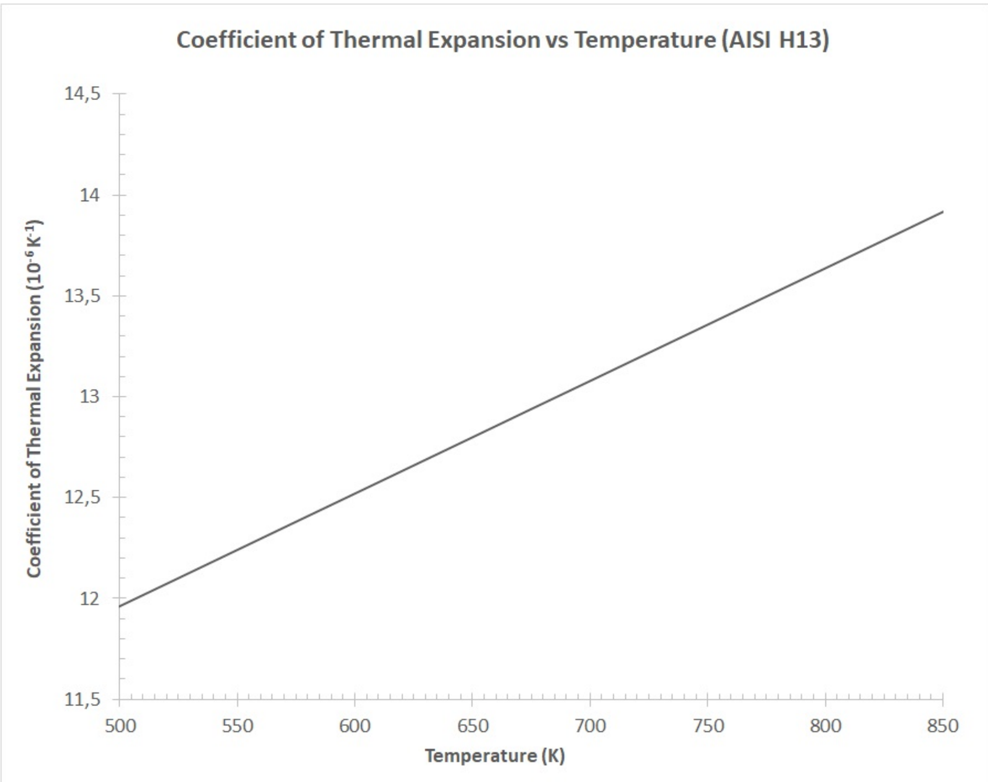

FIG. 3.41: Coefficient of Thermal Expansion versus temperature (AISI H13 steel)

The rest of the numerical model setup remained the same as the one presented in Chapter §2, regardless of the thermal behavior of the tools. Additionally, the mechanical and thermal properties previously presented in Section §2.6 (Table 2.3) were used for the ring in all the conducted simulations of the current analysis.

The solution of each numerical model lasted approximately 300 – 320h, on an Intel Core i7-4790, 32 GB RAM computer with an SSD disk for greater read/ write speeds.

3.3.2 Numerical Model Results and Result Comparisons

After the models were solved and their results were validated and inspected for errors, their comparison was performed. The evaluation of the effects brought by tool elasticity and thermal expansion were investigated through some key properties of the process, namely the dimensions of the produced ring, the main ring rolling force and the conical rolling force. Furthermore, the profile of the tools due to their elastic and thermal deformations were measured in order to correlate them to the ring deformation results. For the measurement of the ring and tool diameters (both inner and outer), twelve sets of diameter results were exported, and the mean diameter results were subsequently calculated. On the other hand, the load results were exported directly from the software.

Before proceeding with the comparisons of the numerical results from the different models, the stress and temperature distributions on each roll will be briefly discussed. Although the author acknowledges that stress and temperature distributions are different at the beginning (Phase 1 in Fig.1.2) and the end of the process (Phase 3 in Fig.1.2), further analyzing them is beyond the scopes of the current analysis.

Stress and Temperature Distributions on the Deformable Tools

In order to analyze the stress and temperature distributions on each tool, the corresponding fields at a timestep of t = 20.5 s were extracted, and they are presented in Figs.3.42 and 3.43, respectively. The stress and temperature fields at this timestep are indicative of the steady–state deformation Phase of Ring Rolling (Phase 2 in Fig.1.2).

In the case of the stress distributions on the tools at t = 20.5 s, these are presented in Fig.3.42:

Observations over Fig.3.42 reveal rather expected stress fields on all the tools. It should be noted that the stress fields presented in Figs.3.42 are focused around the respective contact of each tool with the ring. Also, the color scale in Figs.3.42(a)-(c) was chosen to be the same, to have some kind of comparison, while the color scale in Figs.3.42(d) and (e) was different, in order to avoid shadowing effects on the presented stress fields.

In Fig.3.42(a) the stress fields on the main roll have a mostly linear distribution with two larger areas at its ends. These larger areas are a result of the bulging deformation, created previously in the conical roll bite (**Zhou et al., 2011a**). Additionally, the high – intensity stresses appearing on the aforementioned areas are a result of the increased pressure required to iron out the formed bulges.

Mostly identical, in terms of distribution, stress fields can also be observed on the mandrel (Fig.3.42(b)). The main difference between these two tools lies with the stress fields on the mandrel, after the ring exits main rolling bite (left side of Fig.3.42(b)). These stress fields are heat–related and can be attributed to the mandrel's heating by the much hotter

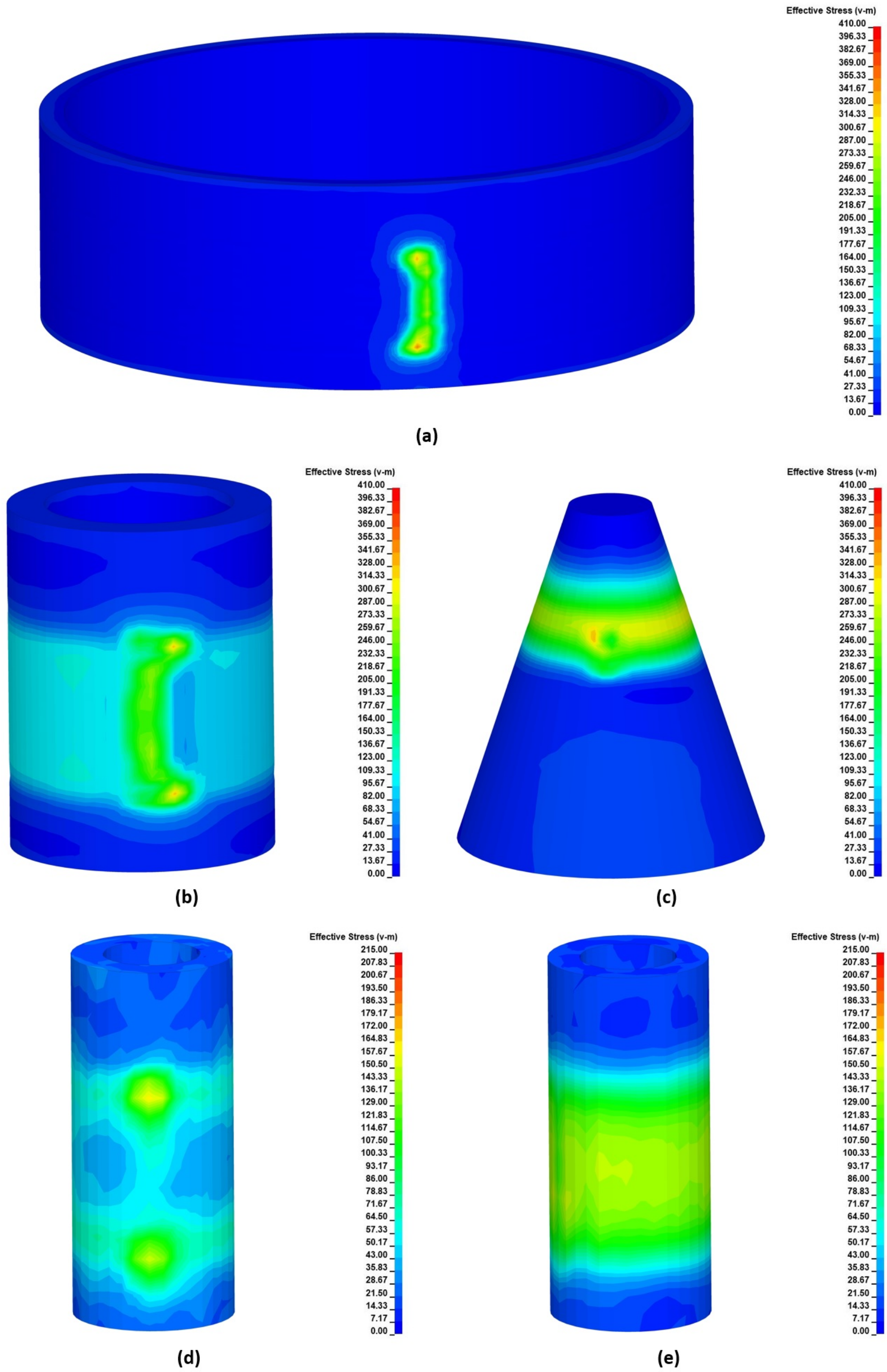

FIG. 3.42: Calculated stress fields on process tools (t = 20.5 s): (a) main roll, (b) mandrel, (c) conical roll (top), (d) support roll 1 and (e) support roll 2

ring. As the mandrel continues to revolve, a part of this heat is lost due to convection and radiation, thus less intense stress fields can be seen on the mandrel near the entrance to the main rolling bite (right side of Fig.3.42(b)). Moreover, two smaller heat–related stress fields are visible around the initial contact with the ring bulges (right side of Fig.3.42(b)), indicating that the ironing of the latter begins prior to the deformation of the rest of the ring. It is worth noting that similar heat–related stress fields are only partially visible on the main roll (Fig.3.42(a)), as its increased mass requires a greater amount of conducted heat in order to have a temperature increase with similar effects.

The stress fields on both conical rolls are mostly identical, thus only the top conical roll is presented in Fig.3.42(c). Near the entrance of the ring to the conical rolling bite (left side of Fig.3.42(c)), the induced stress fields are narrower, while the corresponding stress fields after the conical rolling bite are wider (right side of Fig.3.42(c)). This fact can be attributed to the formation of bulges by the conical roll bite, which makes the contact area between the ring and the conical rolls wider. Right before the ring's entrance to the bite, some high–intensity stress fields can be observed in a semicircular distribution. This specific stress distribution is a result of the fishtail defect edges **Giorleo, Ceretti, and Giardini, 2012** being deformed prior to the rest of the ring. Additionally, in the ring height decrease zone, high – intensity stress fields can be seen in the entire contact length between the ring and the conical roll. These stress fields can be seen extending beyond the height decrease zone, as a result of heat–related induced stresses. Generally, heat–related stress fields can be seen covering the entire perimeter of the conical roll's working zone, although their intensity reduces along the roll's rotation. Furthermore, some relatively high–intensity stress fields are visible towards the minimum diameter of the conical roll, where no stress would be expected. These specific stress fields are a result of heat–related stresses induced at previous timesteps. More specifically, during the process the ring's diameter increases, causing different segments of the conical roll to come in contact with the ring. Thus, the previously heated segments of the conical rolls seem to retain some of the heat–related induced stresses.

Finally, in Figs.3.42(d) and 3.42(e) the stress fields on the support rolls are presented. From the comparison between the two, significant differences can be observed, and thus each roll is analyzed separately below. Regarding the stress fields on support roll 1 (Fig.3.42(d)), two distinct high–intensity stress fields can be observed around the segments where the ring bulges come in contact with this tool. This is a result of a partial ironing of the bulges made by support roll 1. The stress values on the rest of support roll 1 are not so high, indicating a not so intense contact with the ring. Furthermore, the difference observed between the two high–intensity stress fields in terms of stress values, indicates an unsymmetrical formation of the bulges, which can be attributed to the top conical roll being the only one moving towards the ring in the conical roll bite.

On the other hand, the observed stress fields on support roll 2 (Fig.3.42(e)) are rather uniform. The stress intensity is mostly constant in the entirety of the roll's body, which is a result of the ring being constantly pressed against support roll 2. Additionally, the increased interface pressure between the two bodies increases the amount of conducted heat (**Shvets and Dyban, 1964**). As a result, intensified heat–related stress fields can be observed in the entire perimeter of support roll 2 compared to those of support roll 1 (Fig.3.42(d)).

Regarding the temperature distributions on the tools at t = 20.5 s, these are presented in Fig.3.43:

Observations over Fig.3.43 reveal expected temperature distributions on all tools. In this case, too, it should be noted that the temperature fields presented in Fig.3.43 are focused around the respective contact of each tool with the ring. Additionally, each instance in Fig.3.43 has its own color scale, in order to avoid shadowing effects on the results by using a single color scale.

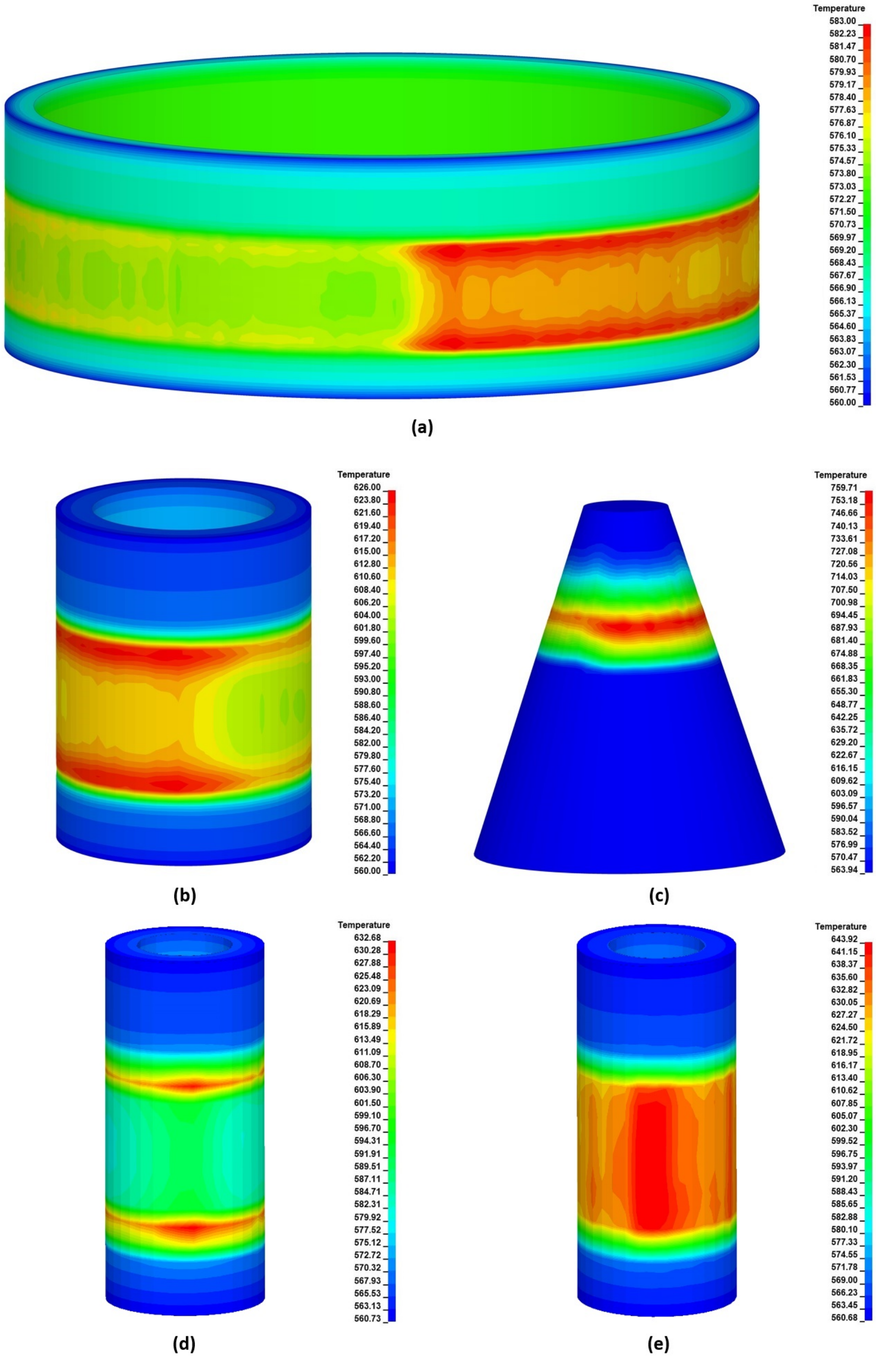

FIG. 3.43: Calculated temperature fields on process tools (t = 20.5 s): (a) main roll, (b) mandrel, (c) conical roll (top), (d) support roll 1 and (e) support roll 2

In Fig.3.43(a), the temperature distribution on the main roll is presented. The main roll is heated around the contact area with the ring, while part of this heat is progressively lost during its rotation. Moreover, the areas where the bulges are ironed present the highest calculated temperature values, as a result of the increased plastic work–turned–to–heat required to deform the increased material volume of these ring segments. As it is expected, the working area of the main roll is warmer than the rest of its body, even if the conducted heat is progressively lost from the segments that are not currently in contact with the ring.

Similar observations to those of the main roll can be made for the mandrel (Fig.3.43(b)). In this case too, the mandrel is heated around the contact area with the ring, with the conducted heat being progressively lost during its rotation. Also, the areas around the ring bulges are warmer.

In the case of the temperature distribution on the top conical roll (Fig.3.43(c)), a temperature increase can be observed around the contact area with the ring. Furthermore, the high–temperature area becomes wider around and after the bite segment, because of the widening of the ring (bulge formation). Additionally, the conical roll segments towards its minimum diameter are warmer, as a result of their contact with the ring during previous time instances.

Finally, the temperature distribution on the support rolls (Figs.3.43(d) and (e)), validate the observations previously made from their respective stress distributions (Figs.3.42(d) and (e)). Thus, support roll 1 is warmer around its contact areas with the ring bulges and colder in the rest of its body, as a result of a not so intense contact with the ring. On the other hand, support roll 2 has increased temperature throughout its working area, with the highest temperature values observed around the contact area with the ring.

R model **- to -** *NO_TE model* **Results Comparison**

Initially, a comparison between the *R model* and the *NO_TE model*, regarding the outer and inner diameters of the ring, was performed. In Fig.3.44, the presented curves are a result of subtraction of the outer and inner ring diameter curves of the *R model* from the corresponding curves of the *NO_TE model*.

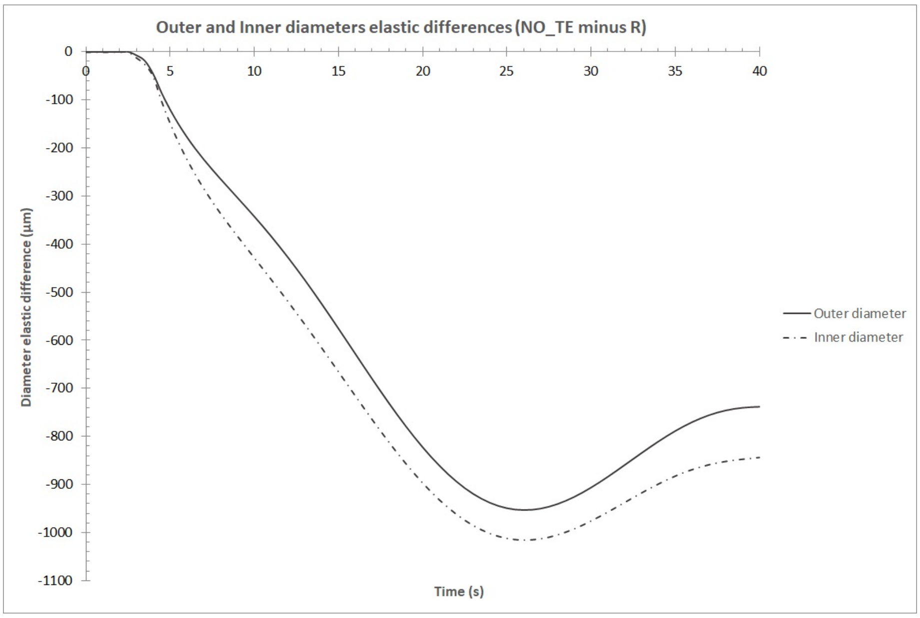

FIG. 3.44: Outer and inner ring diameters elastic differences

In Figs.3.44, the elastic differences in both the outer and the inner diameters of the ring in the two models were observed. More specifically, the outer diameter of the ring in the *R model* was greater than the one in the *NO_TE model* model throughout the process duration, with the difference reaching 0.738 mm at the end of the process, while the maximum difference between the two was approximately 0.953 mm and at t = 26 s. Similarly, a difference of 0.844 mm at the end of the process was observed between the inner ring diameters of the two models, with the maximum difference reaching 1.015 mm at a time of t = 26 s.

In Fig.3.45, a curve resulting from the difference of the average ring height in the *NO_TE model* minus the average ring height in the *R model* is presented:

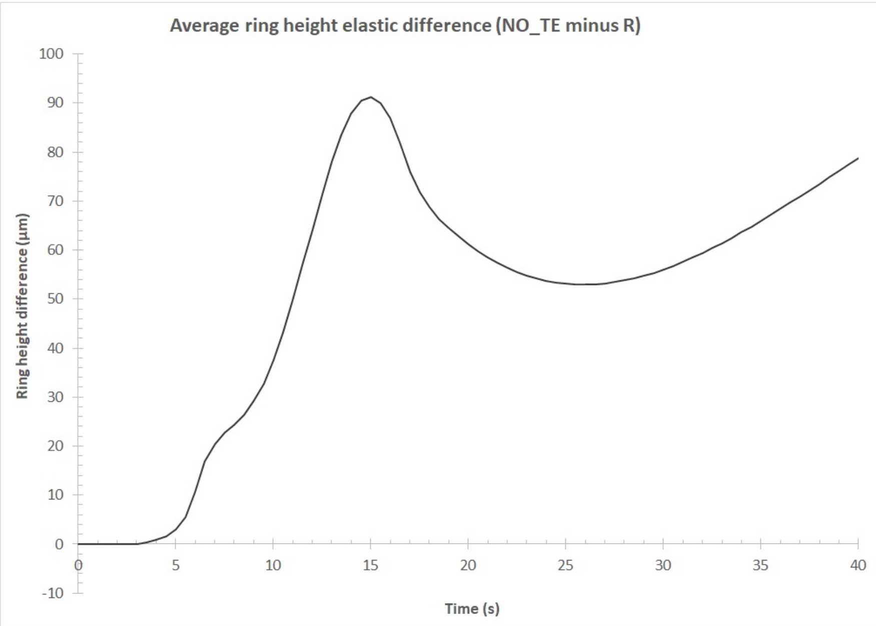

FIG. 3.45: Average ring height elastic difference

Observations over Fig.3.45 revealed an average ring height elastic difference of approximately 0.079 mm at the end of the process, although this difference did not increase monotonically throughout the process's duration. The maximum value was observed at approximately t = 15 s for an elastic deformation value of 0.091 mm.

Next, the elastic deformations of the main roll, the mandrel and the conical rolls were measured and presented in Fig.3.46. Regarding the support rolls, the average elastic deformation curve for each one is presented in Fig.3.47. In Figs.3.46 and 3.47 that follows, the presented curves were a result of subtraction of the corresponding deformation curves of the *R model* from the corresponding deformation curves of the *NO_TE model*.

In Fig.3.46, a similar deformational behavior was observed for the mandrel and the main roll, while a different behavior was observed for the conical rolls.

For the mandrel and the main roll, the maximum elastic deformations of 29 μm for the main roll and 26 μm for the mandrel were observed early at t = 6 s. These deformations gradually converged to approximately 8 μm in the main roll and 10 μm in the mandrel near the end of the process, when the tools reached their final position and the ring continued to rotate with little to no further forming occurring.

On the other hand, in the case of the conical rolls a large deformation of approximately 45 μm was observed at t = 9 s, which remained almost unchanged until t = 18 s. Then,

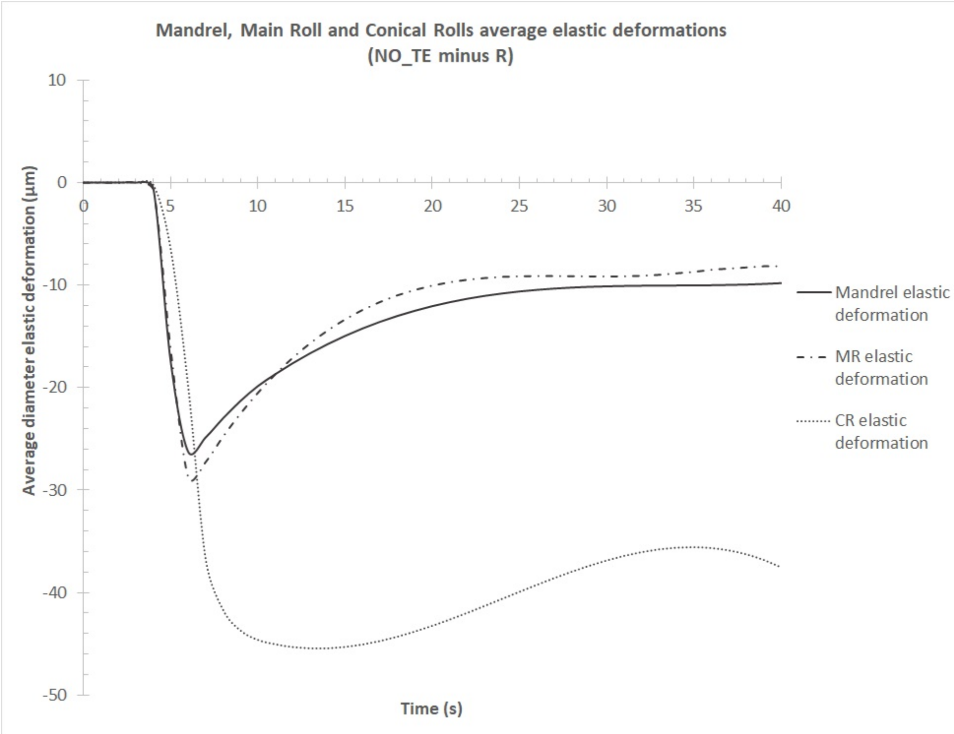

FIG. 3.46: Mandrel, main roll and conical rolls average elastic deformations

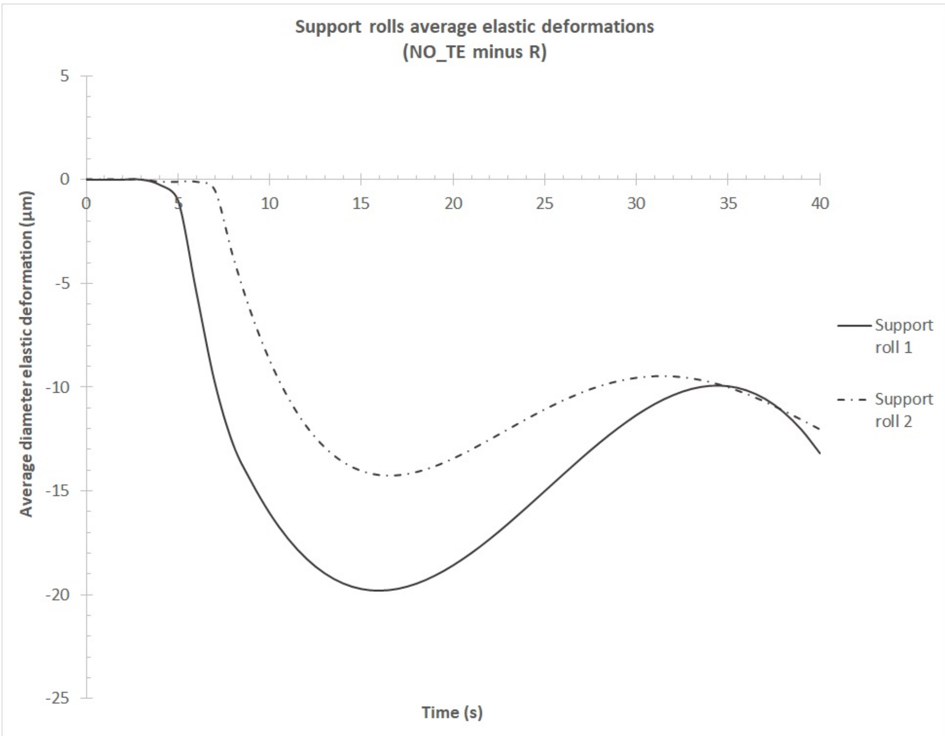

FIG. 3.47: Support rolls average elastic deformations

the deformation began reducing (as an absolute value) continuously until t = 35 s, when it began to increase again (as an absolute value) until the end of the process. The deformation value at the end of the process was approximately 38 μm. It is worth noting that the elastic deformation curves in both conical rolls were almost identical, thus the curve presented in

Fig.3.46 is representative for both conical rolls.

Observations over Fig.3.47 revealed a similar deformation pattern in both tools, however the precise elastic deformation values vary between the two. More specifically, support roll 1 (refer to Fig.3.44), which flattens the ring bulging caused by the conical rolls, had a maximum elastic deformation of approximately 20 μm at t = 16 s, while its final elastic deformation value was approximately 13 μm. On the other hand, support roll 2 (refer to Fig.3.44), which comes in contact with the ring right after its thickness reduction in the roll bite, had a maximum elastic deformation value of approximately 14 μm at t = 17 s, while its elastic deformation at the end of the process was approximately 12 μm. Interestingly, the two support roll had very little difference in their elastic deformation values after t = 35 s. Only a slight difference of approximately 1 μm was observed at the very last timestep of the process.

Finally, the comparison of the main rolling forces and the conical rolling forces are presented in Figs.3.48. As with the previous figures, the force diagrams were a result of the difference between the corresponding force diagrams of the *NO_TE model* minus the corresponding force diagrams of the *R model*.

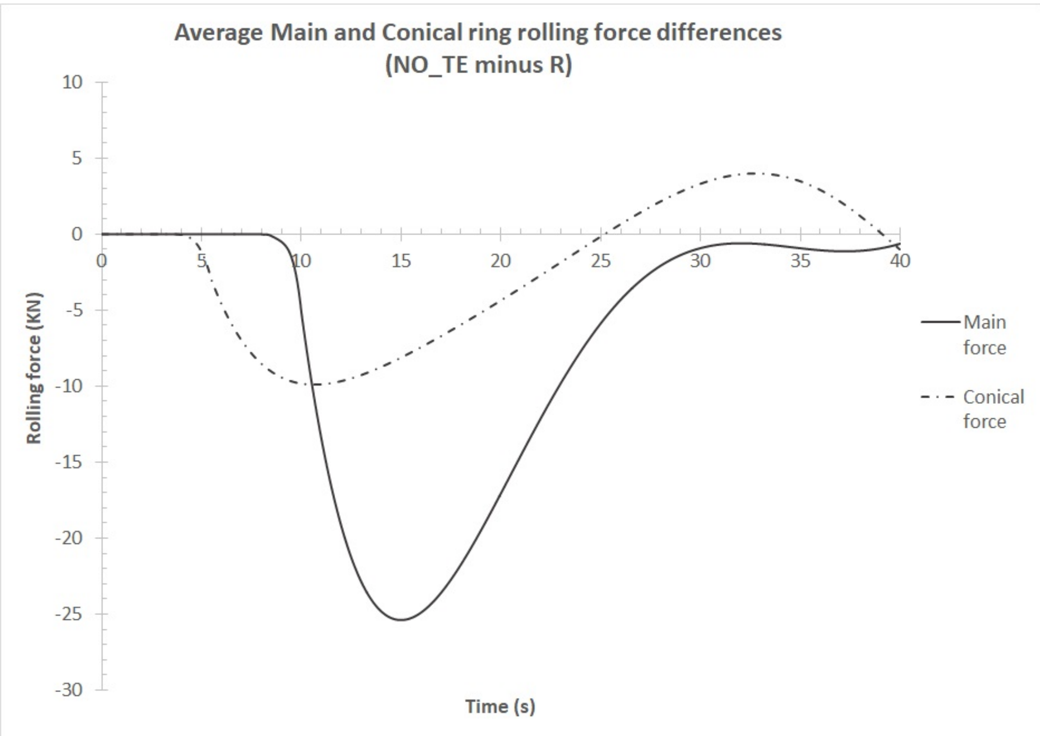

FIG. 3.48: NO_TE minus R average main and conical rolling force differences

Observations over Fig.3.48 revealed that more main rolling load was required in the case of the *R model*. The average main load curves were almost identical for the first 8.5 s of the process, thus their difference during this duration was almost zero. From then on, an increasing difference was observed, which peaked in t = 15 s approximately at 25 KN. Subsequently, the load difference began reducing, until it converged at approximately t = 30 s to an average load value of 1 KN. This load difference hardly changed until the end of the process.

Regarding the average difference in the conical rolling load, a different pattern was presented in Fig.3.48. During the first half of the process the average conical roll of the *R model* was greater with the maximum difference appearing around t = 10 s at a value of 9.9 KN approximately. During the latter half of the process, the conical load difference was reversed, thus the conical load of the *NO_TE model* was greater. The maximum difference in this case appeared around t = 33 s at a value of approximately 4 KN.

NO_TE model - to - *TE model* Results Comparison

Similarly to above, a comparison between the outer ring diameters of the *NO_TE model* and the *TE model* was performed. A curve resulting from subtracting the outer ring diameter curve of the *NO_TE model* from the same curve of the *TE model* is presented in Fig.3.49. Additionally, a curve resulting from the subtraction of the inner ring diameter curve of the *NO_TE model* from the same curve of the *TE model* was calculated and is also presented in Fig.3.49:

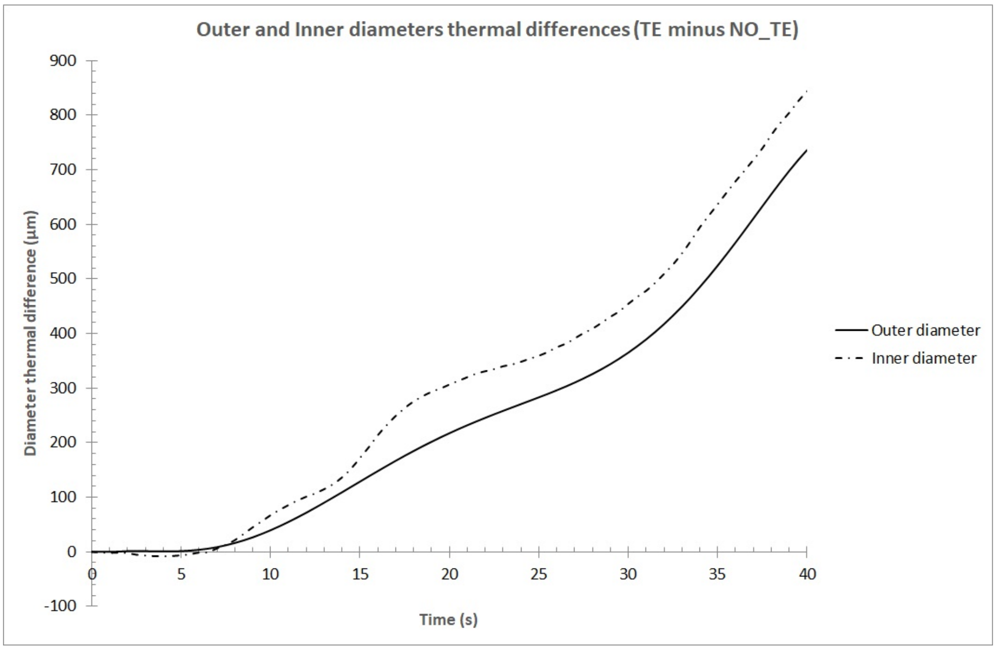

FIG. 3.49: Outer and inner ring diameters thermal differences

Observations over Fig.3.49 revealed a steadily increasing thermal difference between the two curves. The maximum thermal deformation value was observed at the end of the process, for a value of 0.736 mm. Regarding the inner diameter difference, Fig.3.49 revealed a steadily increasing thermal difference in this case too. The maximum thermal deformation value was approximately 0.845 mm and was observed at the end of the process.

Next, a comparison between the average ring heights of the two models was performed, and the resulting curve is presented in Fig.3.50:

In Fig.3.50, an irregular pattern of the average ring height thermal evolution was observed. For most of the process's duration, the average ring height of the *NO_TE model* was greater, until approximately t = 29 s. At this point, the aforementioned trend reversed and the average ring height of the *TE model* became greater. During the first part of the aforementioned curve, the maximum deformation was observed at t = 26 s for a thermal deformation value

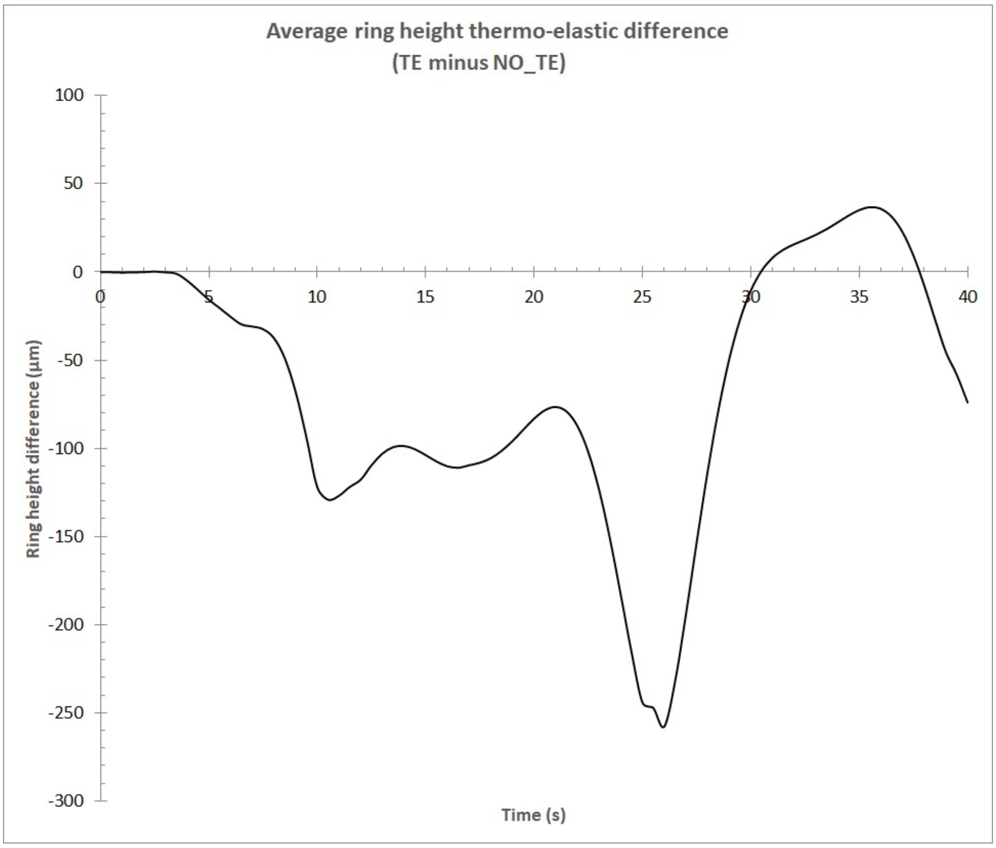

FIG. 3.50: Average ring height thermal difference

of 0.205 mm, while a lesser peak was observed at t = 10.5 s with a deformation value of approximately 0.085 mm. When the trend reversed, a maximum observed deformation value was 0.104 mm at t = 36 s.

Regarding the thermal deformations of the tools, the corresponding curves resulting from subtracting the corresponding deformation curves of the *NO_TE model* from the corresponding deformation curves of the *TE model* for the mandrel, the main roll and the conical rolls are presented in Fig.3.51. As with the conical roll deformation curve presented in the previous chapter, the conical roll curve in Fig.3.51 is representative for both conical rolls.

Observations over Fig.3.51 revealed irregular patterns for all three tools revealed specific patterns for all three tools. In the case of the mandrel, the thermal deformation increased steadily until the end of the process, where it converged on a thermal deformation value of approximately 44 μm. A similar pattern was observed for the main roll thermal deformation curve in Fig.3.51, where a constant but smaller increase rate was presented until approximately t = 36 s. At this point, the maximum thermal deformation value of approximately 13 μm was observed. From then on, the deformation curve decreased until the end of the process, where a thermal deformation value of approximately 11 μm was recorded. Finally, in the case of the conical rolls (Fig.3.51), a peak thermal deformation value of approximately 17 μm was observed at t = 7 s. After this point, the thermal deformation was reduced until approximately t = 23 s, when the thermal deformation value converged at approximately 2 μm and remained almost unchanged until t = 36 s. At the end of the process, the thermal deformation value was slightly reduced to approximately 1 μm.

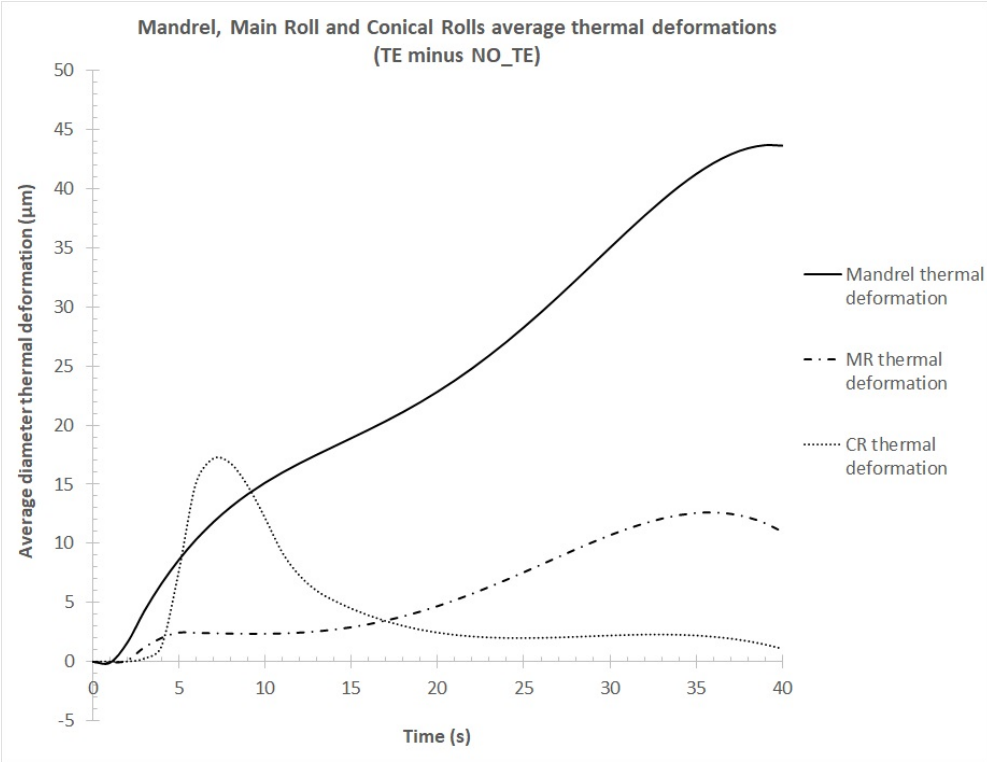

FIG. 3.51: Mandrel, main roll and conical rolls average thermal deformations

In the case of support rolls, the thermal deformation curves resulting from subtracting the deformation curves of the *NO_TE model* from the corresponding curves of the *TE model* were calculated, and they are presented in Fig.3.52.

For both curves of Fig.3.52, a positive thermal deformation pattern was presented. In the case of support roll 1, the thermal deformation presented a maximum value of approximately 59 μm at t = 15 s. Subsequently, the curve began decreasing until approximately t = 33 s, when the curve began increasing again until the end of the process. The last observed thermal deformation value was approximately 13 μm. On the other hand, the thermal deformation curve of support roll 2 was increasing throughout the manufacturing process, with the maximum thermal deformation value at t = 40 s being approximately 40 μm.

Finally, the comparative load curves of the main ring rolling force and of the conical ring rolling force were calculated, and they are presented in Figs.3.53. The load curves presented in Figs.3.53 were calculated from subtracting the corresponding load curves of the *NO_TE model* from the same curves of the *TE model*.

Observations over Fig.3.53 revealed two peaks at t = 6 s and t = 33 s, respectively. The first peak was at a main ring rolling force value of approximately 6.1 KN, while the second peak at a load value of approximately 2.6 KN. At the end of the process, the main ring rolling load difference was approximately zero.

Regarding the conical ring rolling load difference presented in Fig.3.53, a maximum load difference value of approximately 1.5 KN was present at t = 15 s. From that point on, the curve began decreasing until t = 36 s, where the curve reached a negative maximum load value of approximately -0.95 KN. Then, the curve began increasing again until the end of

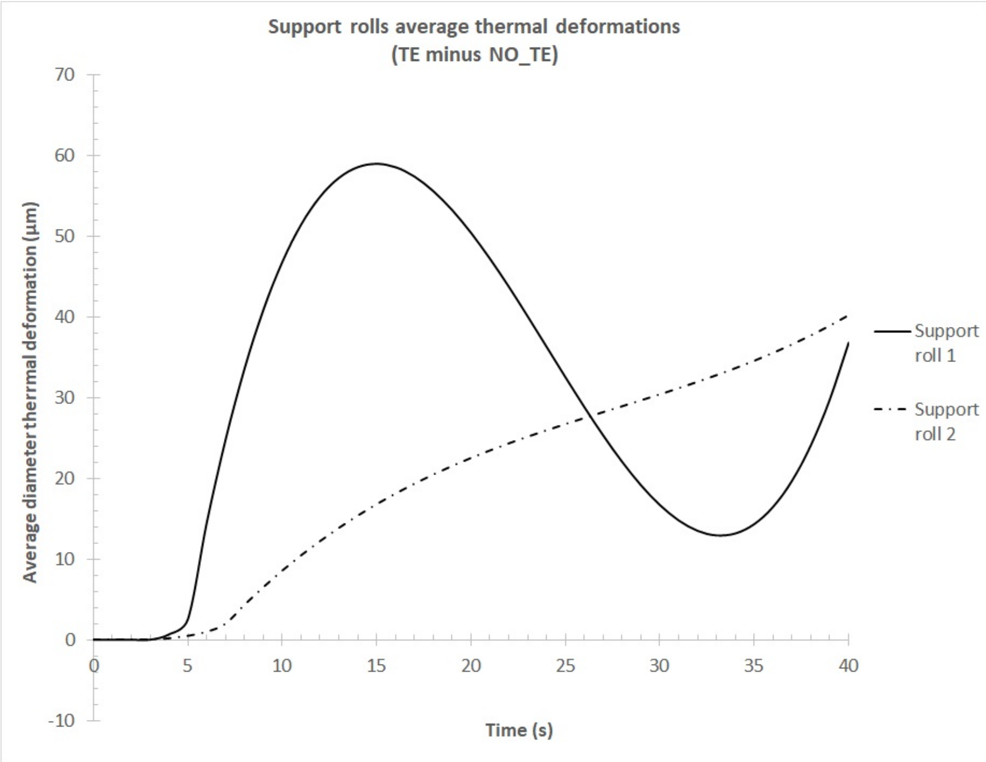

FIG. 3.52: Support rolls average thermal deformations

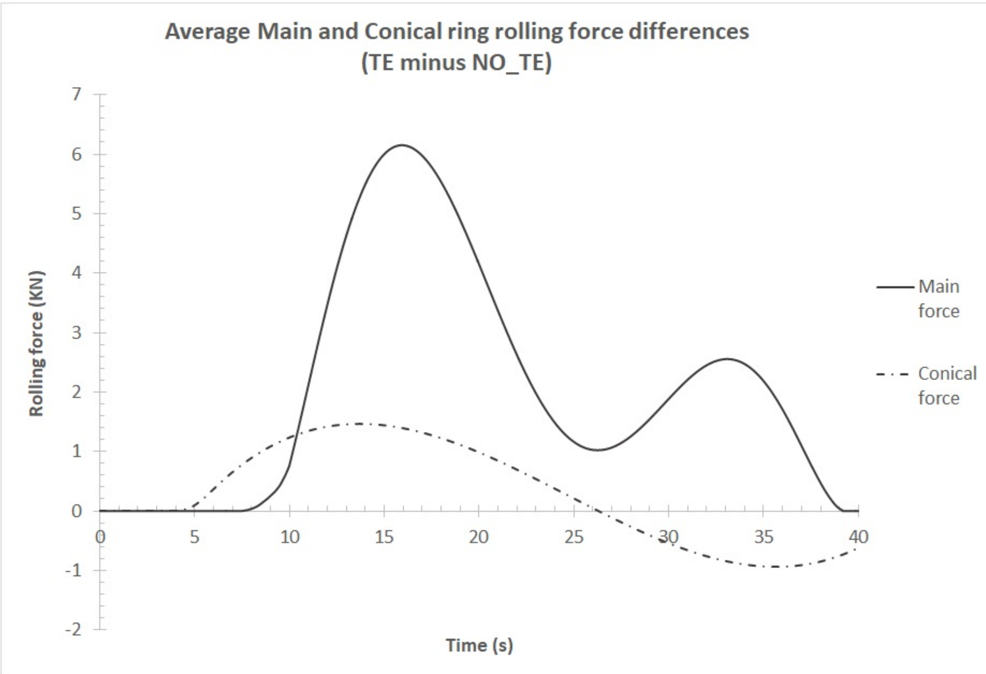

FIG. 3.53: TE minus NO_TE average main and conical rolling force differences

the process, where the load value was approximately -0.63 KN.

Combined Thermo-Elastic Tool Effects

After the separate analysis of the two tool phenomena, their combined effects on ring deformation were analyzed. More specifically, in the current subchapter, ring deformation curves resulting from the subtraction of the R model from the TE model were estimated.

The combined effects on the outer and inner diameters are presented in Fig.3.54, while the combined effects on the average ring height are depicted on Fig.3.55.

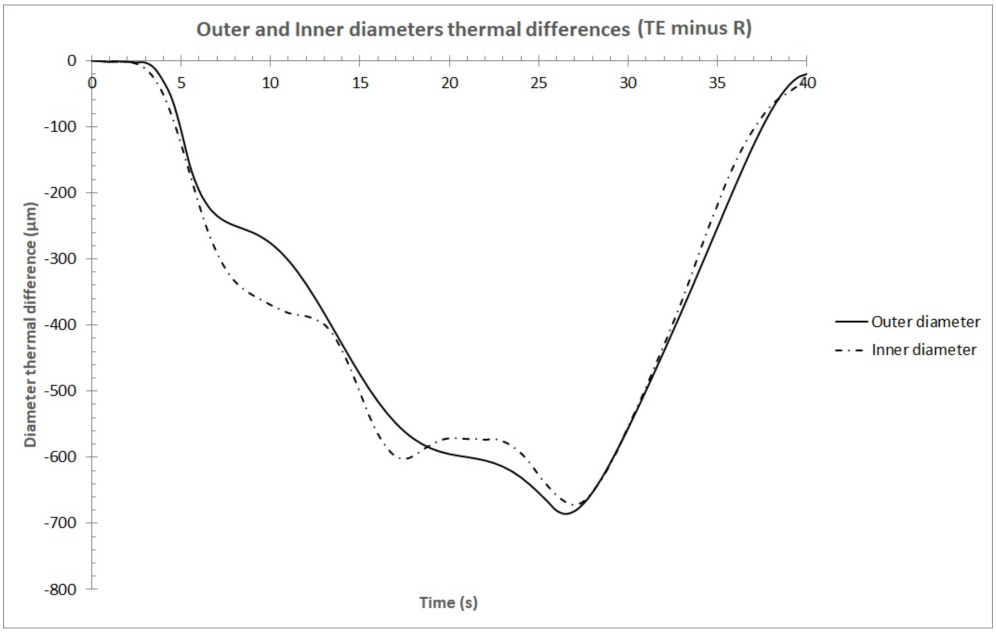

FIG. 3.54: Outer and inner ring diameters thermo-elastic differences

Observations over Fig.3.54 revealed a similar deformation pattern in both the outer and the inner diameters of the ring. Both curves began increasing (as an absolute value) until t = 26.5 s, where the deformation of the outer diameter was approximately 0.686 mm and the deformation of the inner diameter was approximately 0.678 mm. From that point on, the two curves began decreasing (again as an absolute value) until their final values of 20 μm (outer diameter) and 33 μm (inner diameter), at the end of the process. It is worth noting that in Fig.3.54, the negative deformation values indicate a dominant elastic deformation of the rolls.

In the case of the average ring height in Fig.3.55, four different phases were distinguished. On the first phase, the average ring height increased until approximately t = 15 s for a height value of approximately 54 μm. On the second phase, the average ring height decreased until approximately t = 21 s when the curve reversed and began increasing (as an absolute value) until t = 25 s for a height value of approximately -133 μm. On the third phase, the average ring height began decreasing (as an absolute value) again until approximately t = 29 s, when the curve reversed again and began increasing until approximately t = 38 s for a height value of approximately 142 μm. Finally, during phase four, the average ring height began decreasing again until the end of the process, when the deformation value was approximately 64 μm. It is worth noting that in Fig.3.55, the positive values correspond to a dominant elastic deformation of the conical rolls, while the negative values correspond to a dominant thermal deformation of the conical rolls.

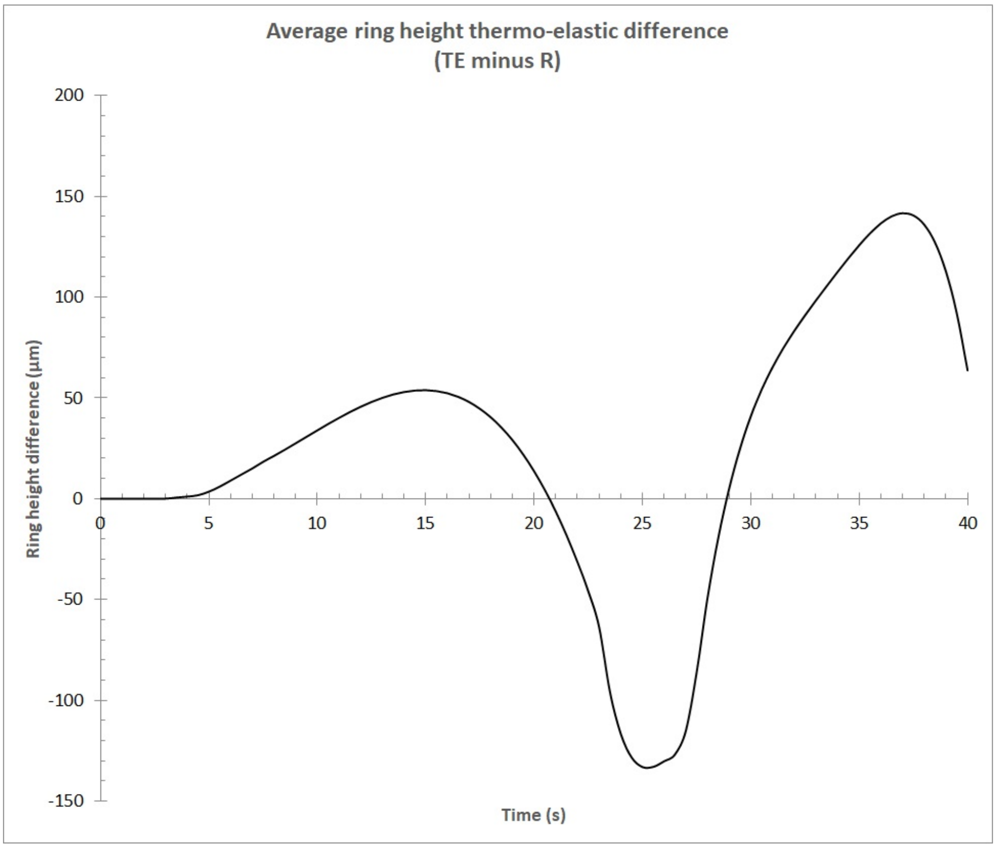

FIG. 3.55: Average ring height thermo-elastic difference

3.3.3 Results and Result Comparisons Discussion

After the presentation of the results from all three models and a brief comparison between them, the presented differences will be further discussed in the current section.

R model - to - _NO_TE model_ Results Comparison Discussion

In all the results of subsection 3.3.2, the presented curves occurred from subtracting the *NO_TE model* results from the *R model* results. This allowed for the effects of tool elasticity to be revealed in their proper nature (e.g. a negative deformation difference value means that a tool radius is reduced due to the elastic deformation of this tool).

Keeping that in mind, the negative values of Fig.3.44 seemed strange at first, as the elastic deformation of the main roll should lead to a greater outer diameter for the ring and thus positive values. However, this behavior can be explained from the basic mechanics of the process. In ring rolling, the reduction of the blank's thickness leads to the increase of the outer diameter of the ring, in order for the law of volume constancy to be satisfied (**Schuler, 1998**). When both the main roll and the mandrel deform inwards (towards their corresponding center of rotation), the created gap is larger than in the case of rigid tools. Thus, the ring thickness in the case of *NO_TE model* is larger in every timestep compared to the ring thickness in the *R model*, which ultimately leads to a smaller outer ring diameter in the *NO_TE model*. This phenomenon is also assisted by the smaller axial deformation caused by the deformation of the conical rolls, which will be further discussed below. On the other hand, the elastic deformation of the rolls has an opposite effect, as it creates more distance between the surface of the main roll and the ring's axis of rotation. However, when comparing the maximum main roll deformation of approximately 29 μm to the 0.3 mm outer diameter reduction at the same time instance (t = 6 s), the increase due to the main roll's elastic deformation is miniscule.

A similar behavior is observed in the mandrel. The negative values in Fig.3.44 indicate a smaller inner ring diameter in the *NO_TE model* than in the *R model*. The elastic deformation of the mandrel in this case acts additively to the reduction of the inner ring diameter, as the distance between the mandrel – ring interface and the ring's axis of rotation is constantly reducing while the mandrel's elastic deformation increases. A comparison between the mandrel deformation (Fig.3.46) and the inner ring diameter reduction reveals that in this case too, the effects of the smaller ring thickness and height reductions to the ring's expansion is orders of magnitude greater than the mandrel's elastic deformation.

Regarding the average ring height, the positive differences observed in Fig.3.45 are expected, as the inwards deformation of the conical rolls creates a larger gap that the ring's material may occupy. A closer inspection of the values in Figs.3.45 and 3.46, regarding the average ring height and the conical rolls elastic deformation respectively, reveal a close correlation between the two. More specifically, in most time instances during the process, the difference of the average ring height between the *NO_TE model* and the*R model* is approximately double the elastic deformation of each conical roll. This remark is not absolute everywhere, as the ring slides across its interface with the conical rolls during the process, thus the conical roll deformation mechanism is relatively complex. Moreover, the deformations of the parallel surfaces of the ring are also more complex, mainly due to the irregular formation behavior of the fishtail defect (**Giorleo, Ceretti, and Giardini, 2012**). However, the correlation of the measured deformation values in the ring and the conical rolls acts as another validation of the proper setup of the simulations.

Next, both support roll deformations presented in Fig.3.47 had similar deformation patterns between one another. These similarities can be attributed to the movement law applied on the support rolls. With this knowledge, a correction can be applied on the movement law of support rolls, equal to the deformation of support roll 2 presented in Fig.3.47. Regarding the difference between the two curves in Fig.3.47, this can be attributed to the slight deformation that support roll 1 makes on the ring's bulges caused by the conical roll bite (**Zhou et al., 2011b**), which in turn slightly deform support roll 1 elastically as well. This fact was verified by the stress distributions presented in Fig.3.42(d), where the stress values on support roll 1 were higher around the ring contact area and especially around the contact with bulge defects. On the contrary, support roll 2 was not so heavily deformed, as it was uniformly in contact with the ring. This was implied by the induced stress fields on support roll 2, which were mostly constant around the ring contact area (Fig.3.42(e)). It is worth noting that in case support roll elastic deformations are not compensated, instabilities are most likely to occur in the process due to poor support of the ring, which would lead to ring oscillations and the subsequent forming of some crucial (or even critical) defects.

Finally, observations over Fig.3.48 revealed differences on both the main and the conical rolling loads. The differences observed in the case of the main rolling load can be attributed to the yielding nature of the tools in the *NO_TE model*, which leads to a lesser radial deformation of the ring in every time instance, compared to the *R model*. Similarly, the differences observed for the conical rolling loads in the first part of the process (until t = 25 s) can be attributed to the yielding nature of the tools, in this case too. For the second part of the process (from t = 25 s until the end of the process), the increase in the conical rolling load of the *NO_TE model* can be attributed to the increase of the ring's height deformation difference observed after t = 25 s in Fig.3.45. However, comparisons between the maximum load differences in Fig.3.48 and the absolute load values required for the process (approximately 1245 KN for the main load and 642 KN for the conical load (**Zhu et al., 2016b**) show a main rolling load reduction of approximately 1.5% and a conical rolling load reduction of approximately 1.6%, which both can be considered negligible.

***NO_TE model* - to - *TE model* Results Comparison Discussion**

The results presented in subsection 3.3.2 were estimated from subtracting the *NO_TE model* results from the *TE model* results. In that way, the elasticity effects could be excluded and only the thermal effects were accounted for.

In Fig.3.49, a constantly increasing deformation was observed for both the outer and the inner diameters of the ring. This behavior is expected, as the ring thickness reduction increases because of the mandrel and main roll thermal expansion (Fig.3.51), and thus both ring diameters further expand.

In the case of the average ring height presented in Fig.3.50, for the greatest part of the process, the ring height of the *NO_TE model* surpassed that of the *TE model*. This behavior was overall expected, as the thermal expansion of the conical rolls in the *TE model* led to a smaller gap than the elastically shrunk conical rolls of the *NO_TE model*. On the other hand, the increase of the ring's height after t = 29 s can be attributed to the increase of the fishtail defect, which is further intensified from the thermal expansion of the main roll and the mandrel.

Regarding the deformations of the main roll and the mandrel (Fig.3.51), a similar deformation behavior was observed, with a continuous increase present throughout the duration of Ring Rolling. This behavior is logical, as the continuous heating of the mandrel and the main roll led to a continuous thermal expansion of the rolls. The deformation difference values themselves were very different between the two tools, which can be attributed to two factors: (a) their difference in mass and (b) their difference in radius. The mass difference between the two tools caused the temperature of the mandrel to increase much faster than the temperature of the main roll, as the conducted heat was distributed in a much larger object in the latter case. Similarly, because of their radius difference, a much larger peripheral area had to be heated in the case of the main roll, compared to that of the mandrel.

The conical roll thermal deformation difference also appearing in Fig.3.51 revealed a rather stable behavior. Apart from a peak increase early in the process, their thermal difference hardly remained the same for almost half of the process's duration. The initial peak was a result of the thermal expansion of a smaller radius of the conical roll, which heated rapidly as the ring remained for an extended period under the same conical roll cross-section (Ring Rolling phase 1). Moreover, the almost stable region of the curve is a result of the ring sliding across its interfaces with the conical rolls, thus different regions of their perimeter were heated during the process. This fact was also indicated by the temperature distribution on the conical rolls (Fig.3.43(c)), where residual increased temperature fields could be observed remaining after the ring had surpassed the corresponding conical roll segments. Thus, a lesser overall average temperature increase – and consequently less thermal expansion – occurred in the conical rolls, as no specific segments were constantly in contact with the ring so that they could overheat. Contrary to the main roll and mandrel corresponding results, no correlation could be made with the average ring height results of Fig.3.50, as the rapid ring expansion and the side effects it had on the deformation behavior of the parallel surfaces of the ring, were too severe and led to a greater difference than double the deformation observed in the conical rolls.

The support roll deformation differences were not similar to one another in this comparison, as depicted in Fig.3.52. More specifically, support roll 1 had a similar deformation behavior to the one presented for the same tool in Fig.3.47, although the deformation of the *TE model* was greater in this case. On the other hand, the deformation behavior of support roll 2 was completely different, as the constant contact with the ring led to a continuous heating of the tool and thus a continuous thermal expansion. The fact that a similar continuous thermal expansion of support roll 1 was not observed, leads to the conclusion that its contact with the ring was not continuous throughout its height. Both of these facts were indicated by their respective temperature distributions presented in Figs.3.43(d) and (e). More specifically, in the case of the temperature distribution on support roll 1, a rapid heating of the tool occurred early on in the process, both because of its contact with the ring and because of the plastic work–turned–to– heat required to iron out the bulge defects. This resulted in the early peak observed in Fig.3.52. From then on, the average temperature of support roll 1 increased, thus the heating of the tool segments causing the ironing of the bulge defects (recorded as a temperature difference ΔT at the moment of the ironing) decreased. As a result, lesser thermal expansions occurred after $t = 15$ s approximately. This phenomenon continued until approximately $t = 30$ s, when ring bulging was reduced (also see Fig.3.50) and support roll 1 came in contact with a larger part of the ring, causing it to heat more uniformly. On the other hand, the temperature distribution on support roll 2 (Fig.3.43(e)) indicated a constant contact between the ring and said roll, thus a constant heating of the latter. Similarly to their elastic deformation, the effects of the support rolls' thermal expansion should be compensated via a correction on the movement law, equal to the thermal deformation difference of support roll 2. In that way, gap creation between the ring and the support rolls could be avoided, thus less forming defects would be expected.

Finally, the main and conical rolling load difference presented in Fig.3.53 had an expected behavior. The main rolling load of *TE model* was greater, with two peaks appearing during the process. The appearance of these two peaks can be correlated to the results in Fig.3.49, where the relative load reduction between the two peaks occurred at the same time as a deformation plateau. The conical rolling load difference had a similar behavior to the one observed in the *R model*-to-*NO_TE model* comparison, where the load difference reverses during the process. The required conical rolling load is greater in the *TE model* until $t = 26$ s. On this point, which coincides with the second large peak in Fig.3.50, the conical load of the *NO_TE model* becomes greater, and the height difference begins to increase. The correlation between the two results can be attributed to a combination of a reduction of the thermal expansion of the conical rolls and an increase of their elastic deformation. Considering the results of Fig.3.51, where the thermal deformation of the conical rolls remains almost the same during the entire process, the rapid increase of the elastic deformation of the conical rolls remains as the only explanation. Such a rapid increase in the elastic deformation can be justified from an equally rapid increase of the fishtail defect occurring during the end of the process, as this phenomenon is mentioned in literature (**Giorleo, Ceretti, and Giardini, 2012**). However, when compared to their respective absolute load values required for the process, the load differences were approximately 0.4% for the main rolling load and 0.2% for the conical rolling load.

Overall, from the current analysis it was made clear that a correction should be applied to the proposed ring outer radius growth rate law (Eq.2.57), which would take into account the effects of both the elastic and thermal deformations of the tools. The corrected law is presented in Eq.3.20.

$$R_{corrected} = \begin{cases} a_{1,2} \cdot t_i^{c_{1,2}} + b_{1,2} - \Delta R_{el}(t_i) - \Delta R_{th}(t_i) & \text{Phases 1,2 of Ring Rolling} \\ a_3 \cdot t_i^{c_3} + b_3 - \Delta R_{el}(t_i) - \Delta R_{th}(t_i) & \text{Phase 3 of Ring Rolling} \end{cases} \tag{3.20}$$

where:

$\Delta R_{el}(t_i)$the elastic deformation difference of the outer radius of the ring

$\Delta R_{th}(t_i)$the thermal deformation difference of the outer radius of the ring

It is worth noting that the application of $\Delta R_{el}(t_i)$ in Eq.3.20, could lead to a slight increase in the elastic deformation of the tools than the one calculated in the current research, as the tools would indent further into the ring. It is advised that a numerical algorithm for the estimation of $\Delta R_{el}(t_i)$ should be used, until a converged solution for this property occurs.

Combined Thermo-Elastic Tool Effects Discussion

The combined thermo-elastic effects of the tools caused some very interesting deformations on the outer and inner diameters of the ring. Observations over Fig.3.54 indicate that in both ring diameters, the effects from the elastic deformations of the tools were dominant. The final deformation values of approximately 30 μm are considerable given the corresponding tolerances of most ring products. For example, the maximum tolerances for common steel seamless ring components as seen in Fig.3.56 **Bolin, 2005**, for a similar ring size to that of the current analysis (OD = 920 mm approximately and h = 115 mm approximately), are +6.4 μm/-9.6 μm in the outer diameter and +9.6 μm/-6.4 μm in the inner diameter. Such tolerance limits can be even stricter in the case of aerospace applications, for which IN718 produced rings are usually aimed at. Furthermore, the existence of much greater deformations during the manufacturing process is also crucial. Such deformations may lead to the formation of more severe defects from instabilities of the ring during the process, especially in case the tools fail to compensate for them with a proper adjustment to their movement route during Ring Rolling. Regarding the combined thermo-elastic tool effects on the average ring height (Fig.3.55), it seems that both the thermal and the elastic roll deformations were dominant at different phases of the process. A closer inspection of the correspond-ing height curves presented in Figs.3.45 and 3.50 verify this point, as the peaks in these curves manifested at different times. This fact indicates that the thermo-elastic conical roll deformations can import significant instabilities in Ring Rolling, especially if there is poor connection with the rest of the rolls. Moreover, a comparison of the maximum calculated deformations from the simulations (approximately 64 μm) to the corresponding tolerances shown in Fig.3.56 (+9.6 μm/-12.7 μm), reveal a great difference between the two. However, it is worth noting that the height of produced seamless ring products is usually machined after Ring Rolling, in order to eliminate any remainder fishtail defects. Thus, the calcu-lated average ring height deformation differences would also be reduced in an actual Ring Rolling process.

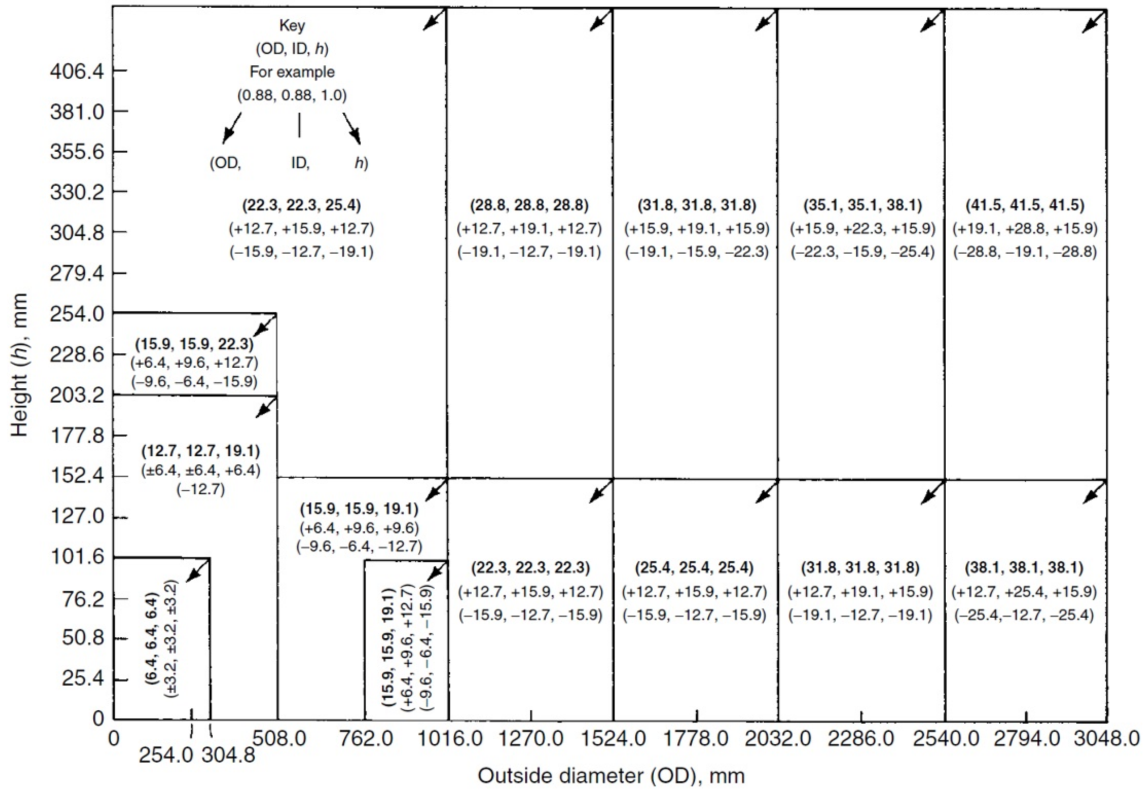

FIG. 3.56: Allowances and tolerance charts for as-rolled carbon, alloy, and stainless steel seamless rings. Allowances are given in **boldface** type; tolerances are in regular type. Closed areas represent the maximum ring sizes for the corresponding allowances and tolerances (both given in μm) (**Bolin, 2005**)

3.4 Support Rolls Movement Law and Ring Material Effects

In sections §2.9 and §3.2.4, the importance of a proper ring growth algorithm was made imminent, since it can affect the quality of the final product through the improper movement of the tools. This is especially important in the case of support rolls, whose movement closely follows the outer radius of the ring. Additionally, because of the non-symmetrical segments of the workpiece and its non-linear growth rate, the exact definition of tool positioning during Ring Rolling can be very challenging.

Until the current point in the dissertation, a combination of a power law (Ring Rolling Phases 1 and 2) and a polynomial (Ring Rolling Phase 3) was used to describe the outer radius expansion of the ring. This ring expansion algorithm produced relatively accurate results, although a series of trial – and – error simulations had to be conducted, in order to determine the exact form of these functions. Seeing that the ring's growth algorithm is a very important parameter for the control of the process, a more thorough analysis of this parameter was attempted in the current section. The main points of research could be summed up to the following:

- Can the aforementioned combination of functions be substituted with a single polynomial?
- How does the material of the ring affect ring growth and thus the aforementioned polynomial function?

In order to further investigate these research points, proper numerical analyses were performed. More specifically, multiple different numerical models, which compared the effects of ring material on the ring growth function in effect, were prepared and subsequently solved. Furthermore, since a numerical model with an alternative ring material was not available, a reference aluminum Ring Rolling process simulation had to be initially conducted. Overall, the steps that were followed for the current analysis involved the following:

1. In the first analysis, the same simulation presented in Chapter 2 is performed, but this time for an AA5754 ring. The scope of this simulation is to function as a reference aluminum ring model, based on the principle presented in Chapter 2.

2. In the second analysis, a *higher* degree polynomial (5^{th} order) was considered for each of the IN718 and AA5754 models.

The results in each analysis step were then compared to one another, as well as to corresponding results of the other steps.

3.4.1 Ring Rolling Simulation of an AA5754 Ring

Aluminum rings are not an uncommon application, as Ring Rolling of aluminum workpieces has already been analyzed by various researchers (e.g. **Koo et al., 2003**, **Zhou et al., 2011a**, etc.). However, the choice of a single aluminum alloy was proven challenging. Considering the mechanics of Ring Rolling, the choice of an aluminum alloy that would be work-hardened in cold seemed to suit the process. Because of this, non-heat treatable aluminum alloys seemed as a good choice. From the majority of non-heat treatable aluminum alloys, series 5xxx can be considered to have a good balance between high strength and commercial availability. For all of the above, AA5754 was finally chosen as the material that would be studied. In general, AA5754 is used in heavy industrial applications, such as ship making, vehicles and nuclear reactors, while it can be manufactured with extrusion processes to produce cylindrical billets (**Al-Helal et al., 2020**).

Aluminum Ring Rolling Model Setup

Likewise, in the Ring Rolling simulation of IN718 presented in Chapter §2, the proper definition of AA5754 material properties was one of the most crucial model parameters. Since experimental thermo-mechanical properties were not available, the corresponding data were found in literature. The thermo-mechanical properties of AA5754 used in the current analysis are presented in Table 3.5 and in Figs.3.57-3.64. In order to input the material properties in LS-DYNA for the current analysis, material models MAT_106 and T10 were used, similarly to the Ring Rolling model of the IN718 workpiece (see Chapter §2).

TABLE 3.5: Material properties (AA5754)

Property	Value or Curve	Reference
AA5754		
Density, d (kg m^{-3})	Fig.3.57	*Hadi, Al-Khafaji, and Subhi, 2022*
Stress - Strain - Temperature surfaces for a Strain Rate Range of $\dot{\epsilon}$ = 0.01 – 10 s^{-1}	Fig.3.58	*Acar et al., 2018, Lin et al., 2013*
Young's Modulus, E (GPa)	Fig.3.59	*Hadi, Al-Khafaji, and Subhi, 2022*
Poisson's Ratio, v	Fig.3.60	*Hadi, Al-Khafaji, and Subhi, 2022*
Yield Strength for a Strain Rate Range of $\dot{\epsilon}$ = 0.01 – 10 s^{-1}, σ_Y (MPa)	Fig.3.61	*Acar et al., 2018, Lin et al., 2013*
Coef. of Th. Expansion, α $\left(\cdot(10^{-6})\ \mathrm{K}^{-1}\right)$	Fig.3.62	*Hadi, Al-Khafaji, and Subhi, 2022*
Thermal Conductivity, K (W m^{-1} K^{-1})	Fig.3.63	*Hadi, Al-Khafaji, and Subhi, 2022*
Specific Heat Capacity, C (J kg^{-1} K^{-1})	Fig.3.64	*Hadi, Al-Khafaji, and Subhi, 2022*

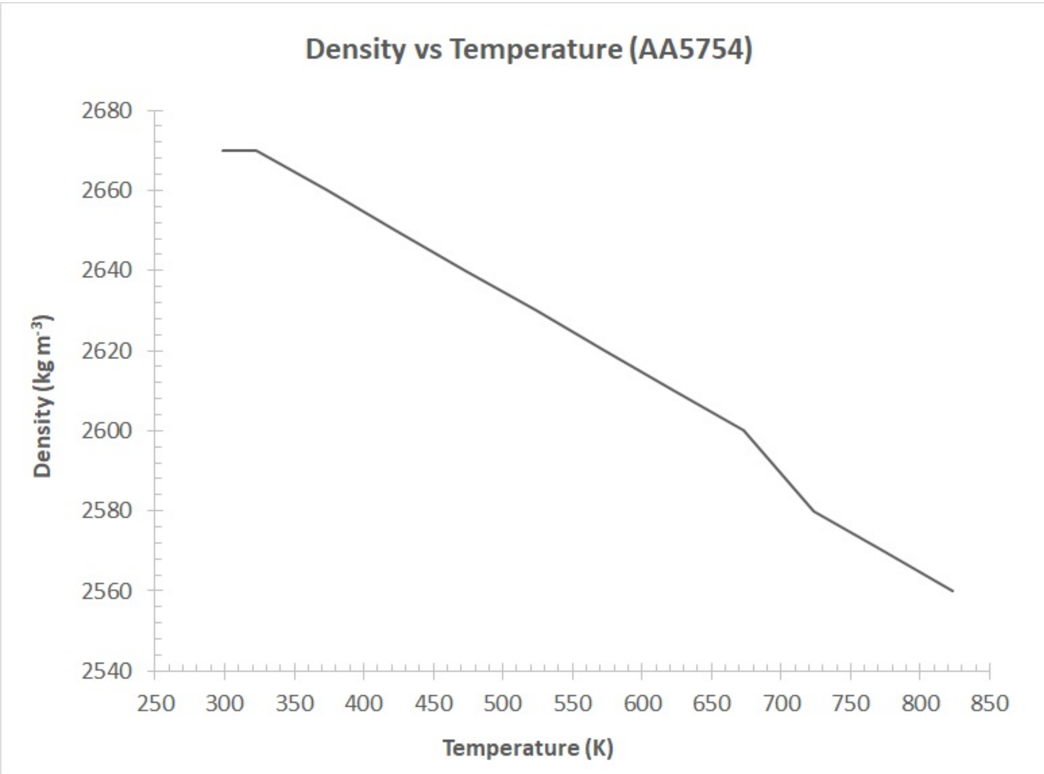

FIG. 3.57: Density vs. Temperature (AA5754)

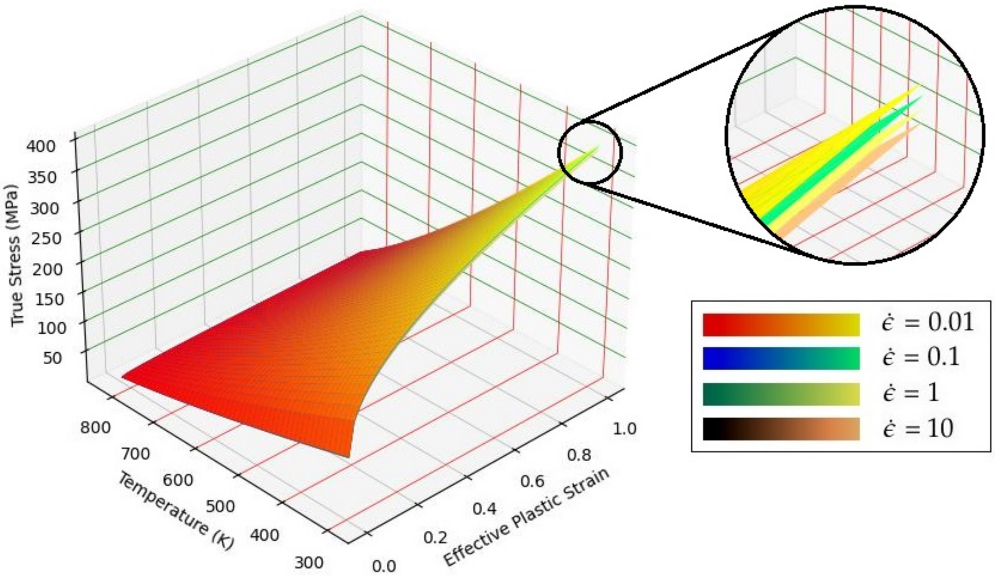

FIG. 3.58: Stress - Strain - Temperature Surfaces for a Strain Rate Range of $\dot{\epsilon} = 0.01 - 10\,\mathrm{s}^{-1}$ (AA5754). The edges of the input surfaces are presented zoomed in, on the upper right corner.

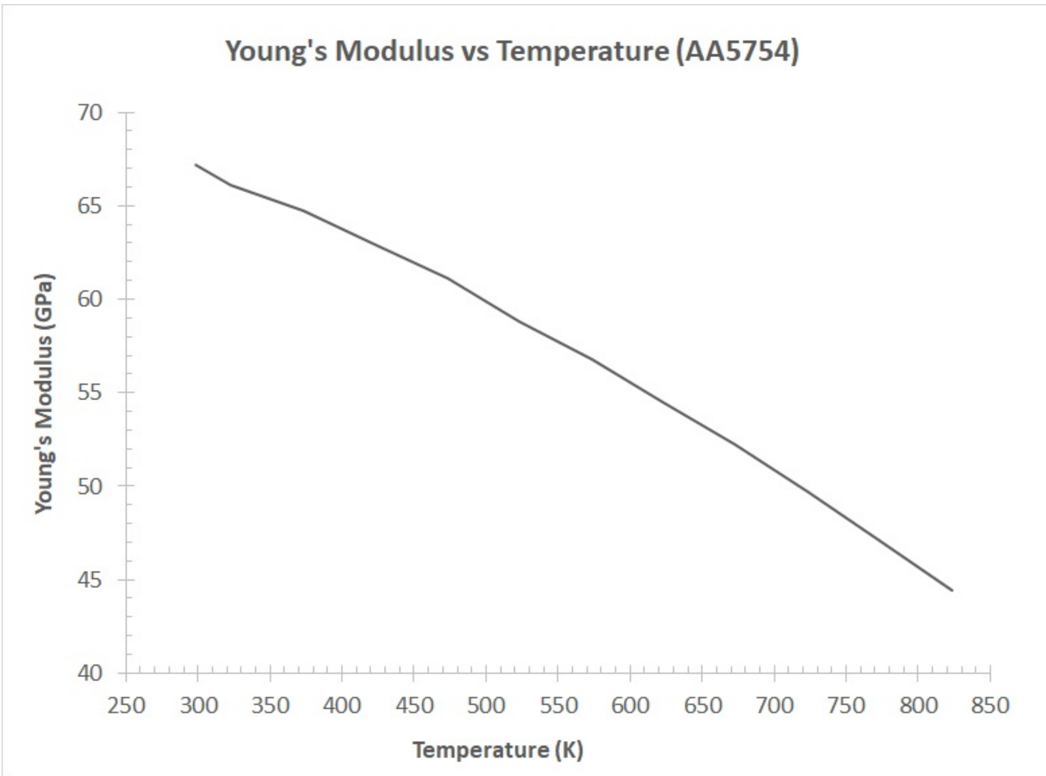

FIG. 3.59: Young's Modulus vs. Temperature (AA5754)

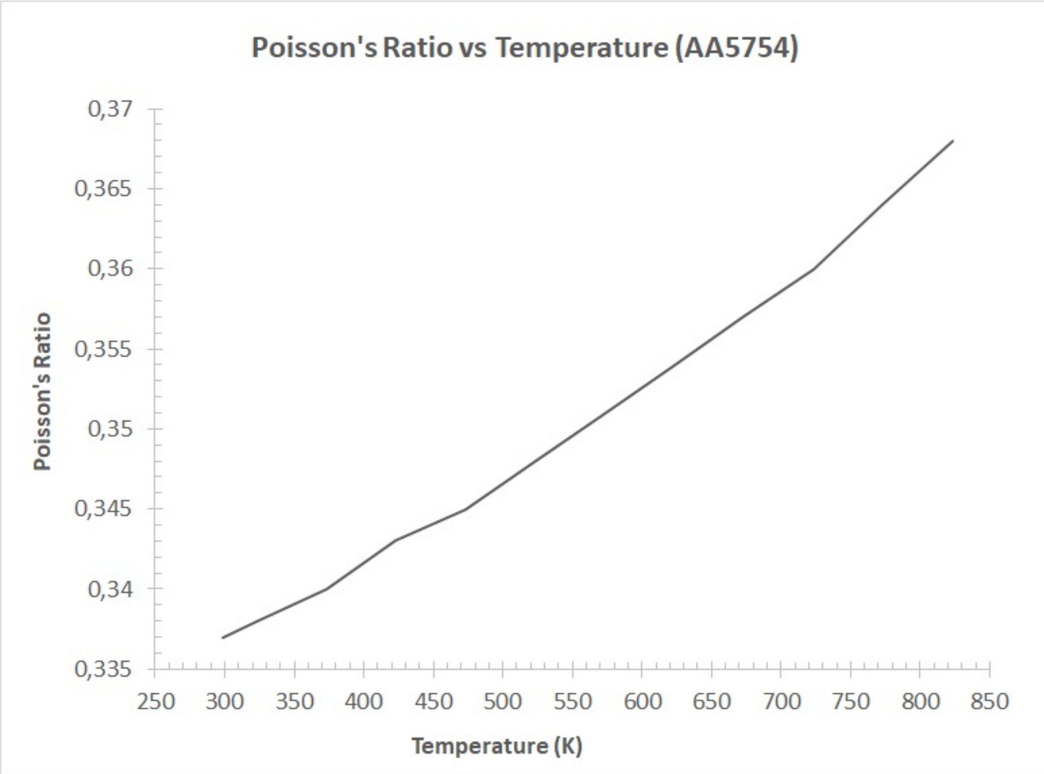

FIG. 3.60: Poisson's Ratio vs. Temperature (AA5754)

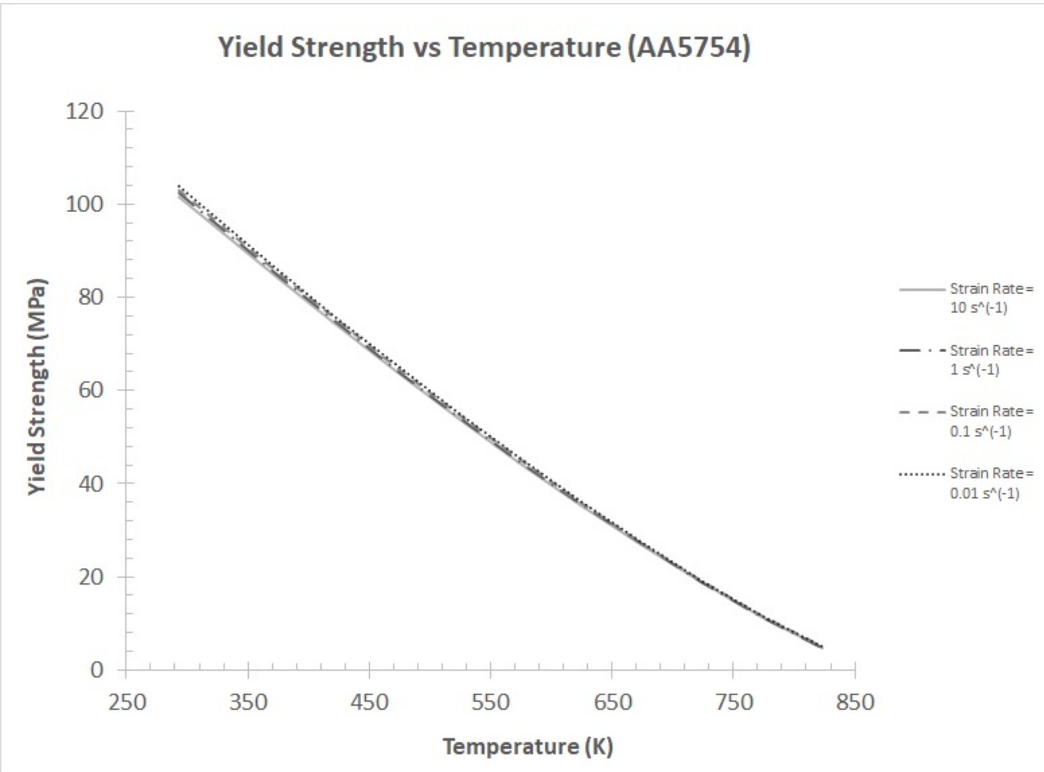

FIG. 3.61: Yield Strength vs. Temperature (AA5754)

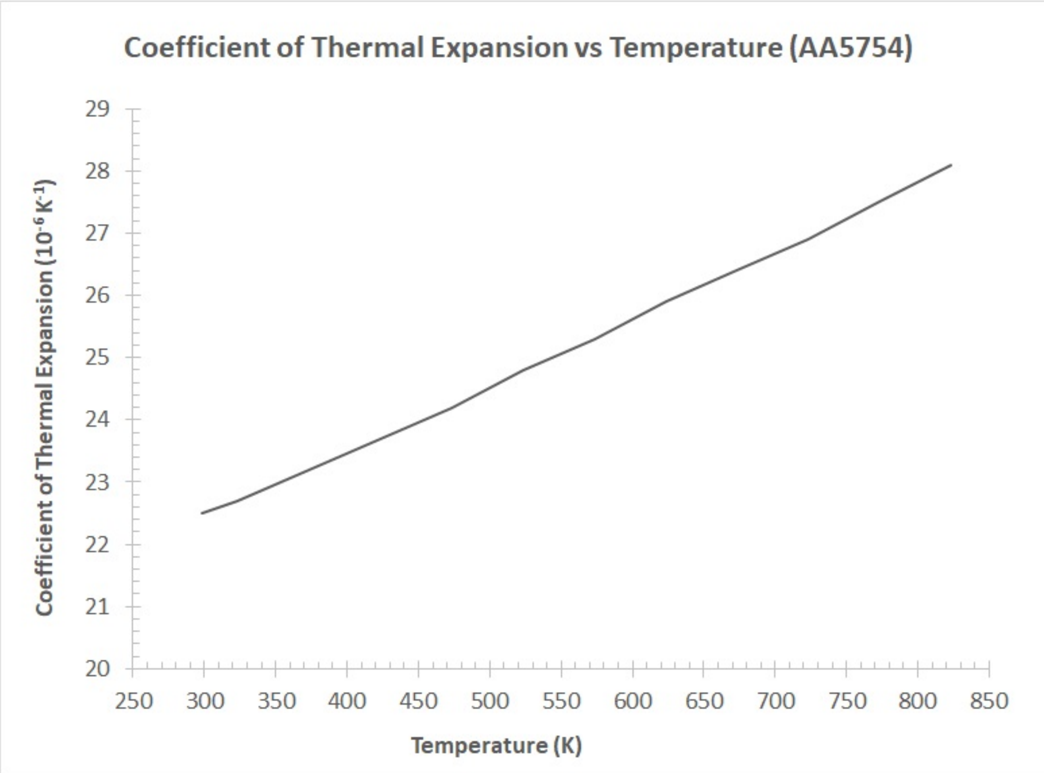

FIG. 3.62: Coefficient of Thermal Expansion vs. Temperature (AA5754)

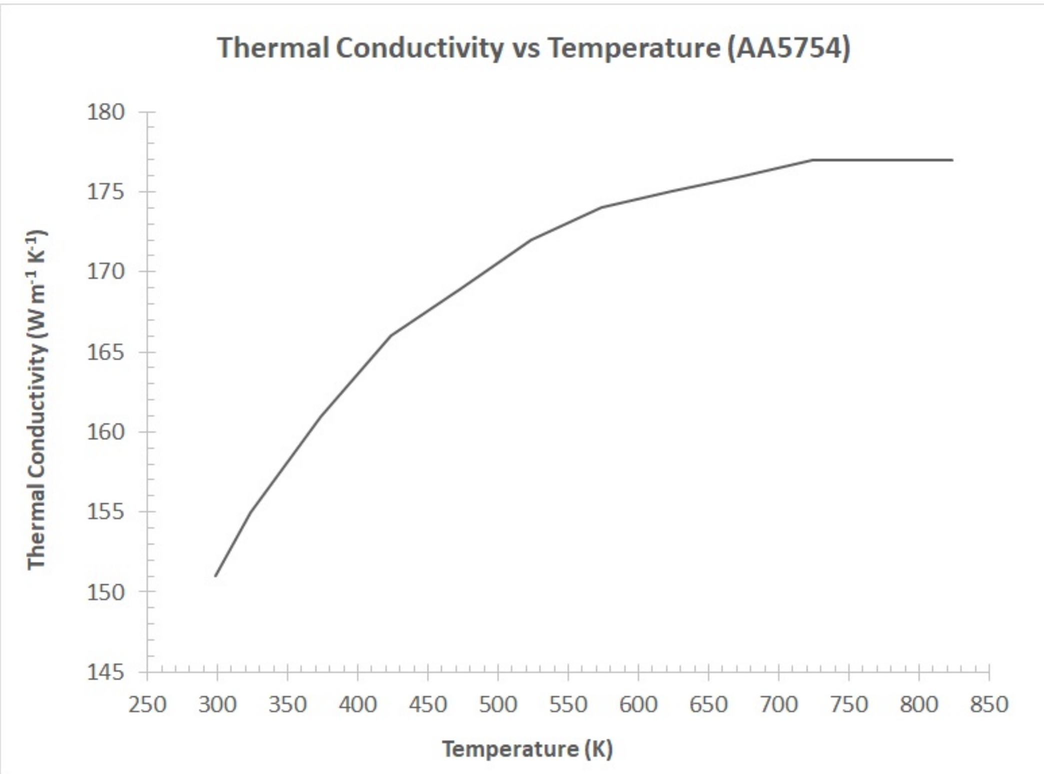

FIG. 3.63: Thermal Conductivity vs. Temperature (AA5754)

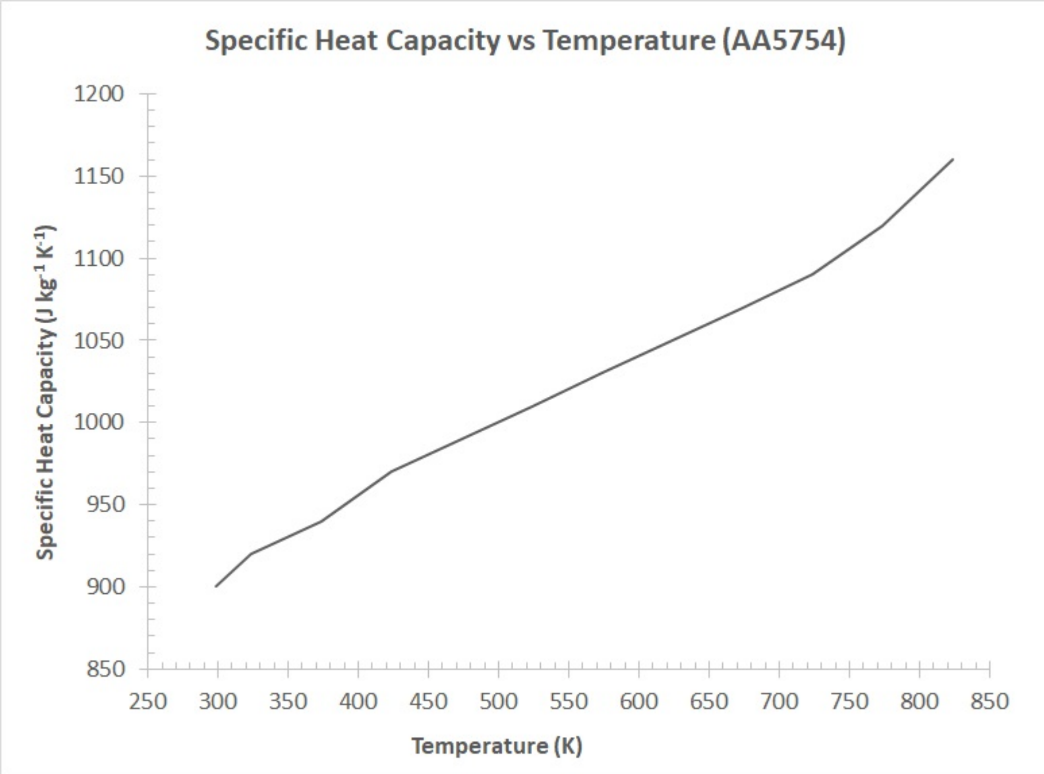

FIG. 3.64: Specific Heat Capacity vs. Temperature (AA5754)

It is worth noting that regarding the Stress – Strain – Temperature surfaces and the corresponding Yield Strength curves (Figs. 3.58 and 3.61, respectively), the presented surfaces/ curves had little to no differences regarding strain rate. Thus, and based on the works of Acar et al. and Lin et al., aluminum alloy 5754 can be considered as strain rate independent.

Since a different material was used in the current simulations, several thermal parameters of the model had to be properly adjusted. In the case of the ring's initial temperature, a temperature of $T_{initial,Al}$ = 773.15 K was considered. This temperature value was input in the *TEMP* option of the INITIAL_TEMPERATURE_SET menu, as this was described in section 2.10. Furthermore, the thermal boundary conditions of the new material had to be reviewed. More specifically, the emissivity factor was considered constant and equal to ϵ_{Al} = 0.32 (**Das and De, 2018**), while the contact conductance was considered equal to H_0 = $h_{contact}$ = 4500 $\frac{W}{m^2 \cdot K}$ (**Yovanovich, n.d.**). The aforementioned material properties were input in the current analysis via the BOUNDARY_RADIATION_SET and the CONTACT_ AUTOMATIC_SURFACE_TO_SURFACE_SMOOTH menus, respectively.

Regarding the movement of the support rolls, initially, the same movement law previously used for the IN718 ring was tested. During these preliminary runs, it was made clear that the aforementioned ring growth algorithm was inadequate, as the movement of the support rolls did not comply with the aluminum ring expansion. This outcome made clear that the constitutive equation of the material affects ring growth pattern, and thus the movement of support rolls should be adjusted properly. Thus, and in order to determine the optimum ring growth algorithm for the current model, a series of trial – and – error simulations had to be conducted. The general form of the tested algorithms was that defined in Eqs.2.57 and 2.58. After the conclusion of the trial simulations, the adjusted algorithms that correspond to the aluminum ring's growth pattern are those presented in Eqs.3.21 and 3.22:

$$R_i = 2.0806 \cdot 10^{-1} \cdot t^{-5.6391 \cdot 10^{-3} \cdot t + 2.0225} + 301.6711 \tag{3.21}$$

$$R_i = -4.1797 \cdot 10^{-1} \cdot t^2 + 36.8289 \cdot t - 332.4106 \tag{3.22}$$

Observations over Eq.3.21 reveal a similar but slightly more complex form than the one hypothesized by Eq.2.57, mainly because of the time-dependent exponent. Nevertheless, with the ring growth algorithm defined, the movement per axis of the support rolls could be estimated via Eqs.2.61 and 2.62. It is worth noting that from the conducted trial runs, the ring center displacement pattern was also estimated (see Eq.2.61 and Fig.2.21), since it was different from the one previously determined for the IN718 ring.

The rest of the model parameters and settings were identical to those presented in Chapter §2. The final aluminum Ring Rolling model was then solved, and its results were subsequently evaluated.

Aluminum Ring Rolling Model Results

In order to evaluate the effects brought by the different ring material, the evolution of specific values during Ring Rolling had to be evaluated. From the plethora of available results, the deformational results were the only that could be compared (to a certain degree) to those received from Chapter §2. On the other hand, results such as equivalent stresses, effective strains, temperature distributions and loads could not be validated in any way, since a corresponding experimental reference did not exist. In the current section, the received deformational results and their comparison to the respective values from the IN718 Ring Rolling simulation will be mainly focused. However, a brief presentation of the rest of the aforementioned results (focused on the main rolling bite and conical rolling bite cross-sections) will be also performed.

Regarding the dimensions of the ring and their evolution during the process, the corresponding values were extracted from the simulation. More specifically, the outer and inner diameter evolution diagrams, as well as the average ring height reduction diagram, were received and subsequently compared to the corresponding results from IN718 ring simulation. The aforementioned comparisons are presented in Figs.3.65 and 3.66:

Observations over Fig.3.65 revealed some interesting results. In both of the outer and inner radii evolution curves, the corresponding values from the two simulations were relatively close, with the radii of the AA5754 ring being slightly lower. However, this trend was completely inverted during Phase 4, when both AA5754 radii surpassed those of the IN718 workpiece. At the end of the process, the outer and inner radii values of the AA5754 ring were $R_{f,Al}$ = 470.46 mm and $r_{f,Al}$ = 419.95 mm, respectively. Compared to the corresponding values received at the end of the IN718 simulation (R_f = 461.03 mm and r_f = 408.16 mm, respectively), differences of ΔR = 2.04% and Δr = 2.89% were observed. These differences can be considered as significant in most engineering applications, thus the importance of ring material to the deformational outcome of Ring Rolling becomes apparent.

In the case of the average ring height, the comparison of the two simulations showed a different overall behavior. More specifically, in Fig.3.66 the average height of the AA5754 ring was greater to that of IN718 for the majority of the process's duration. Only at the very end of the process, the height values from the two methods came very close to one another, with $H_{f,Al}$ = 116.49 mm recorded for the AA5754 workpiece. The difference between the

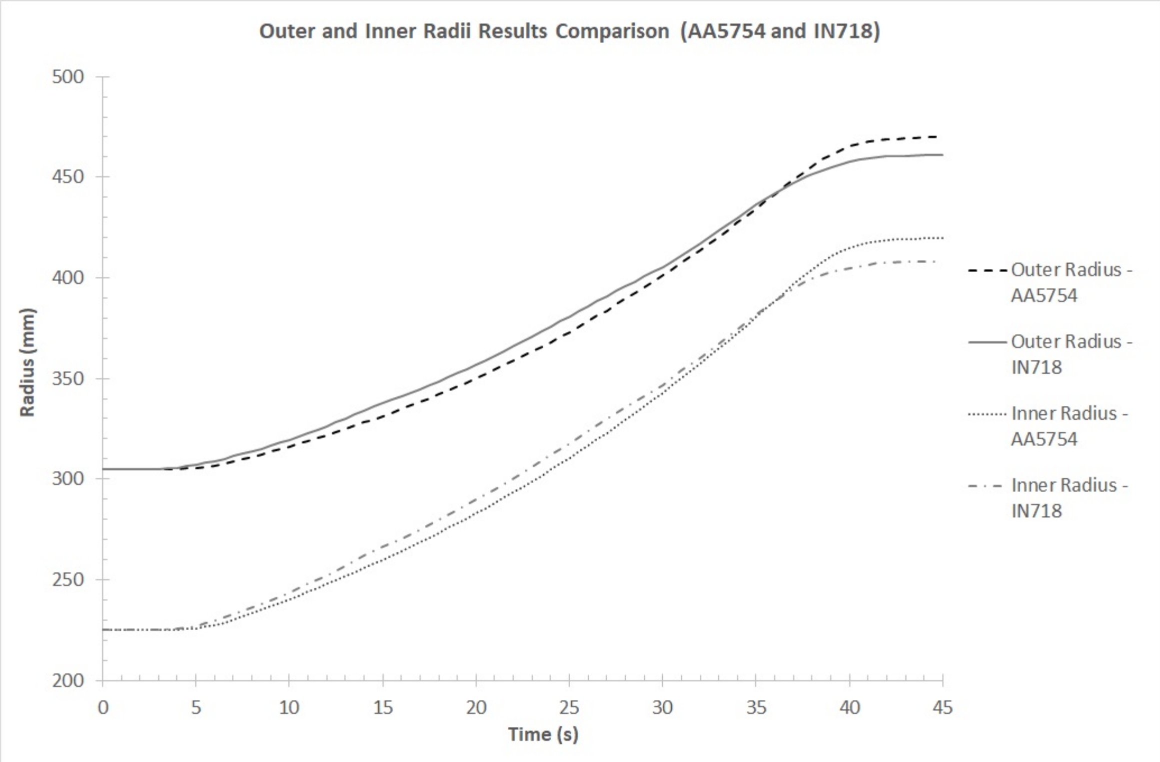

FIG. 3.65: Comparison between the IN718 and AA5754 numerical results of the ring's outer and inner radii

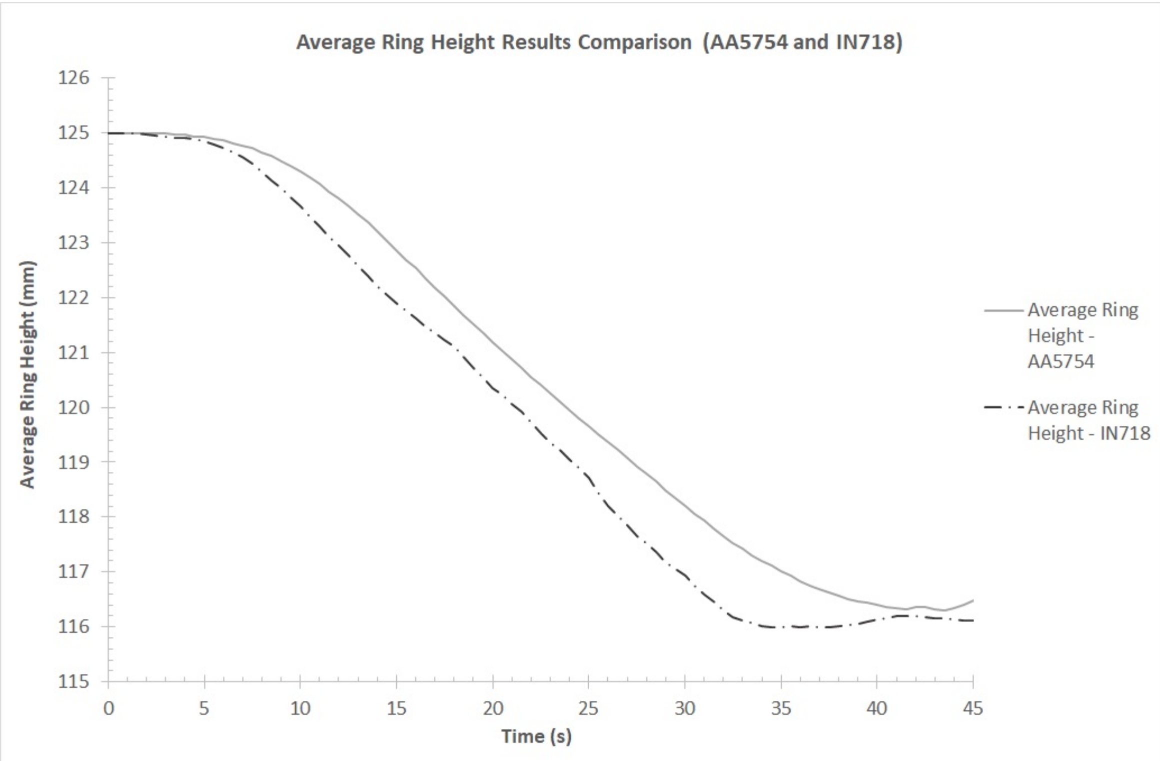

FIG. 3.66: Comparison between the IN718 and AA5754 numerical results of the average ring's height

final average ring height values from the AA5754 and the IN718 (H_f = 116.1 mm) simulations could be estimated at approximately ΔH = 0.33%, which can be considered negligible.

From the combination of the aforementioned results, a difference in the final ring volume can be observed. This inconsistency between the final ring volumes can be explained from a simple consideration of the final thickness from the two simulations. A comparison of the ring thickness from the two simulations is presented in Fig.3.67:

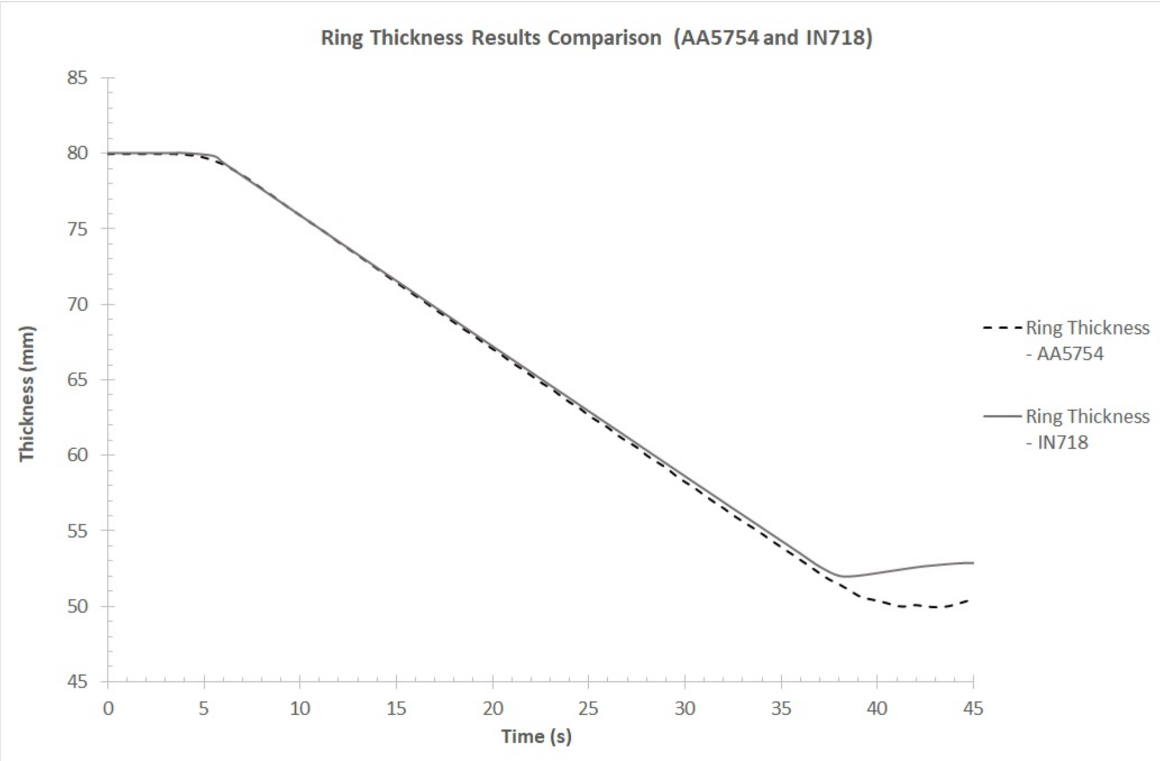

FIG. 3.67: Comparison between the IN718 and AA5754 numerical results of the ring's thickness

Observations over Fig.3.67 revealed a rather expected result. More specifically, the ring's thickness in the case of the IN718 seemed to reduce slower than the corresponding dimension of the AA5754 ring. At the end of the process, the final thickness of the IN718 ring was approximately $f_{f,IN718}$ = 52.87 mm, while the same dimension of the AA5754 ring was approximately $f_{f,Al}$ = 50.51 mm. This inconsistency can be attributed to the average size of bulge defects, which were greater in the case of IN718 (also see Figs.2.34 and 3.70) and were included in the calculation of the average thickness of each model. The corresponding volumes for the two rings were calculated to be equal to V_f = 16,761,239.2 mm^3 and $V_{f,Al}$ = 16,462,537.1 mm^3, which produce a percentage difference of approximately ΔV = 1.78% that can be considered as relatively small. Other reasons that contribute to the inconsistent final ring volumes are the small deviations from the use of average values for the calculations and the small noncompliance caused by the inert numerical defects. It is worth reminding, however, that the presented difference can be generally considered acceptable in most engineering applications.

Other significant deformational results of the current process are the ovalities of the outer and inner diameters. The corresponding curves are presented in Fig.3.68:

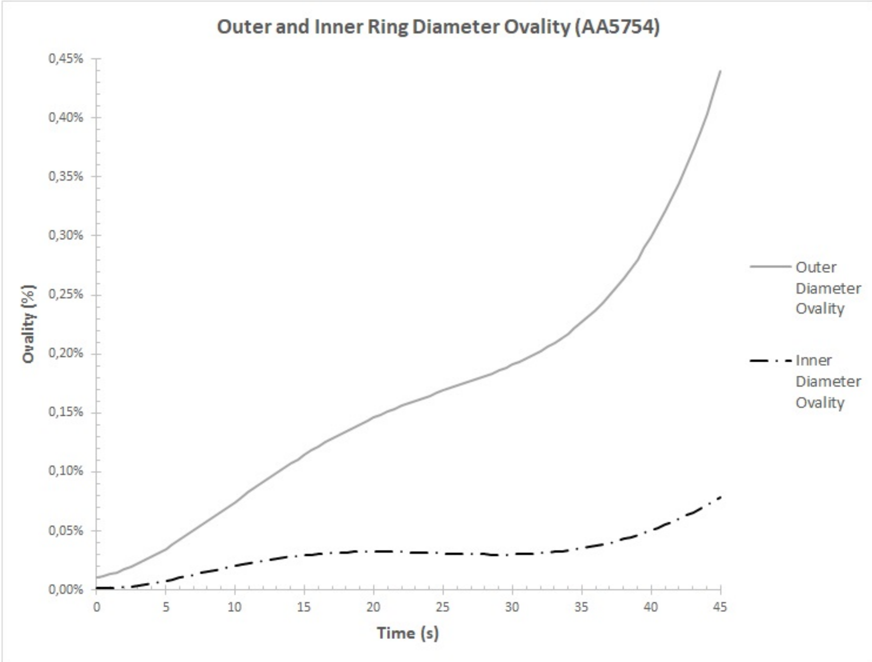

FIG. 3.68: Outer and Inner diameter percentage ovalities during Ring Rolling (AA5754 ring)

Observations over the ovality results (Fig.3.68) revealed relatively small values, similarly to the corresponding results from the IN718 Ring Rolling simulation (see Fig.2.37). In this case, too, the outer diameter ovality was greater than the inner diameter ovality, throughout the duration of the process. The final (and maximum) outer diameter percentage ovality was approximately 0.44%, while the final (maximum) inner percentage ovality was approximately 0.07%. Both of these values are small enough that can be considered negligible, thus the final ring product had an almost perfectly round shape.

Next, the positioning of the support rolls throughout the simulated process was evaluated. For this reason, images of the ring and the support rolls at specific time instances were extracted. The aforementioned images are presented in Fig.3.69:

Observations over Fig.3.69 reveal a very good positioning of the support rolls regarding the expansion of the ring at the corresponding time instances. This fact ensured that the algorithm presented in Eqs.3.21 and 3.22, although more complicated than the one used for the Ring Rolling of IN718, matched the evolution of the ring in the simulation. Thus, it can be concluded that a non-linear expansion of the outer diameter was the governing ring growth mechanism.

The last of the deformational results that was evaluated had to do with the defects formed during Ring Rolling. A graphic representation of these defects is presented in Fig.3.70:

Observations over Fig.3.70 reveal very similar defect geometries to those previously presented in Fig.2.34. More specifically, the same fishtail and bulge formations (as a general shape) were formed after the main rolling bite and the conical rolling bite, respectively, and thus the same conclusions can be drawn in this case, too (also see section §2.16.1).

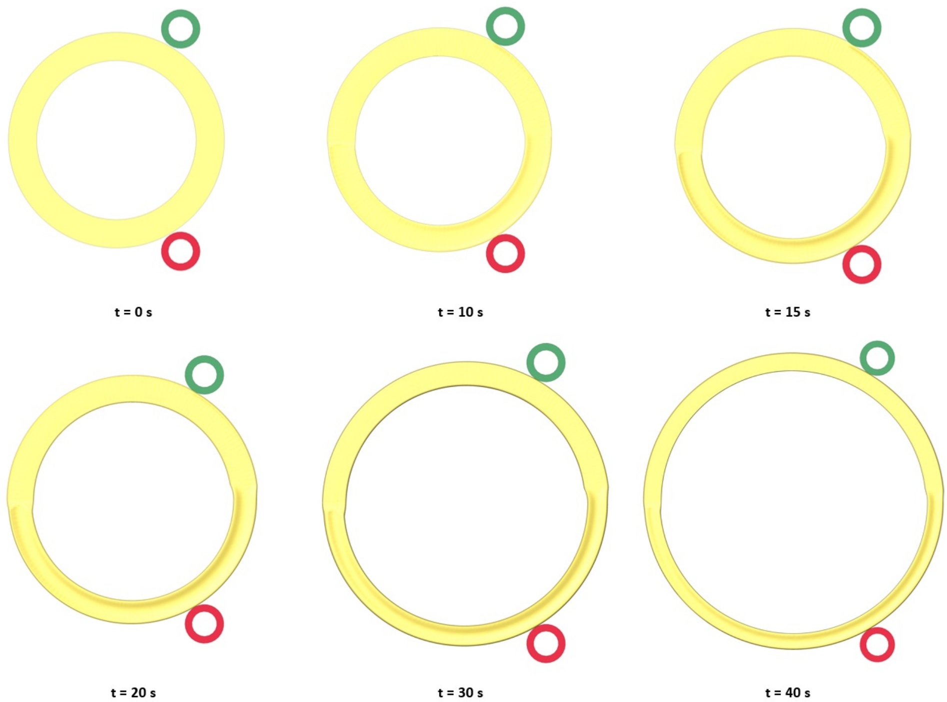

FIG. 3.69: Deformation of AA5754 ring and support roll positions at specific time instance

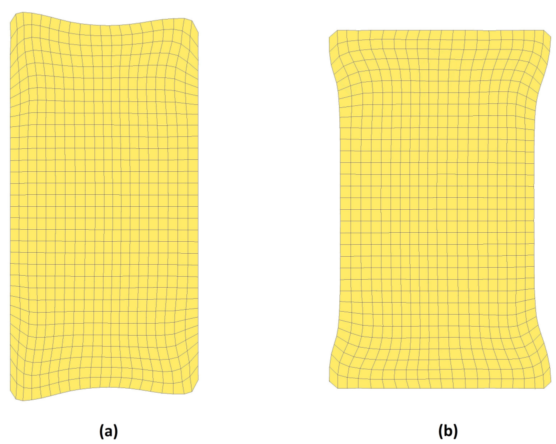

FIG. 3.70: Common defects formed during Ring Rolling at a time instance of t = 24 s (AA5754): (a) Fishtail defect and (b) bulge defect

After the deformational results have been evaluated, an analysis of the equivalent Von Mises and the effective strain results followed. In the case of the equivalent Von Mises stress results, the corresponding distributions in the main rolling bite and the conical rolling bite are presented in Figs.3.71 and 3.72, respectively:

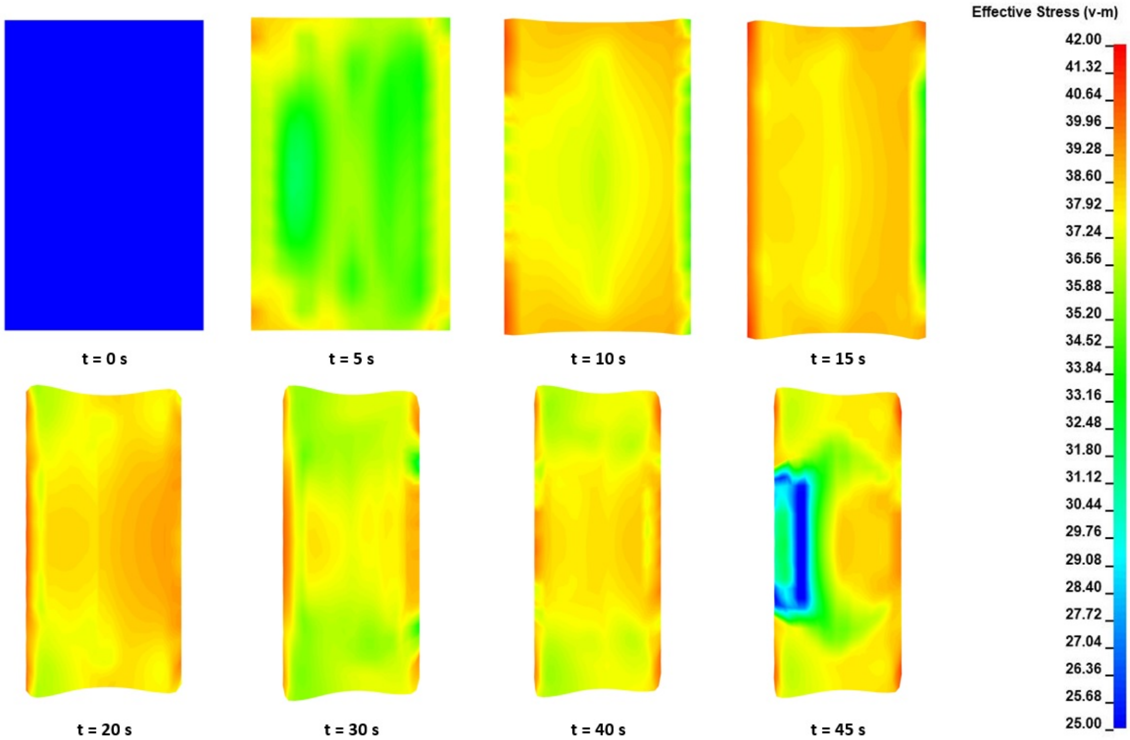

FIG. 3.71: Equivalent Von Mises stress distributions in multiple time instances during the simulation of the AA5754 Ring Rolling process (Cross-section of the workpiece in the main rolling bite)

Observations over Fig.3.71 revealed a similar stress distribution in the ring's main rolling bite cross-section to those previously noted for IN718 (Fig.2.38), although some differences were also present. Before proceeding, it should be noted that in Fig.3.71 the outer peripheral ring surface was on the right side of the presented time instances, while the inner ring peripheral surface was on their left side. During the first few time instances of the process (t = 5–10 s), the highest stresses were concentrated on the inner surface edges, with their maximum recorded values being approximately 40–42 MPa. Also, during the same process duration, the stress distribution around the contact with the main roll seemed to relax from 37-38 MPa at t = 5 s to 30–33 MPa at t = 10 s, while at the same time the stress distribution on the majority of the cross-section significantly increased from 30-32 MPa to 38-40 MPa. The increased stresses along the entire cross-section persisted until t = 20 s, when a stress increase towards the outer peripheral surface could be seen. The corresponding stress values during this period ranged from 30-33 MPa (t = 15 s) to 38–40 MPa (t = 20 s). Additionally, the highest stress distribution around the contact with the mandrel expanded to the whole height of the workpiece, although the same stress values were recorded (40–42 MPa). During the final forming steps of the process (t = 30–40 s), a similar picture to that of the IN718 ring (during the same period) was observed. More specifically, the highest stresses seemed to concentrate around the middle of the ring's height and around its inner and outer surface edges. Similarly to IN718, this distribution indicated the ironing of an overall barrel-like shape produced by the conical roll bite, as well as of the formed bulge

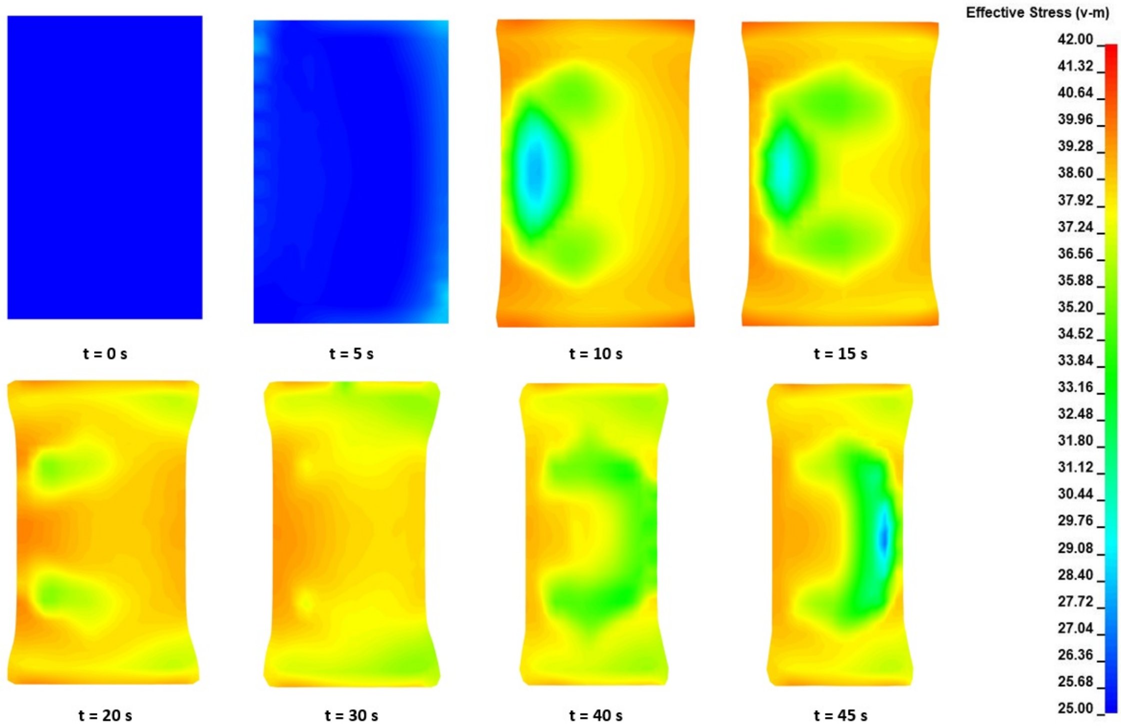

FIG. 3.72: Equivalent Von Mises stress distributions in multiple time instances during the simulation of the AA5754 Ring Rolling process (Cross-section of the workpiece in the conical rolling bite)

defects. The only difference to the IN718 ring was that these central high stress distributions had the tendency to connect between the inner and the outer surfaces. However, the highest stress values at those regions remained almost the same, compared to the previous time instance (t = 20 s). Finally, during the last time instance (t = 45 s), a significant stress decrease was observed around the middle of the inner ring's surface from 38-42 MPa (t = 40 s) to 25–30 MPa (t = 45 s). On the other hand, the stresses in the rest of the cross-section remained almost the same, both in distribution and values. A similar behavior had been observed in the IN718, where the stress decrease around the inner surface region indicated a contact relaxation with the mandrel, apart from its respective edges where the bulge ironing continued to occur.

Regarding the equivalent Von Mises stresses recorded at the conical rolling bite, relatively similar distributions were observed between the AA5754 (Fig.3.72) and the IN718 (Fig.2.39) workpieces in this case too, but with some slight differences. Initially, it should be noted that in Fig.3.72, the inner ring peripheral surface was located on the right side of the presented time instances, while the outer peripheral surface was on their left side. During the first time instances (t = 5 s), some relatively small residual stresses could be observed, mainly on the inner surface edges. The corresponding stress values were approximately 25–28 MPa. From that point onwards, increased stresses could be observed throughout the cross-section. More specifically, during the early forming steps (t = 10–15 s) the highest stresses could be observed along the top and bottom end surfaces of the workpiece, with their corresponding values ranging between 40–42 MPa. Furthermore, increased residual stresses of approximately 38–40 MPa could be observed along the inner ring surface, while the corresponding stresses on the outer peripheral surface were lower (35–38 MPa). Interestingly, the center of the cross-section during the early forming steps had lower stresses, contrary to what was observed in the main rolling bite during the same time instances. Then, during the next forming steps (*t* = 20–30 s) the equivalent stresses at the center of the cross-section increased to approximately 37–40 Mpa, thus bridging the increased residual stress fields of the inner and outer peripheral surfaces. At the same time, the stress fields located just next to the top and bottom end surfaces seemed to gradually relax from 38-40 MPa to approximately 34–37 MPa. Finally, during the last forming and final process steps (*t* = 40–45 s) mostly the same stress distribution could be observed, with the sole major difference being a residual stress relaxation at the middle of the inner peripheral surface. The stress values during these instances decreased from 38-40 MPa, to 32–35 MPa and eventually to 25–30 MPa. This behavior can be explained considering the contact relaxation between the mandrel and the ring, which would result in lower residual stresses.

Regarding the effective strain results observed in the main rolling and conical rolling bites, the corresponding distributions are presented in Figs.3.73 and 3.74, respectively:

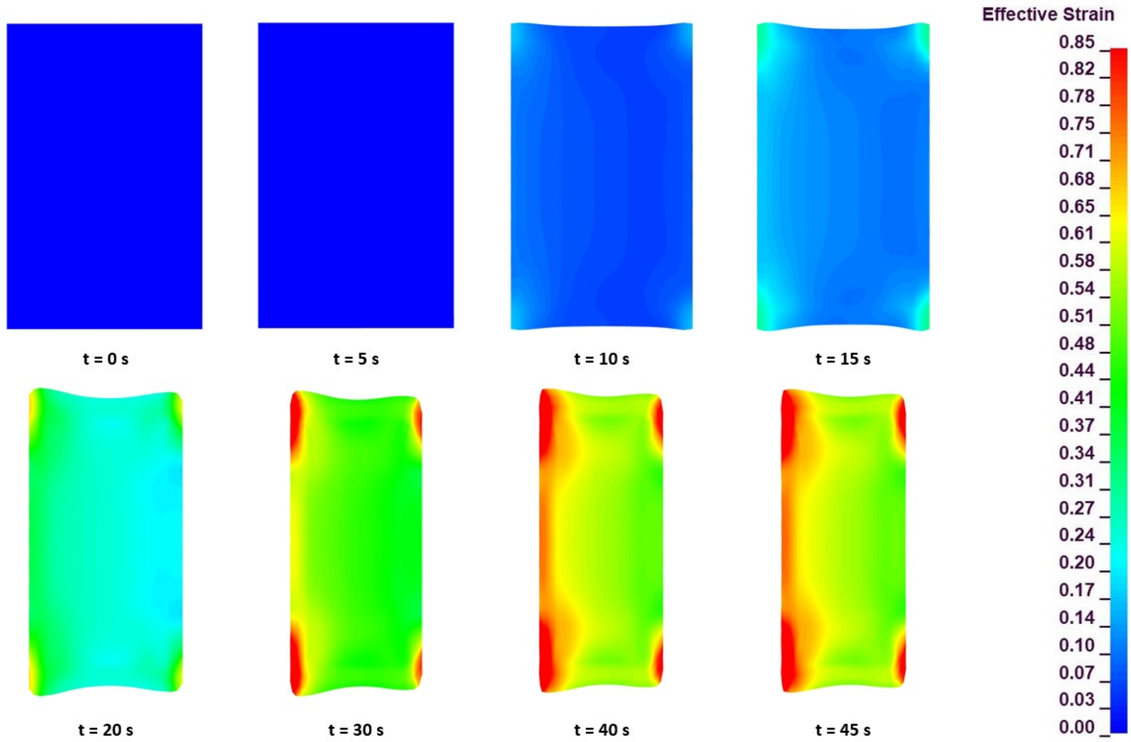

FIG. 3.73: Effective strain distributions in multiple time instances during the simulation of the AA5754 Ring Rolling process (Cross-section of the workpiece in the main rolling bite)

Observations over the effective strains in both Figs.3.73 and 3.74 revealed almost identical distributions to the corresponding previously observed for IN718 (Figs.2.43 and 2.44). In the case of the effective strain distributions in the main rolling bite (Fig.3.73), the highest strains were concentrated on the inner and outer surface edges throughout the duration of the process, with their corresponding values gradually increasing. Other than that, increased strains were also observed around the contact with the mandrel, while the effective strains around the contact with the main roll were significantly lower. The maximum effective strains were recorded at the end of the process (*t* = 40–45 s) around the inner surface edges, with the corresponding values being approximately $\epsilon_{Al,MB,max}$ = 1.3. Overall, the

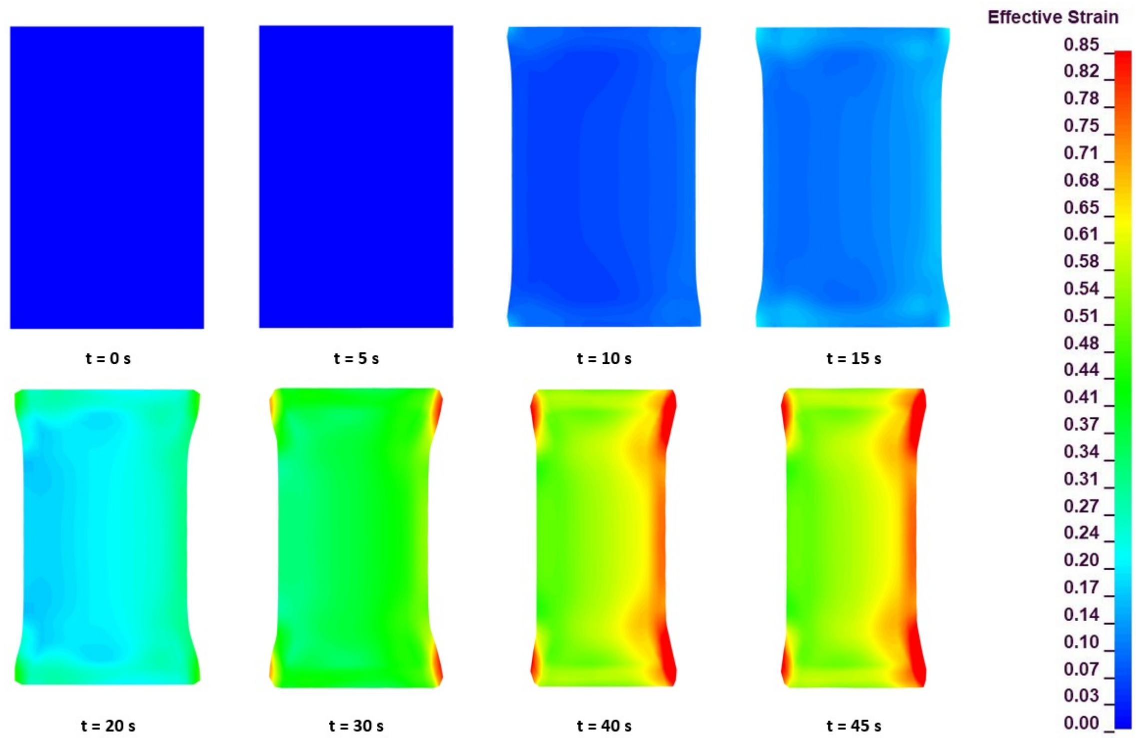

FIG. 3.74: Effective strain distributions in multiple time instances during the simulation of the AA5754 Ring Rolling process (Cross-section of the workpiece in the conical rolling bite)

observed strain fields had the expected behavior as the strains progressively increased during the process, while the maximum values were concentrated on the ironing of the bulges, where the greatest (relative) deformation of the cross-section occurred.

Regarding the effective strains in the conical rolling bite (Fig.3.74), almost identical strains could be observed to the corresponding of the main rolling bite throughout the process, both in terms of their distributions and their values. The only difference was the maximum recorded strain value, which was approximately $\epsilon_{Al,CR,max}$ = 1.15 and was observed around the inner peripheral surface edges, during the end of the process (t = 40–45 s). Since the effective strain results were identical to those of the main rolling bite, the same conclusions can be drawn in this case, too.

Following, the main and axial rolling load results were analyzed. The corresponding curves are presented together in Fig.3.75:

Observations over the main and axial rolling loads presented in Fig.3.75 revealed a similar load distribution to the corresponding load curves of the IN718 Ring Rolling simulation (Figs.2.48 and 2.49, respectively). For both the main and the axial rolling loads, a peak was observed early in the process (at t = 18.5 s for the main rolling load and at t = 19.8 s for the axial rolling load), which decreased from that point and until the end of the process. The maximum recorded load values were $F_{max,MRL,Al}$ = 193.8 KN and $F_{max,ARL,Al}$ = 109.2 KN, respectively. In the case of the main rolling load, the subsequent load decrease after t = 18.5 s occurred with different rates for the rest of the process's duration. On the other hand, the load decrease rate in the case of the axial rolling load was much steadier. From the comparison of the load curves in Fig.3.75 to the corresponding IN718 load curves (Figs.2.48 and

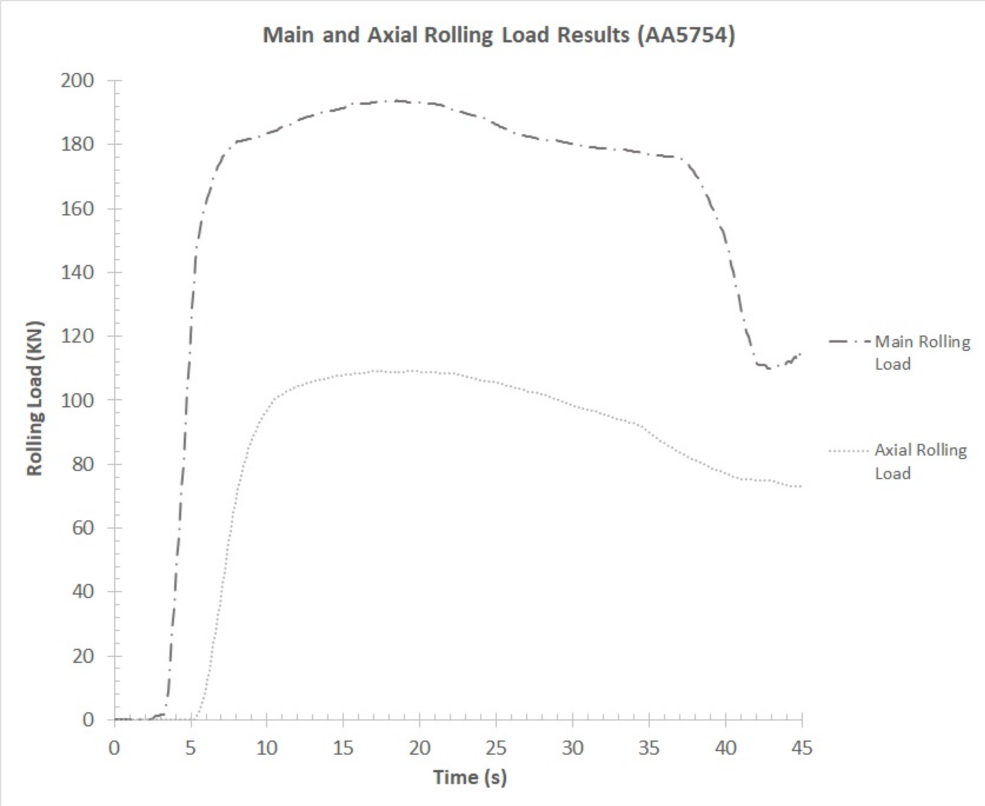

FIG. 3.75: Main and axial rolling loads result curves (AA5754)

2.49) and apart from the absolute load value differences caused by the different mechanical properties, a slight delay in the manifestation of the corresponding maximum loads could be seen between the two materials. More specifically, the maximum loads in the AA5754 process appeared after 5–6 s approximately, compared to IN718. Other than that, the corresponding AA5754 and IN718 load curves had an average overall difference of 83 - 85% to their respective values. Since there were no corresponding experimental data to validate the process, no further conclusions could be drawn.

Finally, the thermal results from the AA5754 simulation were evaluated. The first result evaluation involved the temperature distributions in the main and conical rolling bite cross-sections. The corresponding temperature fields are presented in Figs.3.76 and 3.77, respectively:

Observations over Figs.3.76 and 3.77 revealed very similar temperature distributions in both cross-sections of the workpiece, thus they were analyzed simultaneously. Initially, it should be reminded that in Fig.3.76 the inner peripheral surface is on the left side of the depicted cross-sections, while in Fig.3.77 the same surface is on their right side. From an overview of all time instances, it seems like two separate heating phases took place. During the early to mid time instances (t = 0–10 s), the initial heat of the workpiece seemed to dissipate through the contacts with the tools, as well as through its free surfaces. More specifically, the initial temperature of the workpiece gradually reduced along the surfaces of the ring, while the temperature in each cross-section's core remained hotter. The minimum temperature values at these time instances were always observed around the tool contacting areas, which however seemed to partially reheat as shown at their following time instances on the

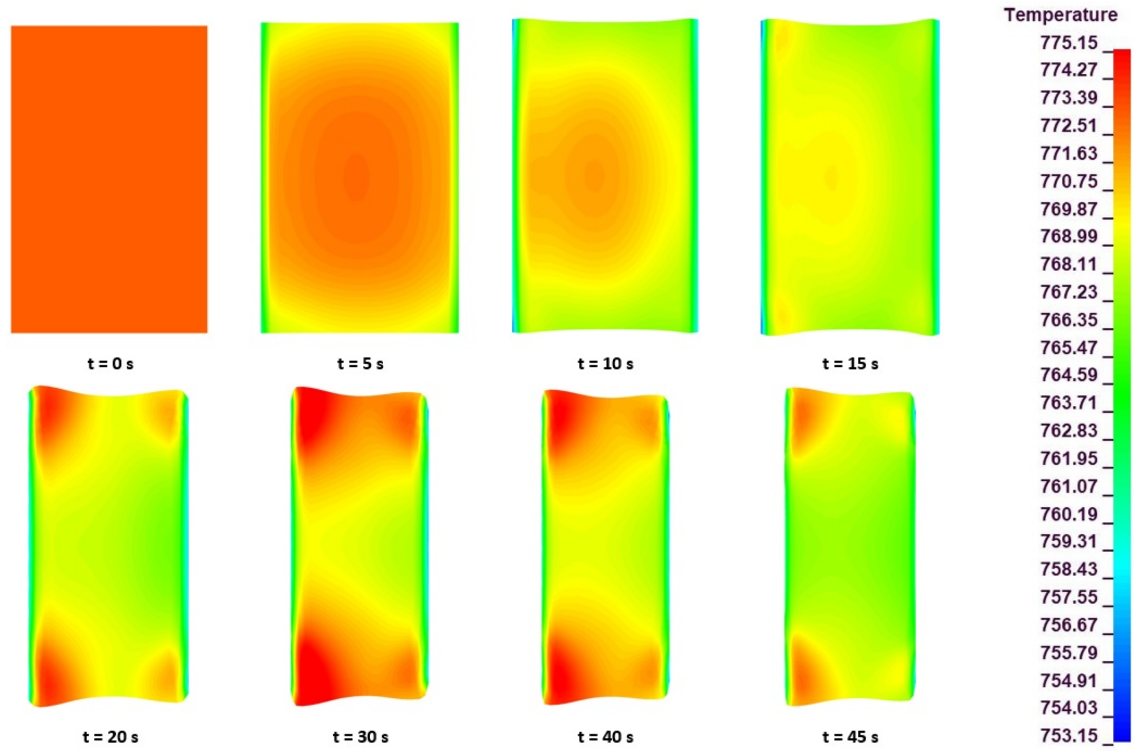

FIG. 3.76: Temperature distributions in multiple time instances during the AA5754 Ring Rolling simulation (Cross-section of the workpiece in the main rolling bite)

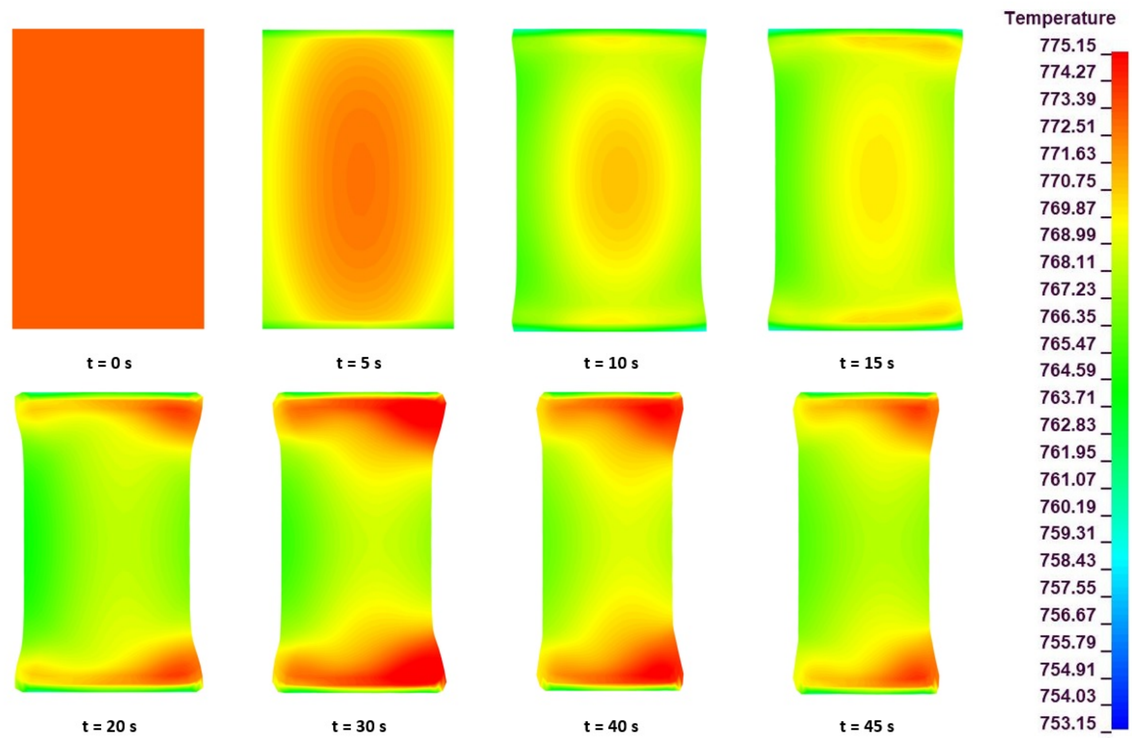

FIG. 3.77: Temperature distributions in multiple time instances during the AA5754 Ring Rolling simulation (Cross-section of the workpiece in the conical rolling bite)

other cross-section (i.e. the cooler upper and lower surfaces of the conical rolling bite cross-section at t = 5 s were slightly hotter when observed at the main rolling bite cross-section at t = 10 s). Eventually, the core temperature in both cross-sections gradually dropped until t = 15 s. From that point onwards, the second heating phase began, which lasted until the end of the simulation. During these time instances (t = 15–40 s), the temperature around the edges of the workpiece began heating, as a result of the plastic work turned to heat from the ironing of the bulge and fishtail defects. Furthermore, the temperature around the inner surface edges was always slightly higher than that around the outer surface edges during the same time instance, regardless of the cross-section. Finally, these increased temperatures began decreasing again near the end of the process, as a result of the reduced ironing of the aforementioned defects. The maximum temperature value from the entire simulation was recorded around the inner peripheral surface edges at approximately $T_{max,Al}$ = 777.3 K and at a time of t = 35.5 s.

The second thermal results evaluation involved the average outer peripheral and upper surface temperature values. The corresponding curves are presented together in Fig.3.78:

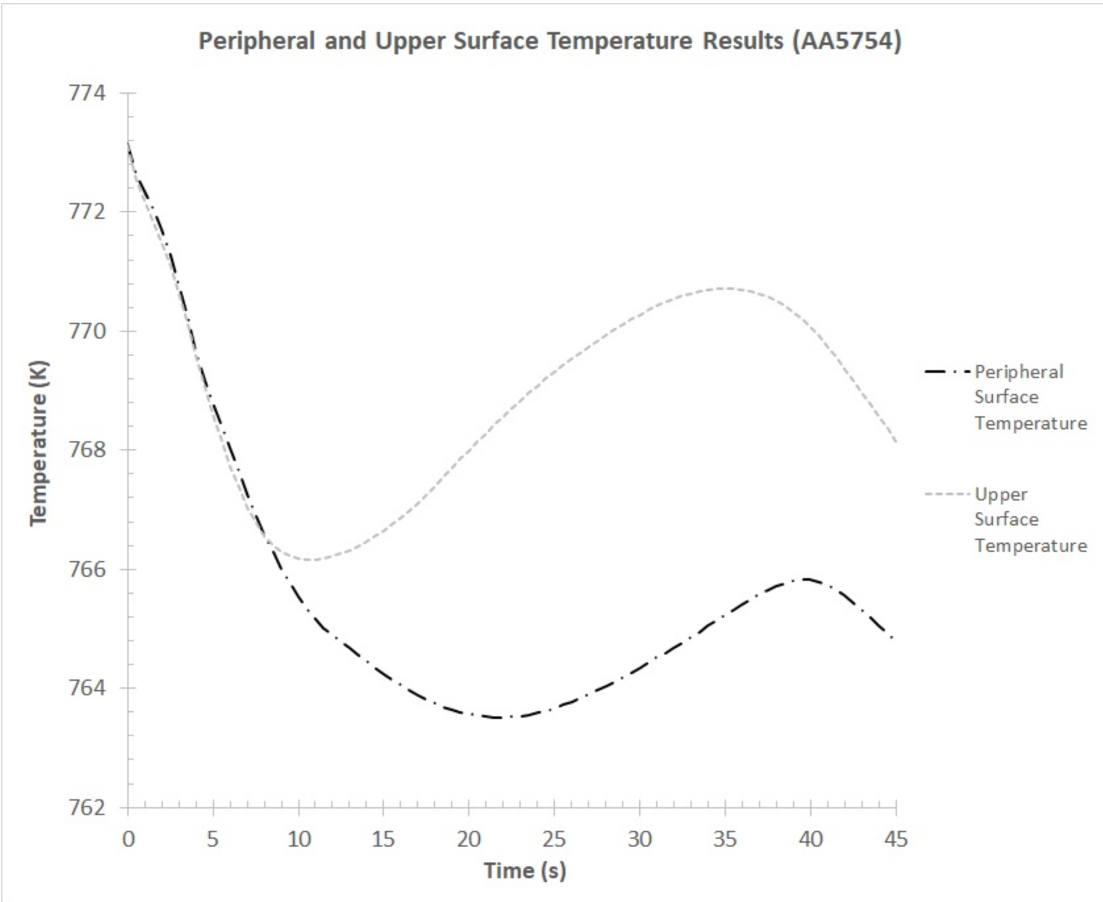

FIG. 3.78: Average outer peripheral and upper ring surface temperature result curves (AA5754)

The presented curves in Fig.3.78 were extracted in the same way as their IN718 counterparts (also see section §2.15.3). Similarly to the corresponding thermal result curves of the IN718 simulation (Fig.2.50), the upper surface of the workpiece seemed to be hotter than the peripheral surface. Unlike IN718, however, both average temperature curves followed a similar pattern, with an initial temperature drop followed by a subsequent temperature increase until the end of the corresponding forming phase and a final temperature decrease during Ring Rolling Phase 4. The corresponding points when the ring's surfaces began heating after cooling and vice versa were different between the two curves, with the extremums of the outer peripheral surface manifesting later. As with the analysis of the rolling load curves, the lack of corresponding experimental results make any further conclusions impossible.

From the entirety of the presented results, it was made clear that the AA5754 Ring Rolling simulation produced rational results. Although different from the validated IN718 Ring Rolling model, the presented results were realistic enough, so that their differences could be attributed to the change of the workpiece's material. Additionally, since no major defects or extreme values were observed, the conducted numerical analysis can be considered safe to be used as a reference model for the following analyses.

3.4.2 Higher Degree Ring Growth Algorithms

The importance of the movement law applied for the support rolls was briefly mentioned in Chapter §2, regarding the dimensional quality of the produced ring. However, the usage of multiple movement laws for different periods within the same manufacturing process, although effective, significantly increased the complexity of the conducted analysis. More specifically, apart from the effective separation of one continuous diameter growth curve to several others, which proved to be quite challenging since the exact separation point should be chosen carefully, ensuring the continuity of these functions was also very difficult. These facts were made even more apparent during the simulation of the AA5754 Ring Rolling process, since an even more complex expression for the ring growth algorithm during Phases 1 and 2 was required. For these reasons, the usage of a single, higher degree polynomial that would describe the movement of support rolls for the whole duration of the process was further investigated. Furthermore, the effects of the ring's material on the aforementioned polynomials were also investigated.

In order to investigate different ring growth algorithms, the reference IN718 (presented in Chapter §2) and the reference AA5754 (presented in section §3.4.1) models were used as the basis for the current analysis. Both of the aforementioned models were used as-is in their corresponding analyses, with the only exception being their respective support roll movement laws. The movement functions of the support rolls were estimated from a higher order degree polynomial for each of the two different ring materials. Thus, two different numerical models were created.

For the determination of the ring growth polynomials, the outer radius results presented in Figs.2.35 and 3.65 were used. More specifically, the corresponding outer radius results were input in the python script presented in Appendix B.2 so that curve fitting would be performed. The minimum degree polynomial with a coefficient of determination of at least $R^2 = 0.999$ for each material would be used. For both ring materials, the minimum functions that satisfied the aforementioned condition were the 5^{th} order polynomials presented in Eq.3.23 (for IN718) and 3.24 (for AA5754):

$$\begin{aligned} R_i = {} & -8.5270 \cdot 10^{-6} \cdot t^5 + 8.5333 \cdot 10^{-4} \cdot t^4 - 3.1678 \cdot 10^{-2} \cdot t^3 \\ & +5.9987 \cdot 10^{-1} \cdot t^2 - 2.2830 \cdot t + 306.4734 \end{aligned} \tag{3.23}$$

$$\begin{aligned} R_i = {} & -6.8514 \cdot 10^{-6} \cdot t^5 + 6.6829 \cdot 10^{-4} \cdot t^4 - 2.4552 \cdot 10^{-2} \cdot t^3 \\ & +5.0627 \cdot 10^{-1} \cdot t^2 - 2.0714 \cdot t + 306.6942 \end{aligned} \tag{3.24}$$

Similarly to previous simulations, the displacement coordinates for each support roll were defined by substituting Eqs.3.23 and 3.24 in Eqs.2.61 and 2.62.

After the created numerical models were solved and inspected for errors, the deformational results from each model were extracted and evaluated. In the following analysis, only the deformational results from the conducted simulations were thoroughly evaluated, since the task at hand was to judge whether the proposed higher degree polynomials would bring any changes to the final ring geometry or not. The corresponding results for each different ring material will be presented separately.

IN718 Ring Material Results

Regarding the IN718 models' results, the outer and inner radii curves from the conducted polynomial simulation were extracted and subsequently compared to the corresponding results from section §2.16.1. The aforementioned comparisons are presented in Fig.3.79:

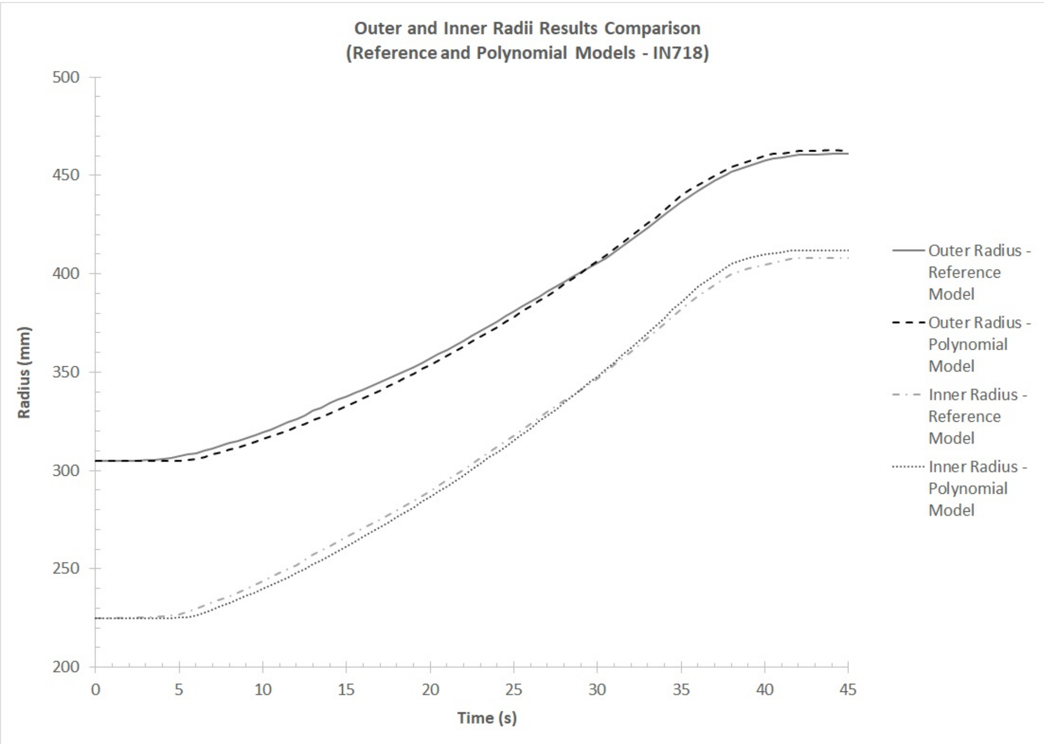

FIG. 3.79: Comparison between the outer and inner radii results from the 5^{th} degree ring growth polynomial and the reference models (IN718)

Observations over Fig.3.79 revealed mostly similar deformations between the reference and the polynomial ring growth algorithm models. However, a closer inspection of the compared curves revealed some slight differences. More specifically, from the beginning of the process and until approximately t = 29 s, the evolutions of both the outer and the inner radii were slower in the polynomial model than the corresponding of the reference model. This trend however completely reversed after t = 29 s, when the outer and the inner radii of the polynomial model were consistently greater. At the end of the process, the outer radius of the polynomial model was approximately $R_{poly,IN718}$ = 462.61 mm while the inner radius was approximately $r_{poly,IN718}$ = 411.61 mm. From these values, the final thickness of the ring can be estimated to be $f_{f,polynomial,IN718}$ = 51 mm approximately, which is less than the final thickness calculated by the reference IN718 model ($f_{f,IN718}$ = 52.87 mm). This difference in ring thickness can be attributed to the smaller bulge defects in the polynomial simulation, as presented in Fig.3.80

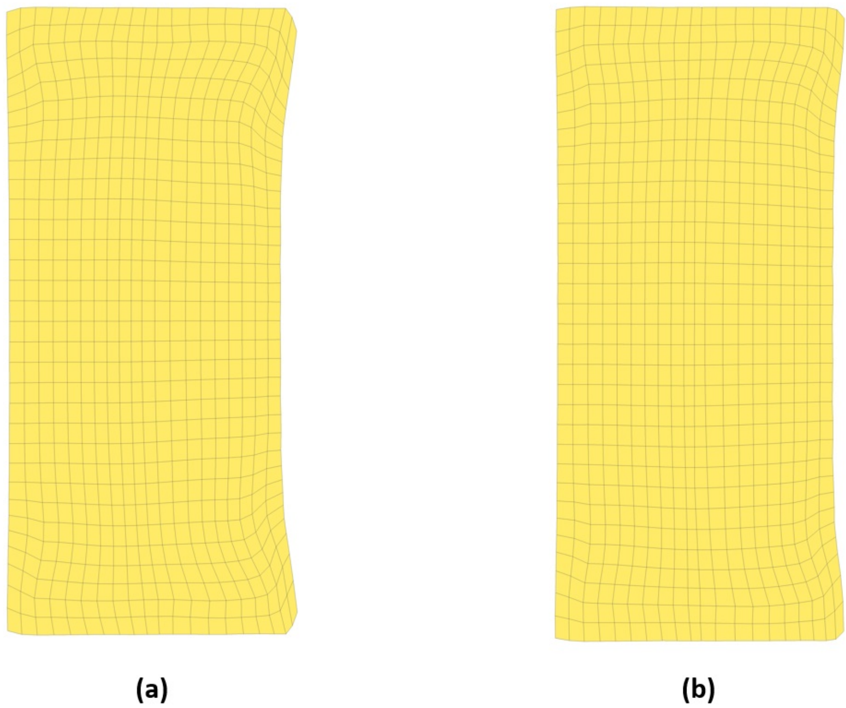

FIG. 3.80: Bulge defect comparison at a time instance of t = 45 s: (a) Reference IN718 model and (b) Polynomial ring growth algorithm model

Similarly to previous figures, in Fig.3.80 the inner peripheral surface is located on the right side of the presented cross-sections and the outer peripheral surface is on their left side. Observations over Fig.3.80 revealed a difference in the size of the bulge defects formed during the process. The two instances presented in Fig.3.80 show the formed bulges at the end of the process from each model, with the cross-sections being those at the exit of the conical rolling bite, where the bulges have not been affected by any ironing yet. A closer inspection over, the bulges created on the inner peripheral surface of the reference model (Fig.3.80(a)) were slightly larger than the corresponding bulges of the polynomial model (Fig.3.80(b)). Since the position of the conical rolls is the same between the two models, the aforementioned differences in bulge size indicate that the ring was slightly pressed towards the mandrel in the case of the polynomial model, which subsequently led to the increased ironing of the bulges and/or the simultaneous reduction in thickness. In general, the difference in the calculated radii prove that the applied movement of the support rolls can affect the dimensional precision of the final product. This fact applies even in cases where the support roll movement is adjusted indirectly, for example through the control of the oil pressure in hydraulic support roll mills.

Regarding the average ring height, the corresponding curves from the reference and the polynomial ring growth algorithm models are presented in Fig.3.81:

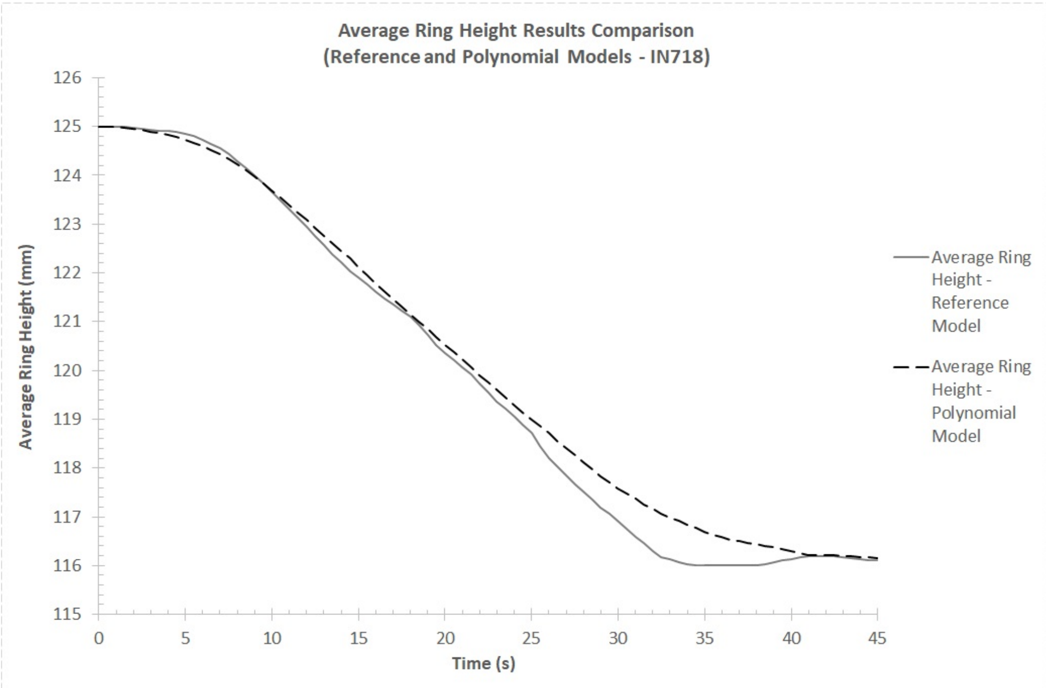

FIG. 3.81: Comparison between the average ring height results from the 5^{th} degree ring growth polynomial and the reference models (IN718)

Observations over Fig.3.81 revealed relatively close average ring height results between the two models. For the majority of the process's duration, the average ring height values from the two methods were almost equal. However, at approximately t = 25 s, the average ring height in the reference model had a sudden reduction until t = 34 s, when it began to slightly increase again. This can mainly be attributed to the form of the movement laws used in the reference model, which resulted in the formation of lesser sized fishtail defects that were considered in the calculation of the average ring height. On the other hand, the average ring height curve from the polynomial model followed a much smoother path, without sudden reductions or increases in the corresponding values. Finally and after t = 41 s, the average ring height curves from the two methods become almost identical, with the final ring height value from the polynomial model being $H_{f,polynomial}$ = 116.2 mm.

Finally, the ovality results from the two models were extracted and evaluated. The corresponding curves from the two models are presented in Fig.3.82:

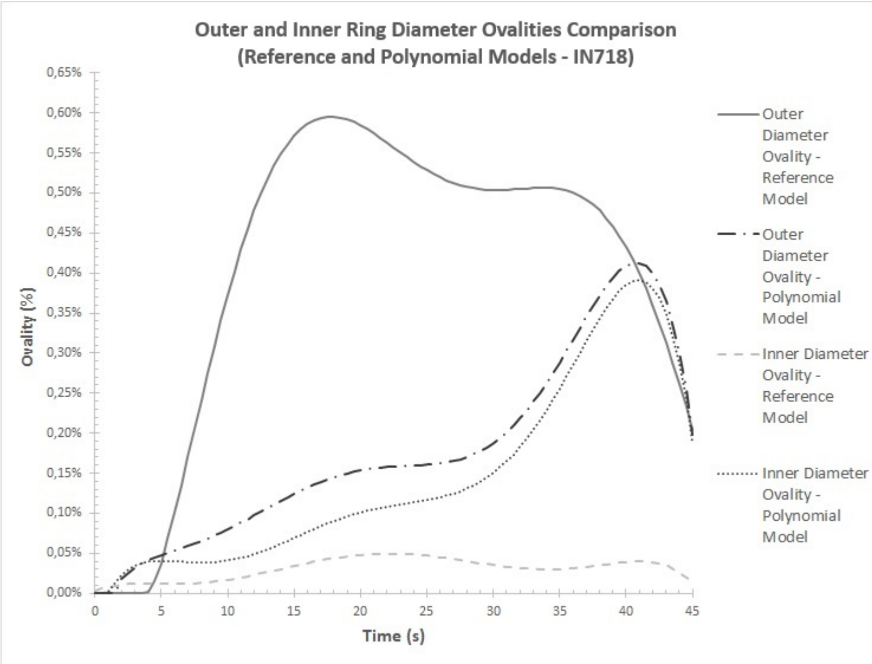

FIG. 3.82: Outer and inner diameter percentage ovality curves calculated during Ring Rolling (Reference and Polynomial Models - IN718)

Observations over Fig.3.82 revealed some rather interesting facts. While in the case of the outer diameter, utilization of the higher degree polynomial algorithm led to a lesser ovality curve but with almost the same final ovality value (compared to the reference model), in the case of the inner diameter ovality, the reference model curve had lower values throughout the duration of the process. Moreover, both the outer and the inner diameter ovality curves of the polynomial model followed very close paths. More specifically, both curves increased steadily until approximately t = 30 s, when their corresponding increase rates maximized. These high increase rates were maintained until approximately t = 40 s, when the corresponding maximum ovality value of each curve was reached, and from that point onwards both curves began decreasing until the end of the process. The final values were almost identical, with the final outer diameter percentage ovality being approximately 0.20% and the final inner diameter percentage ovality being approximately 0.19%. The aforementioned observations indicate that the utilization of a single, higher degree polynomial ring growth algorithm leads to an almost parallel evolution of both ring diameters during the process. Subsequently, this leads to a more uniform forming process, which can be more easily predicted. It is worth noting that although ovality differences were observed between the reference and polynomial models, the corresponding absolute ovality values in all cases were small enough that can be considered negligible.

Overall, from the evaluation of the IN718 polynomial ring growth algorithm model results and their comparison with the corresponding results from the reference model, a smoother and more uniform ring growth was shown by the polynomial model. All dimensional results followed smoother deformation paths, without sudden changes in their rates. Additionally, different localized deformations were observed in the case of the polynomial model, which subsequently affected the final dimensions of the workpiece. From all of the above, the importance of a well-defined support roll movement law for the dimensional precision of the final ring was made apparent, especially considering the complexity of the Ring Rolling process that can be easily affected by any of the key process parameters. However, since the final dimensions of the final products were relatively close, the two support roll movement laws can be considered as equally acceptable.

AA5754 Ring Material Results

Similarly to the IN718 models, the AA5754 outer and inner radii results between the reference and the polynomial models were initially compared. The corresponding curves are presented in Fig.3.83:

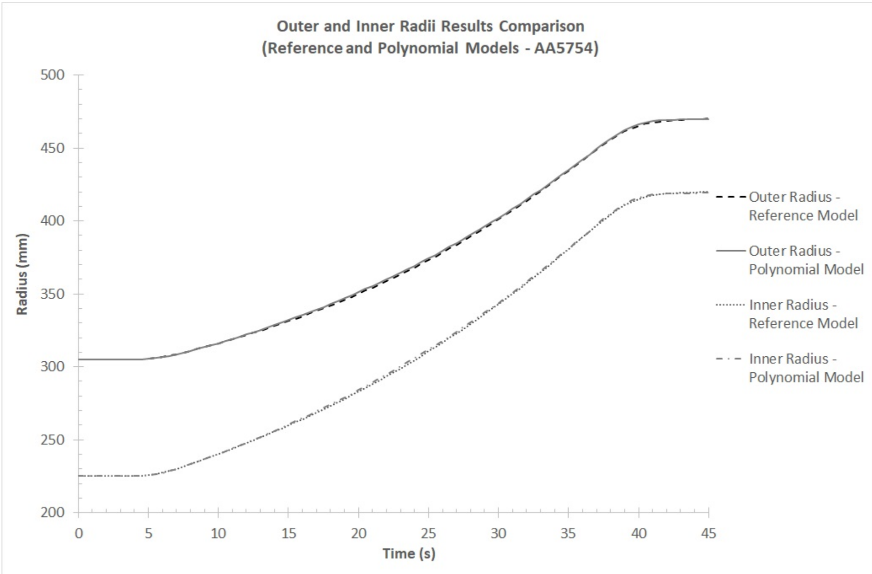

FIG. 3.83: Comparison between the outer and inner radii results from the 5^{th} degree ring growth polynomial and the reference models (AA5754)

Observations over Fig.3.83 revealed almost identical corresponding outer and inner radii curves from the two models. Any differences observed in either of the aforementioned dimensions were so minor that it can be considered negligible.

Regarding the average ring height results comparison between the reference and polynomial AA5754 models, the corresponding curves are presented in Fig.3.84:

Observations over Fig.3.84 revealed almost identical results in this case, too. More specifically, value differences observed between the compared results were small enough to be considered negligible. Thus, in the case of the AA5754 ring and based on the presented results, both of the tested support roll movement laws can be considered interchangeable as they lead to almost identical ring deformations.

Finally, the outer and inner diameter ovalities between the AA5754 reference and polynomial models were compared. The corresponding curves are presented in Fig.3.85:

Observations over Fig.3.85 revealed several differences between the percentage ovalities calculated from the two models. In the case of the polynomial model, both its outer and the inner ovalities followed very close paths. Their corresponding values increased rapidly until approximately t = 8 s, when their increase rate became almost zero. This trend continued until approximately t = 18 s, when both curves began rapidly increasing again. The respective maximum ovality values were reached at slightly different time instances in this case (at t = 31 s in the case of the outer diameter ovality and at t = 34 s in the case of the inner

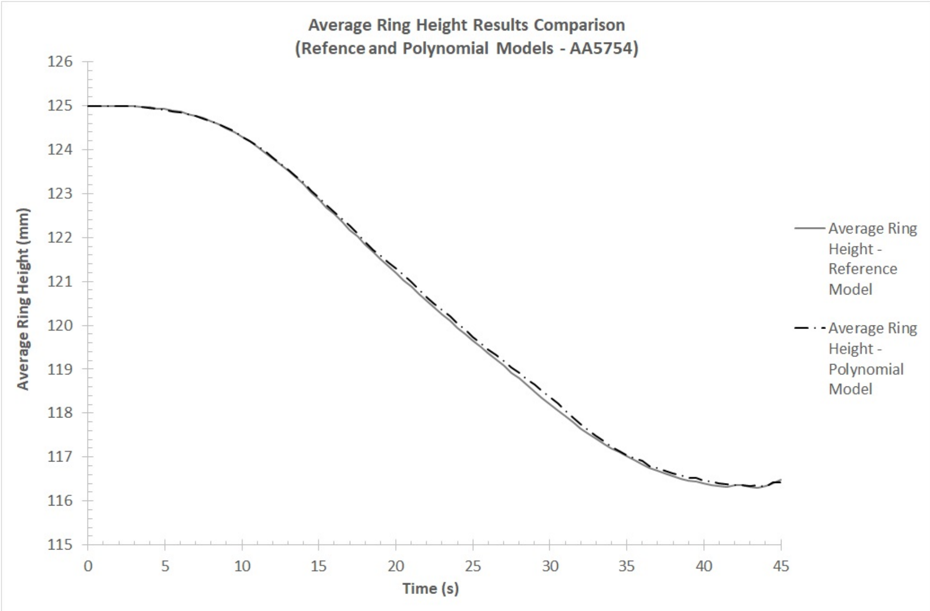

FIG. 3.84: Comparison between the average ring height results from the 5^{th} degree ring growth polynomial and the reference models (AA5754)

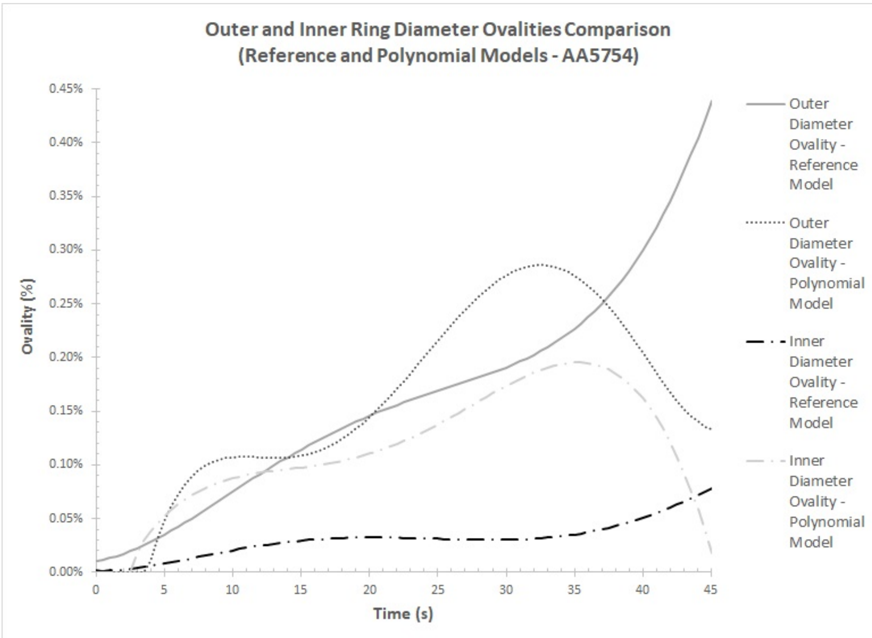

FIG. 3.85: Outer and inner diameter percentage ovality curves calculated during Ring Rolling (Reference and Polynomial Models - IN718)

diameter ovality), while both curves began decreasing after those points. The final ovality values were estimated at approximately 0.13% for the outer diameter and at approximately 0.02% for the inner diameter. Compared to the ovality curves from the reference model, the corresponding polynomial model curves were mostly greater throughout the process, although their respective final ovalities values were comparably lower. Overall, from the comparison of the ovality results from the two models, two quite different behavior patterns could be discerned. More specifically, while the polynomial model ovality curves followed a non-constant evolution rate, the corresponding results from the reference model kept increasing throughout the process. This behavior indicates that a constant defect forming kept occurring in the reference model, which lead to a slight deviation from a perfectly round shape. On the other hand, the circularity of the product in the polynomial model significantly improved during the final phase of the process, which was anticipated based on previous results. It is worth reminding that although the aforementioned facts stand true, the absolute ovality values in all cases were small enough that it could be considered negligible.

3.4.3 Ring Material and Support Roll Movement Law Results and Discussion

From the conducted simulations regarding the effects of the ring's material and the movement laws of the support rolls on the dimensional precision of the final Ring Rolling product, several interesting conclusions were drawn.

In the case of the ring's material, the transition from IN718 to AA5754 caused measurable dimensional divergences in the final product. More specifically, the aluminum ring had slightly greater final dimensions compared to the IN718 workpiece, which were mainly a result of a slightly reduced final thickness. This thickness reduction was caused by the different movement of the support rolls applied by the higher degree polynomial movement law. It should be reminded that the movement laws of the support rolls had to be properly adapted for the AA5754 model, since those used in the reference IN718 model were not compliant. Other than that, the stress, strain and temperature distributions had some differences compared to the corresponding of IN718 (apart from the differences in their respective values, which were expected), although all of them were rational. Finally, the calculated load results followed similar paths to those previously observed in the IN718 reference model, although with different absolute load values. In general, different material Ring Rolling simulations can be performed with the proposed methodology of Chapter §2, if the material and physical properties, as well as the support roll movement laws have been properly adjusted.

Regarding the support roll movement laws, which were based on different ring growth algorithms, the majority of the polynomial models' dimensional results were very close to those calculated by the reference models. The only major difference lied with the average ring height results from the IN718 model, which were slightly divergent for a specific duration of the simulations, although their final values were almost identical. This fact can be attributed to a noncompliance between the two different part of the movement law of the reference model, since the polynomial model results were much smoother. Other than that, the polynomial model results indicated towards a more conforming manufacturing process, since the outer and inner diameters seemed to follow similar evolution paths and with relatively small difference in their final ovalities. Overall, the results of the support roll movement law analysis showed that the reference and polynomial ring growth algorithms can be considered interchangeable, with the latter leading towards a smoother manufacturing process.

3.5 Discussion and Conclusions

In the current Chapter of the dissertation, three common factors that can affect the dimensional precision of ring products, either before or during the Ring Rolling process, were investigated. From the conducted analyses, several crucial factors were identified and discussed.

In the case of the initial billet volume calculation methodology that was proposed, the following conclusions were drawn:

- The proposed initial billet volume calculation methodology seems to produce fairly accurate predictions, based on the corresponding results from the conducted simulations.
- For each of the manufacturing processes that take place, the most crucial parameters were identified and were further discussed.
- In order to have a precise estimation of billet dimensions after the upsetting process, the knowledge of the upsetting factor, B, is essential. The initial billet height and the friction coefficients between the tool and the billet were the most affecting parameters for B.
- The number of forging steps and the velocity of the corresponding tools are two of the most important factors affecting the dimensions of the workpiece after central forging. The estimation of the exact number of forging steps should be made based on the existing constraint factors, while the velocity of the tools should be kept low enough to avoid forming defects, such as dishing. In case a small enough velocity cannot be applied, closed – die forging should be performed instead.
- Billet piercing is mainly affected by tool velocity, as forming defects (e.g. dishing) can occur in this case too. Also, the use of a counter – punch is highly recommended, in order to reduce forming defects and to increase the quality of the final workpiece.
- A good estimation of the tool movement during Ring Rolling is vital for the increased dimensional precision of the manufactured rings.
- Thermal shrinkage of the produced ring from its hot working temperature to room temperature should be taken into account, when estimating the initial volume of the billet.

Regarding the tool elastic deformation and thermal expansion, the following key points were proven:

- The combination of thermal and elastic deformations of the tools in ring rolling can affect the precision of the final products.
- In the analysis conducted in section 3.3, the combined elastic and thermal effects compared to the R model results summed up to a maximum increase of approximately 0.686 mm in the outer ring diameter and of approximately 0.678 mm in the inner ring diameter. Similarly, the average ring height maximum difference deviated significantly between positive and negative values throughout the process, with a maximum recorded value of 0.142 mm. These deformations can cause instabilities to the process, in case the movement routes of the rolls fail to compensate for these deformations.
- Although a specific roll – ring material combination was analyzed in the current analysis, the presented analysis can be repeated for all possible roll – ring material combinations.
- Seeing that the elastic roll effects are mainly a result of the resiliency of the ring and the roll materials, while the thermal roll effects are dependent on the manufacturing temperature and the heat transfer between the bodies and the environment, it is clear that different roll effects are more dominant than others, depending on the material combination analyzed in each case study.

- A newly proposed outer ring radius algorithm can be used to take into account the effects from the thermal and elastic deformations of the tools.

- A consideration of perfectly rigid (undeformable) tools when simulating a ring rolling process can lead to deviations from the actual process results, mainly because of irregularities in the ring growth rate that lead to instabilities and increases the probability of defect formation.

- Regarding the final dimensional deviations of the ring caused by the combined thermo-elastic tool deformations, these were proven to be considerable, especially if high product precision is required.

Finally, the conclusions from the different ring material and the higher degree polynomial ring growth algorithm analyses can be summed up to the following:

- The simulation methodology previously presented in Chapter §2 can be utilized for the simulation of different ring materials, if the corresponding physical (e.g. thermal coefficients, etc.) and material properties have been properly adjusted. Additionally, proper adjustments on the support roll movements law should also be made.

- Ring material change can have a measurable effect on the final dimensions of the produced ring, mainly because of localized deformations that affect the overall deformation of the workpiece.

- Utilizing a single, higher degree polynomial ring growth algorithm to estimate the movement law of the support rolls is possible, since it have minor effects on the final dimensions of the product.

- However, the different support roll movement law can cause unexpected localized deformations on the workpiece during the process, which in some cases can be severe and should be accounted for.

- The conducted analysis showed that considering a single, higher order polynomial ring growth algorithm leads to a smoother deformation of the workpiece.

Overall, the presented analyses have highlighted some key issues that can affect the dimensional precision of the workpiece before and during the Ring Rolling process. Although the results from the aforementioned methodologies were based on validated numerical models, the author of the current dissertation would strongly advise towards additional experimental validations of the presented methodologies (where these can be applied).

Chapter 4

Reverse Ring Rolling Process

4.1 Introduction

As seen previously in Chapter §3, there is room for improvement regarding the accuracy of a Ring Rolling process. The main focus of the presented methodologies in Chapter §3 was to investigate some key factors that may increase the produced ring's dimensional precision before and/or during the Ring Rolling process. However, most industrial Ring Rolling setups cannot manufacture high-precision products, mainly because of the complexity of the process. In order to correct the aforementioned dimensional divergences, several grinding and/or finishing process cycles follow a typical Ring Rolling process. The main drawback of this practice is that the inclusion of the aforementioned post-process cycles can be both time-consuming and fairly costly. Thus, an alternative method aimed at increasing the dimensional precision of the produced rings was further investigated in the current chapter of the dissertation. Since the main goal of the investigated alternative method was to reduce or eradicate any dimensional divergence on the final product, this method can be characterized as post-processing to a typical Ring Rolling process.

The main inspiration for the proposed methodology in the current analysis was the forming of a ceramic pot. In pottery, it is a very common practice for a clay ring to be compressed radially while rotating, leading to a reduction in both of its radii. In case during this practice the clay ring's thickness is kept roughly the same, the aforementioned radial reduction will result in a subsequent increase to the ring's height. Such an example is graphically depicted in Fig.4.1:

FIG. 4.1: Outer and inner radii reduction in pottery (images taken from two time instances of a pottery related video on YouTube)

Seeing that the ring at the end of a hot Ring Rolling process can be of a high enough temperature that it can subdue to further manufacturing, a similar radius reduction practice, let it be called *Reverse Ring Rolling* hereafter, was conceptualized. Since the required equipment to investigate the feasibility of Reverse Ring Rolling was not available, a numerical simulation of this proposed process was conducted as the only possible option to prove it. Furthermore, several key aspects of this process, as well as their effects on the final product, could also be easily investigated via a finite element model, without risking additional costs, damages to the required equipment or hurting the users. It should be clarified that from its conceptualization, Reverse Ring Rolling is primarily intended to correct relatively significant dimensional divergences of several millimeters and not common ring rolling defects like fishtails and/or bulges.

It is worth noting that part of the current chapter was published as a scientific article (**Pressas, Papaefthymiou, and Manolakos, 2024**).

4.2 Characteristics of Reverse Ring Rolling Process

Before proceeding to the simulation of Reverse Ring Rolling, the basic mechanics of the process had to be established. As a first step for this, the movement and positioning of a potter's hands during the reduction of a pot's radii were analyzed. From the plethora of techniques that potters perform in their art, two specific stood out as the most suitable for application in Reverse Ring Rolling. The corresponding techniques are presented in Fig.4.2:

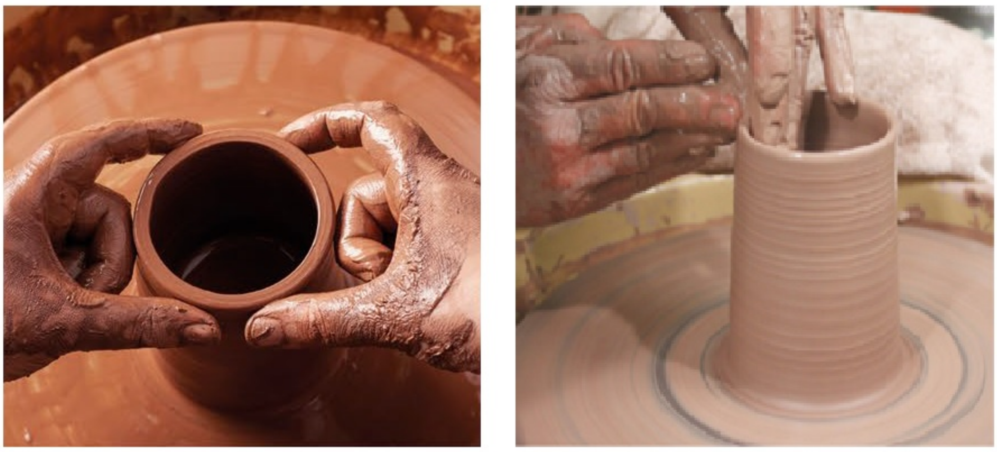

(a) (b)

FIG. 4.2: Applicable pottery techniques to Reverse Ring Rolling: (a) Six-point "Collaring" (image taken from **Hardwicke and Lea, 2019)** and (b) "Pulling" (image taken from **Leach and Dehnert, 2013**)

From the two applicable pottery techniques, the first one (Fig.4.2(a)) is known as "collaring" or "choking" (the term "collaring" will be used hereafter) and involves the axisymmetrical squeezing of the clay ring to reduce both of its radii, while a small simultaneous increase in its height occurs. Usually, the clay ring's thickness is maintained fairly constant during this process. Although there are several alternative forms of the "collaring" technique, the most widely used is the six-point "collaring", in which six fingers are used to perform the radial reduction of the ring. Other notable variations of "collaring" are the four-point and full "collaring" techniques, in which four fingers and the full length of the palms are used, respectively.

The second technique (Fig.4.2(b)) is known as "pulling" and involves the wall thickness reduction of the clay ring, in order to increase its height. For this technique, fingers or sides of both hands are placed on the opposite sides of the clay ring's wall and a slight squeeze is performed. The placement of both hand in "pulling" are reminiscent of the mandrel and main roll positions in Ring Rolling.

Seeing that the main goal of the current analysis was the reduction of specific ring dimensions to achieve the required dimensional precision of a Ring Rolling product, an adaptation of "collaring" and "pulling" techniques was attempted in IN718 rings. Before proceeding to designing the corresponding experiments, however, some core differences between wheel pottery and Ring Rolling needed to be clarified. Apart from some obvious differences (e.g. different materials, substitution of tools by hands in pottery, etc.) the main difference in the mechanics of the two processes was the fixation of the workpiece in pottery. More specifically, in pottery, the clay workpiece is firmly connected to the pottery wheel. This is the result of a combination of the sticking properties of clay when wet and special, anti-slip mats applied on the wheel to increase its adhesion with the clay. On the other hand, the workpiece in Ring Rolling cannot be fixed onto the Ring Rolling mill by any means, instead the support rolls are used to stabilize the ring and ensure its proper manufacturing. This major difference between the two processes should be taken carefully into account when establishing the fundamentals of Reverse Ring Rolling, especially in the case of "pulling" technique.

With the aforementioned points of concern now fully clarified, the pottery techniques presented in Fig.4.2 were attempted to be adapted for Reverse Ring Rolling. More specifically, two separate numerical models were designed to validate the feasibility of the proposed process:

1. One for the adaptation of "collaring", which would simulate the reduction of both ring radii up to a specific point.
2. Another for the adaptation of "pulling", which would simulated the thickness reduction of the ring up to a target outer radius value.

In the case of the "collaring" Reverse Ring Rolling model, the six-point "collaring" technique was chosen as the basis for the model setup. Given that the tools in the main rolling bite would be included in the model as a single point, five additional points would be considered as contacts point of the ring with a separate support roll, in each of them. These contact points would be spaced equally along the periphery of the ring, thus a $\theta_{spacing} = \pi/3$ angular spacing from one point to the next was calculated.Regarding the movement of the tools, all rolls would move linearly and simultaneously towards the center of the ring. In that way, a forming process similar to that of a potter performing "collaring" would be approximated. Additionally, a constant rotational velocity would be provided by the main roll, similarly to a common Ring Rolling process. Because of the simultaneous movement of the tools, the ring wall thickness is expected to remain almost unchanged by the end of the process, while an increase of the ring's height should be observed.

Regarding the "pulling" Reverse Ring Rolling model, the same setup as that of the "collaring" Reverse Ring Rolling model was considered. Since the rotation of the ring would be caused by the main roll in this case, too, the five additional support rolls were maintained in this model to ensure a relative stability of the process. In that way, common stability issues, like e.g. "ring climbing", should be avoided, although other factors, such as the applied linear velocity, also contribute to the manifestation of such instabilities. Other than that, most process parameters would be kept the same (as a first approach, at least) to the corresponding from the "collaring" model. The sole exception to this is the position of the mandrel, which would remain the same throughout the process (after any initial gaps have been closed). Thus, the relative movement between the main roll and the mandrel coupled with the linear movement of the support rolls should result in a stable thickness reduction in the ring and a simultaneous, measurable height increase. It is worth noting that the "pulling" process is designed for a total wall thickness reduction of only a few millimeters, as extending it for more would most probably lead to instabilities and, consequently, to major defects.

A schematic representation of the applied movement on each of the tools in the proposed Reverse Ring Rolling processes is shown in Figs.4.3:

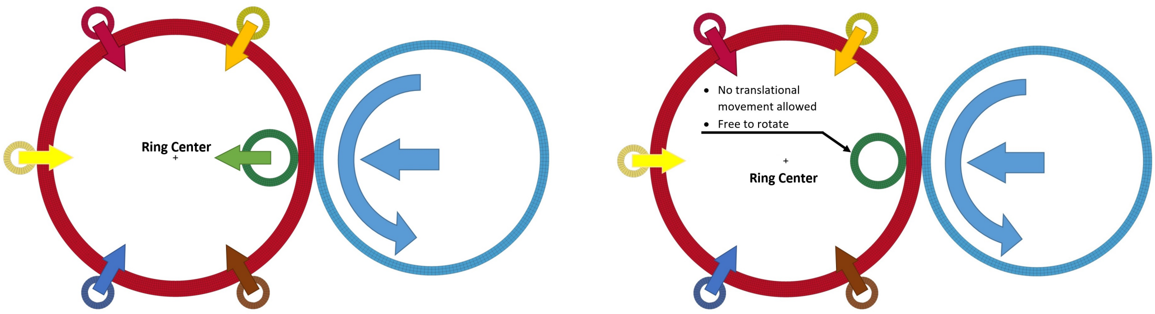

(a) (b)

FIG. 4.3: Applied movement on the rolls in each of the Reverse Ring Rolling process simulations: (a) "Collaring" model and (b) "Pulling" model

From all of the above, it is clear that the successful adaptation of the pottery techniques to Reverse Ring Rolling would require a Ring Rolling mill slightly different from a typical one. More specifically, multiple additional support rolls would be required to perform the necessary stabilization of the workpiece and the reduction of its dimensions. Although uncommon, such Ring Rolling mills with multiple, individually moving tools have already been presented in literature. Most notably, Li, Guo, and Wang in their work **Li, Guo, and Wang, 2021** mentioned the existence of an industrial four support roll mill, which used as a reference for their numerical simulations. Additionally, in **Cleaver and Allwood, 2017** a six support roll mill was used to perform incremental Ring Rolling on profiled rings. The Ring Rolling mill mentioned in **Cleaver and Allwood, 2017** is referenced as "Flexible Ring Rolling" mill and has been used by the researchers of Cambridge University in multiple of their published works (e.g. **Arthington et al., 2015**, **Cleaver et al., 2016**, **Cleaver and Allwood, 2019**, etc.). Although the "Flexible Ring Rolling" mill is not an industrial-sized setup, as it was mainly constructed for research purposes, the construction of an upscaled, industrial-sized version of a similar setup seems feasible. Thus, even if a suitable, industrial-sized Ring Rolling mill for Reverse Ring Rolling processes does not exist at the moment, a potential design and construction of such a mill seems realistically plausible.

Based on the aforementioned, alternative ring rolling mills found in literature, a suitable Reverse Ring Rolling mill should, at minimum, cover the following design points:

- Have more than two support rolls.
- Have a suitable mill table or rollers, which would support the workpiece, without hindering its free rotation.

- Allow for the fully-controllable, independent movement (linear and rotational) of every individual tool.
- Have an appropriate number of measuring subsystems that would provide dimensional feedback of the manufactured workpiece.
- Have a central controller, which would allow for an a priori programming of the synchronous movement of the tools and/or their adaptive correction during the process.
- Have adequate cooling and heating systems to regulate the temperature of the workpiece and the tools.

It is worth noting that a Reverse Ring Rolling mill based on these points could also be used for traditional ring rolling, thus any need for unnecessary breaks between the ring rolling, "collaring" and "pulling" processes would be eliminated, since only a proper tool velocity adjustment would be required to go from one process to the next. As a result, several metallurgical phenomena (e.g. recrystallization) that usually occur between the different processes of the production cycle, due to the movement and cooling of the material, would also be eliminated. Overall, even if a suitable, industrial-sized Reverse Ring Rolling mill does not exist at the moment, a proposed design based on the aforementioned points seems to be realistically plausible.

The Reverse Ring Rolling setup that was considered for both the "collaring" and "pulling" models in the current analysis is presented in Fig.4.4:

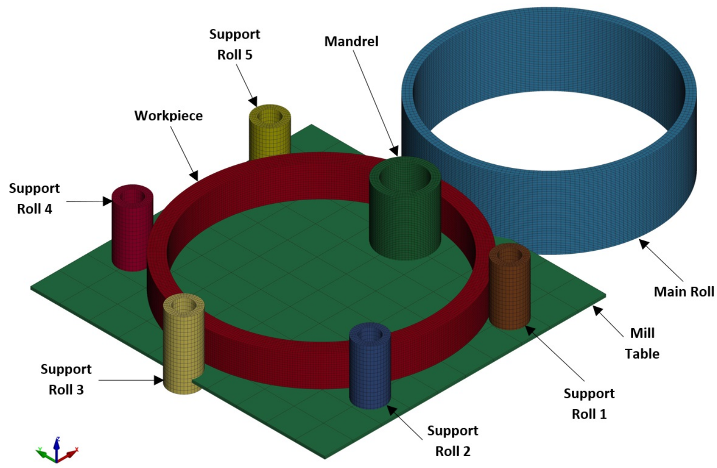

FIG. 4.4: Ring rolling setup used in the simulation of the "collaring" and "pulling" processes

The aforementioned characteristics were used as guidelines for the conducted numerical analyses. A more detailed presentation of the models that were created is made in the following section (§4.3).

4.3 Reverse Ring Rolling Simulations

With the outlines of the analysis defined, some key aspects of the numerical models had to be specified next. The reference model of IN718 Ring Rolling previously presented in Chapter 2 was largely used as the basis for both models. This specific ring rolling model was considered as a good starting point for the current analysis, since it simulated numerous important thermo-mechanical phenomena of the process, such as multiple heat transfer mechanisms, temperature and strain rate dependent material properties and thermal expansion and shrinkage of the workpiece, among others. However, several alterations and adjustments had to be made, in order to properly simulate the proposed forming processes. These differences are further discussed below for each of the "collaring" and "pulling" models. It is worth noting that the main goal of both of the Reverse Ring Rolling models would be to correct at least the outer and inner radii of the manufacturing ring, since the target dimensions mentioned by **Zhu et al., 2016b** diverged from those calculated by the corresponding Ring Rolling model (both in the current analysis and in **Zhu et al., 2016b**).

4.3.1 "Collaring" Model Setup

As a first step, the initial geometry of the ring in the "collaring" model had to be determined. Seeing that Reverse Ring Rolling was proposed as a post-process performed right after a regular Ring Rolling, the final geometry of the workpiece, as this was calculated by the reference model in Chapter §2, was input as the initial workpiece geometry of the "collaring" model. For reasons of simplicity, the initial geometry of the workpiece was modeled as a square cross-section ring having dimensions equal to those calculated at the end of Chapter §2. Thus, the initial workpiece for the current analysis had an outer radius of $R_{collaring,0}$ = 461.03 mm, an inner radius of $r_{collaring,0}$ = 408.16 mm and an initial height of $H_{collaring,0}$ = 116.1 mm. It is worth noting that although there were fishtail and bulge defects in the final product in Chapter §2, these were purposely omitted from the "collaring" model, as they would add an unnecessary level of complexity to the conducted analysis.

Regarding the tools included in the conducted simulations, all the rolls had the same dimensions to their respective counterparts presented in Table 2.1. Apart from the rolls, a mill table was also considered in this analysis. This table was simulated as a simple rectangular plate positioned right beneath the workpiece, with a side length of a_{table} = 1000 mm (also a table thickness of 10 mm was considered, although this dimension was irrelevant). For the sake of simplicity, no roll slots were considered in the table's geometry. Instead, each roll could move freely inside the table with no interaction between them. The reason for the inclusion of a mill table in these models was so that gravity could be added as an additional external load. As mentioned above, there is a great possibility that "ring climbing" could manifest during the process. Similarly to regular Ring Rolling processes, gravity helps counter such instabilities to some extent. Thus and in order to simulate a more realistic behavior, the inclusion of gravity was considered in the Reverse Ring Rolling models. As a result, the addition of a mill table was necessary to support the workpiece and prevent its fall out of the simulation boundaries. Finally, the conical rolls were omitted from the Reverse Ring Rolling models, since the ring height increase was an expected outcome of the process. However, one or more conical rolling bites could be included in a future version of the proposed process, in case height control or further vertical stabilization of the workpiece are required.

In the case of the movement of each tool, these were outlined in the previous section (also see section §4.2) for each of the two models described. A closer inspection of the roll movements for each model and their corresponding effects on the final product would lead to the conclusion that "collaring" and "pulling" models should be considered complimentary, with the final state of the former being input as the initial state of the latter. More specifically, during the "collaring" model, all rolls would choke the workpiece until its inner radius would reach the target value of $r_{f,target}$ = 400 mm (**Zhu et al., 2016b**). Compared to the

$r_{RRR,0}$, a total radial reduction of Δr_{RRR} = 8.16 mm would be performed by all rolls, while the thickness of the workpiece would remain the same. Then and based on the outcome of the "collaring" model, in the "pulling" model the outer radius of the workpiece would be subsequently reduced down to the corresponding target value of $R_{f,target}$ = 450 mm(**Zhu et al., 2016b**). All rolls would perform a linear movement from their starting position towards the ring's center of rotation with the same velocity, while a slight delay would be considered from one roll to the next at the beginning of their movement, in order to compensate for their angular spacing. The linear and rotational velocities of the tools would be equal to $v_{mandrel} = 0.89\ \frac{mm}{s}$ and $\omega_{MR} = 2.09\ \frac{rad}{s}$, same to the corresponding velocities from the reference Ring Rolling model (also see section §2.9). It is worth noting that the rotational velocity was applied only to the main roll, while the rest of the tools were able to rotate freely. The aforementioned velocity values were chosen as an initial approximation for the "collaring" model, since they were low enough not to introduce any dynamic phenomena on the process. In case any stabilization issue would be observed, however, lower velocity values would be applied to the tools.

Regarding the initial conditions, the boundary conditions and the external loads, the majority of these options were imported as-is from the reference model of Chapter §2. The only changes that were made in the Reverse Ring Rolling models, were the following:

- The initial temperature of the ring for the "collaring" model was decreased to $T_{ring,collaring,0}$ = 1313.15 K, based on an approximation from the final temperature results calculated by the IN718 Ring Rolling model. This value was input using the *TEMP* option in the INITIAL_TEMPERATURE_SET menu of LS-DYNA, while it was considered to be the same in the entire ring. The corresponding initial ring temperature for the "pulling" model would be imported from the final state of the "collaring" model.

- The proper boundary conditions for the mill table were applied via its material definition. More specifically, in MAT_20-RIGID that was considered for the mill table, options *CON1* = 7 and *CON2* = 7 (with *CMO* = 1.0 applied) were input, which ensure a full constraint of all translation and rotation degrees-of-freedom (DOFs) for the corresponding body.

- Gravity was introduced in both Reverse Ring Rolling models using option GRAVITY_PART from the LOAD menu. In this option, the part which is subdued to gravitational loads should be defined via *PID* option, while the acceleration of gravity and its direction should be defined via *DOF* and *ACCEL* option, respectively. In the current analysis, the vector of gravity was set parallel to the Z global axis (*DOF* = 3) and the acceleration of gravity was considered equal to *ACCEL* = 9.81 $\frac{m}{s}$. Finally, the gravitational load was considered only for the ring, since the rest of the bodies in the models were not allowed to move along the Z - axis, thus gravity was redundant for these bodies.

- Based on the imposed linear velocity of the tools and the target radii reductions, solution time had to be equal to $t_{collaring}$ = 9.17 s. However, since a minimum of 3 s had to be added so that the final dimensions would be normalized throughout the ring's periphery, the total solution time was set as *ENDTIM* = 12.17 (s) via the CONTROL_TERMINATION menu.

- During the last 3 s of the simulation, when the dimensions of the ring would be normalized, all linear velocities of the tools were set to zero.

The rest of the model parameters were imported as-is from the model in Chapter 2, with no further changes.

4.3.2 "Collaring" Model Results

After the solution of the "collaring" model, the calculated results were observed carefully. An initial overview of the calculated results revealed that the process was completed as intended, with no visible defects or abnormalities. The rotation of the ring was continuous and unobstructed, while no vibrations were observed on the workpiece. Furthermore, both radii reductions were performed as intended (at a macro - scale level at least), while a slight increase of the workpiece's height was also observed. In the following subsections, a more thorough presentation of some crucial results is made.

Deformational Results ("Collaring" Model)

Initially, cross-sections from the main rolling bite (between the mandrel and the main roll) and in contact with a support roll, at the final time instance of the simulation were extracted. These cross-sections are presented in Fig.4.5:

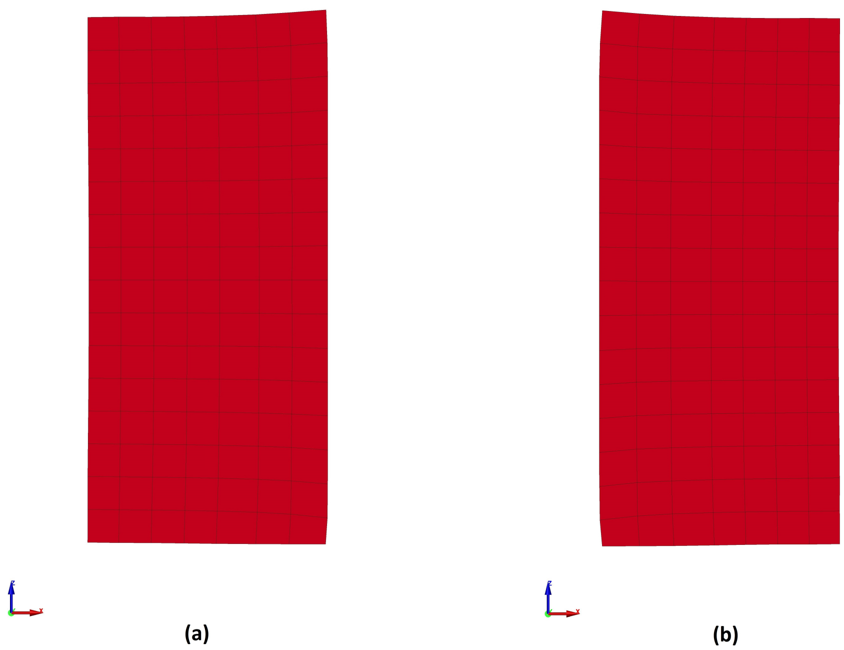

FIG. 4.5: Cross-sections of the ring at the final time instance of the "collaring" model: (a) cross-section at the center of the main rolling bite and (b) cross-section in contact with a support roll

Observations over the cross-sections in Fig.4.5 revealed several interesting formations. Regarding the cross-section observed at the center of the main rolling bite (Fig.4.5(a)), revealed the formation of fishtail defects on the right side of the cross-section, which was in contact with the main roll. The fishtail defect on the bottom side of the ring was significantly smaller than that on the top side, as a result of the mill table restricting its evolution. On the other hand, no fishtail defects were observed on the inner diameter side of the ring, which was in contact with the mandrel. Moreover, a very slight barreling could be observed on the outer diameter surface of the ring. This barreling can be attributed to the vertical movement of the material around the outer diameter ring edges and the friction with the main roll, which caused a small rotation of the formed fishtail defects and thus a barrel-like shape on the cross-section. An almost identical image was observed on the cross-section being in contact with the support roll (Fig.4.5(b)), in which the formed fishtail defects had little to no differences compared to the corresponding defects observed in Fig.4.5(a), while the slight barreling was still present. Overall it can be concluded that during a "collaring" process, the reduction of both ring radii led to the increase of the average ring height mainly on the outer radii side. Additionally, the cross-section remained almost unaltered around the periphery of the workpiece. On that note, it should be noted that although the cross-section in Fig.4.5(b) was taken from the contact of the workpiece with support roll 3 (also see Fig.4.4), the corresponding cross-sections from the contacts with the rest of support rolls were almost identical to that one.

Afterward, the outer and inner radii results, as well as the average ring height results, were evaluated. The corresponding curves are presented in Figs.4.6 and 4.7, respectively:

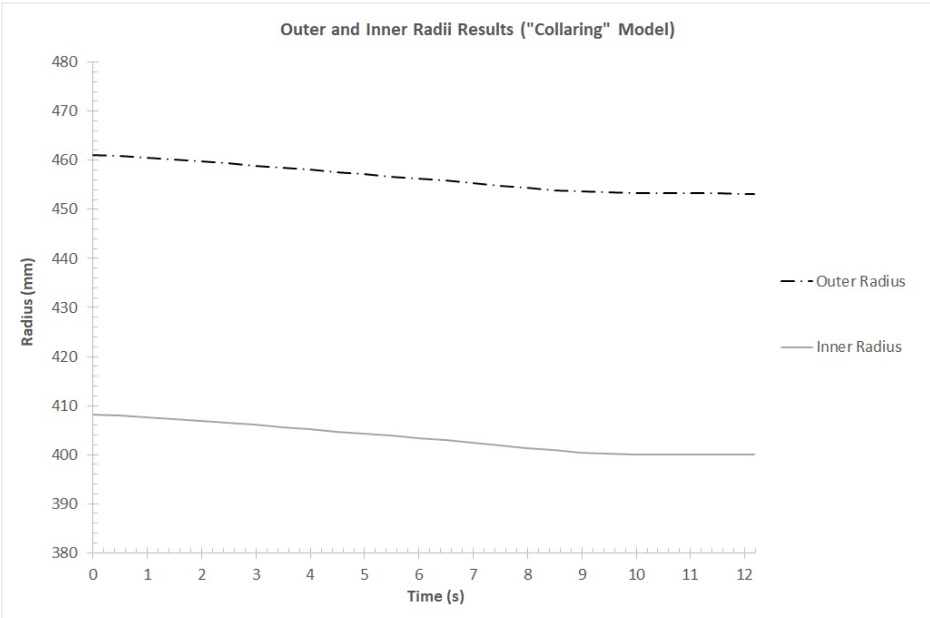

FIG. 4.6: "Collaring" model outer and inner radii results

Observations over Fig.4.6 revealed an overall steady reduction in both radii of the workpiece, throughout the main forming duration of the process. The minimum outer and inner radii values were observed (as expected) at the end of the process's duration, after the end of the dimension normalization phase. The corresponding final radius values were $R_{f,collaring}$ = 453.18 mm and $r_{f,collaring}$ = 400.015 mm, approximately. Since reaching the target value of the inner radius was the main scope of the current process, a comparison between $r_{f,collaring}$ and $r_{f,target}$ was initially performed. From their comparison, a difference of $\Delta r_{collaring}$ = 0.0038% was observed, which can be considered negligible. In the case of the outer radius and compared to the corresponding target value $R_{f,target}$, a difference of $\Delta R_{collaring}$ = 0.71% was observed. This difference, although relatively small, can be considered too large for a high - precision process. However, such differences can be corrected through multiple different processes, in relatively little time. In the current research, the outer radius difference will be attempted to be reduced up to the target value, with the "pulling" Reverse Ring Rolling process.

Regarding the average ring height (Fig.4.7), an overall increase in this dimension was observed. During the forming phase of the process, the overall increase rate of the ring's

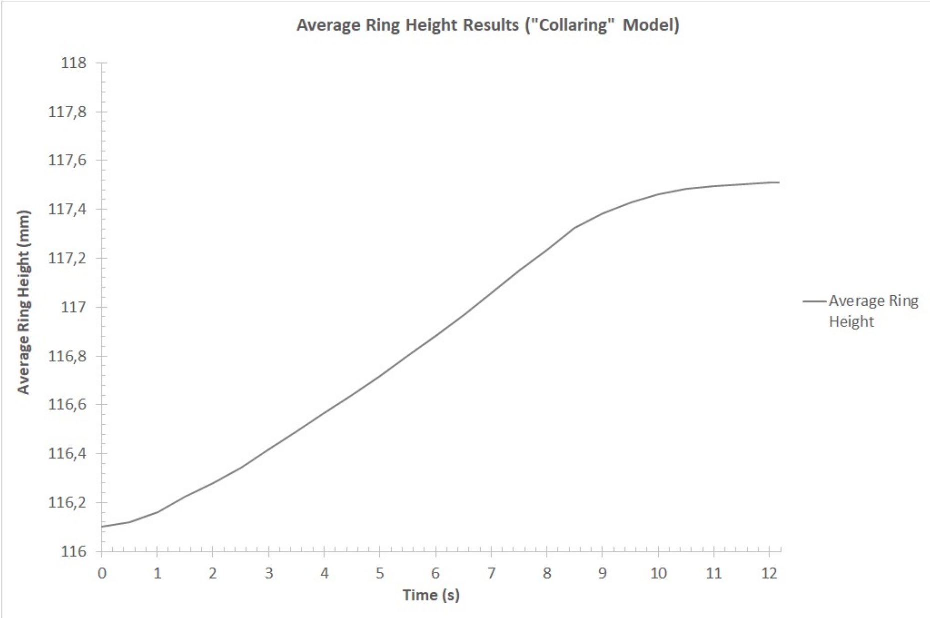

FIG. 4.7: "Collaring" model average ring height results

height can be considered fairly steady. After the main forming phase reached its end (t = 8.5 s approximately), two slower height increase phases could be discerned from the rest of the process. The first of these phases occurred between t = 8.5 s and t = 10 s approximately, and the corresponding increase rate was almost half of that observed until that point. The second of the aforementioned two phases, began at roughly t = 10 s and remained until the end of the simulation. During this phase, the height increase rate became even smaller, with the average ring height remaining almost constant. The final average ring height value at the end of the process was calculated equal to $H_{f,collaring}$ = 117.51 mm, thus the expected behavior of a relatively small height increase was observed. Based on the final average ring height value of the Ring Rolling model in Chapter §2 (H_f = 116.1 mm), the percentage average ring height increase was equal to ΔH = 1.21%, which can be considered relatively small.

Following the main ring dimensions, the outer and inner diameter ovality results were evaluated. For the calculation of the ovality curves, the methodology previously presented in section §2.16.1 was used. The corresponding curves are presented in Fig.4.8:

Observations over the ovality curves in Fig.4.8 revealed relatively small ovality values. A quick overview of the two curves led to the interesting fact of the inner ovality curve being greater than the outer ovality curve, rather than the opposite that was observed in all previous models. Furthermore, both the outer and the inner diameter ovalities followed a similar evolution pattern during the process. More specifically, the ovality of both diameters increased until approximately t = 8 s, when the corresponding maximum ovality values were reached for both diameters. From that point onwards, the ovality values began decreasing at an almost constant rate until t = 10.5 s approximately, when the decrease rate of both curves became lower. The final ovality values were 0.02% and 0.03% for the outer and inner diameters, respectively, which were small enough that the final ring can be considered as almost perfectly circular. This was a rather expected behavior from the "collaring" Reverse Ring Rolling process, since all tools moved simultaneously towards the center of the ring's rotation and with the same linear velocity. Thus, the circular shape of the ring could be easily maintained. It is worth noting that the aforementioned ovalities

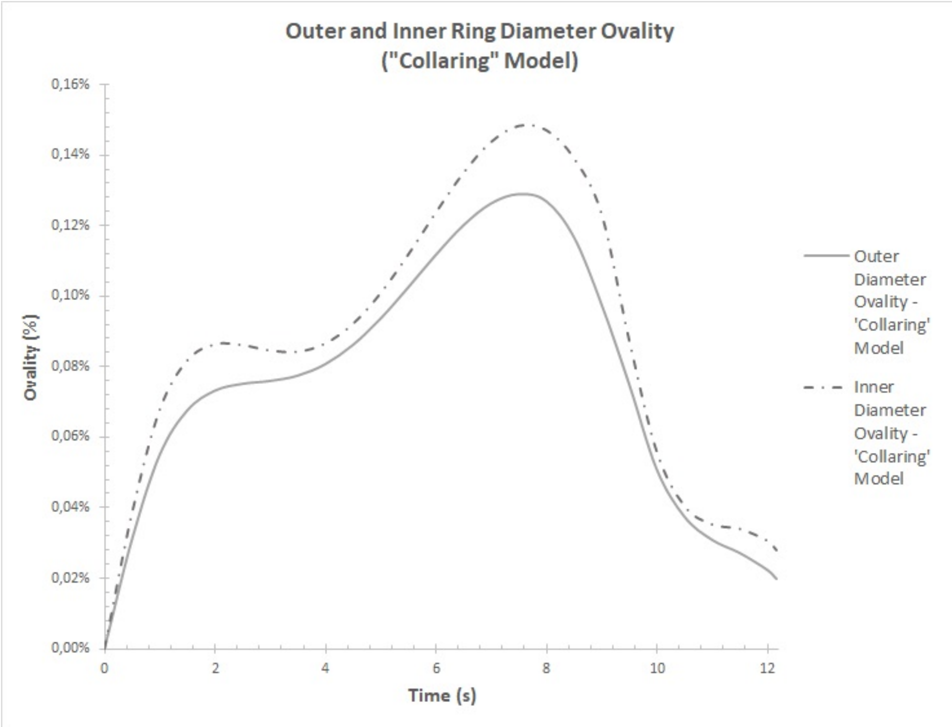

FIG. 4.8: Outer and inner diameter ovality results ("Collaring" model)

would have to be added to the respective pre-existing ovalities from a typical Ring Rolling process, since the "collaring" process is expected to be performed right after Ring Rolling with no intermediate post - processes.

Finally, the ring thickness results from the "collaring" model were evaluated. The corresponding curve is presented in Fig.4.9:

Observations over the ring thickness curve during "collaring" Reverse Ring Rolling (Fig.4.9) revealed an overall small deviation in its size. The recorded thickness changes did not surpass 500 microns, while the difference between the initial and the final recorded thickness values was approximately $\Delta f_{collaring}$ = 295 μm. This difference can be considered as relatively small given the size of the ring's dimensions. In general, the results of Fig.4.9 revealed that the total radii reduction cannot and will not solely translate to a ring height increase. However, since the "collaring" process is not the final part of Reverse Ring Rolling, any deviations in thickness can still be adjusted during the "pulling" process that follows.

Generally, the evaluation of the deformational results from the "collaring" model proved the feasibility of the "collaring" Reverse Ring Rolling process. The whole process performed as intended, with no localized extremities or peculiar formations. The process was very smooth and no oscillations or imbalanced occurred during the process. Overall and based on the deformational results, "collaring" Reverse Ring Rolling process can be considered feasible.

Stress and Strain Results ("Collaring" Model)

Regarding the stress and strain distributions from the "collaring" model, an early review of these results demonstrated different behaviors between the two result sets. More specifically, in the case of the Von Mises stress results, the fringe plots from the main rolling bite

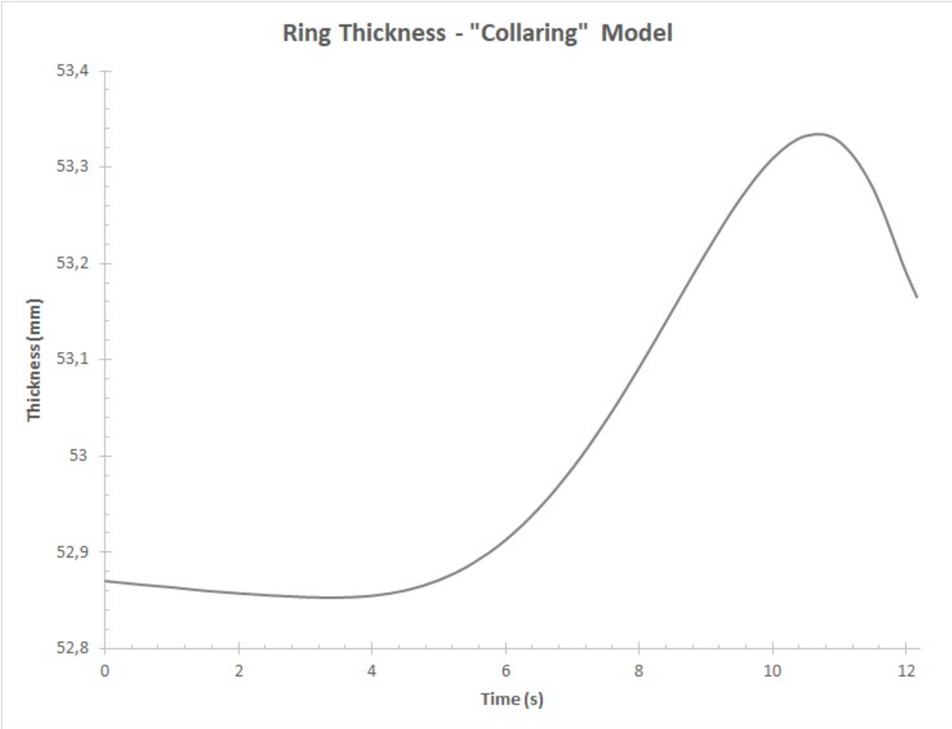

FIG. 4.9: Ring thickness results ("Collaring" model)

cross-section were noticeably different from those of the cross-sections in contact with the support rolls, although the latter were very similar between one another. On the other hand, the effective strain fields were almost identical in every cross-section of the workpiece. Based on these preliminary result reviews, it was finally decided that the Von Mises stress results would be evaluated in two separate cross-sections of the ring (one in the main rolling bite and another in contact with support roll 3), while the effective strain results would be evaluated in a single cross-section (in the main rolling bite).

Initially, the resulting Von Mises stress distributions at eight different time instances of the "collaring" model were evaluated. Contrary to the previous corresponding result analyses of the current dissertation, signed Von Mises stress results were evaluated in this case. The signed equivalent Von Mises stresses have a similar calculation method to the equivalent Von Mises stresses, with the only difference being that the sign of the dominant stress values is maintained. In that way, equivalent tensile and compressive stress results can be distinguished. In the current analysis, use of signed Von Mises stresses was preferred, in order to recognize the governing deformation mechanisms occurring during the "collaring" process. The corresponding signed Von Mises stress fields in each of the two aforementioned cross-sections are presented in Figs.4.10 (in the main rolling bite) and 4.11 (in contact with support roll 3), respectively:

Observations over the signed Von Mises stress distributions of the cross-section in the main rolling bite (Fig.4.10) revealed an interesting stress evolution during the process. Before proceeding to the evaluation of these results, it should be noted that in each of the presented time instances in Fig.4.10 the main roll was located on the right side of the corresponding cross-sections and the mandrel was located on their left side. During the very early stages of the process (t = 0–1 s), a clear stress distribution could be observed in the analyzed cross-section, with a compressive stress field on the main roll side and a tensile stress field on the

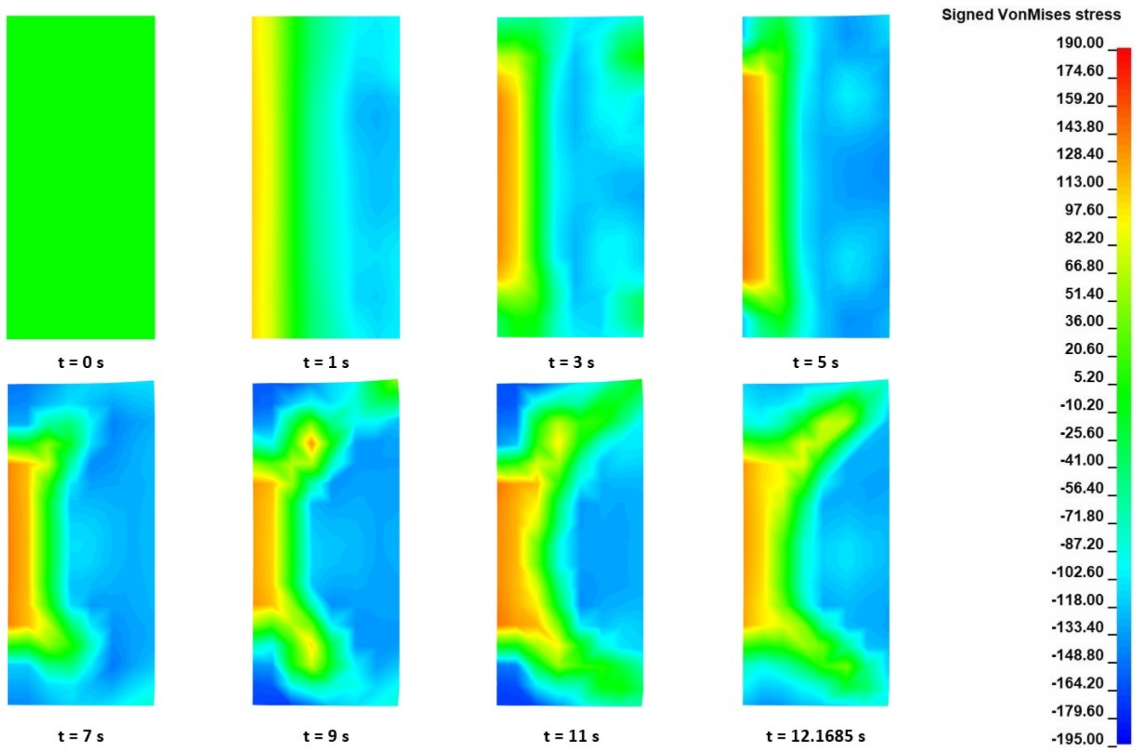

FIG. 4.10: Signed Von Mises stress distributions at multiple time instances of the "collaring" Reverse Ring Rolling process simulation (Main Rolling Bite)

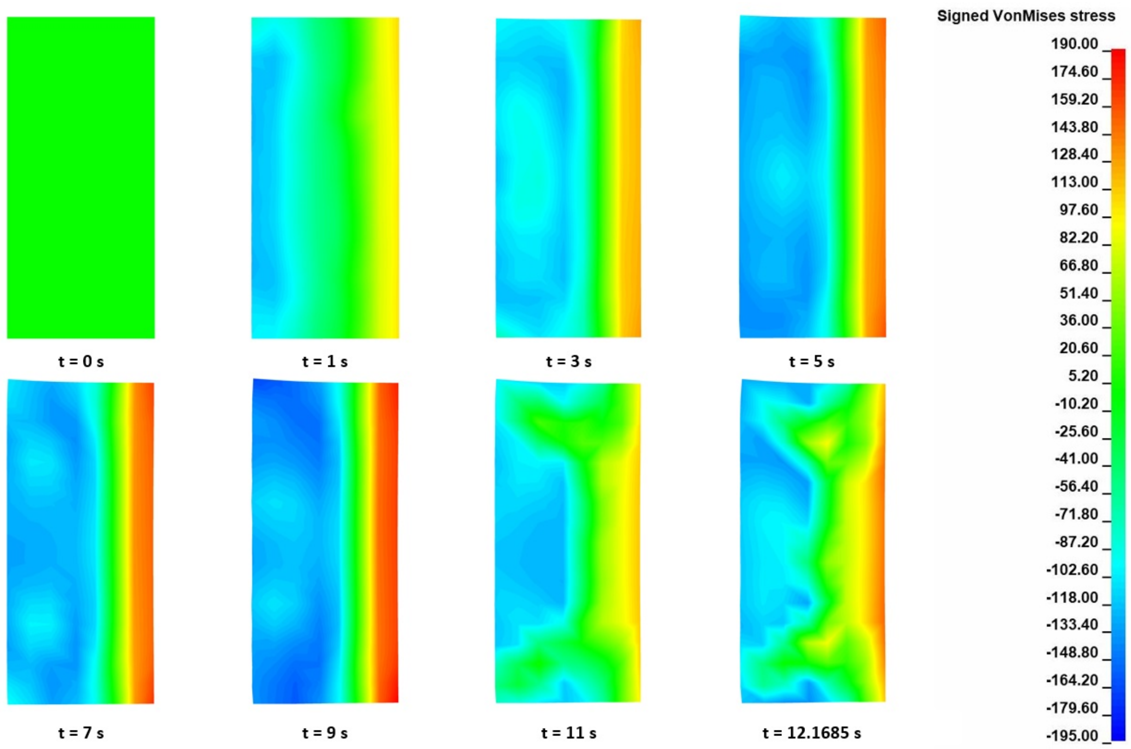

FIG. 4.11: Signed Von Mises stress distributions at multiple time instances of the "collaring" Reverse Ring Rolling process simulation (cross-section in contact with Support Roll 3)

mandrel side. This specific distribution pattern can be attributed to a localized, outwards bending of the workpiece, due to the action of the main roll. As the process proceeded (t = 3–5 s), some divergences were observed in the aforementioned initial stress distribution, located around the edges of the workpiece. More specifically, some compressive stresses began building up around the inner peripheral surface edges, while the corresponding stress fields around the outer peripheral surface edges neutralized at first (t = 3 s) and then a slight compressive field began building up around them again. From that point onwards and until the end of the process, an almost constant stress distribution was mostly observed, with the only exception being the stresses around the outer edges that gradually turned from purely compressive to almost zero. An overview of the aforementioned stress evolution helped clarify the deformational mechanism of the workpiece. More specifically, the initial compression from the main roll caused an outward bending of the ring, which combined with the continuity of the latter's material led to a localized elongation of its inner peripheral surface. At the same time, a slight vertical arching of the cross-section was observed, which led to an early (t = 5 s) separation of the outer edges from the main roll, while pressing only the inner edges against the mandrel. After t = 7 s, the formation of fishtail defects along the outer peripheral surface was observed. The aforementioned defect formation led to the manifestation of compressive stresses around the bottom, outer edge due to the contact with the mill table, while the corresponding upper, outer edge stresses were closer to zero, due to a contact loss with the main roll. Finally, at the very end of the process the corresponding stress fields were noticeably reduced, as a result of the conclusion of the main forming actions and the normalization of the ring dimensions. From the entirety of the process, the maximum recorded (absolute) Von Mises stresses were observed near the end of the process (t = 11 s) around the inner edges of the ring, with the corresponding values being approximately 180–195 MPa.

Regarding the stress results observed in Fig.4.11, which were representative for all cross-sections being in contact with any of the support rolls, some significant differences were observed compared to the corresponding results presented in Fig.4.10. First and foremost, in the current analysis, the corresponding tool was positioned on the left side of the presented cross-sections. For the majority of the process's duration (t = 0–9 s), the same localized, outward bending of the ring, previously observed during the very early time instances of Fig.4.10, was observed in this case, too. After t = 11 s, a notable change was observed in the corresponding stress fields, as the inner surface tensile stresses were significantly reduced and the outer edge stress fields came closer to zero, due to the fishtail defects bending slightly inwards and thus losing contact with the tool. Regarding the maximum recorded (absolute) stresses in Fig.4.11, these were observed near the end of the process's duration (t = 9 s) around the outer edges of the ring, with the corresponding values being approximately 170–190 MPa.

The localized bending deformation mechanism that was observed by the stress results in Figs.4.10 and 4.11 was of particular interest, and thus it was decided to be further analyzed. For this reason, the stress distributions from the entire workpiece at a representative time instance around the middle of the process (t = 5 s) were extracted. The aforementioned results are presented in Fig.4.12:

Observations over Fig.4.12 clarified and confirmed the deformation mechanism that was observed before. More specifically, from the stress fields presented in the top view of the ring (Fig.4.12(a)) tensile stresses appeared around the inner peripheral surface of the ring, exactly opposite to the roll contact points. The only exception to this was the main rolling bite, in which the top view revealed slightly compressive stress values in the corresponding

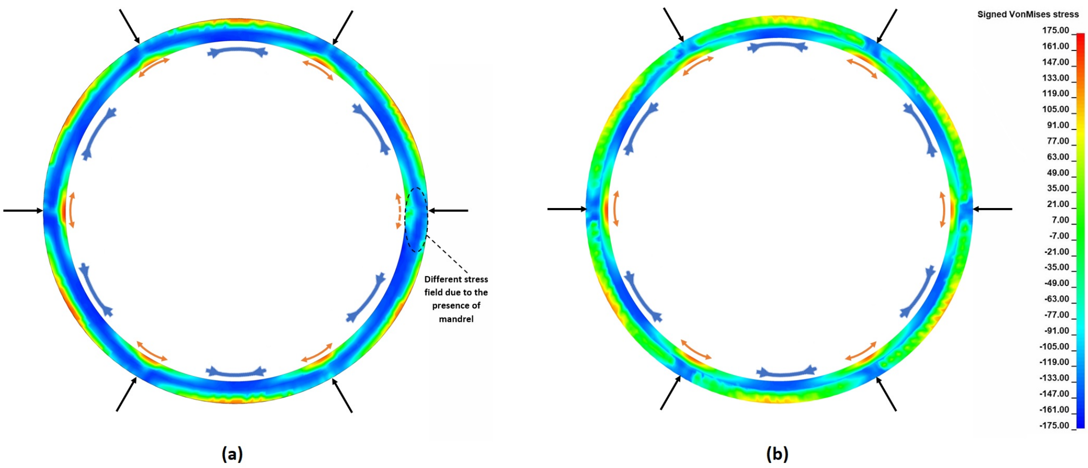

FIG. 4.12: Signed equivalent Von Mises stress distributions at t = 5 s of the "collaring" Reverse Ring Rolling process simulation: (a) Top view and (b) cross-section at the middle of the ring's height. The black arrows indicate the radial compression from the rolls, the red curved double arrows indicate ring segments where tension is dominant, and the blue curve double arrows indicate ring segments where compression is dominant (along the inner peripheral surface).

inner surface segment. However, combining these results to those previously observed in Fig.4.10 led to the conclusion that the compressive stresses observed in Fig.4.12(a) around the mandrel contact at the main rolling bite were a result of the inner ring edges being compressed against the mandrel. This fact is further validated from the middle height cross-section of the ring (Fig.4.12(b)), where there was no contact with the mandrel and almost identical stress fields were observed around every roll contact point. Interestingly, in the arc segments of the workpiece located between two subsequent roll contact points, significant compressive stresses could be seen along the inner peripheral surface. Combined with the aforementioned observations, these compressive stresses indicate the formation of small hinge-like deformations, which were only restrained by the material's own stiffness. Given that "collaring" is expected to be performed as a hot process and that the stiffness of most metals is significantly reduced in increased temperatures, these hinge-like deformations could potentially lead to global shape defects, in case of improper process parameters (mainly the linear and rotational velocities of the tools) are applied.

After the evaluation of the calculated stress results, the effective strain distributions were analyzed. For this analysis, the effective strain fields from only a single cross-section needed to be extracted (the main rolling bite cross-section was chosen), since they were almost identical in every other cross-section of the workpiece. The aforementioned effective strain distributions, at different time instances during the process, are presented in Fig.4.13:

Observations over Fig.4.13 revealed a rather expected strain evolution during the process. Since the main rolling bite cross-section was used for the current analysis, the positioning of the tools in Fig.4.13 was the same as that in Fig.4.10 (mandrel to the left, main roll to the right). Based on the mechanics of the "collaring" process, the main forming work is provided by the main roll and the support rolls to the outer peripheral surface of the workpiece. This phenomenon is clearly depicted in the effective strain results of Fig.4.13, which show a constantly increasing strain field concentrated around the outer peripheral ring surface. These strain fields increased steadily (both in intensity and volume) until approximately t

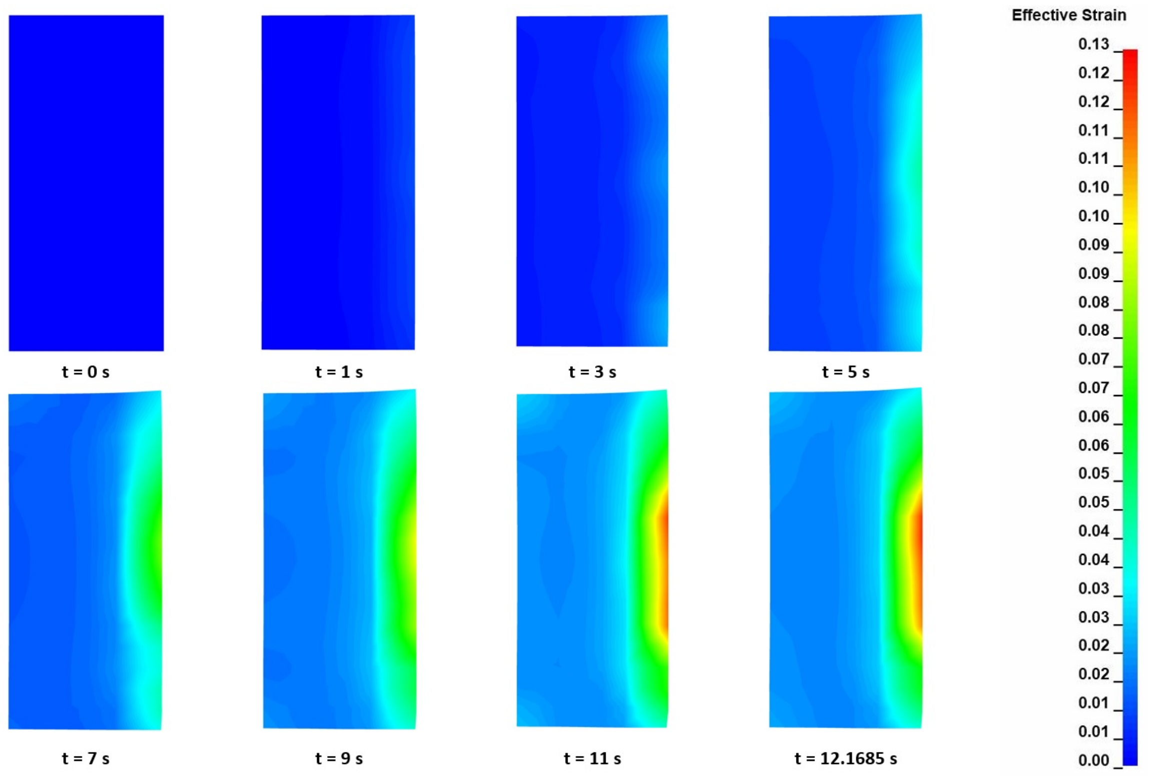

FIG. 4.13: Effective strain distributions at multiple time instances of the "collaring" Reverse Ring Rolling process simulation (Main Rolling Bite)

= 11 s, when no further divergences could be observed from that point and until the end of the simulation (t = 12.1685 s). The maximum recorded effective strains were observed after t = 11 s (and remained the same for the rest of the simulation) around the middle of the ring's outer surface, with the corresponding values being approximately 0.12–0.13. Other than that, some relatively increased effective strain fields also appeared around the inner edges of the ring after t = 5 s, which also increased until the end of the process. The manifestation of these strain fields coincided with the forming and growth of fishtail defects, which caused the vertical arching of the cross-section and the subsequent pressing of the ring against the mandrel. These inner edge strain fields reached their maximum effective strains at t = 11 s, similarly to the outer peripheral surface strains. The maximum recorded inner edge effective strain values were approximately 0.03–0.04.

Overall, the evaluation of the stress and strain results helped to clarify some localized deformational phenomena and better comprehend the deformation mechanism that occurs during the "collaring" Reverse Ring Rolling process. Since the observed results did not show any abnormalities or singularities, they can be considered as realistic and plausible.

Load Results ("Collaring" Model)

In the case of the load results from the "collaring" Reverse Ring Rolling model, the corresponding curves were extracted after the end of the simulation. For a better comprehension, these curves were split into two different figures. In Fig.4.14 the load reactions from the contact of the workpiece with the main roll and the mandrel are presented, while in Fig.4.15 the load reactions from the contact of the workpiece with each of the support rolls are presented:

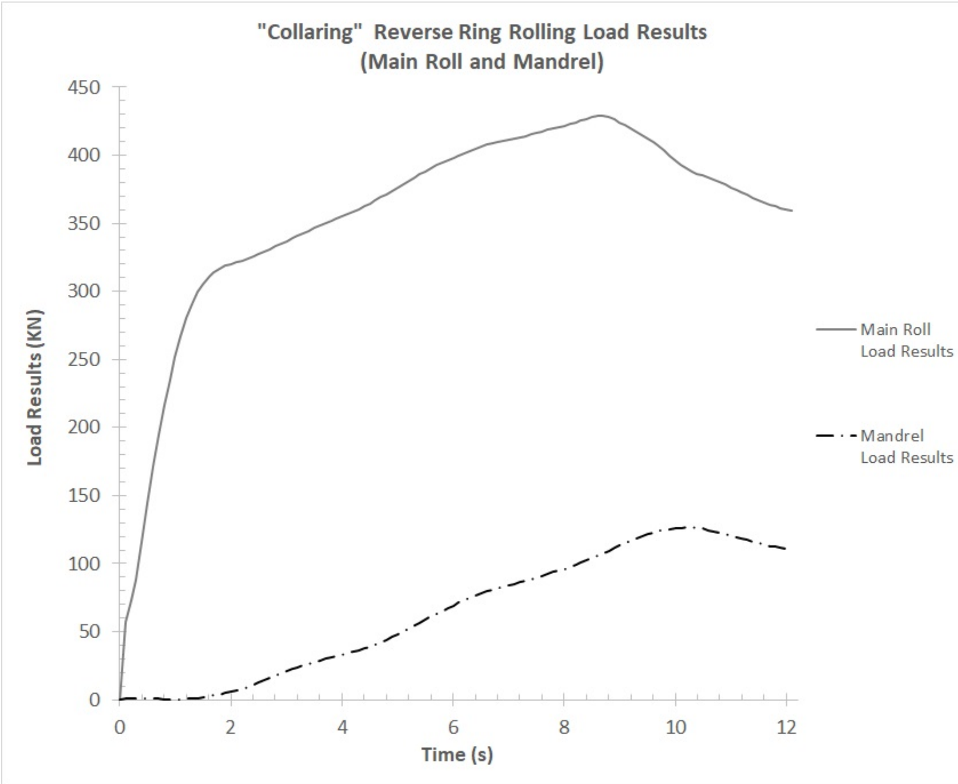

FIG. 4.14: Load result curves from the "collaring" Reverse Ring Rolling process simulation (Main roll and mandrel)

Observations over Fig.4.14 revealed significant differences between the load curves from the main roll and the mandrel. More specifically, in the case of the main roll load curve, a rapid load increase was observed early on in the process (t = 0–1.5 s, approximately). From that point onwards and until approximately t = 8.5 s, the main roll load continued to increase, although at a reduced rate compared to the beginning of the process. Additionally, at t = 8.5 s the maximum load value for the main roll was recorded at 430 KN, approximately. Lastly, from t = 8.5 s and until the end of the process, the main roll load decreased constantly, with a small change in rate after t = 10 s. The final main roll load value was approximately 360 KN. On the other hand, the mandrel load curve was significantly lower compared to that of the main roll. In this case, the calculated load during the early phase of the process (t = 0–2 s, approximately) was negligible, indicating poor or no contact between the mandrel and the workpiece. After t = 2 s and until t = 10 s approximately, a gradual increase at an almost constant rate was observed in the load, which ended at the corresponding curve's peak value of approximately 130 KN. From that point and until the end of the simulation, the mandrel load decreased steadily, with the final value being 110 KN approximately. From the overview of both load curves presented in Fig.4.14, the main roll load curve was measurably higher than the mandrel load curve throughout the process. In other respects, the two curves showed load increases and decreases at very similar rates, while the corresponding load changes mostly occurred at the same time windows during the process. The only differences to that were the first few seconds of the process, when no load was applied on the mandrel, and between t = 8.5 s and t = 10 s, when the main roll load decreased while the mandrel load increased. Especially this last difference indicates that after the conclusion of the tools' linear movement, the only active forming in the entire process was performed by the mandrel. This forming was mainly focused on normalizing

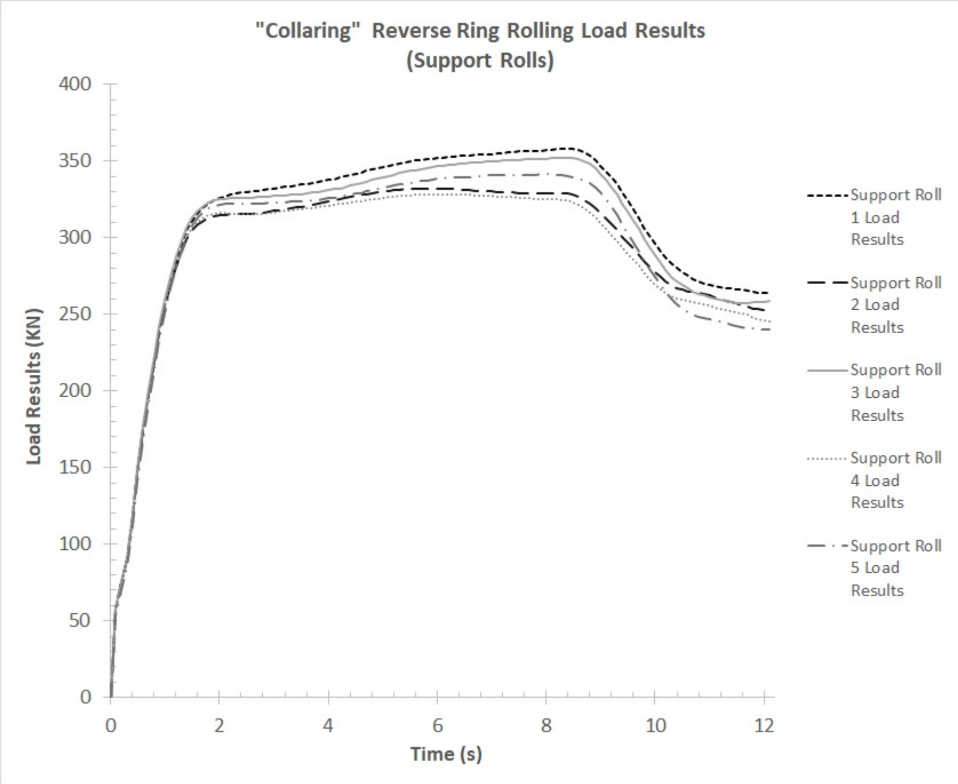

FIG. 4.15: Load result curves from the "collaring" Reverse Ring Rolling process simulation (Support rolls)

the inner radius of the ring, throughout its perimeter.

Regarding the corresponding load results of the support rolls (Fig.4.15), a first overview of the corresponding curves revealed comparable load values between one another and to those of the main roll. In this case, all support roll load curves were relatively close to one another, with the maximum percentage difference being approximately 12.5%. A more thorough analysis of these curves revealed a rapid initial load increase (from t = 0 until t = 1.5 s), which was almost identical to the corresponding segment of the main roll load curve. From that point onwards and until approximately t = 8.5 s, each load curve increased at a slightly different rate. Around t = 8.5 s, each curve reached its respective maximum load value, which ranged from 325 KN to 360 KN, approximately. After the conclusion of the main forming by the main roll and the support rolls, two different load reduction phases could be observed in all curves. The first load reduction phase occurred from t = 8.5 s until t = 10 s, with the corresponding reduction rates being relatively high. The second phase was observed from t = 10 s and until the end of the simulation, while the corresponding load reduction rates were slower. The final recorded load values of the curves in Fig.4.15 ranged from 240 KN to 265 KN, approximately. From the comparison of these load curves between one another, it can deduced that the support rolls closer to the main rolling bite and the one directly opposite of the main roll (support rolls 1, 3 and 5) withstood greater loads compared to the other two support rolls (support rolls 2 and 4). Especially in the case of support roll 1 (also see Fig.4.4), an additional load percentage needed to be counterbalanced, since the dynamic component from the momentum of the ring applied some additional force to the aforementioned tool, as the latter exited the main rolling bite. It is worth noting that in case the rotational velocity had an opposite direction (counterclockwise instead of clockwise), the highest load curve would most probably correspond to the ring's interaction with support roll 5.

From the correlation between the load results (Figs.4.14 and 4.15) and the corresponding deformational results (Figs.4.6 and 4.7), several interesting points can be discerned. Most notably, a clear correlation between the support roll load results and the deformation results was observed, since the corresponding curves in Figs.4.15, 4.6 and 4.7 had divergences in their slope at the same time instances. Furthermore, the slope changes observed in these curves after the linear movement of the rolls is concluded, indicated two different post - forming phases. At first (t = 8.5–10 s), a relatively quick normalization of the outer ring radii could be observed, which in turn caused a relatively larger height increase (compared to the next post - forming phase). After t = 10 s, however, only minor deformations took place (e.g. the ironing of potential defects) since the major ring dimensions had already been normalized and thus the need for additional work (and subsequently load) from the corresponding tools was significantly reduced. Overall, the presented load results had a rather expected behavior, with no extremities or abnormalities.

Temperature Results ("Collaring" Model)

Finally, the thermal results from the "collaring" Reverse Ring Rolling model were evaluated. Similarly to previous analyses, initially, the average temperature curves from the ring's outer peripheral and upper end surfaces were discussed. The aforementioned temperature curves were created using the methodology presented in section §2.15.3, and they are presented in Fig.4.16:

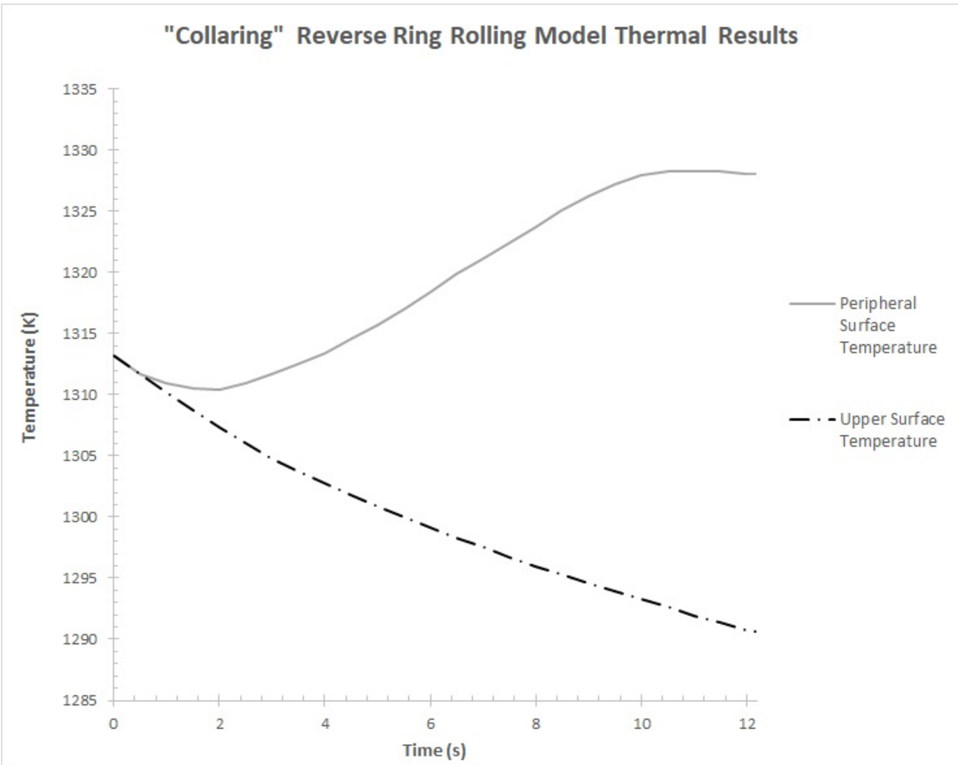

FIG. 4.16: Temperature result curves from the "collaring" Reverse Ring Rolling process simulation

Observations over the temperature curves in Fig.4.16 revealed some rather expected behaviors. In the case of the outer peripheral temperature, a slight temperature drop was observed early in the process (t = 0–2 s), which could be attributed to the relatively small deformations occurring at that time and the relatively high thermal conductivity of the tools, as the latter had not been yet heated from the process. However, after t = 2 s, a gradual temperature increase was observed as a result of the plastic work turned to heat, which lasted almost until the end of the process (a slight temperature drop was observed at the very end of the corresponding curve). The respective temperature increase rate was not constant throughout the process, with noticeable divergences observed at t = 8.5 s, t = 10 s and t = 11.5 s. More specifically, at t = 8.5 s the temperature increase rate was reduced approximately in half, then between t = 10 s and t = 11.5 s almost no temperature increase could be observed and after t = 11.5 s a slight temperature decrease was recorded. These temperature rate divergences coincided with the changes in the forming process that were previously discussed, in combination with the heating of the tools that naturally occurred during the process. The maximum outer peripheral temperature was observed at t = 11 s, with the corresponding value being approximately $T_{peripheral,collaring,max}$ = 1328.3 K. However, the final outer peripheral temperature value was slightly lower at $T_{peripheral,collaring,f}$ = 1328 K.

On the other hand, a constant temperature reduction was observed in the case of the upper end curve. Although the corresponding temperature reduction rate was not linear, an overall smooth temperature transition was recorded. This was a rather expected behavior, since no forming was performed directly on the upper end segments of the workpiece and thus a constant heat transfer from the ring to the environment was the only thermal phenomenon that took place. The maximum temperature recorded in the upper end curve was the initially input value of $T_{upper,collaring,max}$ = 1313.15 K, while the temperature value at the end of the process was approximately $T_{upper,collaring,f}$ = 1290.7 K.

Similarly to previous thermal result reviews conducted in the current dissertation, the peripheral, and upper end temperature curves provided little to no information about the temperature distributions inside the volume of the ring. For this reason, the temperature fields at various time instances of the process were extracted, in order to be further analyzed. A preliminary inspection regarding the temperature fields in various cross-sections of the workpiece and at the same time instances revealed that these fields were almost identical across the ring's body. Thus, the corresponding temperature distributions from a single cross-section of the ring (the main rolling bite cross-section was chosen again) and at different time instances during the process, were finally extracted, and they are presented in Fig.4.17:

Observations over the thermal results presented in Fig.4.17 revealed a rather expected temperature evolution during the process. Before proceeding with the evaluation of these results, it should be noted that since the cross-section of the workpiece in the main rolling bite was used for the current analysis, the positioning of the tools was the same as the corresponding stress and strain field evaluations discussed above. During the early stages of the process (t = 0–3 s), a slight temperature decrease could be observed along the surfaces of the workpiece, with the greatest temperature decrease occurring along the contact with the mill table. After t = 3 s and until t = 11 s, a similar temperature pattern could be observed in all cross-sections. More specifically, the temperature of the bottom and top ring surfaces, as well as along the contact with the mandrel, was constantly decreasing, as a result of heat being transferred towards the tools and the environment. Interestingly, the temperature values recorded along the contact with the mandrel were always slightly higher compared to the corresponding distributions at the top and, especially, the bottom end surfaces, thus

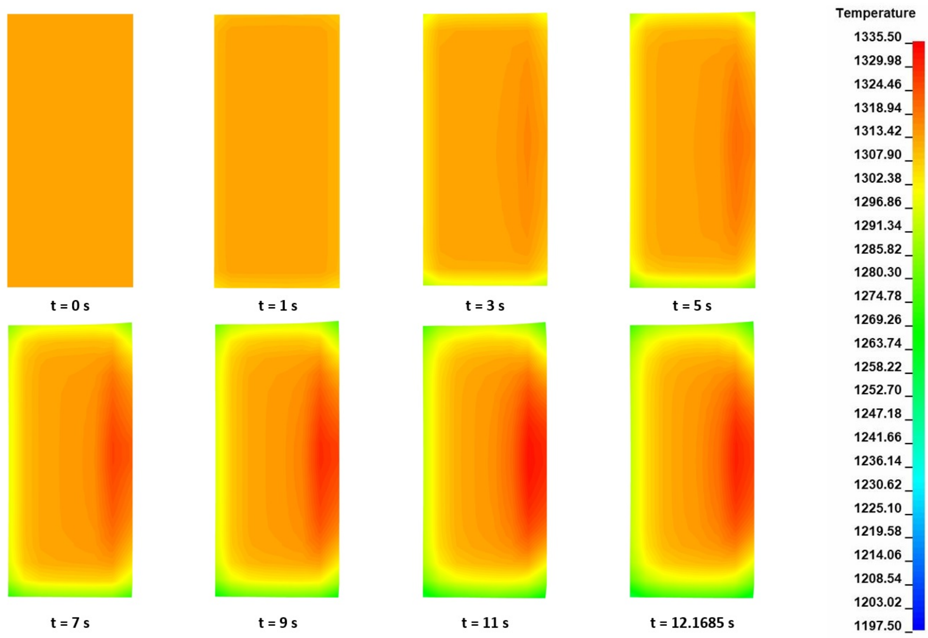

FIG. 4.17: Temperature distributions at multiple time instances of the "collaring" Reverse Ring Rolling process simulation (Main Rolling Bite)

indicating that a percentage of plastic work was introduced by the mandrel, which subsequently raised the temperature of the workpiece by a measurable margin. On the other hand, the temperature along the contact with the main roll kept increasing during the process, mainly due to the significant plastic work introduced by the aforementioned tool. This phenomenon could be observed until t = 11 s, while by the end of the process (t = 12.1685 s) a slight temperature decrease was observed in that area. The maximum recorded temperature from the entire process were observed along the contact with the main roll around t = 11 s, with the corresponding value being approximately $T_{collaring,max}$ = 1335.5 K.

4.3.3 "Pulling" Model Setup

After the inner radius of the ring was reduced almost precisely to the target value by the "collaring" process, a "pulling" process was subsequently setup to adjust the outer ring radius, as well. In general, the "pulling" process has some significant differences in its mechanics, compared to the "collaring" process. Apart from the main difference, which is the lack of linear movement of the mandrel in this process, the velocity values applied on the tools could heavily affect its feasibility. More specifically, a "pulling" process can be considered as being closer to a finishing process in terms of the applied process parameters. Thus, a combination of a high rotational velocity and a (relatively) low linear velocity should be applied to the rolls. This fact was further proven through a number of preliminary trial models, in which the application of different tool velocities (both linear and rotational) was tested. The trial models which had velocities close to those applied on the "collaring" model led to global shape defects on the final product. An example of a failed trial model with global shape defects is presented in Fig.4.18.

Through the conducted preliminary trial models, a realistic model parameter set was determined. With the aforementioned parameter set, the "pulling" model could be setup, subsequently. For this model, the final state of the "collaring" model was used to define the initial geometries of the workpiece and the tools. Additionally, the majority of process and

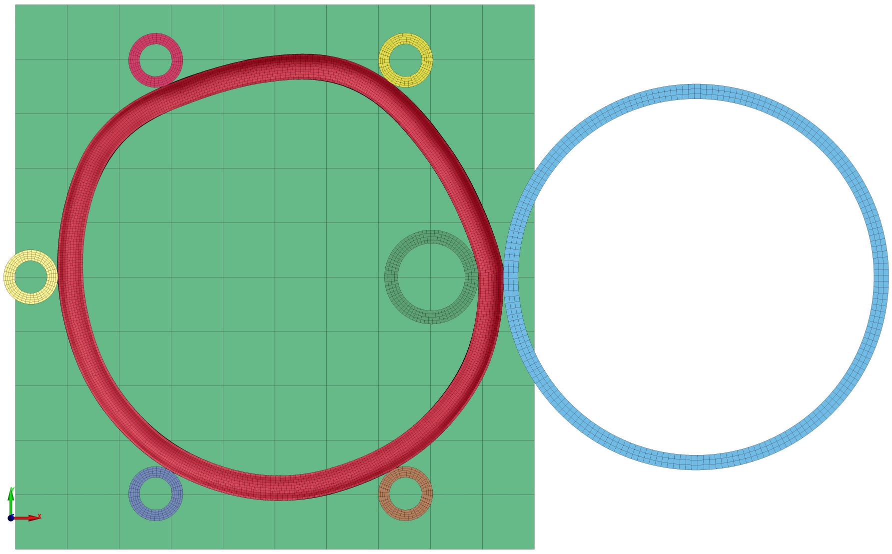

FIG. 4.18: Global shape defects on the final product of a "pulling" process simulation, due to improper tool velocities

model parameters were kept the same, since the general setups of the two processes were quite similar. The properties and parameters that were different in the "pulling" model, can be summed up to the following:

- The initial temperature of the ring in the current analysis was re-evaluated, and it was slightly increased to $T_{ring,pulling,0}$ = 1318.15 K, based on an approximation from the final temperature results of the "collaring" model. This value was once again input using the *TEMP* option in the INITIAL_TEMPERATURE_SET menu. Also, the aforementioned initial temperature value was considered the same in the entire ring.

- The linear immobilization of the mandrel was introduced via MAT_20-RIGID menu, by setting option *CON1* = 7 (with *CMO* = 1.0 applied).

- During some preliminary trial models, the formation of peripheral surface defects was observed. In order to minimize the aforementioned defect formation, the friction coefficients between the rolls and the workpiece were reduced to *FS/FD* = 0.2/0.1 for the main roll - to - ring contact and to *FS/FD* = 0.1/0.05 for the rest of the contacts. Such friction coefficient values can be considered realistic, in cases of well - lubricated finishing processes, in which the quality of the product's surface is a requirement. Additionally, similar low friction coefficients are also considered in cases of cold Ring Rolling application, mainly during Phase 4.

- The rotational and linear velocity values considered in the current analysis were $\omega_{MR,pulling}$ = $\frac{10 \cdot \pi}{3}$ $\frac{rad}{s}$ and $v_{tools,pulling}$ = 0.2 $\frac{mm}{s}$, respectively. These velocity values were introduced in the model via the DEFINE_CURVE menu.

- A slight delay was applied to the linear velocity of the support rolls. This delay was defined based on the respective angular position of each support roll and the angular velocity of the ring. The main reason for the consideration of the aforementioned delay was to minimize the possibility of the workpiece to stuck during the process.

- Based on the final outer radius at the end of the "collaring" model ($R_{f,collaring}$ = 453.18 mm) and the target outer radius ($R_{f,target}$ = 450 mm), a total outer radius reduction of ΔR = 3.18 mm had to be performed during the "pulling" model. Given the linear tool velocity of $v_{tools,pulling} = 0.2 \frac{mm}{s}$, a total simulation time of $t = 15.9$ s had to be applied. Since an additional $\Delta t = 3$ s were at least required for the normalization of the ring's dimensions, a total simulation time of $ENDTIM = 18.9$ s was finally input in the model via the CONTROL_TERMINATION menu.

It is worth noting that no stress, strain, or temperature distributions were transferred from the "collaring" to the "pulling" model, since the effects of the latter process needed to be solely evaluated. However, the existence of residual stresses and/or non-uniform temperature distributions could significantly affect the outcome of an actual "pulling" process.

4.3.4 "Pulling" Model Results

After the solution of the "pulling" model, the calculated results revealed an overall successful conclusion of the process, as this was intended. At a first glance, the outer radius of the workpiece was reduced with a simultaneous increase of its height, while no abnormalities manifested. In the following subsections, a more detailed analysis of the calculated results is conducted.

Deformational Results ("Pulling" Model)

As with the previous analyses, the deformational results from the "pulling" model were initially evaluated. As a first analysis, the cross-sections of the workpiece at the first and last time instance of the "pulling" model were reviewed as they are presented in Fig.4.19. It is worth noting that the cross-sections in Fig.4.19 were almost identical for every cross-section of the ring, at their respective time instances.

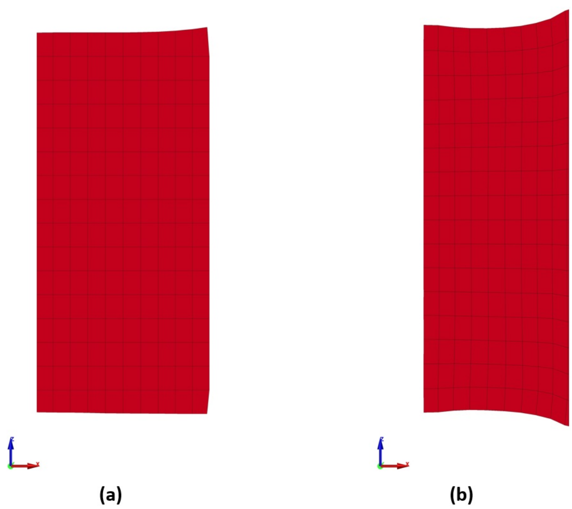

FIG. 4.19: Cross-sections of the ring at different time instances of the "pulling" model: (a) initial time instance and (b) final time instance

Observations over the cross-sections in Fig.4.19 revealed a relatively significant deformation of the workpiece during the "pulling" process. Regarding the orientation of the cross-sections in Fig.4.19, the outer peripheral surface was on their respective right side and the inner peripheral surface was on their left side. Most notably and apart from the thickness reduction, which was the main goal of the current process, large fishtail defects could be observed at the outer surface edges, while smaller fishtail defects were formed at the inner surface edges. The aforementioned fishtail defects were rather expected, as the majority of forming was performed by the main roll and the support rolls. On the other hand, the formation of the inner fishtail defects implied that the workpiece was pressed at a measurable degree against the mandrel, thus the conducted process was reminiscent of Ring Rolling (to a certain degree). It should be noted that the peripheral surfaces of the workpiece at the end of the "pulling" model revealed no arching of the cross-section, as any inwards rotation of the edges was completely ironed out.

Subsequently, the major ring dimension results were evaluated. The outer and inner radii curves and the average ring height curve are presented in Figs.4.20 and 4.21, respectively:

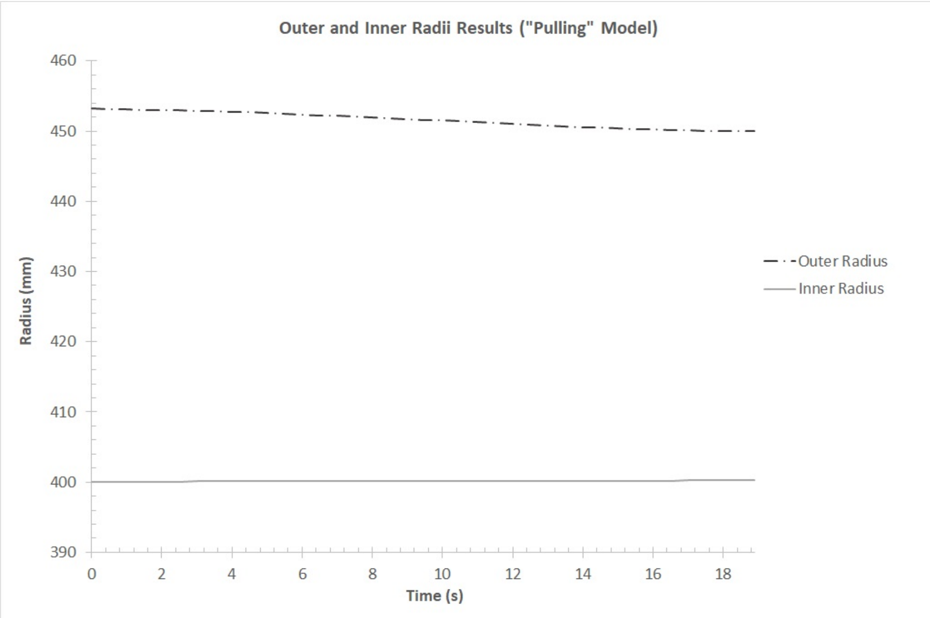

FIG. 4.20: "Pulling" model outer and inner radii results

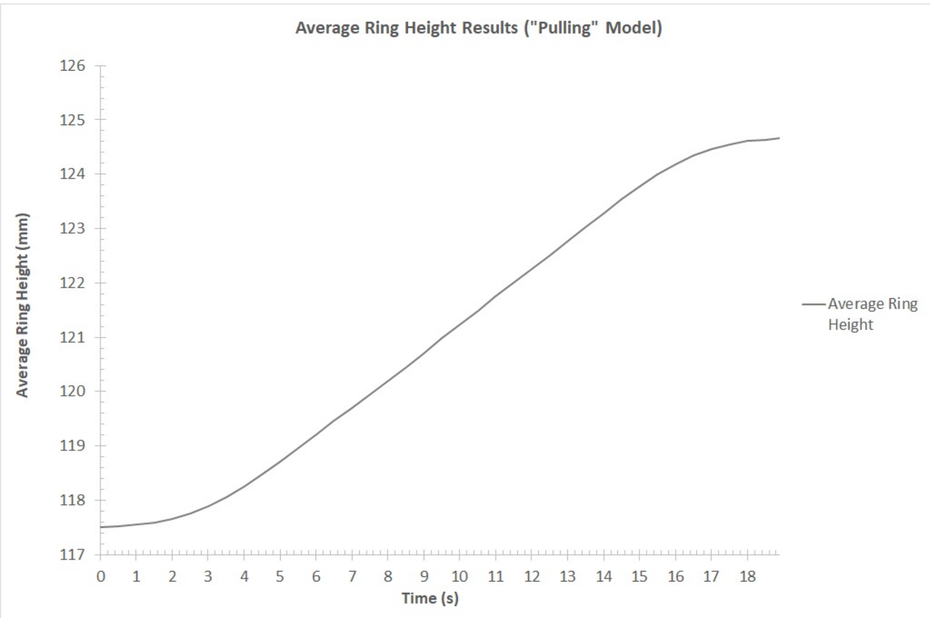

FIG. 4.21: "Pulling" model average ring height results

Observations over the inner and outer radii, results presented in Fig.4.20 revealed a rather expected behavior. In the case of the outer radius results, a smooth (almost linear) reduction was observed for the majority of the process (t = 0–17.5 s), while little to no further deviations were recorded for the remainder of the process (t = 17.5–18.9 s). On the other hand, the inner radius results revealed a slight increase in the corresponding dimension. The inner radius increase occurred gradually throughout the entirety of the process, at an almost linear rate. Regarding the final radii of the workpiece, the outer radius value recorded at the last time instance was approximately $R_{f,pulling}$ = 449.998 mm, while the corresponding inner radius was approximately equal to $r_{f,pulling}$ = 400.31 mm. Compared to their respective target values, the inner radius was larger by a percentage of $\Delta r_{pulling}$ = 0.08%, while the outer radius was smaller by a percentage of $\Delta R_{pulling}$ = 0.0003%. Both of these percentage differences are small enough to be considered negligible, although the inner radius was increased from 0.0038% (at the end of the "collaring" process) to 0.08% greater than its respective target value.

Regarding the average ring height results, a rather expected behavior was observed in Fig.4.21. During the early stages of the "pulling" process (t = 0–3 s), a relatively slow increase of the average ring height was observed. From that point onwards and until the conclusion of the main forming action (t = 3–15.9 s), the aforementioned dimension increased at an accelerated rate, as a result of the ring's thickness reduction occurring at the same time. Finally, from t = 15.9 s and until the end of the process, another relatively slow increase was observed. The maximum average height was recorded at the end of the process, as expected, with the corresponding value being $H_{pulling,f}$ = 124.66 mm. Based on this value, the corresponding percentage difference compared to the target height value was $\Delta H_{pulling}$ = 8.4%. However, both of these values can be considered as misleading, since the average ring height was heavily affected by the greatest ring height measured on the workpiece, which was located on the outer side fishtail defect. In order to have a more meaningful height result and given that the main goal of the ring height analysis was to ensure that there is enough material to grind off the ring so that the required target ring height can be reached, a measurement of the minimum ring height needed to be conducted. After reviewing various cross-sections of the final product, the minimum recorded height was found to be located closer to the inner peripheral surface, with its corresponding value being $H_{pulling,min,f}$ = 121.22 mm at the end of the process. This height was $\Delta H_{pulling,min}$ = 5.41% greater than the corresponding target value, so some additional grinding or machining post - processes could be successfully performed, in order to achieve the prerequisite ring height.

From the rest of deformational results available from the "pulling" model, the ring's ovalities and thickness were also analyzed. In the case of the former, the outer and inner ovality curves were created using the same methodology previously presented in §2.16.1. The corresponding result curves are presented in Fig.4.22:

Observations over the outer and inner ring ovalities (Fig.4.22) revealed some interesting points. More specifically, the results of the current process were the first to introduce ovality curves with notably different behaviors. In the case of the outer diameter ovality and during the very first time instance, an ovality increase was observed, as a result of the asynchronous movement of the tools that affected the ovality of the outer diameter. Subsequently, a slight reduction could be observed until t = 4 s, which was followed by a gradual increase that lasted until the end of the process. Most notably, after the end of the main forming action (t = 15.9 s) a reduction of the outer ovality's increase rate was observed. Based on these observations, it can be concluded that early in the process the main forming action performed by the main rolling bite ironed some pre-existing (from the "collaring"

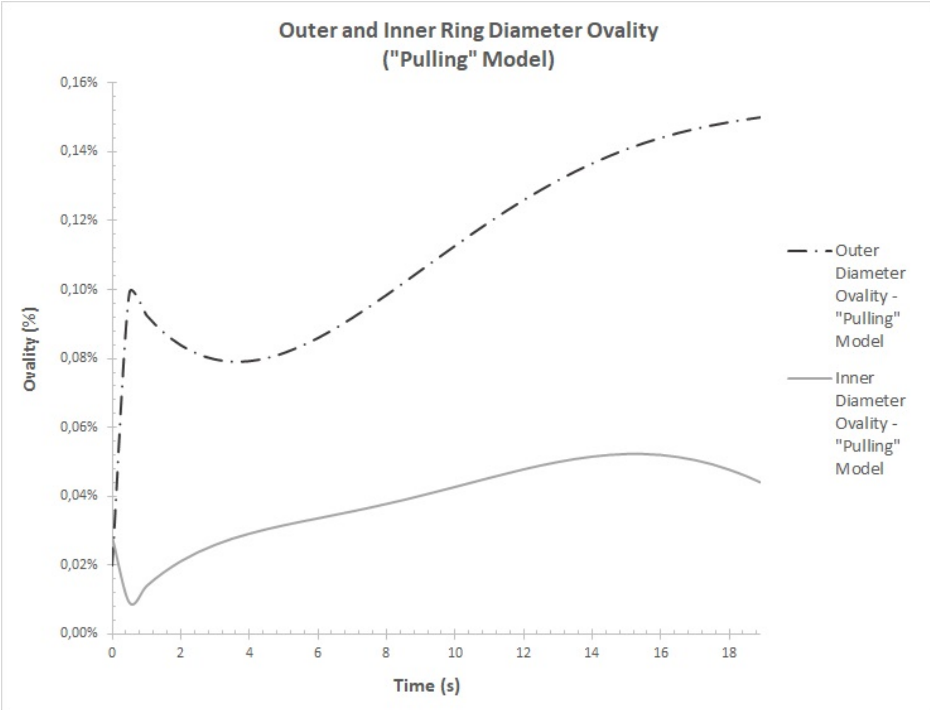

FIG. 4.22: Outer and inner diameter ovality results ("Pulling" model)

process) surface imperfections, thus a slight ovality reduction was observed. After t = 4 s, however, the asynchronous tools' movement caused a more global ovality divergence, which was progressively stabilized when each tool reached its final position. It is highly probable that in case the final finishing phase was simulated for longer, the outer diameter ovality would start decreasing. Regarding the maximum recorded outer ovality, this was observed at the very end of the process, with the corresponding value being approximately 0.15%. Similarly to the "collaring" model, it should be noted that the aforementioned ovalities would have to be added to any pre-existing ovalities from Ring Rolling and "collaring" processes.

In the case of the inner diameter ovality, a sudden decrease was observed early in the process, as the ring's compression against the mandrel lead to the ironing of the pre-existing inner surface imperfections. Afterward, the inner diameter ovality began increasing (although not steadily) from the beginning of the process and until the end of the main forming action (t = 15.9 s), when it reached its peak value of 0.05%, approximately. This phenomenon can be attributed again to the asynchronous movement of the tools. From that point and until the end of the process, the inner diameter ovality slightly decreased, with the corresponding value at the end of the process being approximately 0.04%.

In general, both of the recorded ovality values are small enough so that the produced ring can be considered as perfectly round. However, in case the requirements for low ovalities are even stricter, maintaining the final finishing phase of the "pulling" process (during which the rolls only rotate without moving linearly) for an extended period of time would reduce the calculated ovalities even more.

Finally, the ring thickness results were extracted and evaluated. The corresponding curve is presented in Fig.4.23:

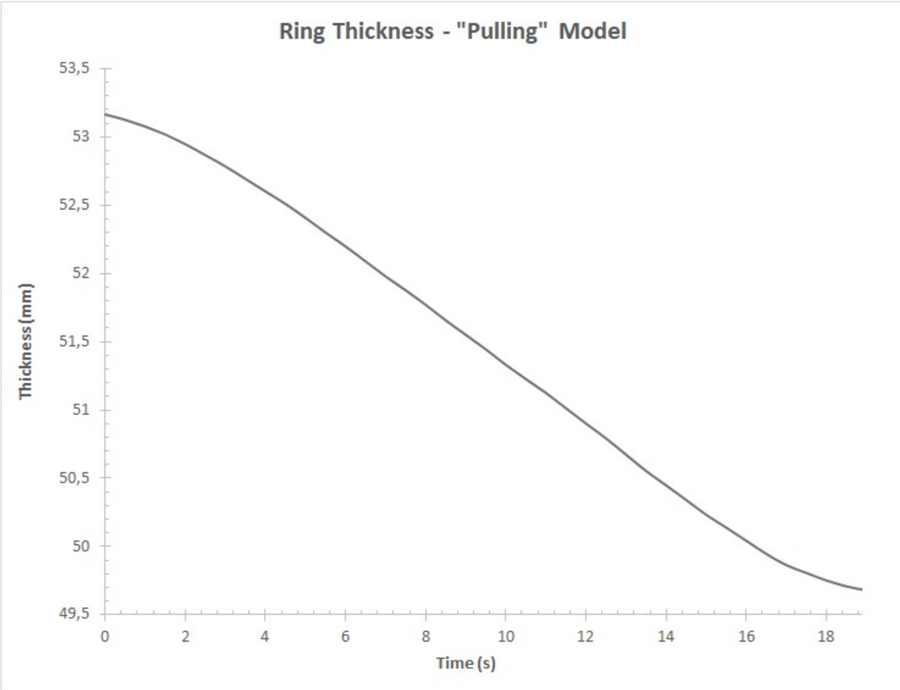

FIG. 4.23: Ring thickness results ("Pulling" model)

Observations over Fig.4.23 revealed a rather expected behavior. More specifically, and during the entire process, a gradual reduction of the ring's thickness was observed, although not at a constant rate. Given that this was the main goal of the current process, any other behavior would be considered unacceptable. The final recorded thickness value was approximately $f_{pulling,f}$ = 49.68 mm, for a percentage difference of $\Delta f_{pulling}$ = 0.64%, thus the calculated thickness was slightly smaller than the corresponding target value.

Overall, the deformational results proved the feasibility of the Reverse Ring Rolling process as a post - Ring Rolling process, which can "correct" the diametrical overshoots to a significant degree. Although the final dimensions from the conducted simulations were not exactly equal to the target dimensions (even if they were very close), this could be easily achieved through some minor adjustment of the corresponding manufacturing durations.

Stress and Strain Results ("Pulling" Model)

Following the deformational results, an analysis of the calculated stress and strain results from the "pulling" model was conducted.

Initially, the signed Von Mises stress results at different time instances during the process were evaluated. Similarly to the "collaring" model, two different cross-sections of the ring were analyzed, namely one in the main rolling bite and another in contact with a support roll (support roll 3 contacting cross-sections were chosen in this case, too). The latter was compared with the corresponding cross-sections being in contact with the rest of support rolls and almost identical stress were observed between one another (if the small delay applied to their linear movement was taken into account). The aforementioned signed Von Mises stress results from the two cross-sections at different time instances during the process are presented in Figs.4.24 and 4.25:

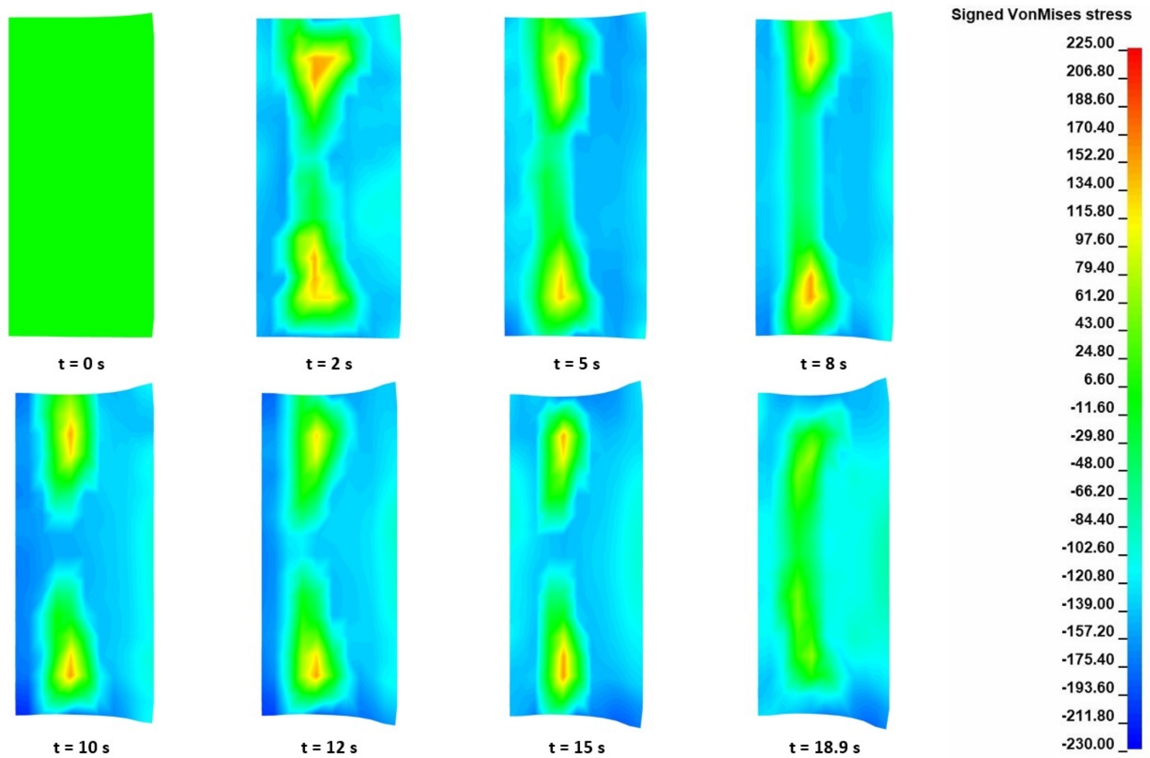

FIG. 4.24: Signed Von Mises stress distributions at multiple time instances of the "pulling" Reverse Ring Rolling process simulation (Main Rolling Bite)

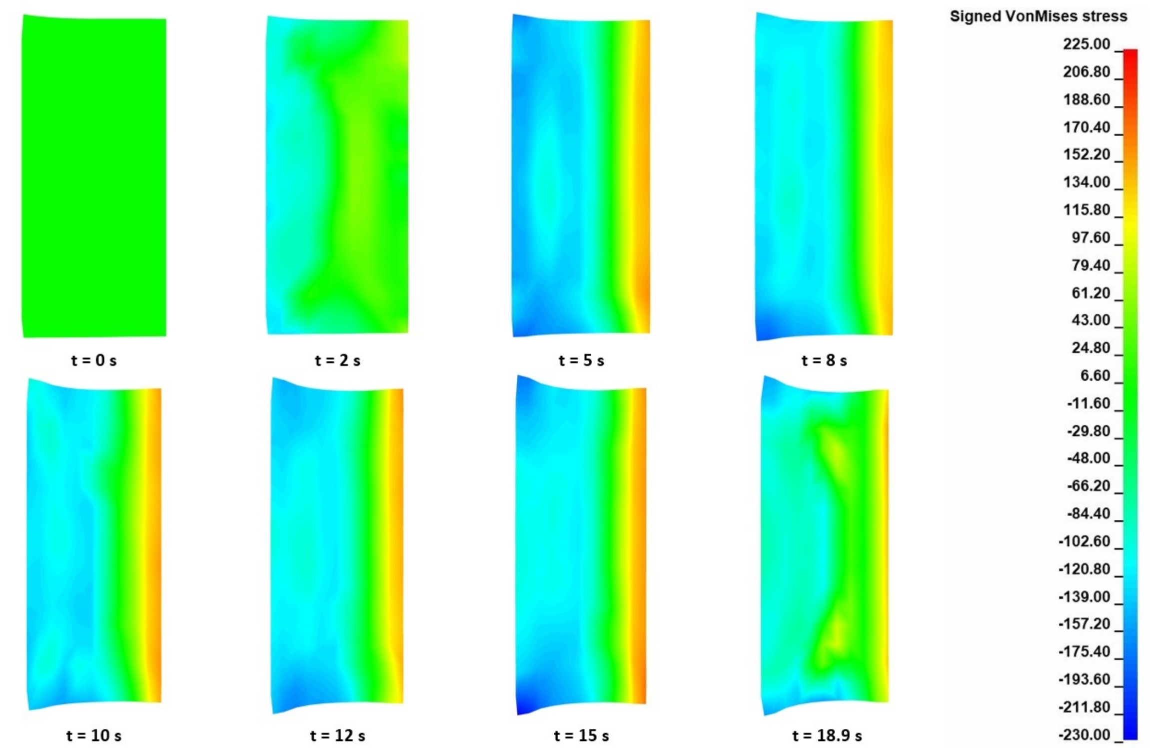

FIG. 4.25: Signed Von Mises stress distributions at multiple time instances of the "pulling" Reverse Ring Rolling process simulation (cross-section in contact with Support Roll 3)

Observations over the signed Von Mises stress results of the material in the main rolling bite (Fig.4.24) revealed some rather expected stress distributions. Before further analyzing the presented stress distributions in Fig.4.24, it should be reminding that the main roll was located on the right side of the depicted cross-sections, while the mandrel was located on their left side. In almost every time instance of Fig.4.24, two relatively high compressive stress fields were observed around the contacts with the main roll and the mandrel, with the latter having slightly greater (absolute) stress values. This fact can be attributed to the smaller contact area between the mandrel and the ring, compared to that between the main roll and the ring. On the other hand, a neutral to tensile stress field could be observed around the center of the corresponding cross-sections. This particular stress field was a result of the ring's height increase, which produced these tensile stresses in areas where the vastly superior compressive stresses were not dominant or were completely absent. These two types of stress fields were observed throughout the process and around the same areas of the cross-section, with some relatively small deviations in shape and size. Finally, during the last stages of the process (t = 15–18.9 s), an additional compressive stress field was seen increasing around the bottom outer edge of the workpiece, as a result of the bottom fishtail defect interacting with the mill table. The maximum (absolute) stresses were observed around the inner edges of the workpiece and at the middle of the process's duration (t = 10–12 s), with the corresponding (compressive) values being approximately 200–230 MPa.

In the case of the signed Von Mises stresses observed in the support roll contacting cross-sections (Fig.4.25), the corresponding distributions were also rather expected. Firstly, it should be reminded that the support roll in this case was located on the left side of the presented cross-sections. For the entirety of the "pulling" process, a relatively high compressive stress field was observed along the outer peripheral surface of the ring, as a result of the forming action of the contacting tool. On the contrary, a moderate tensile stress field could be observed along the inner peripheral surface during the whole process. The latter can be attributed to the same slight outward bending mechanism that was also observed and described in the corresponding results of the "collaring" model. These specific stress fields were observed almost unchanged throughout the process, with some minor deviations observed at the very first and very last time instances of the simulation. The maximum (absolute) Von Mises stresses in this case were observed around the bottom outer edge of the ring at t = 15 s, with the corresponding (compressive) values being approximately 210–230 MPa. The maximum recorded stress values were a result of the combination of the support roll's compressive action and of the bottom fishtail defect's interaction with the mill table.

Finally, the calculated effective strain results from the "pulling" model were evaluated. Similarly to the "collaring" model, the strain results were almost identical throughout the perimeter of the ring (taking into consideration the small delay applied to the tools), thus only a single representative cross-section was analyzed (the main rolling bite cross-section was chosen). The corresponding effective strain distributions for multiple time instances during the process are presented in Fig.4.26:

Observations over the effective strain distributions in Fig.4.26 revealed a rather expected behavior. It is worth reminding that in the main rolling bite cross-section that was chosen for this analysis, the outer peripheral surface is located on the right side of the presented instances, while the inner peripheral surface is located on their left side. During the "pulling" process, two distinct effective strain fields were mainly observed, one on each of the peripheral surfaces of the workpiece. These two effective strain fields increased in size and intensity over the process's duration, with the field on the outer surface size having slightly increased strain values compared to the field on the inner surface side, at the same time

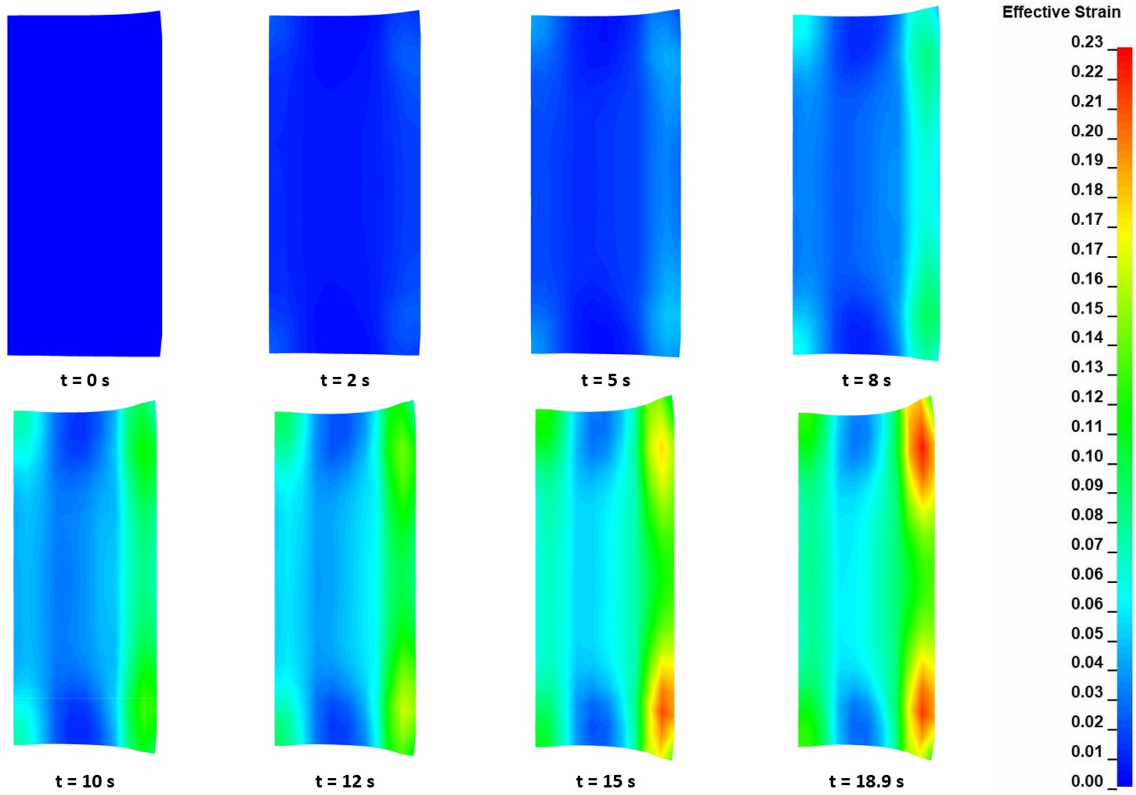

FIG. 4.26: Effective strain distributions at multiple time instances of the "pulling" Reverse Ring Rolling process simulation (Main Rolling Bite)

instances. Interestingly, after t = 10 s and until t = 15 s, the effective strain field around the outer bottom edge of the ring began intensifying at a more accelerated rate than the corresponding field at the upper outer edge. This phenomenon can be attributed to the compression of the outer bottom fishtail defect against the mill table, which contributed some additional strain to the strain field that already existed as a result of the main roll's compressive action. Finally, the maximum recorded effective strains from the entire simulation were observed around the outer edges of the ring at the end of the process, with their corresponding values being approximately 0.20–0.23.

Overall, from the analysis of stresses and strains, some rather expected results were observed, given the deformation mechanism taking place during a "pulling" process. The recorded stress and strain distributions had logical patterns, while no extreme values or abnormalities were observed. Based on these conclusions, the corresponding results can be considered as realistic and plausible.

Load Results ("Pulling" Model)

Next, the load results from the "pulling" model were analyzed. The corresponding load curves from the interaction of the workpiece with each of the tools were extracted directly from the simulation, and they were subsequently compared with one another. Similarly to the corresponding "collaring" model results, the curves of the main roll and mandrel loads were analyzed on a separate figure than the support roll load curves. The aforementioned curve comparisons are presented in Figs.4.27 and 4.28:

Observations over Fig.4.27 revealed some rather expected load results. Both the main roll

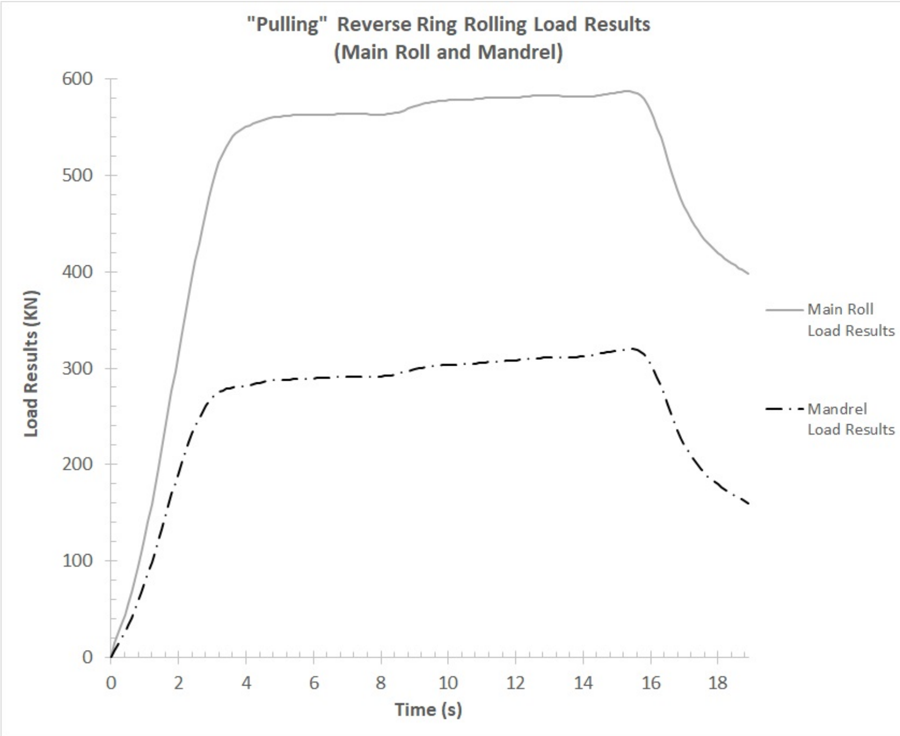

FIG. 4.27: Load result curves from the "pulling" Reverse Ring Rolling process simulation (Main roll and mandrel)

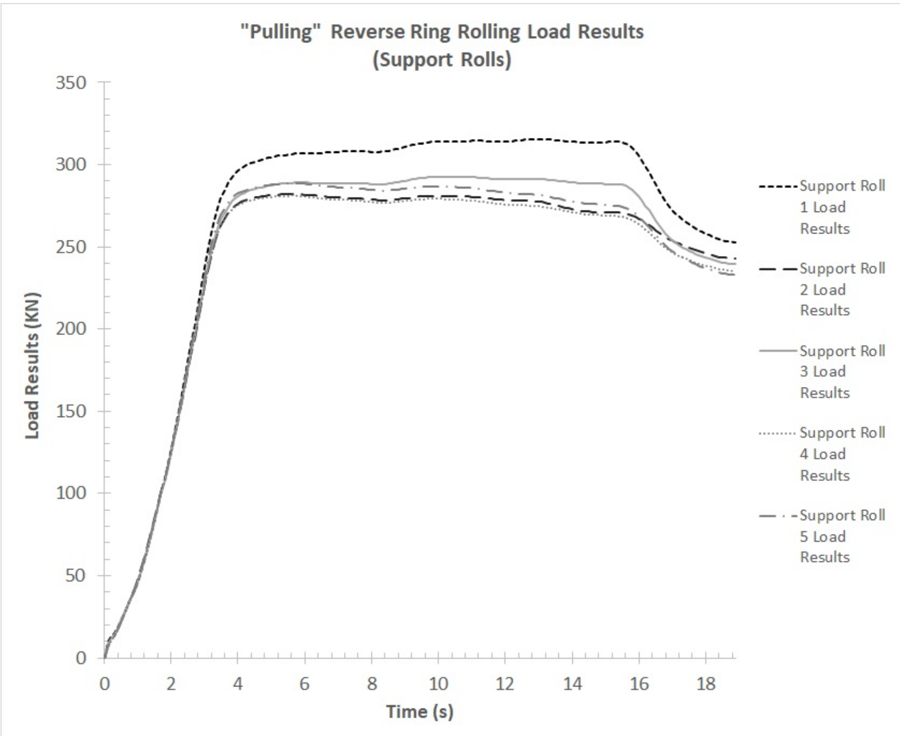

FIG. 4.28: Load result curves from the "pulling" Reverse Ring Rolling process simulation (Support rolls)

and the mandrel load curves had almost identical increase and decrease patterns, although their corresponding values were different. From the beginning of the process and until t

= 3 s, a rapid load increase was observed for both tools. Afterward, the load increase rate decreased significantly, and the recorded load values increased only slightly until the end of the main forming action (t = 15.9 s). On that point, the maximum load for each curve was recorded. After t = 15.9 s and until the end of the process, both curves gradually decreased. The maximum recorded load values for the main roll and the mandrel were 587 KN and 320 KN, respectively. In general, this behavior can be considered as logical, since the applied load by the main roll is counterbalanced partially by the mandrel and in another part by specific support rolls.

Regarding the observed load results from the ring's reaction with each of the support rolls (Fig.4.28), these were very close to the mandrel load curve from Fig.4.27, both in terms of pattern and load values. All the support roll load curves had a rapid initial load increase until t = 3 s approximately, which was subsequently followed by a significant load deviation. Interestingly, only support roll 1 had an increasing load pattern after t = 3 s, while the rest of the curves either maintained an almost constant load value or they had a slightly decreasing loading rate. Finally, after t = 15.9 s, all curves had a relatively fast load decrease until the end of the process. The maximum recorded load among all support roll load curves appeared in support roll 1 curve at t = 15.9 s, with the corresponding value being approximately 315 KN. It is worth noting that although all support roll load curves were relatively close to one another, a quick sorting of the observed curves would position support roll 1 curve as the one with the highest load values, followed by support roll 3 and 5 in order (for the numbering of support rolls, please refer to Fig.**??**). Support roll 2 and 4 curves, on the other hand, had the lowest load values and were almost identical to one another, with support roll 2 curve being ever so slightly greater than support roll 4 curve. This specific sorting was previously observed unchanged from the corresponding "collaring" model support roll load curves.

Generally, the observed load results followed rather expected patterns, while their respective values were within acceptable margins. Thus, the presented load curves can be considered as plausible during an actual "pulling" model.

Temperature Results ("Pulling" Model)

Finally, the thermal results from the "pulling" model were evaluated. At first and similarly to the "collaring" model, the average temperature curves from the ring's outer peripheral and upper end surfaces were analyzed. The corresponding temperature curves are presented in Fig.4.29:

Observations over the temperature curves in Fig.4.29 revealed some rather expected behaviors, which were very similar to the corresponding results from the "collaring" model. In this case, too, the peripheral surface temperature was initially reduced until t = 3 s, as a result of the tools' high cooling rate (the tools had not been heated from the process yet) combined with the relatively small deformation performed on the workpiece up to that point. However, after t = 3 s, a continuous and gradual temperature increase was observed on the peripheral surface, with the maximum temperature value at the end of the process being approximately $T_{peripheral,pulling,max}$ = 1419 K. Interestingly after t = 15.9 s, a slight reduction could be observed on the temperature increase rate of this curve, since the main forming action was concluded on that particular time instance. On the other hand, the upper surface temperature curve was constantly reducing throughout the process. This behavior was expected, since no direct forming was performed on the corresponding segments of the workpiece and thus no plastic work, which would be turned to heat, was introduced

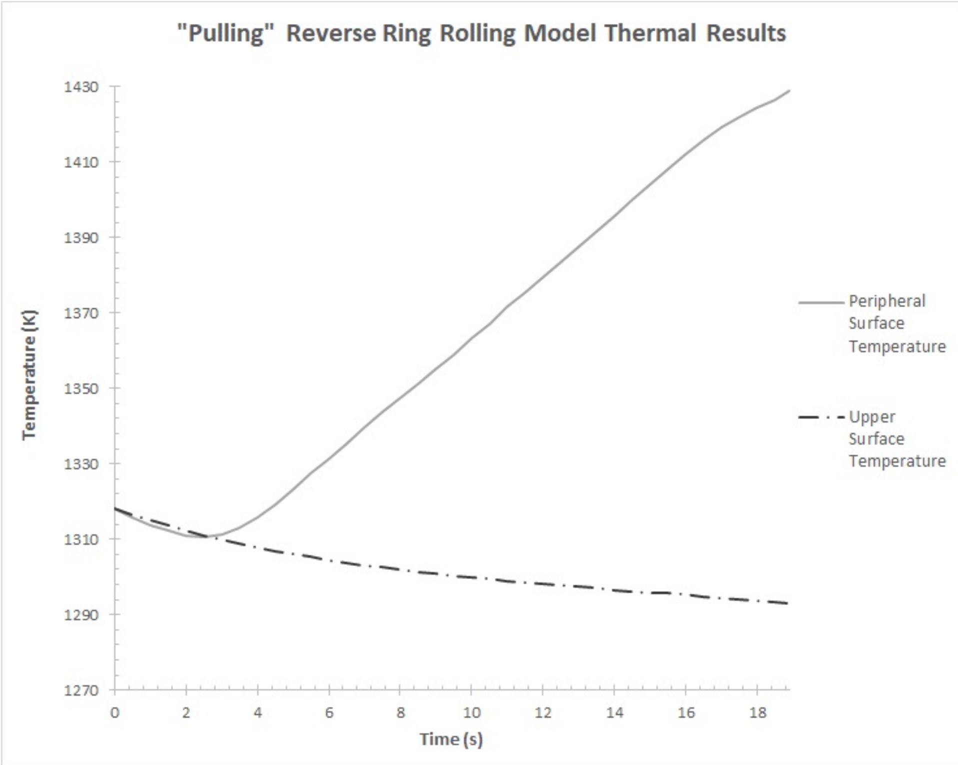

FIG. 4.29: Temperature result curves from the "pulling" Reverse Ring Rolling process simulation

in these areas. The maximum temperature value observed in the upper end curve was the initial input value of $T_{upper,pulling,max}$ = 1318.15 K, while the temperature value at the end of the process was approximately $T_{upper,pulling,f}$ = 1283 K. In general, the analyzed temperature curves had a rather expected behavior, with no particular points of concern.

Finally, in order to analyze the temperature distributions inside the body of the ring, the corresponding fields at multiple time instances during the process were extracted. From a quick review of different cross-sections of the workpiece prior to the extraction of the temperature distributions, it was made clear that the temperature fields were relatively uniform within the body of the ring, in this case too. Thus, only a single cross-section of the ring (that inside the main rolling bite) was analyzed in the current analysis. The corresponding temperature fields are presented in Fig.4.30:

Observations over the temperature distributions in Fig.4.30 revealed rather expected results. Prior to the analysis of the aforementioned results, it should be reminded that in Fig.4.30 the main roll was positioned on the right side of the presented instances, while the mandrel was on their left side. As with the "collaring" model, during the early stages of the process (t = 0–5 s) a temperature reduction could be observed mainly along the bottom surface of the ring, due to the ring's contact with the mill table. From t = 5 s and until the end of the process, this temperature reduction concentrated on the outer bottom edge of the workpiece, while at the same time, a temperature increase was observed along the outer peripheral surface of the ring. The latter was a result of the plastic work (turned to heat) introduced by the main roll's compressive action. This temperature distribution gradually increased both in terms of size and of value over the duration of "pulling" process. Regarding the maximum and minimum temperatures in Fig.4.30 both were observed at the

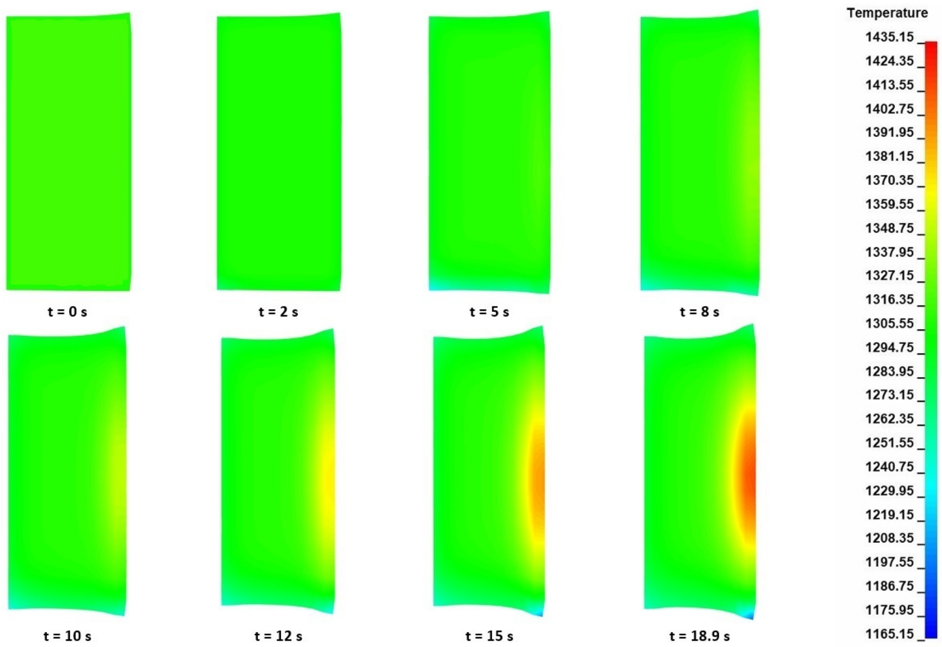

FIG. 4.30: Temperature distributions at multiple time instances of the "pulling" Reverse Ring Rolling process simulation (Main Rolling Bite)

end of the process, with the corresponding values being $T_{pulling,max}$ = 1435 K and $T_{pulling,min}$ = 1165 K, respectively. Generally, the aforementioned temperature distributions followed the expected path, with great similarities (mainly in terms of the observed patterns) to the corresponding results from the "collaring" model.

Since no particular extremities or abnormalities were observed in this case either, the thermal results from the "pulling" model can be considered to be representative of an actual "pulling" process.

4.4 Crucial Reverse Ring Rolling Process Parameters

Given the mechanics of Reverse Ring Rolling as they were described in section 4.2, the two most important aspects of the process are maintaining its stability and achieving the required ring radius reduction at a stable (but relatively fast) reduction rate.

For this reason, the effects of certain parameters on those aspects of the process were further examined in the current section. More specifically, the parameters that were investigated were: (a) the linear velocities of the rolls, (b) the number of support rolls used in the process and (c) the initial temperature of the ring. In order to perform the corresponding analyses, comparative simulations with notable differences on these process parameters were conducted. The calculated results from each of the these simulations were subsequently compared to the corresponding results previously presented in sections §4.3.1 and §4.3.3, since the latter were used as the base models for all other simulations. The conducted comparisons are presented in more depth, in the following sections.

Before proceeding to the analyses of the conducted simulations, there are two keypoints that need to be clarified. Firstly, the main goal of the conducted simulations was to investigate whether similar simulations to those presented in sections §4.3.1 and §4.3.3, but with differences solely on a single, crucial process parameter (per model) could be performed successfully, and subsequently evaluate the quality of the final product from each process. Secondly, the following comparisons were based only on the deformational results of the conducted simulations. The author of the current dissertation is well-aware that facilitation of different parameters can have a significant impact on multiple of the model's quantities, namely the calculated stresses, strains, loads, and temperatures. However, given that in the current section the effectiveness of certain process parameters on the feasibility of the proposed process is investigated and that a thorough analysis of all available results from a successfully simulated Reverse Ring Rolling has already been performed in sections §4.3.2 and §4.3.4, further analyzing additional results calculated by hypothetical case studies would just be needless additions to the dissertation.

4.4.1 Tool Linear Velocity

From the preliminary models conducted for the determination of the proper process parameter sets in the case of the Reverse Ring Rolling models (also see section §4.3), the linear velocity of the tools was proved as one of the most crucial parameters. If the applied linear velocities were too high, global shape defects would manifest on the manufactured workpiece. Based on these results, a more thorough investigation on the effectiveness of tool linear velocity on the governing deformation mechanisms and the quality of the final product was performed.

More specifically, in the current analysis, two different velocity values were tested for each of the two Reverse Ring Rolling processes. The main scope of the current analysis was to test lower and higher velocities than those used in the simulations presented in section §4.3, thus it was decided that velocity values half and double of those applied on the aforementioned simulations would be used. In each of the "collaring" and pulling" models with different linear velocities, the same radial deformation would be planned to be performed on the workpiece. The rest of process parameters would remain the same. It is worth noting that for each of the conducted "pulling" simulations, the final state from their corresponding "collaring" model would be used as their initial state.

Different Velocity Reverse Ring Rolling Models Setup

In order to evaluate the effectiveness of the tool linear velocity on each of the "collaring" and "pulling" processes, the corresponding models from section §4.3 were used as a basis. Then, a number of proper adjustments were made on the basis models, which can be summed up to the following:

- Two different groups of simulations were conducted, namely the half velocity models and the double velocity models. The results of the half velocity "collaring" model would be used as the initial state of the half velocity "pulling" model, while the results from the double velocity "collaring" model would be the initial state of the double velocity "pulling" model. The minor shape differences caused by the different "collaring" processes would be included in their respective follow-up "pulling" model, since the two processes are considered as parts of a continuous Reverse Ring Rolling process.
- Based on the simulations of §4.3, the half velocity values would be $v_{collaring,half} = 0.445$ $\frac{mm}{s}$ and $v_{pulling,half} = 0.1$ $\frac{mm}{s}$, while the double velocity values would be $v_{collaring,double}$ = 1.78 $\frac{mm}{s}$ and $v_{pulling,double} = 0.4$ $\frac{mm}{s}$, respectively. These velocities were input in the model via the DEFINE_CURVE menu and applied to the tools via the BOUNDARY_PRESCRIBED_MOTION_RIGID menu.

- In order to achieve the same radial deformation on the workpiece, different total simulation durations were considered for each model. For these duration values, the extended normalization time and any tool movement delays (mainly in the case of the "pulling" models) were also accounted for, thus the overall simulation times for each model were $t_{collaring,half}$ = 21.34 s, $t_{collaring,double}$ = 7.58 s, $t_{pulling,half}$ = 34.8 s and $t_{pulling,double}$ = 11.45 s, respectively. The corresponding simulation times were input into their respective models via the *ENDTIM* option of the CONTROL_TERMINATION menu.
- Similarly to previous simulations, during the normalization time all tool linear velocities were set equal to zero.

Although the conducted simulations are considered as parts of two - stage processes, the evaluation of their respective results in the following sections will be performed per model category, namely separately for the "collaring" and the "pulling" models. In that way, the effects caused to each process stage by the different tool linear velocities will be better evaluated.

Different Linear Velocity "Collaring" Models Results

After the successful conclusion of each of the conducted simulations, their models were reviewed and evaluated. Initially, a general review of the final state from the half velocity "collaring" and the double velocity "collaring" models was made. The corresponding time instances are presented in Figs.4.31 and 4.32, respectively:

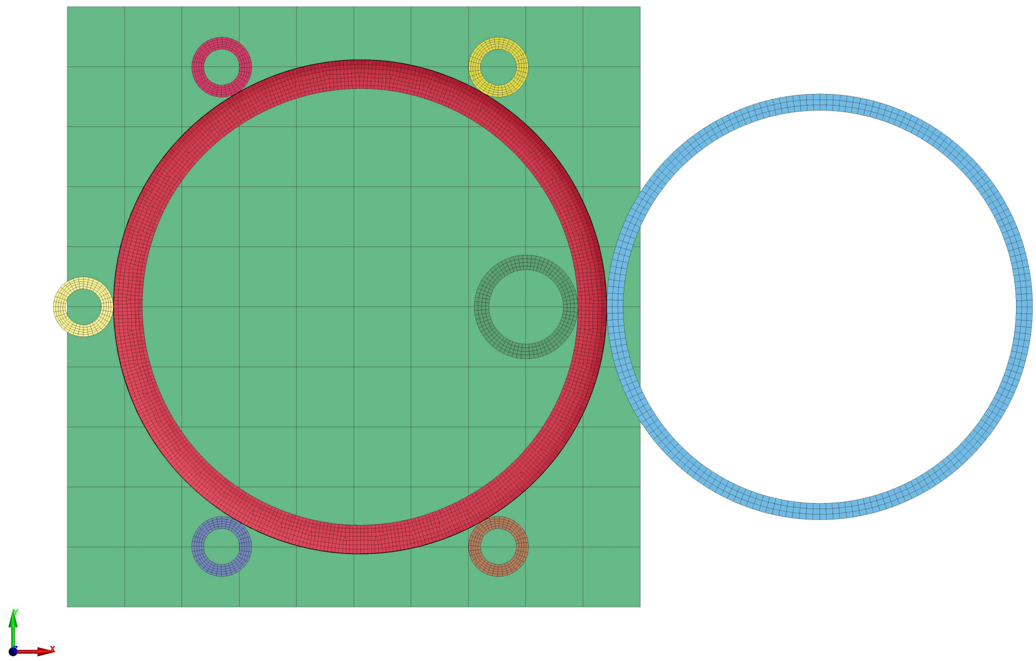

FIG. 4.31: Final time instance of the half velocity "collaring" model

Observations over the final instances from the two models revealed rather expected global shapes. The products from each process were fairly circular, while no overall shape defects could be observed. Based on these results, both of the corresponding processes can be considered successful.

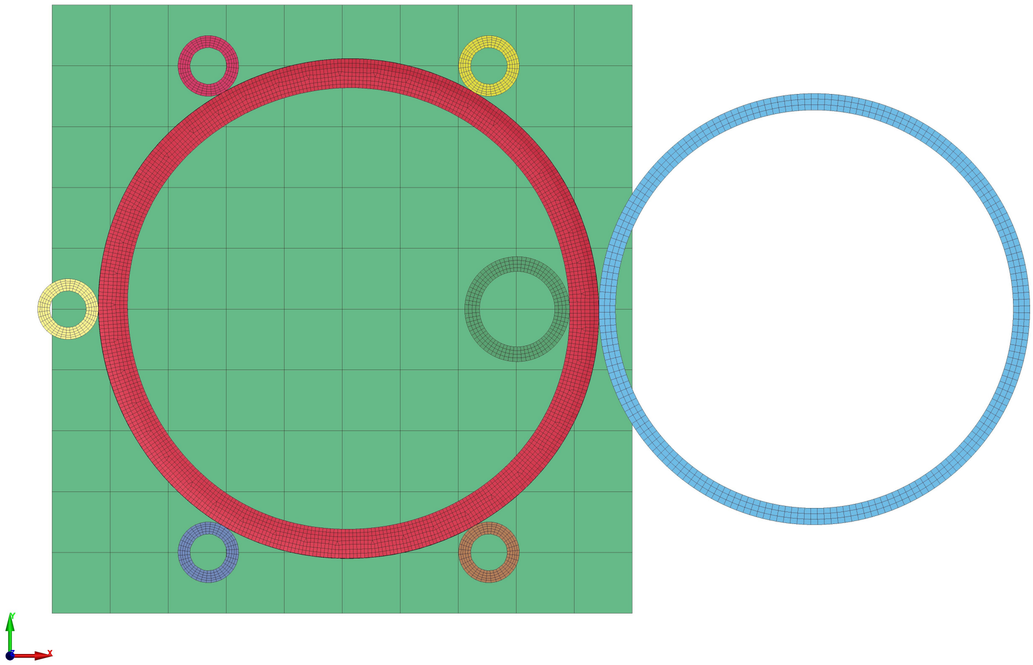

FIG. 4.32: Final time instance of the double velocity "collaring" model

Additionally, a review of the cross-sections from the final products of each model was made. The corresponding cross-sections together with the corresponding cross-section from section §4.3.2 are presented in Fig.4.33:

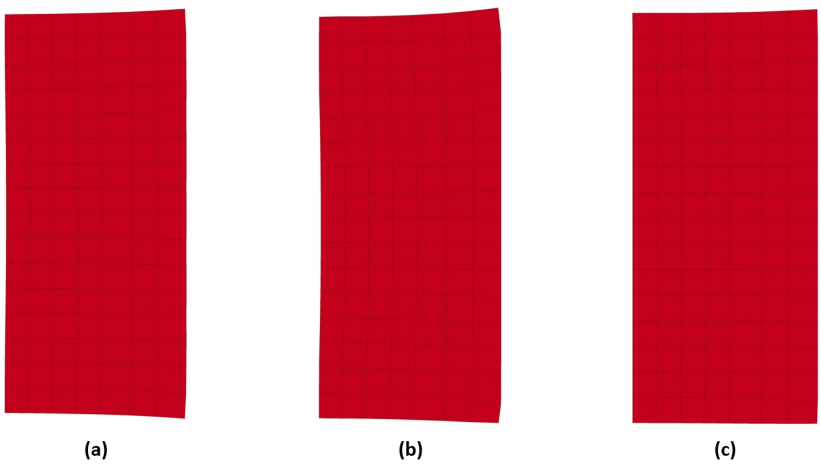

FIG. 4.33: Ring's cross-section at the final time instance of each model: (a) "Collaring" model, (b) Half velocity "collaring" model and (c) Double velocity "collaring" model. All cross-sections were taken from the main rolling bite, thus the outer peripheral surface is located on the right of each cross-section

Observations over the cross-sections in Fig.4.33 revealed quite similar shapes between the three models. The greatest differences could be observed at their corresponding outer surface fishtail defects. More specifically, the size of the aforementioned defects seemed to be inversely proportional to the linear velocity applied, since the corresponding shape from the half velocity "collaring" model had the largest fishtail defects, while the cross-section from the double velocity "collaring" model had the smallest fishtail defects. However, the corresponding fishtail defects from all three cross-sections can be considered as relatively small (e.g. compared to Ring Rolling fishtail defects, as in Fig.2.34).

Afterward, a more in depth analysis of the calculated results was performed. Similarly to previous simulations, at first, the major ring dimensions were evaluated. The outer and inner radii curves from each process and their comparisons to the corresponding curves from the simulations of section §4.3 are presented in Figs.4.34 and 4.35, respectively:

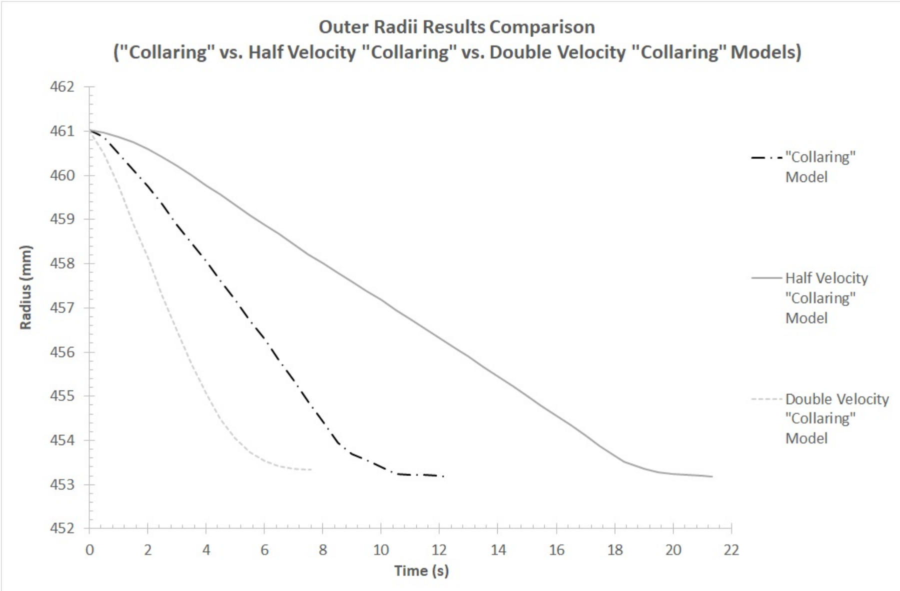

FIG. 4.34: "Collaring" model vs. half velocity "collaring" model vs. double velocity "collaring" model outer radii results comparison

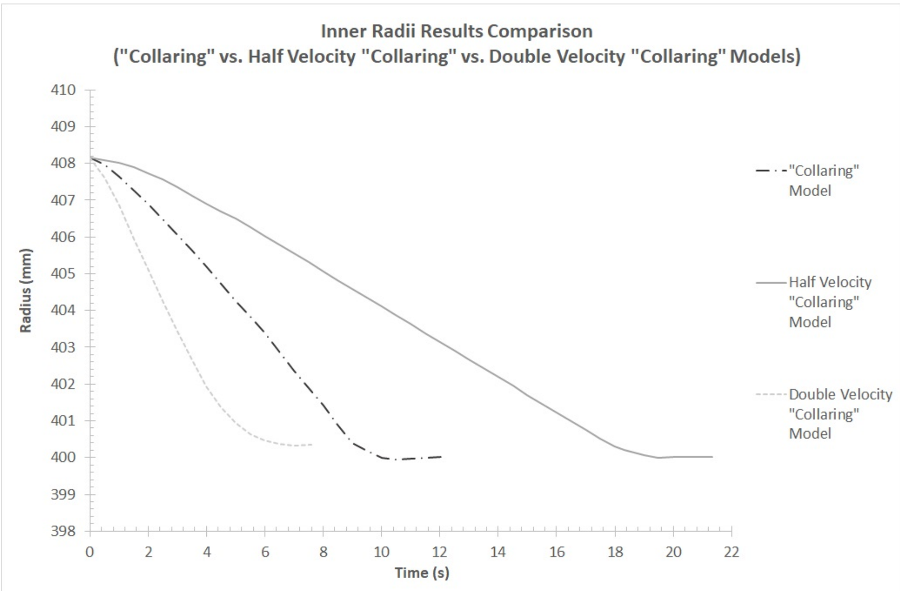

FIG. 4.35: "Collaring" model vs. half velocity "collaring" model vs. double velocity "collaring" model inner radii results comparison

Observations over the outer ring radii curves from the three models (Fig.4.34) revealed some rather interesting behaviors. Apart from the slower evolution of the lower velocity curves, which was rather expected, their overall behaviors were very similar to one another. However, even if the overall radial deformations were planned to be the same, some slight differences were observed among their respective final outer radii values. More specifically, the final recorded values from each model were $R_{f,collaring}$ = 453.18 mm, $R_{f,collaring,half}$ = 453.19 mm and $R_{f,collaring,double}$ = 453.34 mm, while their respective percentage differences compared to the target value of $R_{f,target}$ = 450 mm were $\Delta R_{collaring}$ = 0.707%, $\Delta R_{collaring,half}$ = 0.709% and $\Delta R_{collaring,double}$ = 0.742%. Based on these results, it can be concluded that the higher linear velocity caused some slight defects on the ring (e.g. hinge-like formations between the roll contact points) that led to an increase of the average outer radius of the ring. Furthermore, the outer radii results can also explain the difference in the size of fishtail defects, which was previously observed in Fig.4.33. More specifically, in the models with the lower linear velocities the main forming action from the tools led to an increase of the ring's height around the outer peripheral surface, since the corresponding forming work was applied more gradually. On the other hand, the greater tool velocity in the double velocity "collaring" model led the forming work to be partially directed towards bending the ring, which subsequently created the hinge-like formations. As a result, the aforementioned hinge-like formations were included in the calculation of the outer radius and thus a slightly larger final value was measured.

In the case of the inner radii curves (Fig.4.35), very similar results to those of the outer radii comparisons were observed. The corresponding curves in this case followed almost identical paths to their outer radii counterparts, thus the same conclusions can be drawn. The final recorded inner radii values in this case were $r_{f,collaring}$ = 400.015 mm, $r_{f,collaring,half}$ = 400.015 mm and $r_{f,collaring,double}$ = 400.357 mm, with their respective percentage differences compared to the target value of $r_{f,target}$ = 400 mm being $\Delta r_{collaring}$ = 0.0038%, $\Delta r_{collaring,half}$ = 0.0038% and $\Delta r_{collaring,double}$ = 0.0892%. Based on these final inner radii values, the conclusions previously drawn from the evaluation of the outer radii results seem to be further proven.

The final major dimension that needed to be evaluated was the average ring height. The corresponding results from the three models were compared to one another and the corresponding curves are presented in Fig.4.36:

Observations over the average ring height results in Fig.4.36 revealed some rather interesting behaviors. From the three models, the half velocity "collaring" workpiece appeared to have the largest average height, which was expected considering the cross-section comparisons in Fig.4.33. Most notably, the corresponding final height results from the double velocity "collaring" model were slightly greater than those of the "collaring" model. In other words, the more dynamic behavior of the increased double velocity "collaring" model led to a more uniform height increase, most probably due to a simultaneous thickness reduction. Regarding the aforementioned final ring height values, these were $H_{f,collaring}$ = 117.51 mm, $H_{f,collaring,half}$ = 118.15 mm and $H_{f,collaring,double}$ = 117.74 mm, with their respective percentage differences compared to the target value of $H_{f,target}$ = 115 mm being $\Delta H_{collaring}$ = 2.18%, $\Delta H_{collaring,half}$ = 2.74% and $\Delta H_{collaring,double}$ = 2.38%.

Overall, from the evaluation of the major ring dimensions, the half velocity "collaring" and "collaring" models seemed to have a more stable behavior with fewer defects and the closest results to the corresponding target values. Most interestingly and although the double velocity "collaring" model seemed to be very close to a global shape defect initiation point, its

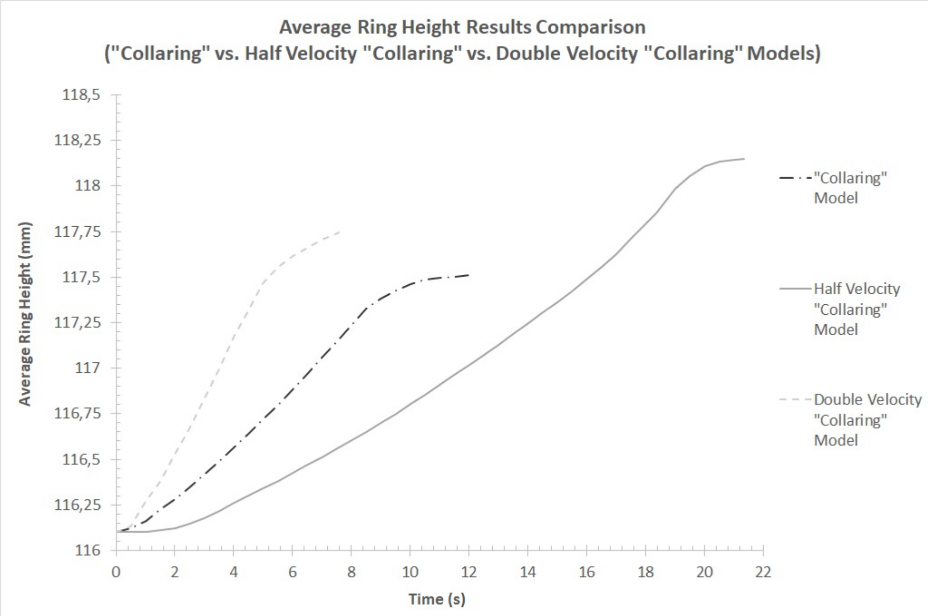

FIG. 4.36: "Collaring" model vs. half velocity "collaring" model vs. double velocity "collaring" model average ring height results comparison

cross-sectional deformation was the most uniform with the smallest fishtail defects. However, based on the best dimensional precision of the final Reverse Ring Rolling product, the lower velocity models seem to have produced the optimum workpiece.

From the evaluation of the average ring height results, a correlation between them and the corresponding thickness results was heavily implied. For this reason, the thickness curves from the three models were compared to one another, and they are presented in Fig.4.37:

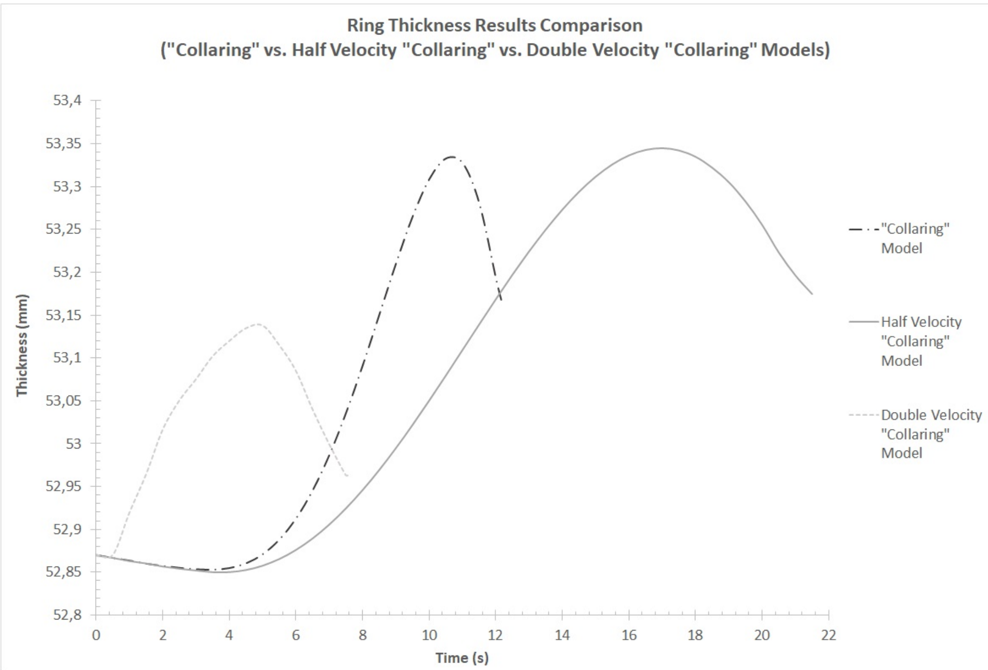

FIG. 4.37: "Collaring" model vs. half velocity "collaring" model vs. double velocity "collaring" model thickness results comparison

Observations over the thickness curves in Fig.4.37 seem to further prove what was previously speculated during the evaluation of the average ring height results. Initially, all three curves appeared to have a similar overall pattern, with a slight initial thickness reduction followed by a thickness increased and then another thickness reduction during the radii normalization phase. Most notably, the double velocity "collaring" model appeared to have the lowest thickness values, thus proving that this more dynamic process indeed led to increased thickness reduction. Regarding the maximum thickness values observed during each model, these were equal to $f_{max,collaring}$ = 53.33 mm, $f_{max,collaring,half}$ = 53.34 mm and $f_{max,collaring,double}$ = 53.14 mm, while the corresponding final thickness values were $f_{f,collaring}$ = 53.16 mm, $f_{f,collaring,half}$ = 53.17 mm and $f_{f,collaring,double}$ = 52.96 mm. Overall, the behavior of all thickness curves can be considered as rather expected based on the mechanics of the process.

Finally, the calculated outer and inner diameter ovalities from the three models were evaluated. The corresponding curves are presented in Fig.4.38:

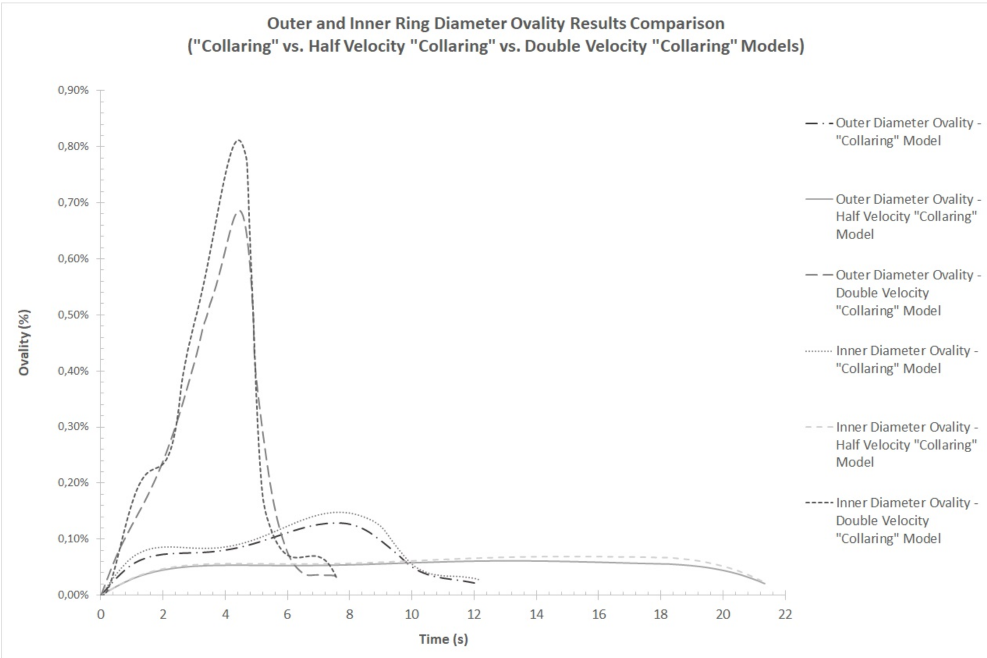

FIG. 4.38: "Collaring" model vs. half velocity "collaring" model vs. double velocity "collaring" model outer and inner ovality results comparison

Observations over the ovality results in Fig.4.38 revealed some interesting points. Initially, the outer and inner diameter ovality curves from the same model followed very similar paths during their respective process's duration. Moreover and as it was speculated, the double velocity "collaring" model appeared to have the worst results in terms of product circularity, thus further proving the potential for global shape defects. However, in all the ovality curves, a relatively significant reduction in their values was observed during their respective radii normalization phase, thus proving the importance of this practice during Reverse Ring Rolling. In case this practice was to be omitted, the best ovality results (having the lowest values) would be those of the half velocity "collaring" model. Regarding the final ovality values, these were equal to 0.020% and 0.028% in the case of the outer and inner ovalities from the "collaring" model, 0.021% and 0.023% in the case of the outer and inner ovalities from the half velocity "collaring" model, and 0.033% and 0.031% in the case of the outer and inner ovalities from the double velocity "collaring" model, respectively. It is worth noting that the constantly increasing ovalities of the double velocity "collaring" model during the initial phase of this process, were the definitive proof for the occurrence of defect formation that was speculated above.

Generally, all three of the facilitated tool velocity values seemed to be viable, although lower velocity models had arguably the best results, in terms of process stability and product dimensional precision. Furthermore, the conducted tool velocity analysis allowed for the evaluation of the effects from more dynamic process conditions. Based on the corresponding results, if a higher velocity was considered for the tools of a "collaring" process, it should lead to a more uniform thickness reduction with less fishtail defects. On the other hand, if the applied velocity was beyond a certain threshold (usually dependent on the initial dimensions of the ring and its material), the potential for global shape defect initiation would highly increase. Overall, the linear velocity of the tools was proven to be one of the most crucial "collaring" process parameters.

Different Linear Velocity "Pulling" Models Results

After the successful solution of the aforementioned "collaring" models, their final instances were used as the initial states for the corresponding "pulling" models. Each of the half velocity "pulling" and the double velocity "pulling" models was subsequently solved and inspected for errors. Then, the extracted results from each model were evaluated and compared to one another.

Similarly to previous analyses, a general review of the final states from each "pulling" model was initially performed. The corresponding time instances from the half velocity and the double velocity "pulling" models are presented in Figs.4.39 and 4.40, respectively:

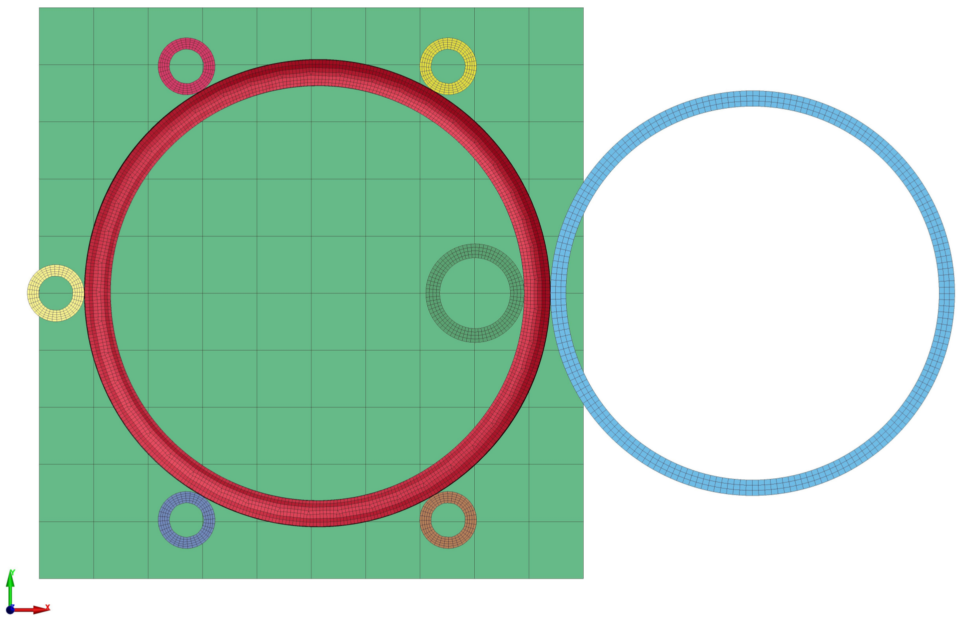

FIG. 4.39: Final time instance of the half velocity "pulling" model

Observations over the final time instances in Figs.4.39 and 4.40 revealed some rather interesting results. Although the half velocity "pulling" model was completed successfully, since

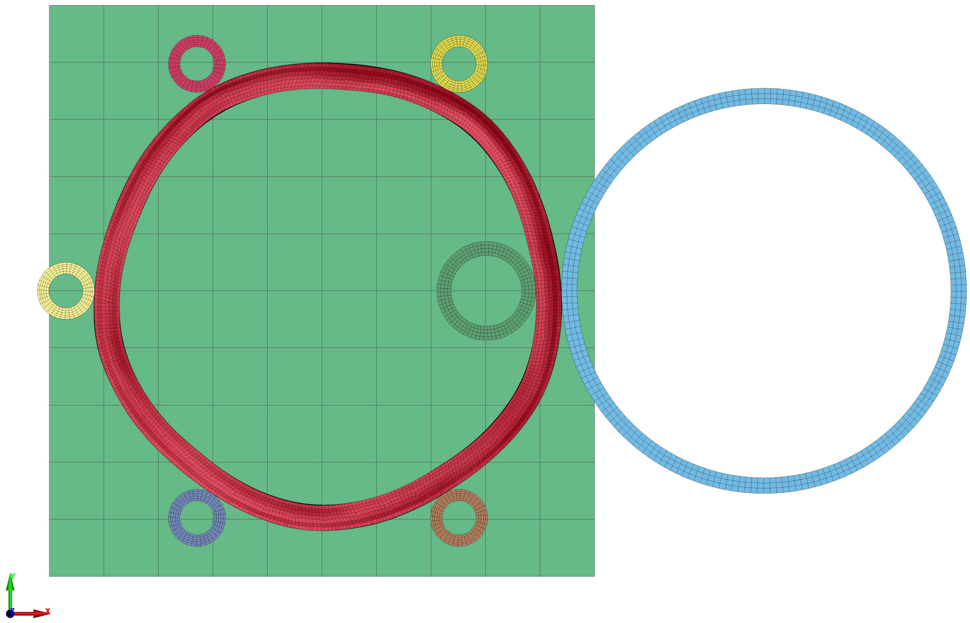

FIG. 4.40: Final time instance of the double velocity "pulling" model

its final product had a fairly circular shape, the double velocity "pulling" model appeared to have some small global shape defects. Because of this, a step-by-step observation of the double velocity process had to be performed. For this analysis, multiple different time instances were extracted from the double velocity "pulling" model, and they are presented in Fig.4.41:

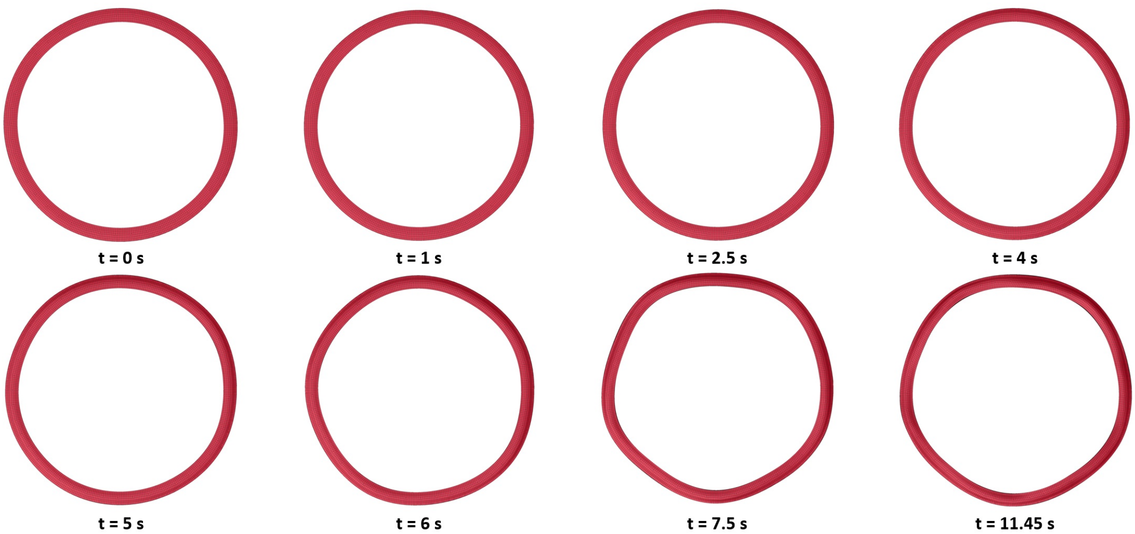

FIG. 4.41: Ring deformation during multiple time instances during the double velocity "pulling" process simulation

Observations over the time instances from the double velocity "pulling" model (Fig.4.41) revealed that the aforementioned global shape defects began manifesting after t = 6 s, approximately. Although these defects were not extensive, for reasons of clarity the current process cannot be considered successful since the final product was obviously not circular.

Thus, in the evaluations of the dimensional results that follow, the corresponding curves only up to t = 6 s will be considered for the double velocity "pulling" model. The only exception to this will be the evaluation of the final cross-section that is presented right below, in which the analysis of any cross-section prior to the last time instance is meaningless. It should be noted that based on the different states presented in Fig.4.41, a comparison between the time instances at t = 7.5 s (right before the normalization phase) and at t = 11.45 s revealed a more circular global shape at the end of the normalization phase, as the corresponding defects appear to have been ironed to a certain degree.

Following the overview of the final states of the aforementioned "pulling" simulations, a review of their respective cross-sections at the end of each simulation was conducted. The corresponding instances are presented in Fig.4.42:

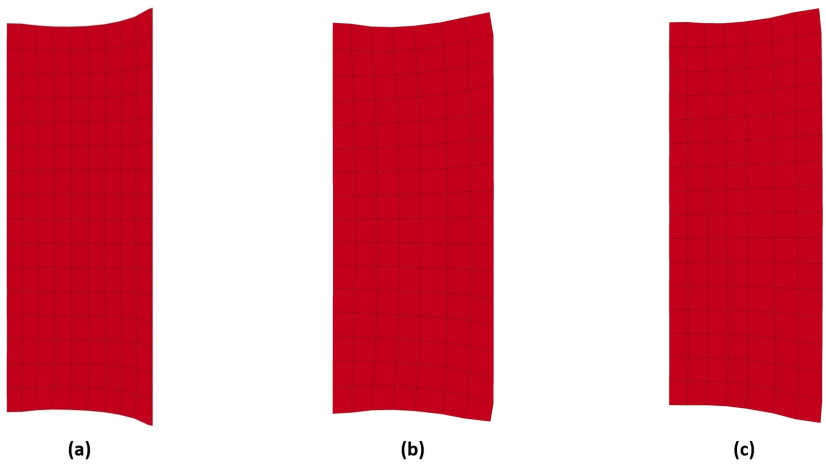

FIG. 4.42: Ring's cross-section at the final time instance of each model: (a) "Pulling" model, (b) Half velocity "pulling" model and (c) Double velocity "pulling" model. All cross-sections were taken from the main rolling bite, thus the outer peripheral surface is located on the right of each cross-section

Observations over the cross-sections in Fig.4.42 revealed some differences. In this case, the largest outer surface fishtail defects were observed in the cross-section of the "pulling" model, followed by those of the double velocity "pulling" model. The corresponding outer surface fishtail defects from the half velocity "pulling" model were slightly smaller than the latter. On the other hand, the inner surface fishtail defects of the "pulling" and the half velocity "pulling" cross-sections were comparable in size, while the corresponding defects of the double velocity model's cross-section were noticeably smaller. Since from the mechanics of the "pulling" process the reduction of the ring's thickness was scheduled, the formation of fishtail defects was inevitable. However, no safe correlations can be made between the tools' linear velocity and the fishtail defect formation, since the results in Fig.4.42 did not have a clear pattern.

Afterward, the major dimension results from the conducted simulations were analyzed. For the comparison of the outer and inner radii results, the corresponding curves were extracted from each model, and they are presented in Figs.4.43 and 4.44, respectively:

Observations over the outer ring radii results in Fig.4.43 revealed some rather expected behaviors. More specifically, the outer radii from all models seemed to decrease steadily, as it was expected. Regarding the final outer radii values from the "pulling" and the half velocity

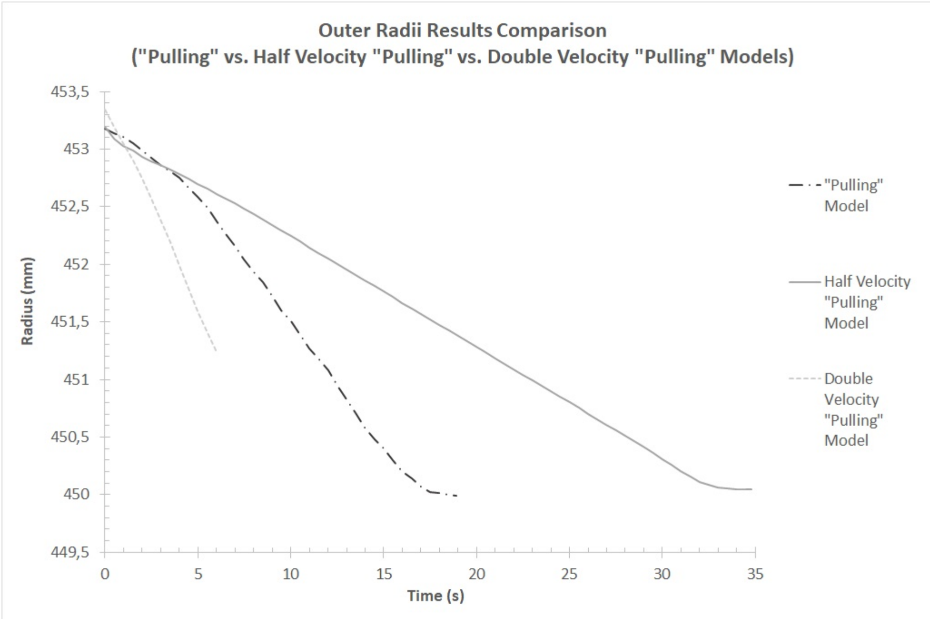

FIG. 4.43: "Pulling" model vs. half velocity "pulling" model vs. double velocity "pulling" model outer radii results comparison

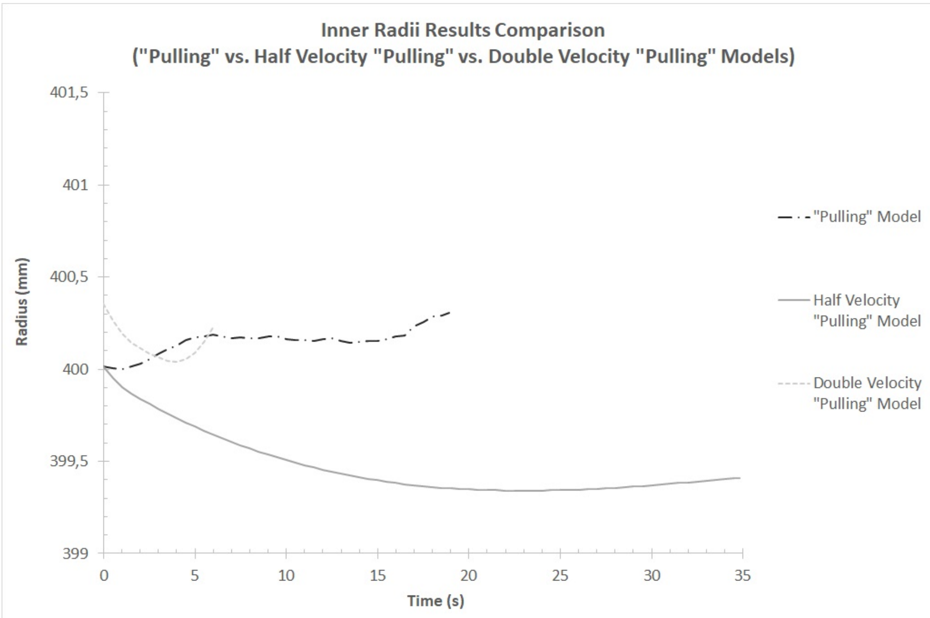

FIG. 4.44: "Pulling" model vs. half velocity "pulling" model vs. double velocity "pulling" model inner radii results comparison

"pulling" models, these were equal to $R_{f,pulling}$ = 449.99 mm and $R_{f,pulling,half}$ = 450.05 mm, respectively, with the corresponding percentage differences compared to the target value of $R_{f,target}$ = 450 mm being $\Delta R_{pulling}$ = -0.002%, $\Delta R_{pulling,half}$ = 0.011%. An evaluation of the final outer radius from the double velocity "pulling" model was not performed, since the corresponding model did not finish successfully.

In the case of the inner radii results, some very interesting observations were made. Initially, all three curves in Fig.4.44 seemed to have completely different patterns. In the case of the "pulling" model, the corresponding curve increased in three distinct phases. In the case of the double velocity "pulling" model, a slight reduction was initially observed in the corresponding inner radius curve, which was followed by a subsequent increase after t = 4 s, approximately. Since global shape defects were observed in this case, this increasing rate should continue until the end of the double velocity process, as additional thinning of the ring would be observed in order to compensate for the greater radial extension of the manifested shape defects. Finally, in the case of the half velocity "pulling" model, a reduction of its inner radius was observed. This behavior can be attributed to the forming action of the support rolls, whose linear movement acted similarly to a "collaring" process and thus reduced both ring radii. The final inner radii values from the two completed simulations were $r_{f,pulling}$ = 400.31 mm and $r_{f,pulling,half}$ = 399.41 mm, with the corresponding percentage differences (regarding the target inner radius) being equal to $\Delta r_{pulling}$ = 0.08% and $\Delta r_{pulling,half}$ = -0.15%, respectively. From the aforementioned inner radii comparisons, a clear correlation between this dimension and the tools' linear velocity was implied. More specifically, the overall inner radius reduction caused by the action of the support rolls appeared to be countered, to some extent, by a dynamic component introduced in the main rolling bite. In other words, as the linear velocity increased, the dynamic component that was introduced by the main roll caused some additional thinning of the ring, which in turn led to the increase of the inner radius. In case this dynamic component was very small or omitted (e.g. in the half velocity "pulling" model), the additional thinning would not be performed and thus the "collaring" action from the support rolls would prevail. Overall, the inner radius of the ring appears to be heavily affected by the linear velocity of the tools.

Subsequently, the average ring height results were evaluated. The corresponding curves from the three models are presented in Fig.4.45:

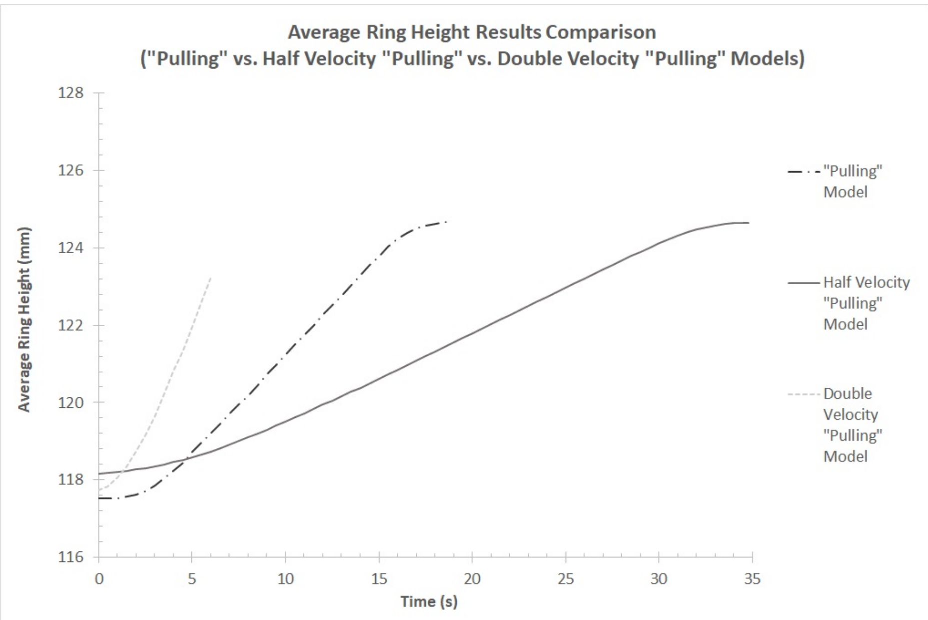

FIG. 4.45: "Pulling" model vs. half velocity "pulling" model vs. double velocity "pulling" model average ring height results comparison

Observations over the average ring height results in Fig.4.45 revealed some rather expected behaviors. All three curves appeared to increase steadily, with no particular points of interest. The final recorded average ring height values from the "pulling" and the half velocity "pulling" models were $H_{f,pulling}$ = 124.67 mm and $H_{f,pulling,half}$ = 124.65 mm, with their percentage differences compared to the target value of $H_{f,target}$ = 115 mm being $\Delta H_{pulling}$ =

8.41% and $\Delta H_{pulling,half}$ = 8.39%, respectively. In this case, too, the average ring height results from the double velocity "pulling" model were not evaluated.

In the case of the ring thickness results from the conducted "pulling" simulations, the corresponding curves are presented in Fig.4.46:

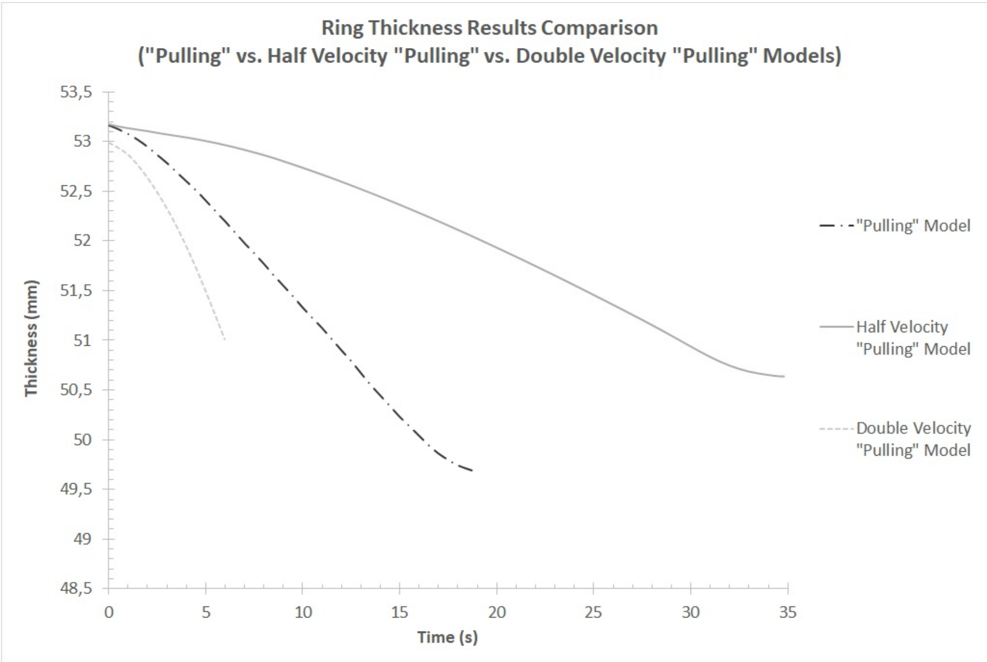

FIG. 4.46: "Pulling" model vs. half velocity "pulling" model vs. double velocity "pulling" model thickness results comparison

Observations over the thickness curves in Fig.4.46 revealed some rather expected behaviors. All three curves decreased steadily during their respective process, while no abnormalities were observed. The only point of interest was the relatively greater final thickness observed in the half velocity "pulling" curve, which further proved the speculations previously made during the evaluation of the inner radii results. The final recorded thickness values of the "pulling" and half velocity "pulling" curves were $f_{f,pulling}$ = 49.68 mm, $f_{f,pulling,half}$ = 50.64 mm, respectively. Once again, the corresponding thickness results from the double velocity "pulling" model were not evaluated.

Finally, the outer and inner diameter ovalities from the three models were analyzed. The corresponding curves are presented in Fig.4.47:

Observations over the ovality results in Fig.4.47 revealed some interesting points. Regarding the ovality curves from the "pulling" model, these were extensively discussed in section §4.3.4. In the case of the ovality curves from the half velocity "pulling" model, relatively constant ovality values were observed for the majority of their process's duration, with these values decreasing only during the corresponding radii normalization phase. On the other hand, the ovality curves from the double velocity "pulling" model revealed a constantly increasing pattern, which would most probably continue to increase even beyond t = 6 s, since the global shape defects began manifesting at that time instance. Regarding, the final recorded ovality values from the two successfully conducted simulations, these were equal to 0.15% and 0.04% in the case of the outer and inner ovalities from the "pulling"

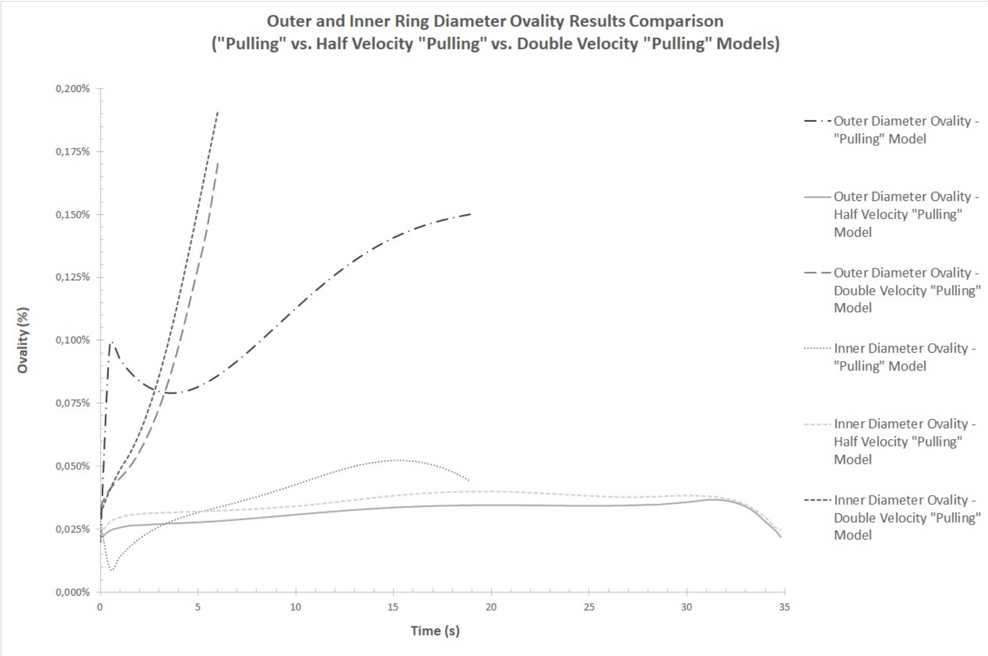

FIG. 4.47: "Pulling" model vs. half velocity "pulling" model vs. double velocity "pulling" model outer and inner ovality results comparison

model, 0.022% and 0.024% in the case of the outer and inner ovalities from the half velocity "pulling" model.

From the current analysis, the feasibility of the "pulling" process was proven to be heavily affected by the facilitated tool velocity. A relatively high tool linear velocity was shown to lead to global shape defects, which would render the final product unacceptable. Additionally, relatively high tool velocities that would not result in shape defects were shown to have a significant impact on the dimensional precision of the workpiece, mainly through the introduction of a dynamic forming component in the process. Arguably, the best performance was observed with the minimum linear velocity, which offered great stability in the process and very good precision in terms of the final dimensions of the product. From all of the above, it can be concluded that the choice of a proper tool linear velocity in a Reverse Ring Rolling process is of utmost importance.

4.4.2 Number of Support Rolls

One of the most important requirements for conducting a Reverse Ring Rolling process is a suitable mill with multiple support rolls. However, using such a Ring Rolling mill can be both more complicated and more costly, since more tools need to be controlled and coordinated together, while the additional rolls increase the power requirements and the maintenance cost of the setup. However, during the literature research in the proposed process's mechanics, an alternative to "six-point collaring" was identified, namely the "four-point collaring" process. In this practice, only four contacting point are used for the reduction of a workpiece's diameter. Since the use of only three support rolls would decrease the complexity and the cost of the process, the possibility of adopting "four-point collaring" into Reverse Ring Rolling was further investigated in the current section.

"Four-Point" Reverse Ring Rolling Models Setup

In pottery, the fundamentals of a "four-point collaring" involves the use of four contact points, which are positioned across one another, in groups of two. This specific positioning strictly defines the position of support rolls during a "four-point" Reverse Ring Rolling. More specifically, since the main rolling bite is positioned in a specific place of a Ring Rolling mill and a support roll should be positioned directly opposite of the main rolling bite, the other set of support rolls can only be positioned in $\pm\frac{\pi}{2}$ angles regarding the main rolling bite, in order to achieve a more balanced process.

Regarding the setup of the two "four-point" Reverse Ring Rolling models (defined as "4P-collaring" and "4P-pulling" models hereafter), the corresponding models from section §4.3 were used as their respective basis. All the necessary alterations that were made on the basis models, in order to set up the "4P" models, can be summarized in the following:

- The number of support rolls was reduced from five to three and they were positioned with an angular difference of $\frac{\pi}{2}$ from their previous tool, along the perimeter of the ring.
- The linear velocity directions were properly adjusted, so that each support roll would move towards the center of the workpiece. Furthermore, the corresponding velocity values were maintained the same as those presented in section §4.3.
- The number of contacts in the model was also reduced, since fewer tools would be considered in the current analysis.
- Similarly to previous analyses, the initial state of the "4P-pulling" model would be taken from the final instance of the "4P-collaring" model.

The rest of the boundary conditions and the process parameters remained the same to those presented in section §4.3. The initial state of the "4P-collaring" model is presented in Fig.4.48:

"Four-Point" Reverse Ring Rolling Models Results - Preliminary Runs

After the "4P-collaring" model was solved, its final state was extracted, and it is presented in Fig.4.49:

Although the solution of the "4P-collaring" model was concluded without warnings or error messages, a review over the final state of the results in Fig.4.49 revealed an unacceptable final product, in terms of its non-circularity. Based on these results, a step-by-step review of the entire process was subsequently performed. The most characteristic time instances from this simulation are presented in Fig.4.50:

Observations over the time instances from the "4P-collaring" model (Fig.4.50) revealed that the corresponding process was performed as intended only during its first few seconds. More specifically, the ring maintained a fairly circular shape until t = 4 s into the process. However, some relatively large shape defects appeared on the workpiece at that time, and they continued to deteriorate until the end of the process. These shape defects seem to indicate that the use of less support rolls with the process parameters of the "collaring" model in effect, would lead to the introduction of significant imbalances in the process. Also, since

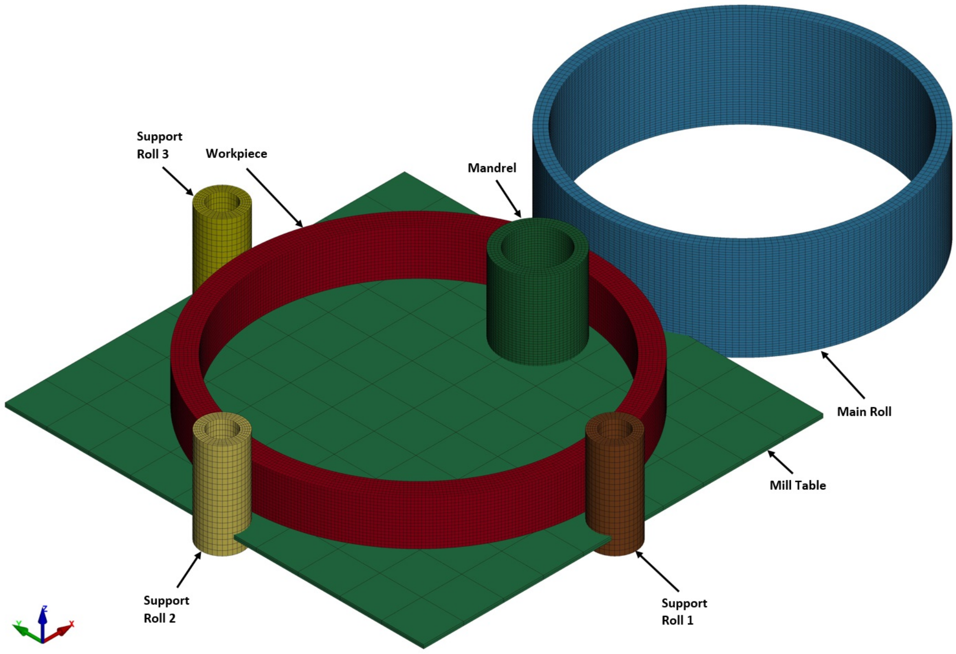

FIG. 4.48: Initial Reverse Ring Rolling numerical model setup ("4P-collaring" model)

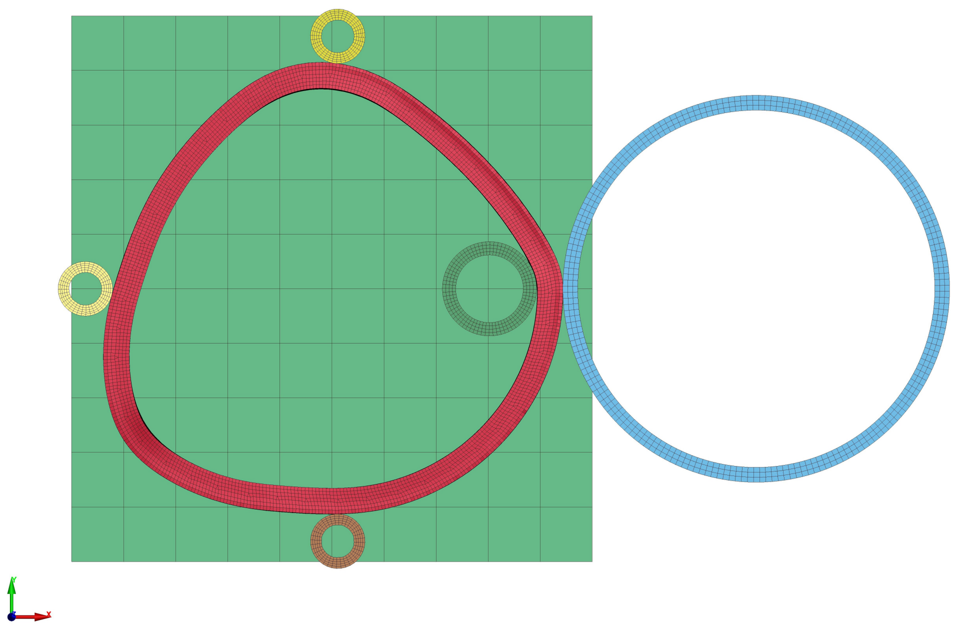

FIG. 4.49: Final time instance of the "4P-collaring" model

the final product of the current process was deemed unacceptable, any further analysis would not be meaningful.

Although the "4P-collaring" process could not produce the anticipated final product and thus could be considered as not viable, the feasibility of the "4P-pulling" process still needed to be evaluated. However, since the final "4P-collaring" product was non-circular, a different initial state for the "4P-pulling" model had to be considered. For this reason, the initial

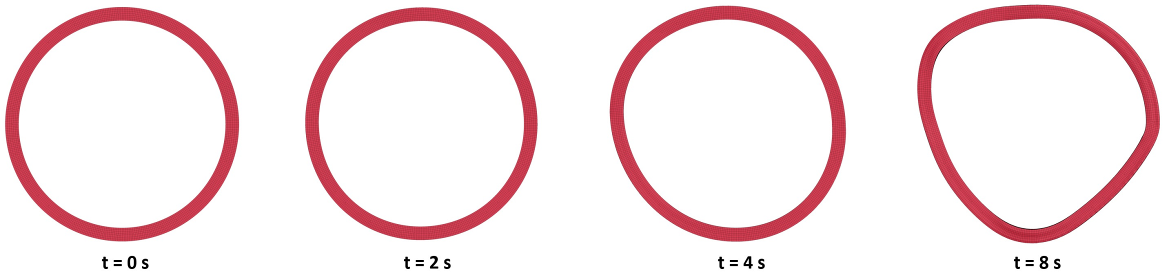

FIG. 4.50: Ring deformation during multiple time instances during the "4P-collaring" simulation

state of the "pulling" model, as this was presented in section §4.3.3, was considered for this analysis. After the necessary alterations were performed, the "4P-pulling" model was solved and its final time instance is presented in Fig.4.51:

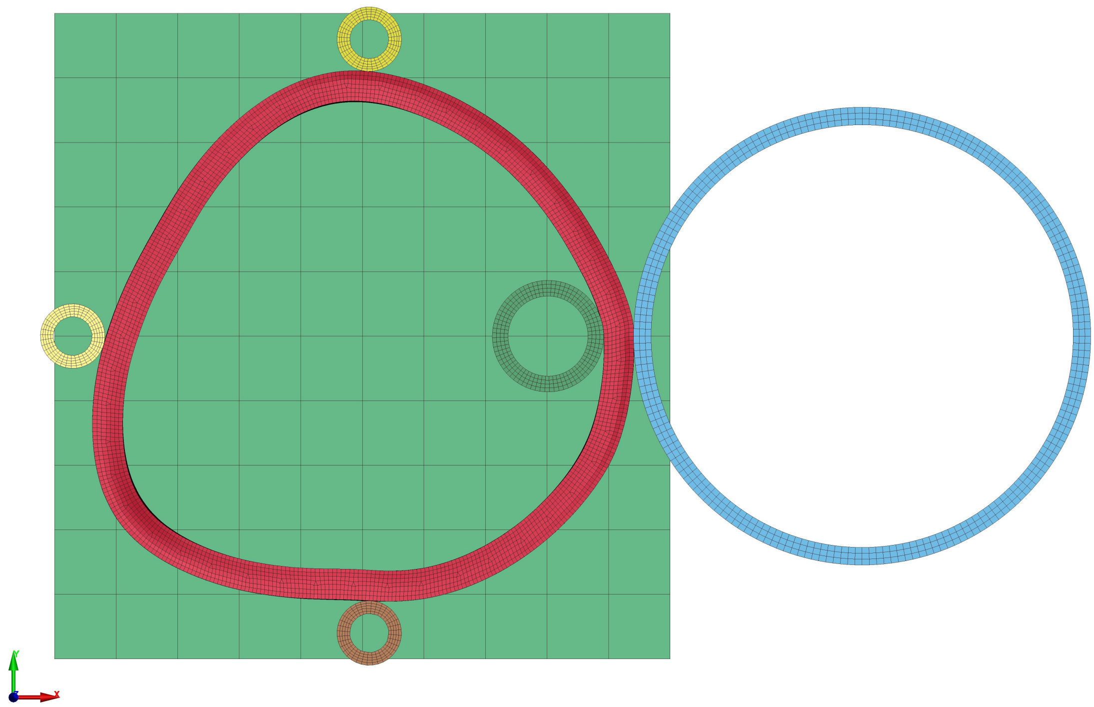

FIG. 4.51: Final time instance of the "4P-pulling" model

A review over the final time instance from the "4P-pulling" revealed that, in this case too, a non-circular final product was manufactured. What is more, from the comparison between Figs.4.50 and 4.51, two very similar final product shapes were observed, thus indicating a correlation between the number of support rolls and the shape defect formation. This conclusion can be safely drawn, since both the tool linear velocity and the time that the shape defects appeared on each model were different. Similarly to the "4P-collaring" model, a step-by-step observation of the ring's deformation during the "4P-pulling" was performed, and it is presented in Fig.4.52:

Observations over the time instances in Fig.4.52 revealed almost identical ring deformations

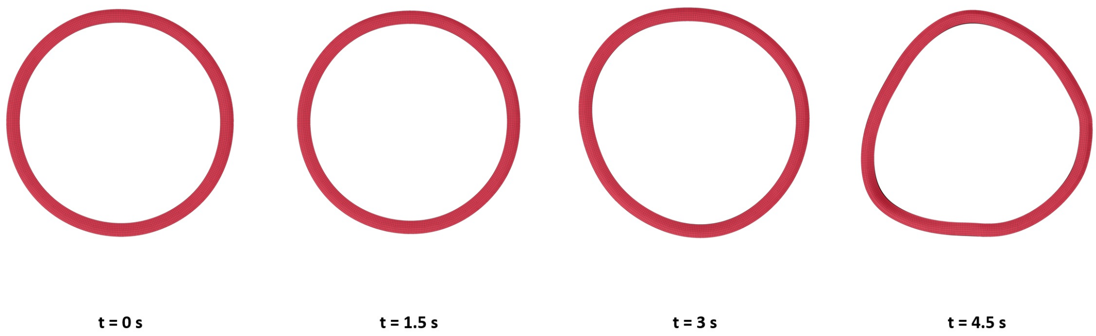

FIG. 4.52: Ring deformation during multiple time instances during the "4P-pulling" process simulation

to those previously observed in Fig.4.50, although at different time instances into their respective processes. In this case also, the process proceeded as initially intended during its first seconds, while the observed shape defects appeared after t = 3 s and deteriorated over the rest of the process.

From both of the conducted "4P-collaring" and "4P-pulling" models, it was proven that a "four-point" Reverse Ring Rolling process cannot be used to manufacture acceptable products with the same process parameters that were previously considered in section §4.3. The main reason for the manufacturing of non-circular products was the imbalance introduced by a combination of the fewer support rolls and the relatively high tool linear velocity. The effectiveness of the tool linear velocity on the current analysis was speculated based on the corresponding results from section §4.4.1, which showed a correlation between the aforementioned process parameter and the formation of global shape defects on the workpiece.

"Four-Point" Reverse Ring Rolling Models Results - Half Velocity Models

From the aforementioned simulations, the feasibility of "four-point" Reverse Ring Rolling was questioned. More specifically, the analyzed results indicated that the current process can only be performed for relatively small radial deformations. However, based on the analysis performed in section §4.4.1, a correlation between tool velocity and global shape defect formation was shown. For this reason and since the results from the corresponding half velocity Reverse Ring Rolling models were available, an updated version of the "4P-collaring" and "4P-pulling" simulations would be attempted. In these updated versions, the corresponding models' setup would remain the mostly same, with the main difference being that the linear velocity values of the tools would be reduced to half (0.445 $\frac{mm}{s}$ for the "updated collaring" model and 0.1 $\frac{mm}{s}$ for the "updated pulling" model, respectively). Because of this change, the total simulation time also needed to be doubled (21.337 s for the "updated collaring" model and 34.8 s for the "updated pulling" model, respectively).

After the aforementioned changes were performed, the updated models were solved. In the case of the "4P-updated collaring" model, its final time instance is presented in Fig.4.53:

Observations over the final time instance of the "4P-updated collaring" model (Fig.4.53) revealed a fairly circular final product. This fact implied that a "4P-collaring" process with a relatively small linear velocity on the tools could be feasible. Since no significant defects were observed, a more thorough analysis on the rest of the results from the "4P-updated collaring" model was subsequently performed.

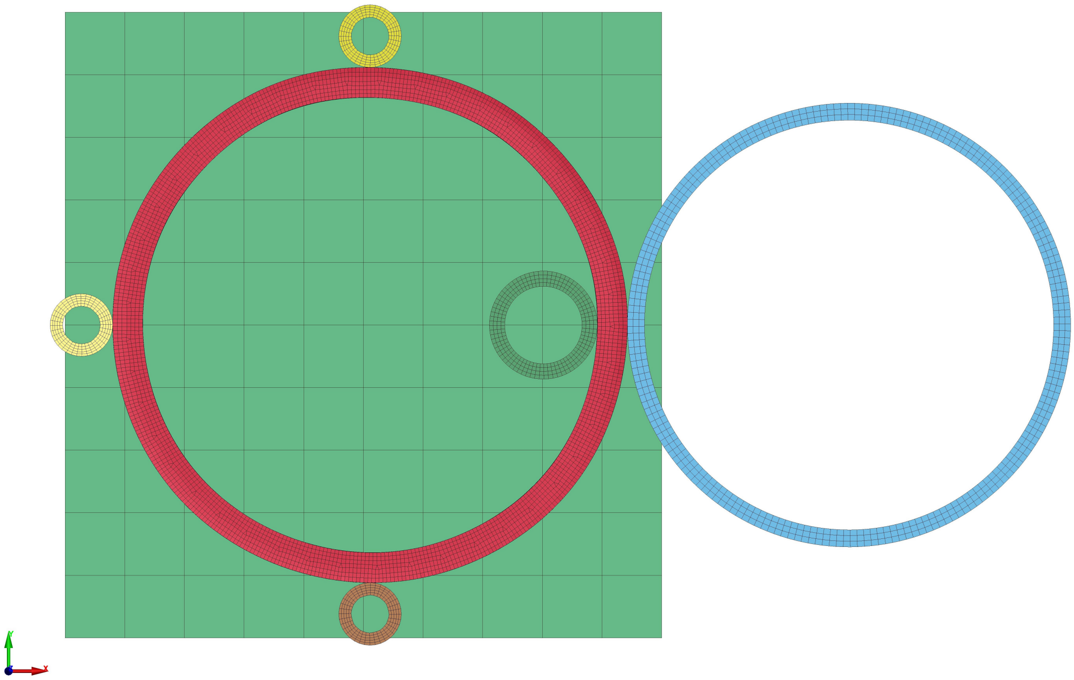

FIG. 4.53: Final time instance of the "4P-updated collaring" model

Similarly to previous simulations, a comparison of the cross-sections of the ring from the two processes was also performed, and it is presented in Fig.4.54. It is worth reminding that for all the following result comparisons, the half velocity "collaring" model was used as a reference point.

Observations over the cross-sections in Fig.4.54 revealed significant differences between the two workpieces. More specifically, the fishtail defects observed at the top surface of the "4P-updated collaring" ring were very small compared to the corresponding defects from the half velocity "collaring" model, while no bottom defects could be observed in the former. Based on these observations, it can be concluded that the formation of fishtail defects during a "collaring" process functions additively from the contact of each roll with the workpiece. Overall, the minimum fishtail defects of the "4R - updated collaring" model indicated a much more uniform ring deformation during the corresponding process.

Afterward, the outer and inner radii results from the two models were compared. The corresponding curves are presented in Figs.4.55 and 4.56, respectively:
Observations over the outer and inner ring radii results in Figs.4.55 and 4.56 revealed very similar deformation patterns between the two processes, but with notable differences between their corresponding values. More specifically, the outer and inner radii curves appeared to have a slight delay very early in the process, which resulted in less radial deformation and thus higher radii values at the end of the process. The aforementioned delay in these curves can be attributed to some early global shape defects (most probably hinge-like formations) during the first contact of the rolls with the workpiece, which were considered in the calculation of the radii curves and thus increased the early recorded values. Regarding the final outer radii values from the two models, these were $R_{f,collaring,half}$ = 453.19 mm and $R_{f,collaring,4P-updated}$ = 453.70 mm, respectively, with the corresponding percentage differences compared to the target value of $R_{f,target}$ = 450 mm being $\Delta R_{collaring,half}$ = 0.71%,

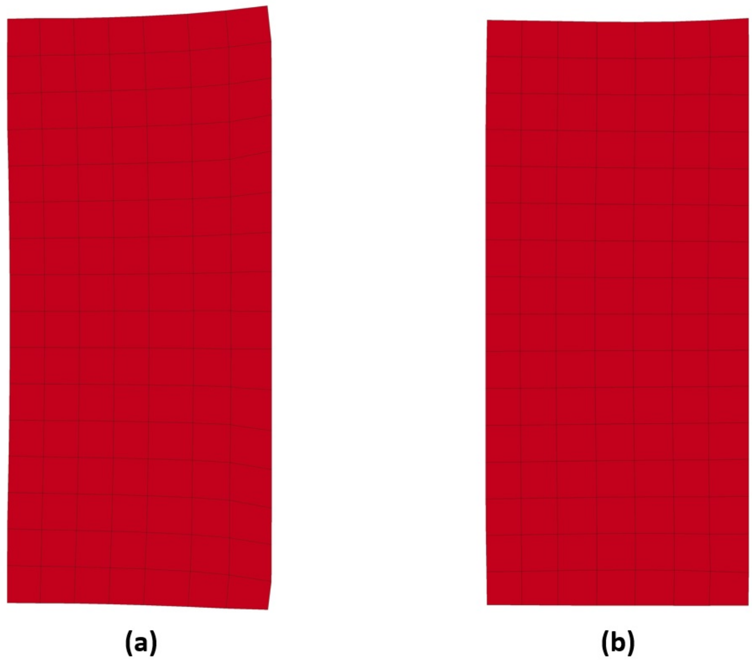

FIG. 4.54: Ring's cross-section at the final time instance of each model: (a) Half velocity "collaring" model and (b) "4P-updated collaring" model. All cross-sections were taken from the main rolling bite, thus the outer peripheral surface is located on the right of each cross-section

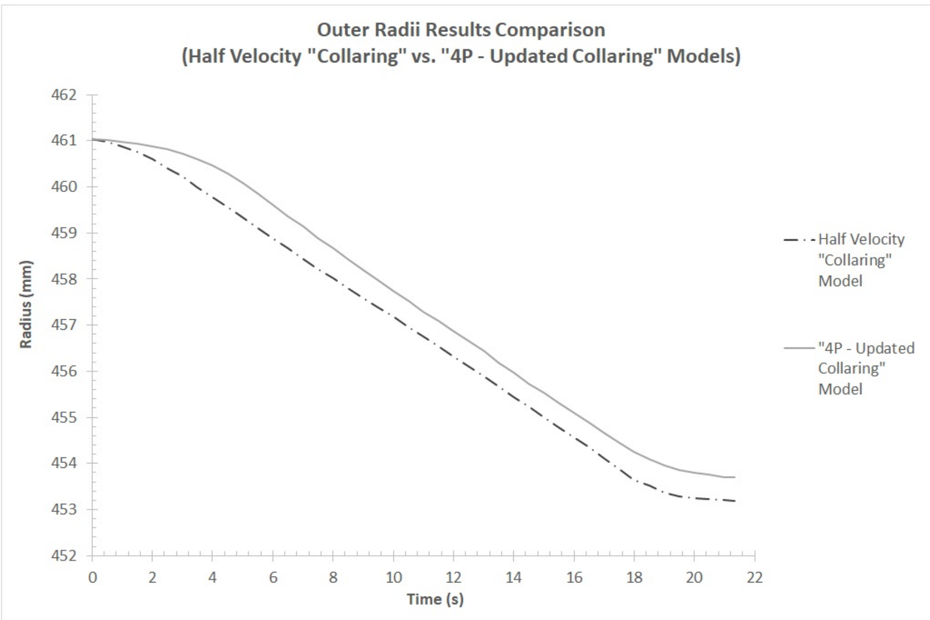

FIG. 4.55: Half velocity "collaring" model vs. "4P-updated collaring" model outer radii results comparison

$\Delta R_{collaring,4P-updated}$ = 0.82%. On the other hand, the final inner radii values from the two models were $r_{f,collaring,half}$ = 400.01 mm and $r_{f,collaring,4P-updated}$ = 400.64 mm, with their respective percentage differences compared to the target value of $r_{f,target}$ = 400 mm being $\Delta r_{collaring,half}$ = 0.0038% and $\Delta r_{collaring,4P-updated}$ = 0.16%. Based on these results, it was made

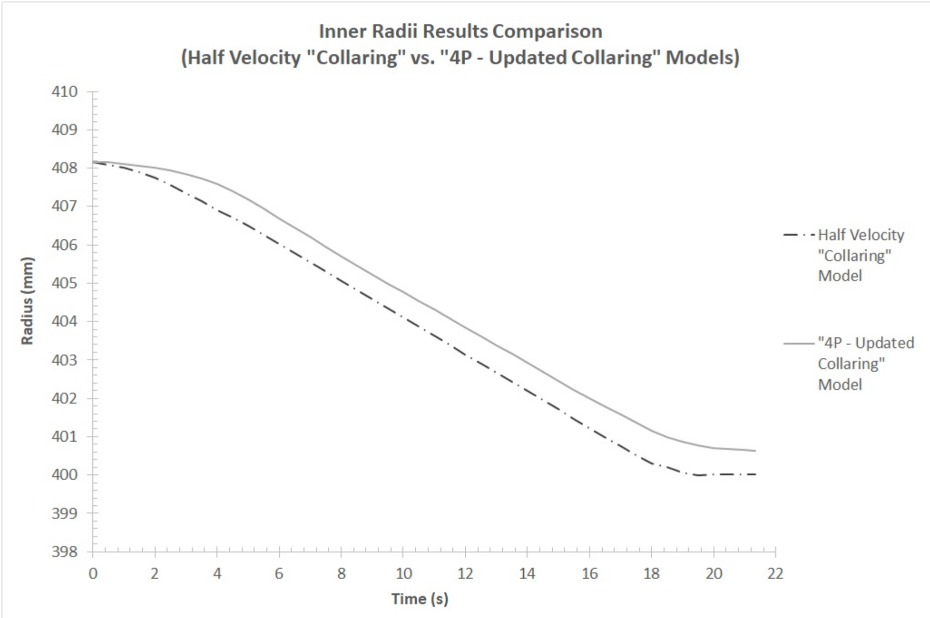

FIG. 4.56: Half velocity "collaring" model vs. "4P-updated collaring" model inner radii results comparison

clear that the initially formed global shape defects affected the overall dimensional precision of the "4P-updated collaring" process. However, a slight extension of the process's duration should make up for the observed dimensional imprecisions.

In the case of the average ring height results, the corresponding curves from the half velocity "collaring" and the "4P-updated collaring" models are presented in Fig.4.57:

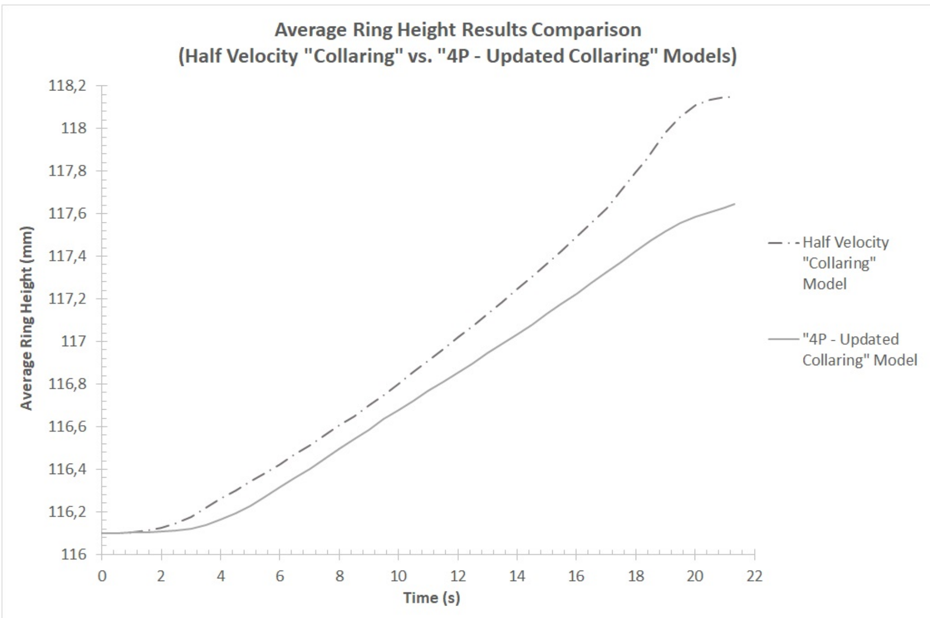

FIG. 4.57: Half velocity "collaring" model vs. "4P-updated collaring" model average ring height results comparison

Observations over the average ring height results in Fig.4.57 revealed some measurable differences in their corresponding values. In this case a deviation in the increase rate of the half velocity "collaring" curve was observed after t = 12 s, approximately, which was not observed in the corresponding curve of the "4P-updated collaring" model. The latter curve was much smoother, with no sudden changes in pace (at least during the main forming phase of the process). Additionally, the initial delay previously observed in the radii results was observed in this case, too. The aforementioned delay can be attributed on the very limited ring thinning that occurred early in the process, which resulted in no height changes during the same time. The final average ring height values in Fig.4.57 were equal to $H_{f,collaring,half}$ = 118.15 mm and $H_{f,collaring,4P-updated}$ = 117.64 mm, while their respective percentage differences compared to the target value of $H_{f,target}$ = 115 mm were $\Delta H_{collaring,half}$ = 2.74% and $\Delta H_{collaring,4P-updated}$ = 2.29%.

From the evaluation of the major ring dimensions, it was shown that the "4P-updated collaring" model had some fairly good results, even if the corresponding process should be extended for some additional time, in order to achieve the required dimensional precision. It is especially important to note that from the initial delays observed in all three result curves, the possibility of the aforementioned initial hinge-like formations becoming unstable and thus resulting in global shape defects on the ring was very high. In order to negate any such possibility, the linear velocity of the tools should be kept at fairly low values. Nevertheless, "four-point collaring" process at a reduced tool velocity seems to be a feasible alternative.

After the major ring dimension results were analyzed, an evaluation of the ring thickness measurements from the two processes was performed. The corresponding curves are presented in Fig.4.58:

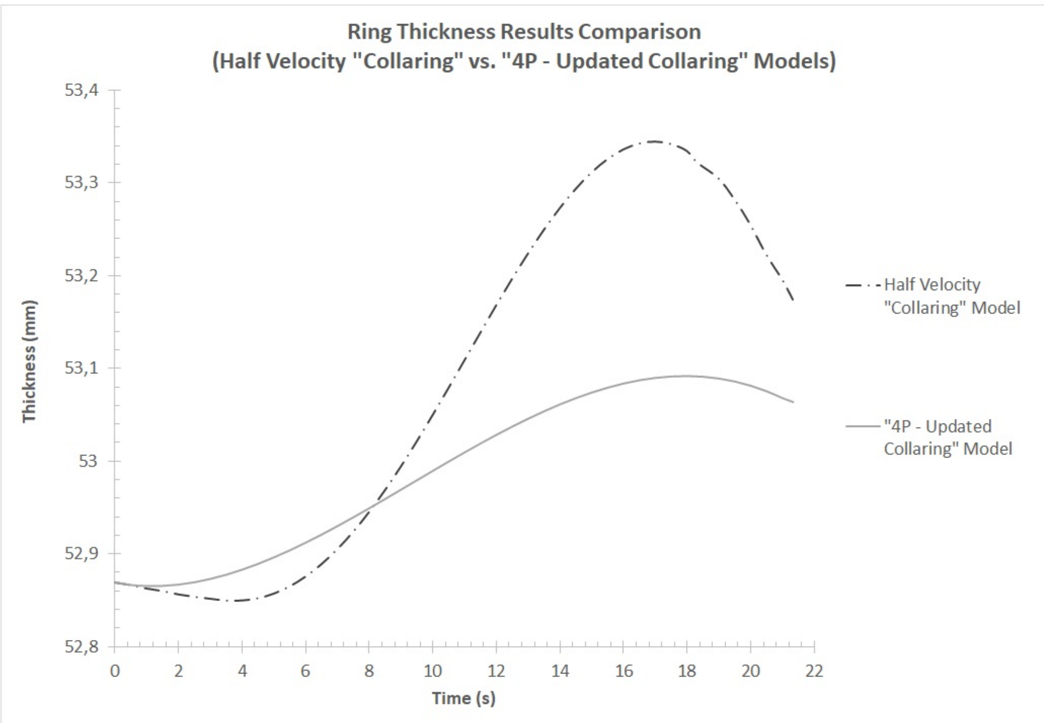

FIG. 4.58: Half velocity "collaring" model vs. "4P-updated collaring" model thickness results comparison

Observations over the thickness curves in Fig.4.58 revealed some significant differences. More specifically, in the half velocity "collaring" model, the ring's thickness was observed to initially decrease slightly, then increase for most of the main forming phase and during the radii normalization phase it decreased again. On the other hand, the ring's thickness from the "4P-updated collaring" model constantly increased during the main forming phase of the process, and decreased during the radii normalization phase. Additionally, the initial delay previously observed in the radii and height results from the "4P-updated collaring" model, could also be seen in the corresponding thickness curve, thus proving that no thickness reduction was performed during the very early stages of the process. Regarding the final thickness values from the two models, these were $f_{f,collaring,half}$ = 53.17 mm and $f_{f,collaring,4P-updated}$ = 53.06 mm, respectively.

Finally, the outer and inner diameter ovality results from the two model were compared with one another. The corresponding curves are presented in Fig.4.59:

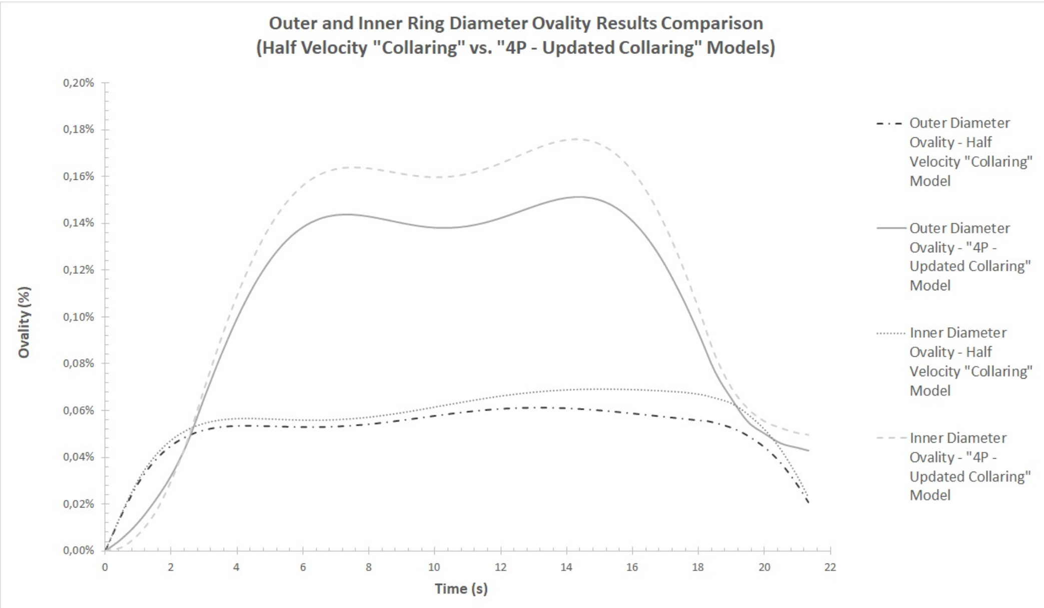

FIG. 4.59: Half velocity "collaring" model vs. "4P-updated collaring" model outer and inner ovality results comparison

Observations over the results in Fig.4.59 revealed some differences between the calculated ovalities from the two methods. Although in both models, the corresponding ovality curves were mostly stable (a slight deviation was observed in the "4P-updated collaring" curves), their values were vastly different. More specifically, the values of both the outer and inner ovality curves from the "4P-updated collaring" model were more than double the corresponding values from the half velocity "collaring" model curves. However, and likewise previous simulations, both ovalities notably decreased during their respective radii normalization phase. Regarding the final outer and inner ovality values from each model, these were 0.043% and 0.049% in the case of the outer and inner ovalities from the half velocity "collaring" model and 0.022% and 0.024% in the case of the outer and inner ovalities from the "4P-updated collaring" model, respectively. This difference indicates a less circular shape of the "4P-updated collaring" final product.

Generally, the results from the "4P-updated collaring" model proved its feasibility. Although the dimensional precision of the current process could be improved compared to the precision of the "six-point" Reverse Ring Rolling processes, the process seemed to be quite stable and with no significant defects appearing. The only major issue with this alternative process was that the linear velocity of the tools should be kept at relatively low values, or else risking the possibility of imbalances and subsequent global shape defects.

After the successful completion of the "4P-updated collaring" simulation, a low velocity "4P-updated pulling" simulation was attempted. Similarly to the previous analysis, in this case the half velocity "pulling" model would be compared to an updated version of the "4P-pulling" model. Those two models would have the same tool linear velocities applied on their respective rolls (as well as the same total duration), with the rest of the process parameters being the same. After the proper setup of the "4P-updated pulling" model and its subsequent solution, an overview over its final time instance was performed. The aforementioned state of the "4P-updated pulling" model is presented in Fig.4.60:

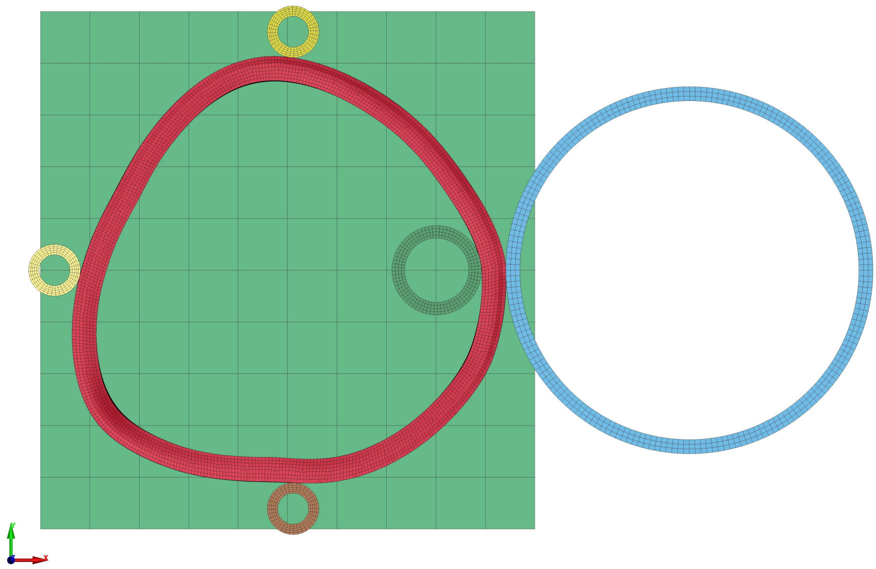

FIG. 4.60: Final time instance of the "4P-updated pulling" model

Observations over Fig.4.60 revealed an unsuccessful "pulling" process. Similarly to the final instance of "4P-pulling" model, some global shape defects were observed on the workpiece. These shape defects deem the final non-circular product as unacceptable.

Since the "4P-updated pulling" model ended with severe shape defects, a step-by-step analysis of the process was subsequently performed. Some characteristic time instances from the process are presented in Fig.4.61:

Observations over the time instances presented in Fig.4.61 revealed a similar deformational path to that of the "4P-pulling" model. More specifically, the consecutive states in Fig.4.61 revealed that the process proceeded as intended only during its first few seconds. After t = 6 s, some initial shape defects began appearing, which rapidly deteriorated from that point onwards. Based on these observations, any further analysis of the calculated results was deemed meaningless.

In general, the "4P-pulling" process with reduced tool linear velocity was proven to be non-feasible, at least for the range of tool velocities that was tested. The corresponding models showed that the process remained stable only for a limited range of radial deformation (less

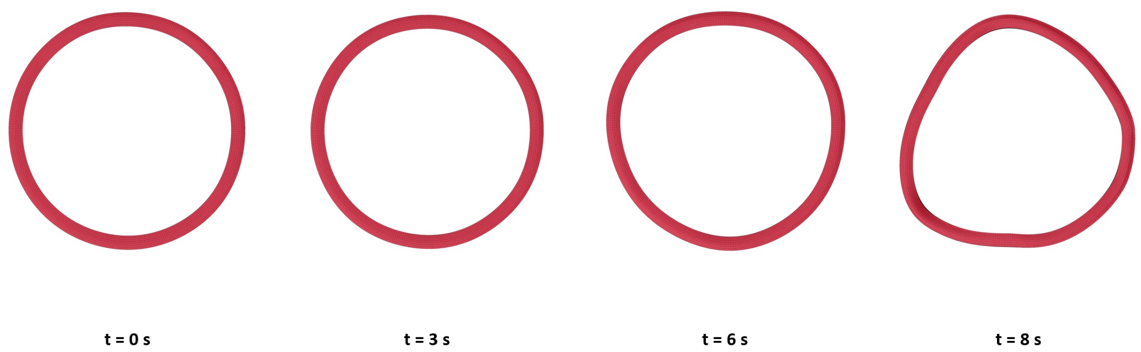

FIG. 4.61: Ring deformation during multiple time instances during the "4P-updated pulling" process simulation

than what was required to achieve the target dimensions). Since the feasibility of the "4P-pulling" process is heavily affected by the tool linear velocity, facilitating even lower tool velocity would perhaps result in a feasible "4P-pulling" process. However, since no results from similar "six-point pulling" processes were available for comparison, no other tool velocities could be tested in the current research. A more thorough feasibility analysis of the "4P-pulling" process could be conducted in a potential future research work.

4.4.3 Initial Ring Temperature

All the aforementioned analyses were performed as hot processes, since the initial concept of Reverse Ring Rolling was as an immediate continuation of the Ring Rolling process. In that way, the already hot workpiece can be further manufactured with relative ease, due to the decreased yield strength of material at high temperatures. However, as it was previously presented in §3.2.4, cooling the final Ring Rolling product down to room temperature will cause a significant and often unpredictable shrinkage, thus reducing the overall ring dimensions by an unknown amount. Furthermore, common surface phenomena occurring during the cooling of the product, such as scaling, can cause additional material loss and thus dimensional imprecision. On the other hand, if Reverse Ring Rolling could be performed as a cold process, the high dimensional precision of its product would be permanent.

Based on these observations, the initial temperature of the ring was further investigated as a crucial Reverse Ring Rolling process parameter. For this analysis, the same simulations previously conducted in section §4.3 were repeated but this time in room temperature. After the successful solution of these models, through which the feasibility of Reverse Ring Rolling would be validated, the calculated results were compared to the corresponding of sections §4.3.2 and §4.3.4, in order to analyze their differences. It is worth noting that the aforementioned comparisons mainly focused on the deformational results from the two processes, since it is well-known that the temperature difference would cause significant deviations to the calculated stress, strain, load and thermal results.

Cold Reverse Ring Rolling Models Setup

In order to setup the cold Reverse Ring Rolling models, several process parameters had to be properly adjusted. More specifically, apart from the initial temperature of the workpiece and the tools that needed to be reduced to room temperature, all material and heat transfer properties had to be checked and/or extend the corresponding curves to involve the temperature range of the current analysis. More specifically, the parameters that had to be adjusted for the current simulation involved the following:

- In order to set the initial temperature of the workpiece and the tools at room temperature, the corresponding initial temperature options were set equal to *TEMP* = 298.15 in the INITIAL_TEMPERATURE_SET menu.

- The workpiece and tool temperatures were reset back to 298.15 K between the cold "collaring" and cold "pulling" models, in order to evaluate the feasibility of both processes at room temperature.

- All material properties, namely, Young's Modulus (E), Poisson's ratio (v), Yield strength (σ_Y), coefficient of thermal expansion (α), thermal conductivity (K) and specific heat capacity (C) as they were given in their respective literature references of Table 2.3 involved values from room temperature, thus the corresponding room temperature values were included in MAT_106 and MAT_T10 via their respective curves defined in DEFINE_CURVE menu.

- In all contacts, the corresponding friction coefficients were maintained the same to those previously presented in sections §4.3.1 and 4.3.3, respectively, thus no difference due to temperature was considered. The author of the current dissertation, however, is well aware that the temperature of the workpiece can significantly affect the friction state between itself and tooling.

- The conductance coefficient for all contacts was considered equal to $K = 0.45\ \frac{W}{mK}$, as per the corresponding rule - of - thumb previously discussed in section §2.8.

- Both of the convection and radiation coefficient curves were extended to room temperature range, based on the corresponding curves found in the literature, as they were presented in section §2.10.2.

The rest of the process parameters were maintained the same, in order to evaluate the effects of solely the ring's initial temperature on the feasibility of Reverse Ring Rolling processes.

Cold Reverse Ring Rolling Models Results Comparison

After the completion of each simulation, their respective results were extracted and subsequently compared to corresponding results from the "collaring" and "pulling" models presented in sections §4.3.2 and 4.3.4, respectively.

Initially, an evaluation of the cold "collaring" model results was conducted. A general overview of the aforementioned model revealed that the process concluded successfully, with no major macro-scaled defects being observed (Fig.4.62).

Then, the rings' cross-sections at the end of the "collaring" and the cold "collaring" models were compared to one another, with the corresponding instances presented in Fig.4.63:

Observations over the cross-section of the workpiece at the final time instance of each of the analyzed models (Fig.4.63) revealed mostly similar deformations with very few differences. Most notably, and although the two cross-sections were almost identical, the bottom fishtail defect in the case of the cold "collaring" product was slightly larger. This fact can be attributed to the greater yield strength of the cold "collaring" workpiece, which caused the bottom fishtail defect to be stiffer and thus deformed less from its interaction with the mill table.

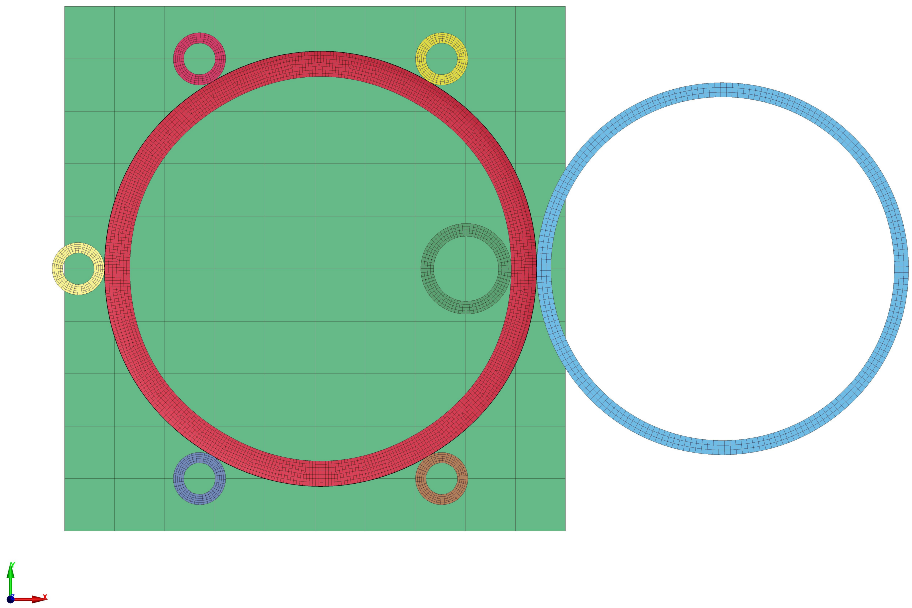

FIG. 4.62: Final time instance of the cold "collaring" model

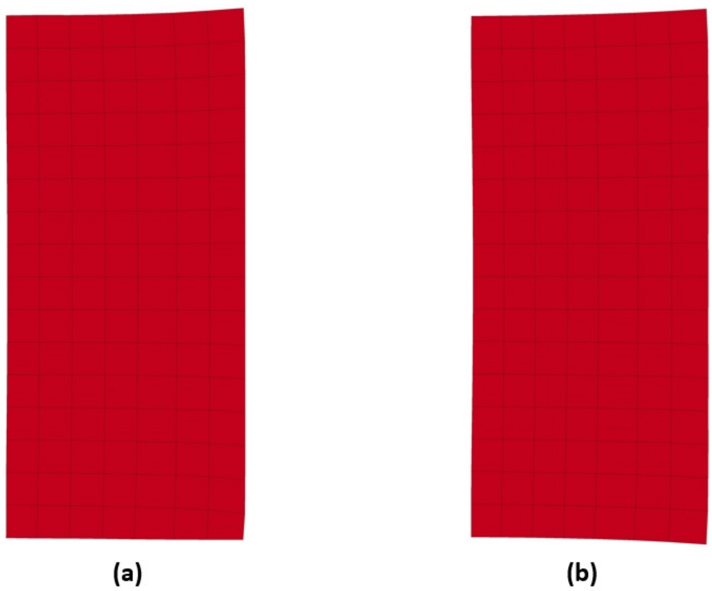

FIG. 4.63: Ring's cross-section at the final time instance of each model: (a) "Collaring" model and (b) Cold "collaring" model

Afterward, the outer and inner radii results of the cold "collaring" model were evaluated. The corresponding curves, as well as, their respective counterparts from section §4.3.2 are compared in Figs.4.64 and 4.65:

Observations over the outer and inner radii results from the two models (Fig.4.64 and 4.65) revealed some differences between the corresponding curves. More specifically, both radii of the cold "collaring" ring decreased at a slower rate compared to the corresponding results

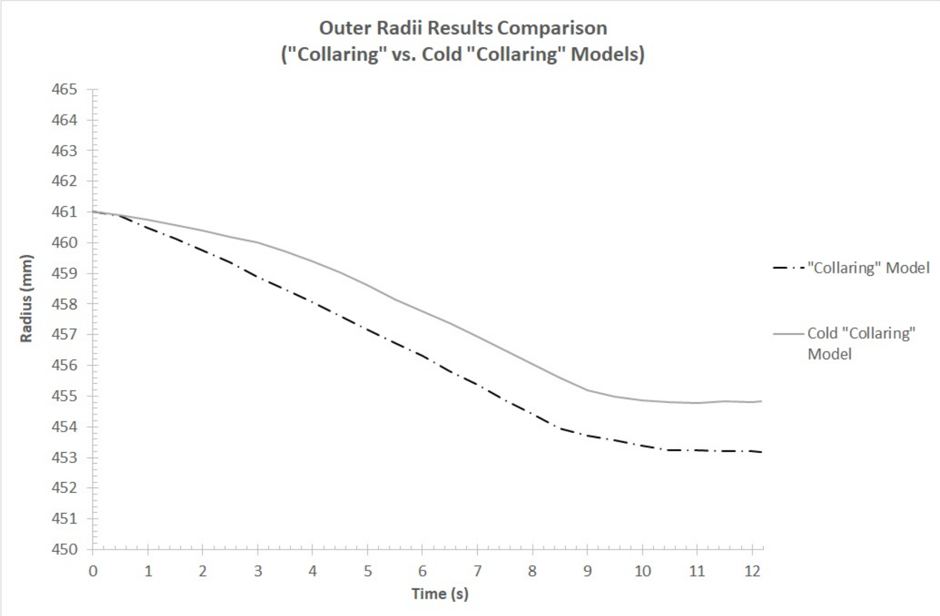

FIG. 4.64: Cold "collaring" model vs. "collaring" model outer radii results comparison

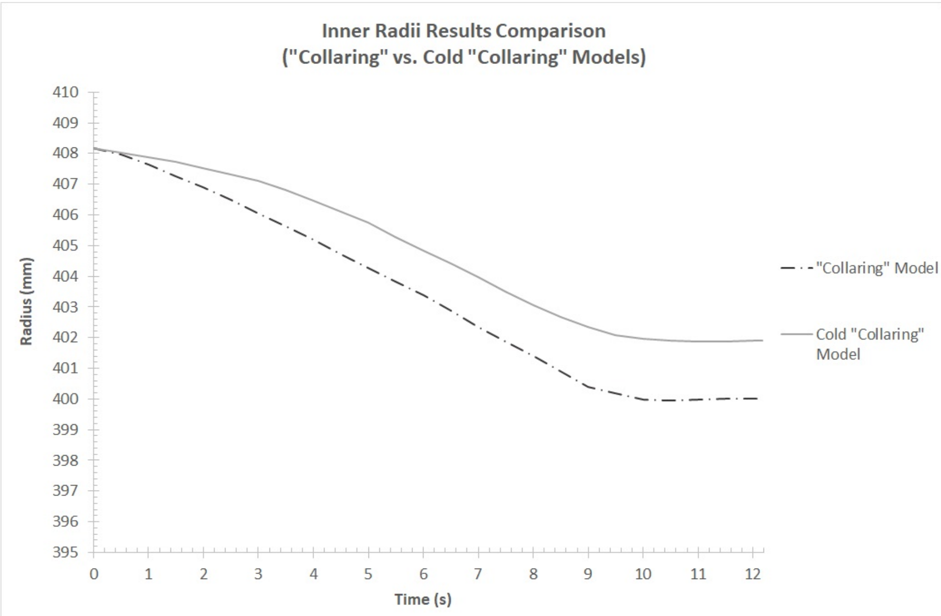

FIG. 4.65: Cold "collaring" model vs. "collaring" model inner radii results comparison

from the "collaring" model. These differences can be attributed to the increased mechanical properties of IN718 in lower temperatures that required additional work to deform up to the desired point. In this case, the predefined inner radius could be reached by the cold "collaring" process, if the linear movement of the tools would be extended for another 3 s, approximately, given that the deformation rate would remain the same. Based on the presented results, the final outer and inner radii in the cold "collaring" model were $R_{f,cold\_collaring}$ = 454.84 mm and $r_{f,cold\_collaring}$ = 401.91 mm, respectively, for a percentage difference of $\Delta R_{cold\_collaring}$ = 0.37% and $\Delta r_{cold\_collaring}$ = 0.47%, compared to the corresponding "collaring" model results.

In the case of the average ring height results from the cold "collaring" model and their comparison to the respective results from the "collaring" model, the corresponding curves are presented in Fig.4.66:

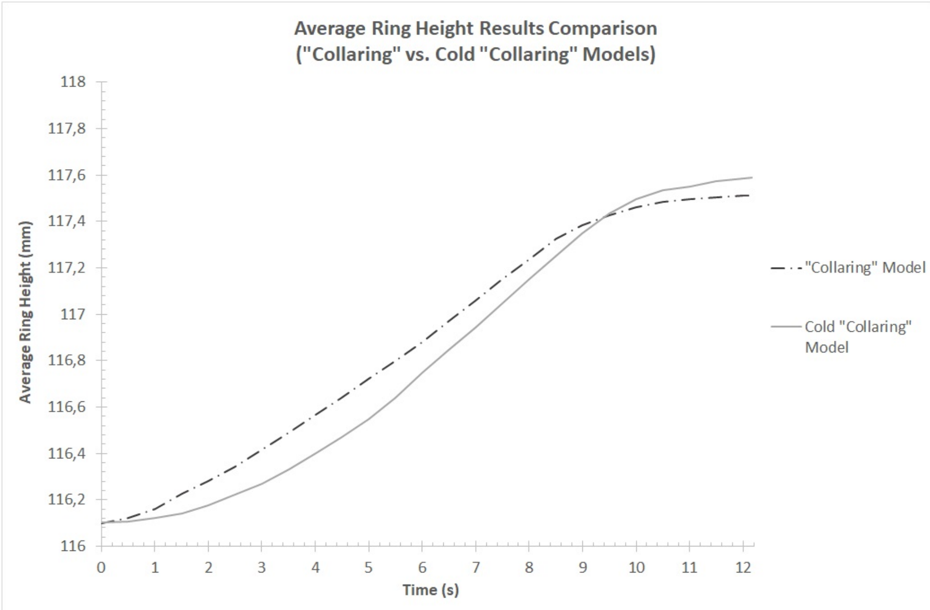

FIG. 4.66: Cold "collaring" model vs. "collaring" model average ring height results comparison

Observations over Fig.4.66 revealed some differences in this case, too. More specifically, the evolution of the average ring height results of the cold "collaring" model had two separate phases. During the first phase (t = 0 - 4.5 s), the average ring height increased at a slower pace than the respective dimension of the "collaring" model. However, after t = 4.5 s, the cold "collaring" ring height began increasing faster than the "collaring" ring height, and it even slightly surpassed the latter after t = 9.2 s. At the end of the process, the average ring height had a value of $H_{f,cold\_collaring}$ = 117.59 mm, for a percentage difference of $\Delta H_{cold\_collaring}$ = 0.068% compared to the final ring height of the "collaring" workpiece. This difference can be attributed to the larger bottom fishtail defect observed in the cold "collaring" model, which especially increased in height during the normalization of the ring's radii (after t = 9.2 s). However, it should be reminded that the average height difference between the two models was still relatively small.

Subsequently, the ring's thickness and ovality results were analyzed. The corresponding comparisons to the respective "collaring" model results are presented in Figs.4.67 and 4.68, respectively:

Observations over the thickness results in Fig.4.67 revealed some differences, both in terms of values and evolution patterns. More specifically, in the case of the thickness results from the cold "collaring" model, some very slight deviations could be observed throughout the process, with the final thickness value being approximately $f_{f,cold\_collaring}$ = 57.93 mm. On the other hand, the corresponding results from the "collaring" model revealed a relatively great thickness increase after the middle of the process. Correlated to the previous demormational results, the aforementioned difference confirmed that in the case of the hotter "collaring" model, the lack of bottom fishtail defect (as a result of its compression against

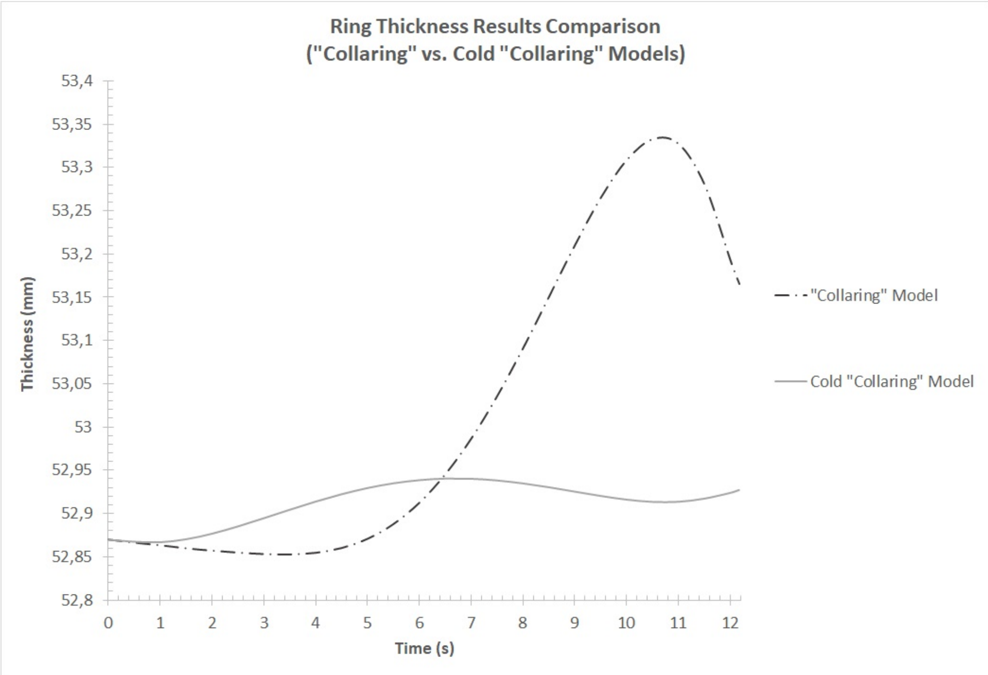

FIG. 4.67: Cold "collaring" model vs. "collaring" model thickness results comparison

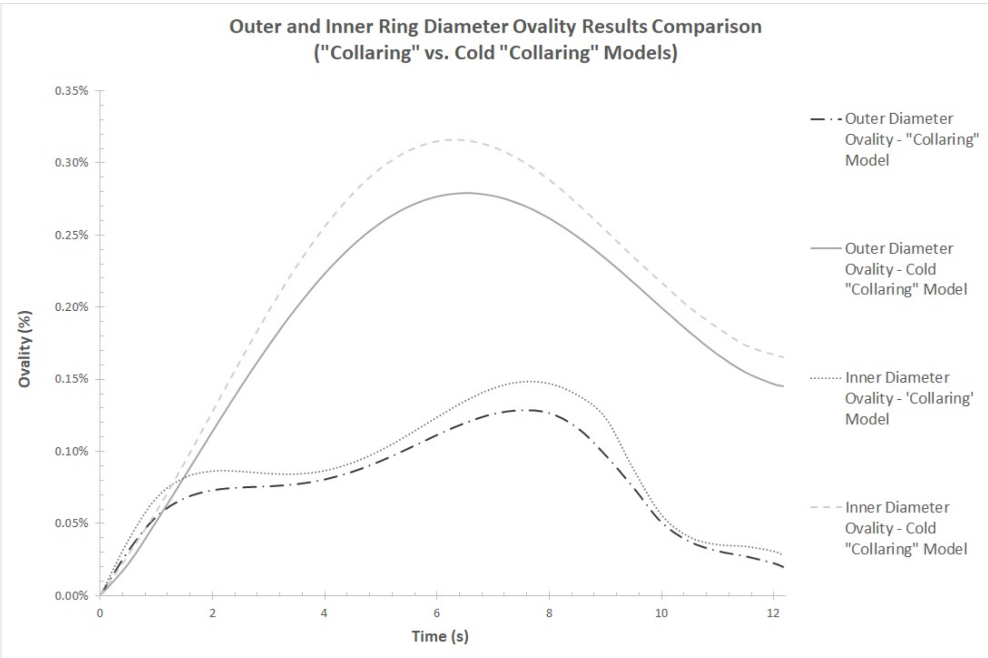

FIG. 4.68: Cold "collaring" model vs. "collaring" model outer and inner ovality results comparison

the mill table) led to a thickening of the workpiece. It should also be mentioned that a greater overall deformation of the "collaring" model was rather expected, due to the increased formability of the material in high temperatures and its decreased stiffness that led to lesser localized bending and elastic deformations. Both of these phenomena, however, were much more prominent in the cold "collaring" model.

In the case of the outer and inner ring ovalities (Fig.4.68), the comparison between the results from the two models revealed some rather increased ovalities in the case of the cold "collaring" models. More specifically, and although the ovality results from both models were relatively small, the ovalities of the cold "collaring" model were almost double compared to those of the "collaring" model. In other words, the deformation mechanism in the cold "collaring" model led to a less circular product compared to that of "collaring" process. The final outer and inner ovalities of the cold "collaring" product were 0.15% and 0.16%, respectively.

Overall, from the review of the deformational result from the cold "collaring" model, the feasibility of the aforementioned process at room temperature was proven, although some slight adjustment may be required. More specifically, from the evaluation of radii and thickness results it was made clear that phenomena like localized bending and high elastic deformations become much more relevant at room temperature, thus leading to lesser radial deformation of the workpiece and slightly larger shape defects. In order to tackle these problems, a proper adjustment (reduction) of the tool velocities and an extension of the process's duration can be recommended. Generally, the cold "collaring" process can be considered as feasible.

Following the cold "collaring" model, an evaluation of the cold "pulling" model results was performed. Initially, a general overview of the ring's deformation during multiple instances of the process was performed. The corresponding results are presented in Fig.4.69:

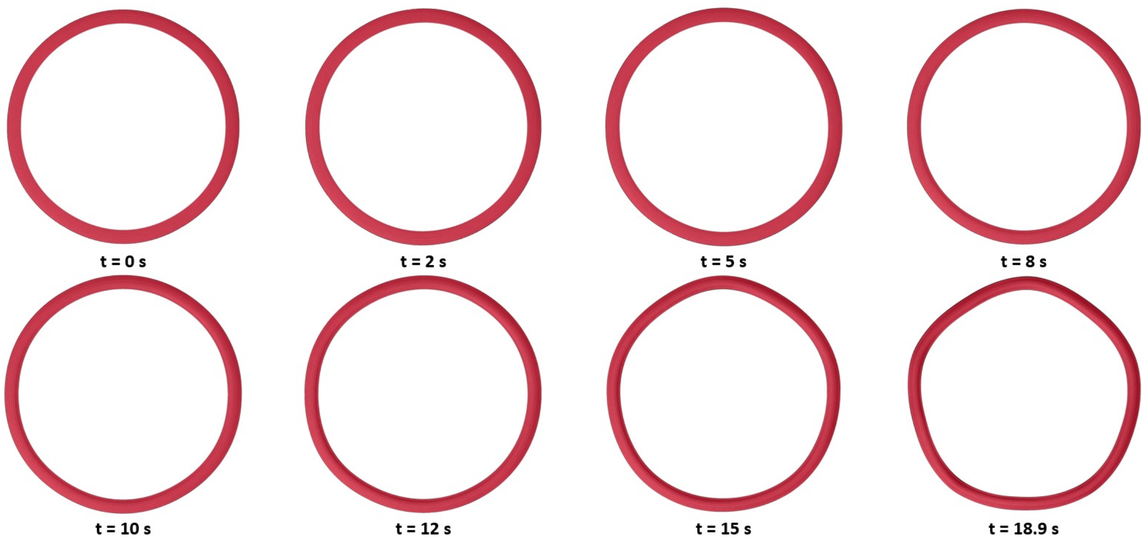

FIG. 4.69: Ring deformation during multiple time instances during the cold "pulling" process simulation

Observations over the ring's deformation at multiple time instances of the cold "pulling" process (Fig.4.69) revealed that the cold "pulling" process could not be completed until the end with the set of parameters defined in section §4.3.3. More specifically, although until t = 10 s the cold "pulling" process product had a fairly circular shape, global shape defects began manifesting from that point onwards and until the end of the process. At the final time instance of the simulation, the ring had an overall shape reminiscent of a pentagon. Such defects were previously discussed as potential problems caused by improper process parameters (also see section §4.3.4), mainly due to some excess localized hinge-like formations. These hinge-like formations were heavily implied by the signed Von Mises stress results observed during the "pulling" process (e.g. Fig.4.12) and were mainly located between the roll contact points. Nevertheless, based on the presented time instances in Fig.4.69, approximately half of the process (until t = 10 s) can only be considered as feasible, thus results from the cold "pulling" model up to that point will be further analyzed below.

Regarding the cross-section of the workpiece at t = 10 s and its comparison to the corresponding cross-section at the same time instance from the "pulling" model, these are presented at Fig.4.70:

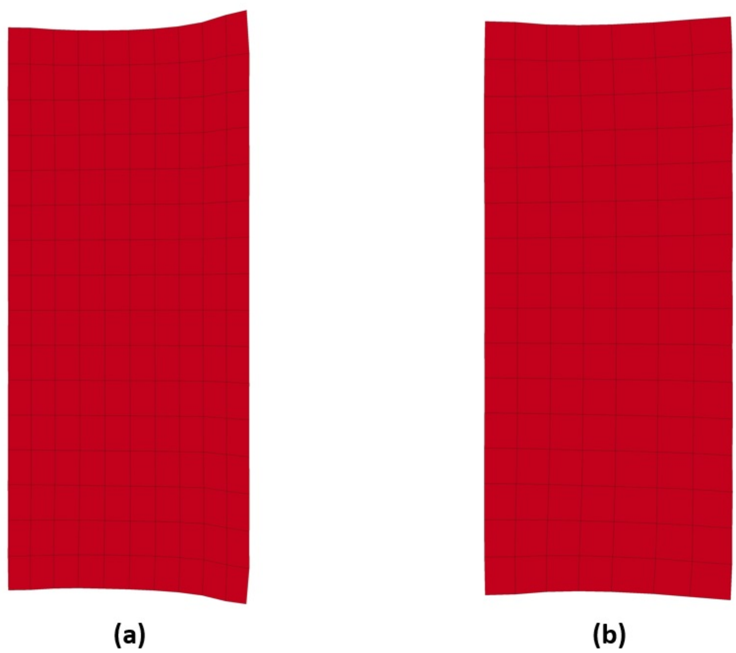

FIG. 4.70: Ring's cross-section at t = 10 s from each model: (a) "Pulling" model and (b) Cold "pulling" model

Observations over the cross-sections presented in Fig.4.70 revealed some slight differences between the two. More specifically, observations over the cross-section from the "pulling" model (Fig.4.70(a)) revealed the formation of rather unsymmetrical fishtail defects, with the outer fishtail defects (right side of Fig.4.70(a)) being larger than the respective inner surface defects (left side of Fig.4.70(a)). On the other hand in the case of the cross-section from the cold "pulling" model (Fig.4.70(b)), the corresponding fishtail defects were formed much more symmetrically, with their size in both the outer and the inner surfaces being almost equal. This difference can be attributed to the divergence in material properties between the hot and cold states of the workpieces, which allowed for different deformation mechanisms to manifest. Based on the cross-sections from the two models, it was implied that more localized deformations occurred during the "pulling" process, whereas a more uniform thinning of the workpiece could be observed during the cold "pulling" process.

Afterwards, the outer and inner radii results from the cold "pulling" process were evaluated. The aforementioned curves and their comparison to the corresponding results from the "pulling" model are presented in Figs.4.71 and 4.72, respectively:

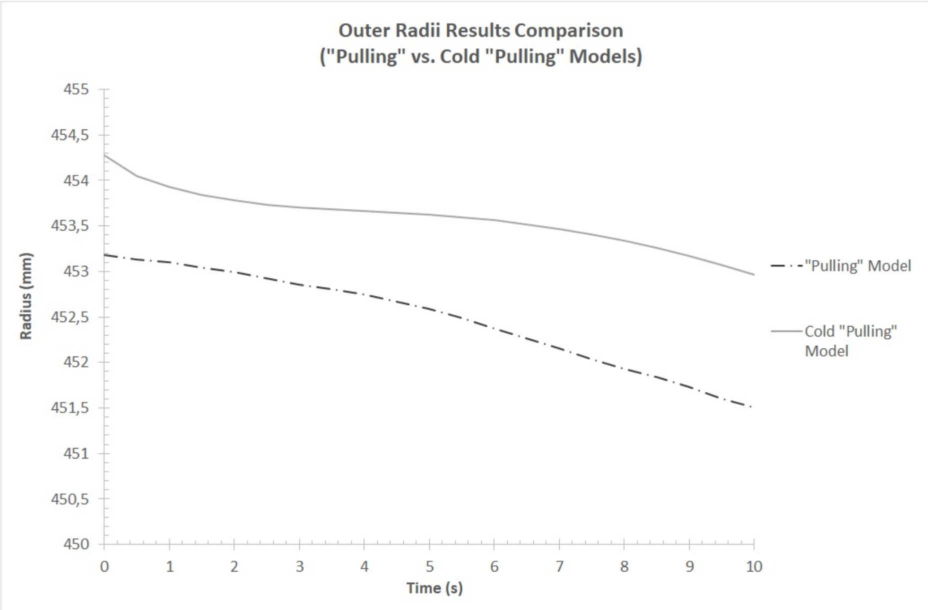

FIG. 4.71: Cold "pulling" model vs. "pulling" model outer radii results comparison

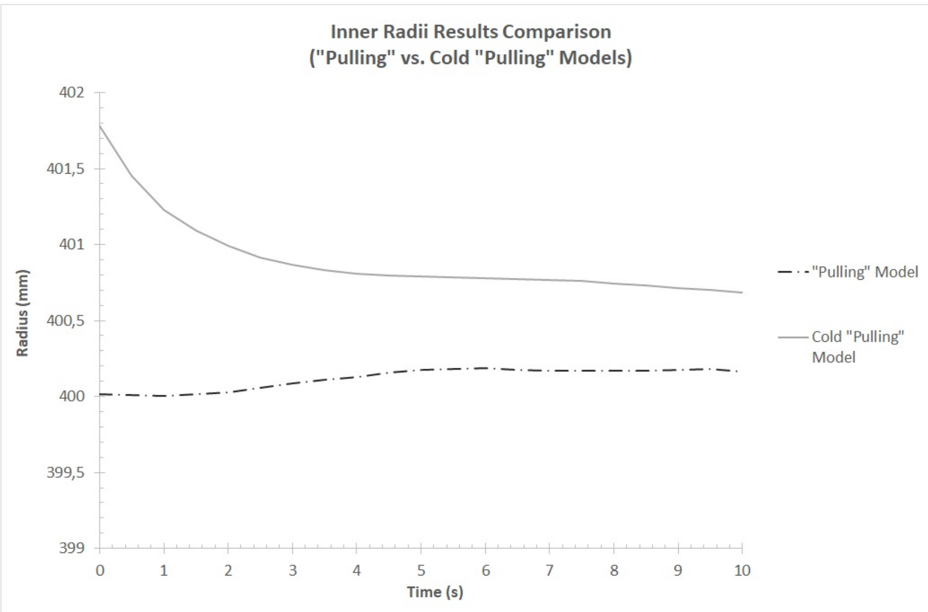

FIG. 4.72: Cold "pulling" model vs. "pulling" model inner radii results comparison

Observations over the outer and inner radii comparisons (Figs.4.71 and 4.72) revealed some very interesting behaviors. Similarly to the corrsponding results from the cold "collaring" model, the outer radius of the current model reduced at a slower pace compared to that of the "pulling", even if an initial fast reduction was observed very early in the process. However, a completely different behavior was observed between the inner radii results (Fig.4.72). More specifically, a gradual reduction was observed in the cold "pulling" inner radius, whereas the corresponding dimension slightly increased for the same duration of the "pulling" model. This difference implies that although a thinning of the workpiece was performed in the main rolling bite, the support rolls performed a process closer to that of cold "collaring". Because of this, the hinge-like formations became gradually worse and eventually some global shape defects manifested. A possible solution to this problem would be the application of different (reduced) linear velocities only on the support rolls, so as to follow the thinning performed by the main rolling bite and not to further deform the workpiece. Regarding the recorded radii values at t = 10 s of the cold "pulling" model, these were $R_{cold\_pulling,10}$ = 452.96 mm and $r_{t=10s,cold\_pulling}$ = 400.68 mm, for a percentage difference of $\Delta R_{cold\_pulling}$ = 0.32% and $\Delta r_{cold\_pulling}$ = 0.13% compared to the corresponding values of the "pulling" model.

Following the radii results, the average ring height results were evaluated. The corresponding curve comparison to the average ring height results of the "pulling" model is presented in Fig.4.73:

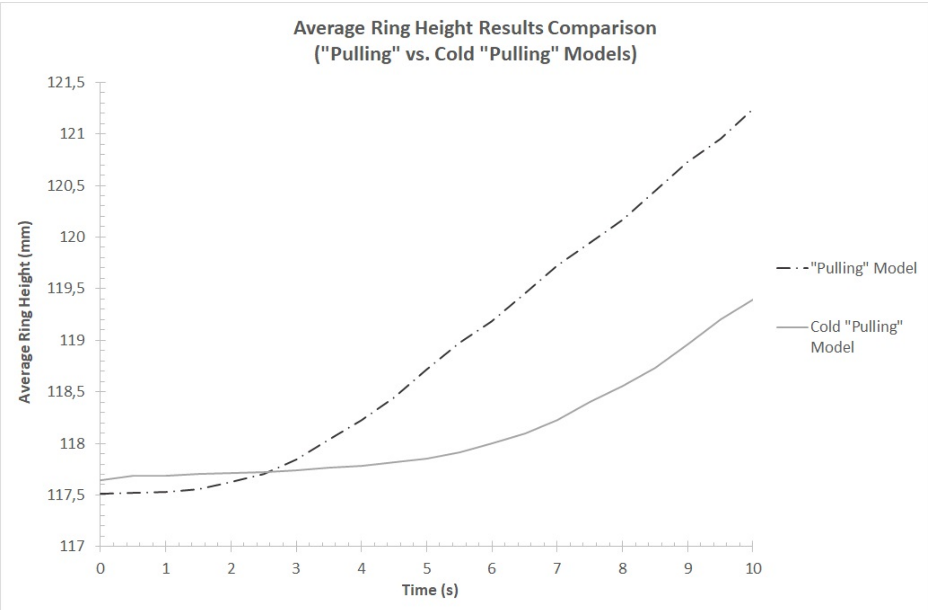

FIG. 4.73: Cold "pulling" model vs. "pulling" model average ring height results comparison

Observations over Fig.4.73 revealed some rather expected behaviors. More specifically, although early in the process both curves increased very slightly, after t = 2 s the average height of the "pulling" workpiece began increasing rapidly. On the other hand, the corresponding rapid height increase of the cold "pulling" workpiece was delayed until after t = 5.5 s. Additionally, these results can be correlated to the cross-section instances presented in Fig.4.70, in which the fishtail defects on the "pulling" ring were comparably larger than those of the cold "pulling" ring. The corresponding cold "pulling" average ring height value at t = 10 s was $H_{t=10s,cold\_pulling}$ = 119.39 mm, for a percentage difference of $\Delta H_{t=10s,cold\_pulling}$ = 1.52% compared to the average ring height calculated by the "pulling" model. However, it should be reminded that a more useful height measurement would be that of the minimum recorded value, which in this case would be $H_{min,cold\_pulling}$ = 118.35 mm for a percentage difference of $\Delta H_{min,cold\_pulling}$ = 0.68% compared to the corresponding dimension of the "pulling" workpiece, at the same time instance.

In the case of the calculated ring thickness, the corresponding results' comparison from the cold "pulling" and the "pulling" models are presented in Fig.4.74:

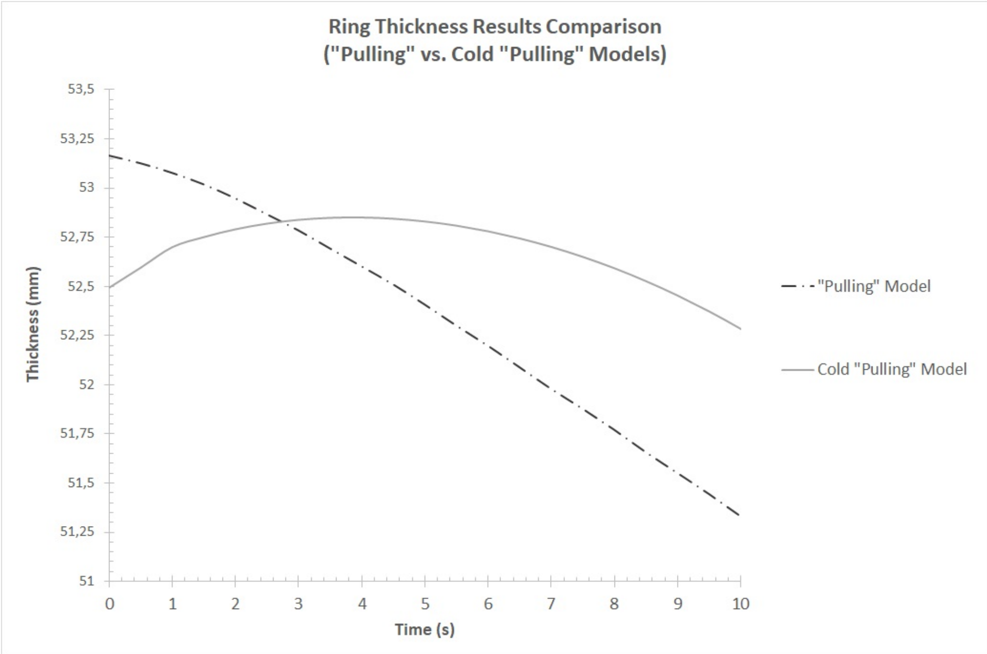

FIG. 4.74: Cold "pulling" model vs. "pulling" model thickness results comparison

Observations over the thickness curves in Fig.4.74 revealed a rather interesting behavior. More specifically, the thickness of the ring in the cold "pulling" model gradually increased until t = 3.5 s and subsequently decreased for the rest of the process. Compared to the "pulling" process that the corresponding ring thickness constantly decreased, the cold "pulling" results indicated that a different deformation mechanism prevailed during the early stages of the current process. Further comparisons of the cold "pulling" thickness curve to the corresponding curve from the cold "collaring" model (Fig.4.67) revealed similarities between the two, thus a deformation mechanism closer to that of cold "collaring" was implied in this case. Regarding the thickness value calculated by the cold "pulling" model at t = 10 s, this was equal to $f_{t=10s,cold\_pulling}$ = 52.28 mm with a percentage difference of $\Delta f_{cold\_pulling}$ = 1.86% compared to the corresponding "pulling" model results.

Finally, the outer and inner ring ovality results from the cold "pulling" model were evaluated. The aforementioned curves along with the respective results calculated by the "pulling" model are presented in Fig.4.75:

Observations over the ovality results of the cold "pulling" workpiece (Fig.4.75) revealed an interesting behavior. Early in the process (until t 2 s, approximately), both ovalities curves decreased, as a result of the normalization of pre-existing roundness defects inherited from the cold "collaring" process. From that point onwards, the inner ovality curve continued to increase for the rest of the process, whereas the outer ovality curve increased until t = 8 s and then slightly decreased until t = 10 s. Although the inner ovality behavior was expected, especially after comparing it to both ovality curves from the "pulling" model, the cold "pulling outer ovality curve's behavior was rather peculiar. The observed deviation with the corresponding curve first increasing and then decreasing implied that the hinge-like formations began becoming sizable after t = 8 s. Thus, it can be concluded that the cold "pulling" process performed as it was initially intended, only for the first 8 s of its total duration. Regarding the recorded outer and inner ovality values at t = 10 s were equal to 0.17% and 0.20%, respectively.

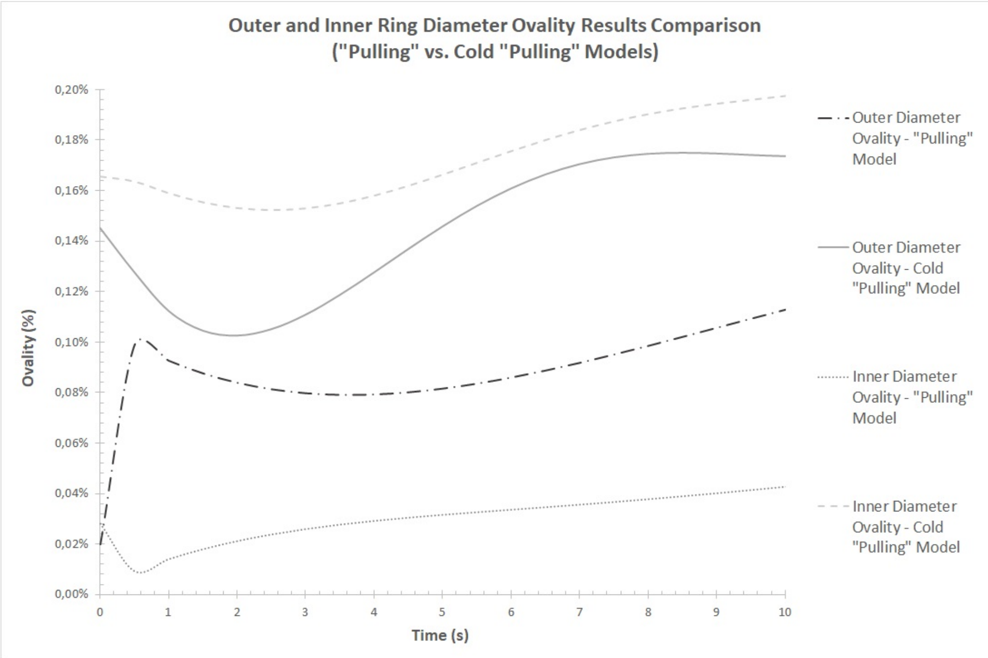

FIG. 4.75: Cold "pulling" model vs. "pulling" model outer and inner ovality results comparison

Overall, the analysis of the deformational results from the cold "pulling" model showed some notable differences in the process's mechanism, especially compared to the aforementioned "pulling" process (also see section §4.3.4). During the first few instances of cold "pulling", an ironing of pre-existing surfaces defects and a normalization of both radii (similarly to a finishing forming process) was performed. From that point onwards, however, two different deformation mechanisms took place. The first mechanism involved the thinning of the ring inside the main rolling bite, which was the expected outcome from this process. The second mechanism involved the overall compression of the ring towards its center by the support rolls (similarly to a cold "collaring" process), which was a rather unintended outcome. In order for the second mechanism not occur and thus perform a successful cold "pulling" process, different linear velocities should be applied on the support rolls and on the main roll, so that the support rolls would stabilize the workpiece during the process, but they would not perform any additional forming on it. A precise determination of the linear tool velocities is mainly affected by the ring's material and the required thinning, thus the corresponding process parameters can be rendered as case specific. In general, a cold "pulling" process can be considered as challenging, since a more in depth and case specific determination of applicable process parameters is required. However, this fact does not render the process as unfeasible. At this point, it should be reminded that the main goals of the current analysis were to investigate whether the hot and cold Reverse Ring Rolling processes could be performed with the same initial workpiece geometry and the same process parameters (excluding the initial temperatures), and secondly how similar would the final products of these two processes be.

4.5 Discussion and Conclusions

From the conducted simulations, the feasibility of a Reverse Ring Rolling process was largely validated. Both parts of this proposed process were simulated successfully, with no prohibitive issues or points of concern being observed during the evaluation of their respective results.

More specifically, in the case of the "collaring" model a smooth reduction of both ring radii was performed, while the average height of the ring was increased. The majority of plastic deformations were performed across the outer peripheral surface of the workpiece, which led to the formation of a single-sided fishtail defect. This fact can reduce the amount of the necessary post-processing even more, since any grinding or machining would have to be performed over a smaller area of the workpiece. From the evaluation of the equivalent stress, the effective strain, the load and the temperature results some rather expected distributions were observed. Most notably, a deformation mechanism involving the creation of multiple hinge-like formations along the periphery of the ring was identified. Although this deformation mechanism caused no issues in the conducted simulation, it provided additional insight on potential global shape defect mechanisms that could manifest, in case improper process parameters were applied on the process. Overall compared to the target dimensions set for this problem, an outer radius difference of $\Delta R_{collaring}$ = 0.71%, an inner radius difference of much less than $\Delta r_{collaring}$ = 0.01% and an average height increase of $\Delta H_{collaring}$ = 1.21% were observed at the end of the "collaring" model. It is worth noting that although these percentages are relatively small, the corresponding differences in absolute values could still be considered as unacceptable for certain applications.

Meanwhile, the case of the "pulling" Reverse Ring Rolling model proved to be slightly more challenging. For this process, a number of preliminary trials had to be initially performed, in order to determine a set of viable process parameters that would allow for the successful conclusion of this process. When these process parameters had been identified, the conducted "pulling" simulation proved to be stable and with very accurate results. The majority of the analyzed results were very similar to the corresponding results from the "collaring" model, thus no further comments will be made. Regarding the accuracy of the "pulling" process in terms of dimensional precision, the reduction of the outer ring radius was performed almost on spot, with its final value being $\Delta R_{pulling}$ = 0.0003% smaller than the target outer radius. At the same time, the average ring height had a percentage increase from $\Delta H_{collaring}$ = 1.21% (at the end of the "collaring" process) to $\Delta H_{pulling}$ = 8.4%, with the minimum recorded height of the ring being greater by $\Delta H_{pulling,min}$ = 5.41% than the target ring height of H_{target} = 115 mm. This fact ensures that enough material still existed on the ring, so that further grinding or machining processes could be performed on the end surfaces of the ring, in order to reach the predefined height. It should be noted that as an immediate result of the main roll pushing the workpiece against the mandrel, a slight inner radius increase was observed at the end of the "pulling" process, from $\Delta r_{collaring}$ = 0.0038% (at the end of "collaring" process) to $\Delta r_{pulling}$ = 0.08%. Although this difference could be considered significant in high-precision applications, it could be easily "corrected" through some minor adjustments on the durations of both processes. More specifically, a small undershoot of the inner radius should be performed during the "collaring" process, which would in turn balance the small overshoot of the same dimension observed at the end of the "pulling" process. At the same time, the duration of the "pulling" process should be also slightly reduced to remedy the small undershoot observed in the outer radius, at the end of the "pulling" process. In general, a proper adjustment on the durations of these processes can (in principle at least) result in the production of rings with two of their dimensions precisely manufactured.

From the crucial process parameters that were researched, the linear velocity of the tools was probably the most important. The application of proper linear velocities on the rolls during Reverse Ring Rolling was proven to affect both the final dimensions of the product and the overall stability of the process. Meanwhile, if the applied linear velocity was adequately low, Reverse Ring Rolling process alternatives with fewer tools could also become viable. On that point, it should be noted that the "four-point pulling" processes tested in the current analysis, were not able to produce an acceptable circular product. However, using even lower tool velocities seems to be a highly promising solution for a successful "four-point pulling" process. Finally, conducting Reverse Ring Rolling at room temperature was proven to be partially successful, since the "cold pulling" process was performed successfully only for half of its total duration, before some slight shape defects appeared. Applying lower linear velocities on the tools could be recommended in this case too, as a potential solution. It should be mentioned that all the unsuccessful processes that were presented in the current section, performed as intended for a certain period of their respective duration. Thus, these processes could be considered as-is for smaller overall radial deformations.

Overall, the proposed process of Reverse Ring Rolling seems to be a highly promising addition to a Ring Rolling production line. The main requirement of the process that is a Ring Rolling mill with additional support rolls has already been explored (to a certain degree) in literature. On the other hands, the potential benefits, which mainly include the significant reduction or complete eradication of further radial post-processing of every product, can significantly reduce the duration and the cost of the total production. Additionally, the production of high-precision ring components at a lower cost may have a significant impact on their working lifetime, as well as on the life expectancy of production lines using these components. It is worth reminding that during the cooling of Ring Rolling products to room temperature, significant dimensional deviations will also occur (also see section §3.2.4), thus the predefined final product dimensions at the end of a Reverse Ring Rolling process should be determined with these deviations considered.

Chapter 5

Polygonal Ring Rolling Process

5.1 Introduction

All the preceding analyses involved numerous reruns for the conducted models, most of which ended in error terminations. During one of these reruns, a rather interesting ring shape was produced. More specifically, due to the improper direction of the support roll movements, a square - shaped final product was formed during the simulation. Upon closer inspection of the corresponding results, a new approach of forming seamless, non-circular polygonal products was identified, and it was decided to be briefly investigated. Since the current investigation is not thematically relevant to the main objective of the current dissertation, the analysis of the current Chapter is presented only as a very brief proof of concept. The author acknowledges that there is room for further research and (of course) improvement in the Polygonal Ring Rolling process.

While reviewing literature for similar processes or observations, some relevant work came to light. More specifically, Johnson, MacLeod, and Needham and Moon et al. in their corresponding works (**Johnson, MacLeod, and Needham, 1968** and **Moon et al., 2004**, respectively) mentioned that an inappropriate setup of the support rolls or a defective movement of these tools can lead to polygon - shaped defects on the workpiece. Later, Arthington et al. and Han, Hua, and Yang (**Arthington et al., 2016** and **Han, Hua, and Yang, 2020**, respectively) attempted to create polygonal ring products, although with some limitations in their processes. In the case of **Arthington et al., 2016**, the research team performed a few polygonal-shaped forming productions in a clay-like material, using their previously established "Flexible Ring Rolling" setup. The whole process did not involve the use of support rolls, while (to the author's best knowledge) a metallic polygonal Ring Rolling was not attempted. On the other hand, in **Han, Hua, and Yang, 2020** the authors described the manufacturing of a polygonal - shaped product, using a combination of an outer metallic sheath in which the workpiece was placed. The outer metallic sheath had a complex geometric, with its outer surface being circular and its inner surface being polygonal. This assembly was subsequently placed inside a Ring Rolling setup, where the mandrel would push the workpiece towards the sheath's inner diameter and the main roll would ensure the assembly's rotation. A slight angular movement of the mandrel would compensate for the lack of support rolls.

Although the few research works found in literature described potential methods for the manufacturing of polygonal - shaped seamless products, their lack of application in metals (**Arthington et al., 2016**) or their increased level of complexity (**Han, Hua, and Yang, 2020**) revealed an opening for further research, which will be conducted (to some extent) in the current Chapter of the dissertation. Since no suitable experimental setup was available in this case either, a numerical proof of concept of the process at hand was left as the only viable option. The author of the current thesis acknowledges that an experimental proof of concept should be conducted before ensuring the feasibility of the proposed process. However, since the conducted simulations are based on a fully validated numerical modeling methodology (also see §2), the current analysis can be considered as a very strong indicator towards the feasibility of the corresponding experiments.

5.2 Mechanics of Polygonal Ring Rolling

The main scope of a Polygonal Ring Rolling is the manufacturing of a seamless polygon from an initial ring, with the same total volume. From the volume constancy law, an estimation of some basic dimensions of the polygon can be made. A figure of a hollow polygon with its basic dimensions noted is presented in Fig.5.1. It is worth noting that in Fig.5.1, a hollow pentagon is presented as a reference regular hollow polygon, however, corresponding dimensions are found in any other regular polygon.

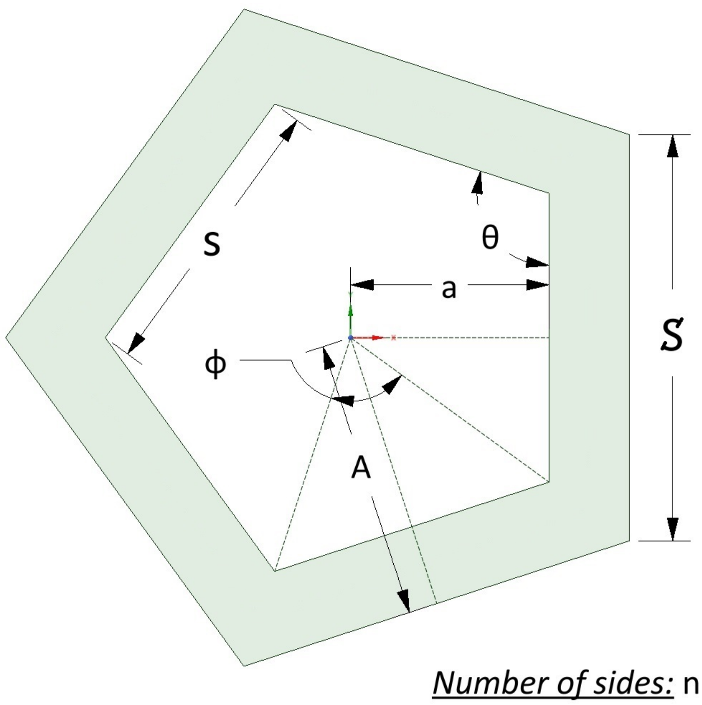

FIG. 5.1: Basic hollow polygon dimensions (a pentagon is presented as a reference design)

From the dimensions in Fig.5.1, the inner side of the polygon, s, is one of the most crucial, since it directly defines the movement of the tools. Additionally, the interior polygon angle (formed between two consecutive sides of the polygon), θ, should also be calculated, since this angle is required for the calculation of the rest of the polygon dimensions.

In Euclidean geometry (**Coxeter, 1969**), the interior angle of a regular polygon can be estimated by Eq.5.1:

$$\theta = \frac{(n-2)}{n} \cdot \pi \tag{5.1}$$

where:

- θ, is the interior angle formed between two consecutive sides of the polygon
- n, is the number of the sides of the polygon

Furthermore, the area of a regular polygon can be calculated using Eq.5.2:

$$\textit{Area of polygon} = \frac{1}{2} \cdot P_i \cdot A_i \tag{5.2}$$

where:

- P_i, is the perimeter of the polygon with $P_i = n \cdot s_i$
- s_i, is the polygon's side
- A_i, is the polygon side's apothem, with $A_i = \frac{s_i}{2} \cdot \tan\left(\frac{\theta}{2}\right)$

With these fundamental equations established, the basic dimensions of the manufactured polygon can be estimated, if the following assumptions stand true:

1. The heights of the initial ring and the manufactured polygon are equal
2. The inner perimeters of the initial ring and the manufactured polygon are equal
3. The volumes of the initial ring and the manufactured polygon are equal

From these three assumptions, the first one simplifies the performed calculations, since it reduces the volume constancy between the two bodies to a simple area equation. From the second assumption, the inner perimeter of the polygon, s, can be estimated via Eq.5.3:

$$\begin{gathered} 2 \cdot \pi \cdot r = n \cdot s \Leftrightarrow \\ \Leftrightarrow s = \frac{2 \cdot \pi \cdot r}{n} \end{gathered} \tag{5.3}$$

where:

- r, is the inner radius of the initial ring
- s, is the inner side of the polygon

Finally through the equation between the two bodies' volumes (reduced to an equation of their respective top view areas), the polygon's outer side can be estimated as per Eq.5.4:

$$\begin{gathered} \pi \cdot \left(R^2 - r^2\right) = \frac{1}{2} \cdot (P \cdot A - p \cdot a) \Leftrightarrow \\ \Leftrightarrow \pi \cdot \left(R^2 - r^2\right) = \frac{n}{4} \cdot \tan\left(\frac{\theta}{2}\right) \cdot \left(S^2 - s^2\right) \Leftrightarrow \\ \Leftrightarrow S = \sqrt{s^2 + \frac{4 \cdot \pi}{n \cdot \tan\left(\frac{\theta}{2}\right)} \cdot \left(R^2 - r^2\right)} \end{gathered} \tag{5.4}$$

where:

- R, is the outer radius of the initial ring
- P, is the outer perimeter of the manufactured polygon

- A, is the outer polygon side apothem
- p, is the inner perimeter of the manufactured polygon
- a, is the inner polygon side apothem

With these basic polygon dimensions defined, a more thorough analysis on the proposed process can be conducted. Based on the movements of (most of) the tools in a typical Ring Rolling mill, as well as the initial and final shape of the workpiece, the fundamental mechanics of the proposed Polygonal Ring Rolling process can be summarized in the following:

- The main rolling bite forms each side of the polygon sequentially, through a linear vertical (regarding the main roll - mandrel center axis) movement of the workpiece guided by the corresponding vertical movement of the support rolls. Although this is not a typical movement pattern of the support rolls, based on the structure of most Ring Rolling mills, such a movement is not prohibited by any means. However, the movement of the support rolls should be fully controllable and not just follow the movement or growth of the workpiece.
- During the process, two distinct phases can be identified in the movement of the workpiece: (a) One when the side of the polygon is formed and (b) a second when the workpiece is rotated.
- When a polygon corner is reached by the main rolling bite, the support rolls should perform a reverse vertical movement. During this action, the workpiece begins rotating about the axis of the mandrel, as if a typical Ring Rolling process was performed.
- The duration of this reverse vertical movement is strictly defined, since an angle of rotation equal to the exterior angle of the polygon should only be travelled.
- After the rotation of the workpiece, the support rolls reverse their vertical movement again, and thus the second side of the polygon begins to form.
- From this point onwards, the two previous steps are repeated in sequence, until all the polygon's sides have been manufactured. A schematic representation of the aforementioned process phases is given in Fig.5.2. It is worth noting that in Fig.5.2 both support rolls were omitted for reasons of clarity.

- Contrary to a typical Ring Rolling, a rotational velocity should be applied to the mandrel in the current process so that the polygon forming is performed more stably. In case a proper rotation velocity is not applied on the mandrel, the workpiece would perform small oscillations during the manufacturing of its sides.
- During the side forming phase, the linear velocities on its two peripheral surfaces (outer and inner) should be equal. Thus and if a constant rotational velocity is considered for the main roll, the rotational velocity of the mandrel during this phase should be calculated through Eq.5.5:

$$\begin{gathered} \omega_{mandrel,l} \cdot r_{mandrel} = \omega_{MR} \cdot r_{MR} \Leftrightarrow \\ \Leftrightarrow \omega_{mandrel,l} = \frac{\omega_{MR} \cdot r_{MR}}{r_{mandrel}} \end{gathered} \tag{5.5}$$

where:

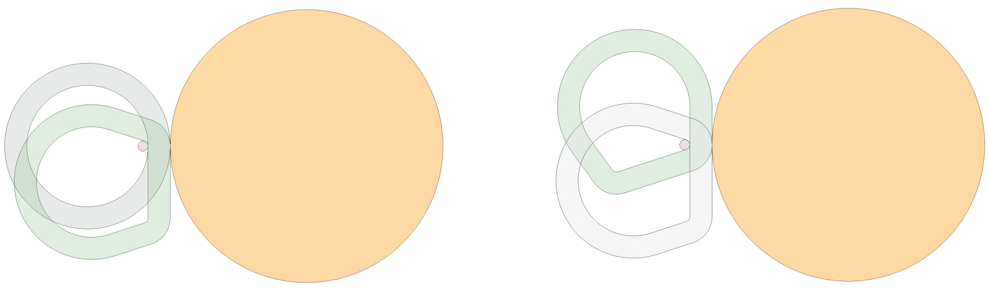

(a) (b)

FIG. 5.2: Main phases of a Polygonal Ring Rolling process: (a) Polygon side formation and (b) Workpiece rotation. In both instances, the green body represents the final state of the corresponding step and the hatched blue body represents its initial state, while the red and orange bodies are the mandrel and the main roll, respectively.

- $\omega_{mandrel,l}$, is the rotational velocity of the mandrel during the side forming phase
- $r_{mandrel}$, is the radius of the mandrel
- ω_{MR}, is the rotational velocity of the main roll
- r_{MR}, is the radius of the main roll

• During the rotation phase, the workpiece rotates about the mandrel's axis. Thus, the rotational velocity of the mandrel in this case should be estimated by Eq.5.6:

$$\begin{aligned} \omega_{mandrel,r} \cdot (r_{mandrel} + f) = \omega_{MR} \cdot r_{MR} \Leftrightarrow \\ \Leftrightarrow \omega_{mandrel,r} = \frac{\omega_{MR} \cdot r_{MR}}{r_{mandrel} + f} \end{aligned} \tag{5.6}$$

where:

- $\omega_{mandrel,r}$, is the rotational velocity of mandrel during the rotation phase
- f, is the thickness of the polygon (considered equal to the initial thickness of the ring, since no thinning should be performed)

• Regarding the linear movement of the mandrel, a very slight initial indentation should only be performed, which would ensure its contact with the workpiece during the current process. In case a constant linear feed was considered for the mandrel, the polygon sides would elongate in addition to straightening, which would significantly increase the complexity of the necessary calculations and thus the complexity of controlling the tools.

• If any sliding is observed between the mandrel and the workpiece during the rotation phase, a slight radial indentation of the mandrel in the workpiece should be performed. However, the mandrel should return to its original position after the end of the corresponding workpiece rotation phase. This practice was also recommended by the authors of **Arthington et al., 2016**.

- For the estimation of the workpiece's vertical travel, l, during the side forming phase, a calculation based on the inner polygon side length and the dimensions of the mandrel should be performed, as per Eq.5.7. A schematic explanation of the aforementioned calculation is presented in Fig.5.3.

$$\begin{gathered} l = s - 2 \cdot x \Leftrightarrow \\ \Leftrightarrow l = s - 2 \cdot r_{mandrel} \cdot \tan\left(\frac{\phi}{2}\right) \end{gathered} \tag{5.7}$$

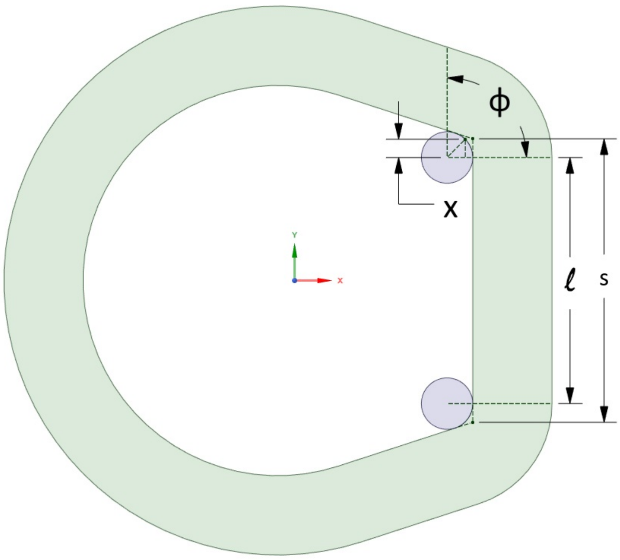

FIG. 5.3: Schematic explanation for the calculation of the workpiece's linear travel

where:

  - ϕ, is the exterior angle of the polygon, with $\phi = \frac{2 \cdot \pi}{n}$.
  - x, is the semi-cord of the contact arc between the mandrel and the workpiece.

- Both support rolls should perform parallel, vertical movements, with their respective total travel being equal to l. At the beginning of the process, a reverse movement compared to that performed during the side forming phase, with a travel distance of $\frac{l}{2}$ should be performed, in order to avoid a corner mismatch at the end of the process.

- The duration of each phase can be estimated using the total travel distance, the exterior angle of the polygon and the corresponding rotational velocity of the mandrel, as per Eqs.5.8:

$$t_l = \frac{l}{\omega_{mandrel,l} \cdot r_{mandrel}} \text{ and } t_r = \frac{\phi}{\omega_{mandrel,r}} \tag{5.8}$$

where:

  - t_l, is the duration of the side forming phase
  - t_r, is the duration of the rotation phase

- Although the conical rolls should be in contact with the ring, no linear velocity should be applied to them. Instead, their role should be limited to the ironing of potential defects that may form during the process.

- Regarding the friction conditions between the tools and the workpiece, some relatively high friction coefficients should be in effect between the workpiece and the main rolling bite tools, while some relatively low friction coefficients should be in effect between the workpiece and the rest of the rolls. In that way, a constant movement of the formed polygon can be ensured, while avoiding sliding that would lead to potential global shape defects on the workpiece.

It is worth noting that an even more precise estimation of the basic polygon dimensions can be approached, if the area of a rounded corner is used instead of Eq.5.2. The corresponding calculations can then be made as per Eq.5.9. An explanatory figure with the basic dimensions of a rounded corner polygon is presented in Fig.5.4.

$$\begin{aligned} \textit{Area of rounded corner polygon} = n \cdot \Bigg\{ \frac{(s+2\cdot b)^2}{4\cdot \tan\left(\frac{\theta}{2}\right)} - \frac{k}{2}\cdot\sqrt{\frac{4\cdot b^2-k^2}{4}} + \\ + r_{corner}^2 \cdot \frac{\pi}{n} - \frac{k}{2}\cdot\left[r_{corner} - r_{corner}\cdot\left(1-\cos\frac{\theta}{2}\right)\right]\Bigg\} \end{aligned} \tag{5.9}$$

where:

- s, is the linear segment of the polygon's side
- b, is the linear extension of the polygon's side
- k, is the cord of the rounded corner
- r_{corner}, is the radius of the rounded corner
- θ, is the interior angle of the polygon

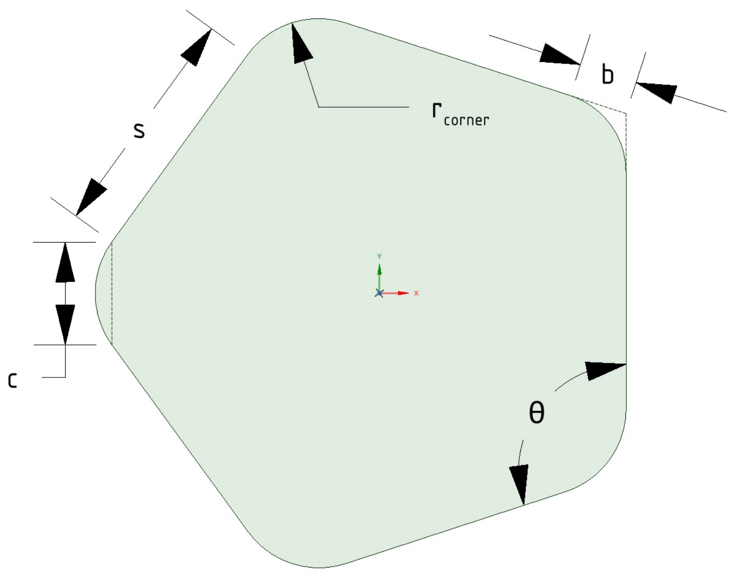

FIG. 5.4: Basic rounded corner polygon dimensions (a pentagon is presented as a reference design)

However, using Eq.5.9 to calculate the basic dimensions of the polygon can significantly increase the complexity of the proposed methodology, so much so that the inner polygon side (supposing a hollow rounded corner polygon) can only be estimated numerically. Furthermore, the more simplistic approach of Eq.5.2 is expected to produce fairly accurate results, thus using a more complex methodology would be meaningless.

With the mechanics of the process fully defined, a numerical proof of concept for the proposed Polygon Ring Rolling process can be performed.

5.3 Polygonal Ring Rolling Simulation

The Polygonal Ring Rolling process is presented in the current thesis more as a proposed concept, since a corresponding experimental process does not still exist at the moment of writing this dissertation. Similarly to Reverse Ring Rolling (which was also a newly proposed process) and since the author had no access to a modifiable Ring Rolling mill, performing a numerical proof of concept for Polygonal Ring Rolling was the only alternative.

In the current section, the feasibility of the Polygonal Ring Rolling process was evaluated via finite element analysis. The conducted simulation was based on the validated methodology previously presented in Chapter §2, with multiple model parameters implemented as-is in the current analysis. A more thorough presentation of the corresponding model is presented below.

5.3.1 Polygonal Ring Rolling Model Setup

As mentioned above, the created numerical model for the Polygonal Ring Rolling was based on the Ring Rolling simulation methodology presented in Chapter §2. However, in order to adjust the Ring Rolling model of §2 to the mechanics and fundamentals of Polygonal Ring Rolling, various changes had to be made.

Initially, different geometries were decided to be implemented for both the initial ring and most of the tools. Some crucial dimensions of these bodies are presented in Table 5.1:

TABLE 5.1: Polygonal Ring Rolling initial ring and tool dimensions

Body	Outer Radius (mm)	Inner Radius (mm)	Height (mm)	Semi-conical angle (°)
Initial Ring	241.55	180	84.8	–
Main roll	550	500*	200	–
Mandrel	20.4	10*	200	–
Support rolls	130	100*	200	–
Conical rolls	450	–	730	18

* The corresponding dimensions had no functional role in the analysis

The initial ring and main roll dimensions were taken from **Zhu et al., 2014**, since a smaller workpiece was decided to be used. The main reasons for this difference (compared to the Ring Rolling model of Chapter 2) were: (a) because the manufacturing of a smaller workpiece was considered to be more challenging, thus more potential problems could arise, and (b) because it would be less time-consuming, thus more preliminary models could be tested. During some early preliminary runs, the dimensions of mandrel and support rolls were also taken from the same reference, however, it was soon discovered that a smaller mandrel and larger support rolls were necessary for the corresponding process. Thus, after some more preliminary runs, the mandrel and support roll dimensions presented in Table 5.1 were determined. Finally, the conical roll dimensions remained the same as those used in the Ring Rolling simulation of Chapter 2, for reasons of simplicity.

As a proof of concept, the manufacturing of a pentagon was decided to be simulated in the current analysis. Based on the initial dimensions of the workpiece and the tools, the basic polygon dimensions and some fundamental process parameters could now be estimated via Eqs.5.1 - 5.8. The corresponding values are presented in Table 5.2:

TABLE 5.2: Basic polygon dimensions and fundamental process parameters used in the Polygonal Ring Rolling simulation

Dimension/ Parameter	Symbol	Value	Units
Number of sides	n	5	–
Outer polygon side	S	313.91	mm
Inner polygon side	s	226.19	mm
Interior polygon angle	θ	108	$^\circ$
Exterior polygon angle	ϕ	72	$^\circ$
Tool travel distance	l	196.57	mm
Main roll rotational velocity	ω_{MR}	0.22	$^{rad}/_{s}$
Mandrel rotational velocity - Side forming phase	$\omega_{mandrel,l}$	5.93	$^{rad}/_{s}$
Mandrel rotational velocity - Rotation phase	$\omega_{mandrel,r}$	1.48	$^{rad}/_{s}$
Side forming phase duration	t_l	1.62	s
Rotation phase duration	t_r	0.85	s
Total simulation time	t_{total}	13.1	s

With the aforementioned process parameters defined, the movement patterns of the tools could be defined. In the case of the main roll, a constant rotational velocity with the corresponding value from Table 5.2 was applied. On the other hand, two separate movement patterns were applied on the mandrel. The first was a slight linear indentation towards the workpiece of approximately 10 μm, which was momentarily increased every time the tool reached a corner of the formed polygon. The values of these larger indentations were approximately 1.25 mm and after their application, the mandrel began immediately moving towards its previous position, which it reached at the end of the corresponding rotation phase. This momentarily larger indentation ensured a better connection between the mandrel and the workpiece during the rotation phase, when relative sliding between the two bodies were more frequent. The second movement pattern was the step-like application of the two rotational velocity values presented in Table 5.2. Both of the aforementioned movement pattern are presented in Fig.5.5:

Regarding the movement of support rolls, these tools oscillated vertically during the process. Although initially two specific limits were considered for the movement of each support roll, it was soon discovered that during the manufacturing of the latter polygon sides, a slight adjustment of these limiting positions should be applied to account for the geometry of the formerly formed polygon sides. The initial limiting positions were equal to $\pm\frac{l}{2}$.

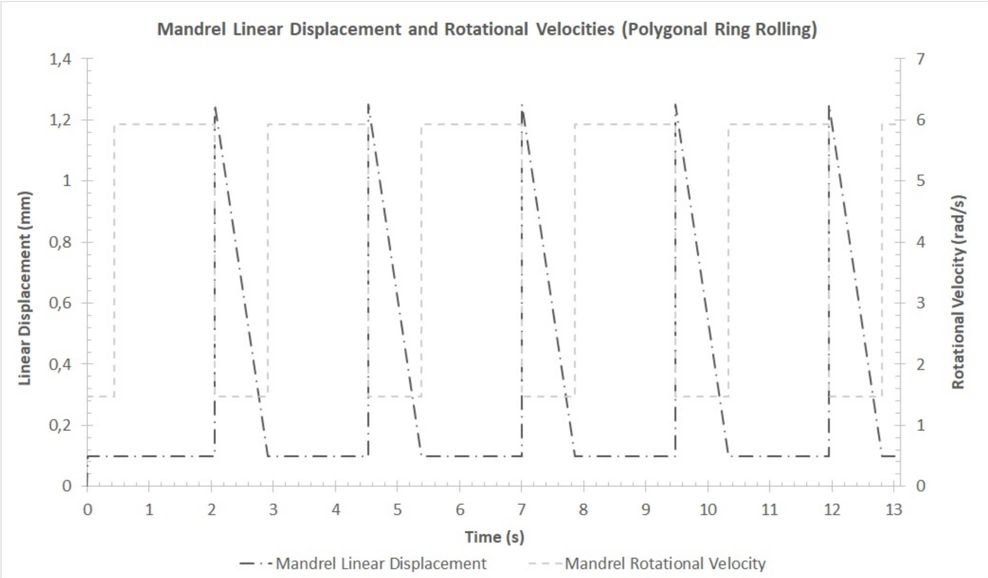

FIG. 5.5: Linear displacement and rotational velocity applied on mandrel during Polygonal Ring Rolling simulation

During the formation of the latter polygon sides, however, the movement limits for each support roll deviated from these initial positions and from one another, since the geometrical complexity of a moving, rotating and deforming workpiece needed to be accounted for. Finally, the movement pattern for each support roll was determined through a series of preliminary models, where the contact points of the ring with each support roll were tracked and properly adjusted between runs. A schematic representation of the applied support roll movement patterns is given in Fig.5.6:

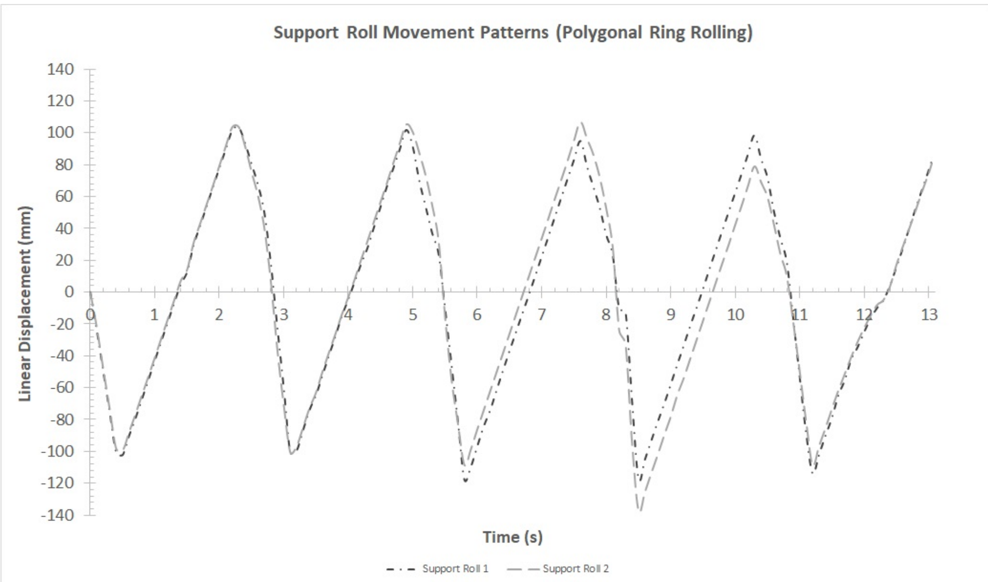

FIG. 5.6: Linear displacement applied on both support rolls during Polygonal Ring Rolling simulation

Finally, both conical rolls were free to revolute about their corresponding rotation axes, however no linear or rotational velocity was applied on them.

In the case of the element mesh applied on the workpiece, an average element size of 6.5 mm was considered. Although a thorough mesh independence analysis was not performed in this case, a similar mesh density (average element size = 4 mm) was shown to produce mesh independent results in the very similar simulation of Ring Rolling (also see section §2.5). Given that the current analysis is conducted solely as a proof of concept rather than an accurate simulation of an actual process, some slight inaccuracies in the calculated results can be overlooked. Should this simulation be used for an actual Polygonal Ring Rolling application, however, a thorough mesh independence analysis should be one of the first steps of the corresponding numerical analysis.

The rest of the model parameters, namely the finite element type, the material of each body and their respective properties, the initial temperature of each body, the applied contact and boundary conditions and the software parameter, were introduced directly from the Ring Rolling model of Chapter 2. The reader should refer to the corresponding sections of Chapter 2 for more information on each of these model parameters. An overview of the Polygonal Ring Rolling model prior to its solution is presented in Fig.5.7:

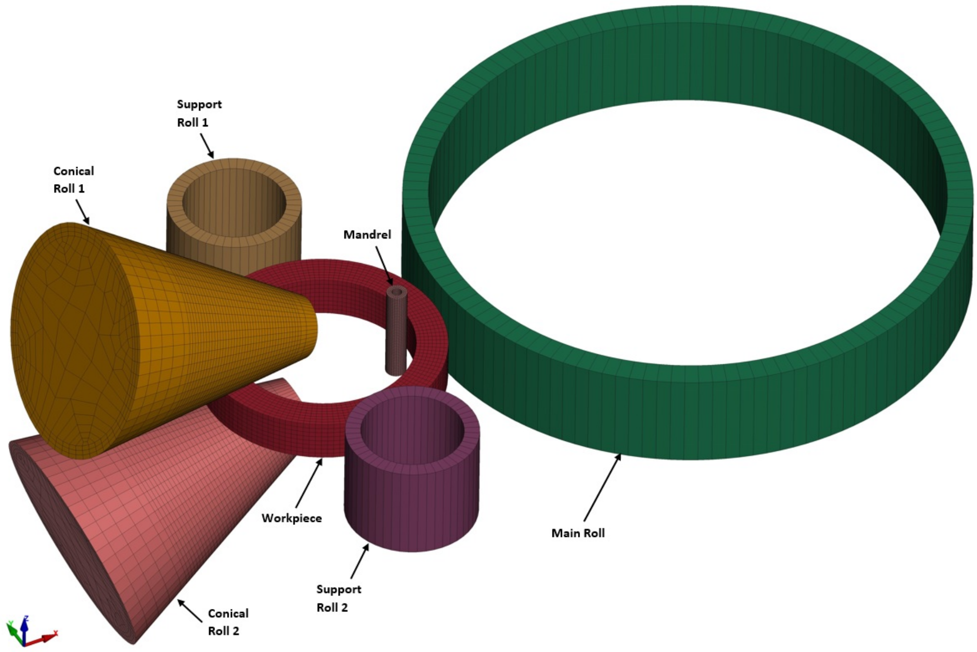

FIG. 5.7: Polygonal Ring Rolling numerical model setup

After the Polygonal Ring Rolling model was properly setup, the model was solved and its results were subsequently evaluated.

5.3.2 Polygonal Ring Rolling Model Results

With the completion of the model's solution, the calculated results were inspected for any significant errors and were subsequently evaluated. Similarly to the previous analyses of the current dissertation, the main result categories that were evaluated were: (a) some crucial deformational results, (b) the signed Von Mises stress distributions in specific phases during the process, (c) the effective strain distributions at the end of the process, (d) the reaction load curves from every tool in the model and (e) the temperature distribution at the end of the process. The evaluation of the aforementioned results was performed mainly qualitatively, since the calculated values could not be validated in any way and thus were of little importance. Additionally, given that Polygon Ring Rolling was conceptualized as a near-net process, little importance should be paid to the measured dimensions of the final product, since further processes would be required to manufacture a near-perfect seamless polygon. However, some geometrical measurements will be presented below for the sake of completion. The author acknowledges that there is still room for improvement in the parameters that affect the dimensions and overall quality of the final product of Polygonal Ring Rolling.

It is worth noting that in all the presented figures of the current section, some or all of the tools have been hidden from view, so that the presented results can be more comprehensive.

Deformational Results

Initially, an evaluation of the workpiece's deformation over multiple steps during the process was performed. The corresponding instances are presented in Fig.5.8:

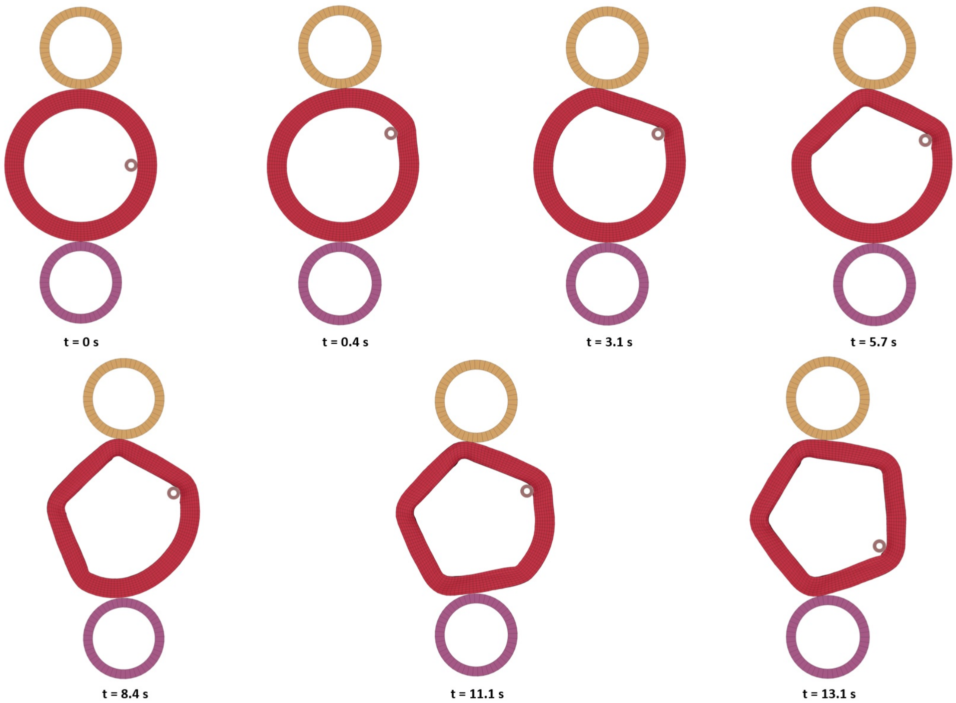

FIG. 5.8: Deformation of the workpiece at multiple time instances of a Polygonal Ring Rolling process simulation (Top view)

Observations over Fig.5.8 revealed several interesting points. First and foremost, the time instances that were chosen for Fig.5.8 corresponded to moments when the formation of each polygon's side had just been concluded. In that way, the evaluation of these results could be more efficient. A quick overview of all time instances revealed that the whole process was rather stable, as a result of a continuous contact of the workpiece with both support rolls. Furthermore, the manufactured sides were fairly straight and relatively close in length. Regarding the quality of the manufactured sides, the one manufactured at the very end of the process seemed to be the worst, as a slight curvature could still be observed after the end of the process. Possible ways to tackle this phenomenon would be to reduce the linear velocity of the workpiece, thus allowing for a more gradual deformation of the workpiece, or to perform a double pass of each side, thus introducing more plastic work in the process (and as a result greater plastic strains). Other notable defects involved some slight "radial" protrusion around some corners, which were a result of the mandrel's increased indentation at the corners and the action support roll 1 that pushed the workpiece against the mandrel. Furthermore, the increased indentation of the mandrel at the corners led to the formation of fishtail defects around these areas. An example of a fishtail defect is presented in Fig.5.9. It is worth noting that these fishtail defects were subsequently ironed, when they reach the conical rolls.

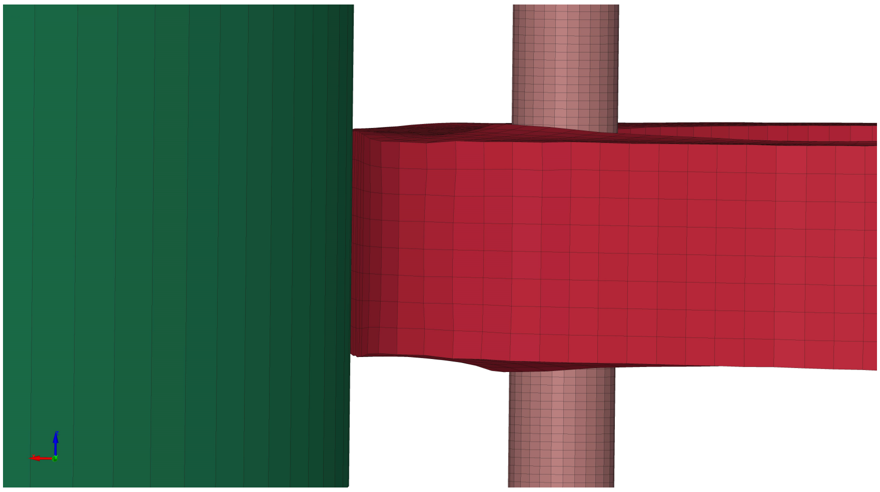

FIG. 5.9: Example of fishtail defects formed around the top and bottom surfaces of the manufactured polygon's corners

The maximum recorded length among all of the manufactured inner sides, s, was measured to be approximately s_{max} = 244.85 mm and the minimum recorded side length was approximately s_{min} = 237.84 mm. The total percentage difference between these two values was approximately Δs = 2.95%. Compared to the theoretical value of s = 226.19 mm presented in Table 5.2, both of these values were larger, thus indicating that a slight elongation due to thinning was performed in all polygon sides. The percentage difference calculated between the maximum length of the manufactured sides and the theoretical side length was approximately $\Delta s_{theoretical,max}$ = 8.25%. Such phenomena could potentially be reduced, in case no initial indentation was applied, however they cannot be completely avoided, since a slight thinning of the workpiece occurred during the straightening of its sides, as a result of its compression against the main roll. Additionally, a slight adjustment on the duration of the latter sides' manufacturing could allow for equal side lengths to be achieved.

In general, the deformational results from the Polygonal Ring Rolling simulation were rather satisfactory. The manufactured polygon was fairly symmetric, with relatively close lengths among its individual sides. Although some slight defects and/or inconsistencies were observed in the final workpiece, these could be significantly improved via the use of a lower linear velocity, of double passes on each side or of slight differentiations of the manufacturing durations in each side. Overall, the deformational results indicate that Polygonal Ring Rolling is feasible, especially under the scope of a near-net process. It is worth mentioning that during the design of Polygonal Ring Rolling process, all of the desired polygon's sides should be inscribed inside the polygonal workpiece manufactured by the process, thus an over- and underestimation of the respective outer and inner sides of the workpiece should be taken into account.

Stress and Strain Results

Following the deformational results, a review of some crucial stress and strain results was performed. In the case of the calculated stress results, an overview of the stress distributions at each of the two phases of the process was performed. Through these results, a better explanation of the deformation mechanisms during these phases could be performed. The corresponding signed equivalent Von Mises stress fields during the side forming and rotation phases are presented in Figs.5.10 and 5.11, respectively:

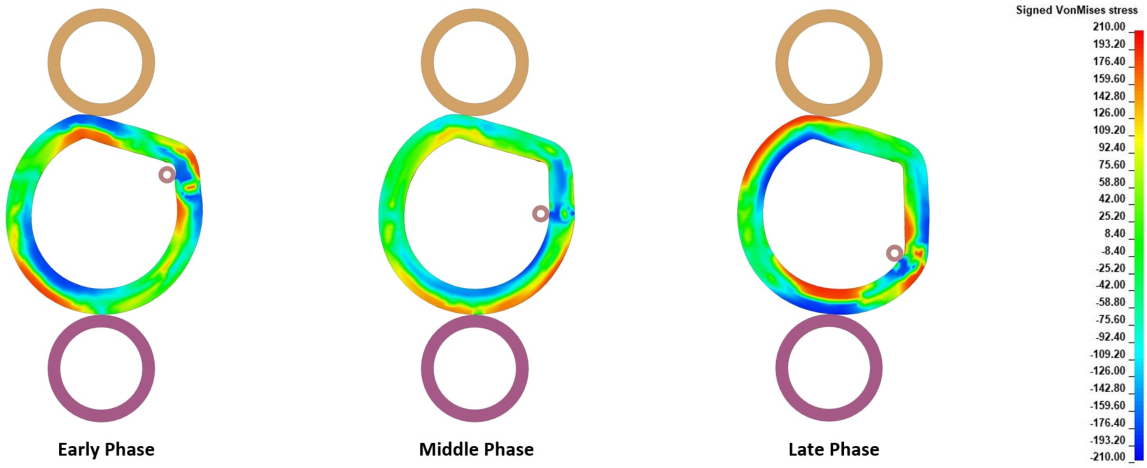

FIG. 5.10: Signed equivalent Von Mises stress distributions during the side forming phase of a Polygonal Ring Rolling process simulation (Top view)

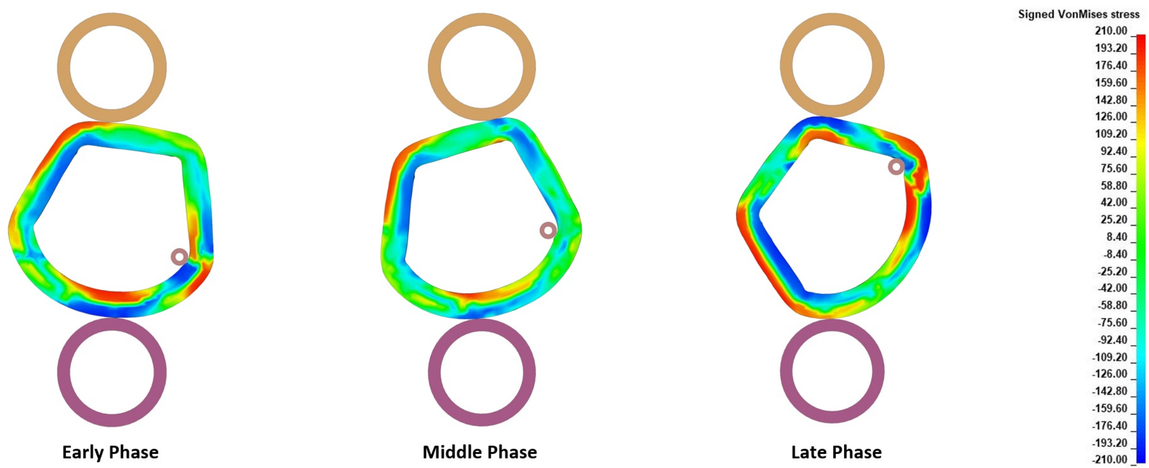

FIG. 5.11: Signed equivalent Von Mises stress distributions during the rotation phase of a Polygonal Ring Rolling process simulation (Top view)

Observations over the signed equivalent Von Mises stress distributions calculated during the side forming phase of Polygonal Ring Rolling (Fig.5.10) revealed several interesting points. During the early stages of the side forming phase, the corner closer to the mandrel had a tendency to close, as a result of the lever mechanism caused by the movement of support roll 1 and the pinning from the mandrel. As the workpiece passed through the main rolling bite (middle phase), the segment of the material below the main rolling bite had the tendency to rotate, which was again caused by the vertical movement of support roll 2 and the stable position of the mandrel. However, this rotation was restricted by support roll 1 leading to a slight bending of the bottom part of the workpiece, which was indicated by the corresponding stress fields observed around that area. Finally, during the late stages of side forming phase, a more intense bending of the workpiece was observed around the follow-up corner, which can be attributed to the straightening and bending of the material at that point. Moreover, the rather intense stress fields observed above the mandrel at that time, were also a result of the material's straightening, which caused tension around the inner peripheral surface of the workpiece. It should be mentioned that during this entire phase, several other bends were observed on the rest of the workpiece, indicated by the stress distributions around the corresponding areas. These bends can be attributed to a combination of the movements of the workpiece and the tools during each time instance, which led to certain points of the workpiece being pressed against their neighboring tools.

Regarding the stress distributions during the rotation phase of the process (Fig.5.11), several interesting points were observed in this case, too. During the entirety of this phase, a shift in the compression of the workpiece was observed. More specifically, at the early stages of the rotation phase, the workpiece was mainly pressed against support roll 2, which led to bends occurring around the contact areas with each support roll. However, as the rotation phase proceeded, the workpiece began being compressed more by support roll 1, thus the aforementioned bends were inverted. Moreover, during the early and middle stages of the rotation phase, a more extensive bending of the workpiece was observed around the contact with support roll 2. Interestingly, the corresponding bending stress fields seemed to have persisted until the late stages of the process, when this small bending rotated below the main rolling bite, thus indicating a plastic deformation of the material at that area. Based on this observation, it can be concluded that during the rotation phase a preliminary pre-straightening can be performed by the support roll 2, which benefits the manufacturing of a more linear polygon side. Regarding the stress fields around the main rolling bite, these were rather expected. More specifically, during the early and late stages of the current phase a relatively increased bending of the corresponding corner was observed, which was to be expected since the presence of a support roll close to the corner during those time instances allowed for the deformation of the material through a lever mechanism. On the other hand, the corresponding stress fields were quite relaxed during the middle stages of the process, thus further proving the contribution of the lever mechanism.

In general, the evaluation of the characteristic signed equivalent Von Mises stress results helped to better understand some more localized phenomena that occur during Polygonal Ring Rolling. One important such phenomenon was the pre-straightening that occurred during the rotation phase, which could further optimize the final geometries of the polygon's sides. Regarding the rest of the observations, the existence of multiple smaller bends during both phases, especially in areas out of the main rolling bite, should be seriously taken into account. In case these bends increase, they could potentially affect the geometry of the sides and the corners that have already been manufactured or even result in global shape defects. This fact is especially crucial in cases of hot Polygonal Ring Rolling processes, where the workpiece is much more deformable. The proper positioning of support rolls during the process is perhaps the most crucial parameter to control such phenomena.

For the evaluation of the effective strains, the corresponding distributions at the end of the process were extracted. The reason for only considering the final effective strain fields for the current analysis was that the corresponding results were rather straightforward. The aforementioned effective strain distributions are presented in Fig.5.12:

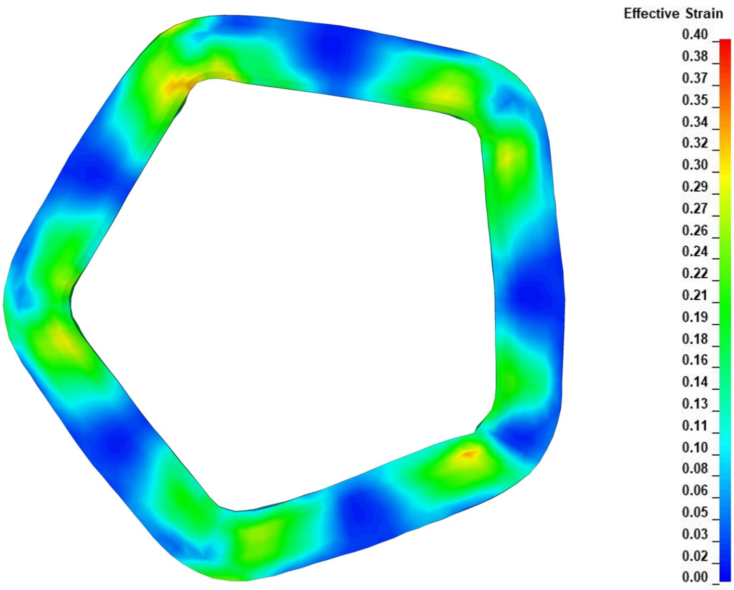

FIG. 5.12: Effective strain distributions at the final times instance (t = 13.1 s) of a Polygonal Ring Rolling process simulation (Top view)

Observations over the final effective strain fields in Fig.5.12 revealed some rather expected distributions. More specifically, the greatest effective strains were observed around the corners of the workpiece, as a result of the permanent bending that occurred around these areas. Furthermore, some rather increased strain fields were also observed around the outer radius of most corners (except for the bottom right corner), which can be attributed to their compression against the main roll during the corresponding rotation phases. The only area, where some slightly greater strains were observed, was the inner surface of the uppermost corner in Fig.5.12. However, given that a larger indentation was also observed in that area, these increased strain fields were rather logical.

Load Results

Afterward, the load results from the Polygonal Ring Rolling simulation were evaluated. Initially, the resultant reaction loads of the tools in the main rolling bite were analyzed. The corresponding load curves are presented in Fig.5.13:

Observations over the reaction load results of the tools in the main rolling bite (Fig.5.13) revealed relatively close patterns between the corresponding curves. More specifically, both load curves had their respective values increased during the side forming phases and decreased during the rotation phases. However, the load of the mandrel was slightly greater in most cases, as a result of its additional loading caused by the action of the support rolls. This fact was heavily implied by the load increases during the beginning and the end of each side forming phase, when the previously discussed lever mechanism became more dominant. Other than that, the only point of interest was a slight load difference observed during the third rotation phase (t = 8.1 s, approximately), with the load values in both curves being greater than the corresponding values in the rest of the rotation phases. This fact can be correlated to the effective strain results previously observed at the corresponding corner of the workpiece (uppermost corner in Fig.5.12), thus implying a slight imbalance occurring at that time.

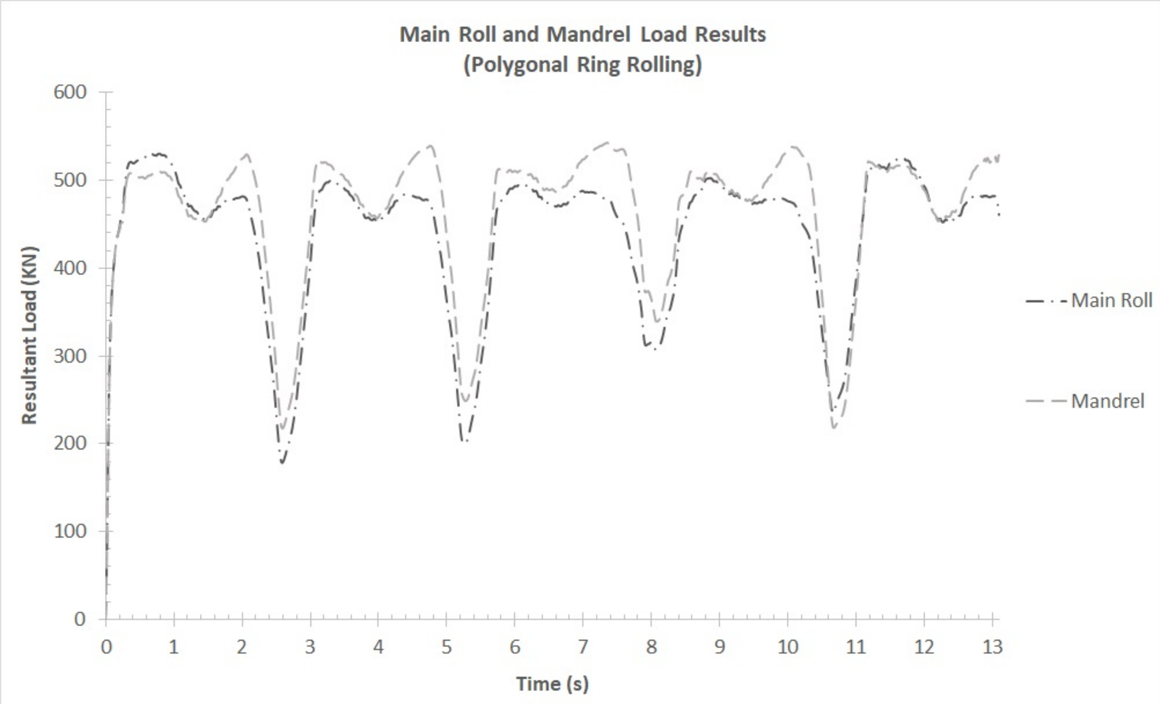

FIG. 5.13: Main roll and mandrel resultant reaction load curves

Regarding the load reaction curves of the support rolls, these are presented in Fig.5.14:

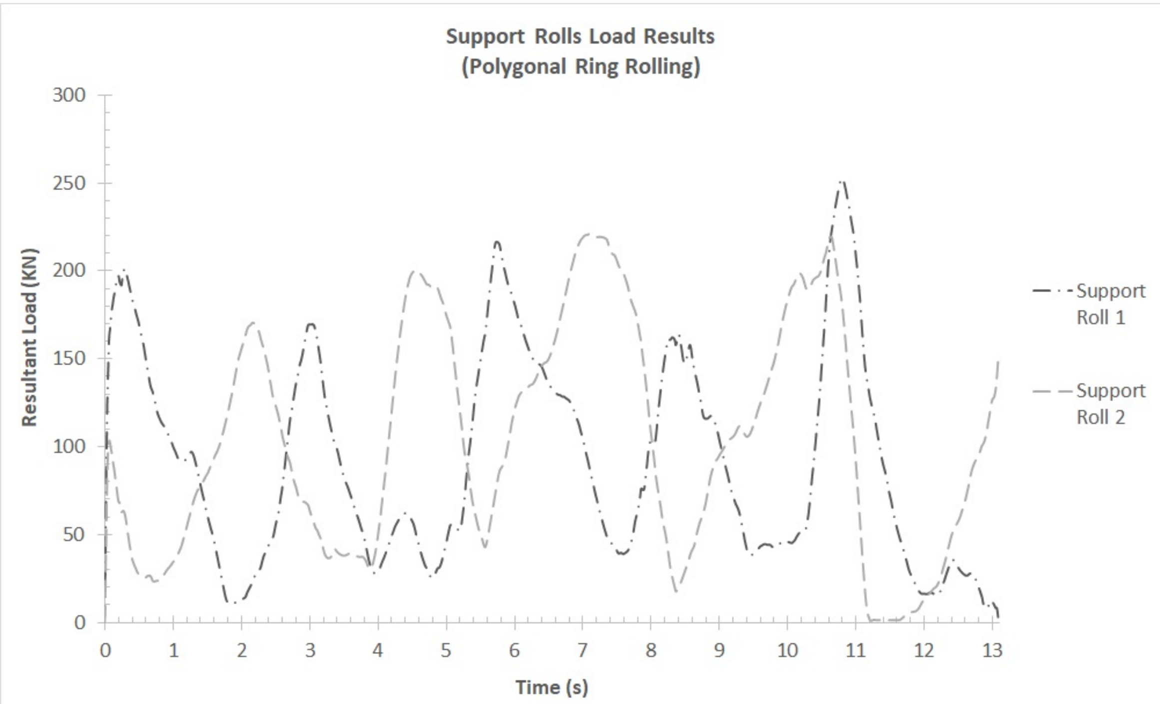

FIG. 5.14: Support rolls resultant reaction load curves

Observations over the load curves in Fig.5.14 revealed some rather interesting load patterns. More specifically, for most of the process's duration the load curves of the two support rolls followed complementary paths, with the load curve of support roll 1 increasing when the corresponding curve of support roll 2 decreased (and vice versa). What is more, the load peaks in each curve did not reveal any specific pattern, thus indicating a rather complex movement of the workpiece that was stabilized by these tools. Only during the final side formation phase (after t = 11.2 s), the two load curves seemed to follow closer paths, thus implying a more stable movement of the workpiece at that time.

Lastly, the reaction load results for the conical rolls are presented in Fig.5.15:

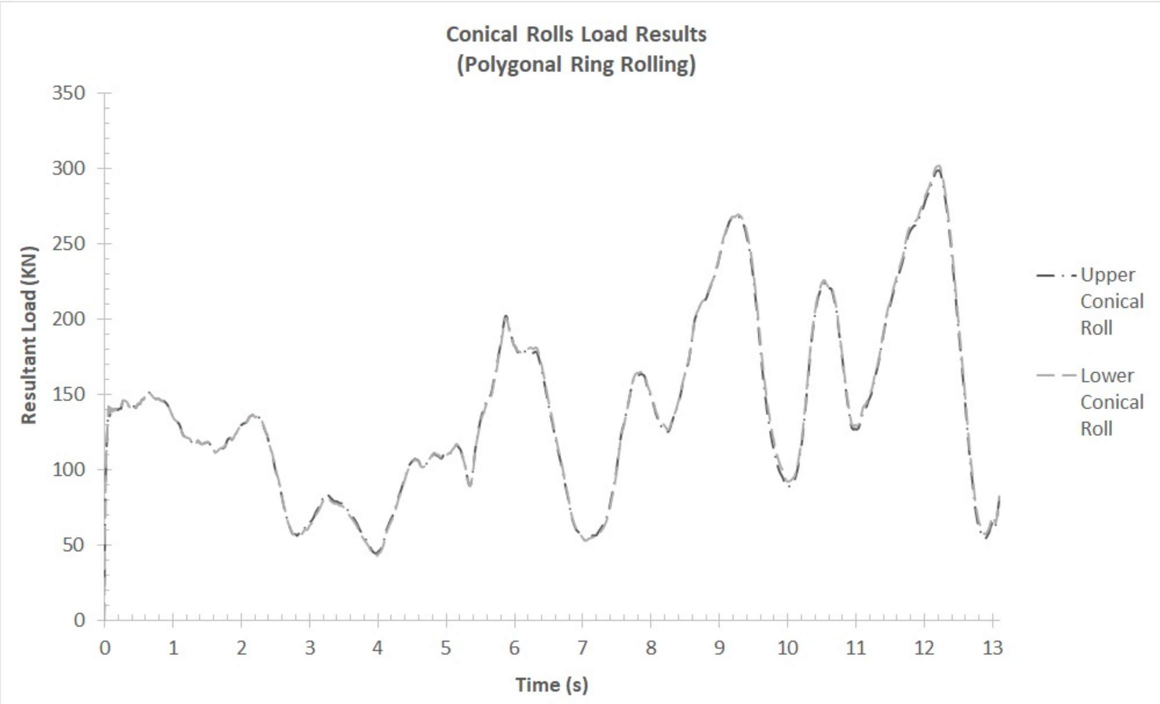

FIG. 5.15: Conical rolls resultant reaction load curves

Observations over the load results in Fig.5.15 revealed almost identical curves between the two tools. During the early stages of the process, relatively low load values were observed in both curves, which were a result of the stabilization of the workpiece against "climbing" imbalances. However, after t = 6 s approximately, additional loads were observed at specific moments during the process. These additional loads can be attributed to the ironing of the corner fishtail defects that occurred at each of these moments.

Thermal Results

Finally, the temperature results from the Polygonal Ring Rolling simulation were evaluated. The corresponding temperature distributions, at the end of the process, are presented in Fig.5.16:

Observations over the temperature distributions at the end of Polygonal Ring Rolling simulation (Fig.5.16) revealed some rather expected results. More specifically, both the inner and outer peripheral surfaces of the workpiece had the lowest temperature values, as a result of their constant cooling by the main rolling bite and the support rolls. Furthermore, a relative temperature increase was observed around the corners of the workpiece, as a result of the plastic work introduced during their permanent bending. These corner temperature distributions were reminiscent of the corresponding strain fields around the same

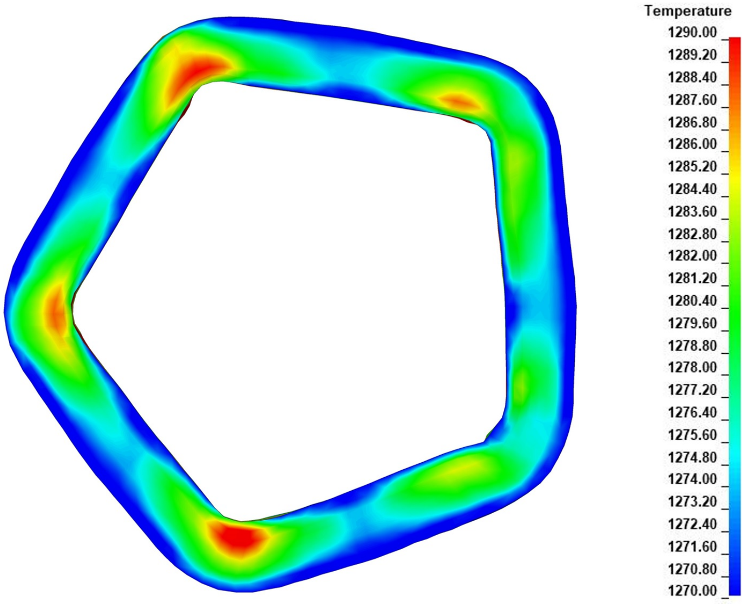

FIG. 5.16: Temperature distributions at the final times instance (t = 13.1 s) of a Polygonal Ring Rolling process simulation (Top view)

areas, thus proving a connection between these two results. Finally, an intensification of the temperature fields around the corners that had passed through the conical roll bite was also observed. This phenomenon was also rather expected, since the introduction of plastic work to iron the fishtail defects formed at the corners led to the aforementioned temperature increase. Overall, the aforementioned temperature distributions were quite logical and straightforward.

5.4 Discussion and Conclusions

From the conducted analysis, Polygonal Ring Rolling seems to be a fairly feasible forming process. The produced polygon was manufactured quite fast, with the current process being able to follow a hot Ring Rolling production, thus having relatively low additional cost per item produced. In other words, the evaluation of the results from the conducted simulation seems to heavily imply the viability of Polygon Ring Rolling as a hot process, thus scheduling it as an immediate follow-up process to that of Ring Rolling, would eliminate any warehousing, transportation, positioning and reheating costs that would be applied otherwise. The fact that only a typical Ring Rolling mill (with fully controllable support rolls, however) is required for the current process, contributes significantly to that point.

From a more thorough evaluation of the numerical results, Polygonal Ring Rolling was shown to be a near-net process, since the final product should be proceeded for some additional post-processing. However, any shape inconsistencies observed were not very far from the theoretically estimated values. In the current example, the sides of the produced pentagon had relatively close lengths between one another, while the maximum percentage difference was approximately 8.25% compared to the corresponding theoretical value presented in Table 5.2. The major factor that caused this difference was the slight elongation of the manufactured sides, which occurred during their compression against the main roll and which was not accounted for in the theoretical methodology. Since the conducted simulation acts as a proof of concept with a lot of room for additional research on this proposed process, further optimization of the quality and the dimensions of the manufactured polygon is a rather realistic prospect.

From the rest of the calculated results, several localized deformation mechanisms came to light. Most of these involved small scale bends that occurred along the perimeter of the workpiece, with the proper positioning of the support rolls being the most crucial parameter that controlled the extent of these bends. Furthermore, an early pre-straightening of each side during its previous rotation phase (before they passed through the main rolling bite) was considered to be a beneficial mechanism that can improved the linearity of these sides. Potential parameters that can affect this pre-straightening are the positioning and the size of support rolls. Moreover, the evaluation of the thermal and strain fields revealed rather expected behaviors, with their corresponding maximum values appearing around the corners of the workpiece, where the largest plastic deformations occurred. Finally, from the analysis of the load results, most of the presented curves had some rather expected behaviors, with the sole exception of the support roll load curves. The evaluation of the latter revealed a rather unstable movement of the workpiece during the process that is mainly restricted by the support rolls, thus proving the significance of their positioning as a very crucial parameter of this process.

Overall, Polygonal Ring Rolling seems to be a very viable process. However, the author of the current dissertation acknowledges the need for additional research on the subject.

Chapter 6

General Conclusions and Future Research

6.1 General Conclusions

The initial scope of the current thesis was the identification of potential aspects and methodologies that could improve the dimensional precision of a flat Ring Rolling process. Since the necessary equipment for an experimental research on this subject was not available, a numerical approach was the only alternative.

Before proceeding to any further analysis, a fully validated model had to be initially established. For this matter, the commercial FEA software ANSYS/LS-DYNA was used. From the plethora of routines and algorithms available in LS-DYNA, the most suitable options that would allow for a physics - based numerical simulation had to be determined. These options were finally determined through some rather extensive trials of preliminary runs for each model parameter. However, a positive aspect of this work was the identification of the most crucial model and, as a result, process parameters of a typical Ring Rolling. After a fully validated model (compared to experimental results found in literature) was established, the rest of numerical analyses could be conducted.

As a first stage of the research, each individual step of a full Ring Rolling production line - from billet to final product - was analyzed in depth, in order to determine the most important aspects that could affect the dimensions of the final ring product and which could be further optimized. This in depth analysis led to the isolation of three crucial process parameters, namely: (a) the initial volume of the preform, (b) the thermo-elastic deformations of the tools and (c) the positioning of support rolls (estimated through the growth pattern of the ring) and its correlation to the material of the workpiece. Each of these parameters was analyzed and evaluated, while methodologies that would consider and optimize the effects of these parameters on Ring Rolling were also proposed.

The second stage of the conducted research involved potential methods that could "correct" any dimensional imprecisions introduced by Ring Rolling. The answer to this problem came from pottery, in which a reverse radial action can be applied on the clay, in order to reduce its radii. With this practice as the main inspiration, the novel process of "Reverse Ring Rolling" was proposed and further analyzed. When the feasibility of this process was numerically proven, some of its most crucial parameters were further investigated. The final results from these analyses heavily indicated towards the feasibility of this process, with some alternatives setups being proposed. With the completion of the research on "Reverse Ring Rolling", the results from each individual step of both stages could be applied either solely or in combination with one another to an actual Ring Rolling process.

The final stage of the current research involved a proof of concept for a newly proposed seamless polygon production process. Since multiple different simulations were conducted for the current thesis (of the order of magnitude of several hundreds), it is only logical that most of them would result in errors. However, during one of these defective simulations, the systematic production of polygonal workpieces was simulated. This process was then further analyzed, and thus the novel process of Polygonal Ring Rolling was proposed. Although corresponding papers have been found in literature around the same (or at least similar) subject, none of them approached this process in the same way. However, since this process was not relevant to the initial scope of the current dissertation, the conducted analysis was limited to that of a simple proof of concept. Although the feasibility of Polygonal Ring Rolling was mostly proved by the conducted simulations, the author acknowledges the need for a more in depth analysis of this subject.

As an epilogue, the author of the dissertation hopes that some researchers will find the contents of this work useful and will be inspired to further investigate some presented concepts.

6.2 Future Research

The conducted analyses of the current dissertation were (to the author's best ability) investigated as thoroughly as possible. However, each of the presented processes and techniques could be used as a starting point for further investigation. Below, some ideas for future research are presented:

- Since all the presented work was performed solely at a numerical level, due to the lack of the necessary experimental equipment, an experimental validation of the conducted processes could help further validate the current research. Moreover, the imperfections and imbalances that are inherent in real - world processes could be identified and included in the proposed methodologies, thus further refining the corresponding calculations.

- The lack of some necessary parameters or properties for a physics - based simulation of the Ring Rolling process was tackled through trial - and - error in the current analysis. However, and since the most crucial parameters were identified from the conducted models, experimental measurements for these properties could be performed for validation purposes.

- The proposed Ring Rolling modeling methodology was based on experimental results for IN718. Applying the same methodology for other workpiece metals would further validate the presented work.

- The inclusion of material loss in the initial billet calculation is related to certain physical phenomena occurring during the corresponding processes (e.g. scaling). A correlation of the material and physical parameters that govern these phenomena could help identify a methodology for the calculation of a correction factor that could, in turn, be applied to the presented initial billet volume calculation methodology.

- The effects of the tool thermo-elastic behavior on other precision manufacturing process could be further investigated.

- From the conducted analysis, a correlation between the ring growth algorithm and ring's material was identified. A correlation of the aforementioned ring growth algorithm with specific material properties could help establish a more generalized ring growth algorithm that could apply to several metallic materials.

- Although some crucial Reverse Ring Rolling parameters were analyzed in the current research, only a part of the proposed processes has been investigated so far. Additional process parameters and alternatives can be researched in a future work. For example, the application of even lower tool linear velocities (compared to those tested in the current dissertation) in the "four - point pulling" and "cold pulling" processes could be investigated as a potential solution that would render them feasible.

- In the current dissertation, only a brief introduction to Polygonal Ring Rolling was made, with only a single example presented. The author of the current thesis believes that there is a lot of room for further research on this subject.

- The main concept of the entirety of this work was to analyze different pieces of a single high - precision manufacturing process line. The combination of the presented methodologies to a complete manufacturing line simulation can be performed and further refined in a future work.

Appendix A

LS-DYNA Example Keyword File

$# LS-DYNA Keyword file created by LS-PrePost(R) V4.9.6-12Jul2022 $# Created on Jan-5-2023 (09:31:58) *KEYWORD
*TITLE
$# title
LS-DYNA keyword deck by LS-PrePost
*CONTROL_ACCURACY

$#	osu	inn	pisodu	iacc	exacc
	1	3	0	0	0

*CONTROL_CONTACT

$#	slsfac	rwpnal	islchk	shlthk	penopt	thkchg	orien	enmass
	0.1	0.0	1	0	1	0	1	0
$#	usrstr	usrfrc	nsbcs	interm	xpene	ssthk	ecdt	tiedprj
	0	0	0	0	4.0	0	0	0
$#	sfric	dfric	edc	vfc	th	th_sf	pen_sf	
	0.0	0.0	0.0	0.0	0.0	0.0	0.0	
$#	ignore	frceng	skiprwg	outseg	spotstp	spotdel	spothin	
	0	0	0	0	0	0	0.0	
$#	isym	nserod	rwgaps	rwgdth	rwksf	icov	swradf	ithoff
	0	0	1	0.0	1.0	0	0.0	0
$#	shledg	pstiff	ithcnt	tdcnof	ftall	unused	shltrw	igactc
	0	0	0	0	0		0.0	0

$*CONTROL\_HOURGLASS$

$#	ihq	hq
	5	0.01

$*CONTROL\_SOLUTION$

$#	soln	nlq	isnan	lcint	lcacc	ncdcf	nocop
	2	0	0	100	0	1	0

$*CONTROL\_TERMINATION$

$#	endtim	endcyc	dtmin	endeng	endmas	nosol
	45.0	0	0.0	0.0	1.0000+E8	0

$*CONTROL\_THERMAL\_NONLINEAR$

```
$#  refmax    tol   dcp   lumpbc   thlstl   nlthpr   phchpn
      10      0.0   0.5     0       0.0       0       0.0
*CONTROL_THERMAL_SOLVER
$#  atype   ptype   solver        -        gpt   eqheat   fwork   sbc
      1       2       11                   8      1.0      1.0    5.67E-11
$#  msglvl  maxitr  abstol      reltol     omega  unused   unused  tsf
      0      500    1.0000E-10  1.0000E-4  1.0                    1.0
*CONTROL_THERMAL_TIMESTEP
$#  ts  tip   its   tmin   tmax   dtemp   tscp   lcts
    1   0.5   0.0   0.0    0.0    20.0    0.5    0
*CONTROL_TIMESTEP
$#  dtinit   tssfac   isdo   tslimt   dt2ms      lctm   erode   ms1st
      0.0     0.9      0      0.0     4.0000E-6   0      0       0
$#  dt2msf   dt2mslc  imscl  unused   unused     rmscl  emscl   ihdo
      0.0     0        1                          1.0            1
*BOUNDARY_CONVECTION_SET
$#  ssid   pserod
     1       0
$#  hlcid   hmult   tlcid   tmult    loc
      0     0.025     0     293.15    0
      9       0
      ⋮
*BOUNDARY_PRESCRIBED_MOTION_RIGID_ID
$#  id     heading
    1    MR_Rotation
$#  pid   dof   vad   lcid   sf    vid   death        birth
     8     7     0     1     1.0    0    1.0000+E28    0.0
     ⋮
*BOUNDARY_RADIATION_SET
$#  ssid   type
     1      1
$#  rflcid   rfmult       tilcid   timult   loc
     47     5.6704E-11     0       293.15    0
     ⋮
*INTERFACE_SPRINGBACK_LSDYNA
```

$#	psid	nshv	ftype	-	ftensr	nthhsv	rflag	intstrn
	1	100	2		0	100	0	0
$#	optc	sldo	ncyc	fsplit	ndflag	cflag	hflag	
OPTCARD		0		1	0	0		

∗*CONTACT_AUTOMATIC_SURFACE_TO_SURFACE_SMOOTH_THERMAL_FRICTION_ID*

$#	cid	title
	1	*Ring − MR*

$#	ssid	msid	sstyp	mstyp	sboxid	mboxid	spr	mpr
	1	3	0	0	0	0	0	0
$#	fs	fd	dc	vc	vdc	penchk	bt	dt
	0.6	0.5	0.0	0.0	0.0	0	0.0	1.0000E+20
$#	sfs	sfm	sst	mst	sfst	sfmt	fsf	vsf
	1.0	1.0	0.0	0.0	1.0	1.0	1.0	1.0
$#	k	frad	h0	lmin	lmax	ftosa	bc_flg	algo
	0.6	0.0	0.45	0.5	1.0	0.5	1	0
$#	lcfst	lcfdt	formula	a	b	c	d	lch
	0	0	0	0	0	0	0	48
$#	soft	sofscl	lcidab	maxpar	sbopt	depth	bsort	frcfrq
	2	0.1	0	1.2	2.0	5	0	1

∗*SET_SEGMENT_TITLE*
Ring

$#	sid	da1	da2	da3	da4	solver
	1	0.0	0.0	0.0	0.0	MECH

$#	n1	n2	n3	n4	a1	a2	a3	a4
	4711559	4711560	4744393	4744392	0.0	0.0	0.0	0.0
	5039890	5039891	5072724	5072723	0.0	0.0	0.0	0.0
	⋮							

∗*SET_SEGMENT_TITLE*
MR

$#	sid	da1	da2	da3	da4	solver
	3	0.0	0.0	0.0	0.0	MECH

$#	n1	n2	n3	n4	a1	a2	a3	a4
	1882362	1882361	1892505	1892506	0.0	0.0	0.0	0.0
	1872237	1872236	1882380	1882381	0.0	0.0	0.0	0.0
	⋮							

(the rest of contacts and segment sets are defined similarly)

```
*NODE
  $#      nid           x            y          z      tc    rc
       394675       181.5     347.5917      -50.0     0     0
       394676    176.4792     346.9081      -50.0     0     0
       394677    171.0507     345.8385      -50.0     0     0
          ⋮
*DATABASE_BNDOUT
  $#      dt     binary    lcur    ioopt
         0.1          1       0        1
*DATABASE_GLSTAT
  $#      dt     binary    lcur    ioopt
         0.1          1       0        1
*DATABASE_MATSUM
  $#      dt     binary    lcur    ioopt
         0.1          1       0        1
*DATABASE_RBDOUT
  $#      dt     binary    lcur    ioopt
         0.1          1       0        1
*DATABASE_RCFORC
  $#      dt     binary    lcur    ioopt
         0.1          1       0        1
*DATABASE_TPRINT
  $#      dt     binary    lcur    ioopt
         0.1          1       0        1
*DATABASE_BINARY_D3PLOT
  $#      dt      lcdt     beam     npltc     psetid
         0.5         0        0         0          0
  $#   ioopt      rate   cutoff    window       type     pset
           0       0.0      0.0       0.0          0        0
*DATABASE_EXTENT_BINARY
  $#   neiph     neips   maxint    strflg     sigflg    epsflg    rltflg    engflg
           0         0        3         0          1         1         1         1
  $#  cmpflg    ieverp   beamip     dcomp       shge     stssz    n3thdt   ialemat
           0         0        0         1          1         1         2         1
  $# nintsld   pkp_sen     sclp     hydro      msscl     therm    intout    nodout
           0         0      1.0         0          0         2       ALL       ALL
```

$#	dtdt	resplt	neipb	quadsld	cubicsld	deleres
	1	1	0	0	0	

**DEFINE_COORDINATE_SYSTEM_TITLE*
CR1

$#	cid	xo	yo	zo	x1	y1	z1	cidl
	2	-620.8439	0.0	-221.8432	-651.4767	0.0	356.7966	0

$#	xp	yp	zp
	-620.8439	1.0	346.8432

**DEFINE_VECTOR_TITLE*
CR1

$#	vid	xt	yt	zt	xh	yh	zh	cid
	6	0.0	0.0	0.0	1.0	0.0	0.0	1

(the rest of coodinate systems and vectors are defined similarly)

**DEFINE_TABLE_TITLE*

	$#	tbid	sfa	offa
		94	1.0	0.0
	$#		value	lcid
IN718_1173			0.01	70
			0.1	76
			1.0	82
			10.0	88

**DEFINE_CURVE_TITLE*

	$#	lcid	sidr	sfa	sfo	offa	offo	dattyp	lcint
IN718_001_1173		70	0	1.0	1.0	0.0	0.0	0	0

$#	a1	o1
	0.0	308.0551
	0.0057461	317.7656
	⋮	

**DEFINE_TABLE_3D_TITLE*

	$#	tbid	sfa	offa
		98	1.0	0.0
IN718	$#		value	lcid
			1173.15	94
			1223.15	95
			⋮	

(the rest of tables and curves are defined similarly)

**ELEMENT_SOLID*

$#	eid	pid	n1	n2	n3	n4	n5	n6	n7	n8
	1	1	81	655	1051	745	656	656	656	1465
	2	1	745	1051	1052	746	1465	1465	1466	1466
	3	1	746	1052	1053	747	1466	1466	1467	1467
	⋮									

**SET_PART_LIST_TITLE*
Ring_and_tools

$#	sid	da1	da2	da3	da4	solver		
	1	0.0	0.0	0.0	0.0	MECH		
$#	pid1	pid2	pid3	pid4	pid5	pid6	pid7	pid8
	4	9	10	12	14	239	242	

(the rest of part sets are defined similarly)

**INITIAL_TEMPERATURE_SET*

$#	nsid	temp	loc
	1	1290.1	0
	2	573.15	0
	5	1291.17	0

**PART*

$#	title							
	Ring							
$#	pid	secid	mid	eosid	hgid	grav	adpopt	tmid
	4	2	69	0	0	0	0	2

**SECTION_SOLID_TITLE*
Solid

$#	secid	elform	aet	unused	unused	unused	cohoff	gaskeit
	2	2	2				0.0	0.0

**MAT_ELASTIC_VISCOPLASTIC_THERMAL_TITLE*
IN718

$#	mid	ro	e	pr	sigy	alpha	lcss	fail
	69	8.2400E-9	0.0	0.0	0.0	0.0	98	0.0
$#	qr1	cr1	qr2	cr2	qx1	cx1	qx2	cx2
	0.0	0.0	0.0	0.0	0.0	0.0	0.0	0.0
$#	c	p	lce	lcpr	lcsigy	lcr	lcx	lcalph
	0.0	0.0	102	103	108	0	0	99
$#	lcc	lcp	tref	lcfail	nuhis	t1phas	t2phas	tol
	0	0	298.15	0.0				

```
∗HOURGLASS
$#   hgid   ihq   qm     ibq   q1    q2     qb/vdc   qw
     1      5     0.01   0     1.5   0.06   0.1      0.1
∗MAT_THERMAL_ISOTROPIC_TD_LC_TITLE
H13_T
$#   tmid   tro   tgrlc   tgmult   tlat      hlat
     5      0.0   0.0     0.0      1580.15   1.700E+11
$#   hclc   tclc  hchsv   tchsv    tghsv
     44     43
```

(the rest of parts, materials, element types and hourglass algorithms are defined similarly)

```
∗SET_NODE_LIST_TITLE
Tools
$#   sid    da1    da2    da3    da4    solver
     2      0.0    0.0    0.0    0.0    MECH
$#   nid1   nid2   nid3   nid4   nid5   nid6   nid7   nid8
     28421  28422  28423  28424  28425  28426  28427  28428
     28429  28430  28431  28432  28433  28434  28435  28436
     ⋮
*END
```

Appendix B

Python Scripts

B.1 3D Surface Plot Script

```
import matplotlib.pyplot as plt
from matplotlib import cm
from matplotlib.ticker import LinearLocator
import numpy as np
from scipy.interpolate import griddata

#create the first surface
x = np.array([-2, . . . (first parameter values)])
y = np.array([-1, . . . (second parameter values)])
z = np.array([0.5, . . . (third parameter values)])
xv = np.linspace(np.min(x), np.max(x))
yv = np.linspace(np.min(y), np.max(y))
[X, Y] = np.meshgrid(xv, yv)
Z = griddata((x, y), z, (X, Y), method='linear')
fig, ax = plt.subplots(subplot_kw="projection": "3d")
surf = ax.plot_surface(X, Y, Z, cmap='winter', linewidth=0, antialiased=True, alpha = 1,
zorder = 1)
ax.set_zlim(0, 15)
ax.zaxis.set_major_locator(LinearLocator(17))
ax.set_xlim(-1, 1)
ax.xaxis.set_major_locator(LinearLocator(12))
ax.set_ylim(-2, 1)
ax.yaxis.set_major_locator(LinearLocator(11))

ax.xaxis._axinfo["grid"].update("linewidth": .5)

# changing grid lines thickness of Y axis to 1 and color to red
ax.yaxis._axinfo["grid"].update("linewidth": .5, 'color': 'red')

# changing grid lines thickness of Z axis to 1 and color to green
ax.zaxis._axinfo["grid"].update("linewidth": .5, 'color': 'green')

ax.set_xlabel('(first parameter name)')
ax.set_ylabel('(second parameter name)')
ax.set_zlabel('(third parameter name)')
fig.colorbar(surf, shrink=0.6)
plt.show()
```

B.2 Polynomial Function Calculation Script

```
import numpy as np
import warnings
import matplotlib.pyplot as plt
from numpy import poly1d

#calculate the polynomial function that fits to the FEA model edge points

warnings.simplefilter('ignore', np.RankWarning)
x = np.array([10.13251591, . . . (x coordinate of the upset billet peripheral nodes)])
y = np.array([223.6506653, . . . (y coordinate of the upset billet peripheral nodes)])
z: poly1d = np.poly1d(np.polyfit(x, y, 12))
plt.scatter(x, y)
print(z)
plt.show()

#print fitted polynomial function coefficients (adjusted for 12th order polynomial)

a0=np.array(z.coefficients[0])
a1=np.array(z.coefficients[1])
a2=np.array(z.coefficients[2])
a3=np.array(z.coefficients[3])
a4=np.array(z.coefficients[4])
a5=np.array(z.coefficients[5])
a6=np.array(z.coefficients[6])
a7=np.array(z.coefficients[7])
a8=np.array(z.coefficients[8])
a9=np.array(z.coefficients[9])
a10=np.array(z.coefficients[10])
a11=np.array(z.coefficients[11])
a12=np.array(z.coefficients[12])

print(a0, a1, a2, a3, a4, a5, a6, a7, a8, a9, a10, a11, a12)

#define function to calculate adjusted r-squared

def adjR(x, y, degree):
results =
coeffs = np.polyfit(x, y, degree)
p = np.poly1d(coeffs)
yhat = p(x)
ybar = np.sum(y)/len(y)
ssreg = np.sum((yhat-ybar)**2)
sstot = np.sum((y - ybar)**2)
results['r_squared'] = 1- (((1-(ssreg/sstot))*(len(y)-1))/(len(y)-degree-1))

return results

#calculated adjusted R-squared for each order of polynomial function
```

```
print(adjR(x, y, 1))
print(adjR(x, y, 2))
print(adjR(x, y, 3))
print(adjR(x, y, 4))
print(adjR(x, y, 5))
print(adjR(x, y, 6))
print(adjR(x, y, 7))
print(adjR(x, y, 8))
print(adjR(x, y, 9))
print(adjR(x, y, 10))
print(adjR(x, y, 11))
print(adjR(x, y, 12))
```

B.3 Squared Polynomial Function Calculation Script

(The script presented in Appendix B.2) must have been run before the current

```
#calculation of the [y(x)]**2 function and its coefficients ai

z2 = P.polypow(z,2)
z21 = np.poly1d(z2)
print(z21)
print(z2)
```

B.4 Squared Polynomial Function Integral Calculation Script

(The scripts presented in Appendix B.2) and B.3 must have been run before the current

```
#calculation of the polynomial integral and its coefficients bi

z3 = np.polyint(z2)
z31 = np.poly1d(z3)
print(z31)
print(z3)
```

Bibliography

Acar, D. et al. (2018). "Warm Hydromechanical Deep Drawing of AA 5754-O and Optimization of Process Parameters". In: *Journal of Engineering Materials and Technology* 140.1, p. 011012.

Al-Helal, K. et al. (2020). "Melt Conditioned Direct Chill (MC-DC) Casting and Extrusion of AA5754 Aluminium Alloy Formulated from Recycled Taint Tabor Scrap". In: *Materials (Basel)* 13.12, p. 2711.

Al-Mohaileb, M. M. (2000). "Computer Modeling of the Temperature Profile During the Ring Rolling Process". MA thesis. College of Engineering and Technology, Ohio University.

Alexis, J. S. and X. A. Satheesh (2004). "An Analysis on the Parameter Optimization in Ring Rolling Process". In: *Proceedings of the* 10^{th} *International Conference on Metal Forming*, pp. 399–402.

Alfozan, A. and J. S. Gunasekera (2002). "Design of Profile Ring Rolling by Backward Simulation Using Upper Bound Element Technique (UBET)". In: *Journal of Manufacturing Processes* 4 (2), pp. 97–108.

Alkorta, J. et al. (2014). "Reverse vs. Effective Strain in the Ring-Rolling of Superalloy 718". In: *8^{th} International Symposium on Superalloy 718 and Derivatives*. Ed. by E. Ott et al. Wiley-Blackwell, pp. 119–128.

Allegri, G., L. Giorleo, and E. Ceretti (2018). "Ring Rotational Speed Trend Analysis By FEM Approach In A Ring Rolling Process". In: *Proceedings of the 21st International ESAFORM Conference on Material Forming, AIP Conference Proceedings 1960*. AIP Publishing, pp. 040001–1–040001–6. ISBN: 978-0-7354-1663-5. DOI: 10.1063/1.5034855.

— (2019). "Roll Gap per Rotation Optimization in a Radial Ring Rolling Process". In: *Proceedings of the 22nd International ESAFORM Conference on Material Forming, AIP Conference Proceedings 2113*. AIP Publishing, pp. 040008–1–040008–6. ISBN: 978-0-7354-1847-9. DOI: 10.1063/1.5112542.

Allwood, J. M., A. E. Tekkaya, and T. F. Stanistreet (2005a). "The development of ring rolling technology". In: *Steel research* 76.2/3, pp. 111–120.

— (2005b). "The development of ring rolling technology - Part 2: Investigation of process behaviour and production equipment". In: *Steel research* 76.7, pp. 491–507.

Allwood, J. M. et al. (2005). "The Technical and Commercial Potential of an Incremental Ring Rolling Process". In: *CIRP Annals* 54 (1), pp. 233–236.

Anjami, N. and A. Basti (2010). "Investigation of Rolls Size Effects on Hot Ring Rolling Process by Coupled Thermo-Mechanical 3D-FEA". In: *Journal of Materials Processing Technology* 210, pp. 1364–1377.

— (2011). "A Comparison between Isothermal and Coupled Thermo-Mechanical FE Analyses of the Ring Rolling Process". In: *Advances in Materials and Processing Technologies II*. Vol. 264. Advanced Materials Research. Trans Tech Publications, pp. 235–240.

Anton, H. (1984). *Volumes by Cylindrical Shells*. New York: Wiley, pp. 367–373.

Arthington, M. R., J. Havinga, and S. R. Duncan (2020). "Control of Ring Rolling with Variable Thickness and Curvature". In: *International Journal of Material Forming* 13, pp. 161–175.

Arthington, M. R. et al. (2014). "Real-Time Measurement of Ring-Rolling Geometry Using Low-Cost Hardware". In: *2014 UKACC International Conference on Control (CONTROL)*, pp. 603–608.

Arthington, M. R. et al. (2015). "Measurement and Control of Variable Geometry During Ring Rolling". In: *2015 IEEE Conference on Control Applications (CCA)*, pp. 1448–1454.

Arthington, M. R. et al. (2016). "Curvature Control in Radial-Axial Ring Rolling". In: *International Federation of Automatic Control–PapersOnLine* 49 (20), pp. 244–249.

Barve, P. (Feb. 2005). "Special Machines for Forging". In: *Cold and Hot Forging: Fundamentals and Applications*. 1st Edition. ASM International, pp. 143, 144, 146, 147. ISBN: 0-87170-805-1.

Berti, G. A., L. Guagliato, and M. Monti (2015). "Set-Up of Radial-Axial Ring-Rolling Process: Process Worksheet and Ring Geometry Expansion Prediction". In: *International Journal of Mechanical Sciences* 99, pp. 58–71.

Bohdal, Ł. et al. (2022). "Experimental and Numerical Studies of Tool Wear Processes in the Nibbling Process". In: *Materials* 15.1.

Bolin, R. (2005). "Ring Rolling". In: *ASM Handbook, Volume 14A: Metalworking: Bulk Forming*. Ed. by S. L. Semiatin. Vol. 14. ASM Handbooks. ASM International, pp. 142–143, 154. ISBN: 087170708X, 9780871707086.

Boucly, P., J. Oudin, and Y. Ravalard (1988). "Simulation of Ring Rolling with New Wax-Based Model Materials on a Flexible Experimental Machine". In: *Journal of Mechanical Working Technology* 16, pp. 119–143.

Brosius, A., M. Tulke, and C. Guilleaume (2019). "Non-Linear Model-Predictive-Control for Thermomechanical Ring Rolling". In: *XV International Conference on Computational Plasticity. Fundamentals and Applications. COMPLAS 2019*. Ed. by E. Oñate et al. International Centre for Numerical Methods in Engineering (CIMNE), pp. 499–509. ISBN: 978-84-949194-7-3.

Buckingham, R.C. et al. (2016). "The effect of strain distribution on microstructural developments during forging in a newly developed nickel base superalloy". In: *Materials Science and Engineering: A* 654, pp. 317–328.

Burge, D. H. (1996). "Experimental Validation of Roll Force and Profile Fill for a Profile Ring Rolling Computer Model". MA thesis. College of Engineering and Technology, Ohio University.

Büscher, M. and T. Witulski (2018). "Ring Rolling of IN 718 for Critical Engine Applications". In: *Proccedings of the 9th International Symposium on Superalloy 718 and Derivatives: Energy, Aerospace, and Industrial Applications*. Ed. by E. Ott et al. The Minerals, Metals & Materials Series. Springer International Publishing, pp. 1001–1011. ISBN: 978-3-319-89479-9. DOI: 10.1007/978-3-319-89480-5.

Butcher, J. C. (2003). *Numerical Methods for Ordinary Differential Equations*. John Wiley & Sons, Ltd., pp. 45–57. ISBN: 0-471-96758-0.

Caddell, R. M., G. Needham, and W. Johnson (1968). "Yield Strength Variation in Ring-Rolled Aluminum". In: *International Journal of Mechanical Sciences* 10, pp. 749–756.

Casotto, S. et al. (2005). "Thermo-mechanical-metallurgical model to predict geometrical distortions of rings during cooling phase after ring rolling operations". In: *International Journal of Machine Tools and Manufacture* 45 (6), pp. 657–664.

Ceretti, E., C. Giardini, and L. Giorleo (2010). "3D Simulation of a Hot Ring Rolling Industrial Process". In: *International Journal of Material Forming* 3 (Suppl 1), pp. 323–326.

Chaudhury, P. K. and D. Zhao (July 1992). *Atlas of Formability: Inconel 718*. 1450 Scalp Avenue, Johnstown, Pa 15904: National Center for Excellence in Metalworking Technology.

Choi, H. D. and H. S. Cho (1986). "An adaptive controller for ring rolling processes". In: *The Winter Annual Meeting of ASME, Anaheim California, DSC-Vol.* 4, pp. 95–107.

— (1989). "An adaptive control approach to the ring geometry control for radial-axial ring rolling processes". In: *Proceedings of the Institution of Mechanical Engineers, Part C: Journal of Mechanical Engineering Science* 204, pp. 243–254.

Choi, H. D., H. S. Cho, and C. O. Lee (1990). "Application of an Adaptive Control Method to the Guide Roll Force Control for Ring Rolling Processes". In: *IFAC Proceedings Volumes* 23 (8), pp. 335–340.

Cleaver, C. J. and J. M. Allwood (2017). "Incremental Profile Ring Rolling with Axial and Circumferential Constraints". In: *CIRP Annals - Manufacturing Technology* 66, pp. 285–288.

— (2019). "Curvature development in ring rolling". In: *Journal of Materials Processing Technology* 267, pp. 316–337.

Cleaver, C. J., J. Lohmar, and S. Tamimi (2021). "Limits to making L-shape ring profiles without ring growth". In: *Journal of Materials Processing Technology* 292, p. 117062.

Cleaver, C. J. et al. (2016). "Ring Rolling with Variable Wall Thickness". In: *CIRP Annals – Manufacturing Technology* 65, pp. 281–284.

Clough, R. W. (Sept. 1960). "The finite element method in plane stress analysis". In: *Proceedings of the Second ASCE Conference on Electronic Computation*.

Courant, R., K. Friedrichs, and H. Levy (1967). "On the Partial Difference Equations of Mathematical Physics". In: *IBM Journal of Research and Development* 11 (2), pp. 215–234.

Coxeter, H. S. M. (1969). *Introduction to Geometry (2nd Edition)*. John Wiley and Sons, Inc., pp. 26–38.

Das, A. and A. De (2018). "Gas Metal Arc Lap Joining of Aluminum Alloys and Steel Sheets". In: *Journal of Welding and Joining* 36.5, pp. 19–26.

Davey, K. and M. J. Ward (2000). "An efficient solution method for finite element ring-rolling simulation". In: *International Journal for Numerical Methods in Engineering* 47, pp. 1997–2018.

— (2002a). "A Practical Method for Finite Element Ring Rolling Simulation using the ALE Flow Formulation". In: *International Journal of Mechanical Sciences* 44, pp. 165–190.

— (2002b). "The Practicalities of Ring Rolling Simulation for Profiled Rings". In: *Journal of Materials Processing Technology* 125–126, pp. 619–625.

— (2003). "An ALE Approach for Finite Element Ring–Rolling Simulation of the Profiled Rings". In: *Journal of Materials Processing Technology* 139, pp. 559–566.

Deshpande, A. A. et al. (2011). "Combined butt joint welding and post weld heat treatment simulation using SYSWELD and ABAQUS". In: *Proceedings of the Institution of Mechanical Engineers, Part L: Journal of Materials: Design and Applications* 225 (L1), pp. 1–10.

Dewasurendra, L. (1998). "A Finite Element Method for Ring Rolling Processes". PhD thesis. College of Engineering and Technology, Ohio University.

Dolci, S. (2021). "The Influence of Strain Rate, Temperature Effects, and Instabilities in Failure Modeling for Metal Alloys". PhD thesis. George Mason University, Fairfax VA.

Dolci, S. et al. (2016). "Incorporation of Inconel-718 material test data into material mode input parameters for *MAT_224". In: 14^{th} International LS-DYNA Users Conference (Detroit, USA).

Żaba, K. et al. (2021). "Coupled Thermomechanical Response Measurement of Deformation of Nickel-Based Superalloys Using Full-Field Digital Image Correlation and Infrared Thermography". In: *Materials* 14 (2163), pp. 1–32.

Egan, P. F. (1974). *The Cold Roll Forming of Shapes of Revolution With Particular Reference to Ball-Bearing Inner and Outer Races*. Palgrave, London, pp. 759–769. ISBN: 978-1-349-01921-2.

El-Wakil, S.D. (2019). *Processes and Design for Manufacturing, Third Edition (3rd ed.)* CRC Press, pp. 219–220.

Eruç, E. and R. Shivpuri (1992a). “A Summary of Ring Rolling Technology - I. Recent Trends in Machines, Process and Production Lines”. In: *International Journal of Machine Tools and Manufacture* 32 (3), pp. 379–398.

— (1992b). “A Summary of Ring Rolling Technology - II. Recent Trends in Process Modeling, Simulation, Planning, and Control”. In: *International Journal of Machine Tools and Manufacture* 32 (3), pp. 399–413.

Feng, Z. and H. Champliaud (2013). “Modelling and Simulation of Radial Ring Rolling Process Based on Finite Element Analyses”. In: *ASME 2013 Pressure Vessels and Piping Conference, Volume 2: Computer Technology and Bolted Joints*.

— (2014). “Analyses of Profile Radial-Axial Ring Rolling Process Based on Explicit Finite Element Method”. In: *ASME 2014 Pressure Vessels and Piping Conference, Volume 2: Computer Technology and Bolted Joints*.

Ferralloy (n.d.). *5 Surprising Uses for Rolled Rings*. URL: `https://ferralloy.com/tag/rolled-ring/`. (accessed: 28.12.2021).

Ford, H. and J. M. Alexander (1963–64). “Simplified Hot Rolling Calculations”. In: *Journal of the Institute of Metals* 92, pp. 397–404.

Forouzan, M. R., M. Salimi, and M. S. Gadala (2003). “Three-Dimensional FE Analysis of Ring Rolling by Employing Thermal Spokes Method”. In: *International Journal of Mechanical Sciences* 45, pp. 1975–1998.

Forouzan, M. R. et al. (2003). “Guide roll simulation in FE analysis of ring rolling”. In: *Journal of Materials Processing Technology* 142, pp. 213–223.

Franchi, R. et al. (2017). “Ring Rolling Process Simulation for Microstructure Optimization”. In: *AIP Conference Proceedings* 1896.1, 100005:1–7.

Frost, H. J. and M. F. Ashby (1982). *Deformation – Mechanism Maps*. The Plasticity, Creep of Metals, and Ceramics, Pergamon Press, Oxford, pp. 54–55.

Gavalas, E., I. S. Pressas, and S. Papaefthymiou (July 2018). “Mesh Sensitivity analysis on implicit and explicit method for rolling simulation”. In: *International Journal of Structural Integrity* 9 (4), pp. 465–474. DOI: `10.1108/IJSI-07-2017-0046`.

Gellhaus, M. and M. Langejürgen (n.d.). *Induction heating increases productivity during ring rolling*. URL: `https://www.sms-group.com/sms-group-magazine/overview/induction-heating-increases-productivity-during-ring-rolling`. (accessed: 28.12.2021).

Gheisari, A. H., M. R. Forouzan, and A. A. Maracy (2011). “Investigation of Process Parameters on Hot Ring Rolling by Coupled Thermo-Mechanical 3D-FEA”. In: *International Journal of Advanced Design and Manufacturing Technology* 4 (4), pp. 33–38.

Giorleo, L., E. Ceretti, and C. Giardini (2012). “Investigation of the Fishtail Defect in Ring Rolling by a FEM Approach”. In: *Proceedings of NAMRI/SME* 40.

— (2013). “Energy consumption reduction in Ring Rolling processes: A FEM analysis”. In: *International Journal of Mechanical Sciences* 74, pp. 55–64.

Giorleo, L., C. Giardini, and E. Ceretti (2013). “Validation of hot ring rolling industrial process 3D simulation”. In: *International Journal of Material Forming* 6, pp. 145–152.

Gontarz, A. and P. Surdacki (2019). “Investigation of Slip Occurrence in the Ring Rolling Process”. In: *MATEC Web of Conferences, ICMSC 2019* 291 (02006), pp. 1–4.

Greene, G. A., C. C. Finfrock, and T. F. Jr. Irvine (1999). *Dependence of Total Hemispherical Emissivity of Inconel-718 on Surface Oxidation and Temperature*. Brookhaven National Laboratory, Department of Advanced Technology, p. 17.

Group, SMS (n.d.[a]). *Ring and wheel rolling: Top quality for discerning customers*. URL: `https://www.sms-group.com/plants/all-plants/ring-and-wheel-rolling-machines`. (accessed: 28.12.2021).

Group, The Use Less (n.d.[b]). *Flexible Ring Rolling*. URL: `https://www.uselessgroup.org/inventions/flexible-ring-rolling`. (accessed: 28.12.2021).

Guenther, S., G. Schwich, and G. Hirt (2020). "Investigation of bond formation behaviour in composite ring rolling". In: *Journal of Materials Processing Technology* 275, p. 116364.

Guenther, S. et al. (2017). "Investigation of a Composite Ring Rolling Process Considering Bonding Behaviour in FEM and Experiment". In: *Procedia Engineering* 207, pp. 1236–1241.

Guo, L. G. et al. (2004). "Simulation for Guide Roll in 3D-FE Analysis of Cold Ring Rolling". In: *Material Science Forum* 471–472, pp. 760–764.

Guo, L.G. and H. Yang (2011a). "Numerical Modelling and Simulation of Radial-Axial Ring Rolling Process". In: *Numerical Analysis – Theory and Application*. Ed. by Prof. J. Awrejcewicz. InTech, pp. 373–394. ISBN: 978-953-307-389-7.

— (2011b). "Towards a Steady Forming Condition for Radial-Axial Ring Rolling". In: *International Journal of Mechanical Sciences* 53 (4), pp. 286–299.

Guo, W. et al. (2020). "Effects of deformation temperature on the evolution of second-phase and mechanical properties of large 2219 Al-Cu alloy rings". In: *Materials Characterization* 160, p. 110094.

Hadi, M.M., M.M.H. Al-Khafaji, and A.D. Subhi (2022). "A Numerical Study of Friction Stir Welding for AA5754 Sheets to Evaluate Temperature Profile and Plastic Strain". In: *Engineering and Technology Journal* 40.12, pp. 1683–1694.

Hahn, Y. H. and D. Y. Yang (1991). "UBET Analysis of Roll Torque and Profile Formation During the Profile Ring-Rolling of Rings Having Rectangular Protrusions". In: *Journal of Materials Processing Technology* 26, pp. 267–280.

— (1994). "UBET Analysis of the Closed-Pass Ring Rolling of Rings having Arbitrarily Shaped Profiles". In: *Journal of Materials Processing Technology* 40, pp. 451–463.

Hallquist, J. O. (2006). *LS-DYNA – Theory Manual*. Livermore Software Technology Corporation (LSTC), Livermore.

Han, X. and L. Hua (2014). "Effect of Friction on Combined Radial and Axial Ring Rolling Process". In: *Tribology International* 73, pp. 117–127.

Han, X., L. Hua, and S. Yang (2020). "A novel polygonal ring rolling method". In: *Journal of Manufacturing Processes* 59, pp. 389–402.

Han, X. et al. (2014a). "A New Cylindrical Ring Rolling Technology for Manufacturing Thin-Walled Cylindrical Ring". In: *International Journal of Mechanical Sciences* 81, pp. 95–108.

— (2014b). "FE Simulation and Experimental Research on Cylindrical Ring Rolling". In: *Journal of Materials Processing Technology* 214, pp. 1245–1258.

Han, X. et al. (2014c). "Ring blank design and its effects on combined radial and axial ring rolling". In: *International Journal of Advanced Manufacturing Technology* 72, pp. 1161–1173.

Han, X. et al. (2017). "An Innovative Eccentric Ring Rolling Method for Fabricating Eccentric Rings". In: *International Journal of Mechanical Sciences* 120, pp. 120–135.

Harbord, F. W. and J. W. Hall (1904). *The metallurgy of Steel*. Griffin's metallurgical series, Metallurgical series. London: Charles Griffin and company, limited, pp. 326, 397, 435, 458.

Hardwicke, K. and M. Lea, eds. (2019). *Complete Pottery Techniques (1st American Edition)*. Dorling Kindersley Limited, a Division of Penguin Random House LLC, pp. 92–111.

Harewood, F. J. and P. E. McHugh (2007). "Comparison of the implicit and explicit finite element methods for crystal plasticity". In: *Computational Materials Science* 39 (2), pp. 481–494.

Hawkyard, J. B., E. Appleton, and W. Johnson (1973). "An Experimental Wide Ring Rolling Mill of Novel Design". In: *Proceedings of the Thirteenth International Machine Tool Design and Research Conference*. Ed. by S. A. Tobias and F. Koenigsberger. Palgrave, London, pp. 547–553. ISBN: 978-1-349-01857-4.

Hawkyard, J. B. and P. Ingham (1979). "An investigation into Profile Ring Rolling". In: *Proceedings of the* 1^{st} *International Conference on Rotary Metalworking Processes (ROMP), London*, pp. 309–320.

Hawkyard, J. B., F. R. Navaratne, and W. Johnson (Sept. 1975). "Cold Rolling of Ring Gears". In: *Proceedings of the Fifteenth International Machine Tool Design and Research Conference*. Ed. by S. A. Tobias and F. Koenigsberger. Palgrave, London, pp. 507–513. ISBN: 978-1-349-01986-1.

Hawkyard, J. B. et al. (1973). "Analyses for Roll Force and Torque in Ring Rolling, with some Supporting Experiments". In: *International Journal of Mechanical Sciences* 15, pp. 873–893.

Hayama, M. (1982). "Theoretical Analysis on Ring Rolling of Plain Rings". In: *Bulletin of the Faculty of Engineering, Yokohama National University* 31, p. 131.

Hill, R. (1950). *The Mathematical Theory of Plasticity*. Oxford Classic Texts in the Physical Sciences. Oxford University Press, Great Clarendon Street, Oxford, pp. 128–160. ISBN: 0-19-850367-9.

— (1963). "A General Method of Analysis for Metal-Working Processes". In: *Journal of the Mechanics and Physics of Solids* 11, pp. 305–326.

Hu, Z. M. et al. (1994). "Three-dimensional finite-element modelling of ring rolling". In: *Journal of Materials Processing Technology* 45, pp. 143–148.

Hua, L. and J. Deng (2017). "Recent Development of Ring Rolling Theory and Technique". In: *International Journal of Materials and Product Technology* 54.1/2/3, pp. 65–87.

Hua, L., J. Deng, and D. Qian (2015). "Precision Ring Rolling Technique and Application in High-Performance Bearing Manufacturing". In: *MATEC Web of Conferences presented in the* 4^{th} *International Conference on New Forming Technology (ICNFT 2015)* 21, 03002, pp. 1–7.

Hua, L., D.-S. Qian, and L.-B. Pan (2009). "Deformation Behaviors and Conditions in L-Section Profile Cold Ring Rolling". In: *Journal of Materials Processing Technology* 209, pp. 5087–5096.

Hua, L. et al. (2007). "Research on Following Motion Rule of Guide Roller in Cold Rolling Groove Ball Ring". In: *Journal of Materials Processing Technology* 187–188, pp. 743–746.

Hua, L. et al. (2016). "Modeling and Application of Ring Stiffness Condition for Radial-Axial Ring Rolling". In: *International Journal of Machine Tools & Manufacture* 110, pp. 66–79.

Hua, L. et al. (2018). "Effects of Rolling Curve on Recrystallization Evolution during Hot Radial-Axial Ring Rolling of Super Lager Alloy Steel Ring". In: *Procedia Manufacturing* 15. Proceedings of the 17th International Conference on Metal Forming METAL FORMING 2018 September 16 – 19, 2018, Loisir Hotel Toyohashi, Toyohashi, Japan, pp. 72–80.

Huez, J., J.-L. Noyes, and J. Coupu (2001). "Three–Dimensional Finite–Element Simulation of Hot Ring Rolling". In: *Superalloys 718, 625, 706 and Various Derivatives*. Ed. by E. A. Loria. TMS (The Minerals, Metals & Materials Society), pp. 249–258.

Husmann, S. and B. Kuhlenkötter (2016). "Determination of Influencing Factors on Ring Climbing in Radial-Axial Ring Rolling via Design of Experiments". In: *Advanced Materials Research* 1140, pp. 19–26.

— (2017). "Investigation for an Automated Avoidance of Ring Climbing in Radial-Axial Ring Rolling". In: *Procedia Engineering* 207, pp. 1242–1247.

Husmann, T., S. Husmann, and B. Kuhlenkötter (2017). "Online-analysis of process-data to avoid ovality in radial-axial ring rolling process". In: *Proceedings of the 20th International ESAFORM Conference on Material Forming* 1896, pp. 190009–1–190009–6.

Hutcheon, K. F. and J. B. Hawkyard (1984). "Production of Jointless Light Alloy Cycle Wheel Rims by Ring Rolling". In: *Proceedings of the Twenty-Fourth International Machine Tool Design and Research Conference*. Ed. by B. J. Davies. Palgrave, London, pp. 13–18. ISBN: 978-1-349-81247-9.

Iturbe, A. et al. (2017). "Mechanical characterization and modelling of Inconel 718 material behavior for machining process assessment". In: *Materials Science and Engineering: A* 756, pp. 441–453.

Jacquotte, O.-P. (1985). "Stability, Accuracy and Efficiency of some Underintegrated Methods in Finite Element Computations". In: *Computer Methods in Applied Mechanics and Engineering* 50, pp. 275–293.

Jarugula, R. et al. (2020). "High Temperature Deformation Behavior and Constitutive Modeling for Flow Behavior of Alloy 718". In: *Journal of Materials Engineering and Performance* 29, pp. 4692–4707.

Jenkouk, V., G. Hirt, and J. Seitz (2013). "Numerical Simulations Supporting the Process Design of Ring Rolling Processes". In: *AIP Conference Proceedings* 1532, pp. 695–700.

Jenkouk, V. et al. (2012). "Finite Element Analysis of the Ring Rolling Process with Integrated Closed-Loop Control". In: *CIRP Annals - Manufacturing Technology* 61, pp. 267–270.

Jiadong, D. et al. (2020). "An experimental study on a novel constructive hot ring rolling process". In: *Procedia Manufacturing* 50, pp. 134–138.

Johnson, W., I. MacLeod, and G. Needham (1968). "An Experimental Investigation into the Process of Ring or Metal Tyre Rolling". In: *International Journal of Mechanical Sciences* 10, pp. 455–468.

Johnson, W. and G. Needham (1968a). "Experiments on Ring Rolling". In: *International Journal of Mechanical Sciences* 10 (2), pp. 95–113.

— (1968b). "Plastic Hinges in Ring Indentation in Relation to Ring Rolling". In: *International Journal of Mechanical Sciences* 10 (6), pp. 487–490.

Joun, M. S., J. H. Chung, and R. Shivpuri (1998). "An axisymmetric forging approach to perform design in ring rolling using a rigid-viscoplastic finite element method". In: *International Journal of Machine Tools and Manufacture* 38, pp. 1183–1191.

Kang, J. H. (2014). "Research on Filling Limit of Profile Ring Rolling on Circumferential Surface". In: *International Journal of Emerging Technology and Advanced Engineering* 4 (12), pp. 40–45.

Kebriaei, R., J. Frischkorn, and S. Reese (2013). "A New Method of Intelligent Control for System Stabilization in Process-Integrated Powder Coating by Radial Axial Rolling of Rings". In: *Journal of Computational and Applied Mathematics* 246, pp. 301–311.

Kebriaei, R. et al. (2013). "Numerical Modelling of Powder Metallurgical Coatings on Ring-Shaped Parts Integrated with Ring Rolling". In: *Journal of Materials Processing Technology* 213, pp. 2015–2032.

Keenan, J. H., J. Chao, and J. Kaye (1983). *Gas tables: International version second edition (SI units)*. John Wiley and Sons, New York.

Kil, T.-D., J.-M. Lee, and Y.-H. Moon (2014). "Formability Estimation of Ring Rolling Process by Using Deformation Processing Map". In: *Procedia Engineering* 81, pp. 298–303.

— (2015). "Quantitative Formability Estimation of Ring Rolling Process by Using Deformation Processing Map". In: *Journal of Materials Processing Technology* 220, pp. 224–230.

Kim, B.-S. et al. (2013). "A Dual-Mesh Approach to Ring-Rolling Simulation with Emphasis on Remeshing". In: *Journal of Manufacturing Processes* 15, pp. 635–643.

Kim, K.-J. et al. (2007). "Ring-Rolling Process for Manufacturing Ti-6Al-4V Plane and Profiled Ring-Products". In: *Advanced Materials Research* 26-28, pp. 429–432.

Kim, K.-R. and Y.-S. Kim (2015). "Development of the Hot Ring Rolling Processes for Multilayered Ring Parts with a Large Outer Diameter". In: *Journal of the Korea Academia-Industrial cooperation Society* 16 (2), pp. 952–962.

Kim, N., H. Kim, and K. Jin (2012). "Optimal Design to Reduce the Maximum Load in Ring Rolling Process". In: *International Journal of Precision Engineering and Manufacturing* 13 (10), pp. 1821–1828.

Kim, N., S. Machida, and S. Kobayashi (1990). "Ring Rolling Process Simulation by the Three Dimensional Finite Element Method". In: *International Journal of Machine Tools and Manufacture* 30 (4), pp. 569–577.

Kohnke, P., ed. (2009). *Theory Reference for the Mechanical APDL and Mechanical Applications*. ANSYS, Inc.

Komori, Y. et al. (2022). "Fine Piercing of Amorphous Electrical Steel Sheet Stack by Micro-/Nano-Textured Punch". In: *Materials* 15.5, p. 1682.

Koo, S. W. et al. (2003). "Analysis of Aluminium Ring Rolling Process Using Thermo-Rigid-Plastic Finite Element Method". In: *Transactions of the Korean Society of Mechanical Engineers* 27, pp. 815–822.

Koppers, U. (1992). "Optimizing the Ring-Rolling Operation with Process Control". In: *Journal of the Minerals (JOM)* 44 (2), pp. 24–27.

Koppers, U. et al. (1986). "Methods for Reducing Materials and Energy Input in Ring Rolling". In: *Stahl und Eisen* 106 (14–15), pp. 789–795.

Krämer, A.M. et al. (2017). "Online-coupled FE simulation and microstructure prediction for the process chain of an Inconel 718 turbine disk". In: *Proceedings of 7th WGP-Jahreskongress, Aachen*. Ed. by R. Schmitt and G. Schuh. Apprimus Wissenschaftsverlag, Aachen, Germany, pp. 3–10. ISBN: 978-3-86359-620-0.

Kuhlenkötter, B. et al. (2020). "Investigation of compaction by ring rolling on thermal sprayed coatings". In: *Procedia Manufacturing* 50, pp. 192–198.

Kumar, V.P. and A.V. Jebaraj (2021). "Influence of Double Aging Heat Treatment on Phase Transformation and Dimensional Accuracy of Inconel 718 Alloy made Through Laser-Based Additive Manufacturing". In: *Transactions of the Indian Institute of Metals* 74, pp. 3103–3117.

Lafarge, R. et al. (2021). "Data based model predictive control for ring rolling". In: *Production Engineering Research and Development* 15, pp. 821–831.

Leach, S. and B. Dehnert (2013). *Simon Leach's Pottery Handbook*. Ed. by L. Allday. Steward, Tabori and Chang, ABRAMS, New York, pp. 66–76.

Lee, K.-H. and B.-M. Kim (2013). "Advanced Feasible Forming Condition for Reducing Ring Spreads in Radial-Axial Ring Rolling". In: *International Journal of Mechanical Sciences* 76, pp. 21–32.

Lee, K.-H. et al. (2014). "Design Method for Intermediate Roll in Multi-Stage Profile Ring Rolling Process: The Case for Excavator Idler Rim". In: *International Journal of Precision Engineering and Manufacturing* 15 (3), pp. 503–512.

Lee, S.-W. et al. (2017). "Poster: A Study on Cold Ring Rolling of Copper for Fabrication of End Ring's Preform". In: *International Symposium on Green Manufacturing and Applications (ISGMA 2017)*, p. 286.

Li, H.-W., L. Feng, and H. Yang (2013). "Deformation Mechanism of Cold Ring Rolling in View of Texture Evolution Predicted by a Newly Proposed Polycrystal Plasticity Model". In: *Transactions of Nonferrous Metals Society of China* 23, pp. 3729–3738.

Li, L. et al. (2008). "A Control Method of Guide Rolls in 3D-FE Simulation of Ring Rolling". In: *Journal of Materials Processing Technology* 205, pp. 99–110.

Li, L. et al. (2016). "A Quantitive Planning Method of Variable Feed Rates for Cold Profiled Ring Rolling Process". In: *International Journal of Advanced Manufacturing Technology* 86 (9–12), pp. 2585–2593.

Li, X., L. Guo, and F. Wang (2021). "On a plastic instability criterion for ultra-large radial-axial ring rolling process with four guide rolls". In: *Chinese Journal of Aeronautics* 35 (6), pp. 391–406.

Li, X. et al. (2018). "Motion Control of Guide Rolls in Intelligent Simulation for Profiled Ring Rolling Process". In: *Procedia Manufacturing* 15. Proceedings of the 17th International Conference on Metal Forming METAL FORMING 2018 September 16 – 19, 2018, Loisir Hotel Toyohashi, Toyohashi, Japan, pp. 97–104.

Li, X. et al. (2019). "Rolling paths design assisted by target-temperature driven intelligent FE simulation of radial-axial ring rolling". In: *Manufacturing Review* 6 (20), pp. 1–17.

Liang, L. et al. (2018). "Intelligent Simulation for Real-Timely Force-Controlled Radial-Axial Rolling Process of Supersized Aluminium Alloy Rings". In: *Procedia Manufacturing* 15. Proceedings of the 17th International Conference on Metal Forming METAL FORMING 2018 September 16 – 19, 2018, Loisir Hotel Toyohashi, Toyohashi, Japan, pp. 105–112.

Lim, T., I. Pillinger, and P. Hartley (1998). "A Finite-Element Simulation of Profile Ring Rolling Using a Hybrid Mesh Model". In: *Journal of Materials Processing Technology* 80–81, pp. 199–205.

Lin, H. and Z. Z. Zhi (1997). "The Extremum Parameters in Ring Rolling". In: *Journal of Materials Processing Technology* 69, pp. 273–276.

Lin, J. et al. (2013). "The Development of Continuum Damage Mechanics-Based Theories for Predicting Forming Limit Diagrams for Hot Stamping Applications". In: *International Journal of Damage Mechanics* 23.5, pp. 684–701.

Lindgren, L. E. and J. Edberg (1990). "Explicit versus Implicit finite element formulation in simulation of rolling". In: *Journal of Materials Processing Technology* 24, pp. 85–94.

Lisiecki, Ł. et al. (2020). "Numerical modelling of the multi-stage production process of large-size rings rolling for the shipbuilding industry including analysis of internal discontinuities". In: *Procedia Manufacturing* 50, pp. 168–172.

Lohmar, J., C. J. Cleaver, and J. M. Allwood (2020). "The influence of constraint rolls on temperature evolution and distribution in radial ring rolling". In: *Journal of Materials Processing Technology* 282, p. 116663.

LS-DYNA_Support, FAQ (2019). *Mass Scaling*. URL: `https://ftp.lstc.com/anonymous/outgoing/support/FAQ/mass_scaling`. accessed: 07.12.2022.

LS-DYNA Keyword Use's Manual – Volume 1 (2020). Vol. 1. Livermore Software Technology Corporation (LSTC), Livermore.

Lu, J. P. et al. (2011). "Research of Radial-Axial Ring Rolling Process Curve". In: *Manufacturing Process Technology*. Vol. 189. Advanced Materials Research. Trans Tech Publications, pp. 589–594.

Lu, X. et al. (2014). "Stress rupture properties of GH4169 superalloy". In: *Journal of Materials Research and Technology* 3 (2), pp. 107–113.

Lugora, C. F. and A. N. Bramley (1987). "Analysis of Spread in Ring Rolling". In: *International Journal of Mechanical Sciences* 29 (2), pp. 149–157.

Luo, X. et al. (2014). "Effect of driver roll rotational speed on hot ring rolling of AZ31 magnesium alloy". In: *Journal of Magnesium and Alloys* 2 (2), pp. 154–158.

Lv, W. et al. (2021). "Simulation Analysis and Optimization of Rolling Process of Steel Rim". In: *World Journal of Mechanics* 11, pp. 34–51.

Ma, Z. et al. (2021). "Microstructural evolution and enhanced mechanical properties of Mg-Gd-Y-Zn-Zr alloy via centrifugal casting, ring-rolling and aging". In: *Journal of Magnesium and Alloys*.

Magazine, Forge (n.d.). *World's Largest Ring-Rolling Machine for Production of Engine Rings Ordered*. URL: `https://www.forgemag.com/articles/85081-worlds-largest-ring-rolling-machine-for-production-of-engine-rings-ordered`. (accessed: 28.12.2021).

Mamalis, A. G. (1975). “Profile Ring–Rolling”. PhD thesis. University of Manchester Institute of Science and Technology (UMIST).
Mamalis, A. G., J. B. Hawkyard, and W. Johnson (1975). “Cavity Formation in Rolling Profiled Rings”. In: *International Journal of Mechanical Sciences* 17 (8), pp. 669–672.
— (1976). “Spread and Flow Patterns in Ring Rolling”. In: *International Journal of Mechanical Sciences* 18, pp. 11–16.
Mamalis, A. G., W. Johnson, and J. B. Hawkyard (1976a). “Neue Untersuchungen beim Ringwalzen”. In: *Arch. Eisenhuttenwes.* 47 (10), pp. 613–618.
— (1976b). “On the Pressure Distribution between Stock and Rolls in Ring Rolling”. In: *Journal of Mechanical Engineering Science* 18 (4), pp. 184–195.
— (1976c). “Pressure Distribution, Roll Force and Torque in Cold Ring Rolling”. In: *Journal of Mechanical Engineering Science* 18 (4), pp. 196–209.
— (1976d). “Ring–Rolling: Literature Review and Some Recent Experimental Results”. In: *Metallurgia and Metal Forming*, pp. 132–140.
— (1976e). “Untersuchungen über die Breitung und den Werkstoffffluß beim Ringwalzen”. In: *Arch. Eisenhuttenwes.* 47 (10), pp. 619–622.
Mao, X. et al. (2020). “Second phase particles and mechanical properties of 2219 aluminum alloys processed by an improved ring manufacturing process”. In: *Materials Science and Engineering A* 781, p. 139226.
Matsui, T., H. Takizawa, and H. Kikuchi (2004). “Numerical Simulation of Ring Rolling Process for Ni-Base Articles”. In: *Proceedings of the International Symposium on Superalloys*, pp. 907–915.
Meng, W. and G.-Q. Zhao (2014). “Effects of Key Simulation Parameters on Conical Ring Rolling Process”. In: *Procedia Engineering* 81, pp. 286–291.
Meng, W., G.-Q. Zhao, and Y. Guan (2014a). “A Mandrel Feeding Strategy in Conical Ring Rolling Process”. In: *Mathematical Problems in Engineering, Article ID: 364274* 2014, pp. 1–13.
— (2014b). “The Effects of Forming Parameters on Conical Ring Rolling Process”. In: *The Scientific World Journal, Article ID: 235656* 2014.
Michl, D., A. Neumann, and A. Brenner (n.d.). *Ring Rolling Machine Having Device For Ring Manipulation (Pattent No. WO/2021/170550).* URL: `https://patentscope.wipo.int/search/en/detail.jsf?docId=WO2021170550`. (accessed: 28.12.2021).
Michl, D., B. Sydow, and M. Bambach (2020). “Ring rolling of pre-forms made by wire-arc additive manufacturing”. In: *Procedia Manufacturing* 47, pp. 342–348.
Milutinović, M. et al. (2005). “Hot Ring Rolling in Bearing Production”. In: *Journal for Technology of Plasticity* 30 (1–2), pp. 61–74.
Moon, H. K., M. C. Lee, and M. S. Joun (2008). “Predicting polygonal-shaped defects during hot ring rolling using a rigid-viscoplastic finite element method”. In: *International Journal of Mechanical Sciences* 50 (2), pp. 306–314.
Moon, H. K. et al. (2004). “Prediction of Defect Formation in Ring Rolling by the Three-Dimensional Rigid-Plastic Finite Element Method”. In: *Transactions of the Korean Society of Mechanical Engineers A* 28 (10), pp. 1492–1499.
Mori, K.-I. and N. Hiramatsu (2001). “Simplified Three–Dimensional Simulation of Ring Rolling with Grooved Rolls by Rigid–Plastic Finite Element Method Using Generalized Plane–Strain Modeling”. In: *Transactions-North American Manufacturing Research Institution of SME*, pp. 3–8.
Moussa, G. and J. B. Hawkyard (1986). “Investigation into the Multi-Stage Ring Rolling of Aluminum Bicycle Wheel Rims”. In: *International Journal of Mechanical Sciences* 28 (12), pp. 841–851.
Oh, I.-Y. et al. (2018). “Analysis of Defects in L-Section Profile Ring Rolling”. In: *Procedia Manufacturing* 15. Proceedings of the 17th International Conference on Metal Forming

METAL FORMING 2018 September 16 – 19, 2018, Loisir Hotel Toyohashi, Toyohashi, Japan, pp. 81–88.

Oh, S. and H. Ki (2019). "Deep learning model for predicting hardness distribution in laser heat treatment of AISI H13 tool steel". In: *Applied Thermal Engineering* 153, pp. 583–595.

Olovssin, L., K. Simonsson, and M. Unosson (2005). "Selective mass scaling for excplicit finite element analyses". In: *International Journal for Numerical Methods in Engineering* 63 (10), pp. 1436–1445.

Omori, S. et al. (Sept. 1984). "Experiment on Roll Forming for Disk-Shaped Blanks". In: *Proceedings of the 3rd International Conference on Rotary Metalworking Proceses: 8-10 September, 1984, Kyoto, Japan*. Ed. by M. Kobayashi. IFS (Publications) and North Holland, pp. 311–320. ISBN: 978-0-903-60855-8.

Ong, L. I. (1990). "Investigations into profile ring rolling of aluminium alloy bicycle wheel rims through experiments and numerical process simulations". PhD thesis. Brunel University.

Onoda, Y. and T. Nakagawa (Sept. 1984). "Spline and gear forming by expanding type ring rolling". In: *Proceedings of the 3rd International Conference on Rotary Metalworking Proceses: 8-10 September, 1984, Kyoto, Japan*. Ed. by M. Kobayashi. IFS (Publications) and North Holland, pp. 291–300. ISBN: 978-0-903-60855-8.

Paetzold, I. et al. (2018). "Determination of the minimum possible damage due to shear cutting using a multi-stage shear cutting process". In: *IOP Conf. Series: Materials Science and Engineering* 418.012070, pp. 1–8. DOI: 10.1088/1757-899X/418/1/012070.

Park, M. et al. (2016). "Development of L-sectioned ring for construction machines by profile ring rolling process". In: *International Journal of Precision Engineering and Manufacturing* 17 (2), pp. 233–240.

Parvizi, A. and K. Abrinia (2012). "An Upper Bound Analysis of the Ring Rolling Process". In: *Manufacturing Science and Technology, ICMST2011*. Vol. 383. Advanced Materials Research. Trans Tech Publications, pp. 2819–2826.

— (2014). "A Two Dimensional Upper Bound Analysis of the Ring Rolling Process with Experimental and FEM Verifications". In: *International Journal of Mechanical Sciences* 79, pp. 176–181.

Parvizi, A., K. Abrinia, and M. Hamedi (2012a). "A Generalized Three Dimensional Upper Bound Analysis of the Profiled Ring Rolling Process". In: *Steel Research International*, pp. 83–86.

— (2012b). "An Analytical Approach to Ring Rolling Using Modified Slab Analysis". In: *Manufacturing Science and Technology, ICMST2011*. Vol. 383. Advanced Materials Research. Trans Tech Publications, pp. 4634–4641.

Parvizi, A., K. Abrinia, and M. Salimi (2011). "Slab Analysis of Ring Rolling Assuming Constant Shear Friction". In: *Journal of Materials Engineering and Performance* 20 (9), pp. 1505–1511.

Patil, S., F. Baratzadeh, and H. Lankarani (2017). "Preliminary Study on Modeling of the Deformation and Thermal Behavior of FSSW using SPH Approach". In: 11th European LS-DYNA Conference 2017 (Salzburg, Austria).

Pauskar, P. M., K. Sawamiphakdi, and D. Q. Jin (2004). "Static Implicit vs. Dynamic Explicit Finite Element Analysis for Ring Rolling Process Modeling". In: *AIP Conference Proceedings* 712, pp. 412–417.

Peng, W. F. et al. (2017). "A 3D-FEM of Adaptive Movement Control of Guide and Conical Rolls in Ring Rolling Process". In: *International Journal of Advanced Manufacturing Technology* 92.9–12, pp. 3287–3298.

Polutin, P. I. et al. (1972). "Investigation of Spread when Rolling Rings". In: *Izvestiya VUZ "Chernaya Metallurgiya"* 9, p. 69.

Potter, D. M. (1960). *Aircraft Production: The Journal of the Aircraft Manufacturing Industry*. Vol. 22. Aircraft Production. Iliffe., pp. 468–474.

Pressas, I. S., S. Papaefthymiou, and D. E. Manolakos (2022). "Evaluation of the roll elastic deformation and thermal expansion effects on the dimensional precision of flat ring rolling products: A numerical investigation". In: *Simulation Modelling Practice and Theory* 117, p. 102499. DOI: 10.1016/j.simpat.2022.102499.

— (2024). "On the Fundamentals of Reverse Ring Rolling: A Numerical Proof of Concept". In: *Materials* 17 (9), p. 2055. DOI: 10.3390/ma17092055.

Puller, S. (2003). "Simulation des Werkstoffflusses beim Ringwalzen mittels elementarer Plastizitätstheorie". PhD thesis. Fachbereich Maschinenbau, Universität Hannover.

Qi, H. and Y. Li (2017). "Research Status and Developing Trends on the Ring Rolling Process of Profile Ring Parts". In: *Procedia Engineering* 207, pp. 1260–1265.

Qian, D. and Y. Pan (2013). "3D Coupled Macro-Microscopic Finite Element Modelling and Simulation for Combined Blank-Forging and Rolling Process of Alloy Steel Large Ring". In: *Computational Materials Science* 70, pp. 24–36.

Qian, D., Z. Zhang, and L. Hua (2013). "An Advanced Manufacturing Method for Thick-Wall and Deep-Groove Ring – Combined Ring Rolling". In: *Journal of Materials Processing Technology* 213, pp. 1258–1267.

Qian, D. et al. (2017). "Experiment Study on Warm Ring Rolling of 52100 Bearing Steel Coupling Microstructure Spheroidisation". In: *Procedia Engineering* 207, pp. 1224–1229.

Quagliato, L. and G. A. Berti (2016). "Mathematical Definition of the 3D Strain Field of the Ring in the Radial-Axial Ring Rolling Process". In: *International Journal of Mechanical Sciences* 115–116, pp. 746–759.

— (2017). "Temperature Estimation and Slip-Line Force Analytical Models for the Estimation of the Radial Forming Force in the RARR Process of Flat Rings". In: *International Journal of Mechanical Sciences* 123, pp. 311–323.

Rachakonda, S. et al. (1991). "Computer-Aided Process Design for the Manufacture of Rolled Rings". In: *International Journal of Computer Integrated Manufacturing* 4 (2), pp. 97–104.

Ramaprasad, P. (2009). "Finite Element Modeling and Analysis of Cold Ring Rolling". MA thesis. Department of Mechanical Engineering, Wichita State University.

Ranatunga, V. et al. (2004). "Three-Dimensional UBET Simulation Tool for Seamless Ring Rolling of Complex Profiles". In: *Journal of Manufacturing Processes* 6 (2), pp. 179–186.

Rittel, D., L.H. Zhang, and S. Osovski (2017). "The Dependence of the Taylor-Quinney Coefficient on the Dynamic Loading Mode". In: *Journal of Mechanics and Physics of Solids* 107 (Suppl 1), pp. 323–326.

Rodríguez-Millán, M. et al. (2021). "Experimental and Numerical Analysis of Conical Impact on Inconel 718 Plates". In: *Metals* 9.6, pp. 1–12.

Roebuck, B. et al. (2002). "Measurement good practice guide No 3: Measuring flow stress in hot axisymmetric compression tests". In: *Measurement good practice guide No 3*. National Physical Laboratory. Hampton Road, Teddington, Middlesex, UK.

Ryoo, J. S., D. Y. Yang, and W. Johnson (1984). "Ring Rolling; The Inclusion of Pressure Roll Speed for Estimating Torque by Using a Velocity Superposition Method". In: *Proceedings of the Twenty-Fourth International Machine Tool Design and Research Conference*. Ed. by B. J. Davies. Palgrave, London, pp. 19–24. ISBN: 978-1-349-81247-9.

— (1986). "The Influence of Process Parameters on Torque and Load in Ring Rolling". In: *Journal of Mechanical Working Technology* 12, pp. 307–321.

Sahli, M. et al. (2020). "Numerical Investigation on Key Process Parameters Affecting Blanking of Steel Sheet by Using Finite Element Method". In: *Materials Science Forum* 1009, pp. 89–94.

Sahli, M. et al. (2021). "Finite element simulation and experimental investigation of the effect of clearance on the forming quality in the fine blanking process". In: *Microsystem Technologies* 27, pp. 871–881.

Salimi, M. (1988). “Investigations into and rolling of thick and thin walled pro led rings”. PhD thesis. University of Manchester Institute of Science and Technology (UMIST).

Salimi, M. and J. B. Hawkyard (1988). “Forming of Thin V-Section Rings by Ring Rolling”. In: *International Journal of Mechanical Sciences* 30 (7), pp. 517–532.

Schafstall, H. and C. Barth (2010). “An innovate Approach to Automated Simulation of Full 3D Ring Rolling Processes and Other Incremental Forming Processes”. In: *Proceedings of the* 13th *International Conference on Metal Forming "Metal Forming 2010", September 19–22, 2010, Toyohashi, Japan; Steel Research International*. Ed. by K.-I. Mori et al. Vol. 81. 9. Verlag Stahleisen GmbH, Düsseldorf, Germany, pp. 202–205.

Schmied, C. and T. Erhart (2018). “Updated Review of Solid Element Formulations in LS-DYNA”. In: *Deutsches LS-DYNA Forum*.

Schuler, GmbH, ed. (1998). *Metal Forming Handbook*. Springer-Verlag Berlin Heidelberg, p. 27. ISBN: 978-3-642-63763-6.

Schwich, G., V. Jenkouk, and G. Hirt (2016). “Realistic modelling of the tool kinematics of radial-axial ring rolling machines in finite element simulation”. In: *ESAFORM 2016, AIP Conference Proceedings 1769*. AIP Publishing, pp. 130018–1–130018–6. ISBN: 978-0-7354-1427-3. DOI: 10.1063/1.4963537.

Schwich, G. et al. (2014). “Prediction of Microstructure and Resulting Rolling Forces by Application of a Material Model in a Hot Ring Rolling Process”. In: *Metal Forming 2014*. Vol. 622. Key Engineering Materials. Trans Tech Publications, pp. 970–977.

Seitz, J., V. Jenkouk, and G. Hirt (2013). “Manufacturing dish shaped rings on radial-axial ring rolling mills”. In: *Production Engineering - Research and Development* 7, pp. 611–618. DOI: 10.1007/s11740-013-0486-y.

Seitz, J., F. Kordtomeikel, and G. Hirt (2016). “Improvement of the dishing process in ring rolling using conical guide rolls”. In: *Production Engineering Research and Development* 11 (1), pp. 29–39.

Seitz, J. et al. (2016). “Investigation of a Composite Ring Rolling Process by FEM and Experiment”. In: *MATEC Web of Conference* 80, p. 15011.

Shapiro, A. (2012). *Using LS-DYNA for Heat Transfer & Coupled Thermal-Stress Problems*. Livermore Software Technology Corporation, pp. 6–1 –7–48.

Shivpuri, R. and E. Eruç (1993). “Planning and Simulation of the Ring Rolling Process for the Improved Productivity”. In: *International Journal of Machine Tools and Manufacture* 33 (2), pp. 153–173.

Shvets, J. T. and E. P. Dyban (1964). “Contact Heat Transfer Between Plane Metal Surface”. In: *International Chemical Engineering* 4 (4), p. 621.

Silveira, R. A. M., W. L. A. Pereira, and P. B. Gonalves (2008). “Nonlinear analysis of structural elements under unilateral contact constraints by a Ritz type approach”. In: *International Journal of Solids and Structures* 45 (9), pp. 2629–2650.

Song, J. L. et al. (2002). “Coupled Thermo–Mechanical Finite–Element Modelling of Hot Ring Rolling Process”. In: *Journal of Materials Processing Technology* 121, pp. 332–340.

Special_Metals_Corp. (2020). “Inconel alloy 718. Publication No. SMC-045, Huntington, WV”. In: pp. 1–2. accessed: 16.06.2022.

Stanistreet, T. F., J. M. Allwood, and A. M. Willoughby (2006). “The design of a flexible model ring rolling machine”. In: *Journal of Materials Processing Technology* 177, pp. 630–633.

Sun, B., J. Xu, and C. Xing (2018). “Numerical and experimental investigations on the effect of mandrel feeding speed for high-speed rail bearing inner ring”. In: *International Journal of Advanced Manufacturing Technology* 100, pp. 1993–2006.

Sun, J. S., K. H. Lee, and H. P. Lee (2000). “Comparison of implicit and explicit finite element methods for dynamic problems”. In: *Journal of Materials Processing Technology* 105 (1-2), pp. 110–118.

Swift, K.G. and J.D. Booker (2013). "Chapter 4 - Forming Processes". In: *Manufacturing Process Selection Handbook*. Ed. by K.G. Swift and J.D. Booker. Oxford: Butterworth-Heinemann, pp. 93–140. ISBN: 978-0-08-099360-7. DOI: `https://doi.org/10.1016/B978-0-08-099360-7.00004-5`.

Szabo, Z. J. and E. Dittrich (1996). "Manufacturing systems for the production of seamless-rolled rings". In: *Journal of Materials Processing Technology* 60, pp. 67–72.

Tang, X. et al. (2017). "Study on the microstructure evolution during radial-axial ring rolling of IN178 using a unified internal state variable material model". In: *International Journal of Mechanical Sciences* 128–129, pp. 235–252.

Teja, P. S. et al. (2019). "Simulation and Optimization Studies on the Ring Rolling Process Using Steel and Aluminum Alloys". In: *Journal of Engineering Sciences* 6 (2), E36–E40.

Thomas, A. et al. (2006). "High Temperature Deformation of Inconel 718". In: *Journal of Materials Processing Technology* 177 (1), pp. 469–472.

Tiedemann, I. et al. (2007). "Material flow determination for radial flexible profile ring rolling". In: *Production Engineering Research and Development* 1, pp. 227–232.

Tolcha, M. A. and H. G. Lemu (2019). "Modeling Thermomechanical Stress with H13 Tool Steel Material Response for Rolling Die under Hot Milling". In: *Metals* 9 (5), p. 495.

Touloukian, Y. S., P. E. Liley, and S. C. Saxena (Jan. 1970). "Thermophysical properties of matter - the TPRC data series. Volume 3. Thermal conductivity - nonmetallic liquids and gases. (Reannouncement). Data book".

Touloukian, Y. S., S. C. Saxena, and P. Hestermans (Jan. 1975). "Thermophysical properties of matter - the TPRC data series. Volume 11. Viscosity. (Reannouncement). Data book".

Traoré, K. F., P. Montmitonnet, and M. Souchet (2000). "Parallel Finite Element Modelling of the Ring Rolling Process Using a Quasi Eulerian Description". In: *European Congress on Computational Methods in Applied Sciences and Engineering (ECCOMAS)*, pp. 1–20.

Tszeng, T. C. and T. Altan (1991). "Investigation of Ring Rolling by Pseudi Plane-Strain FEM Analysis". In: *Journal of Materials Processing Technology* 27, pp. 151–161.

Uchibori, T., R. Matsumoto, and H. Utsunomiya (2018). "Peripheral Speed of Steel Ring during Hot Ring Rolling". In: *Procedia Manufacturing* 15. Proceedings of the 17th International Conference on Metal Forming METAL FORMING 2018 September 16 – 19, 2018, Loisir Hotel Toyohashi, Toyohashi, Japan, pp. 89–96.

Uddeholm (2020). *Uddeholm Orvar Supreme, Edition 11*, p. 4.

Utsunomiya, H. et al. (2002). "Elastic–Plastic Finite Element Analysis of Cold Ring Rolling Process". In: *Journal of Materials Processing Technology* 125–126, pp. 613–618.

Vimalnathan, S. and L. Mears (2010). "Finite Element Simulation of Ring Rolling Process". In: *SAE Technical Paper*.

Wang, C. (2016). "Simulation of Damage Evolution during Hot Ring Rolling". PhD thesis. University of Twente. ISBN: 978-94-91909-35-1.

Wang, C., H. Geijselaers, and T. Van den Boogaard (2013). "Multi–Stage FE Simulation of Hot Ring Rolling". In: *AIP Conference Proceedings* 1532, pp. 1014–1019.

Wang, C. et al. (2014a). "Influence of Feed Rate on Damage Development in Hot Ring Rolling". In: *Procedia Engineering* 81, pp. 292–297.

Wang, C. et al. (2016). "Influence of ring growth rate on damage development in hot ring rolling". In: *Journal of Materials Processing Technology* 227, pp. 268–280.

Wang, M. (2011). "Comparison of Evolution Laws of Stress and Strain Fields in Hot Rolling of Titanium Alloy Large Rings with Different Sizes". In: *Transactions of Nonferrous Metals Society of China* 21, pp. 1611–1619.

Wang, M., H. Yang, and L. G. Guo (2012). "Numerical Study on Motions of Rolls in Hot Rolling of Titanium Alloy Large Rings". In: *Rare Metal Materials and Engineering* 41 (1), pp. 0014–0018.

Wang, M. et al. (2006). "Dynamic Explicit FE Modeling of Hot Ring Rolling Process". In: *Transactions of Nonferrous Metals Society of China* 16, pp. 1274–1280.

Wang, M. et al. (2009). "Analysis of Coupled Mechanical and Thermal Behaviors in Hot Rolling of Large Rings of Titanium Alloy Using 3D Dynamic Explicit FEM". In: *Journal of Materials Processing Technology* 209, pp. 3384–3395.

Wang, M. et al. (2013). "Microstructure evolution modeling of titanium alloy large ring in hot ring rolling". In: *International Journal of Advanced Manufacturing Technology* 66, pp. 1427–1437.

Wang, X. and L. Hua (2011). "Analysis of Guide Modes in Vertical Hot Ring Rolling and their Effects on the Ring's Dimensional Precision Using FE Method". In: *Journal of Mechanical Science and Technology* 25 (3), pp. 655–662.

— (2013). "Modeling of on-line measurement for rolling the rings with blank size errors in vertical hot ring rolling process". In: *International Journal of Advanced Manufacturing Technology* 68, pp. 257–262.

Wang, X. et al. (2014b). "Numerical Simulation and Experimental Study on Geometry Variations and Process Control Method of Vertical Hot Ring Rolling". In: *International Journal of Advanced Manufacturing Technology* 73, pp. 389–398.

Wang, Z. W. et al. (2007). "The key technology and realization of virtual ring rolling". In: *Journal of Materials Processing Technology* 182 (1-3), pp. 374–381.

Wang, Z. W. et al. (2010). "Complete Modeling and Parameter Optimization for Virtual Ring Rolling". In: *International Journal of Mechanical Sciences* 52, pp. 1325–1333.

Weber, K. H. (1959). "Das Walzen von Ringen und der Aufbau der Ringwalzwerke". In: *Stahl und Eisen* 79, pp. 1912,1923.

Wu, Q. et al. (2019). "Analysis and homogenization of residual stress in aerospace ring rolling process of 219 aluminum alloy using thermal stress relief method". In: *International Journal of Mechanical Sciences* 157–158, pp. 111–118.

Xiaotao, G. and Y. Fan (2012). "Research of PEEQ for Conical Ring with Outer Steps Ring Rolling". In: *Physics Procedia* 25, pp. 257–261.

Xie, C. et al. (2000). "Rigid-Viscoplastic Dynamic Explicit FEA of the Ring Rolling Process". In: *Internation Journal of Machine Tools & Manufacture* 40, pp. 81–93.

Xu, S. G., J. C. Lian, and J. B. Hawkyard (1991). "Simulation of Ring Rolling Using a Rigid-Plastic Finite Element Model". In: *International Journal of Mechanical Sciences* 33 (5), pp. 393–401.

Xu, S. G. et al. (1997). "Simulation of the Hot Ring Rolling Process by Using a Thermo-Coupled Three-Dimensional Rigid-Viscoplastic Finite Element Method". In: *Journal of Manufacturing Science and Engineering* 119, pp. 542–549.

Xu, W. et al. (2012). "A New Mathematical Model for Predicting for Predicting the Diameter Expansion of Flat Ring in Radial-Axial Ring Rolling". In: *International Journal of Advanced Manufacturing Technology* 60 (9–12), pp. 913–921.

Xu, W. et al. (2014). "Quantitative Design Methodology for Flat Ring Rolling Process". In: *Procedia Engineering* 81, pp. 280–285.

Xu, W. et al. (2015). "Feeding Interval Design Considering Multiconstraints in Flat Ring Rolling Process". In: *International Journal of Advanced Manufacturing Technology* 81 (1–4), pp. 219–229.

Yan, F.-L., L. Hua, and Y.-Q. Wu (2007). "Planning Feed Speed in Cold Ring Rolling". In: *International Journal of Machine Tools & Manufacture* 47, pp. 1695–1701.

Yanagimoto, J. and M. Kiuchi (1989). "Composite Numerical Method for Ring Rolling Analysis". In: *Proceedings of the* 40^{th} *Japanese Joint Conference for Technology of Plasticity*, pp. 377–380.

Yang, D. Y. and K. H. Kim (1988). "Rigid - Plastic Finite Element Analysis of Plane Strain Ring Rolling". In: *International Journal of Mechanical Sciences* 30 (8), pp. 571–580.

Yang, D. Y., K. H. Kim, and J. B. Hawkyard (1991). "Simulation of T-Section Profile Ring Rolling by the 3-D Rigid-Plastic Finite Element Method". In: *International Journal of Mechanical Sciences* 33 (7), pp. 541–550.

Yang, D. Y. and J. S. Ryoo (1987). "An Investigation into the Relationship between Torque and Load in Ring Rolling". In: *Journal of Engineering for Industry* 190 (3), pp. 190–196.

Yang, D. Y. et al. (1981). "Analysis of Roll Torque in Profile Ring-Rolling of L-Sections". In: *Proceedings of the Twenty-First International Machine Tool Design and Research Conference*. Ed. by J. M. Alexander. Swansea : Department of Mechanical Engineering, University College of Swansea in association with Macmillan, pp. 69–74. ISBN: 978-1-349-05861-7.

Yang, D. Y. et al. (1984). "Development of a New Computer-Aided Manufacturing System for the Hot Ring-Rolling Process". In: *Proceedings of the* 3*rd* *International Conference on Rotary Metalworking Processes (ROMP), Kyoto*, pp. 229–238.

Yang, H., L. Guo, and M. Zhan (2005). "Role of Friction in Cold Ring Rolling". In: *Journal of Materials Science & Technology* 21 (6), pp. 914–920.

Yang, H. et al. (2006). "Research on the influence of material properties on cold ring rolling processes by 3D-FE numerical simulation". In: *Journal of Materials Processing Technology* 177, pp. 634–638.

Yea, Y. et al. (2003). "Prediction of Spread, Pressure Distribution and Roll Force in Ring Rolling Process Using Rigid-Plastic Finite Element Method". In: *Journal of Materials Processing Technology* 140, pp. 478–486.

Yeom, J.-K. et al. (2014). "Ring-Rolling Design of Yaw Ring for Wind Turbines". In: *Metals and Materials International* 20 (3), pp. 521–526.

Yovanovich, M.M. (n.d.). "Thermal Interface (Joint) Conductance and Resistance". In: *University of Waterloo. ECE 309: Introduction to Thermodynamics and Heat Transfer Course Notes* (), pp. 19–26.

Yun, J. S. and H. S. Cho (1985). "A Suboptimal Design Approach to the Ring Diameter Control for Ring Rolling Processes". In: *Journal of Dynamic Systems, Measurement, and Control* 107, pp. 207–212.

Zamani, M. R. (2014). "New Method of Determination for Pressure and Shear Frictions in the Ring Rolling Process as Analytical Functions". In: *Journal of Solid Mechanics* 6 (3), pp. 322–333.

Zhang, Y. et al. (2019). "The dynamic position compensation method of the online laser detection system for the ring workpiece". In: *Measurement* 135, pp. 555–564.

Zhao, Y. and D. Qian (2010). "Effect of Rolling Ratio on Groove-Section Profile Ring Rolling". In: *Journal of Mechanical Science and Technology* 24 (8), pp. 1679–1687.

Zhou, G., L. Hua, and D. S. Qian (2011). "3D Coupled Thermo-Mechanical FE Analysis of Roll Size Effects on the Radial-Axial Ring Rolling Process". In: *Computational Materials Science* 50, pp. 911–924.

Zhou, G., W. Wei, and Q. Liu (2020). "Infuence of Plastic Deformation on Microstructural Evolution of 100Cr6 Bearing Ring in Hot Ring Rolling". In: *Materials* 13 (19), p. 4355.

Zhou, G. et al. (2012). "Effects of Axial Rolls Motions on Radial-Axial Rolling Process for Large-Scale Alloy Steel Ring with 3D Coupled Thermo-Mechanical FEA". In: *International Journal of Mechanical Sciences* 59, pp. 1–7.

Zhou, J. et al. (2011a). "Study on Forming Defects in the Rolling Process of Large Aluminum Alloy Ring via Adaptive Controlled Simulation". In: *International Journal of Advanced Manufacturing Technology* 55, pp. 95–106.

— (2011b). "Study on forming defects in the rolling process of large aluminum alloy ring via adaptive controlled simulation". In: *International Journal of Advanced Manufacturing Technology* 55, pp. 95–106.

Zhu, S. et al. (2012). "Investigation of Deformation Degree and Initial Forming Temperature Dependences of Microstructure in Hot Ring Rolling of TA15 Titanium Alloy by Multi-Scale Simulations". In: *Computational Materials Science* 65, pp. 221–229.

Zhu, S. et al. (2014). "Research on the Effects of Coordinate Deformation on Radial-Axial Ring Rolling Process br FE simulation Based on In-Process Control". In: *International Journal of Advanced Manufacturing Technology* 72 (1–4), pp. 57–68.

Zhu, X. et al. (2016a). "Effects of Blank Dimension on Forming Characteristics During Conical-Section Ring Rolling of Inco718 Alloy". In: *International Journal of Advanced Manufacturing Technology* 84, pp. 2707–2718.

Zhu, X. et al. (2016b). "Optimization on Cooperative Feed Strategy for Radial-Axial Ring Rolling Process of Inco718 Alloy by RSM and FEM". In: *Chinese Journal of Aeronautics* 29 (3), pp. 831–842.

Zienkiewicz, O. C., R. L. Taylor, and J. Z. Zhu (2013). *The Finite Element Method: Its Basis and Fundamentals* [7th. Edition]. Butterworth-Heinemann.

Zuo, Z. J., X. Tan, and Y. Li (2011). "Design on Thin Ring Rolling Machine with Fixed Driven Rollers". In: *Applied Mechanics and Materials* 44–47, pp. 436–440.

Ioannis **Pressas**

Profile

Innovative and passionate **mechanical engineer** with a keen interest in numerical simulation, programming, data analysis and problem-solving. Possessing a high expertise in ANSYS and LS-DYNA simulation softwares, I have simulated a wide variety of industrial applications and processes, mainly around the thermo-mechanical response of manufacturing and structural systems. Proficient in Python programming, I have successfully developed many code scripts, while lately I am training on Neural Network development with TensorFlow. I demonstrate strong problem-solving skills with the aim of tackling industrial problems and improving system performance.

Contact details

@ johnpressas@gmail.com

+30 698 304 7885

github.com/Agamemnon-Kanenas

72^{nd} Dim. Gounari, Peristeri 121 31, GR

Personal information

Citizenship: **Greece**

Family: **Married with one child**

Languages:

- **Greek** (native)
- **Engish** (C2)
- **French** (A1)
- **Japanese** (N4)

Skills

- Python, C++, C, Fortran 77
- Matlab, PyCharm, Jupyter Notebook, Anaconda
- MS Office Suite, MS Project
- AutoCAD, SolidWorks, SpaceClaim
- ANSYS, LS-DYNA

Experience

Senior Engineer at *ELKEME S.A.*. **2016–Present**

◇ Numerical simulations regarding a large variety of industrial problems, applications and manufacturing systems. R&D on the optimization of existing industrial processes.

Private Tutor. *Math, Physics and Chemistry (Middle and High School).* **2012–2016**

◇ Provided tutoring in middle and high school students in Math, Physics and Chemistry.

Seasonal Worker at *"Apollonas" Book Distribution Warehouse.* **2006–2007**

◇ Preparation and sending of book orders, during high season.

Education

Ph.D. in Mechanical Engineering School of Mechanical Engineering. *National Technical University of Athens.* **2012–Present**

◇ Thesis title: *Manufacturing of Advanced Materials: Simulation of High Precision Ring Rolling via Finite Element Analysis*

◇ Numerical analysis and optimization of a hot ring rolling process, in order to increase the dimensional precision of the manufactured products. Development of novel practices and methods that can adjust dimensional imperfections. Novel approach to polygonal ring rolling process.

Master in Mechanical Engineering. School of Mechanical Engineering. *National Technical University of Athens.* **2006–2011**

◇ 5-year degree in Mechanical Engineering (300 credit units).

Additional education

Certificate of Proficiency in the Python Programming Language - PCEP. *Python Institute* **2021**

◇ Basic Programming Concepts, Techniques and Best Practices; Data Types, Evaluations and Basic Input-Output Operations; Flow Control: Loops, and Conditional Blocks; Data Collections: Lists, Tuples, and Dictionaries; Functions

Introductory training on OrcaFlex software. *Orcina* **2018**

◇ Simulate the global response of naval and submarine systems and structures

Introductory training on UFlex software. *SINTEF* **2018**

◇ Estimate the structural response of complex, submarine cable structures.

Adobe Rich Media Communication Flash 8. *Adobe* **2008**

◇ Rich media website development

Hobbies

Crafting: STEM, metalcrafting, woodcrafting, electronics.

Tinkering: Fixing simple and complex machines.

Music: Piano, keyboards and listening to it.

Other: Reading, playing with my child, video games.

Εκτεταμένη Περίληψη

Διαμορφωσιμότητα Προηγμένων Υλικών:
Προσομοίωση Έλασης Δακτυλίων Υψηλής Ακρίβειας με Ανάλυση Πεπερασμένων Στοιχείων

Ιωάννης Πρέσσας, Ph.D.

Περίληψη

Η παρούσα έκθεση αποτελεί την εκτεταμένη περίληψη της διδακτορικής διατριβής με τίτλο: *"Διαμορφωσιμότητα Προηγμένων Υλικών: Προσομοίωση Έλασης Δακτυλίων Υψηλής Ακρίβειας με Ανάλυση Πεπερασμένων Στοιχείων"*, η οποία εκπονήθηκε από τον υποψήφιο διδάκτορα Ιωάννη Πρέσσα. Η εκπονηθείσα έρευνα περιστρέφεται γύρω από μεθόδους και παραμέτρους, οι οποίες μπορούν να αυξήσουν τη διαστασιακή ακρίβεια των προϊόντων της κατεργασίας έλασης δακτυλίων. Η έλαση δακτυλίων θεωρείται ευρέως ως μία κατεργασία ημι-τελικών προϊόντων, εξαιτίας των τραχέων και σχετικά ανακριβών τελικών εργοτεμαχίων, τα οποία χρήζουν περαιτέρω επεξεργασίας προκειμένου να επιτευχθεί η επιθυμητή ακρίβεια στις διαστάσεις τους. Για τον λόγο αυτό, και ελλείψει διάταξης για τη διεξαγωγή πειραματικής διερεύνησης, αρχικά αναπτύχθηκε και πιστοποιήθηκε ένα αριθμητικό μοντέλο πεπερασμένων στοιχείων μιας εν θερμώ έλασης δακτυλίων, βασισμένο σε δεδομένα που βρέθηκαν στη βιβλιογραφία. Για το συγκεκριμένο αριθμητικό μοντέλο, χρησιμοποιήθηκε το εμπορικό λογισμικό πεπερασμένων στοιχείων ANSYS/LS-DYNA. Έπειτα, το μοντέλο πεπερασμένων στοιχείων που αναπτύχθηκε, χρησιμοποιήθηκε ως βάση για την αριθμητική διερεύνηση μεθόδων και των παραμέτρων, με σκοπό την αύξηση της ακρίβειας της κατεργασίας. Τα κύρια στοιχεία μελέτης ήταν: (α) ο ορθότερος υπολογισμός του αρχικού όγκου του εργοτεμαχίου, (β) η επίδραση των θερμο-ελαστικών παραμορφώσεων των εργαλείων και (γ) η επίδραση της κινηματικής των υποστηρικτικών ραούλων, συναρτήσει του υλικού του δακτυλίου. Ιδιαίτερη έμφαση δόθηκε, επίσης, και στην ανάπτυξη μιας νέας κατεργασίας, η οποία μπορεί να πραγματοποιηθεί απευθείας μετά το πέρας μιας τυπικής έλασης δακτυλίων, με σκοπό τη "διόρθωση" διαστασιακών σφαλμάτων, χωρίς να υπάρχει ανάγκη απομάκρυνσης ή/και επανατοποθέτησης του κατεργαζόμενου τεμαχίου. Τέλος, διερευνήθηκε εν είδει απόδειξης της ιδέας (proof of concept), μια νέα προσέγγιση για την κατεργασία πολυγωνικών τεμαχίων, με χρήση μιας τυπικής διάταξης έλασης δακτυλίων.

Λέξεις Κλειδιά: Έλαση δακτυλίων, ANSYS/LS-DYNA, Κατεργασία Υψηλής Ακριβείας, Προετοιμασία Μπιγιέτας, Θερμο-ελαστικές Παραμορφώσεις Εργαλείων, Αντίστροφη Έλαση Δακτυλίων, Έλαση Πολυγωνικών Τεμαχίων

1. Εισαγωγή

Η κατεργασία της έλασης δακτυλίων είναι μια κατεργασία διαμόρφωσης υλικού, η οποία εφαρμόζεται για την παραγωγή εκ περιστροφής προϊόντων, χωρίς ραφή σε κάποιο σημείο. Οι διατομές των εν λόγω προϊόντων μπορούν να έχουν ποικιλία ως προς τη μορφή τους. Ως κατεργασία, η έλαση δακτυλίων μπορεί να πραγματοποιηθεί και εν ψυχρώ και εν θερμώ, με έναν συνδυασμό των δύο να εφαρμόζονται συνήθως στον ίδιο κύκλο παραγωγής, προκειμένου να αυξηθεί η ποιότητα των τελικών προϊόντων. Με βάση την επιθυμητή γεωμετρία των προϊόντων, καθορίζεται η γεωμετρία και ο αριθμός των εργαλείων της διάταξης, αν και η γενικότερη κινηματική τους δε μεταβάλλεται σημαντικά. Επιπλέον, οι κρίσιμες παράμετροι της κατεργασίας καθορίζονται σε μεγάλο βαθμό από το υλικό και την πολυπλοκότητα των παραγόμενων προϊόντων. Μια τυπική διάταξη έλασης δακτυλίων παρουσιάζεται στο Σχ.1:

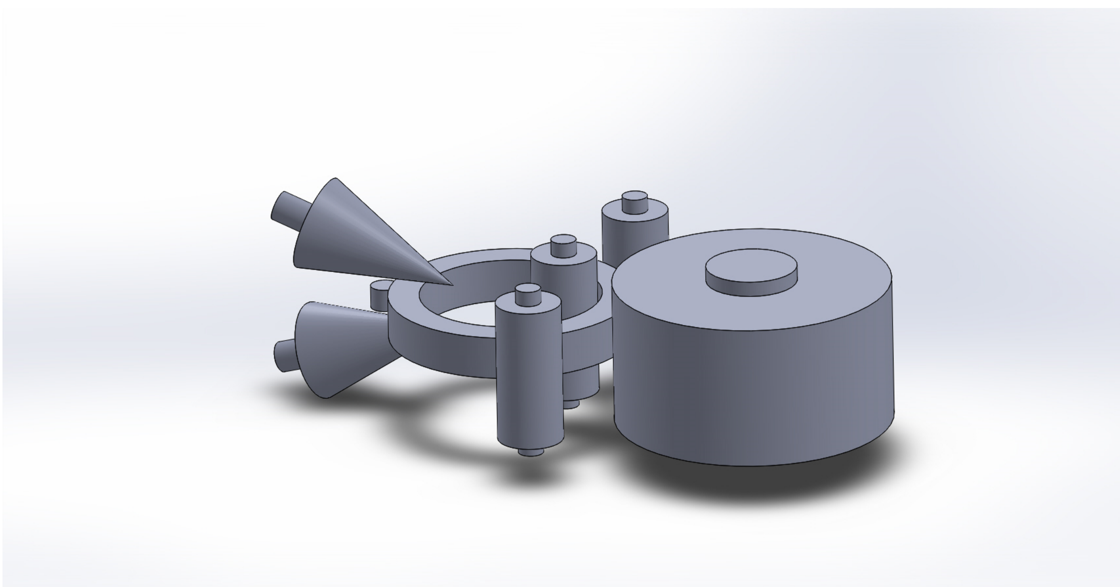

Σχήμα 1: Τυπική διάταξη έλασης δακτυλίων ορθογωνικής διατομής

Οι φάσεις μιας τυπικής κατεργασίας έλασης δακτυλίων παρουσιάζονται στο Σχ.2 (**Yun and Cho, 1985**):

Στο Σχ.2 διακρίνονται τέσσερις διαφορετικές φάσεις της κατεργασίας. Οι διαφορές που παρατηρούνται στις εν λόγω φάσεις, συνοψίζονται παρακάτω:

- Στην *1η Φάση (στάδιο εγκλωβισμού εργοτεμαχίου)*, το μαντρέλ ξεκινά να κινείται προς το κυρίως ράουλο με σταθερή ταχύτητα, ενώ το κυρίως ράουλο ξεκινά να περιστρέφεται με σταθερή επιτάχυνση μέχρι να φτάσει την τελική γωνιακή του ταχύτητα. Εφόσον η

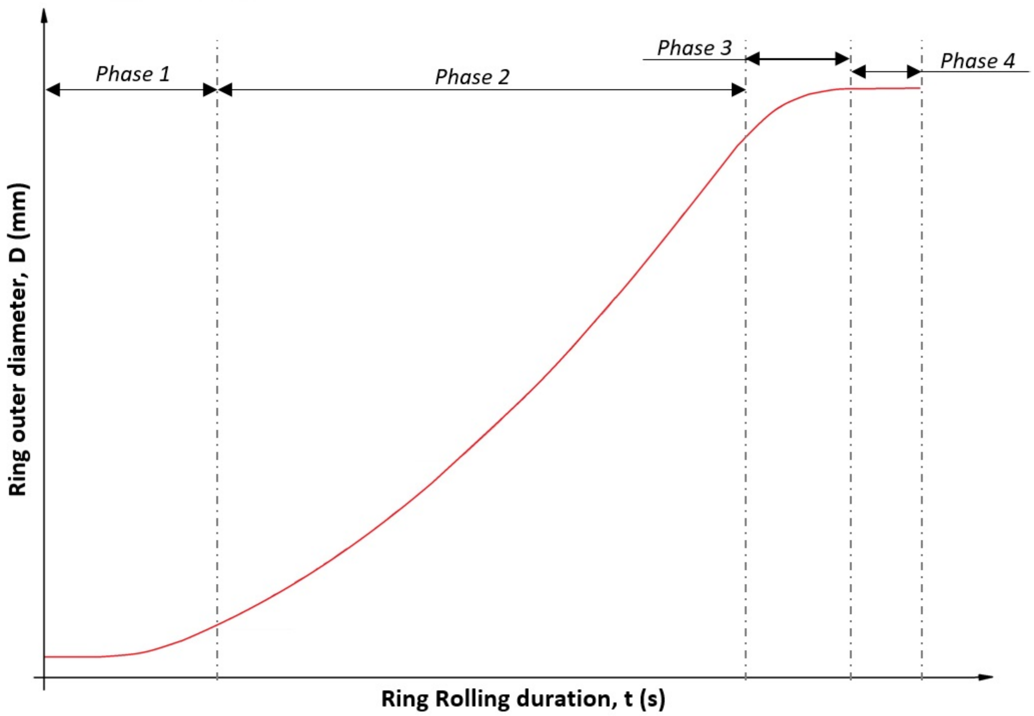

Σχήμα 2: Φάσεις μιας τυπικής κατεργασίας έλασης δακτυλίων

γραμμική ταχύτητα του μαντρέλ είναι σχετικά μικρή, η αύξηση της εξωτερικής διαμέτρου του δακτυλίου σε αυτήν τη φάση δεν είναι πολύ μεγάλη (σε σύγκριση με αυτήν του τελικού τεμαχίου). Επιπλέον, τα κωνικά ράουλα ξεκινούν την καθοδική τους κίνηση, προκειμένου να μειωθεί το ύψος του δακτυλίου. Η συνολική διάρκεια της *1ης Φάσης* εξαρτάται από τη διάταξη και το αρχικό εργοτεμάχιο (γεωμετρία και υλικό), αφού η μάζα των εργαλείων και η αρχική απόσταση που πρέπει να καλύψει το μαντρέλ, μπορεί να ποικίλουν σημαντικά.

- Στη *2η Φάση (στάδιο σταθερής παραμόρφωσης)*, όλα τα εργαλεία έχουν αποκτήσει τις τελικές τους ταχύτητες, ενώ η μείωση του πάχους και του ύψους του δακτυλίου του εργοτεμαχίου πραγματοποιούνται με σταθερό ρυθμό. Κατά τη διάρκεια αυτής της φάσης, πραγματοποιείται το μεγαλύτερο ποσοστό της συνολικής παραμόρφωσης του εργοτεμαχίου, ενώ το τέλος της *2ης Φάσης* οριοθετείται από το πέρας της γραμμικής κίνησης του μαντρέλ και των κωνικών ραούλων.

- Στην *3η Φάση (τελικό στάδιο έλασης)*, οι γραμμικές κινήσεις του μαντρέλ και των κωνικών ραούλων έχουν ολοκληρωθεί, ενώ ο δακτύλιος συνεχίζει να περιστρέφεται, μέχρις ότου ολόκληρη η περίμετρος του να διασχίσει το τελικό διάκενο μαντρέλ-κυρίως ραούλου, με αποτέλεσμα αυτός να έχει το ίδιο πάχος σε όλη την περιφέρειά του.

- Στην *4η Φάση (στάδιο διόρθωσης κυκλικότητας)*, ο δακτύλιος συνεχίζει να περιστρέφεται για λίγο ακόμα, με αυξημένη γωνιακή ταχύτητα. Το αποτέλεσμα αυτής της φάσης, είναι η διόρθωση των όποιων ελαττωμάτων κυκλικότητας έχουν προκύψει, ενώ επίσης μπορούν να διορθωθούν και μεγαλύτερα ελαττώματα, όπως η "ουρά ψαριού" και οι άνω και κάτω διογκώσεις. Επιπλέον, πολύ συχνά κατά τη συγκεκριμένη φάση αυξάνεται και ο ρυθμός ψύξης του δακτυλίου, ώστε οι τελευταίες περιστροφές να πραγματοποιηθούν εν ψυχρώ. Έτσι, τα προαναφερθέντα ελαττώματα μπορούν να εξαλειφθούν πλήρως, ενώ παράλληλα αυξάνεται και η επιφανειακή σκληρότητα του προϊόντος.

Παρόλο που πολλά από τα ελαττώματα της έλασης δακτυλίων μπορούν να ελεγχθούν ως κάποιο βαθμό, στις περισσότερες βιομηχανικές παραγωγές οι ακριβείς διαστάσεις των τελικών τεμαχίων δεν μπορούν ποτέ να επιτευχθούν. Η κύρια αιτία αυτού είναι η χονδροειδής προσέγγιση στον υπολογισμό του αρχικού όγκου του εργοτεμαχίου, η οποία συνήθως υπερδιαστασιολογείται ώστε να αντισταθμίσει τα διαστασιακά σφάλματα που πραγματοποιούνται κατά τη σφυρηλάτηση και τη διάτρηση της αρχικής μπιγέτας. Επιπλέον, άλλες παράμετροι καθεαυτής της έλασης δακτυλίων, όπως ο κακός έλεγχος θέσης των εργαλείων, επιδεινώνουν τη διαστασιακή ανακρίβεια των τελικών προϊόντων. Λόγω των παραπάνω, είναι επιτακτική η ανάγκη πολλαπλών κύκλων κατεργασιών αποβολής υλικού, ώστε να επιτευχθούν οι ακριβείς διαστάσεις και η απαιτούμενη ποιότητα επιφάνειας των παραγόμενων δακτυλίων, αυξάνοντας παράλληλα τον συνολικό χρόνο και το συνολικό κόστος ανά τεμάχιο (**Wu et al., 2019**). Γίνεται, λοιπόν, αντιληπτό ότι μια πιθανή αύξηση στη διαστασιακή ακρίβεια των προϊόντων της έλασης δακτυλίων θα μπορούσε να μειώσει σημαντικά το κόστος παραγωγής ανά τεμάχιο και θα συνέβαλε σημαντικά στην αύξηση της παραγωγικότητας δακτυλιοειδών προϊόντων, πολλά εκ των οποίο αποτελούν μέρος κρίσιμων εφαρμογών (π.χ. δακτύλιοι ρουλεμάν).

Προκειμένου να μπορέσουν να βελτιστοποιήσουν την κατεργασία, διάφοροι ερευνητές ανά τον κόσμο πραγματοποίησαν πολλές διαφορετικές προσεγγίσεις. Πολλοί εξ αυτών προσέγγισαν πειραματικά ή/και αναλυτικά το πρόβλημα με στόχο είτε να βελτιστοποιήσουν την αποτελεσματικότητα των εργαλείων της διάταξης (π.χ. **Hawkyard, Appleton, and Johnson, 1973; Stanistreet, Allwood, and Willoughby, 2006**), είτε να ελέγξουν την ανάπτυξη του εργοτεμαχίου κατά τη διάρκεια της κατεργασίας (π.χ. **Szabo and Dittrich, 1996; Uchibori, Matsumoto, and Utsunomiya, 2018**), είτε να προσδιορίσουν τις οριακές τιμές ορισμένων κρίσιμων παραμέτρων αυτής (π.χ. **Zhao and Qian, 2010; Xu et al., 2015**). Επιπροσθέτως, από τις αρχές της δεκαετίας του 1990 παρουσιάστηκαν πολλαπλές εργασίες που χρησιμοποιούσαν αναλύσεις με τη μέθοδο των πεπερασμένων στοιχείων, είτε συμπληρωματικά με άλλες πειραματικές προσεγγίσεις (π.χ. **Xu, Lian, and Hawkyard, 1991; Wang et al., 2009**), είτε ως μέθοδο πιστοποίησης αναλυτικών και πειραματικών μεθοδολογιών (π.χ. **Parvizi and Abrinia, 2014; Li, Guo, and Wang, 2021**). Αν και οι προαναφερθείσες προσεγγίσεις έδωσαν απαντήσεις σε κάποια ερωτήματα σχετικά με την κατεργασία, η έρευνα γύρω από την εξάλειψη των διαστασιακών σφαλμάτων των τελικών τεμαχίων της έλασης δακτυλίων ήταν ελλιπής. Ακόμα, αν και αριθμητικές μοντελοποιήσεις της κατεργασίας έχουν δημοσιευτεί από πολλούς ερευνητές, οι αντίστοιχες αναλύσεις ευαισθησίας των αριθμητικών παραμέτρων των εν λόγω μοντέλων δεν παρουσιάζονται και πολλές σημαντικές παράμετροι των μοντελοποιήσεων δε δημοσιοποιούνται, με αποτέλεσμα η αναπαραγωγή των εν λόγω προσομοιώσεων, χωρίς αριθμητικά προβλήματα, να είναι αδύνατη.

Με βάση την προηγηθείσα βιβλιογραφική μελέτη, στην παρούσα διδακτορική διατριβή διερευνήθηκαν σε βάθος ορισμένες κρίσιμες παράμετροι και μεθοδολογίες, οι οποίες θα μπορούσαν εν δυνάμει να αυξήσουν τη διαστασιακή ακρίβεια μιας ορθογωνικής έλασης δακτυλίων. Η διερεύνηση πραγματοποιήθηκε μέσω πιστοποιημένων, θερμο-μηχανικών προσομοιώσεων. Πιο συγκεκριμένα, η δομή της παρούσας διατριβής είναι η ακόλουθη:

- Στο *δεύτερο κεφάλαιο*, η ανάπτυξη μιας συζευγμένης, θερμο-μηχανικής προσομοίωσης μιας εν θερμώ έλασης δακτυλίων αναλύεται διεξοδικά. Στα πλαίσια αυτής της μελέτης παρουσιάζονται οι καταλληλότερες παράμετροι για το τελικό μοντέλο, μαζί με μια επεξήγηση γύρω από την καταλληλότητά τους. Τα αποτελέσματα της εν λόγω προσομοίωσης θα συγκριθούν, στη συνέχεια, με αντίστοιχα πειραματικά αποτελέσματα από τη βιβλιογραφία (**Zhu et al., 2016**), προκειμένου το αριθμητικό μοντέλο που αναπτύχθηκε να μπορεί να θεωρηθεί πιστοποιημένο. Τέλος, θα αναλυθούν και άλλες κατηγορίες αποτελεσμάτων, οι οποίες υπό κανονικές συνθήκες δεν μπορούν να μετρηθούν σε πειραματικές εφαρμογές.

- Στο *τρίτο κεφάλαιο*, διερευνώνται τρεις κρίσιμες παράμετροι αύξησης της διαστασιακής ακρίβειας των προϊόντων της έλασης δακτυλίων. Αρχικά, προτείνεται και επιβεβαιώνεται μια μεθοδολογία υπολογισμού του αρχικού όγκου του εργοτεμαχίου. Έπειτα, εξετάζεται η επίδραση των θερμο-ελαστικών παραμορφώσεων των εργαλείων στις τελικές διαστάσεις των δακτυλίων. Τέλος, μελετώνται οι επιδράσεις της κινηματικής των υποστηρικτικών ραούλων στις διαστάσεις των προϊόντων, συναρτήσει του υλικού αυτών.

- Στο *τέταρτο κεφάλαιο*, παρουσιάζεται μια καινοτόμα κατεργασία "διόρθωσης" διαστασιακών σφαλμάτων των τελικών δακτυλιοειδών προϊόντων. Εκτός από τον κύριο μηχανισμό αυτής της νέας μεθόδου, διερευνάται ακόμα και η επίδραση κάποιων κρίσιμων παραμέτρων στα τελικά αποτελέσματα της εν λόγω κατεργασίας.

- Τέλος, στο *πέμπτο κεφάλαιο* παρουσιάζεται μια νέα προσέγγιση για την παραγωγή πολυγωνικών προϊόντων, με χρήση μιας τυπικής διάταξης έλασης δακτυλίων. Η εν λόγω ανάλυση δεν επεκτείνεται σε μεγάλο βάθος, αφού το θέμα της αποκλίνει από το κύριο θέμα της παρούσας διατριβής. Αντίθετα, παρουσιάζεται στον αναγνώστη απλά ως μια απόδειξη της ιδέας.

2. Αριθμητική Προσομοίωση της Κατεργασίας Έλασης Δακτυλίων

2.1. Μεθοδολογία Ανάπτυξης Αριθμητικού Μοντέλου

Προκειμένου να διερευνηθούν αριθμητικά οι παράμετροι και οι μεθοδολογίες αύξησης της διαστασιακής ακρίβειας της κατεργασίας έλασης δακτυλίων, ένα πιστοποιημένο και απαλλαγμένο από ελαττώματα αριθμητικό μοντέλο της κατεργασίας έπρεπε να αναπτυχθεί αρχικά. Παρόλα αυτά, στη σχετική βιβλιογραφία σπανίως έως ποτέ δεν παρέχονται όλες οι απαραίτητες παράμετροι για την αναπαραγωγή των αντίστοιχων μοντέλων έλασης δακτυλίων. Επιπλέον, οι συγγραφείς πολλές φορές κάνουν παραδοχές προκειμένου να απλοποιήσουν τις προσομοιώσεις τους ή να ξεπεράσουν δυσκολίες κατά την επίλυση τους, χωρίς όμως πάντα να αξιολογούν τις επιπτώσεις των εν λόγω παραδοχών στα τελικά αποτελέσματα των μοντέλων τους. Αυτός ο συνδυασμός ελλιπών δεδομένων και παραδοχών, καθιστά την αναπαραγωγή των μοντέλων έλασης δακτυλίων πολύ δύσκολη.

Με βάση όλα τα παραπάνω, η ανάπτυξη ενός αριθμητικού μοντέλου έλασης δακτυλίων από το μηδέν ήταν η μόνη εναλλακτική στα πλαίσια της παρούσας διατριβής. Το μοντέλο που αναπτύχθηκε, βασίστηκε στα πειραματικά δεδομένα που παρουσίασαν οι Zhu et al. στην εργασία τους για την έλαση ενός δακτυλίου από IN718 (**Zhu et al., 2016**). Η προαναφερθείσα εργασία επιλέχθηκε, μεταξύ άλλων, επειδή παρουσίαζε την πλειονότητα των κρίσιμων παραμέτρων της κατεργασίας, ενώ τα αντίστοιχα πειραματικά αποτελέσματα ήταν επαρκή για την πιστοποίηση του μοντέλου που αναπτύχθηκε. Οι ιδιότητες υλικού λήφθηκαν είτε από την εργασία αναφοράς, είτε μετά από έρευνα στη σχετική βιβλιογραφία, ενώ η μία παράμετρος που δεν ήταν διαθέσιμη σε καμία από τις δύο πηγές, προσδιορίστηκε μέσα από έναν κύκλο προσομοιώσεων δοκιμής-και-σφάλματος.

Για την ορθή ανάπτυξη ενός αριθμητικού μοντέλου μιας κατεργασίας μέσω ανάλυσης πεπερασμένων στοιχείων, μια σειρά από συγκεκριμένα και πολύ ακριβή βήματα θα πρέπει να ακολουθούνται. Για το μοντέλο της παρούσας ανάλυσης, τα βήματα που ακολουθήθηκαν καθώς και μια σύντομη επεξήγηση των επιλογών που πραγματοποιήθηκαν, παρουσιάζονται παρακάτω:

1. **Επιλογή μεταξύ 2D και 3D προσομοίωσης:**

   Στην κατεργασία πραγματοποιείται παραμόρφωση του τεμαχίου και στις τρεις διαστάσεις, με αποτέλεσμα μια 2D προσομοίωση να είναι μη ρεαλιστική. Έτσι, επιλέχθηκε να γίνει μια **3D προσομοίωση**, παρά τον αυξημένο βαθμό δυσκολίας και ανάγκης υπολογιστικών πόρων.

2. **Προσδιορισμός της βέλτιστης μεθόδου επίλυσης των πεπερασμένων στοιχείων:**

   Η επίλυση ενός μοντέλου πεπερασμένων στοιχείων μπορεί να προσεγγιστεί είτε μέσω αριθμητικής παραγώγισης (implicit method), είτε μέσω αριθμητικής ολοκλήρωσης (explicit method). Οι δύο μέθοδοι έχουν σημαντικές διαφορές με αποτέλεσμα η καταλληλότητά τους να διαφέρει ανάλογα με το φαινόμενο που προσομοιώνεται. Ένας εμπειρικός χάρτης καταλληλότητας κάθε μεθόδου παρουσιάζεται στο Σχ.3:

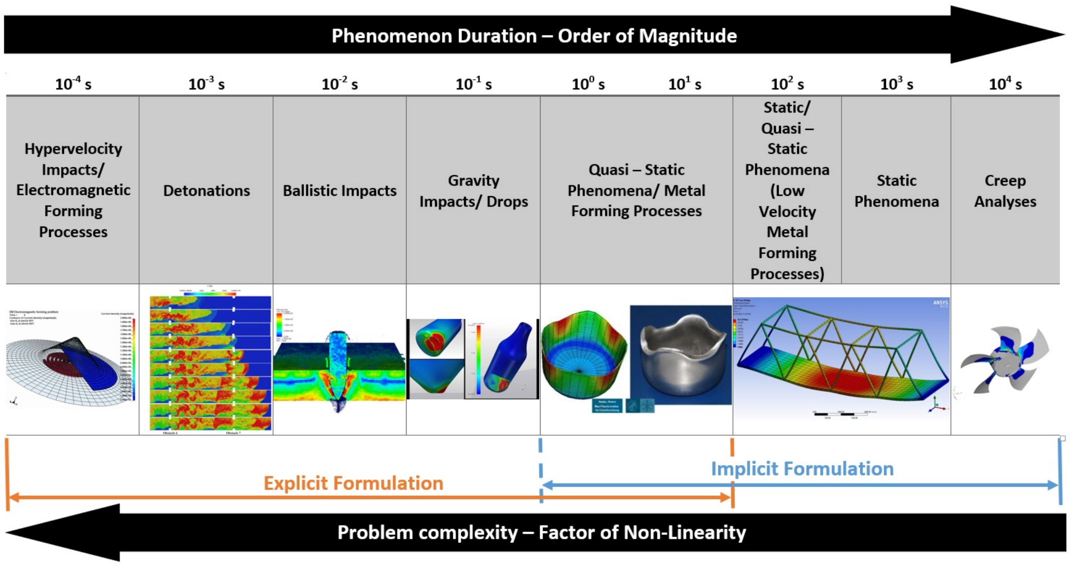

Σχήμα 3: Προτεινόμενες μέθοδοι επίλυσης αναλύσεων πεπερασμένων στοιχείων για διαφορετικές εφαρμογές

Προκειμένου να γίνει επιλογή της βέλτιστης μεθόδου επίλυσης, μελετήθηκε μια παρεμφερής συζευγμένη προσομοίωση μιας θερμο-μηχανικής κατεργασίας έλασης ενός φύλλου αλουμινίου, τα συμπεράσματα της οποίας μπορούσαν να γενικευτούν και για την κατεργασία έλασης δακτυλίων, λόγω των ομοιοτήτων των δύο κατεργασιών στην κινηματική των εργαλείων τους. Από τα συμπεράσματα της εν λόγω μελέτης προέκυψε ότι σε μοντέλα με μεγάλο αριθμό πεπερασμένων στοιχείων (και άρα πολλών κόμβων), η επίλυση μέσω αριθμητικής ολοκλήρωσης είναι η προτεινόμενη μέθοδος, λόγω του σημαντικά μικρότερου χρόνου επίλυσης. Η αντίστοιχη καμπύλη που περιγράφει αυτά τα αποτελέσματα, παρουσιάζεται στο Σχ.4:

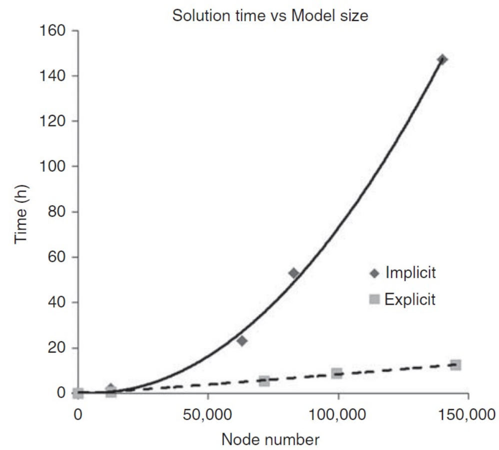

Σχήμα 4: Σύγκριση του χρόνου επίλυσης ενός μοντέλου έλασης φύλλου αλουμινίου μέσω αριθμητικής παραγώγισης και αριθμητικής ολοκλήρωσης, συναρτήσει του αριθμού των κόμβων που περιλαμβάνονται στο μοντέλο

Με βάση όλα τα παραπάνω, επιλέχθηκε τελικά η μέθοδος της **αριθμητικής ολοκλήρωσης (explicit method)** για την επίλυση όλων των μοντέλων της παρούσας ανάλυσης.

3. **Ακριβής δημιουργία της γεωμετρίας του προβλήματος:**

   Όλα τα εργαλεία και το αρχικό δοκίμιο της κατεργασίας αναπαράχθηκαν βάσει της περιγραφόμενης γεωμετρίας από τη δημοσίευση των Zhu et al.. Τα εν λόγω σώματα απεικονίζονται στο Σχ.5:

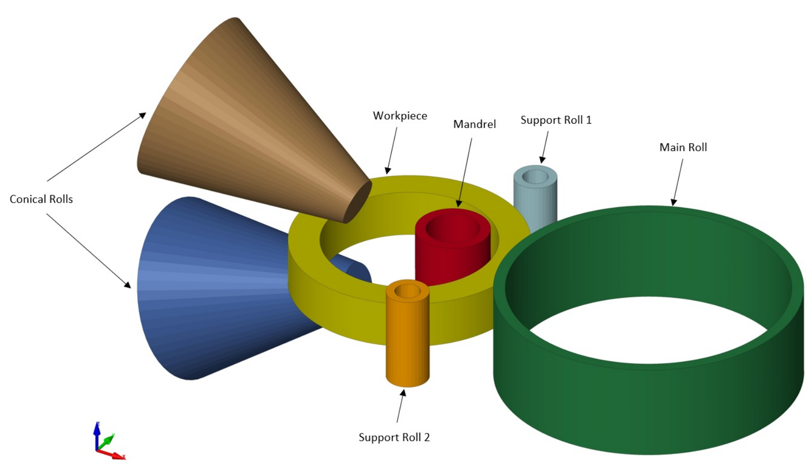

Σχήμα 5: Σχηματική αναπαράσταση των σωμάτων της προσομοίωσης έλασης δακτυλίων

4. **Βέλτιστη πυκνότητα αριθμητικού πλέγματος:**

Προκειμένου να είναι αξιόπιστα τα αποτελέσματα της προσομοίωσης, χρειάστηκε να ανεξαρτητοποιηθούν από την επίδραση της διακριτοποίησης του σώματος με πεπερασμένα στοιχεία. Αυτό μπορεί να γίνει όταν τα πεπερασμένα στοιχεία γίνουν αρκετά μικρά σε μέγεθος, ώστε να σταματήσουν να συμπεριφέρονται ως κρίκοι μιας αλυσίδας ή ενός δικτυώματος, αλλά ως τμήματα ενός συνεχούς μέσου. Για τον λόγο αυτόν, πραγματοποιήθηκε μελέτη ανεξαρτησίας πλέγματος, στα πλαίσια της οποίας πραγματοποιήθηκε επανάληψη της ίδιας προσομοίωσης με ολοένα μικρότερο μέγεθος πεπερασμένων στοιχείων. Όταν τα αποτελέσματα άρχισαν να παραμένουν τα ίδια, παρά τη μείωση του μεγέθους των πεπερασμένων στοιχείων, το μοντέλο μπορούσε πλέον να θεωρείται ανεξάρτητο της επίδραση του αριθμητικού πλέγματος. Ένα παράδειγμα της επίδρασης του αριθμητικού πλέγματος στα αποτελέσματα του μοντέλου παρουσιάζεται στο Σχ.6:

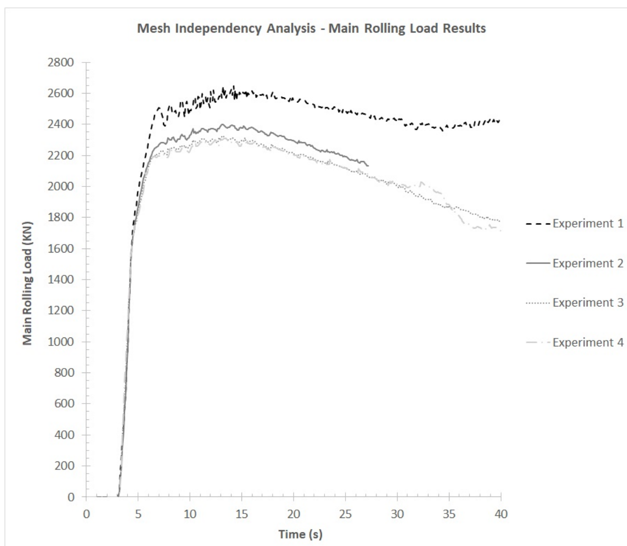

Σχήμα 6: Αποτελέσματα κυρίως φορτίου έλασης δακτυλίου κατά την ανάλυση ανεξαρτησίας πλέγματος

Από την εν λόγω ανάλυση προέκυψε ότι το μοντέλο ήταν ανεξάρτητο του αριθμητικού πλέγματος για μέση διάσταση πεπερασμένων στοιχείων μικρότερη ή ίση των **4 mm**. Αξίζει να αναφερθεί ότι η ανάλυση ανεξαρτησίας πλέγματος αφορά κυρίως το πλέγμα του δοκιμίου.

5. **Προσδιορισμός ιδιοτήτων υλικών:**

Για την εκτέλεση της αριθμητικής προσομοίωσης της κατεργασίας, η επιλογή των σωστών θερμο-μηχανικών ιδιοτήτων είναι από ένα από τα πιο χρονοβόρα, αλλά κρίσιμα βήματα της όλης διαδικασίας. Στα πλαίσια της παρούσας διατριβής πραγματοποιήθηκε ενδελεχής βιβλιογραφική ανασκόπηση για την εύρεση των σωστών ιδιοτήτων υλικού, με τις τελικές ιδιότητες να λαμβάνονται από τις εργασίες **Zhu et al., 2016**, **Iturbe at al., 2017**, **Deshpande et al., 2011**, **Tolcha and Lemu, 2019**, κ.α.. Αξίζει να αναφερθεί ότι για όλα τα εργαλεία, επιλέχθηκε αυθαίρετα ως υλικό ο εργαλειοχάλυβας AISI H13, αφού η συγκεκριμένη πληροφορία δεν είχε συμπεριληφθεί στην εργασία των **Zhu et al., 2016**. Κάποια χαρακτηριστικά παραδείγματα θερμο-μηχανικών ιδιοτήτων που συμπεριλήφθηκαν στο μοντέλο έλασης δακτυλίων της παρούσας διατριβής, παρουσιάζονται στα Σχ.7 - 8:

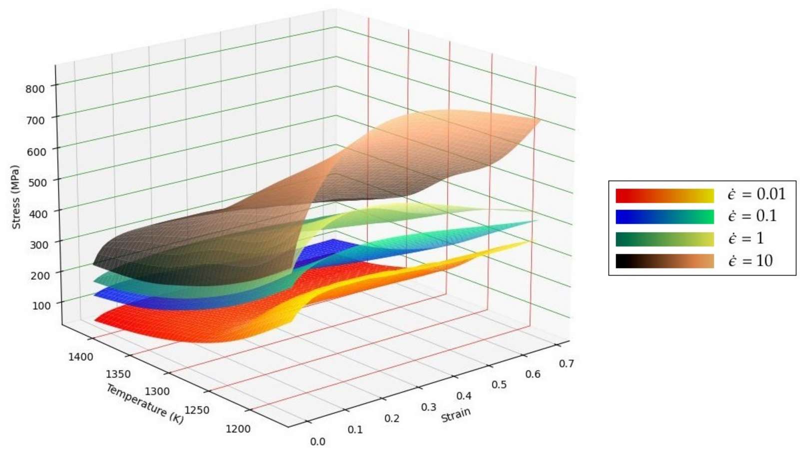

Σχήμα 7: Επιφάνειες πραγματικών τάσεων - πραγματικών παραμορφώσεων - θερμοκρασίας για πολλαπλούς ρυθμούς παραμόρφωσης (IN718)

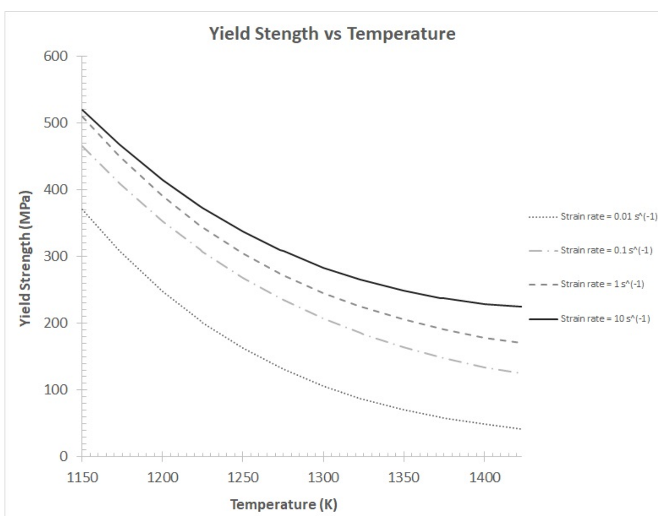

Σχήμα 8: Όριο διαρροής για πολλαπλές θερμοκρασίες (IN718)

Αξίζει να αναφερθεί ότι οι ιδιότητες που συμπεριλήφθηκαν στο μοντέλο ήταν όλες εκείνες που απαιτούνται για την περιγραφή μιας πλήρους θερμο-μηχανικής κατεργασίας, ήτοι οι ελαστοπλαστικές, μηχανικές ιδιότητες συναρτήσει της θερμοκρασίας και του ρυθμού παραμόρφωσης, καθώς και οι θερμικές ιδιότητες για την περιγραφή της μεταφορά θερμότητας μέσα από κάθε σώμα, από το ένα σώμα στο άλλο και από κάθε σώμα προς στο περιβάλλον.

6. **Προσδιορισμός του κατάλληλου τύπου πεπερασμένων στοιχείων:**

Το λογισμικό LS-DYNA παρέχει πολλούς διαφορετικούς τύπους πεπερασμένων στοιχείων για διαφορετικούς τύπους αναλύσεων. Από τους διαθέσιμους τύπους πεπερασμένων στοιχείων για αναλύσεις τρισδιάστατων στερεών και κατόπιν έρευνας για την καταλληλότητα τους ως προς την προσομοίωση της εν λόγω κατεργασία, επιλέχθηκε τελικά ο τύπος **SOLID_ELEMENT_2: 8-Node Hexahedron** για το παρομορφώσιμο δοκίμιο και ο τύπος **SOLID_ELEMENT_1: Constant Stress Solid Element** για τα εργαλεία. Με αυτόν τον συνδυασμό εξασφαλίστηκε ότι η παραμόρφωση του δοκιμίου θα γινόταν με ακρίβεια, ενώ ο υπολογιστικός χρόνο θα παρέμενε σε (σχετικά) χαμηλά επίπεδα.

7. **Ορισμός επαφών μεταξύ διαφορετικών σωμάτων:**

Ο ορισμός των επαφών είναι άλλη μια κρίσιμη παράμετρος κατά την προσομοίωση κατεργασιών. Οι δύο ιδιότητες που πρέπει να προσδιοριστούν κατά τον ορισμό των επαφών είναι: (α) οι κατάλληλοι συντελεστές τριβής και (β) οι συντελεστές μεταφοράς θερμότητας μεταξύ των σωμάτων σε επαφή. Από τους διαθέσιμους τύπους επαφών επιλέχθηκε ο τύπος **AUTOMATIC_SURFACE_TO_SURFACE_SMOOTH**, ως ο καταλληλότερος για την επαφή κυλινδρικών σωμάτων. Ακόμα, από τις προαναφερθείσες ιδιότητες, οι συντελεστές τριβής επιλέχθηκαν με βάση τις αντίστοιχες συνθήκες μιας εν θερμώ έλασης δακτυλίων, ενώ για τον προσδιορισμό του συντελεστή θερμικής αγωγής μεταξύ των σωμάτων χρειάστηκε να εκπονηθεί μια ενδελεχής μελέτη, αφού η συγκεκριμένη παράμετρος ήταν η μόνη άγνωστη με βάση τα στοιχεία που δίνονταν στην εργασία των Zhu et al.. Στα πλαίσια τις εν λόγω μελέτης, χρειάστηκε να πραγματοποιηθεί μια εκτεταμένη σειρά προσομοιώσεων δοκιμής-και-σφάλματος, προκειμένου να προσδιοριστεί η καμπύλη που περιέγραφε το συντελεστή θερμικής αγωγής μεταξύ εργαλείων και δοκιμίου. Τελικά, η δοκιμή κατέληξε στον προσδιορισμό δύο μοτίβων του συντελεστή: (α) ένα μεταξύ του δοκιμίου και κωνικών ραούλων και (β) ένα μεταξύ του δοκιμίου και των υπόλοιπων εργαλείων. Τα εν λόγω μοτίβα του συντελεστή θερμικής αγωγής παρουσιάζονται στο Σχ.9:

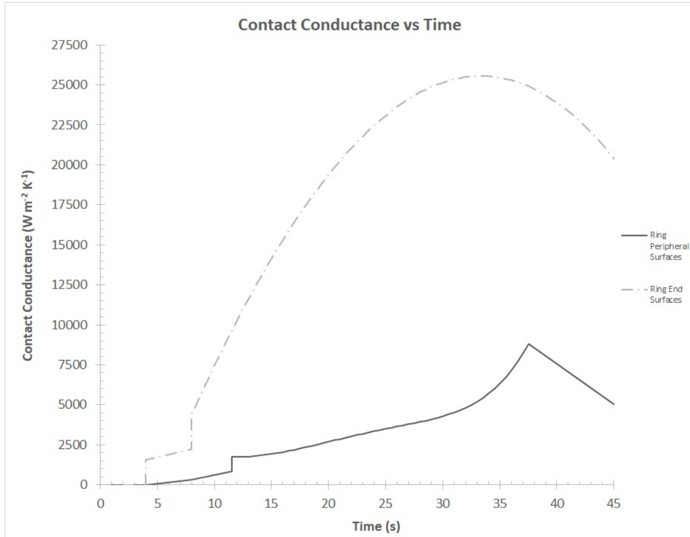

Σχήμα 9: Μοτίβα συντελεστών θερμικής αγωγής μεταξύ δοκιμίου και εργαλείων

8. Ορισμός της κινηματικής των εργαλείων:

Σχετικά με την κινηματική των εργαλείων, οι περισσότερες ταχύτητες και συνθήκες κίνησης περιγράφονται με ακρίβεια στην εργασία των Zhu et al.. Σύμφωνα με την ανωτέρω βιβλιογραφική πηγή, όλα τα κύρια εργαλεία της κατεργασίας εκτελούν κινήσεις με σταθερές γραμμικές και γωνιακές ταχύτητες. Οι εν λόγω ταχύτητες παρουσιάζονται στο Πίνακα 1:

Πίνακας 1: Ταχύτητες εργαλείων

Τύπος ταχύτητας	**Τιμή**
Γραμμική ταχύτητα μαντρέλ, $v_{mandrel}$ $(\frac{mm}{s})$	0.89
Γωνιακή ταχύτητα κυρίως ραούλου, ω_{MR} $(\frac{rad}{s})$	2.09
Γραμμική ταχύτητα άνω κωνικού ραούλου, v_{CR} $(\frac{mm}{s})$	0.35
Γωνιακή ταχύτητα κωνικών ραούλων (μέση), ω_{CR} $(\frac{rad}{s})$	7.71

Εξαίρεση αποτελούν τα υποστηρικτικά ράουλα, των οποίων η κίνηση δεν περιγραφόταν στη βιβλιογραφική πηγή. Για τον λόγο αυτό, η κίνησή τους βασίστηκε στον ρυθμό ανάπτυξης του δακτυλίου κατά την κατεργασία, όπως αυτός προέκυπτε από τα πειραματικά δεδομένα. Κατά την επισκόπηση των πειραματικών δεδομένων, προέκυψε ότι ο ρυθμός ανάπτυξης της εξωτερικής ακτίνας του δακτυλίου μπορεί να προσδιοριστεί από δύο συμπληρωματικές εξισώσεις (Εξ.1 και 2):

$$R_i = 3.1003 \cdot 10^{-1} \cdot t^{1.7} + 301.7273 \qquad \text{(φάσεις 1 και 2 της κατεργασίας)} \quad (1)$$

$$R_i = -2.5097 \cdot 10^{-1} \cdot t^2 + 22.6085 \cdot t - 45.5521 \quad \text{(φάση 3 της κατεργασίας)} \quad (2)$$

Οι προσδιορισθέντες ρυθμοί ανάπτυξης του δακτυλίου χρησιμοποιήθηκαν για τον ορισμό της κίνησης των υποστηρικτικών ραούλων, μέσω των Εξ.3:

$$\begin{aligned} X_{SR} &= R_i \cdot cos\phi - \Delta c \\ Y_{SR} &= \pm R_i \cdot sin\phi \end{aligned} \tag{3}$$

Αξίζει να αναφερθεί ότι στην πρώτη από τις Εξ.3, η παράμετρος Δc περιγράφει τη μετατόπιση του κέντρου περιστροφής του δακτυλίου, ως αποτέλεσμα της αύξησης της διαμέτρου του (το σημείο συμπίεσης του δακτυλίου από το μαντρέλ και το κυρίως ράουλο παραμένει σταθερό καθ΄ όλη τη διάρκεια της κατεργασίας). Επίσης κατά την αντικατάσταση της γωνίας φ στις Εξ.3, η φορά περιστροφής του δακτυλίου και οι γωνιακές θέσεις των υποστηρικτικών ραούλων χρειάστηκε να ληφθούν υπόψιν και να αντισταθμιστούν.

9. **Προσδιορισμός των οριακών και των αρχικών συνθηκών:**

Οι υπόλοιπες φυσικές παράμετροι της προσομοίωσης προσδιορίστηκαν είτε ως αρχικές, είτε ως οριακές συνθήκες. Οι μόνες αρχικές συνθήκες που χρειάστηκε να οριστούν για τη συγκεκριμένη προσομοίωση ήταν οι αρχικές θερμοκρασίες των σωμάτων. Αυτές ήταν $\mathbf{T}_{ring,periphery} = \mathbf{1290.1\ K}$, $\mathbf{T}_{ring,ends} = \mathbf{1291.1\ K}$ και $\mathbf{T}_{tools} = \mathbf{573.15\ K}$ (**Zhu et al., 2016**). Από την άλλη μεριά, οι οριακές συνθήκες που χρειάστηκε να οριστούν στη συγκεκριμένη προσομοίωση ήταν η συναγωγή θερμοκρασίας των σωμάτων με τον αέρα (**BOUNDARY_CONVECTION_SET**) και η ακτινοβόληση θερμοκρασίας προς το περιβάλλον (**BOUNDARY_RADIATION_SET**). Οι αντίστοιχοι συντελεστές προσδιορίστηκαν από τη σχετική βιβλιογραφία (**Keenan, Chao, and Kaye, 1983**, **Touloukian, Liley, and Saxena, 1970** και **Greene, Finfrock, and Irvine, 1999**). Αξίζει να αναφερθεί ότι οι συντελεστές για τις ανωτέρω οριακές συνθήκες είναι θερμοκρασιακά εξαρτώμενοι και άρα υπολογίζονταν εκ νέου σε κάθε χρονικό βήμα της ανάλυσης, βάσει της θερμοκρασίας κάθε πεπερασμένου στοιχείου.

10. **Ορισμός των παραμέτρων του λογισμικού:**

Αφού ορίστηκαν όλες οι παράμετροι που περιέγραφαν τα φυσικά φαινόμενα της κατεργασίας, ήταν απαραίτητο να οριστούν στη συνέχεια και οι παράμετροι λειτουργίας του λογισμικού. Οι εν λόγω παράμετροι κατηγοριοποιούνται σε δύο κατηγορίες: (α) στις παραμέτρους ελέγχου του προγράμματος και (β) στις παραμέτρους καταγραφής των αποτελεσμάτων. Οι παράμετροι ελέγχου του προγράμματος καθορίζουν παράγοντες όπως τον συνολικό χρόνο επίλυσης του μοντέλου, την ευστάθεια του μηχανικού και θερμικού επιλύτη, την ακρίβεια των υπολογισμών, κ.α.. Οι παράμετροι καταγραφής των αποτελεσμάτων καθορίζουν ποια φυσικά μεγέθη θα εξάγονται ως αποτελέσματα και σε ποια συχνότητα κατά την επίλυση του μοντέλου.

11. **Προσδιορισμός της βέλτιστης κλιμάκωσης μάζας:**

    Λόγω του μεγάλου αριθμού πεπερασμένων στοιχείων που χρησιμοποιήθηκαν στην εν λόγω προσομοίωση, χρειάστηκε να επιταχυνθούν με κάποιον τρόπο οι υπολογισμοί. Η βέλτιστη τεχνική για την εν λόγω επιτάχυνση είναι η λεγόμενη "κλιμάκωση μάζας". Με την εν λόγω τεχνική, το λογισμικό αυξάνει πλασματικά τη μάζα ορισμένων πεπερασμένων στοιχείων και έτσι δύναται να αυξήσει και το χρονικό βήμα των υπολογισμών. Το μειονέκτημα είναι ότι υπερβολική αύξηση της μάζας των στοιχείων, μπορεί να οδηγήσει σε αφύσικη συμπεριφορά των σωμάτων και άρα σε λανθασμένα αποτελέσματα. Το LS-DYNA δίνει τη δυνατότητα τόσο για "συνήθη κλιμάκωση μάζας", όσο και για "επιλεκτική κλιμάκωση μάζας". Ύστερα από ενδελεχή μελέτη και την πραγματοποίηση ορισμένων δοκιμαστικών προσομοιώσεων, επιλέχθηκε τελικά η **"επιλεκτική κλιμάκωση μάζας"**. Τα υπολογιζόμενα αποτελέσματα δεν παρουσίασαν αφύσικη συμπεριφορά, σύμφωνα με τα όρια που τίθενται από τη σχετική βιβλιογραφία (**Patil, Baratzadeh, and Lankarani, 2017**).

12. **Επίλυση του μοντέλου:**

    Μετά από τη διεκπεραίωση όλων των απαραίτητων βημάτων για την ανάπτυξη του μοντέλου έλασης δακτυλίων, στη συνέχεια αυτό τέθηκε προς επίλυση. Η επίλυση του τελικού μοντέλου, καθώς και όλες οι προκαταρκτικές προσομοιώσεις κατά την προετοιμασία του, επιλύθηκαν από έναν τυπικό οικιακό υπολογιστή, με μέσω χρόνο επίλυσης κάθε μοντέλου (για την πλήρη διάρκεια της προσομοίωσης) τις 300 - 320 ώρες.

13. **Πιστοποίηση των αποτελεσμάτων:**

    Τα αποτελέσματα από το τελικό μοντέλο έλασης δακτυλίου που αναπτύχθηκε στο παρόν κεφάλαιο συγκρίθηκαν με τα αντίστοιχα πειραματικά αποτελέσματα από την εργασία των Zhu et al., ώστε να διαπιστωθεί η εγκυρότητα του μοντέλου. Τρία χαρακτηριστικά διαγράμματα που παρουσιάζουν τη σύγκριση αριθμητικών και πειραματικών αποτελεσμάτων παρουσιάζονται στα Σχ.10-12:

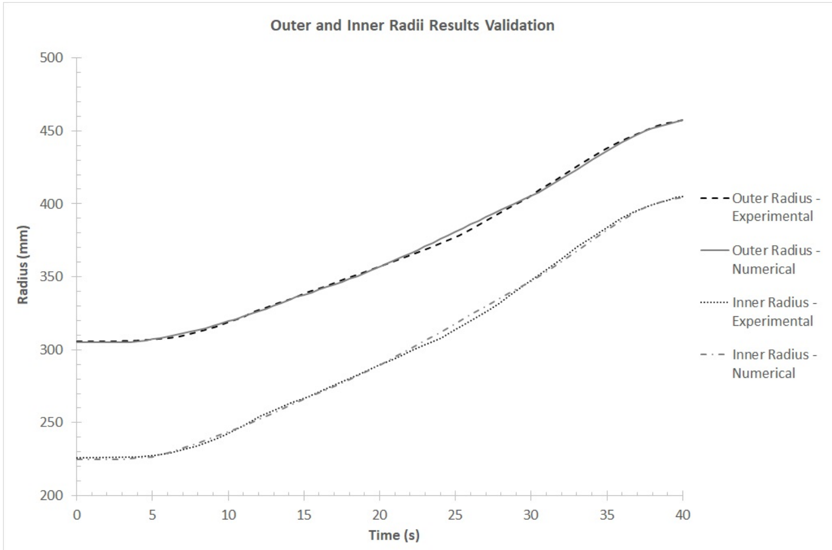

Σχήμα 10: Σύγκριση αριθμητικών και πειραματικών αποτελεσμάτων της εξωτερικής και εσωτερικής ακτίνας του δοκιμίου

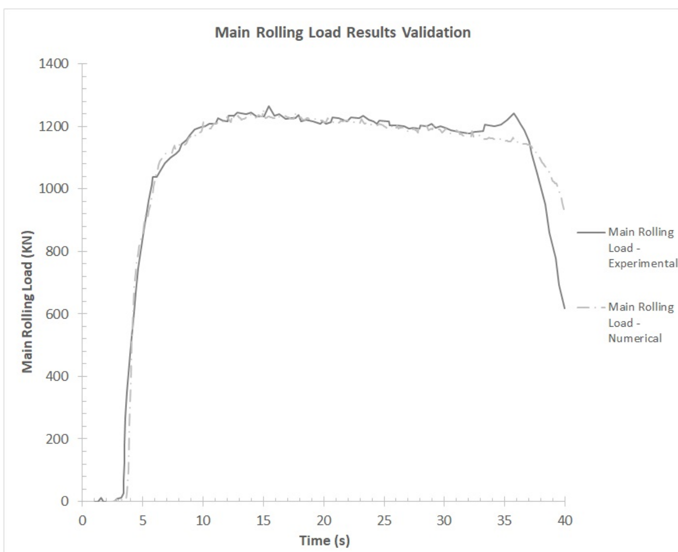

Σχήμα 11: Σύγκριση αριθμητικών και πειραματικών αποτελεσμάτων του κύριου φορτίου έλασης

Από τη σύγκριση των αριθμητικών και πειραματικών αποτελεσμάτων διαπιστώθηκε ικανοποιητική ακρίβεια μεταξύ των δύο, ώστε το αριθμητικό μοντέλο που αναπτύχθηκε να θεωρείται πιστοποιημένο.

Αξίζει να αναφερθεί ότι από την ανάλυση των αποτελεσμάτων παραμόρφωσης της εργασίας των Zhu et al., φαίνεται να απουσιάζει εντελώς η φάση 4 της κατεργασίας.

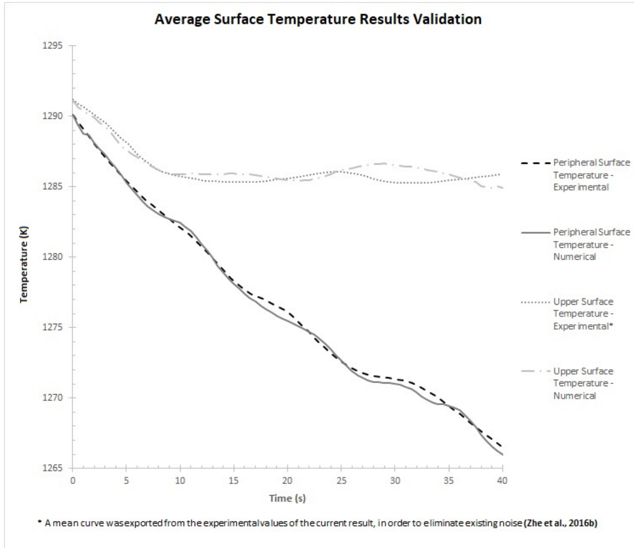

Σχήμα 12: Σύγκριση αριθμητικών και πειραματικών αποτελεσμάτων της περιφερειακής και άνω επιφανειακής θερμοκρασίας του δοκιμίου

2.2. Λοιπά Αποτελέσματα

Πέρα από τα αποτελέσματα που πιστοποιήθηκαν κατά τη σύγκριση του μοντέλου με την αντίστοιχη πειραματική εφαρμογή, η προσομοίωση προσέφερε τη δυνατότητα επισκόπησης και άλλων αποτελεσμάτων, μερικά από τα οποία δεν μπορούν να ληφθούν άμεσα κατά τη διάρκεια της πειραματικής διαδικασίας. Μερικά χαρακτηριστικά παραδείγματα των εν λόγω αποτελεσμάτων παρουσιάζονται στα Σχ.13 - 15:

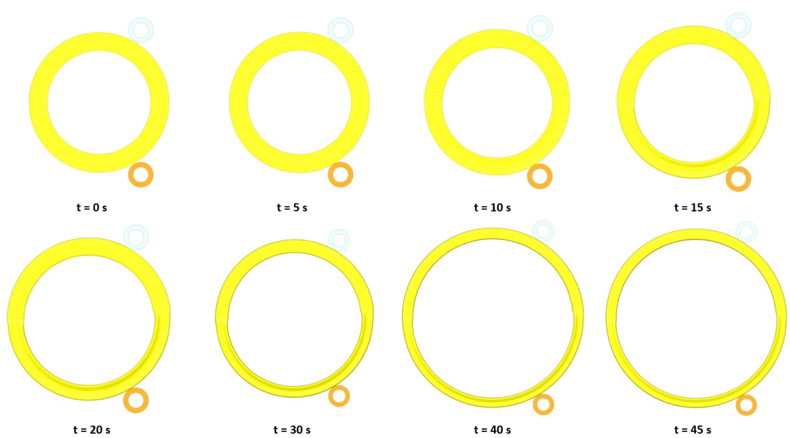

Σχήμα 13: Οπτικοποίηση της ανάπτυξης του δακτυλίου κατά τη διάρκεια της κατεργασίας

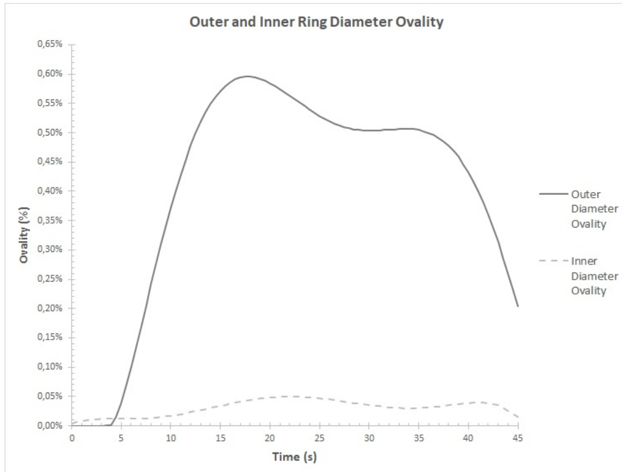

Σχήμα 14: Αποτελέσματα εξέλιξης της κυκλικότητας του δακτυλίου κατά τη διάρκεια της κατεργασίας

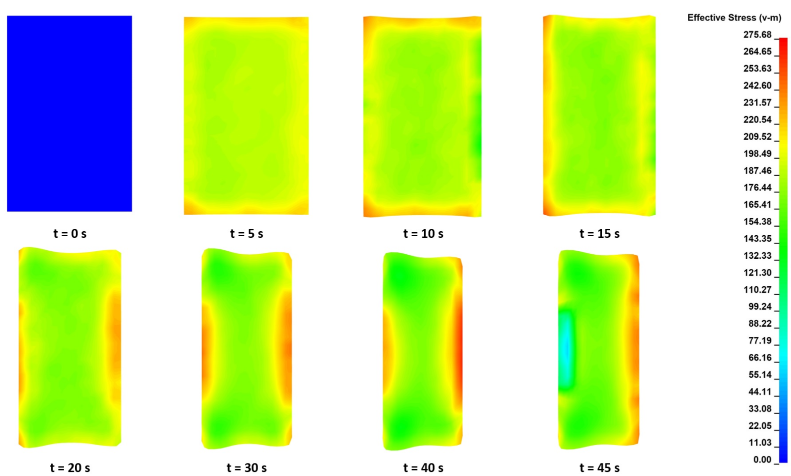

Σχήμα 15: Απεικόνιση των ισοδύναμων τάσεων κατά Von Mises, στην τομή του δακτυλίου που βρίσκεται μεταξύ του κυρίως ραούλου και του μαντρέλ

2.3. *Συμπεράσματα κεφαλαίου*

Από την ανάλυση που εκπονήθηκε στο παρόν κεφάλαιο εξήχθησαν τα παρακάτω συμπεράσματα:

- Οι πιο κρίσιμες παράμετροι για την ορθή μοντελοποίηση της εν θερμώ κατεργασίας έλασης δακτυλίων ήταν οι παρακάτω: (α) η ανεξαρτησία πλέγματος, (β) ο προσδιορισμός των συντελεστών μετάδοσης θερμότητας, (γ) η επιλογή κατάλληλου μαθηματικού μοντέλου υλικού και οι τιμές των απαραίτητων θερμο-μηχανικών ιδιοτήτων (με εξάρτηση των εν λόγω ιδιοτήτων από τη θερμοκρασία ή/και τον ρυθμό παραμόρφωσης), (δ) η κινηματική των υποστηρικτικών ραούλων και (ε) η επιλογή κατάλληλης κλιμάκωσης μάζας.

- Αν και αρκετές ιδιότητες αναφέρονταν στη βιβλιογραφική πηγή των Zhu et al., ορισμένες δεν παρέχονταν και χρειάστηκε να προσδιοριστούν είτε από τη βιβλιογραφία, είτε από διεξαγωγή δοκιμαστικών προσομοιώσεων δοκιμής-και-σφάλματος.

- Η γεωμετρική ανάπτυξη του δακτυλίου ήταν σχεδόν ταυτόσημη με αυτήν του πειράματος, αν και οι δύο απείχαν από τις επιθυμητές τελικές διαστάσεις που είχαν οριστεί στη δημοσίευση των Zhu et al.. Επιπλέον, οι κυκλικότητες που υπολογίστηκαν στις δύο περιφέρειες του δακτυλίου έδειξαν μια σχεδόν τέλεια κυκλική γεωμετρία.

- Τα τασικά, παραμορφωσιακά και θερμοκρασιακά πεδία που εξάχθηκαν από το μοντέλο κατέδειξαν τον μηχανισμό διαμόρφωσης του δοκιμίου, καθώς και ορισμένα κρίσιμα σημεία αυτού (π.χ. ελαττώματα που δημιουργήθηκαν).

- Τα υπολογισμένα διαγράμματα φορτίων και θερμοκρασιών κατέδειξαν ότι ολόκληρη η φάση 4 είχε παραληφθεί από την αντίστοιχη βιβλιογραφική πηγή (**Zhu et al., 2016**), ενώ επίσης αποκάλυψαν και ορισμένα σημεία όπου η πειραματική διαδικασία δεν ήταν ομαλή, όπως θα αναμενόταν.

3. Αύξηση της Ακρίβειας της Κατεργασίας Έλασης Δακτυλίων: Αποδείξεις Ιδεών

Από την προσομοίωση της έλασης δακτυλίων φάνηκε ότι οι επιθυμητές διαστάσεις στον κατεργαζόμενο δακτύλιο πολύ σπάνια μπορούν να εξασφαλισθούν από την κατεργασία. Εφόσον το αριθμητικό μοντέλο της κατεργασίας είχε πλέον πιστοποιηθεί, μπορούσε να χρησιμοποιηθεί σαν βάση για περαιτέρω διερευνήσεις. Έτσι, στο παρόν κεφάλαιο της διατριβής αναπτύχθηκαν μεθοδολογίες (και τα αντίστοιχα αριθμητικά μοντέλα) που θα μπορούσαν να αυξήσουν την ακρίβεια της έλασης δακτυλίων. Στη φάση της προκαταρκτικής μελέτης, αποφασίστηκε να εστιαστεί η έρευνα σε τρεις συγκεκριμένες, κρίσιμες παραμέτρους της κατεργασίας, οι οποίες ήταν:

- Ο ακριβής προσδιορισμός του αρχικού όγκου του εργοτεμαχίου

- Η επίδραση των ελαστικών και θερμικών παραμορφώσεων των εργαλείων

- Η επίδραση της κινηματικής των υποστηρικτικών ραούλων και η εξάρτησή της από το υλικό του δοκιμίου

Οι τρεις αυτές παράμετροι εξετάστηκαν ξεχωριστά σε επιμέρους υποκεφάλαια.

3.1. Ακριβής προσδιορισμός του αρχικού όγκου του εργοτεμαχίου

Για την ανάπτυξη της μεθοδολογίας, η οποία θα προέβλεπε με ακρίβεια τον αρχικό όγκο του εργοτεμαχίου, χρειάστηκε να διερευνηθούν σε βάθος όλες οι προκαταρκτικές φάσεις/κατεργασίες της έλασης δακτυλίων, ώστε να προσδιοριστούν οι παράγοντες που εισάγουν αβεβαιότητα στον ανωτέρω υπολογισμό. Οι εν λόγω κατεργασίες πραγματοποιούνται ως επί των πλείστων εν θερμώ και είναι: (α) η σφυρηλάτηση της αρχικής μπιγέτας και (β) η διάνοιξη της κεντρικής οπής. Αξίζει να αναφερθεί ότι για το μεγαλύτερο μέρος των δύο αυτών κατεργασιών είναι κοινώς αποδεκτό ότι ισχύει η αρχή διατήρηση του όγκου (**Schuler, 1998**).

3.1.1. Διερεύνηση σφυρηλάτησης αρχικής μπιγιέτας

Κατά τη διάρκεια της σφυρηλάτησης της αρχικής μπιγέτας, ένα κυλινδρικό εργαλείο συμπιέζει την αρχική μπιγέτα μέχρι το ύψος της να γίνει ίσο με το αρχικό ύψος του εργοτεμαχίου. Λόγω της τριβής με τα εργαλεία, το τελικό σχήμα μετά το πέρας της σφυρηλάτησης είναι βαρελοειδές, ενώ διαφορετικές παράμετροι της κατεργασίας μπορούν να επηρεάσουν την ακριβή γεωμετρία του βαρελοειδούς. Οι κυριότερες τέτοιες παράμετροι είναι:

- Οι αρχικές και τελικές διαστάσεις της μπιγέτας
- Η ταχύτητα του εργαλείου
- Οι συντελεστές τριβής μεταξύ δοκιμίου και εργαλείων

Η επίδραση των εν λόγω παραμέτρων μελετήθηκε μέσω ενός αξονοσυμμετρικού μοντέλου πεπερασμένου στοιχείων (Σχ.16):

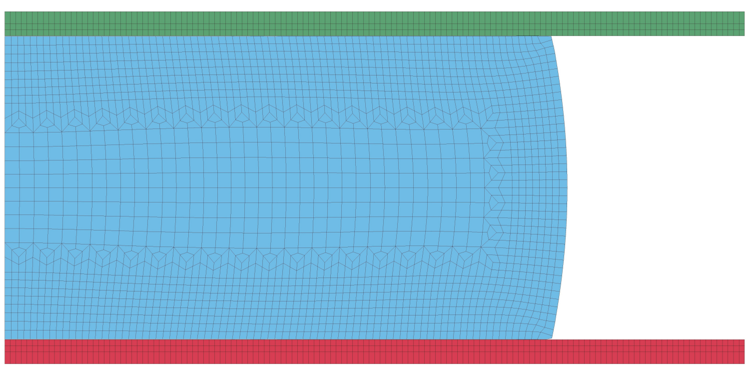

Σχήμα 16: Αξονοσυμμετρικό μοντέλο της κατεργασίας σφυρηλάτησης της αρχικής μπιγέτας του εργοτεμαχίου

Από την εν λόγω μελέτη, επετεύχθη ο προσδιορισμός μίας ημι-αναλυτικής σχέσης που μπορούσε σε συνεργασία με το ανωτέρω αξονοσυμμετρικό μοντέλο να προσδιορίσει έναν ισοδύναμο κύλινδρο με όγκο ίσο με αυτόν του εργοτεμαχίου μετά τη σφυρηλάτηση (Εξ.4):

$$r_{eq} = \sqrt{\frac{1}{y_u - y_l} \cdot \int_{y_l}^{y_u} \left[f(y)\right]^2 dy} \tag{4}$$

Ο υπολογισμός ενός ισοδύναμου πλήρους κυλίνδρου αντί του αρχικού βαρελοειδούς απεδείχθη κρίσιμος για την απλοποίηση της προς ανάπτυξη μεθοδολογίας.

3.1.2. Διάνοιξη κεντρικής οπής εργοτεμαχίου

Μετά τη σφυρηλάτηση της αρχικής μπιγέτας, ακολούθησε η μελέτη της κατεργασίας διάνοιξης της κεντρικής οπής του εργοτεμαχείου. Η εν λόγω κατεργασία πραγματοποιείται συνήθως σε τουλάχιστον δύο διακριτά στάδια: (α) την εντοπισμένη σφυρηλάτηση του κέντρου της μπιγέτας (πραγματοποιείται συνήθως σε πολλαπλά βήματα) και (β) την απότμηση ενός μικρού δίσκου που παρέμεινε μετά το πρώτο στάδιο. Και στην περίπτωση αυτή, η επίδραση των πιο σημαντικών παραμέτρων των δύο σταδίων της κατεργασίας διερευνήθηκαν αριθμητικά με δύο ξεχωριστά αξονοσυμμετρικά μοντέλα (Σχ.17 και 18):

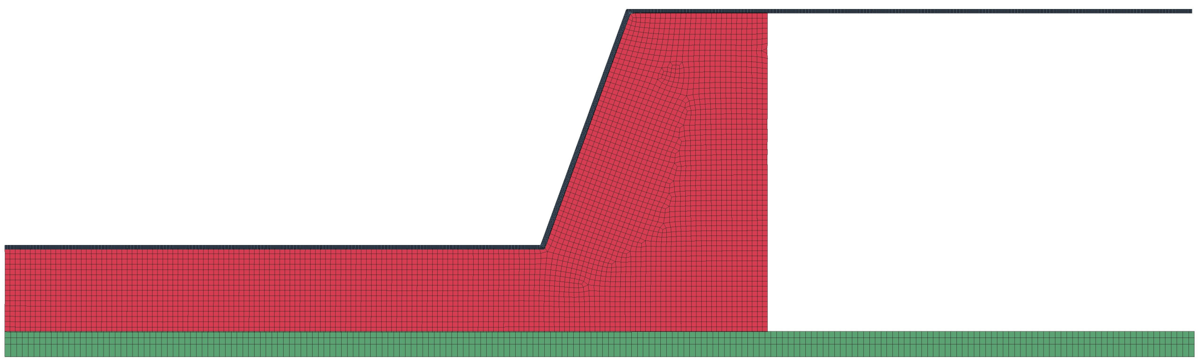

Σχήμα 17: Αξονοσυμμετρικό μοντέλο της κατεργασίας εντοπισμένη σφυρηλάτηση του κέντρου της μπιγέτας

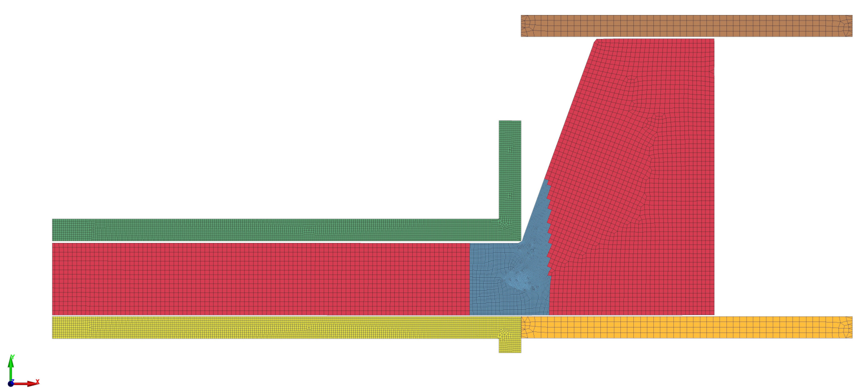

Σχήμα 18: Αξονοσυμμετρικό μοντέλο της κατεργασίας τελικής διάνοιξης της κεντρικής οπής του εργοτεμαχίου

Μετά το πέρας της διερεύνησης της κατεργασίας διάνοιξης της κεντρικής οπής του εργοτεμαχίου, προσδιορίστηκε και πάλι μια ημι-αναλυτική σχέση, η οποία μπορούσε μαζί με το αντίστοιχο αριθμητικό μοντέλο της κατεργασίας, να υπολογίσει τον αρχικό όγκο του εργοτεμαχίου (Εξ.5), μέσω ενός ισόογκου, διάτρητου κυλίνδρου με ισοδύναμη εξωτερική ακτίνα, r' (Εξ.6):

$$V_{billet} = \pi \cdot h_f \cdot \left(r'^2 - \frac{d^2}{4} \cdot v \right) \tag{5}$$

$$r' = \sqrt{r_{eq}^2 + \frac{1}{3 \cdot h_f} \cdot \left[h_t \cdot (r_t^2 + r_t \cdot R_t + R_t^2) + h_b \cdot (r_b^2 + r_b \cdot R_b + R_b^2)\right]} \tag{6}$$

3.1.3. Μεθοδολογία υπολογισμού αρχικού όγκου εργοτεμαχίου

Τα συμπεράσματα που προέκυψαν από τη μελέτη των ανωτέρω κατεργασιών χρησιμοποιήθηκαν ώστε να αναπτυχθεί μια μεθοδολογία για τον υπολογισμό του αρχικού όγκου του εργοτεμαχίου. Συνοπτικά, τα επιμέρους βήματα αυτής της μεθοδολογία είναι τα παρακάτω:

1. Από τις επιθυμητές διαστάσεις του τελικού προϊόντος, υπολογίζεται ο συνολικός όγκος του αρχικού υλικού.
2. Με βάση τον συνολικό όγκο, επιλέγονται δύο από τις τρεις κρίσιμες διαστάσεις του αρχικού εργοτεμαχίου, δηλαδή η εσωτερική ακτίνα του, η εξωτερική ακτίνα του ή/και το ύψος του. Η τρίτη διάσταση προκύπτει από την αρχή διατήρησης του όγκου.
3. Θεωρώντας σταθερή την εξωτερική ακτίνα σε όλο του ύψος του εργοτεμαχίου, αυτή τίθεται ίση με r'.
4. Μέσω της Εξ.6 υπολογίζεται το r_{eq}, δεδομένου ότι ορισμένες από τις υπόλοιπες παραμέτρους είναι γνωστές (π.χ. το πάχος του τελικού δίσκου, v που θα παραμείνει μετά την εντοπισμένη σφυρηλάτηση).
5. Με δεδομένο το ύψος του εργοτεμαχίου πριν την έλαση δακτυλίων και το πάχος του δίσκου μετά την εντοπισμένη σφυρηλάτηση, v, υπολογίζεται το βάθος διείσδυσης της εντοπισμένης σφυρηλάτησης, h.
6. Με όλες τις παραμέτρους γνωστές, μπορεί να υπολογιστεί πλέον ο όγκος της αρχικής μπιγέτας, μέσω της Εξ.5.
7. Ελέγχονται οι υπολογισμένες παράμετροι και συγκρίνονται με τις αντίστοιχες οριακές συνθήκες της βιβλιογραφίας (**Xu et al., 2014**), ώστε να διασφαλιστεί ότι καμία συνθήκη δεν παραβιάζεται. Συνήθως, στο εν λόγω βήμα αποδεικνύεται ότι η εντοπισμένη σφυρηλάτηση θα πρέπει να πραγματοποιηθεί σε πολλαπλά βήματα.
8. Μέσω του αρχικού όγκου της μπιγέτας, των διαθέσιμων διαστάσεων από τους προμηθευτές και των συνθηκών σφυρηλάτησης (θεωρούνται ότι είναι ήδη προσδιορισμένες), επιλέγεται μία από τις δύο διαστάσεις της αρχικής μπιγέτας (συνήθως η διάμετρος, d_0, και σπανιότερα το ύψος, h_0) και στη συνέχεια υπολογίζεται η δεύτερη.

3.1.4. Πιστοποίηση της προταθείσας μεθοδολογίας

Η μεθοδολογία που προτάθηκε έπρεπε να πιστοποιηθεί ως προς την εγκυρότητά της. Για τον λόγο αυτόν, επιχειρήθηκε η χρήση της εν λόγω μεθοδολογίας για την επίτευξη του επιθυμητού δακτυλίου που είχε αρχικά επισημανθεί στην εργασία αναφοράς (**Zhu et al., 2016**). Οι διαστάσεις του επιθυμητού αυτού δακτυλίου ήταν $900 \times 800 \times 115$ ($D_f \times d_f \times H_f$), ενώ οι αντίστοιχες τελικές διαστάσεις από την πειραματική διαδικασία ήταν $914 \times 810 \times 116.2$. Η προταθείσα μεθοδολογία οδήγησε στον υπολογισμό του όγκου του αρχικού υλικού του εργοτεμαχίου, καθώς και στις επιμέρους λεπτομέρειες κάθε επιμέρους κατεργασίας πριν την έλαση δακτυλίων (π.χ. διαστάσεις ενδιάμεσων προϊόντων, αριθμός πάσων εντοπισμένης σφυρηλάτησης, κλπ.). Εν συνεχεία, τα αριθμητικά μοντέλα που αναπτύχθηκαν στο παρόν κεφάλαιο, καθώς και το μοντέλο έλασης δακτυλίων που αναπτύχθηκε στο Κεφ.2 εφαρμόστηκαν στην αρχική μπιγέτα που προέκυψε από τη μεθοδολογία, ώστε να κατεργαστεί (αριθμητικά) ο επιθυμητός δακτύλιος. Ορισμένα από τα τελικά διαστασιολογικά αποτελέσματα μετά την ολοκλήρωση της επίλυση του αντίστοιχου μοντέλου έλασης δακτυλίου, παρουσιάζονται στο Σχ.19:

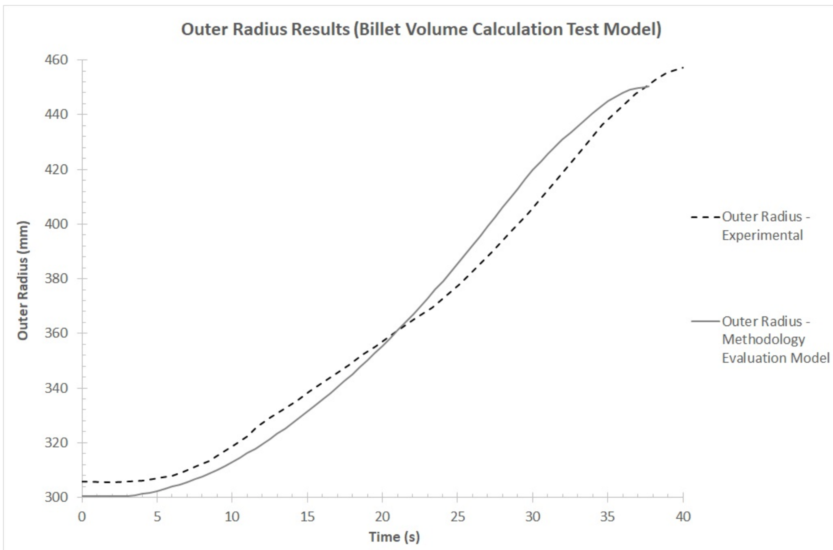

Σχήμα 19: Σύγκριση αποτελεσμάτων εξωτερικής διαμέτρου πειραματικής διαδικασίας και μεθοδολογίας ακριβούς προσδιορισμού αρχικού όγκου εργοτεμαχίου

Τα αποτελέσματα έδειξαν συνάφεια μεταξύ των τελικών διαστάσεων του δακτυλίου από την προσομοίωση και των επιθυμητών διαστάσεων, με απόκλιση πολύ μικρότερη του 1%.

3.1.5. Λοιπές παράμετροι που επηρεάζουν την προταθείσα μεθοδολογία

Στα πλαίσια της εν λόγω μελέτης, πολλές από τις παραμέτρους των επιμέρους κατεργασιών χρειάστηκε να διερευνηθούν ως προς την επίδρασή τους. Στις περιπτώσεις αυτές πραγματοποιήθηκαν επιμέρους κύκλοι προσομοιώσεων δοκιμής-και-σφάλματος και τα αντίστοιχα αποτελέσματα παρουσιάστηκαν στην εργασία. Ακόμα, μελετήθηκε περαιτέρω και η επίδραση της συστολής του τελικού δακτυλίου από τη θερμοκρασία της εν θερμώ κατεργασίας σε θερμοκρασία περιβάλλοντος. Τέλος, σημειώθηκε ότι ορισμένα αστάθμητα φαινόμενα της όλης παραγωγικής διαδικασίας (π.χ. απώλεια υλικού λόγω φολίδωσης, κλπ.) θα πρέπει να αντισταθμιστούν μέσω κατάλληλης προσαρμογής των τελικών διαστάσεων που προκύπτουν από την προταθείσα μεθοδολογία.

3.2. Επίδραση των θερμο-ελαστικών παραμορφώσεων των εργαλείων

Εν συνεχεία, μελετήθηκε η επίδραση των ελαστο-ελαστικών παραμορφώσεων των εργαλείων κατά τη διάρκεια μιας κατεργασίας έλασης δακτυλίων. Σε όλες τις σχετικές αριθμητικές αναλύσεις που πραγματοποιούνται στη βιβλιογραφία, τα εργαλεία θεωρούνται ως απαραμόρφωτα στερεά. Στις πραγματικές εφαρμογές, όμως, κάτι τέτοιο δεν ευσταθεί, καθώς οι θερμο-ελαστικές παραμορφώσεις των εργαλείων δεν μπορούν να απομονωθούν με κάποιον τρόπο. Παρόλα αυτά, η απομόνωση των θερμικών ή/και ελαστικών ιδιοτήτων των εργαλείων είναι δυνατή στις αριθμητικές προσομοιώσεις. Με βάση τα παραπάνω, για τη μελέτη της επίδρασης των θερμικών και ελαστικών παραμορφώσεων πραγματοποιήθηκε αριθμητική διερεύνηση, για την οποία αναπτύχθηκαν τα παρακάτω μοντέλα:

- Ένα μοντέλο με απαραμόρφωτα εργαλεία (Μοντέλο R).
- Ένα δεύτερο μοντέλο, στο οποίο τα εργαλεία μπορούσαν να παραμορφωθούν ελαστικά, αλλά όχι θερμικά (Μοντέλο NO_TE).
- Ένα τρίτο μοντέλο, στο οποίο τα εργαλεία μπορούσαν να παραμορφωθούν και ελαστικά και θερμικά (Μοντέλο TE).

Βάση και για τα τρία αριθμητικά που αναφέρθηκαν, αποτέλεσε το μοντέλο έλασης δακτυλίων που αναπτύχθηκε στο Κεφ.2. Τα αποτελέσματα από τα τρία μοντέλα, στη συνέχεια συγκρίθηκαν μεταξύ τους ανά δύο, ώστε να μπορεί να αξιολογηθεί η επίδραση της ελαστικής και θερμικής παραμόρφωσης των εργαλείων, ξεχωριστά.

Βασικό στοιχείο για την ανάπτυξη των προαναφερθέντων μοντέλων ήταν η ανεύρεση των κατάλληλων θερμο-ελαστικών μηχανικών ιδιοτήτων του υλικού των εργαλείων (AISI H13), οι οποίες βρέθηκαν στη σχετική βιβλιογραφία (π.χ. **Tolcha and Lemu, 2019**, **Oh and Ki, 2019**, κλπ.). Αξίζει να αναφερθεί ότι στα ανωτέρω μοντέλα δεν εισήχθησαν οι μηχανικές ιδιότητες της πλαστικής περιοχής του υλικού των εργαλείων, αφού τα αντίστοιχα σώματα αναμένονταν να υποστούν μόνο ελαστικές (πλήρως αντιστρεπτές) παραμορφώσεις.

Μετά την ολοκλήρωση των αντίστοιχων επιλύσεων, πραγματοποιήθηκαν οι παρακάτω τρεις συγκρίσεις των μοντέλων ανά δύο:

- Σύγκριση μοντέλου R και μοντέλου NO_TE.
- Σύγκριση μοντέλου NO_TE και μοντέλου TE.
- Σύγκριση μοντέλου R και μοντέλου TE.

Στα πλαίσια των εν λόγω διερευνήσεων, συγκρίθηκαν οι παραμορφώσεις που υπολογίστηκαν για τα εργαλεία, και για το κατεργαζόμενο τεμάχιο. Μερικές χαρακτηριστικές καμπύλες των προαναφερθέντων συγκρίσεων παρουσιάζονται στα Σχ.20 - 22:

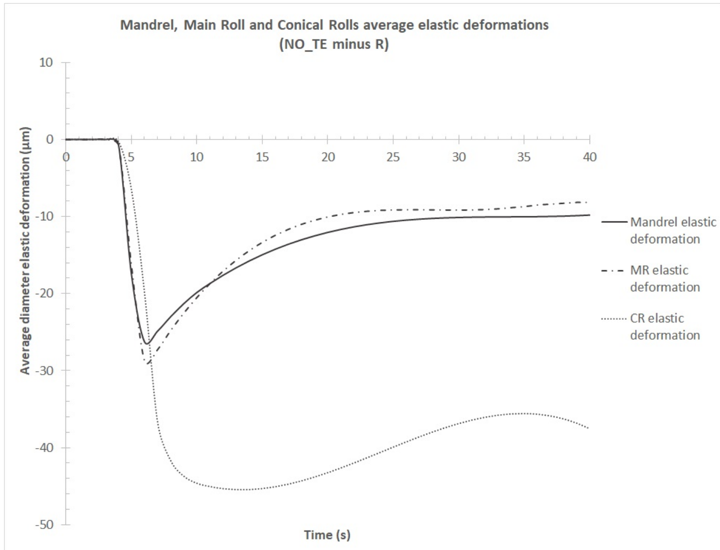

Σχήμα 20: Σύγκριση αποτελεσμάτων εξωτερικής διαμέτρου κυρίως ραούλου, μαντρέλ και κωνικού ραούλου (Σύγκριση μοντέλων R και NO_TE)

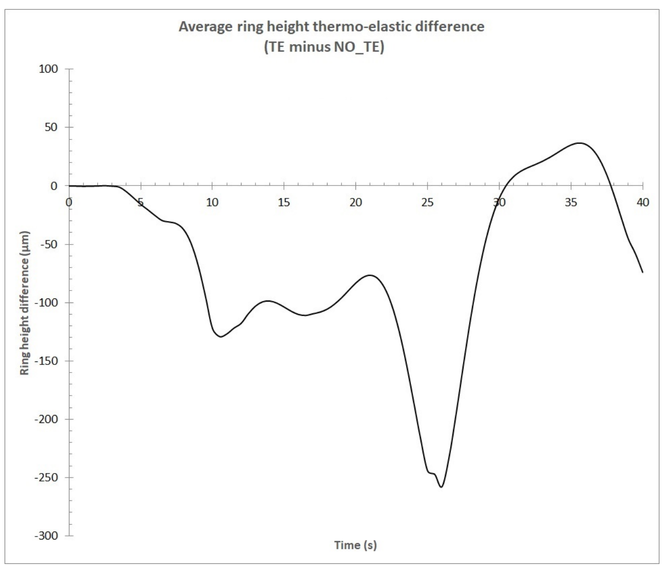

Σχήμα 21: Σύγκριση αποτελεσμάτων ύψους τεμαχίου (Σύγκριση μοντέλων NO_TE και TE)

Επισκόπηση επί των συγκρινόμενων αποτελεσμάτων οδήγησαν στο συμπέρασμα ότι οι θερμο-ελαστικές παραμορφώσεις των εργαλείων έχουν σημαντική επίδραση στις τελικές διαστάσεις του δοκιμίου. Πιο συγκεκριμένα, σχετικά μικρές παραμορφώσεις στα εργαλεία (της τάξεως των μερικών δεκάδων μm) οδήγησαν σε συγκριτικά μεγαλύτερες διαστασιακές διαφορές στο κατεργαζόμενο τεμάχιο (της τάξεως των μερικών εκατοντάδων μm), μεμονωμένα από κάθε φαινόμενο. Επίσης, αποδείχθηκε ότι η επίδραση των ελαστικών παραμορφώσεων των εργαλείων

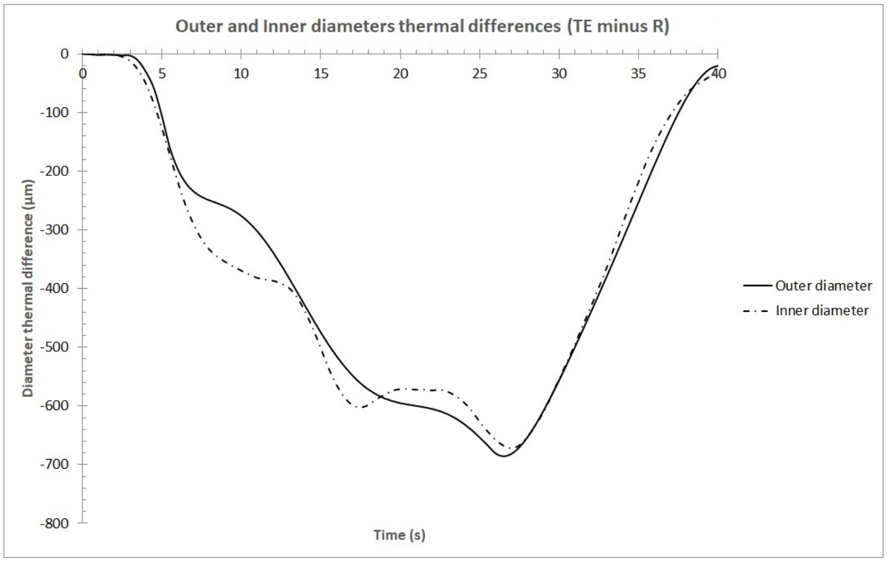

Σχήμα 22: Σύγκριση αποτελεσμάτων εξωτερικής και εσωτερικής διαμέτρου τεμαχίου (Σύγκριση μοντέλων R και TE)

στο κατεργαζόμενο τεμάχιο αντιτίθεται αυτής των θερμικών παραμορφώσεων των εργαλείων, με αποτέλεσμα η συνολική διαφορά στο συγκεκριμένο παράδειγμα να ήταν σχετικά μικρή (περίπου 5 - 15 μm). Παρόλα αυτά, το ίδιο μπορεί να μην ισχύει σε άλλες περιπτώσεις έλασης δακτυλίων και άρα οι αντίστοιχες διαφορές μπορεί να είναι σημαντικά μεγαλύτερες. Για τον λόγο αυτόν, στα πλαίσια της παρούσας μελέτης προτάθηκε η θέσπιση διορθωτικών παραγόντων για τις εν λόγω διαφορές ($\Delta R_{el}(t)$ και $\Delta R_{th}(t)$ για τις ελαστικές και θερμικές παραμορφώσεις, αντίστοιχα). Τέλος, αν και οι διαφορές που μετρήθηκαν στο τελικό τεμάχιο ήταν σχετικά μικρές, μπορούν να θεωρηθούν σημαντικές για προϊόντα υψηλής ακρίβειας, καθώς ήταν μεγαλύτερες από τα επίπεδα των συνήθων ανοχών αντίστοιχων εφαρμογών.

3.3. *Επίδραση της κινηματικής των υποστηρικτικών ραούλων και η εξάρτησή αυτής από το υλικό του δοκιμίου*

Η τελευταία κρίσιμη παράμετρος που διερευνήθηκε ως προς την επίδραση της στην έλαση δακτυλίων ήταν η κινηματική των υποστηρικτικών ραούλων και το κατά πόσο αυτή εξαρτάται από το υλικό του κατεργαζόμενου τεμαχίου. Στο αριθμητικό μοντέλο έλασης δακτυλίων που παρουσιάστηκε στο Κεφ.2, η κίνηση των υποστηρικτικών ραούλων περιγράφηκε μέσω δύο διαφορετικών πολυωνυμικών σχέσεων, οι οποίες στηρίζονταν στον ρυθμό ανάπτυξης του δακτυλίου: (α) μίας για τη φάση 1 και 2 της κατεργασίας και (β) μίας δεύτερης για τη φάση 3 της κατεργασίας (Εξ.1 και 2, αντίστοιχα). Με βάση τα παραπάνω, τέθηκαν δύο ερευνητικά ερωτήματα στο παρόν κεφάλαιο:

- Μπορεί η κίνηση των υποστηρικτικών ραούλων να περιγραφεί με μία μόνο πολυωνυμική σχέση;

- Έχει το υλικό του δακτυλίου επίδραση στον ρυθμό ανάπτυξης του, και άρα και στην προαναφερθείσα πολυωνυμική σχέση;

Προκειμένου να απαντηθούν τα παραπάνω ερευνητικά ερωτήματα, πραγματοποιήθηκε μία νέα αριθμητική διερεύνηση, στα πλαίσια της οποίας εκπονήθηκαν οι παρακάτω αναλύσεις:

1. Ανάπτυξη ενός αριθμητικού μοντέλου έλασης δακτυλίων βάσει του μοντέλου του Κεφ.2, με το υλικό του δακτυλίου να είναι κράμα αλουμινίου AA5754.
2. Χρήση των δύο μοντέλων έλασης δακτυλίων (με υλικό IN718 και AA5754), αλλά με την κίνηση των υποστηρικτικών ραούλων να ορίζεται από ένα πολυώνυμο $5^{ης}$ τάξης.

3.3.1. Μοντέλο έλασης δακτυλίου με υλικό τεμαχίου AA5754

Όπως αναφέρθηκε και παραπάνω, ως δεύτερο υλικό δακτυλίου για τη σύγκριση με το IN718 επιλέχθηκε το κράμα αλουμινίου AA5754. Προκειμένου να μπορεί να πραγματοποιηθεί με επιτυχία η προσομοίωση της κατεργασίας με το υλικό αυτό, έπρεπε να μεταβληθούν κατάλληλα τρία στοιχεία του υπάρχοντος μοντέλου: (α) οι θερμο-μηχανικές ιδιότητες του κατεργαζόμενου τεμαχίου, (β) η αρχική θερμοκρασία του τεμαχίου και (γ) οι εξισώσεις κίνησης των υποστηρικτικών ραούλων. Οι υπόλοιπες παράμετροι του μοντέλου παρέμειναν οι ίδιες. Οι θερμο-μηχανικές ιδιότητες του κράματος AA5754 προσδιορίστηκαν από αντίστοιχες πηγές της βιβλιογραφίας (π.χ. **Acar et al., 2018**, **Hadi, Al-Khafaji, and Subhi, 2022**, κ.α.). Αντίστοιχα, η αρχική θερμοκρασία του δοκιμίου τέθηκε ίση με $T_{0,Al} = 773.15$ K, μια τυπική θερμοκρασία για εν θερμώ κατεργασίες του AA5754. Για την περίπτωση των εξισώσεων κίνησης των υποστηρικτικών ραούλων σε αυτήν την περίπτωση, χρειάστηκε να πραγματοποιηθεί εκ νέου ένας κύκλος προσομοιώσεων δοκιμής-και-σφάλματος, με τις τελικές σχέσεις να παρουσιάζονται παρακάτω (Εξ.7 και 8):

$$R_i = 2.0806 \cdot 10^{-1} \cdot t^{-5.6391 \cdot 10^{-3} \cdot t + 2.0225} + 301.6711 \tag{7}$$

$$R_i = -4.1797 \cdot 10^{-1} \cdot t^2 + 36.8289 \cdot t - 332.4106 \tag{8}$$

Αξίζει να αναφερθεί ότι η ανάγκη ανάπτυξης νέων σχέσεων κίνησης για τα υποστηρικτικά ράουλα, καθώς και η αύξηση της πολυπλοκότητας των εν λόγω σχέσεων για την περίπτωση του κράματος αλουμινίου, λειτουργούν ως μία έμμεση απόδειξη της κρισιμότητας των θερμο-μηχανικών ιδιοτήτων του υλικού του δακτυλίου στον ρυθμό ανάπτυξής του.

Μετά την επίλυση του μοντέλου με δακτύλιο AA5754 πραγματοποιήθηκε επισκόπηση στα αποτελέσματα αυτού, μερικά από τα οποία παρουσιάζονται στα Σχ.23 - 25. Αξίζει να αναφερθεί ότι τα διαστασιακά αποτελέσματα από το συγκεκριμένο μοντέλο συγκρίθηκαν με τα αντίστοιχα αποτελέσματα του μοντέλου με δακτύλιο IN718.

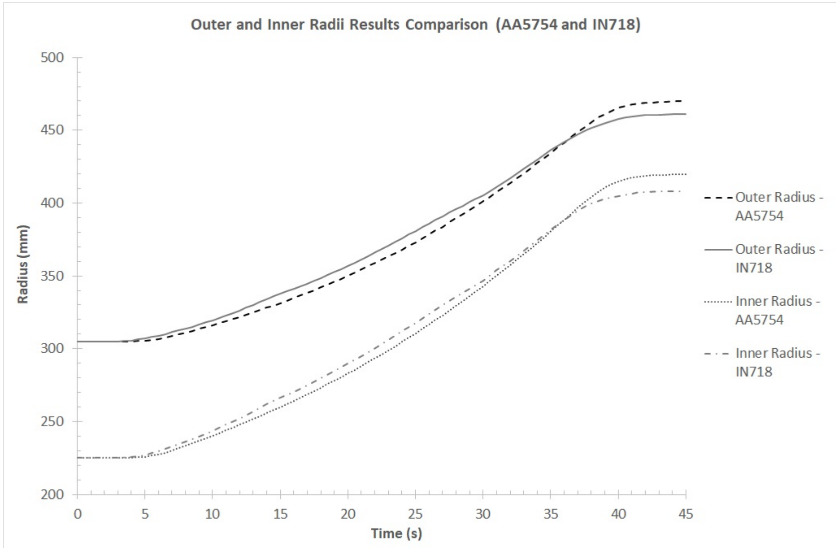

Σχήμα 23: Ανάπτυξη εξωτερικής και εσωτερικής ακτίνας δακτυλίου AA5754 κατά τη διάρκεια της κατεργασίας, και σύγκριση με αντίστοιχα αποτελέσματα δακτυλίου IN718

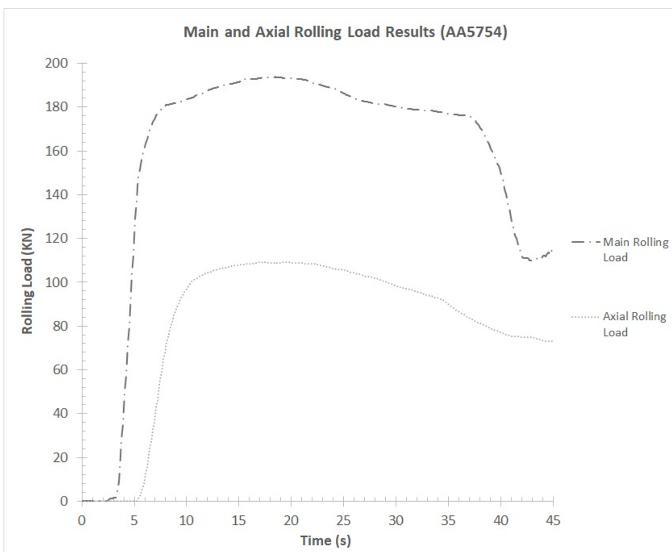

Σχήμα 24: Κύριο και κάθετο φορτίο έλασης δακτυλίου (AA5754)

Από τα αποτελέσματα του μοντέλου έλασης δακτυλίου για το AA5754, αποδείχθηκε ότι η μορφή του τελικού προϊόντος στη συγκεκριμένη περίπτωση ήταν μεγαλύτερη στις κύριες διαστάσεις της σε ποσοστό 0.5 - 3%, περίπου, σε σύγκριση με τον τελικό δακτύλιο IN718. Τα υπόλοιπα αποτελέσματα (π.χ. κατανομές τάσεων και παραμορφώσεων, θερμοκρασίες, φορτία, κλπ.), απείχαν σημαντικά από αυτά του IN718, όπως ήταν αναμενόμενο λόγω των μεγάλων αντιθέσεων στις θερμο-μηχανικές ιδότητες των δύο υλικών, καθώς και λόγω των διαφορετικών

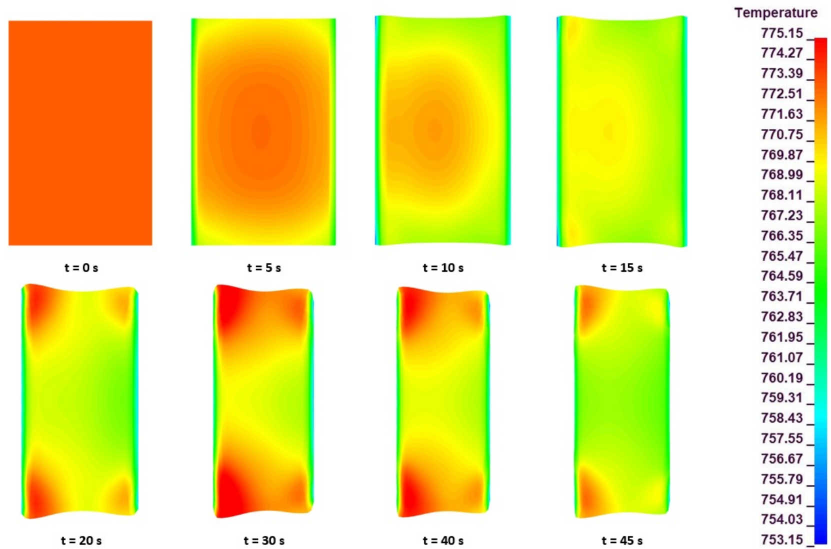

Σχήμα 25: Κατανομή θερμοκρασιών σε διαφορετικές χρονικές στιγμές της τομής του δακτυλίου AA5754 που βρίσκεται μεταξύ του κυρίως ραούλου και του μαντέλ

αρχικών συνθηκών στα δύο μοντέλα. Ένα γενικό συμπέρασμα που μπορεί αν εξαχθεί είναι ότι το υλικό του δακτυλίου επηρεάζει σημαντικά την τελική μορφή του προϊόντος, ακόμα και με την ίδια κινηματική στα κύρια εργαλεία της έλασης δακτυλίων.

3.3.2. Επιβολή πολυωνύμου μεγαλύτερης τάξης στην κίνηση των υποστηρικτικών ραούλων

Με τα μοντέλα των δύο διαφορετικών υλικών δακτυλίων να έχουν ολοκληρωθεί, στη συνέχεια διερευνήθηκε η επιβολή ενός μόνο πολυωνύμου μεγαλύτερης τάξης για την κινηματική των υποστηρικτικών ραούλων. Για τη διερεύνηση του κατάλληλου πολυωνύμου για το κάθε μοντέλο, χρησιμοποιήθηκαν τα αποτελέσματα της ανάπτυξης της εξωτερικής διαμέτρου από τα δύο μοντέλα που είχαν ήδη επιλυθεί. Μετά από πολλαπλές δοκιμές πολυωνύμων διαφορετικής τάξης για κάθε υλικό, οι τελικές πολυωνυμικές σχέσεις προσδιορίστηκαν και παρουσιάζονται στην Εξ.9 για το IN718 και στην Εξ.10 για το AA5754:

$$\begin{aligned} R_i = -8.5270 \cdot 10^{-6} \cdot t^5 + 8.5333 \cdot 10^{-4} \cdot t^4 - 3.1678 \cdot 10^{-2} \cdot t^3 \\ +5.9987 \cdot 10^{-1} \cdot t^2 - 2.2830 \cdot t + 306.4734 \end{aligned} \tag{9}$$

$$\begin{aligned} R_i = -6.8514 \cdot 10^{-6} \cdot t^5 + 6.6829 \cdot 10^{-4} \cdot t^4 - 2.4552 \cdot 10^{-2} \cdot t^3 \\ +5.0627 \cdot 10^{-1} \cdot t^2 - 2.0714 \cdot t + 306.6942 \end{aligned} \tag{10}$$

Τα δύο πολυώνυμα των Εξ.9 και 10 κατόπιν εφαρμόστηκαν στα δύο μοντέλα έλασης δακτυλίων (με δακτύλιο IN718 και AA5754) και επιλύθηκαν εκ νέου. Τα αποτελέσματα από κάθε νέο μοντέλο συγκρίθηκαν με τα αποτελέσματα των αρχικών, αντίστοιχων μοντέλων. Μερικά χαρακτηριστικά διαγράμματα από τις εν λόγω συγκρίσεις παρουσιάζονται στα Σχ.26 και 27:

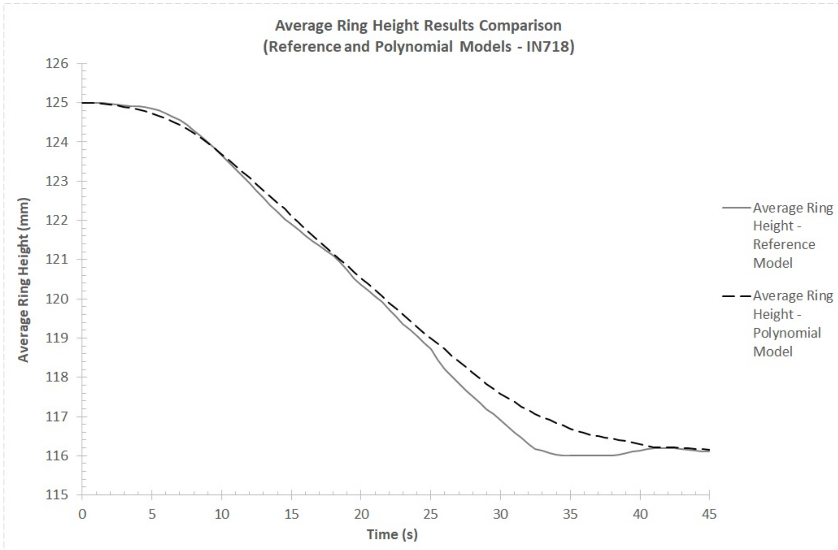

Σχήμα 26: Σύγκριση της εξέλιξης του μέσου ύψους δακτυλίου μεταξύ του αρχικού μοντέλου και του μοντέλου με πολυώνυμο μεγαλύτερης τάξης (IN718)

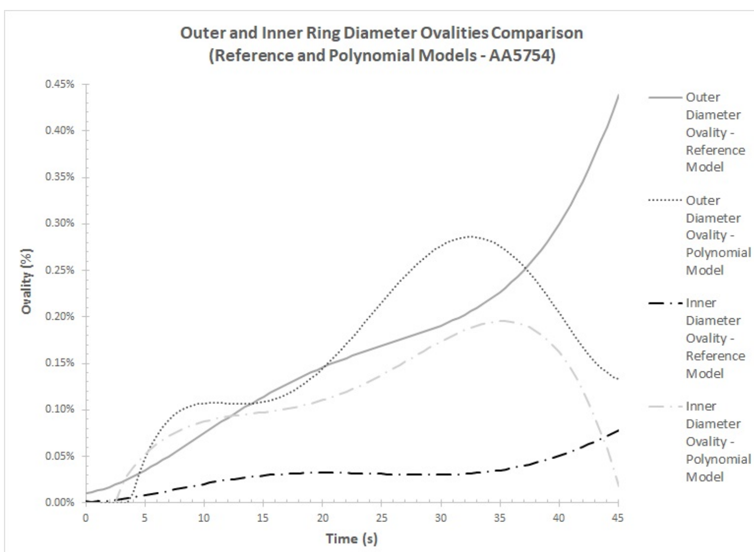

Σχήμα 27: Σύγκριση των σφαλμάτων κυκλικότητας της εξωτερικής και εσωτερικής ακτίνας μεταξύ του αρχικού μοντέλου και του μοντέλου με πολυώνυμο μεγαλύτερης τάξης (AA5754)

Από την επισκόπηση των τελικών αποτελεσμάτων, αποδείχθηκε ότι η χρήση μιας μόνο πολυωνυμικής σχέσης $5^{ης}$ τάξης οδήγησε σε πιο ομαλές παραμορφώσεις των εργοτεμαχίων, ενώ οι τελικές διαστάσεις του παραγόμενου δακτυλίου είχαν εξάρτηση επιπλέον και από το υλικό αυτού.

3.4. Συμπεράσματα κεφαλαίου

Από τις διαφορετικές αναλύσεις που διεκπεραιώθηκαν στα πλαίσια του παρόντος κεφαλαίου, αποδείχθηκε η εξάρτηση της ακρίβειας των τελικών διαστάσεων του κατεργαζόμενου δακτυλίου και από τις τρεις παραμέτρους που μελετήθηκαν. Τα συμπεράσματα από κάθε επιμέρους μελέτη συνοψίζονται στα παρακάτω:

- Με βάση τα αποτελέσματα των αντίστοιχων προσομοιώσεων, η μεθοδολογία υπολογισμού του όγκου της αρχικής μπιγέτας απέδωσε πολύ ακριβείς τελικές διαστάσεις στον κατεργασμένο δακτύλιο.
- Ένα σημαντικό στοιχείο για την αποδοτικότητα της εν λόγω μεθοδολογίας είναι η γνώση ορισμένων παραμέτρων κάθε προγενέστερης κατεργασίας, καθώς και η αντιστάθμιση ορισμένων φυσικών φαινομένων που οδηγούν σε απώλεια υλικού ή σε μεταβολή των τελικών διαστάσεων μετά την έλαση δακτυλίων.
- Οι θερμικές και ελαστικές παραμορφώσεις των εργαλείων κατά τη διάρκεια της έλασης δακτυλίων μπορούν να επιφέρουν σημαντικές διαστασιακές αποκλίσεις στο τελικό προϊόν, στα πλαίσια μιας κατεργασίας υψηλής ακρίβειας.
- Δεδομένου ότι τα αποτελέσματα από τις ελαστικές παραμορφώσεις των εργαλείων είναι αντίθετα από αυτά των θερμικών τους παραμορφώσεων, καθώς και το γεγονός ότι τα δύο είδη παραμορφώσεων εξαρτώνται από διαφορετικές ιδιότητες των υλικών, τα συνδυαστικά αποτελέσματα από τους δύο τύπους παραμορφώσεων μπορεί να είναι πολύ σημαντικά σε ορισμένες περιπτώσεις και αμελητέα σε άλλες.
- Το υλικό του δακτυλίου παίζει καθοριστικό ρόλο στις διαστάσεις του τελικού προϊόντος της έλασης δακτυλίων.
- Ο καθορισμός ενός υψηλής τάξης πολυωνύμου για την κινηματική των υποστηρικτικών ραούλων μπορεί να επιφέρει διαφορές στις τελικές διαστάσεις του κατεργαζόμενου δοκιμίου, συναρτήσει και του υλικού αυτού.

4. Αντίστροφη Έλαση Δακτυλίων

Στο προηγούμενο κεφάλαιο επισημάνθηκαν ορισμένες παράμετροι που μπορούν εν δυνάμει να βελτιστοποιηθούν, ώστε να αυξηθεί η ακρίβεια της κατεργασίας έλασης δακτυλίων. Παρόλα αυτά, στις περισσότερες βιομηχανικές παραγωγές αυτής της κατεργασίας ορισμένα διαστασιακά σφάλματα εμμένουν μετά το τέλος αυτής, με αποτέλεσμα να απαιτούνται αρκετοί κύκλοι κατεργασιών αποβολής υλικού, ώστε να επιτευχθούν οι επιθυμητές τελικές διαστάσεις στο προϊόν. Προκειμένου να περιοριστεί ή να εξαλειφθεί η ανάγκη αυτών των επιπλέον βημάτων, στο παρόν κεφάλαιο διερευνήθηκε μια νέα κατεργασία, η οποία μπορεί να πραγματοποιηθεί στις διατάξεις έλασης δακτυλίων, χωρίς να απαιτείται επανατοποθέτηση ή αρχικοποίηση του δακτυλίου. Η κατεργασία αυτή πήρε το όνομα *"Αντίστροφη Έλαση Δακτυλίων"*. Δεδομένου ότι η εν λόγω κατεργασία είναι νεωτεριστική, η απόδειξη των ιδέας αυτής πραγματοποιήθηκε στην παρούσα διατριβή μέσω αριθμητικών αναλύσεων.

4.1. Βασικές αρχές Αντίστροφης Έλασης Δακτυλίων

Βασική προϋπόθεση για τη διεξαγωγή της Αντίστροφης Έλασης Δακτυλίων είναι η χρήση διατάξεων έλασης δακτυλίων, με περισσότερα των δύο υποστηρικτικών ραούλων και με δυνατότητα αυτόνομης κίνησης στο καθένα από αυτά. Τέτοιες διατάξεις, αν και όχι ευρέως διαδεδομένες στη βιομηχανία, έχουν παρουσιαστεί σε μερικές δημοσιεύσεις (π.χ. **Arthington et al., 2015**, **Li, Guo, and Wang, 2021**). Αξίζει να αναφερθεί ότι αν και η χρήση κωνικών ραούλων δεν είναι απαγορευτική για τη συγκεκριμένη κατεργασία, στα πλαίσια της εν λόγω μελέτης αυτά δε συμπεριλήφθηκαν ως μέρος της διάταξης.

Ως προς τα στάδια υλοποίησης της κατεργασίας, η Αντίστροφη Έλαση Δακτυλίων αποτελείται από δύο επιμέρους βήματα:

1. Τον περιμετρικό "στραγγαλισμό" του δακτυλίου ("collaring").
2. Την ομοιόμορφη μείωση του πάχους τοιχώματος του δακτυλίου ("pulling").

Τα δύο αυτά βήματα διέπονται από ορισμένες διαφορές στην κινηματική των εργαλείων, οι οποίες και επιφέρουν διαφορετικά τελικά αποτελέσματα στο κατεργαζόμενο τεμάχιο. Πιο συγκεκριμένα στο βήμα του "στραγγαλισμού", όλα τα εργαλεία κινούνται συντονισμένα προς το κέντρο του δακτυλίου, ενώ στο βήμα της ομοιόμορφης μείωσης του πάχους τοιχώματος του δακτυλίου, το μαντρέλ σταματάει τη γραμμική του κίνηση, και όλα τα υπόλοιπα εργαλεία συνεχίζουν τη συντονισμένη τους κίνηση προς το κέντρο του δακτυλίου. Θα πρέπει να αναφερθεί ότι και στα δύο βήματα της κατεργασίας, η περιστροφική κίνηση επιβάλλεται από το κυρίως ράουλο, ενώ όλα τα υπόλοιπα εργαλεία μπορούν να περιστρέφονται ελεύθερα. Μια γραφική αναπαράσταση της κινηματικής των εργαλείων στα δύο βήματα της Αντίστροφης Έλασης Δακτυλίων, παρουσιάζεται στο Σχ.28:

Αποτέλεσμα των ανωτέρω διαφορών στην κινηματική των εργαλείων κάθε βήματος είναι η συνολική μείωση της εσωτερικής και εξωτερικής διαμέτρου στο βήμα του "στραγγαλισμού", ενώ στο βήμα της ομοιόμορφης μείωσης του πάχους τοιχώματος πραγματοποιείται μείωση μόνο της εξωτερικής διαμέτρους του δακτυλίου. Άμεση συνέπεια της μείωσης των διαμέτρων του δακτυλίου είναι η ταυτόχρονη αύξηση του μέσου ύψους αυτού, ώστε να μην παραβιάζεται η αρχή διατήρησης του όγκου. Παρόλα αυτά, η μείωση του ύψους του δοκιμίου στα επιθυμητά επίπεδα μπορεί να πραγματοποιηθεί μέσω πιο απλών κατεργασιών αποβολής υλικού (π.χ. πλάνισμα, επίπεδο ρεκτιφιέ, κλπ.), οι οποίες είναι πιο εύκολες ως προς την αρχικοποίηση της θέσης του τεμαχίου.

Το βασικότερο πλεονέκτημα που προκύπτει από την υλοποίηση της Αντίστροφης Έλασης Δακτυλίων είναι ότι μπορεί να πραγματοποιηθεί αμέσως μετά από μια τυπική κατεργασία έλασης δακτυλίων, χωρίς την ανάγκη ενδιάμεσων διακοπών ή/και επανατοποθέτησης του κατεργαζόμενου τεμαχίου. Το γεγονός αυτό οφείλεται, εν μέρει, στο ότι η απαραίτητη διάταξη για την

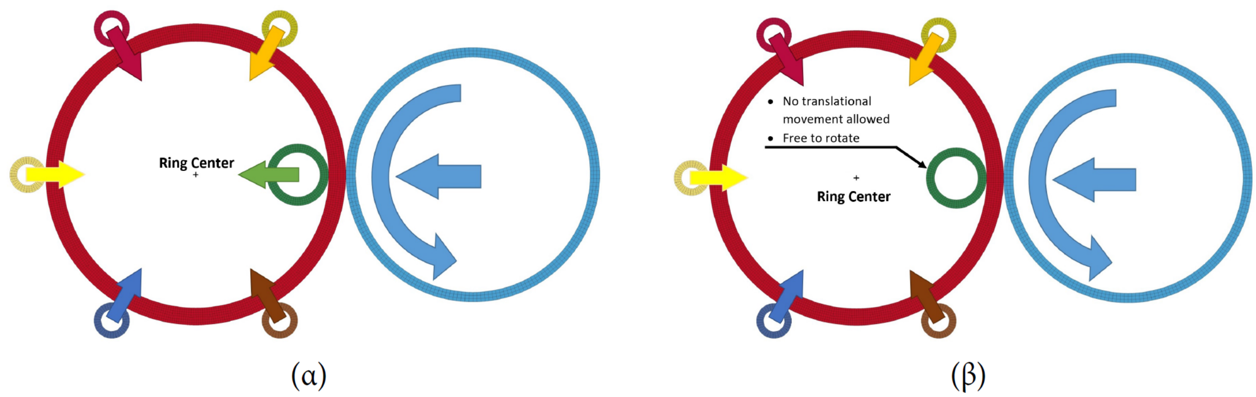

Σχήμα 28: Κινηματική εργαλείων κατά την Αντίστροφη Έλαση Δακτυλίων: (α) Βήμα "στραγγαλισμού" και (β) βήμα ομοιόμορφης μείωσης πάχους τοιχώματος

Αντίστροφη Έλαση Δακτυλίων μπορεί να χρησιμοποιηθεί και για τυπικές ελάσεις δακτυλίων, ενώ η μετάβαση από τη μία κατεργασία στην επόμενη απαιτεί μια απλή ρύθμιση των ταχυτήτων των εργαλείων. Επιπροσθέτως, μεταλλουργικά φαινόμενα που πραγματοποιούνται στα διαλείμματα μεταξύ των κατεργασιών και τα οποία οφείλονται κυρίως στην ψύξη του προϊόντος στο διάστημα αυτό (π.χ. ανακρυστάλλωση, κλπ.), στη συγκεκριμένη περίπτωση δε θα πραγματοποιηθούν.

4.2. Προσομοίωση Αντίστροφης Έλασης Δακτυλίων

Προκειμένου να αποδειχθεί η βιωσιμότητα της Αντίστροφης Έλασης Δακτυλίων, χρειάστηκε να πραγματοποιηθεί η αντίστοιχη αριθμητική ανάλυση. Το μοντέλο που αναπτύχθηκε στα πλαίσια αυτής της ανάλυσης βασίστηκε, σε αρκετά σημεία, στο μοντέλο έλασης δακτυλίων του Κεφ.2. Πιο συγκεκριμένα, επιχειρήθηκε να "διορθωθούν" οι διαστασιακές ατέλειες που προέκυψαν κατά την έλαση δακτυλίων της βιβλιογραφικής αναφοράς των Zhu et al., σε σχέση με τις επιθυμητές διαστάσεις του τελικού δακτυλίου που είχαν ορίσει αρχικά οι συγγραφείς.

Για το βήμα του "στραγγαλισμού", το αντίστοιχο μοντέλο πήρε ως αρχική κατάσταση την έξοδο του μοντέλου έλασης δακτυλίων. Εν συνεχεία, προστέθηκαν κάποια επιπλέον υποστηρικτικά ράουλα στην περιφέρεια του δακτυλίου και ρυθμίστηκαν κατάλληλα οι ταχύτητες όλων των εργαλείων. Παράλληλα, αφαιρέθηκαν από την ανάλυση τα κωνικά ράουλα και προστέθηκε μία εργαλειοτράπεζα, ώστε να μπορέσει να συμπεριληφθεί στην ανάλυση και η επίδραση της βαρύτητας.

Αντίστοιχα για το βήμα της ομοιόμορφης μείωσης πάχους τοιχώματος, το μοντέλο που αναπτύχθηκε είχε ως αρχική κατάσταση την έξοδο του μοντέλου "στραγγαλισμού". Για την προσομοίωση του βήματος αυτού έπρεπε να ρυθμιστούν κατάλληλα οι ταχύτητες των εργαλείων, αφού από κάποιες προκαταρκτικές προσομοιώσεις αποδείχθηκε ότι το συγκεκριμένο μοντέλο ήταν αρκετά ευαίσθητο στη συγκεκριμένη παράμετρο.

Μετά από την επίλυση και των μοντέλων των δύο βημάτων, πραγματοποιήθηκε επισκόπηση στα αποτελέσματά τους. Από αυτά, οι τελικές διάμετροι του δακτυλίου είχαν απόκλιση από αντίστοιχες επιθυμητές διαστάσεις σε ποσοστό σημαντικά μικρότερο του 1%, κάτι που υπαινίσσεται ότι η Αντίστροφη Έλαση Δακτυλίων μπορεί να καταταγεί στις κατεργασίες υψηλής διαστασιακής ακρίβειας. Ακόμα και στην περίπτωση, όμως, που οι αποκλίσεις από τις τιμές στόχου θα ήταν μεγαλύτερες, μια απλή ρύθμιση της διάρκεια κάθε βήματος της κατεργασίας, θα ήταν αρκετή για τη διόρθωσή τους. Από την άλλη μεριά, παρατηρήθηκε μια συνολική αύξηση του ύψους του δοκιμίου σε ποσοστό περίπου 5%. Μερικά χαρακτηριστικά αποτελέσματα από τις δύο προσομοιώσεις παρουσιάζονται στα Σχ.29 και 30:

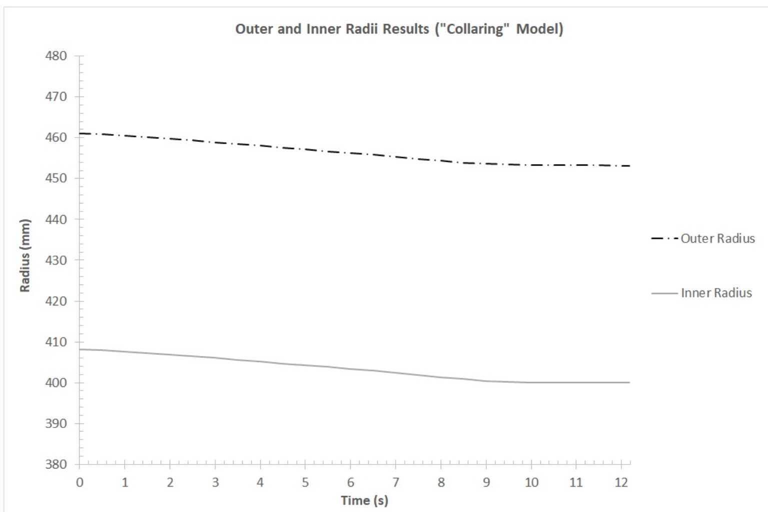

Σχήμα 29: Εξέλιξη της εσωτερικής και εξωτερικής ακτίνας του δακτυλίου (βήμα "στραγγαλισμού")

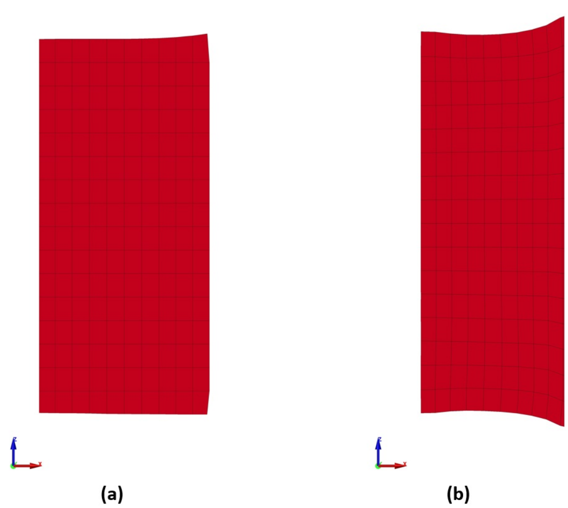

Σχήμα 30: Μεταβολή της διατομής του δακτυλίου κατά το βήμα της ομοιόμορφης μείωσης πάχους τοιχώματος

Αξίζει να αναφερθεί ότι και σε αυτήν την περίπτωση, άλλοι παράγοντες όπως η συστολή του δακτυλίου κατά την ψύξη του σε θερμοκρασία περιβάλλοντος θα πρέπει να έχουν ληφθεί υπ΄ όψιν πριν τη διεξαγωγή μιας Αντίστροφης Έλασης Δακτυλίων και να έχουν αντισταθμιστεί.

4.3. Ανάλυση κρίσιμων παραμέτρων Αντίστροφης Έλασης Δακτυλίων

Κατά την ανάπτυξη του μοντέλου Αντίστροφης Έλασης Δακτυλίων αποκαλύφθηκε ότι ορισμένες παράμετροι ήταν πιο επιδραστικές στα τελικά αποτελέσματα της κατεργασίας. Αποφασίστηκε, λοιπόν, να πραγματοποιηθεί περαιτέρω ανάλυση στις πιο κρίσιμες από αυτές τις παραμέτρους, οι οποίες ήταν: (α) οι γραμμικές ταχύτητες των εργαλείων, (β) ο αριθμός των υποστηρικτικών ραούλων και (γ) η αρχική θερμοκρασία του εργοτεμαχίου. Εφόσον ο κύριος στόχος της εν λόγω ανάλυσης είναι η μελέτη της επίδρασης των προτεινόμενων παραμέτρων, χρησιμοποιήθηκαν τα μοντέλα των δύο βημάτων της Αντίστροφης Έλασης Δακτυλίων, με μεταβολή μίας μόνο παραμέτρου κάθε φορά (τουλάχιστον κατά τον σχεδιασμό της μελέτης). Θα πρέπει να αναφερθεί ότι μελετήθηκαν μόνο τα τελικά διαστασιακά αποτελέσματα από κάθε μοντέλο, στα πλαίσια της αξιολόγησης των ανωτέρω κρίσιμων παραμέτρων.

Για τη διερεύνηση της επίδρασης της γραμμικής ταχύτητας των εργαλείων αναπτύχθηκαν δύο διαφορετικά ζεύγη μοντέλων: (α) ένα ζεύγος με τις μισές γραμμικές ταχύτητες εργαλείων από αυτές που τέθηκαν στο αρχικό ζεύγος μοντέλων και (β) ένα δεύτερο ζεύγος με τις διπλάσιων των αρχικών γραμμικών ταχυτήτων. Υπενθυμίζεται ότι κάθε ζεύγος μοντέλων αποτελείται από το μοντέλο του βήματος "στραγγαλισμού") και το μοντέλο του βήματος ομοιόμορφης μείωσης πάχους τοιχώματος. Κατ΄ αντιστοιχία της μεταβολής των γραμμικών ταχυτήτων σε κάθε νέο ζεύγος μοντέλων, προσαρμόστηκαν κατάλληλα και οι συνολικοί χρόνοι των αντίστοιχων βημάτων, ώστε η συνολική παραμόρφωση να παραμένει κατ΄ αρχήν ίδια. Τα τελικά αποτελέσματα της εν λόγω ανάλυσης απέδειξαν ότι τα μοντέλα με τη μικρότερη ταχύτητα είχαν τη βέλτιστη διαστασιακή ακρίβεια. Από την άλλη μεριά, τα μοντέλα με τη μεγαλύτερη ταχύτητα είχαν τη μικρότερη διαστασιακή ακρίβεια, ενώ συγκεκριμένα το μοντέλο του βήματος ομοιόμορφης μείωσης πάχους τοιχώματος με τη μεγαλύτερη ταχύτητα παρουσίασε γενικευμένα γεωμετρικά ελαττώματα (πολυγωνική διαμόρφωση).

Η διερεύνηση της επίδρασης του αριθμού των υποστηρικτικών ραούλων αποδείχθηκε πιο απαιτητική. Στα πλαίσια αυτής της μελέτης, αποφασίστηκε η χρήση τριών υποστηρικτικών ραούλων στη διάταξη, αντί για πέντε που συμμετείχαν στο αρχικό ζεύγος μοντέλων. Παρόλα αυτά, η χρήση λιγότερων υποστηρικτικών ραούλων με τις ίδιες γραμμικές ταχύτητες εργαλείων με αυτές των αρχικών μοντέλων οδήγησε στη δημιουργία γενικευμένων γεωμετρικών σφαλμάτων ήδη από το βήμα του "στραγγαλισμού". Η παρατήρηση αυτή απέδειξε την εξάρτηση του αριθμού των εργαλείων και των ταχυτήτων τους, ως έναν καθοριστικό παράγοντα για την επιτυχημένη διεξαγωγή της Αντίστροφης Έλασης Δακτυλίων. Προκειμένου να εξαχθούν περαιτέρω συμπεράσματα σχετικά με την επίδραση του αριθμού των εργαλείων, αποφασίστηκε, λοιπόν, να χρησιμοποιηθούν τα μοντέλα με τις μισές γραμμικές ταχύτητες από την προηγούμενη ανάλυση. Το μοντέλο του βήματος "στραγγαλισμού" με τα λιγότερα εργαλεία ολοκληρώθηκε με επιτυχία και έδειξε μικρότερες (κατ΄ απόλυτη τιμή) παραμορφώσεις του δακτυλίου, σε σύγκριση με το μοντέλο μισής ταχύτητας με τα πέντε υποστηρικτικά ράουλα. Αντίθετα, το μοντέλο του βήματος ομοιόμορφης μείωσης πάχους τοιχώματος δεν κατάφερε να ολοκληρωθεί λόγω της πρόωρης εμφάνισης γενικευμένων γεωμετρικών σφαλμάτων, ενισχύοντας ακόμα περισσότερο την εξάρτηση του αριθμού των εργαλείων από την ταχύτητά τους.

Τέλος, η διερεύνηση της επίδρασης της αρχικής θερμοκρασίας του δακτυλίου πραγματοποιήθηκε με την προσομοίωση των βημάτων της κατεργασίας εν ψυχρώ. Αν και τα δύο βήματα κατάφεραν να ολοκληρωθούν μέχρι το πέρας της διάρκειάς τους, κάποια σχετικά περιορισμένα γενικευμένα γεωμετρικά ελαττώματα εμφανίστηκαν στο τέλος του βήματος ομοιόμορφης μείωσης πάχους τοιχώματος. Επιπλέον, η επισκόπηση των αποτελεσμάτων της εν λόγω μελέτης έδειξε μικρότερες (κατ΄ απόλυτη τιμή) παραμορφώσεις στο μοντέλο της εν ψυχρώ κατεργασίας, με σημαντικά μικρότερα τοπικά ελαττώματα (π.χ. ελάττωμα "ουράς ψαριού") στο τεμάχιο. Συμπερασματικά, η εν ψυχρώ Αντίστροφη Έλαση Δακτυλίων μπορεί να είναι ρεαλιστικά εφαρμόσιμη, εφόσον το εύρος της διαστασιακής μείωσης ή/και η ταχύτητα των εργαλείων είναι κατάλληλα επιλεγμένα.

Μερικές χαρακτηριστικές εικόνες αποτελεσμάτων από τις αναλύσεις επιδράσεων των ανωτέρω κρίσιμων παραμέτρων στην Αντίστροφη Έλαση Δακτυλίων παρουσιάζονται στα Σχ.31 - 33:

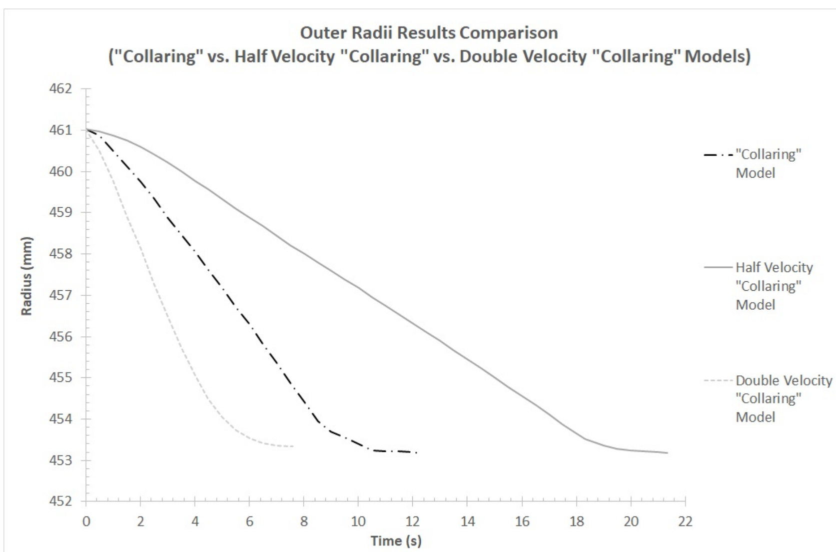

Σχήμα 31: Σύγκριση της εξέλιξης της εξωτερικής ακτίνας του δακτυλίου για διαφορετικές ταχύτητες εργαλείων (βήμα "στραγγαλισμού")

4.4. Συμπεράσματα κεφαλαίου

Από τις διεξαχθείσες αναλύσεις του παρόντος κεφαλαίου προέκυψαν τα παρακάτω συμπεράσματα:

- Οι προσομοιώσεις που διεξήχθησαν, απέδειξαν σε μεγάλο βαθμό τη βιωσιμότητα της κατεργασίας Αντίστροφης Έλασης Δακτυλίων.

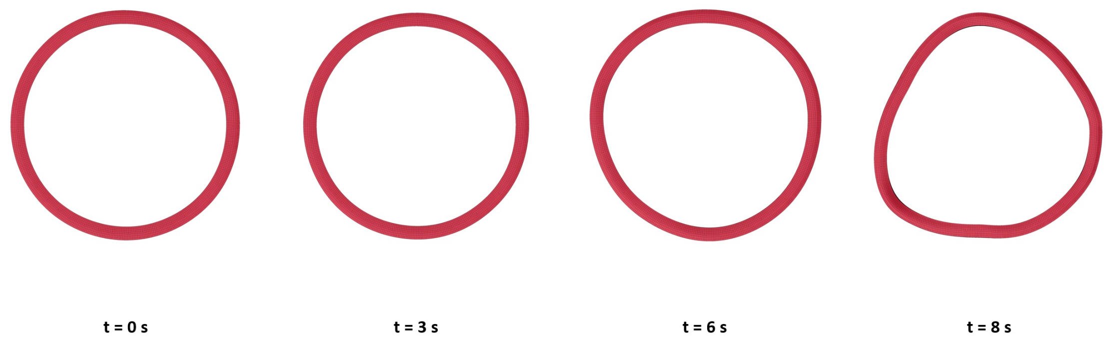

Σχήμα 32: Παραμόρφωση δακτυλίου σε πολλαπλές χρονικές στιγμές του βήματος ομοιόμορφης μείωσης πάχους τοιχώματος στο μοντέλο με τρία υποστηρικτικά ράουλα και μικρότερη ταχύτητα

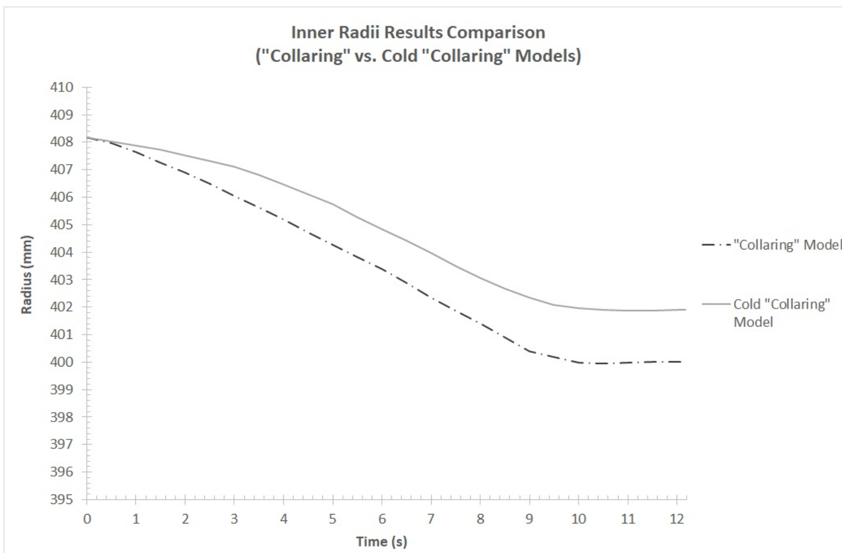

Σχήμα 33: Σύγκριση της εξέλιξης της εσωτερικής ακτίνας του δακτυλίου μεταξύ εν θερμώ και εν ψυχρώ κατεργασίας (βήμα "στραγγαλισμού")

- Αν και το μοντέλο του βήματος "στραγγαλισμού") ήταν αρκετά σταθερό στις περισσότερες περιπτώσεις, το μοντέλο του βήματος ομοιόμορφης μείωσης πάχους τοιχώματος αποδείχθηκε πιο ευαίσθητο από τις τιμές των παραμέτρων που θα επιλεγούν.

- Οι συνολικές αποκλίσεις από τις τιμές στόχου στο παράδειγμα που προσομοιώθηκε ήταν σημαντικές μικρότερες του 1%, για την περίπτωση της εσωτερικής και εξωτερικής ακτίνας του κατεργαζόμενου δακτυλίου.

- Οι όποιες διαστασιακές αποκλίσεις προκύψουν από την Αντίστροφη Έλαση Δακτυλίων μπορούν να διορθωθούν με μια απλή ρύθμιση του συνολικού χρόνου κάθε βήματος της κατεργασίας.

- Από τις κρίσιμες παραμέτρους της κατεργασίας που μελετήθηκαν, μεγαλύτερη επίδραση φάνηκε να έχει η γραμμική ταχύτητα των εργαλείων και ο αριθμός των υποστηρικτικών ραούλων.
- Κατά την ανάλυση της επίδρασης του αριθμού των ραούλων, αποδείχθηκε εξάρτηση μεταξύ της εν λόγω παραμέτρου και της γραμμικής ταχύτητας των εργαλείων, με αποτέλεσμα ένας κατάλληλος συνδυασμός των δύο να μπορεί να καταστήσει τη συγκεκριμένη κατεργασία εφικτή.
- Η Αντίστροφη Έλαση Δακτυλίων μπορεί δυνητικά να εφαρμοστεί και εν ψυχρώ, αν ο κατάλληλος συνδυασμός των υπολοίπων παραμέτρων της κατεργασίας μπορέσει να προσδιοριστεί σωστά.

5. Πολυγωνική Έλαση Δακτυλίων

Στα πλαίσια της παρούσας διατριβής πραγματοποιήθηκαν πολλαπλές προσομοιώσεις που κατέληξαν σε σφάλματα. Σε μία από αυτές, μία λανθασμένη ρύθμιση στην κινηματική των υποστηρικτικών ραούλων οδήγησε στη μορφοποίηση του δακτυλίου σε ένα τετραγωνικής γεωμετρίας τεμάχιο. Με βάση αυτό, αποφασίστηκε να μελετηθεί περαιτέρω η δυνατότητα κατεργασίας πολυγωνικών τεμαχίων μέσω μια τυπικής διάταξης έλασης δακτυλίων. Αξίζει να αναφερθεί ότι εφόσον η συγκεκριμένη μελέτη δε συνάδει με το κύριο θέμα της διατριβής που είναι η αύξηση της ακρίβειας της κατεργασίας έλασης δακτυλίων, μόνο μια πρωταρχική απόδειξη της ιδέας πραγματοποιήθηκε στο παρόν κεφάλαιο.

5.1. Βασικές αρχές της Πολυγωνικής Έλασης Δακτυλίων

Η αρχή λειτουργίας της Πολυγωνικής Έλασης Δακτυλίων βασίζεται στη συντονισμένη κίνηση των υποστηρικτικών ραούλων και του μαντρέλ. Πιο συγκεκριμένα, οι βασικές αρχές της εν λόγω προταθείσας κατεργασίας είναι οι κάτωθι:

- Το κυρίως ράουλο και το μαντρέλ είναι υπεύθυνα για τον σχηματισμό των πλευρών του πολυγώνου, με την ευθύγραμμη κίνηση του τεμαχίου να οδηγείται από τα υποστηρικτικά ράουλα.
- Κατά τη διάρκεια της κατεργασίας, διακρίνονται δύο διαφορετικές κινήσεις του τεμαχίου: (α) η ευθύγραμμη κίνησή του κατά τη διαμόρφωση μιας πλευράς και (β) η περιστροφή του τεμαχίου σε κάθε γωνία του πολυγώνου. Οι εν λόγω κινήσεις παρουσιάζονται στο Σχ.34:
- Η περιστροφή του τεμαχίου επιβάλλεται από το κυρίως ράουλο και το μαντρέλ, με την ταυτόχρονη αντίστροφη κίνηση των υποστηρικτικών ραούλων (σε σχέση με την κίνηση που εκτελούν κατά τον σχηματισμό των πλευρών).
- Η χρονική διάρκεια κάθε φάσης της κατεργασίας είναι αυστηρά καθορισμένες από τη γεωμετρία του τεμαχίου και την ταχύτητα των εργαλείων.

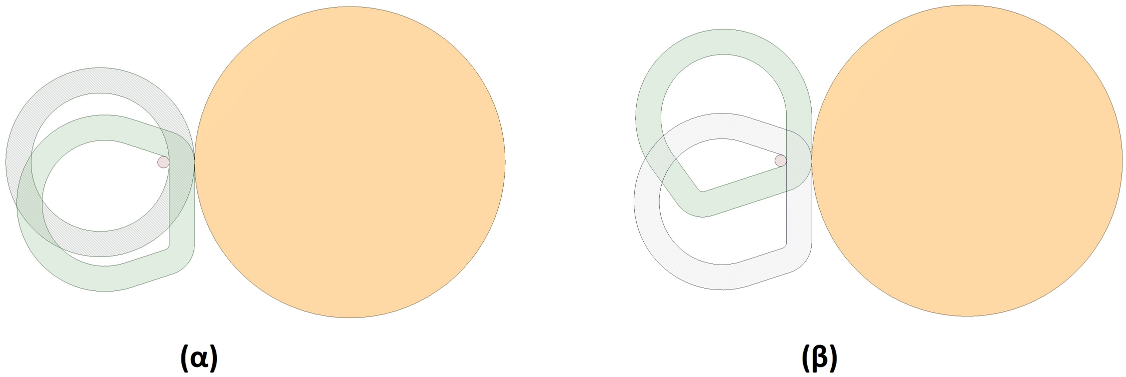

Σχήμα 34: Βασικές κινήσεις της Πολυγωνικής Έλασης Δακτυλίων: (α) Ευθύγραμμη κίνηση τεμαχίου και (β) περιστροφή του τεμαχίου

- Η αλληλουχία των προαναφερθεισών κινήσεων επαναλαμβάνεται μέχρι να ολοκληρωθεί η διαμόρφωση όλων των πλευρών του πολυγώνου.
- Οι γωνιακές ταχύτητες του κυρίως ραούλου και του μαντρέλ καθορίζονται έτσι ώστε οι αντίστοιχες περιφερειακές γραμμικές ταχύτητές τους να είναι ίσες.
- Κατά την περιστροφή του τεμαχίου, η προκαταρκτική μελέτη απέδειξε τη χρησιμότητα μιας μικρής εισχώρησης του μαντρέλ στις γωνίες του πολυγώνου.
- Δεν προτείνεται η συνεχής μείωση του πάχους των πλευρών του πολυγώνου, αφού αυξάνει σημαντικά την πολυπλοκότητα της κατεργασίας.
- Μόνο κατά τη διαμόρφωση της πρώτης πλευράς του πολυγώνου, προτείνεται να πραγματοποιηθεί αρχικά μια αντίθετη κίνηση των υποστηρικτικών ραούλων και του τεμαχίου κατά μισή πλευρά πολυγώνου, και στη συνέχεια να εκκινήσει η κατεργασία που περιγράφηκε ανωτέρω.
- Τα κωνικά ράουλα δε θα πρέπει να κινούνται γραμμικά, ώστε να μην εισάγουν ανισορροπία στην κατεργασία. Αντί αυτού μπορούν να παραμένουν σταθερά και έτσι να διορθώνουν τις τοπικές επιφανειακές ατέλειες του τεμαχίου.
- Θα πρέπει να υπάρχει πολύ καλή πρόσφυση των εργαλείων με το τεμάχιο, ώστε να μην υπάρχουν ολισθήσεις που θα οδηγούν σε γενικευμένα γεωμετρικά σφάλματα.

5.2. Προσομοίωση της Πολυγωνικής Έλασης Δακτυλίων

Για την απόδειξη της βιωσιμότητας της Πολυγωνικής Έλασης Δακτυλίων πραγματοποιήθηκε και σε αυτήν την περίπτωση μια αριθμητική διερεύνηση. Το μοντέλο του Κεφ.2, χρησιμοποιήθηκε μόνο ως βάση για τις αριθμητικές παραμέτρους, αφού τόσο οι γεωμετρίες του τεμαχίου και των εργαλείων, όσο και οι υπόλοιπες παράμετροι της κατεργασίας διέφεραν σημαντικά. Η γεωμετρία του παραγόμενου πολυγώνου επιλέχθηκε αυθαίρετα να είναι αυτή ενός πενταγώνου για τη συγκεκριμένη απόδειξη της ιδέας. Βάσει της αρχικής και της επιθυμητής γεωμετρίας του πολυγώνου και τιμών των ταχυτήτων των εργαλείων, προσδιορίστηκαν με ακρίβεια τα προφίλ της κινηματικής των εργαλείων, με ένα χαρακτηριστικό παράδειγμα να παρουσιάζεται στο Σχ.35:

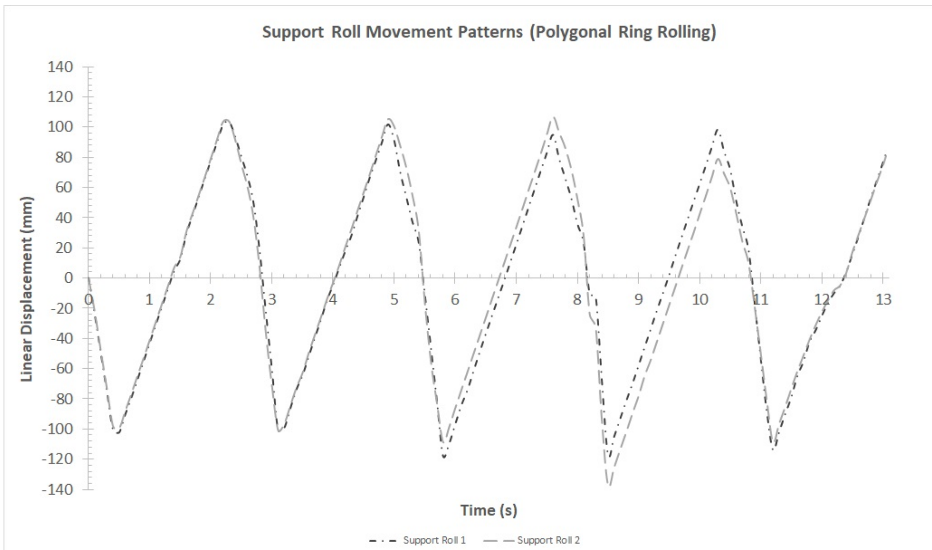

Σχήμα 35: Προφίλ ταχυτήτων των υποστηρικτικών ραούλων κατά την Πολυγωνικής Έλασης Δακτυλίων

Μετά την επίλυση του αριθμητικού μοντέλου, ακολούθησε μια ενδελεχής επισκόπηση στα αποτελέσματα αυτού. Σε γενικές γραμμές, τα αποτελέσματα της προσομοίωσης έδειξαν ότι η τελική μορφή του τεμαχίου ήταν πολύ κοντά σε αυτήν ενός κανονικού πενταγώνου, ενώ ορισμένα μικρά τοπικά ελαττώματα παρατηρήθηκαν στις γωνίες του. Η μέγιστη απόκλιση στο μήκος μιας πλευράς ήταν περίπου 8%, σε σύγκριση με τις αρχικά υπολογισμένες πλευρές του αντίστοιχου κανονικού πενταγώνου. Επίσης, τα τασικά, παραμορφωσιακά και θερμοκρασιακά πεδία είχαν την αναμενόμενη μορφή, χωρίς ιδιαίτερα σημεία αβεβαιότητας. Τέλος, αναλύθηκαν και τα αποτελέσματα φορτίων των εργαλείων, χωρίς όμως να υπάρχει κάποιο μέτρο σύγκρισης για αυτά. Ορισμένα από τα προαναφερθέντα αριθμητικά αποτελέσματα παρουσιάζονται στα Σχ.36 - 38:

5.3. Συμπεράσματα κεφαλαίου

Από τη διεκπεραιωθείσα αριθμητική ανάλυση της Πολυγωνικής Έλασης Δακτυλίων, εξήχθησαν τα κάτωθι συμπεράσματα:

- Η επιτυχής μοντελοποίηση οδήγησε στο συμπέρασμα ότι η Πολυγωνική Έλαση Δακτυλίων αποτελεί μια ρεαλιστικά υλοποιήσιμη κατεργασία.
- Η όλη διαδικασία μπορεί να πραγματοποιηθεί αμέσως μετά το πέρας μιας τυπικής έλασης δακτυλίων, όπου το τελικό πάχος του δακτυλίου θα έχει επιτευχθεί.

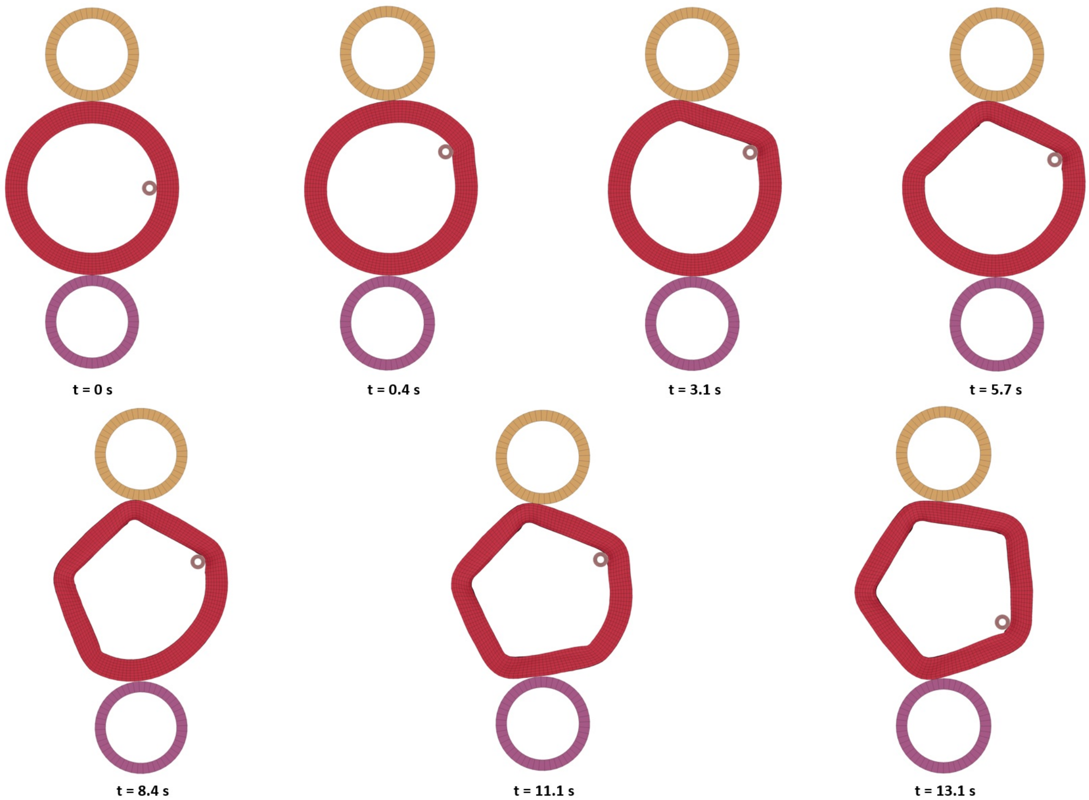

Σχήμα 36: Διαμόρφωση του τεμαχίου σε διάφορες χρονικές στιγμές της Πολυγωνικής Έλασης Δακτυλίων

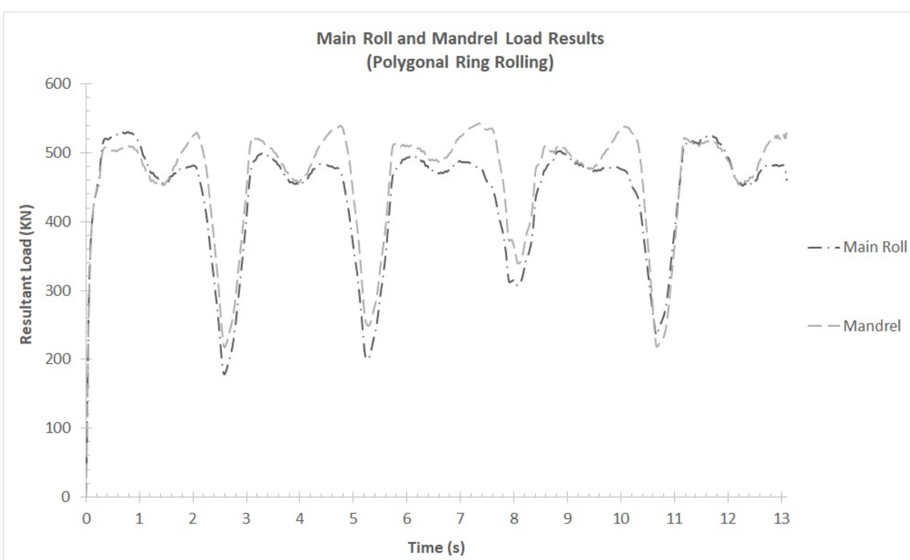

Σχήμα 37: Κύρια φορτία διαμόρφωσης κατά την Πολυγωνική Έλαση Δακτυλίων

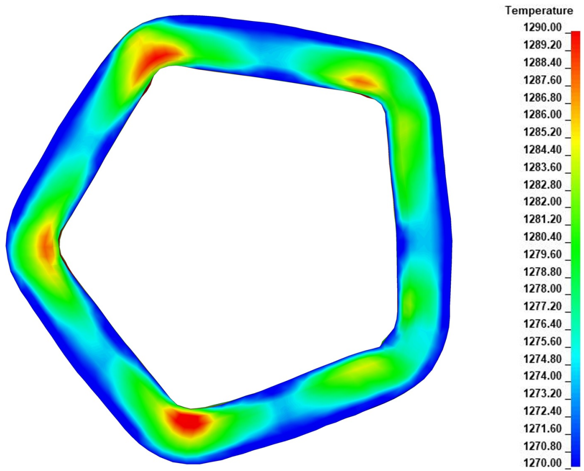

Σχήμα 38: Τελική κατανομή θερμοκρασιών στο τεμάχιο της κατεργασίας Πολυγωνικής Έλασης Δακτυλίων

- Η μέγιστη απόκλιση από τις θεωρητικά υπολογισμένες τιμές ήταν περίπου 8%, το οποίο μπορεί να θεωρηθεί αποδεκτό για μια κατεργασία ημι-τελικών προϊόντων.
- Τα τασικά, παραμορφωσιακά και θερμοκρασιακά πεδία που υπολογίστηκαν από το αριθμητικό μοντέλο, βοήθησαν στο να εξηγηθεί ο μηχανισμός διαμόρφωσης της κατεργασίας.
- Αν και διαπιστώθηκε η επίδραση ορισμένων παραμέτρων στα αποτελέσματα της εν λόγω κατεργασίας (π.χ. το μέγεθος των εργαλείων), εντούτοις προτείνεται η διεξαγωγή μιας πιο ενδελεχούς μελέτης πάνω σε αυτές.

6. Γενικά Συμπεράσματα και Συζήτηση

Τα γενικά συμπεράσματα της παρούσας διατριβής μπορούν να συνοψισθούν στα παρακάτω:

- Η παρούσα μελέτη μπορούσε να πραγματοποιηθεί μόνο μέσω αριθμητικής προσομοίωσης όλων των διερευνώμενων μεθόδων, αφού δεν υπήρχε ο απαραίτητος εξοπλισμός για να διεξαχθεί πειραματικά.
- Η ανάπτυξη ενός πλήρως πιστοποιημένου αριθμητικού μοντέλου της κατεργασίας, το οποίο προσομοίωνε την πλειονότητα των φυσικών φαινομένων που διέπουν την κατεργασία, πραγματοποιήθηκε με το εμπορικό λογισμικό ανάλυσης πεπερασμένων στοιχείων ANSYS/LS-DYNA.
- Ο προσδιορισμός των βέλτιστων αριθμητικών και φυσικών ιδιοτήτων για την προσομοίωση έγινε μέσα από εκτενή βιβλιογραφική έρευνα και πολλαπλούς κύκλους αριθμητικών δοκιμών.

- Οι αριθμητικές και φυσικές ιδιότητες που προσδιορίστηκαν και πιστοποιήθηκαν, αποτέλεσαν τη βάση για όλες τις περαιτέρω προσομοιώσεις που πραγματοποιήθηκαν στα πλαίσια της παρούσας διατριβής.
- Οι πιο κρίσιμες παράμετροι και οι μεθοδολογίες που μπορούν να επηρεάσουν τη διαστασιακή ακρίβεια των προϊόντων της έλασης δακτυλίων χωρίστηκαν σε αυτές που πραγματοποιούνται πριν και κατά τη διάρκεια της κατεργασίας και σε άλλες που μπορούν να πραγματοποιηθούν αμέσως μετά από αυτήν, εν είδει "διορθωτικών" ενεργειών.
- Η μελέτη των παραμέτρων και μεθοδολογιών που πραγματοποιούνται πριν και κατά τη διάρκεια της κατεργασίας πρόκρινε: (α) τον ακριβή όγκο του αρχικού εργοτεμαχίου, (β) τις θερμο-ελαστικές παραμορφώσεις των εργαλείων και (γ) την κινηματική των υποστηρικτικών ραούλων, συναρτήσει του υλικού του τεμαχίου, ως τις πιο κρίσιμες για περαιτέρω μελέτη και βελτιστοποίηση.
- Η επίδραση των ανωτέρω παραμέτρων αξιολογήθηκε ποιοτικά και ποσοτικά, μέσω εκτεταμένων κύκλων προσομοιώσεων, ενώ παράλληλα προτάθηκαν μεθοδολογίες που λάμβαναν υπόψιν και μπορούσαν να βελτιστοποιήσουν τις εν λόγω παραμέτρους προς όφελος της διαστασιακής ακρίβειας των τελικών προϊόντων.
- Σχετικά με τις "διορθωτικές" ενέργειες μετά την κατεργασία, προτάθηκε η νεωτεριστική κατεργασία της Αντίστροφης Έλασης Δακτυλίων.
- Το βασικό πλεονέκτημα της Αντίστροφης Έλασης Δακτυλίων είναι ότι μπορεί να πραγματοποιηθεί σε συνέχεια της κατεργασίας έλασης δακτυλίων με την ίδια διάταξη, και χωρίς να απαιτείται επανατοποθέτηση και αρχικοποίηση της θέσης του τεμαχίου.
- Η βιωσιμότητα της Αντίστροφης Έλασης Δακτυλίων αποδείχθηκε αριθμητικά, ενώ μελετήθηκε ακόμα και η επίδραση κάποιον κρίσιμων παραμέτρων στην κατεργασία αυτή.
- Τέλος, προσεγγίστηκε μια νέα μέθοδος για την παραγωγή πολυγωνικών προϊόντων, χωρίς ραφή, μέσω μια τυπικής διάταξης έλασης δακτυλίων.
- Η βιωσιμότητα και αυτής της μεθόδου αποδείχθηκε αριθμητικά, αν και δεν πραγματοποιήθηκε ανάλυση σε μεγαλύτερο βάθος όλων των κρίσιμων παραμέτρων, αφού η συγκεκριμένη μελέτη απέκλινε από το κύριο θέμα της παρούσας διατριβής.

7. Περαιτέρω Έρευνα

Ως βήματα για περαιτέρω έρευνα, βάσει των αποφθεγμάτων της παρούσας διδακτορικής διατριβής, ο συγγραφέας προτείνει τα παρακάτω:

- Οι μελέτες της παρούσας διατριβής πραγματοποιήθηκαν αριθμητικά, ελλείψει του απαραίτητου πειραματικού εξοπλισμού. Μια πειραματική πιστοποίηση των προτεινόμενων μεθοδολογιών θα επιβεβαίωνε περαιτέρω τα αποτελέσματα των εκπονηθέντων αναλύσεων.

- Επίσης, τυχόν παράγοντες αβεβαιότητας των πραγματικών εφαρμογών θα μπορούσαν να χρησιμοποιηθούν για την περαιτέρω βελτιστοποίηση των εν λόγω μεθοδολογιών.
- Ορισμένες φυσικές παράμετροι που προσδιορίστηκαν μέσω κύκλων δοκιμής-και-σφάλματος, θα μπορούσαν να μετρηθούν και να επιβεβαιωθούν κατά τη διάρκεια μιας αντίστοιχης πειραματικής δοκιμής.
- Το βασικό μοντέλο έλασης δακτυλίων αναπτύχθηκε για δακτύλιο από IN718. Η ίδια μεθοδολογία προσομοίωσης θα μπορούσε πιθανώς να πιστοποιηθεί περαιτέρω και για άλλα υλικά δακτυλίων, σε αντιπαραβολή με τα αντίστοιχα πειράματα.
- Η συμπερίληψη φαινομένων απώλειας υλικού κατά την προετοιμασία του εργοτεμαχίου της έλασης δακτυλίων (π.χ. λόγω του φαινομένων φολίδωσης), θα μπορούσε να βελτιστοποιήσει περαιτέρω την προταθείσα μεθοδολογία υπολογισμού του αρχικού όγκου της μπιγέτας.
- Η επίδραση των θερμο-ελαστικών παραμορφώσεων των εργαλείων μπορούν να διερευνηθούν και σε άλλες κατεργασίες υψηλής ακρίβειας.
- Αν και διαπιστώθηκε/επιβεβαιώθηκε η σύνδεση μεταξύ του ρυθμού ανάπτυξης του δακτυλίου κατά την έλαση δακτυλίων και του υλικού αυτού, η διερεύνηση και για άλλα υλικά θα μπορούσε να οδηγήσει στην ανάπτυξη μιας πιο γενικευμένης σχέσης για τη συσχέτιση των δύο.
- Αν και οι πιο κρίσιμες παράμετροι της Αντίστροφης Έλασης Δακτυλίων διερευνήθηκαν σε μεγάλο βαθμό, υπάρχει περιθώριο για περαιτέρω έρευνα σε αυτήν τη νεωτεριστική κατεργασία.
- Η Πολυγωνική Έλαση Δακτυλίων με βάση την προταθείσα μεθοδολογία αναλύθηκε σχετικά επιφανειακά και σαν απόδειξη της ιδέας μόνο. Υπάρχουν αρκετές παράμετροι που αφορούν την εν λόγω κατεργασία, οι οποίες μπορούν να διερευνηθούν περαιτέρω.
- Οι προταθείσες μεθοδολογίες αναλύθηκαν ξεχωριστά στα πλαίσια της παρούσας διατριβής. Ο συνδυασμός όλων αυτών των μεθοδολογιών σε μια κοινή παραγωγική γραμμή, θα μπορούσε να οδηγήσει σε περαιτέρω βελτιστοποίησή τους.

8. Δημοσιεύσεις που Προέκυψαν από τη Διατριβή

Από την παρούσα διατριβή, προέκυψαν οι παρακάτω τρεις δημοσιεύσεις σε peer-reviewed περιοδικά:

- Gavalas, E., I. S. Pressas, and S. Papaefthymiou (July 2018). “Mesh Sensitivity analysis on implicit and explicit method for rolling simulation”. In: *International Journal of Structural Integrity* 9 (4), pp. 465–474. DOI: 10.1108/IJSI-07-2017-0046.

- Pressas, I. S., S. Papaefthymiou, and D. E. Manolakos (2022). "Evaluation of the roll elastic deformation and thermal expansion effects on the dimensional precision of flat ring rolling products: A numerical investigation". In: *Simulation Modelling Practice and Theory* 117, p. 102499. DOI: 10.1016/j.simpat.2022.102499.

- Pressas, I. S., S. Papaefthymiou, and D. E. Manolakos (2024). "On the Fundamentals of Reverse Ring Rolling: A Numerical Proof of Concept". In: *Materials* 17 (9), p. 2055. DOI: 10.3390/ma17092055.

Αναφορές

Acar, D. et al. (2018). "Warm Hydromechanical Deep Drawing of AA 5754-O and Optimization of Process Parameters". In: *Journal of Engineering Materials and Technology* 140.1, p. 011012.

Arthington, M. R. et al. (2015). "Measurement and Control of Variable Geometry During Ring Rolling". In: *2015 IEEE Conference on Control Applications (CCA)*, pp. 1448–1454.

Deshpande, A. A. et al. (2011). "Combined butt joint welding and post weld heat treatment simulation using SYSWELD and ABAQUS". In: *Proceedings of the Institution of Mechanical Engineers, Part L: Journal of Materials: Design and Applications* 225 (L1), pp. 1–10.

Greene, G. A., C. C. Finfrock, and T. F. Jr. Irvine (1999). *Dependence of Total Hemispherical Emissivity of Inconel-718 on Surface Oxidation and Temperature*. Brookhaven National Laboratory, Department of Advanced Technology, p. 17.

Hadi, M.M., M.M.H. Al-Khafaji, and A.D. Subhi (2022). "A Numerical Study of Friction Stir Welding for AA5754 Sheets to Evaluate Temperature Profile and Plastic Strain". In: *Engineering and Technology Journal* 40.12, pp. 1683–1694.

Hawkyard, J. B., E. Appleton,and W. Johnson (1973). "An Experimental Wide Ring Rolling Mill of Novel Design". In: *Proceedings of the Thirteenth International Machine Tool Design and Research Conference*. Ed. by S. A. Tobias and F. Koenigsberger. Palgrave, London, pp. 547–553. ISBN: 978-1-349-01857-4.

Iturbe, A. et al. (2017). "Mechanical characterization and modelling of Inconel 718 material behavior for machining process assessment". In: *Materials Science and Engineering: A* 756, pp. 441–453.

Keenan, J. H., J. Chao, and J. Kaye (1983). *Gas tables: International version second edition (SI units)*. John Wiley and Sons, New York.

Li, X., L. Guo, and F. Wang (2021). "On a plastic instability criterion for ultra-large radial-axial ring rolling process with four guide rolls". In: *Chinese Journal of Aeronautics* 35 (6), pp. 391–406.

Oh, S. and H. Ki (2019). “Deep learning model for predicting hardness distribution in laser heat treatment of AISI H13 tool steel”. In: *Applied Thermal Engineering* 153, pp. 583–595.

Patil, S., F. Baratzadeh, and H. Lankarani (2017). “Preliminary Study on Modeling of the Deformation and Thermal Behavior of FSSW using SPH Approach”. In: 11th European LS-DYNA Conference 2017 (Salzburg, Austria).

Parvizi, A. and K. Abrinia (2014). “A Two Dimensional Upper Bound Analysis of the Ring Rolling Process with Experimental and FEM Verifications”. In: *International Journal of Mechanical Sciences* 79, pp. 176–181.

Pressas, I. S., S. Papaefthymiou and D. E. Manolakos (2024). "On the Fundamentals of Reverse Ring Rolling: A Numerical Proof of Concept". In: *Materials* 17 (9), p. 2055. DOI: 10.3390/ma17092055.

Schuler, GmbH, ed. (1998). *Metal Forming Handbook*. Springer-Verlag Berlin Heidelberg, p. 27. ISBN: 978-3-642-63763-6.

Stanistreet, T. F., J. M. Allwood, and A. M. Willoughby (2006). “The design of a flexible model ring rolling machine”. In: *Journal of Materials Processing Technology* 177, pp. 630– 633.

Szabo, Z. J. and E. Dittrich (1996). “Manufacturing systems for the production of seamless-rolled rings”. In: *Journal of Materials Processing Technology* 60, pp. 67–72.

Tolcha, M. A. and H. G. Lemu (2019). “Modeling Thermomechanical Stress with H13 Tool Steel Material Response for Rolling Die under Hot Milling”. In: *Metals* 9 (5), p. 495.

Touloukian, Y. S., P. E. Liley, and S. C. Saxena (Jan. 1970). “Thermophysical properties of matter - the TPRC data series. Volume 3. Thermal conductivity - nonmetallic liquids and gases. (Reannouncement). Data book”.

Uchibori, T., R. Matsumoto, and H. Utsunomiya (2018). “Peripheral Speed of Steel Ring during Hot Ring Rolling”. In: *Procedia Manufacturing* 15. Proceedings of the 17th International Conference on Metal Forming METAL FORMING 2018 September 16 – 19, 2018, Loisir Hotel Toyohashi, Toyohashi, Japan, pp. 89–96.

Wang, M. et al. (2009). “Analysis of Coupled Mechanical and Thermal Behaviors in Hot Rolling of Large Rings of Titanium Alloy Using 3D Dynamic Explicit FEM”. In: *Journal of Materials Processing Technology* 209, pp. 3384–3395.

Wu, Q. et al. (2019). “Analysis and homogenization of residual stress in aerospace ring rolling process of 219 aluminum alloy using thermal stress relief method”. In: *International Journal of Mechanical Sciences* 157–158, pp. 111–118.

Xu, S. G., J. C. Lian, and J. B. Hawkyard (1991). “Simulation of Ring Rolling Using a Rigid- Plastic Finite Element Model”. In: *International Journal of Mechanical Sciences* 33 (5), pp. 393–401.

Xu, W. et al. (2014). “Quantitative Design Methodology for Flat Ring Rolling Process”. In: *Procedia Engineering* 81, pp. 280–285.

Xu, W. et al. (2015). “Feeding Interval Design Considering Multiconstraints in Flat Ring Rolling Process”. In: *International Journal of Advanced Manufacturing Technology* 81 (1–4), pp. 219–229.

Yun, J. S. and H. S. Cho (1985). “A Suboptimal Design Approach to the Ring Diameter Control for Ring Rolling Processes”. In: *Journal of Dynamic Systems, Measurement, and Control* 107, pp. 207–212.

Zhao, Y. and D. Qian (2010). “Effect of Rolling Ratio on Groove-Section Profile Ring Rolling”. In: *Journal of Mechanical Science and Technology* 24 (8), pp. 1679–1687.

Zhu, X. et al. (2016). “Optimization on Cooperative Feed Strategy for Radial-Axial Ring Rolling Process of Inco718 Alloy by RSM and FEM”. In: *Chinese Journal of Aeronautics* 29 (3), pp. 831–842.